Université Pierre et Marie Curie

Géosciences, Ressources Naturelles et Environnement

Institut des Sciences de la Terre de Paris

Mountain building at a subduction-collision transition zone, Taiwan

Insights from morphostructural analysis and thermochronological dating

Par Lucas Mesalles

Thèse de doctorat de Sciences de la Terre

Dirigée par Frédéric Mouthereau et Chung-Pai Chang

Présentée et soutenue publiquement le XX septembre 2014

Devant un jury composé de :

Peter van der Beek (Professeur), rapporteur.

Stéphane Bonnet (Professeur), rapporteur.

Olivier Lacombe (Professeur), examinateur.

Jacques Malavieille (Directeur de recherche CNRS), examinateur.

Matthias Bernet (Maître de conférences), examinateur.

Chung-Pai Chang (Professeur), co-directeur de thèse.

Frédéric Mouthereau (Maître de conférences), directeur de thèse.

Except where otherwise noted, this work is licensed under
http://creativecommons.org/licenses/by-nc-nd/3.0/

Résumé :
La croissance des chaînes de montagnes actives est contrôlée par les processus tectoniques qui interagissent avec les processus de surface dépendant du climat. Apporter des contraintes sur le développement de ces chaînes est clef pour comprendre les processus qui contrôlent la formation des paysages de la surface de la Terre. Cette étude se concentre sur la chaîne de Taiwan, un prisme orogénique emblématique où la tectonique, très active, est associée à de l'érosion très rapide pour former un des paysages les plus dynamiques sur la Terre. J'ai plus particulièrement focalisé mon travail sur le Sud de la Chaîne Centrale de Taiwan, situé à la transition entre la subduction et la collision arc-continent. Trois approches différentes ont été associées dans le but d'apporter une comprehension, la plus complète possible, des mécanismes de construction orogénique, et son évolution depuis le début de la collision jusqu'au développement du paysage actuel.
L'étude de terrain apporte l'information générale sur la géologie de surface et l'évolution long-terme du prisme orogénique. La thermochronologie basse-température apporte des contraintes sur le calendrier du refroidissement et l'exhumation, et son évolution temporelle. Finalement, l'analyse géomorphologique permet d'étudier des processus contrôlant le développement du paysage actuel.
La déformation du Sud de l'île est caractérisée par deux domaines distincts structuralement : une unité à vergence Ouest définie autour des plus hauts sommets, et une unité à vergence Est observée dans les vallées de l'Est. Ces deux unités montrent une schistosité pénétrative associée à de grands plis qui soulignent ensemble un éventail. Les unités sont bordées par de grandes zones de cisaillement inclinées vers l'Ouest qui indiquent une phase d'extension tardive réactivant des décrochements senestres plus anciens. Une dernière unité structurale est observée plus à l'Est qui est caractérisée par une schistosité horizontale, associée à un grand pli couché. J'interprète le Sud de l'île comme une chaîne à double-vergence caractérisée par une déformation tardive généralement transtensive.
Le résultat des datations par traces de fission sur zircon le long d'un profil vertical contraint l'âge du début de collision et l'histoire d'exhumation en relation avec la transition depuis la collision d'une marge hyper-amincie vers la collision de la marge proximale de la Mer de Chine du Sud. Ces données révèlent un début de refroidissement à 7.2 Ma un taux minimum de 21°C/Ma, suivi d'une accélération de l'exhumation d'un ordre de grandeur après 3.2 Ma et d'une augmentation du gradient géothermique de ~41°C/km à 65°C/km. Cette dernière phase est interprétée comme la phase majeure de croissance orogénique lorsque la marge proximale a été impliquée dans la collision. Les traces de fission sur zircon et apatite détritiques des sédiments syn-orogéniques Plio-Pléistocène de l'avant-pays occidental suggèrent l'exhumation de la couverture à l'Ouest de la chaîne. L'ensemble des âges obtenus confirme une phase à ~3.2 Ma qui a conduit à exhumer la partie Est de la chaîne lors de l'extrusion du cœur métamorphique.
L'analyse géomorphologique au Sud de la Chaîne Centrale révèle l'existence de zones à faible relief à hautes altitudes, à l'aplomb de la ligne de partage des eaux actuelle et du cœur métamorphique. Ces régions sont caractérisées par la présence de lacs de forme ovoïde, de sols latéritiques, et de faibles taux d'érosion. Des considérations morphologiques et climatiques indiquent une origine probablement glaciaire pour ces surfaces qui sont préservées depuis au moin 50 ka (fin du *Marine Isotope Stage 4*), comme le suggèrent les données climatiques qui montrent que ce refroidissement a été le plus important du dernier cycle glaciaire. La coïncidence spatiale entre les surfaces de faibles reliefs, la position du cœur métamorphique et l'empreinte glaciaire remarquable observée dans quelques bassins de l'Est suggère le rôle potentiel des glaciations lors de l'exhumation récente du cœur de la chaîne, et confirment potentiellement un forçage climatique des orogènes aux basses latitudes.

Abstract:

The growth of active mountain belts is driven bydeep tectonic processes, interacting with climate-dependent surface processes. Providing constraints on their development is key to understanding the controlling processes shaping the Earth's surface.

The present study focuses on Taiwan mountain belt, an archetypical orogenic wedge where very active tectonics is combined with an efficient eroding system to build one of the most dynamic landscapes on Earth. I focus on the southern Taiwan Central Range, located at the transition between subduction and arc-continent collision. Three approaches were combined to provide a complete picture on how a young mountain belt builds up, and evolved since the early collisional stage to the more recent morphological development of the orogen.

Fieldwork provides the general constraint on surface geology and on long-term evolution of the orogenic wedge. Low-temperature thermochronology constrains the timing of cooling and exhumation, and its evolution through time. And finally, morphological analysis brings to light the major processes controlling the present-day landscape development.

Deformation in the southern Central Range presents two major and distinct structural domains: a west-verging structural unit roughly limited to the western divide, and an east-verging unit, covering most of the eastern divide. Both units present a pervasive schistosity associated with large-scale folding that delineates a fan-shaped pattern. The structural units are limited by a steeply west-dipping shear zones displaying a dominant late stage normal faulting and an early strike-slip faulting stage. An additional structural unit is found in the east characterized by a flat-lying schistosity probably related to recumbent folding of unknown vergence. Overall, southern Taiwan displays a bivergent structure marked by orogen-parallel transtensive deformation zones.

The results of zircon fission track (FT) dating along a vertically sampled profile provide constraints on the onset of collision and exhumational history that reflect transition from collision of hyper-extended distal margin to collision of thick proximal South China Sea margins. These data reveal onset of cooling at 7.2 Ma at a minimum rate of 21°C/m.y., followed by an order of magnitude acceleration of exhumation after ca. 3.2 Ma and increase of geothermal gradients from ~41°C/km to 65°C/km. This phase is interpreted as a major stage of topographic growth and erosion, and is probably related to the involvement of normal thickness passive margin crust in the collision. Additionally, detrital zircon and apatite FT derived from Plio-Pleistocene sediments from the southwestern foreland basin display the erosion of the western divide cover rocks with ages similar to the early phase seen in the hinterland. Combined with existing FT data of the eastern divide, our data indicates that the ~3.2 Ma phase seen in the vertical profile, exhumes preferably the eastern divide rocks, and probably marks the onset of the metamorphic core eastward extrusion.

Geomorphic analysis of the southern Central Range reveals the existence of low relief at high altitudes, located along the drainage divide and on top of the metamorphic core. These areas are characterized by the common presence of oval shaped lakes, lateritic soils and very slow erosion rates. Morphological and climatic considerations indicate the likely glacial origin of these surfaces that are preserved since maybe at elast 50 kyr (end of Marine Isotope Stage 4), when the climatic record indicates the strongest atmospheric cooling of the last glacial cycle. The spatial coincidence of the southern low-relief surfaces with the exposure of the metamorphic core and the marked glacial imprint of some of eastern basins, suggest a potential role of glaciations in the recent exhumation of the metamorphic core in Taiwan, and probably in other orogens, and potentially confirm a Late Cenozoic climatic forcing on orogens at all latitudes.

摘要：
造山帶的地表變形是由深部構造和表面侵蝕相互作用所控制，要了解地表形貌的變化過程，深部構造和表面侵蝕速率因此成為首要研究課題。
近期台灣造山帶的研究中，一般認為活躍的構造活動加上快速的侵蝕速率是造成台灣現有地形景觀的主要原因。本研究區域位於台灣中央山脈南段，為隱沒作用至弧陸碰撞的過渡帶。本研究結合野外調查、定年分析及地形分析三種方法，以 完整了解台灣山脈的構造演化以及地形發育過程。
地表的地質調□結果能提供造山帶在長時間尺度下的演化過程資訊。配合低溫定年分析，可得知岩石冷卻和快速抬升發生的時間，以及其隨著時間的變化過程。最後，地形分析可幫助了解現今地形的主要控制因素。
中央山脈南段的變形可分為兩個主要且截然不同的構造單元，一為向西發育的構造單元，大致分布於分水嶺的西側，另一為向東發育的構造單元，主要位於分水嶺的東翼。在兩構造單元中都具有大尺度的褶皺構造並伴隨著扇狀分布的片理，各單元以陡峭向西傾斜的剪切帶為界，剪切帶的運動模式包括最後一期的正斷層和早期的走向滑移斷層。除上述兩個主要的構造單元外，另有一具平緩的褶皺並伴隨著水平片理的構造單元沿山脈的最東緣分布。整體而言，台灣南段展示了橫跨擠壓造山帶的兩個相反方向發育的構造單元。
垂直的岩石樣本剖面可以提供重建碰撞到抬升過程的資訊。鋯石核飛跡定年的結果顯示，從南中國海邊緣開始碰撞時(約從7.2百萬年前開始)，此區域以約21°C/my的速率開始冷卻。約在3.2百萬年前，伴隨著巨大的加速抬升事件，地溫梯度約從41°C/km增加至65°C/km。此現象可解釋為地形成長和侵蝕作用發生的主要階段，可能和碰撞時期被動大陸邊緣正常的增厚現象相關。此外，台灣西南部前陸盆地的上新世-更新世時期的□石岩屑及磷灰石的核飛跡定年分析資料顯示，在分水嶺西翼表層岩石的侵蝕年齡和內陸十分相似。結合分水嶺東側的核飛跡資料，顯示在3.2百萬年前，抬升主要發生在分水嶺東側的岩石，這也是台灣東部的變質岩開始出露的階段。
中央山脈南段的地形分析顯示在高海拔地區的地勢起伏較緩，包括流域盆地的分水嶺地區和變質岩區的頂部。這些區域的地形特徵一般為橢圓形的湖泊及風化的紅土，反映非常低的侵蝕速率。此區域 5 萬年前可能開始進入冰河時期，氣候紀錄亦指出在末代冰期階段此區有很強的大氣冷卻效應。在空間上，由於此區之地形起伏較緩，以及在東部盆地中留有冰川的痕跡，都暗指冰河作用在在台灣的變質岩出露過程扮演很重要的角色，在世界其他造山帶亦可能如此。此現象也間接證實高緯度地區在晚新生代氣候條件的推動下，有較發達的造山運動。

A los de la isla y de la península, a los de la galia y de la sinica.

Acknowledgments

I am grateful for the patience and encouragement of Frédéric Mouthereau and Chung-Pai Chang, who supervised this work throughout from the beginning. Wen-Rong Chi and Andrew T.-S. Lin introduced me to Taiwan stratigraphy and sedimentology, and were of great help in my understanding of Taiwanese geology, I thank them both. I thank Matthias Bernet and Elisabeth Hardwick for their help and availability during thermochronological analysis in Grenoble. Thanks to Finlay Stuart and Luigia Di Nicola for the welcome and help in the helium laboratory in SUERC (Glasgow, UK). Thanks to Tzen-Fu Yui (Academia Sinica) for providing access to his mineral separation lab to process some of the samples used in this research. Thanks to Sean Willett for discussion of the data and modelling results and for providing his code for thermal modelling before final publication. Thanks to Pietro Sternai for providing his code for hypsokyrtome computing and for the help during processing and interpretation.

During this past years I have had inspiring discussions which improved my understanding on Taiwan geology and helped building up what is presented in this piece of writing: Tim Byrne (U. of Connecticut), Kamil Ustayenky (U. of Basel), Bruce Shyu (National Taiwan University), Yu-Chang Chan (Academia Sinica), Jian-Cheng Lee (Academia Sinica), John Suppe (National Taiwan University), Francis Wu (U. of Binghamton), Cornelia Spiegel (U. of Bremen), Matthias Bernet (U. Joseph Fourier), Louis Teng (National Taiwan University), Geoffrey Batt (U. of Western Australia), Jiun-Yee Yen (National Dong Hwa University), Mariline Lebéon (Academia Sinica), Laetitia Mezzonati (Academia Sinica), Owen Chen (National Central University), Hao Kuo-Chen (National Central University), Lionel Siame (U. Aix-Marseille), Luis Teng (National Taiwan University), Arthur Chen (Tainan University), Pien-Mei Liew (National Taiwan University), Hao-Tsu Chu (Central Geological Survey), Chin-Ho Tsai (National Dong Hwa University), Xavier Robert (U. Joseph Fourier), Thibault Simon-Labric (U. Joseph Fourier) and Kerry Gallagher (U. Rennes). Corrections and comments from P. van der Beek of an earlier version of this manuscript substantially improved the present work. I should thank the fundamental help of Academia Sinica's Earth Science Institute librarians April Chen and her assistant, for their availability and efficiency during the mining of Taiwanese publications related to this research.

I am indebted to the professors and mentors I have had during my first steps as an undergraduate and graduate student for encouraging me to continue towards a PhD and for stimulating and feeding my curiosity. I am particularly thankful to: Jocelyn Barbarand, Yves Missenard, Maurice Pagel, Hermann Zeyen, Cécile Gautheron, Julien Gargani, Bertrand Saint-Bézar, Pierre Vergely, Denis Sorel, Antonio Benedicto, Beate Orberger, Jean Bébien, Giuseppe Siani and Cécile Quentin. My thanks go to Geoffrey Batt who consolidated my knowledge and self-confidence needed to pursue the PhD during my year as a master exchange student in Royal Holloway-University of London.

I am also grateful to GRSL (National Central University) students and non-geologist friends for their help during sampling in sometimes rough conditions: Xiao-Xiong, Xiao-Ba, Zhi-Hua, Suavek, Remigio, Siegfried, Xavier, Brusco, Iván, Yu-Yi, Sasha & Katerina, Konstantin and Uli. I should thank Yi-An Chen and Ting-Hsuen (GRSL) for assisting with translation and Chia-Chen and the entire GRSL lab for the welcome and help with the tough administrative procedures. I should

thank the ISTeP laboratory in Paris for their help and support during the last stretch of the manuscript writing, especially to Alexandre, Arnaud, Leila, Manfred, Yamar and Mme. Tristiani.

I would not have finished this work if it wasn't for all the support brought by my friends in Taiwan, Grenoble and Paris: Sławek & Olympia, Remy & Irene, Cécile & Xavier, Alma Itana, Diego, Memo, Carol, Oscar, Joselin, Oliver, Ramses, Luis, Kaivin, Uli, Fugu, Marco, Brusco, Miguel, Navcha, Berni, Matteo, Mansoureh, George (dorm), George (chemistry), Yan, Jan, Rakesh, Krishna, Ashish, Vathan, Yu-yi, Ina, Leon, Leo, Silver, Claire, Piero, Ema, Fabri, Nando, Rachel, Jakub and Martin.

I would not have survived without the funding-feeding-hosting provided sometimes by institutions but mainly by friends and family: LIA (Taiwan –France plane tickets trips), Taiwan International Graduate Program (TIGP, for the 1st year monthly stipend), GRSL-NCU (field trips), ISTeP (last two months funding), Luisa, Marisa, Víctor, Gracia, Laura, Sławek-Olimpia-Helena Gyletisz, Gérome (Gé), Luis and Ramses (La Caja de Música), Pero Kovk, Amélie & Mathieu, Carol Avila, Navcha Nergui, Wu family (Taimali), JinShan family (Tawu), Jonathan, Stanko, and Charlotte & Frédéric.

Last but not the least, this would not have come to good end without my parents (Luisa and Víctor), grandmother (Marisa) and Laura, always here to support me.

Table of contents

INTRODUCTION **15**
I. Conceptual background *15*
II. Mountains belts: a privileged natural laboratory *18*
III. Controlling factors in mountain building: state of the art *20*
A. Tectonic forcing on mountain building 20
1) First-order control on collisional crustal shortening: plate convergence and inherited pre-collisional properties 20
2) Mountain building processes 24
B. Late Cenozoic climate change and theoretical orogenic response 36
1) Sedimentation rates increase in the late Cenozoic 36
2) Climatic forcing of an orogens and Late Cenozoic climatic change 39
IV. Statement of the general topic *41*

Chapter 1: The Taiwan mountain belt **45**
I. Geodynamic setting *45*
A. The South China Sea margin and Philippine Sea plate in the geodynamic framework of SE Asia 45
1) The South China Sea margin and the Himalayan collision 47
2) The South China Sea margin and the geodynamics of the proto-SCS 48
3) The Philippine Sea plate motion 52
B. Margins in the South-China Sea and inversion tectonics 53
II. Geology of Taiwan *58*
A. Present-day kinematics and main active faults 58
B. Geological provinces 61
C. Exhumation and metamorphic history 68
1) Pre-Cenozoic metamorphism and deformation recorded in the Tananao metamorphic complex 68
2) Cenozoic metamorphism 72
D. Models of mountain building 73
1) Thermo-kinematic models with dominant subduction of the Chinese margin crust 75
2) A thermo-mechanical model with dominant accretion of the Chinese margin crust 76

Chapter 2: Structure of the southern Taiwan Central Range **79**
I. Southern Taiwan: bridging the gap between oceanic subduction and arc collision *79*
II. Active tectonics and long-term deformation of the southern Central Range *82*
A. Seismological and geodetic observations in the Central Range: implications for crustal thickening 82
B. Geology and deformation of the Central Range: a review 86
1) Major contacts: Crustal-scale faults and reactivated sedimentary contacts 86
2) Existing structural studies of the Central Range 90
III. Structure and geology of the Taimali-Taiwu area, southern Central Range *93*
A. General geology and structural units southern Central Range 95
B. Lithostratigraphic and structural units along the Taimali-Taiwu transect 97
1) Lithostratigraphy and depositional age constrains 97
2) Characterisation of the main structural units and bounding faults 105
IV. Cross-section, relative chronology of deformation and discussion *112*
V. Conclusive remarks *115*

Chapter 3: Thermochronological constraints from southern Taiwan 117
I. General thermochronological principles 117
A. Closure temperature and partial annealing zone 119
B. Tectonics and topographic effects on thermochronological age 120
II. Thermochronology in Taiwan 121
A. *Insitu* thermochronology in the Central Range mountains 121
B. Detrital thermochronology of the syn-orogenic sediments 131
C. Exhumation of the western fold-and-thrust belt 134
III. Adopted approach 135
A. Sampling strategy in southern Taiwan 135
1) Eastern Central Range: vertical profile and horizontal transect along the retro-wedge 137
2) Plio-Pleistocene foreland sediments: record of a recent tectonic-erosive phase 138
3) Western Central Range: pro-wedge exhumation and source rocks of the western foreland sediments. 143
B. Analytical methods 146
IV. Results 148
A. Age-elevation profile in the Taimali valley 148
1) ZFT ages and age-elevation relationship 148
2) Thermal modelling of the vertical profile 154
B. Horizontal iso-altitude profile in the Taimali valley 157
C. Fission-track detrital record from Plio-Pleistocene foreland sediments 159
D. Laonung fault samples 165
V. Discussion and implications 171
A. Young-peak age approach 171
B. The thermal record of a two-phased collision in the Taiwan mountain belt 177
1) From underwater continental crust underthrusting to arc-continent collision 177
2) Relationship between mélange formations and the two-phased collisional events. 195
C. Constraints on the timing of tectonic events of the Central Range 197
1) General considerations 197
2) Southern Taiwan deformation 199
VI. Conclusions 201

Chapter 4: Morphological elements of southern Taiwan 203
I. Erosion in the Taiwan orogeny: questioning steady-state in Taiwan 205
A. Climate and sediment discharge in Taiwan 205
B. Recent erosion rates: Suspended sediment load and Holocene incision rates in Southern Taiwan 207
II. Morphometry and landscape development 209
A. Low relief areas as evidenced by relief and slopes maps 210
1) Methods 210
2) General morphology of southern Taiwan 211
3) Results 213
4) Discussion: potential glacial imprint on low-relief areas 227
B. Hypsometry and hypsokyrtome: markers of glaciated landscape 232
1) Method and validation 234
2) Results 238
III. Conclusions 243

GENERAL CONCLUSIONS 245

Bibliography 248

ANNEXES 292
Annex 1: Old geological map of southern Taiwan 293
Geologic map of Taiwan: Daibuzan sheet (Usami & Matsumoto, 1940) 293
Geological map along the South Link Railroad *(Hu and Tsan, 1984)* 295

Annex 2: Summary of deformation phases from the main existing studies *296*
Annex 3: Hypsometry of Taiwan's geological provinces. *300*
Annex 4: Thermochronological raw data *301*
Zircon fission track 301
Apatite fission track 330

INTRODUCTION

This chapter presents the motivation, background and a short review on the state of the art of my PhD research project. It aims to give the reader an overview of the purpose and pertinence of the following chapters.

I. Conceptual background

The landscape is the critical interface between two interacting systems: an internal tectonic system, and an external climate-governed system [e.g. *Allen*, 2005]. Landscape is the platform from which live raised, human evolved and scientist observe. Apprehending the governing forces shaping landscape, not only has numerous immediate applications, from disaster mitigation and engineering to natural resources and ecology, but is the key element for solving some of the outstanding challenges humankind is facing in the 21st century.
The traditional view of landscape, resulting from the passive consumption of tectonically created topography (e.g. seminal work of Davis 1899, considered by many as the birth of geomorphology as a science) is now known too simplistic, as multiple interactions and feedbacks are involved in the process (Fig. 1). Indeed, because the rates at which each of the earth science subsystems operates are similar [e.g. *Bonnet and Crave*, 2003; *Whipple and Meade*, 2006], complex coupling is likely to occur [e.g. *Roe*, 2009; *von Elverfeldt*, 2012].

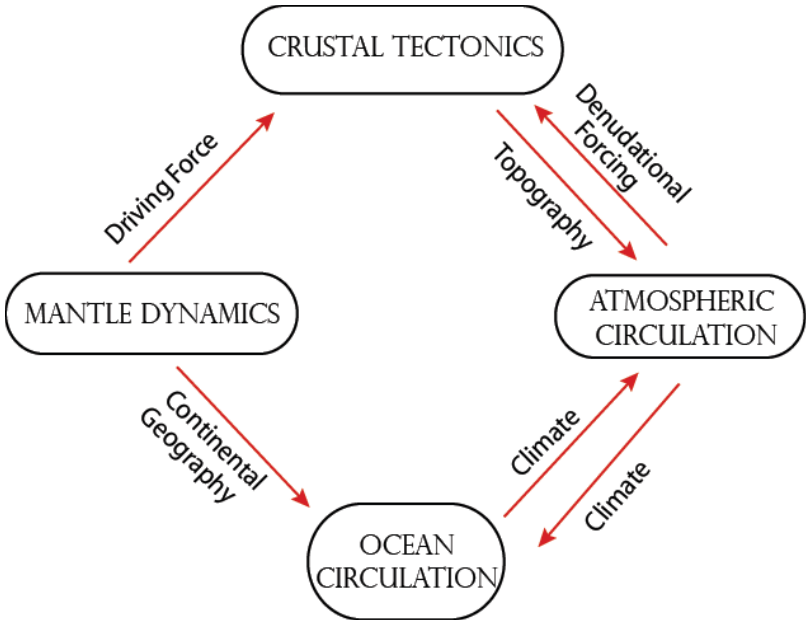

Fig. 1: *Synthetic earth science system's interactions and feedbacks for the development of macro-scale landforms (modified from Beaumont et al., 2000).*

The understanding of these feedbacks and interactions starts from the understanding of the processes behind it. This was stated by *Leighly* [1940] as follows:

"Davis's great mistake was the assumption that we know the processes involved in the development of land forms. We don't; and until we do we shall be ignorant of the general course of their development."

While empirical *laws* have greatly improved the way we understand the earth science system and are the base of most of present-day knowledge, current research tends to focus on the extraction of process-based theories. Indeed the understanding of the process behind a given observation or statistical relation is fundamental for predictions in the dynamic earth system, and more fundamentally, allows to quantify the degree of dependency and response times to perturbations within each sub-system and between the sub-systems themselves [*Allen*, 2008b]. Critical for establishing process-based theories is empirical *data*. Rates, precise timings constraints, and absolute quantification are fundamental measurable quantities upon which the theoretical consideration should be based on [e.g. *Allen*, 2008a].

Quantification of tectonic and erosive processes is presently possible through numerical tools for landscape analysis, absolute dating of relief development, erosion and tectonic processes, and numerical modelling of erosion and tectonics (see Table 1).

Method	**Time-scale**	**Space-Scale**	**Outcome**
Sediment discharge of rivers	Modern	Drainage basin scale	Erosion
Evaluation of old and recent sedimentary record *(i.e. stratigraphy and recent sea-floor sediments, respectively)* through modern geophysical technics *(e.g. seismic reflection, sonar)*	Modern *(10's yrs)* to geological *(i.e. 10^5-10^6 yrs)*	Regional	Sedimentation
Ocean, fresh-water and speleotheme isotopic ratios in modern deposits and in the stratigraphic record *(e.g. $^{16/18}O$, $^{87/86}Sr$, $^{10/9}Be$)*	Modern to geological	Local, regional and global scale erosion	Global scale erosion
Geodetic data, digital elevation models *, interferometry	Modern	Local, regional and global	Erosion and tectonics
Low-temperature thermochronology *	Holocene *(i.e. 10^4 yrs)* to geological timescale *(i.e. 10^5 - 10^6 yrs)*	Local and regional	Erosion and cooling
Cosmogenic dating			

Numerical modelling	Virtually any time-scale, but mostly at *(10^3 -10^4 yrs)*	Virtually any scale, but mostly local *(i.e. drainage basin scale)* or regional scale	Interaction between erosion and tectonics

Table 1: *Methods to estimate erosion and tectonics at different time and space scales. Note that distinguishing the erosive and tectonic signals is not an obvious task, and it is in many cases we measure a mixed signal. Asterisk (*) indicates the methods used in this study, although existing data based on other techniques is compiled from other studies.*

In general terms, the framework of the present PhD thesis follows the general research tendency aiming to quantitatively constrain the main forces shaping the landscape. The focus is putted on the tectonic and climatic/erosive processes, the main controlling players in the development reshaping the earth surface (Fig. 1). Tectonism controls the geographical distribution of topographic lows, caused by subsidence and accommodating eroded sediment input (Fig. 2), and highs such as mountain ranges (Fig. 5), the expression of exhumation and uplift. Climate controls the rates at which erosion happens and assures the transport of sediments towards the topographic lows (Fig.2 and Fig.3).

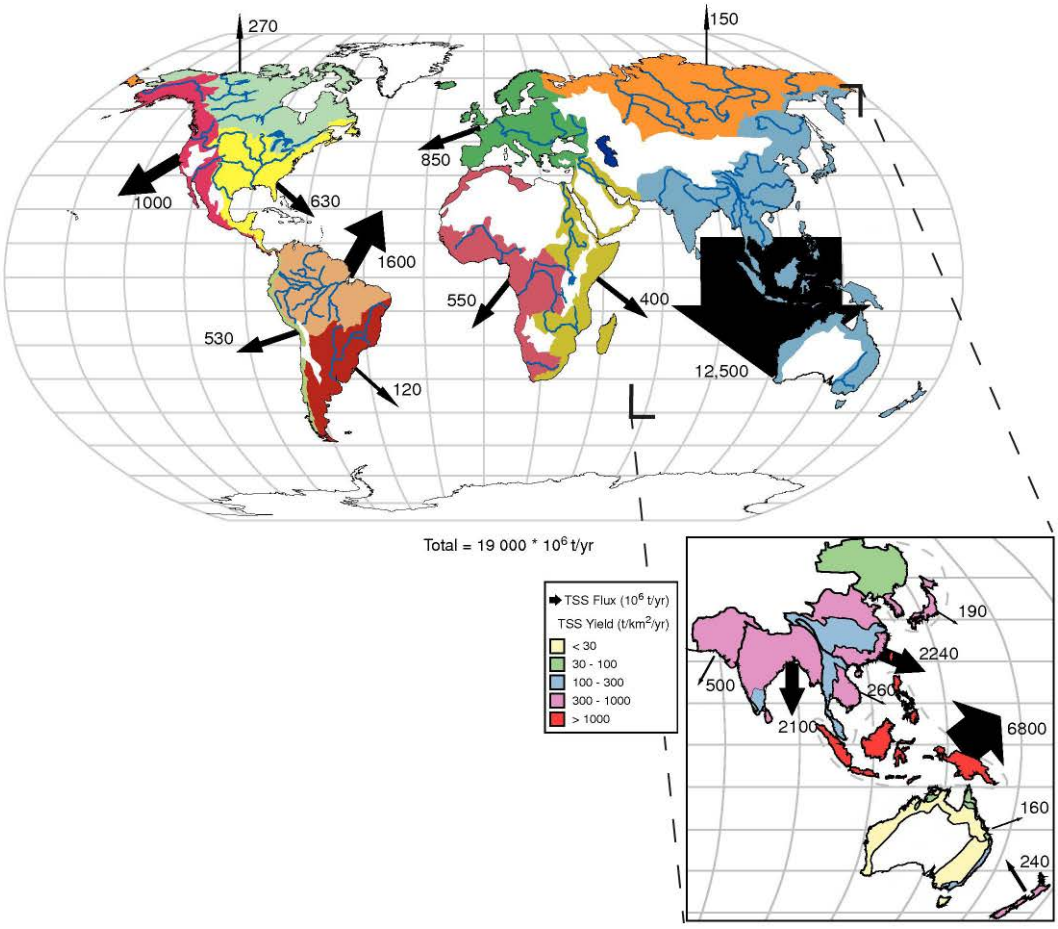

Fig. 2: *Annual discharge of fluvial sediment delivered to the ocean in tonnes/year. Controlled by topographic factors and climate. Sediment discharge can be taken as a proxy*

for tectonic divergence/convergence rates modulated by climate, as seen by the dramatic difference between sediment delivery coming from passive (low delivery) and active (high delivery) margins (cf. Fig. 3). Note the outstanding contribution of Southeast Asian and Oceania rivers, discharging ~66% of the total sediment output to the oceans (upper panel), ~50% of which is delivered by the southeast Asian islands (inset). Modified from [*Milliman and Farnsworth*, 2011].

II. Mountains belts: a privileged natural laboratory

The study of tectonically active mountainous landscape is particularly adapted to assess the tectonic-climatic interplay. There are two main reasons justifying this choice.

First, active mountainous landscapes are areas of high erosion rates, accounting for most of the world's sediment flux to the ocean (Fig. 2 and 3). Wet (runnof >750mm/yr) mountaineous (topography>1000m) landscapes may account for as much as ~60% and ~40% of the cumulative global suspended and dissolved sediments, respectively, delivered to the oceans, while representing only ~14% of the drained area (fig. 3 top panel; *Milliman and Syvitski*, 1992; *Milliman and Farnsworth*, 2011). Similarly, Southeast Asian islands alone may account for almost ½ of the global sediment delivery to the oceans (Fig. 2, inset).

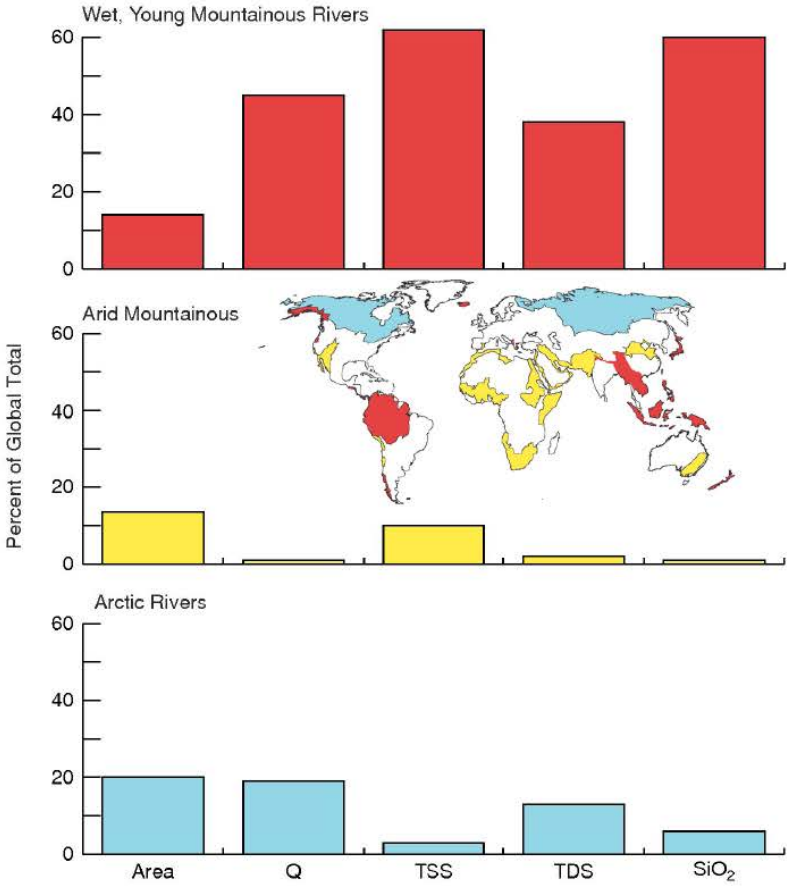

Fig. 3: *Global percentage of cumulative drainage basin area, discharge (Q), suspended-sediment (TSS), dissolved solid (TDS), dissolved silica (SiO_2) from wet young mountains*

(high altitude terrains _>1000m_ with high precipitation and runnoff _ >750mm/yr, and active tectonism; in red), arid mountains (high altitude with low precipitation and runoff _ <300mm/yr; in yellow) and arctic rivers (in blue). TSS is taken as a proxy of mechanical weathering, while TDS and SiO2 are function of chemical weathering. Areas considered are shown in the world map with the same colour coding. Altogether theses areas drain ~44% but greatly contribute to the global suspended and dissolved sediment delivery to the ocean. Modified from (Milliman and Farnsworth, 2011).

Secondly, active orogenic settings show high rates of convergence and deformation, concentrating most of high magnitude earthquakes (Fig. 4). Plate convergence in active margins is accommodated through subduction, shortening of the upper plate and/or through shortening of the plunging plate, the latter mainly occurring when continental crust starts being involved (i.e. collision). Shortening leads to crustal thickening which, through isostatic compensation, eventually generates subaerial topography, exposing the deforming rocks to erosive processes.

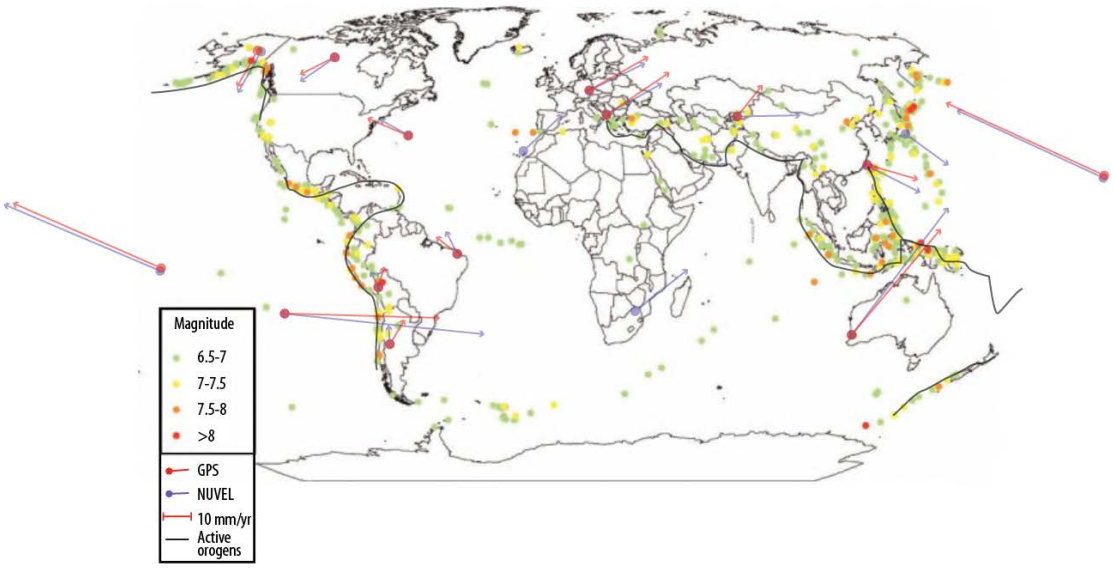

Fig. 4: *World map with major earthquakes (magnitude >6.5, 1950-2000, data from the USGS data base; from Milliman & Farnsworth, 2010), selected tectonic plate motion vectors (NUVEL model and measured GPS; from Frisch et al., 2011) and orogenic plate boundaries. Note how active margins, accommodating plate's differential motion, and particularly young active mountain belts concentrate seismicity.*

Because active orogens concentrate crustal deformation and erosion and because those two processes happen at similar rates, a certain number of distinguishing feedbacks are likely to occur (Fig. 5). It is worth mentioning that among the potential climatic effects on orogen development, the growth of glaciers in high-altitude areas after the instauration of glacial/interglacial periods in the late Cenozoic had possibly a major effect on orogen development [e.g. *Herman et al.*, 2013].

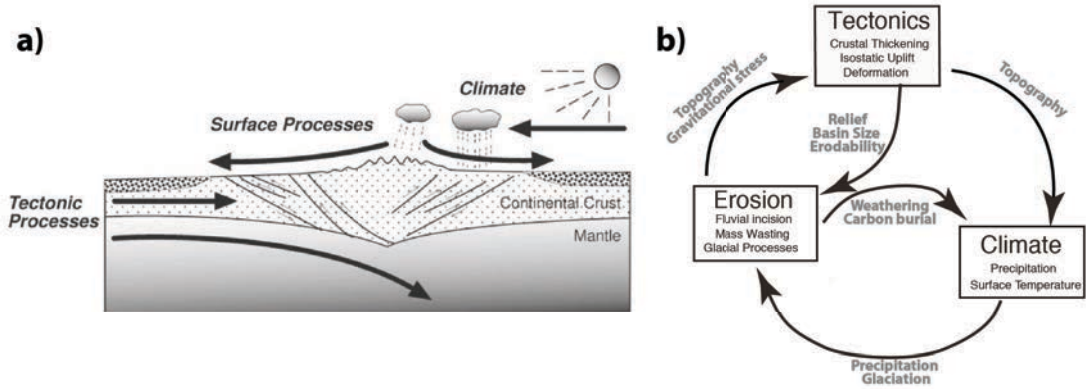

Fig. 5: *The orogenic system interactions and feedbacks. a) Cartoon showing the three main subsystems controlling orogen morphology and tectonic development (from Roe et al., 2008). b) Feedbacks and interactions acting in an orogen (modified from Willett et al., 2006).*

III. Controlling factors in mountain building: state of the art

The following is a short review on the current understanding of the main features controlling the evolution of mountain belts. The section is subdivided into the tectonic and climatic/erosive factors, the main controlling processes on the development of mountain belts.

A. Tectonic forcing on mountain building

In this work, we concentrate on convergent plate boundaries, which host the major collisional orogens (Fig.4). Contractional mountain ranges involving collision can implicate two continents (e.g. Himalaya, European Alps), a continent and an oceanic plateau (e.g. Southern Alps of New Zealand) or a continent and an island arc (e.g. Papua New Guinea, Timor Banda-arc, Taiwan, and Kamchatka). Orogens can also form at subduction zones in retro-arc position (e.g. American Cordilleras, Andes), where coupling at the plate interphase transmits the stress beyond the subduction zone to the overriding plate inducing shortening. Similar processes are at play in intraplate contractional mountain ranges (e.g. Tian-Shan, Atlas mountains, Pyrenees belt) where, as in the subduction related mountain building, a far stress field is transmitted from the plate boundary to the inner plate domain.

1) First-order control on collisional crustal shortening: plate convergence and inherited pre-collisional properties

The main controls on the anatomy and mechanism of collisional orogens are:

- The geodynamic setting, in particular convergence rates and plate motion direction (i.e. oblique or orthogonal to place boundary or suture zone) driven by deep mantle processes (Fig. 4 and Fig. 5).

- The pre-collisional histories, particularly the inherited rheology of the affected lithospheres. Additionally, because collision, in most cases, involves continental passive margins, the inherited faults, passive margin sedimentary architecture are also of primary importance (Fig. 6).

The reason why the continental drift theory of A. Wegener [*Wegener*, 1912] was not consensual until the second half of the XXth century, despite consistent evidences (e.g. coastline match, geological and faunal continuity across shorelines, paleo-climatic consideration) lies in the lack of plausible mechanism driving plate motion (A. Wegener invoked earth's rotation derived forces as a possible mechanism). It is now generally accepted that the lithospheric plates are mechanically coupled so that mantellic convection is the main mechanism orchestrating plate motion and indirectly controlling the main forces acting on tectonic plates (i.e. oceanic ridge push and subducting slab pull).

While it is easy to conceive the relation between the ascending and descending limbs of the mantle's convection cells with the oceanic spreading and subduction zones, on may wonder what happen when the oceanic domain is totally consumed so that the attached continental crust meets its conjugate margin or a volcanic arc, that is, when collision starts. Deep processes are able to sustain large plate convergence rates after collision onset. Even small-scale convection currents originating between the base of the lithosphere and 400 km, may be dominant in the mobility of small crustal fragments as proposed for the Mediterranean region [*Faccenna and Becker*, 2010].

However, while deep mantle processes provide an essential component of the necessary forces driving plates, orogenic belts are built by crustal shortening, implying a mechanical decoupling between crust and mantle. The rheology of the continental lithosphere involved during collision is therefore central to understand mountain building processes. In particular the rheology of passive margin (Fig. 6), as collision involve at least one passive margin.

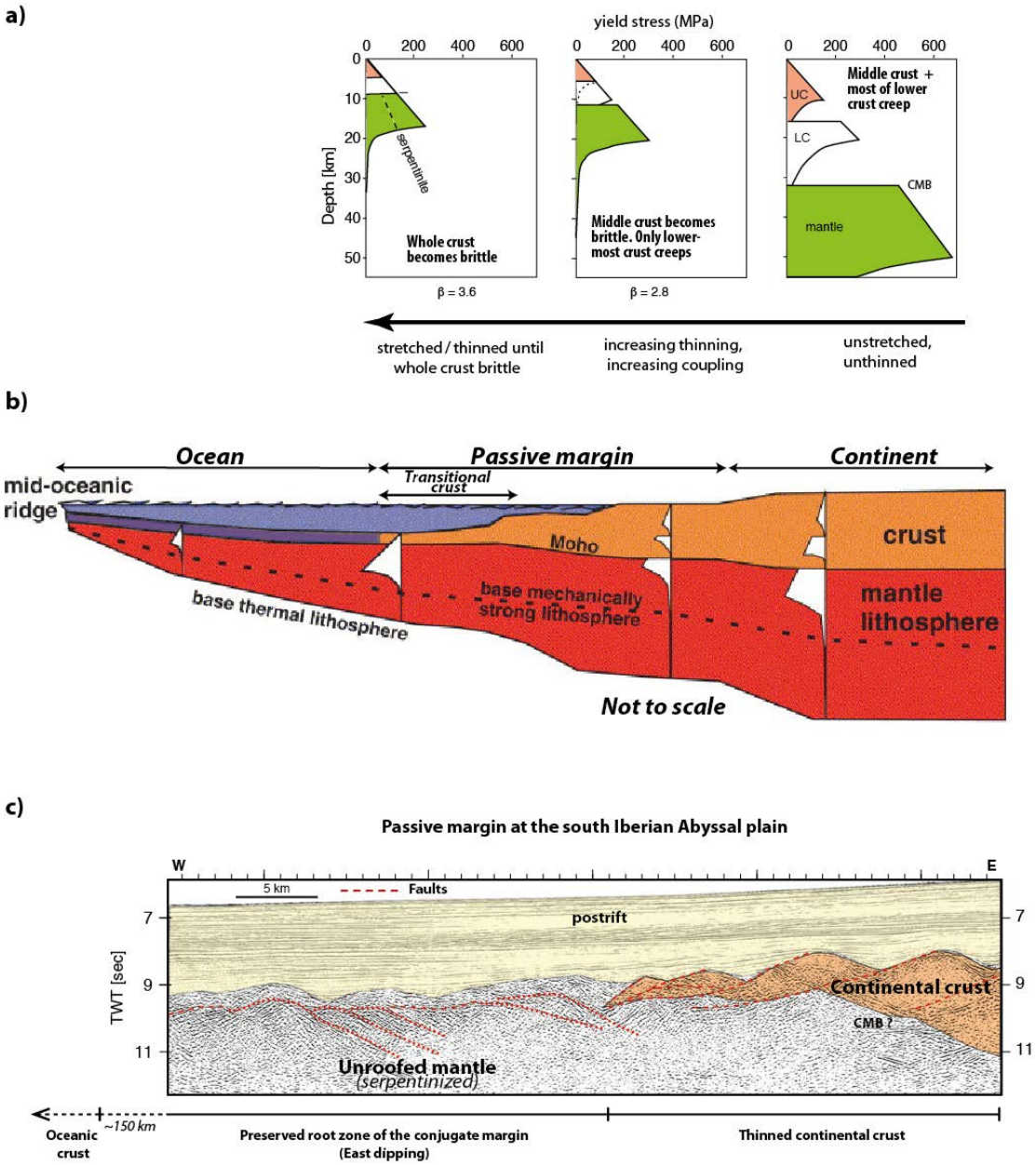

Fig. 6*: Rheological variation along section in a passive margin. a) Continental lithosphere rheology (yield stress vs. depth) evolution with increasing pure shear stretching (i.e. increasing β factor). Modified from* [*Reston and Manatchal*, 2011]*. b) Schematic cross-section of the continent-ocean boundary, displaying variation in thickness and typical brittle-ductile strength variations. Modified form* [*Cloetingh et al.*, 2005]*. c) Seismic reflection line showing extremely thinned transitional continental crust in the south Iberian passive margin with exhumed mantle right below the post-rift sediments. Modified from* [Reston and Manatchal*, 2011*]*. Note how the whole crust becomes brittle with increasing extension, eventually leading to surface exposure and serpentinisation of the lithospheric mantle.*

A first control on the rheological structure of the crust is the inherited architecture of passive margins (Fig. 6a and Fig. 6b). Passive margins are key players in the collisional processes as the their arrival to the subduction zone mark the beginning of collision. The transition between continental and oceanic crust is materialised by a wide band (Fig.6; up to 200km, *Reston and Manatchal*,

2011) of progressively thinner continental crust, from normal thickness continental crust (~30km) down to extremely thinned crust (~5km) with occasional locally exhumed mantle (Fig. 6c). Differential stretching of the lithosphere modifies its rheological properties (Fig. 6a and Fig.6b) that will subsequently control the deformation style during collision (coupling or decoupling at mid-crustal levels?; thick or thin skinned deformation?; Fig. 8a).
It is now well established that the relation between long-term strength of continents, which can be assimilated to the effective elastic thickness (Te) (Fig. 7) reflects variations in the strength of the lithospheric mantle [Fig.7; *Burov and Watts*, 2006]. Elastic thickness can thus be used as a proxy assessing the coupling between the lithospheric mantle and the overlying crust, and thus can help assessing the stability of subduction and deformation style [Fig.8a; *Mouthereau et al.*, 2013].

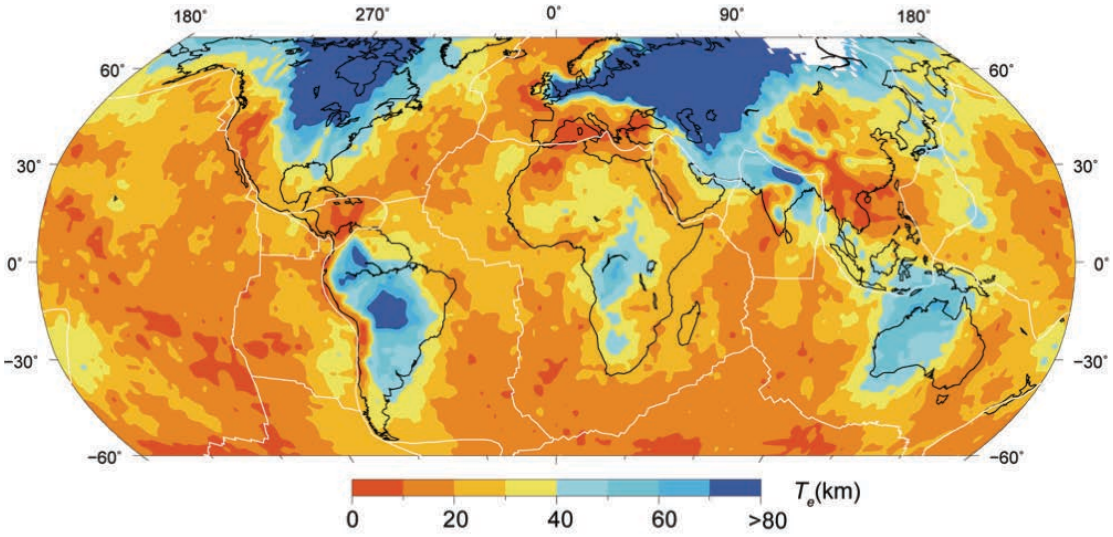

Fig. 7*: Global eleastic thickness (Te) structure of the lithosphere (2° × 2) reflecting the rheological properties of lithosphere. The rheology of the lithosphere, particularly in collided or present-day passive margins control the way deformation of the continental lithosphere occurs. After Mouthereau et al. (2013).*

It has recently been suggested that the age-dependent properties of the passive-margin lithosphere are key to explain variations in the accommodation of continental deformation in external orogens; two distinct groups have been distinguished (Fig. 8b): the first comprises localized (subduction-style) and simple-shear deformation; and the second comprises distributed (collision-style) and pure-shear deformation [Fig, 8b; *Mouthereau et al.*, 2013].
The first group (Fig. 8b) is characterized by high crustal strain (up to 70%) with deformation localized above a shallow-dipping detachment in the weak sedimentary cover. This is observed for old cratonized lithosphere (>1 Gyr; Fig.7). In such cold lithosphere, the subducted lower crust is coupled with the mantle. The latter group (Fig. 8b) is characterized by reduced crustal strain (<40%), revealing that deformation is distributed between brittle crustal thrust ramps in the upper brittle crust and the ductile middle-lower crust. This appears to be more commonly observed in thrust belts built on Phanerozoic lithosphere (Fig. 7).

These differences are interpreted to illustrate the dependence of the lower crust and mantle strength on lithosphere thermal-age (i.e. age of the last thermal event). One main implication is that in external domains, where syn-collisional burial is limited, transient deformation and dynamic weakening processes in the lithosphere do not significantly alter the effect of the pre-collisional rheological layering. Thus, for instance, shortening of young lithosphere is characterized by basement-involved deformation, which reflects decoupling at the brittle-ductile transition or in the viscous lower crust [Fig. 6a and Fig. 6b; *Mouthereau et al., 2013*].

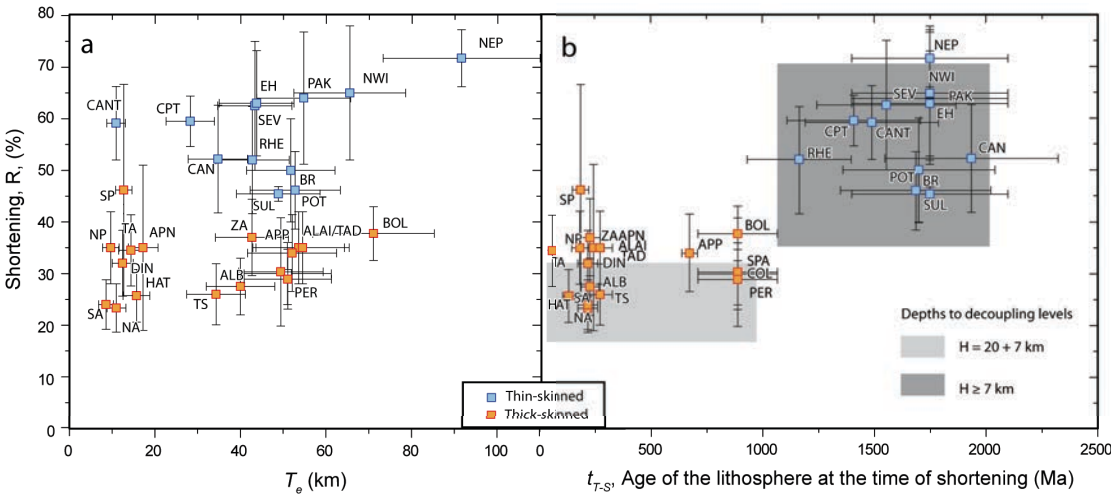

Fig. 8: *Empirical relationships between lithosphere properties, style of deformation and shortening. a) Shortening from wordwide orogens vs. elastic thickness (Te) estimates. b) Shortening vs. age of foreland lithosphere.* Shortening extracted from balanced cross-sections. t_{TS} *is the thermal age (i.e. time since last thermal event) of foreland lithosphere at the time of shortening. Note how in a) thick and thin skinned belts comprises a wide range of Te values although, the overall tendency shows increasing Te with increasing shortening rates. Note how in b) lower shortening rates in thick-skinned belts is associated with a relatively younger (~Phanerozoic) thermal age, while high-shortening rates of thick-skinned belts is associated with an older (~Proterozoic) thermal age. Abbreviations: ALAI, Alai Ranges; ALB, Alborz; APN, Apennines; APP, Appalachians; BOL, Sub-Andean Bolivian thrust belt; BR, Brooks Ranges; CAN, Canadian Rockies; CANT, Cantabrian Mountains; COL, Sub-Andean Colombian trust belt; CPT, Carpathians; DIN, Dinarides; EH, Eastern Himalayas thrust belt; HAT, High Atlas; NA, Northern Alps; NEP, Nepalese thrust belt; NP, Northern Pyrenees; NWI, North-western Himalaya; PAK, Pakistan Himalayan thrust belt; PER, Peruvian thrust belt; POT, Potwar Plateau; RHE, Rheno-hercynian thrust belt; SA, Southern Alps; SEV, Sevier thrust belt; SP, Southern Pyrenees; SPA, Sierras Pampeanas; SUL, Sulaiman Range; TA, Taiwan; TAD, Tadjik thrust belt; TS, Tien-Shan; ZA, Zagros. After [Mouthereau et al., 2013].*

2) Mountain building processes

a) Brittle accretionary wedges

The strength of the continental crust is understood to be a combination of pressure-dependent brittle strength of the upper crust and the viscous,

temperature-dependent and strain-rate dependent strength of the lower continental crust [*Burov and Watts*, 2006; *Ranalli and Murphy*, 1987; fig. 9].

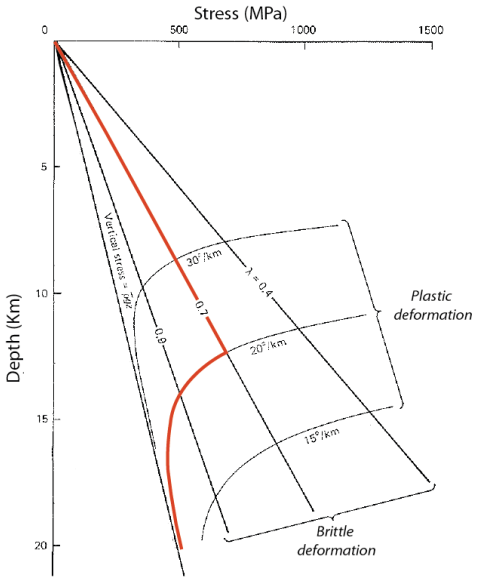

Fig. 9*: Idealized strength profile of the crust with different pore fluid pressure ratios (λ,) and geotherms. Maximum horizontal stress (x axis) based on laboratory measurements for a Quartz rich crust. The intersection of the linear brittle curves and plastic, or ductile, curves marks the boundary between the upper and lower crust. λ is 0 for dry rocks and 1 when the fluid pressure is equal to the overburden stress. The red line show the strength profile for a crust with a pore-fluid pressure of 0.7 and a geothermal gradient of 20°C/km. Modified from Suppe (1984).*

Using geometric considerations initially applied to oceanic accretionary wedges, wedge-shaped collisional mountain belts have been described by the theory of frictional critically-tapered wedges [*Suppe*, 1981; *Davis et al.*, 1983; *Dahlen*, 1984, 1990; *Dahlen et al.*, 1984]. Critical taper or critical wedge theory forms the basis of an elegant and straightforward approach to explain mountain building at convergent plate boundaries (Fig. 10). It assumes that shape of mountain belts reflect the balance between gravitational forces that arise from thickening of the brittle upper crust, and the frictional resistance to sliding on a regional detachment surface, which is the plate interface in subduction-style orogeny. This formulation allows a simple description of the distribution of deformation within the orogen, which enables prediction of the width, topography, and time-temperature paths of rock particles in tectonic/erosion coupled systems [e.g. *Brandon et al.*, 1998; *Willett et al*., 2003].

The critical wedge theory was originally applied to accretionary wedges and fold-and-thrust belts at the front of the orogen. However, later on, its application was successfully extended to the totality of the orogenic system, when limited ductile deformation existed.
Based on sand-box experiments, analytical treatment of field stresses and field observations, the model states that fold-and-thrust belts and accretionary prism belts form a wedge-shaped package of rocks that deform internally as new material is incorporated, until a critical taper (i.e. critical topographical angle) is reached. From this point, the internal strength allows the activation of basal décollement (i.e. mechanically weak layer allowing sliding), and the wedge will grow in a self-similar way (i.e. keeping invariant its cross-sectional shape, angles and geometry) (Fig. 9), such that:

$$\alpha + \beta = \mu\, b\, (1 - \sin\varphi) / (1 + \sin\varphi) = \text{Constant}$$

with α = *Topographic slope,* β = *Dip of the basal detachment,*
μb = *Coefficient of friction of the basal detachment,* and
Φ = *Angle of internal friction of material in the wedge*

From this equation we can see that the two parameters controlling the critical wedge geometry are the strength of the wedge (Φ) and the coefficient of friction at the basal detachment (μb).

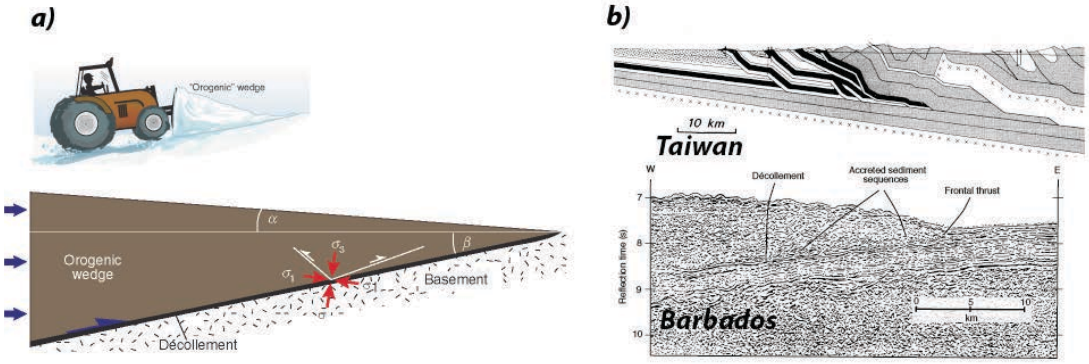

Fig. 10*: Critical wedge model in theory and practice. a) Bulldozer wedge analogy (top) and sketch of the wedge with the angular parameter* [*Fossen*, 2010]*. b) Natural cases: submarine and subaerial wedge. Interpretative cross-section of the Taiwan fold-and-thrust belt (Western Foothills) by Suppe (1981) on the top panel, and seismic reflection line in the Barbados submarine accretionary prism* [*Nemcok, et al.*, 2005]*, bottom panel.*

b) Feedbacks with surface processes

The effect of erosion on the critical wedge orogen is two-folded:
First, it counteracts the addition of new material by redistributing sediments across the surface through erosion and sedimentation. One important consequence is the redistribution of mass changes, which modifies the internal stress state of the wedge, leading to a departure from equilibrium, and thus the cessation of the activity of the décollement. The system will tend to re-establish equilibrium (i.e. the critical taper) in order to overpass the friction on the décollement and allow the frontal advancement of the thrust belt. The reestablishment of the critical taper is mainly done through deformation in the inner part of the belt, such as [*Nemcok, et al.*, 2005]:

- Out-of-sequence thrusting along pre-existing thrusts;
- Activation of back-thrusting;
- Duplexing along the basal décollement (also called underplating);
- Contractional inversion of former basins (such as piggy-back or fore-arc basins)

Thus, theoretically, erosion may trigger deformation; it obviously does not create mountain belts but controls its geometry, style and pattern of deformation [e.g. *Avouac and Burov*, 1996; *Willett*, 1999; *Whipple*, 2009].

Erosion in the mountain belt implies sedimentation in the foreland. The effect of syn-tectonic sedimentation is dual. It can either inhibit forward propagation of

the frontal thrusts by increasing the load on them [*Storti and McClay*, 1995; Fig. 11].

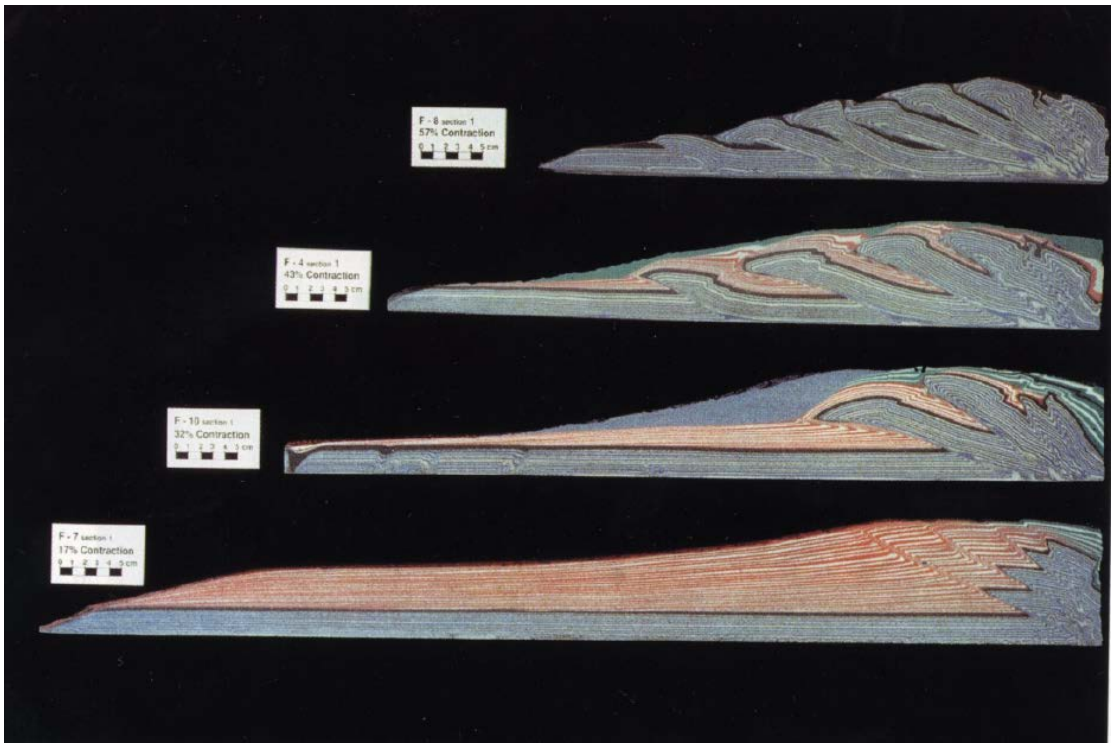

Fig. 11*: Effect of sedimentation on the frontal propagation of the wedge. Sedimentation increases from the top model to the bottom. As sedimentation increase short, steep thrust develop at the rear of the model. The number of this thrust decrease with increasing sedimentation. In short, sedimentation inhibits forward propagation of thrusts. Note that only sedimentation is depicted in this model, no erosion is taking place. After Storti and McClay* [1995].

Alternatively, provided that an efficient décollement is present in the foreland, deformation can be transmitted farther into the foreland on top of larger thrust sheets, as seen in the Pyrenees [e.g. *Fillon et al.*, 2013].

Instead of frontal accretion, wedges with multiple décollements show variable components of frontal accretion of the incoming material, and basal accretion (underplating) of thrusts units below the upper décollement, similar to the formation of duplexes (fig. 12). Underplating is more likely to occur in the hinterland of mountain belts where interactions between tectonics and erosion are most significant [*Malavieille*, 2010; Fig. 12].

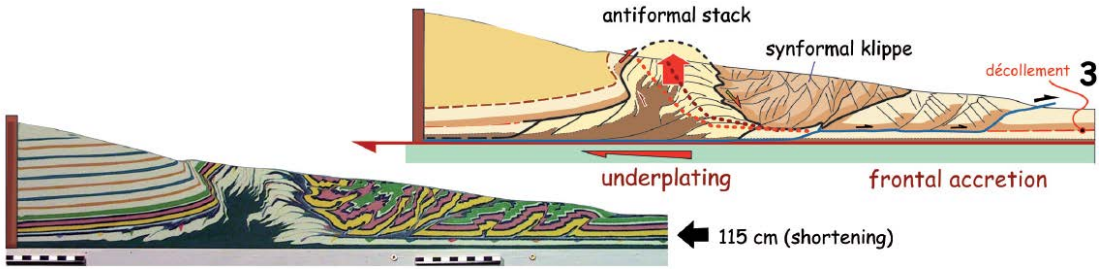

Fig. 12*: Analogue sand-box model (left) and interpretation (right). Frontal accretion and*

underplating are the main modes of accretion of material into the orogen. Underplating balanced by erosion creates an antiformal stack and exhumes the deepest rocks to the surface. A back-thrust is also developed, although not much shortening is accommodated along it. This model reproduces surprisingly well the surface geology of some orogens such as Taiwan. After Malavieille [2010].

The multiple décollement wedge model (fig. 12) highlights what is often considered (by numerical modellers) as a completely different mode of accretion: underplating. But in fact, underplating can simply be viewed as the results of a more complex wedge behaviour of the wedge's frontal accretion in presence of multiple décollements. Nevertheless, we shouldn't forget that such analogue models and most numerical models assume the rheology of the crust to behave as a pressure-dependent brittle rheology without considering depth-changing rheology (e.g. ductile behaviour). This approximation may be true for the first 10-15km of the crust but not above that. In any case, natural cases are certainly more complex.

Numerical models of critical wedges can predict the orogen behaviour to different dominant modes of accretion of material (Fig. 13). If material is added uniformly along the base and erosion is constant and uniform (Fig. 13B), the overlying wedge would be uplifted uniformly, with little or no internal strain, so that the resultant velocity field is quite different from that of frontal accretion, where surface horizontal component decrease toward the rear of the wedge (Fig. 13A). In fact, the horizontal component of the surface velocity could be zero, so the surface velocity is specified entirely by the vertical component (i.e. wedges with no surface shortening) [*Willett et al.*, 2001].

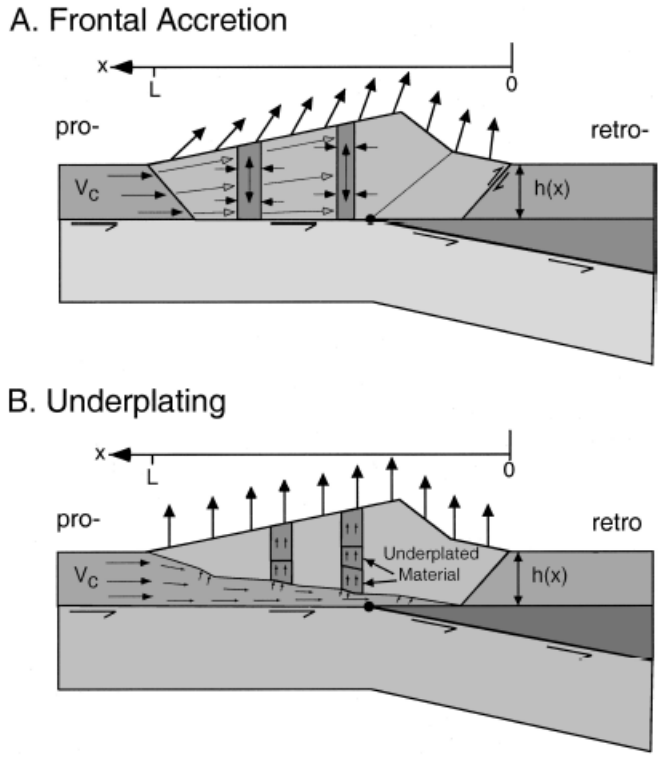

Fig. 13*: End-member kinematic models of orogenic wedge growth. A) Frontal accretion. Wedge shortens such that a vertical column extends vertically and shortens horizontally.*

Vertical component of surface velocity is relatively constant. B) Underplating. Wedge does not shorten horizontally and thus has no horizontal velocity. Columns of rock move vertically at a constant rate in response to addition of new material at base of the wedge. From [*Willett et al.*, 2001].

In cases where accretion and erosion are matched, so that overall, there is no net increase of the wedge volume, steady-state is reached (Fig. 14). Effectively dynamical systems with strong negative feedbacks (e.g. enhanced elevation→ increased erosion→ reduction of elevation) tend to reach a state of equilibrium [*Phillips*, 1992; *Willett and Brandon*, 2002]. The steady-state assumption is a key element for numerical models as it allows assessing how the studied systems behave to perturbation.

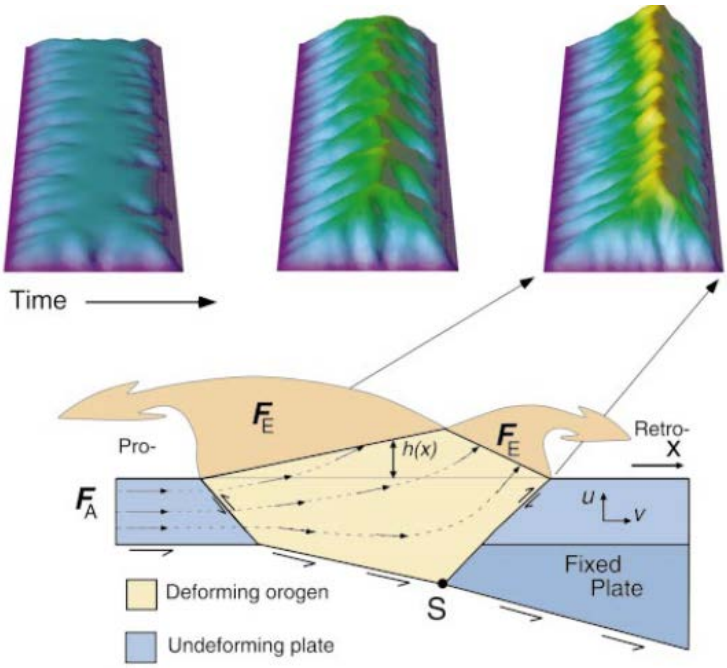

Fig. 14*: Kinematic model of a collisional orogen in which erosion flux is balanced by accretion flux, leading to a flux steady-state system. After Willett and Brandon (2002).*

Using a coupled kinematic and erosion approach, *Barr and Dahlen* [1989] and *Dahlen and Barr* [1989] were the first to model the thermal structure in a steady state critical wedge and predict the particle path and metamorphism along the wedge. They found that the metamorphic rocks distribution in Taiwan orogeny is produced mostly by frontal accretion of 75%, and the remaining 25% are accommodated by underthrusting [*Dahlen and Barr*, 1989]. In the Taiwan case, with the accumulation of low-temperature thermochronological data indicating localized exhumation in the internal part of the orogeny, percentage of underplating has increased to 90% [e.g. *Simoes et al.*, 2007].

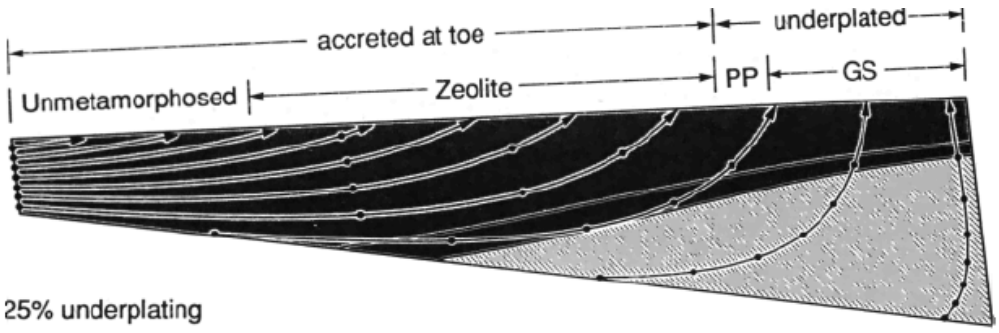

Fig. 15*: Some of the first coupled tectonic and erosion numerical models showing the particle path through the orogen and its control on metamorphism distribution (Dahlen and Barr, 1989).*

More detailed thermo-kinematic and thermo-mechanical models were then developed [e.g. *Beaumont et al.*, 1992, 1996, 2000; *Willett et al.*, 1993; *Batt and Braun*, 1997; *Willett*, 1999; *Braun et al.*, 2010]. Some of the main results of these models are:

- Backthrusting is recurrent in all the models. The orogen forms a doubly vergent accretionary wedge.
- Material from the subducting plate is accreted through underthrusting of upper crust sediments or through ductile extrusion of the subducted lower crust.
- Erosion localizes strain and exhumation.

Additionally, normal faulting can be a way the wedge reequilibrates from an excessive growth. Effectively, normal faulting is not limited to extensional tectonics settings, they are common feature of orogens such as the Himalayas, European Alps and most of the active or decaying orogens (e.g. *Molnar and Tapponnier, 1975*). Normal faulting can be interpreted as the collapse of a decaying orogen, but also can be the result of a fast tectonic growth overtaking the critical stable angle of crustal material. The same way the critical wedge will tend to grow if the system is "under" equilibrated, if this equilibrium is surpassed, the system will tend to re-establish it, by increasing the width of the wedge or, less likely, change the dip of the décollement.
Consequently, syn-orogenic normal faulting can be an effective way to exhume deeply formed rocks, in combination with the two other main exhumational processes, namely erosion and ductile flow [*Ring et al.*, 1999; Fig. 16].

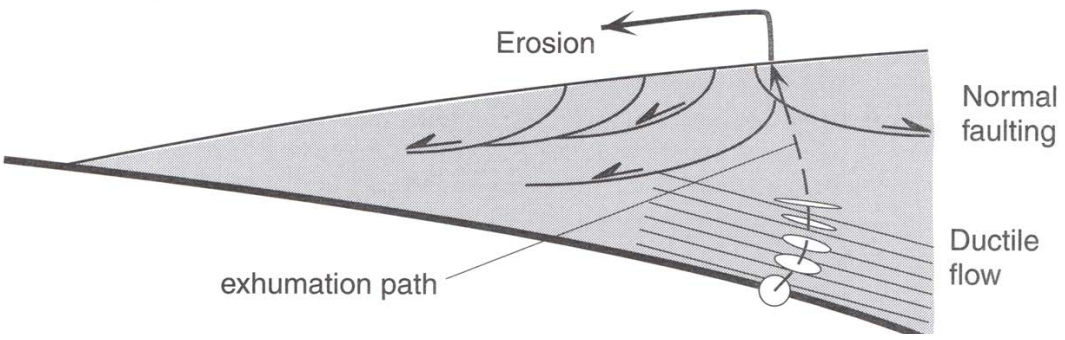

***Fig. 16**: Exhumational processes. Erosion, normal faulting and ductile flow. The later is symbolized by the strained circle (Ring et al., 1999)*

c) Limitation of the models of brittle orogenic wedges

Some of the limitation of the original critical wedge theory is unlimited size of the backstop (i.e. buttress or bulldozer's plow) against which the sediments are accreted. This resulted in unrealistic one sided wedge geometries as natural orogens and accretionary prisms often form doubly-vergent wedges [e.g. *Koons*, 1990; *Silver and Reed*, 1988; *Willett et al.*, 1993]. Beaumont et al. (1996) showed that the activation of a back fold and thrust characterize the transition from subduction to collision. As discussed in the next chapter for the Taiwan case, one can even state that such rigid backstop does not really exist in natural cases and that deformation develops on the lower plate as well as in the upper plate.

Moreover, coupling between faulting and ductile flow must occur in orogenic belts. For instance, the outward flow of ductile lower crust beneath large collision zones or plateau regions is known to control their surface expression [*Royden*, 1996; *Royden et al.*, 1997]. In contrast, the dynamic coupling between horizontal shortening and erosion produces inward flow of the lower crust, an efficient process to maintain topography over geological times [*Avouac and Burov,* 1996]. Ductile flow has been proposed to occur on the flanks of the eastern and south-eastern Tibetan plateau, where the lower crust flow is most significant due to high topographic gradients [*Royden et al.*, 1997; *Clark et al.*, 2005]. This process can eventually lead to the persistence of a low viscosity channel flow where geothermal gradients are high and coupling with erosional removal efficient. This mechanism was proposed to explain exhumation from deep crustal levels like the Greater Himalaya Sequence [*Beaumont et al.*, 2001]. Ultimately, extrusion of lower crustal materials is able to trigger earthquake in the topographic front as suggested for the Wenchuan earthquake in 2009 [*Burchfiel et al.*, 2008].

The processes involved in orogenic metamorphism implied by the critical wedge model (Fig. 15 and Fig 17A) differ from what geologists have traditionally interpreted from field-based studies in more mature orogens, where deeper crustal levels are interpreted to be involved in the collisional processes. In the original conceptualisation of critical wedge models in Taiwan [*Suppe*, 1980a, 1981] basement involvement only came into play in the inner(eastern)most part of the belt where evidences of lower plate affinity basement rocks were seen in the surface geology. There, a ramp rooting into the basement was the locus of basement duplexes; similarly to what has been reproduces in sand-box experiment (Fig. 12). Alternative interpretations in Taiwan involve lower crustal levels since the beginning of collision and imply thickening and ductile extrusion of the metamorphic core (Fig.17B) [*Yamato et al.*, 2009].
Based on whether one interpret the orogenic wedge as involving only the top-most brittle crustal levels or deeper levels one can distinguish two different cases: a first case where deformation remains localized at the plate interface (subduction-type; Fig. 17A); a second case where deformation is distributed along the whole crustal thickness (collision-type; Fig. 17B). The latter is probably

most active when a pre-orogenic weak lower-crust exist and is shortened under high erosion rates.

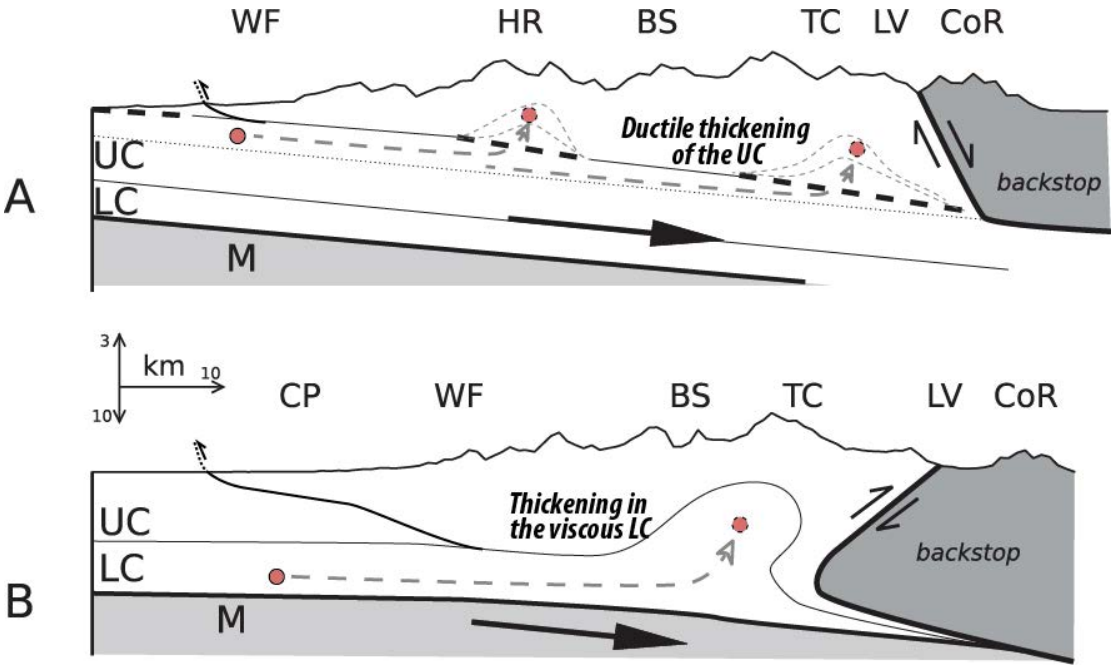

Fig. 17: *Different models of ductile accretion in orogenic wedges, applied to the Taiwan case A) subduction-type in which the upper crust, weakened during burial by subduction, is accreted by underplating. Dashed lines indicate underplating windows, corresponding to the basement ramps in the original critical wedge model by Suppe [1980]. B) collision-type in which the native lower crust is accreted by ductile extrusion, together with the upper crust undergoing preferentially brittle deformation. Black dots materialize the particle trajectory (from left to right) of a given particle from the subducting crust incorporated into the wedge. Letters on top of the topographic trasnect refer to the different geological units in the Taiwan described in more detail in Chapter 2. WF – Western Foothills; HR – Hsuehshan Range; BS – Backbone Slates; TC – Tananao Metamorphic core; LV – Longitudinal Valley; CoR – Coastal Range. Modified from* [*Mouyen et al.*, 2014].

In the first type (Fig. 17A), subduction below the plate interface brings upper crustal rocks and faults to lower crustal depths. The dynamic transition from brittle to viscous regime promotes ductile accretion and thickening accommodated across ductile shear zones below upper brittle wedge [*Dunlap et al.*, 1997]. Such accretion by underplating has been proposed in many orogens, to explain tectonic denudation or exhumation in absence of thrusting at the surface, including Taiwan [*Simoes et al.*, 2007b]. In the second type (Fig. 17B), frontal accretion dominates such that faulting and ductile shearing does occur in the same vertical section of crust. Involvement of the mid-to-lower crust is argued by field-based observation that documents ancient mid to lower crustal shear zones from which rheology at brittle-ductile transition or below can be inferred [*Fusseis et al.*, 2006; *Bürgmann and Dresen*, 2008; *Burov*, 2011]. Eventually, constraints on strain rates across active continental faults [Appenines; *Cowie et al.*, 2013] or based on post-seismic geodetic data in collisional belt [Taiwan; *Rousset et al.*, 2012] argue for loading processes by lower crustal flow. This has been also argued in many orogens based on geophysical data [*Mouthereau and Lacombe*, 2006; *Mouthereau et al.*, 2012] and is supported by mechanical

modeling of weak continental crust [*Yamato et al.*, 2009; *Jammes and Huismans*, 2012; *Nilfouroushan et al.*, 2013].

Whether metamorphism and ductile thickening in orogens results from duplexing of subducted upper crust or by accretion of inherited ductile lower crust has strong impact on the amount and nature of crustal material that is transferred from lower to upper plates and in the nature and origin of metamorphism on orogens.

d) Thermal state in orogens controlled by erosion and topography

The thermal state of the orogens is essential for the understanding of deformation, as it controls material rheology and thus deformation (e.g. fig. 9).
In orogens, rocks are heated. This is observed by the increased heat flow in modern orogens and by high-temperature metamorphism in exhumed ancient orogens, only possible at high geothermal conditions [*Stüwe*, 2007].
Some of the reasons are:

- Crustal thickening brings cold crustal material to depth and to greater temperatures. Although this process does not increase the heat flow at the surface (as heat coming from the underlying mantle can be considered constant), it heats previously cold rocks leading to metamorphism.
- Thickening of the crust will lead to an increased contribution of the radioactive heat. In some cases, combining it with other processes, this can lead to anatexy (i.e. partial melting of crustal material), as seen in the Himalayas [*Law et al.*, 2006].
- Thickening of the crust leads to the creation of sub-aerial topography, which in turns initiates surface processes action. Erosion and topography lead to perturbation of the thermal structure. Particularly erosion leads to an increasing surface heat-flow through advection of hot rocks towards the surface (Fig. 20).
- Frictional heating may arguably be an important heat source, especially along the basal décollement faults, and has been estimated to have a contribution greater than radioactive heat production [*Barr and Dahlen*, 1989]. Nevertheless its significance is still a matter of debate.

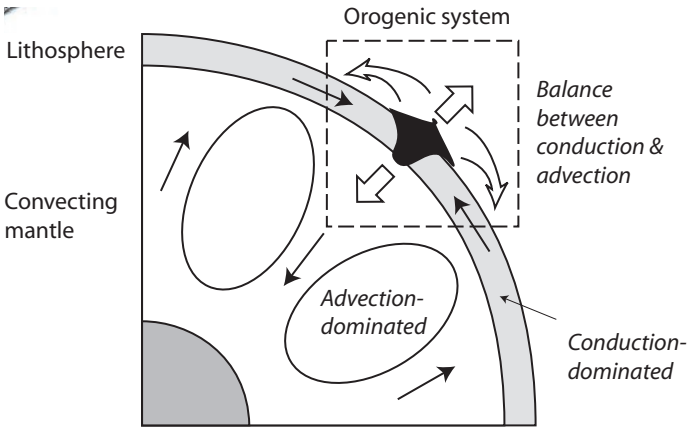

***Fig. 18**: Modes of heat transport in the earth. From Braun et al. (2006).*

Heat is mostly transported by conduction (transfer through molecular vibration energy) and advection (transport of matter itself). In the mantle heat is mostly dissipated by thermally driven advection (i.e. convection) creating convection cells, which in turn drive the movement of tectonic plates (Fig. 18). The tectonic plates may eventually collide, thicken the crust and uplift the earth surface. The topographic gradient created in this setting results in mass transfer at the earth surface (i.e. erosion and deposition), causing heat advection. Thus, in this setting, the heat is transferred by conduction but also advection [*Stüwe et al.*, 1994; *Braun et al.*, 2006; *Stüwe*, 2007].

Lets consider now what are the processes potentially perturbing the shallow (first ~15km) crust thermal structure, giving a special focus to the orogenic system. As introduced earlier, heat advection is a major process in orogens, mainly through the rock transport towards the surface due to erosion and thrusting, but also through fluid circulation. We can expect a higher geothermal gradient where advection of rocks is important, while the isotherms will be more spaced (i.e. lower geothermal gradient) in places of less advection (Fig. 19). Thermal structure of the crust is thus controlled by the location of erosion and deformation.

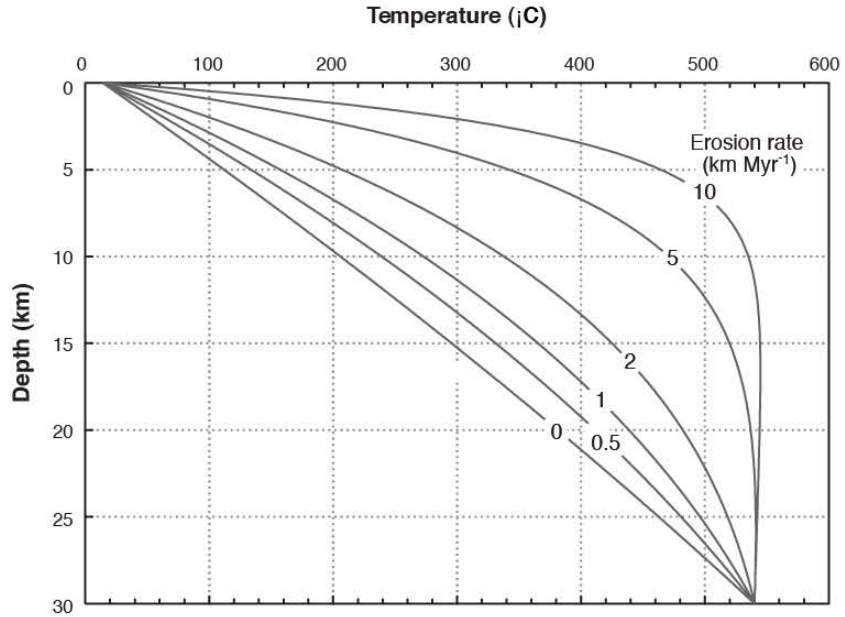

Fig. 19*: Geothermal gradient for different erosion rates, showing the effect of isotherm advection by erosion (modified from Reiners and Brandon, 2006)*

A related effect is the topographic disturbance of the isotherms close to the surface. The magnitude and depth of the perturbation depends on the wavelength and amplitude of the topography, which in turn determines the depth of thermal perturbation (Fig. 20). .
In nature, however, the topographic and exhumational effects are combined. Figure 20b shows how, as exhumation rate increase in a given fixed topography, the geothermal gradient increase due to heat advection towards the surface resulting in a topographic thermal perturbation reaching deeper levels. In both cases (Fig. 20a and b) the geothermal gradient in the valleys is steeper than in

the crests. This effect is amplified as exhumation increases. Note that figure 21b assume an homogenous exhumation, equal in the valleys and in the crest. We can imagine a different scenario were valleys are lowered faster than crests, in which case the geothermal gradient difference between valleys and crests will be even more important.

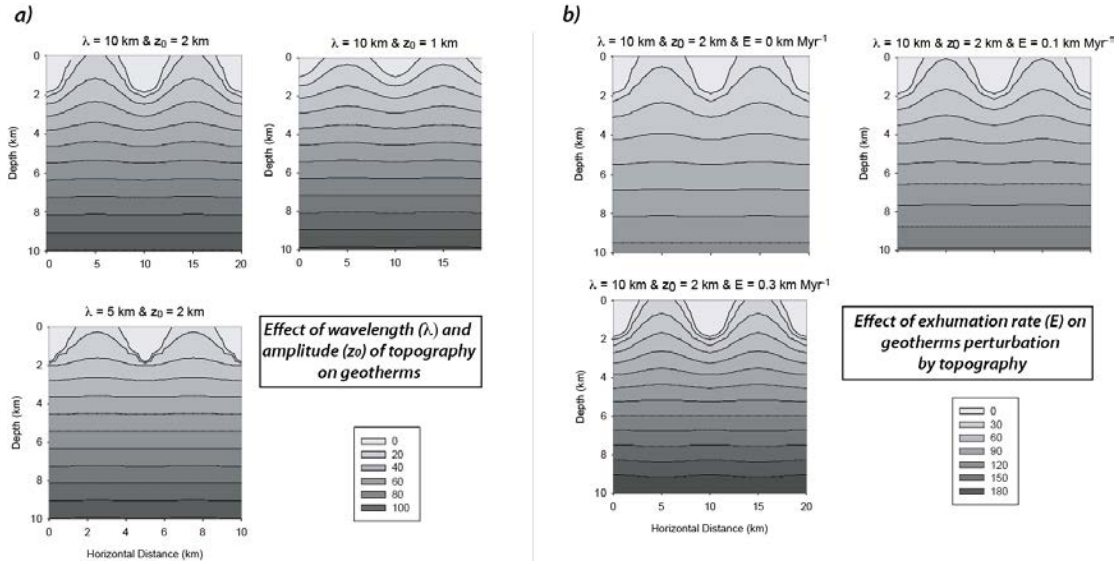

Fig. 20*: Topography and exhumation effect on geotherms. a) Variable amplitude and wavelength topography and its effect on geotherms. The depth of the effect of topography depends on the characteristics (i.e. amplitude and wavelength) of the topography. Note the different scale of the x-axis in the lower panel. b) Effect of exhumation rates on the topographic perturbation of the geotherms. Here topography is constant, only exhumation rates changes. Note that higher exhumation rates increases the geothermal gradient and provokes a topographic effect on higher isotherms. Modified from (Braun et al., 2006).*

B. Late Cenozoic climate change and theoretical orogenic response

With the advent of the critical wedge theory and its implicit relation between deformation and topography, a whole world of new perspective linking tectonic and climate were brought to birth. Particularly, because a well-documented climatic change took place in Late Cenozoic, one could expect an orogenic response to a passage towards an increased climatic variability and the start of glaciation in high latitudes and altitudes.

Although tectonic/surface-process coupled numerical and analogue models show erosive controls on deformation, there is a lack of evidence in natural cases confirming a causal relationship. As stated by [*Braun*, 2006]: "*one must be reminded that the demonstration that a coupling between erosion and tectonics exists has so far been limited to the results of computer modelling of the system*". However, recent research have provided with compelling evidences arguing for an erosional driven change in orogen kinematics in the St. Elias mountains in Alaska [*Berger et al.*, 2008] and in the European Alps [*Willett et al.*, 2006b; *Willett*, 2010], suggesting such a kinematic change may have occurred in other orogens. Such a global behaviour is further supported by a simultaneous global increase of exhumation at all latitudes [*Herman et al.*, 2013].

In the following I briefly review the main climatic factors argued to control the global sedimentation and erosion rates increase in the Late Cenozoic and then introduce the theoretical behaviour of orogens to an increased erosional efficiency.

1) Sedimentation rates increase in the late Cenozoic

In spite of some opposing views [e.g. *Willenbring and von Blanckenburg*, 2010], it is generally believed that the Late Cenozoic period has witnessed a net increase in sedimentation (Fig. 21) resulting from a global climatic shift towards colder and more variable atmospheric conditions (Fig. 22) [e.g. *Hay et al.*, 2002; *Molnar*, 2004].

Part of the Plio-Quaternary terrigenous accumulation increase results from erosion of continental shelves due to the onset of glaciations and sea level drop, but continental sedimentation also increased during the same time span (Fig.21). The sedimentation accumulation rate increase affected equally active as well as quiescent tectonic areas, suggesting the change affected both kind of landscapes [*Molnar*, 2004]. The only satisfying global explanation appears to be climatic rather than tectonic, although some the initial trigger and complex feedbacks could involve some tectonic component [e.g. *Raymo and Ruddiman*, 1992; *Ruddiman and Prell*, 1997].

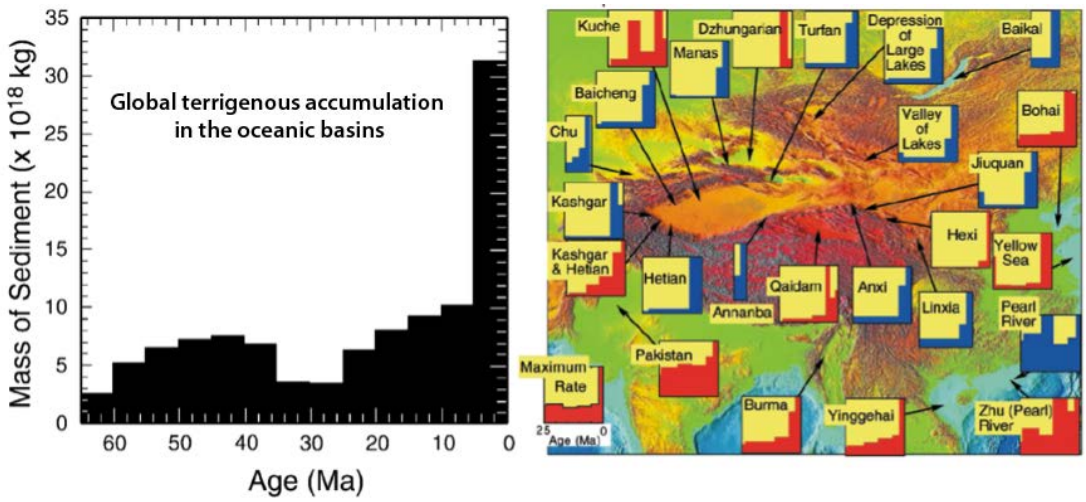

Fig. 21*: Global terrigenous accumulation during Cenozoic times deduced from the Ocean Drilling Program; b) sedimentation since 25Ma in the Himalayan endoreic basins and foreland (Molnar, 2004).*

Glacial erosion has been recognized as a very effective erosive agent [e.g. *Montgomery*, 2002] controlling the height of mountain ranges [*Brozovic et al.*, 1997; *Egholm et al.*, 2009], although its high erosive efficiency relatively to fluvial erosion has been turned down recently [*Koppes and Montgomery*, 2009]. The sedimentary record at high latitudes and at high altitudes shows that glacial derived sediments dominate these settings, and thus the onset of glacial erosion in these areas can satisfactorily explain the increased sedimentary accumulation [*Molnar*, 2004].

Glaciation at low latitudes and altitudes is more limited [e.g. *Hastenrath*, 2009] and the late Cenozoic sedimentation rate increase is likely not linked to glaciation. In theses settings, both short and long-term climatic variability appear to control erosion rates. Annual climatic variability affects erosion and sediment transport, through catastrophic events, such as typhoons, annual storms or other non-climatic events such as large earthquakes, as demonstrated to occur in Taiwan [*Dadson et al.*, 2003; *Huang and Montgomery*, 2013]. At geological time-scales climatic variability may have similar effects. The Earth climate has gone through a well-known change since Mid-Miocene times, when the global cooling trend of the Cenozoic was accentuated (Fig. 22). Simultaneously with the Northern Hemisphere glaciations (i.e. incipient glaciations at ~5 Ma; Fig. 22), an increase of the amplitude and frequency of the climatic variations increased markedly (Fig. 22; *Hay et al., 2002*). Time-series spectral analyses of benthic foraminifera $\partial^{18}O$ revealed a change in the dominant orbital periods from a long period dominated frequency in the Late Miocene (400 kyr, 126kyr, 95kyr and 41kyr), opposed to dominant 100kyr periods with marked 41kyr periods increasing significantly, indicating a strong influence of the earth's precession favouring polar ice preservation (*Molnar, 2004*).

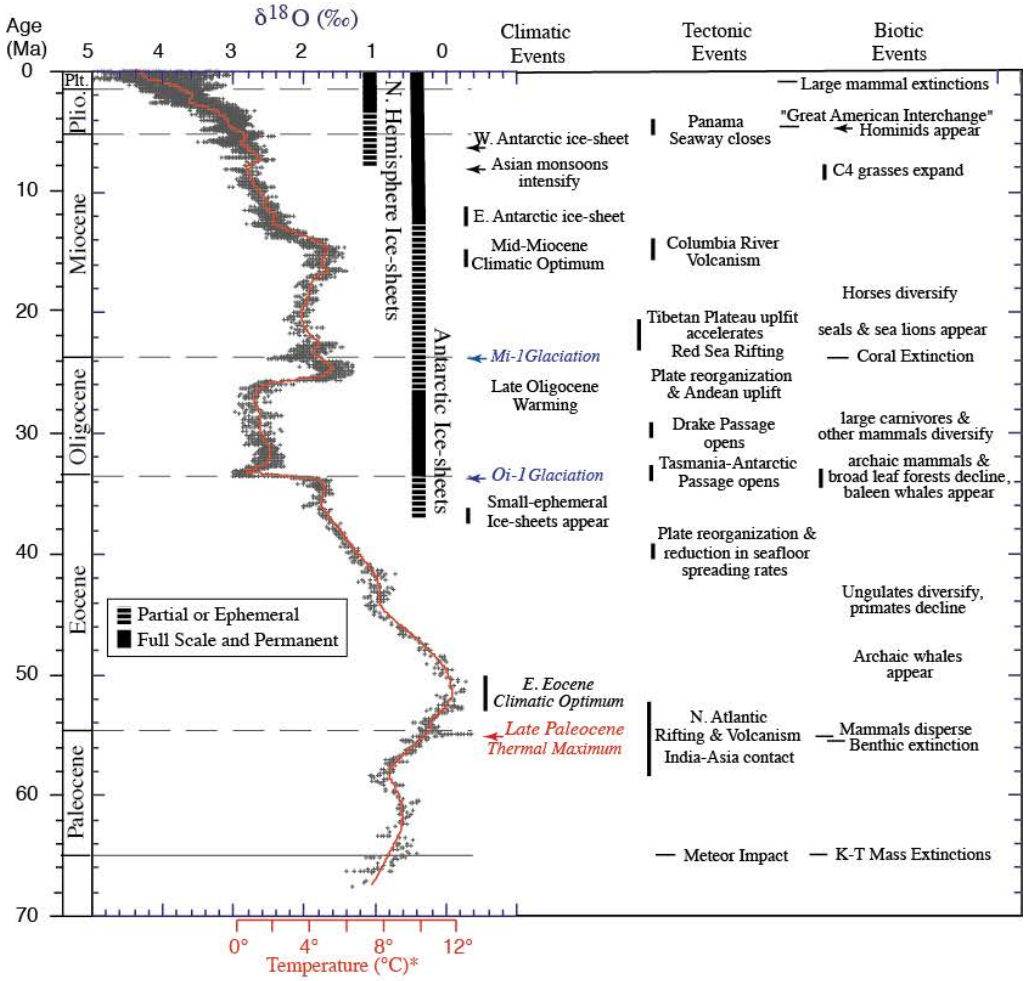
Age (Ma)
δ18O (‰)
Climatic Events
Tectonic Events
Biotic Events
Plt.
Plio.
Miocene
Oligocene
Eocene
Paleocene
N. Hemisphere Ice-sheets
Antarctic Ice-sheets
Partial or Ephemeral
Full Scale and Permanent
W. Antarctic ice-sheet
Asian monsoons intensify
E. Antarctic ice-sheet
Mid-Miocene Climatic Optimum
Mi-1 Glaciation
Late Oligocene Warming
Oi-1 Glaciation
Small-ephemeral Ice-sheets appear
E. Eocene Climatic Optimum
Late Paleocene Thermal Maximum
Panama Seaway closes
Columbia River Volcanism
Tibetan Plateau uplfit accelerates Red Sea Rifting
Plate reorganization & Andean uplift
Drake Passage opens
Tasmania-Antarctic Passage opens
Plate reorganization & reduction in seafloor spreading rates
N. Atlantic Rifting & Volcanism
India-Asia contact
Meteor Impact
Large mammal extinctions
"Great American Interchange"
Hominids appear
C4 grasses expand
Horses diversify
seals & sea lions appear
Coral Extinction
large carnivores & other mammals diversify
archaic mammals & broad leaf forests decline, baleen whales appear
Ungulates diversify, primates decline
Archaic whales appear
Mammals disperse
Benthic extinction
K-T Mass Extinctions
Temperature (°C)*

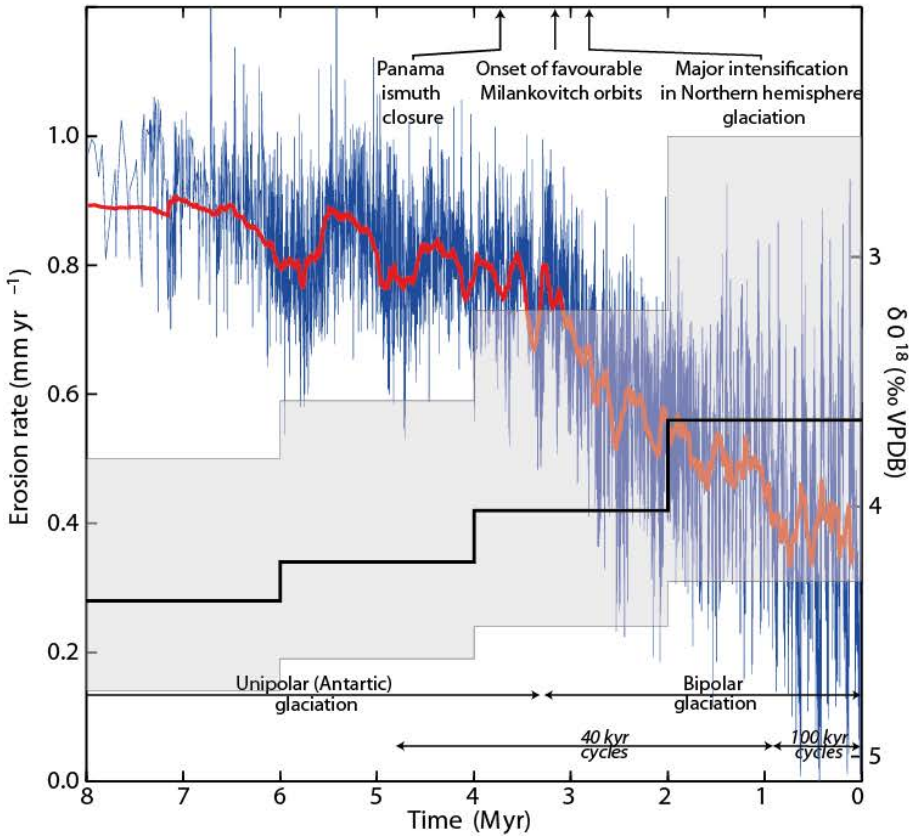
Panama ismuth closure
Onset of favourable Milankovitch orbits
Major intensification in Northern hemisphere glaciation
Erosion rate (mm yr −1)
δO18 (‰ VPDB)
Unipolar (Antartic) glaciation
Bipolar glaciation
40 kyr cycles
100 kyr cycles
Time (Myr)

Fig. 22: *Top panel: Temporal relation between the main tectonic, climatic and biotic events for the Cenozoic; modified from* [*Zachos et al.*, 2001]*. Lower panel: Detail on the climatic (right axis) and erosion rates over 2-Myr time interval (left axis) derived from cooling histories of sediment-source regions for the past 8 Ma;* modified from [*Herman et al.*, 2013]*. Lower panel also shows the significant tectono-climatic events having potentially caused the erosion rate increase including the dominant Milankovitch periods* defined by *Hay et al.* [2002]*. $\delta^{18}O$ for both panels derived from benthic foraminifera from the ODP drilling project. VPDB is the Vienna Pee-Dee belemnite standard.*

Overall, three main climatically-dependent factors have been identified as main controlling factors of erosion:

- Sea level changes responsible of continental shelf erosion and base level drop.
- Glacial erosion in high latitudes and altitudes settings.
- Climatic variability, been the global and most important factor.

2) Climatic forcing of an orogens and Late Cenozoic climatic change

The characteristic steep topographic gradients and high erosion rates of mountain ranges make this setting a particularly sensible place to erosional efficiency changes, particularly in wet and active orogens (Fig. 3).

Early studies demonstrated qualitatively that rate and pattern of erosion of critical taper orogenic wedges dictates the width, structural style, the longevity of exhumation structures, the rate and pattern of internal strain, near surface uplift rate, the P-T-t pathways of rocks and spatial distribution of metamorphic facies [e.g. *Dahlen et al.*, 1984; *Davis et al.*, 1983]. Later numerical experiments coupling deformation and homogenous erosion provided more quantitative constraint on the thermal effects and metamorphism [*Barr and Dahlen*, 1989; *Barr et al.*, 1991]. Finally, the effects of asymmetrical erosional efficiency the importance of erosion on the orogen geometry and strain distribution [*Willett*, 1999]. Importantly the latter model matched well with the near surface measures of uplift and metamorphic grade of several mountain ranges such as the Southern Alps in New Zealand, the Olympic mountains in the Washington state (USA) and the Himalayas.
The analog laboratory experiments documented a direct and significant control of erosion on the style, pattern and rate of deformation mainly on the single-structure scale view. Particularly, concentration of strain on the pro- and retro-thrust and particle trajectories appeared to be controlled by erosion. Consequently P-T-t path and the associated distribution of metamorphic rocks at the surface can be predicted. As numerical models, analogue models showed the potential for highly localized deformational response to erosion [e.g. *Malavieille*, 2010].

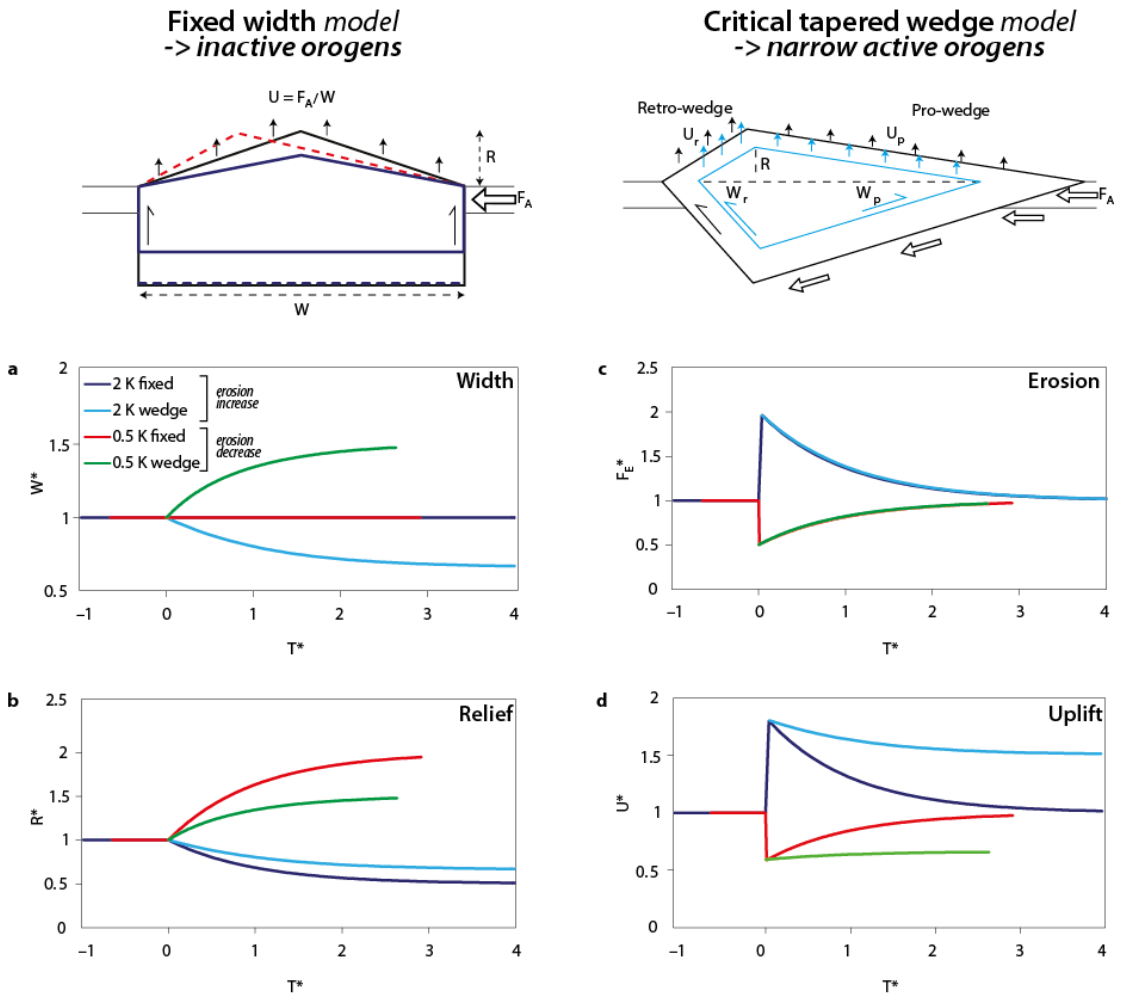

Fig. 23: *Analytical landscape-evolution models (top panel) and results for an increase (2 K) and decrease (0.5 K) in erosion efficiency. Solid lines in both panels show topography and crustal root for low (black) and high (blue) erosional efficiency. Two models are shown, fixed-width orogeny (top-left) and critically tapered wedge (top-right). Ur and Up are near-surface rock uplift rates (the length of the arrows are proportional to the uplift rates) on the retro and pro- sides of the wedge, which have widths Wr and Wp, respectively. Lower four panels show mountain-belt response to erosional efficiency changes. Response to both an increase (twice; 2K) and decrease (half; 0.5K) in erosional efficiency are tested using an analytical model. Predicted variables include: a, normalized mountain belt half-width (W*), b, normalized topographic relief (R*), c, normalized total erosional efflux (FE*) and d, normalized rock uplift rate (U*). All variables are normalized by their initial steady-state values and are plotted against dimensionless time (T*), which is the ratio of time to system response time (τ). Curves are shown for both the simple fixed-width model ('fixed') and a coupled erosion-tectonic model ('wedge'). Modified from* [*Whipple*, 2009].

Whipple [2009] provided a comparison of the fundamental characteristics and behaviour of various orogenic systems to a change in erosive efficiency (Fig. 23). The author, based on a reference "fixed-width" system that can be assimilated to an inactive orogen (although with positive accretionary flux; Fig. 23), aimed distinguishing the simple physical response of the crust to increased erosion from a real forcing of the orogen. In this reference model an increase in erosional efficiency leads to an increase of erosive efflux, reduction of topographic relief

and a short-lived isostatic-related increase of rock uplift (Fig. 23). In the critical taper wedge model, the erosive efficiency increase has similar effects on the erosive efflux and relief but conversely to the fixed-width model, the rock uplift is persistent beyond the initial isostatic response. The initial isostatic resulting from the erosion unload is likely to affect the adjacent foreland basin by reducing their subsidence. Additionally the critical taper wedge displays a decrease of its width indication the activation of internal thrust of the wedge (i.e. out-of-sequence) (Fig. 23). Elsewhere, it is generally known that a tectonically forced orogen is associated to forward propagation of the deformation front (i.e. increased width) resulting increased foreland basin subsidence [e.g. *DeCelles and Giles*, 1996].
To summarise, the distinction between a climatic and a tectonic forcing can be demonstrated if simultaneity of the following is proved:

Climatic forcing if simultaneous:	***Tectonic forcing if simultaneous:***
- Erosion flux increase - Foreland isostatic rebound - Activation of internal thrust (i.e. reduction of orogen width) - Relief reduction	- Erosion flux increase - Foreland increased subsidence - Uplift persistence beyond system response time. - Activation of frontal thrust (i.e. increase of orogen width) - Increased relief

As for any highly coupled system, causes and consequences are difficult to distinguish, and the chicken or egg question will prevail until the system is better understood. As highlighted in the effective field-tests of *Whipple* [2009] above, for proving a climatic forcing in orogens, synchronicity in the timing of tectono-erosive-morphological events is critical. Only this way a causal relationships can be established beyond simple spatial relationships [e.g. *Reiners et al.*, 2003].

IV. Statement of the general topic

The present research works focus on the tectonic-erosive system of an active orogenic setting. Orogenic settings are characterised by high erosion rates and active deformation, ideal to characterize the interactions between erosion and deformation (if any).

The present study focuses on the Taiwan mountain belt, an archetypical active orogen at the origin of the much of the funding works on the critical wedge model [*Suppe*, 1981, 1984a; *Davis et al.*, 1983; *Dahlen*, 1984; *Dahlen et al.*, 1984]. Based on this pioneer works a whole generation of tectonic and coupled numerical models came to live [e.g. *Beaumont et al.*, 1992, 1996, 2000a; *Willett et al.*, 1993; *Willett*, 1999; *Stolar et al.*, 2006; *Whipple and Meade*, 2006; *Fisher et al.*, 2007; *Roe et al.*, 2008; *Whipple*, 2009] improving considerably the understanding of the orogenic system.

This study addresses a number of aspects on the orogenic development of Taiwan. In general terms, this thesis aims constraining the timing of the different deformation phases, the associated kinematics and identify some of the processes behind each of the phases. To this end I used structural data, thermochronology and geomorphological analysis, the combination of which gives multi-temporal constraints on orogenic development.

Despite the relatively well studied geology of the Taiwan island, a number of fundamental questions remain unanswered or controversial:

What is the age of collision and of the main mountain building phases?

Considering that collision should start as the first involvement and accretion of continental crust occur in the subduction wedge, the onset of collision should be addressed in light of the current knowledge of the South China Sea passive margin architecture, this is, considering the previously overlooked wide (~250 km) and ultra-thinned continental crust, as recently proven by a number of studies [*Byrne et al.*, 2011; *Lester et al.*, 2013; *McIntosh et al.*, 2013; *Eakin et al.*, 2014]. This question is addressed through a combination of structural analysis in southern Taiwan's Central Range mountains (*Chapter 2*) combined with timing constrains of the major tectono-erosive events using thermochronological tools (*Chapter 3*) (Fig. 24). The results are partly presented in an accepted article (*Geology* - GSA publication) entitled "*From submarine continental accretion to arc-continent orogenic evolution: the thermal record in the Taiwan mountain belt"* included at the end of the *Chapter 3.*

What are the major controls on the long-term morphological evolution of sub-tropical mountains belt?

In order to evaluate the potential tectono-erosive feedbacks in the orogen, the major controls on morphological evolution of the Taiwan orogen need to be assessed. Climatic reconstructions indicates that, although cyclically alternating (Fig. 23), the Late Cenozoic climatic signal is dominated by longer cold, glacial periods [e.g. *Porter*, 1989], arguably at the origin of the Late Cenozoic worldwide sediment rate increase (Fig.23, e.g. *Molnar*, 2004; *Herman et al.*, 2013]. Literature treating Taiwanese morphology and paleo-climate has systematically assumed fluvial processes as dominating short and long-term erosive processes, given the present sub-tropical monsoonal climate with frequent typhoons, relegating the significance of glacial processes to the highest mountain peaks [e.g. *Cui et al.*, 2000; *Böse*, 2004; *Böse and Hebenstreit*, 2008; *Siame et al.*, 2012]. Nevertheless, a number of evidences tend to give a more important role to glaciation in the long and short term morphological and erosive evolution of the orogen, namely the long forgotten presence of low-relief paleo-surfaces [*Tomita*, 1939; *Lin*, 1957] and paleo-climatic and sedimentological elements supporting for a much lower snow-line in last glacial cycle (from ~110kyr to ~15 kyr) [*Liew*, 1986, 1991; *Liew and Huang*, 1994; *Cui et al.*, 2000, 2002; *Liew et al.*, 2006]. To test the potential important role of glaciation on the morphological development we exploit digital elevation models and satellite image using

classic morphological mapping, morphometric tools and available paleo-climatic data. The results are presented in *Chapter 3* (Fig. 24).

To answer to the above-mentioned problematics, the aim is to constrain deformation and exhumation at different times-scales, through the combination of traditional geological techniques (i.e. geological mapping, structural analysis) and low-temperature thermochronological tools and geomorphological analysis. Ultimately, because our data will allow to assess the processes involved and timing of orogenic development, I will be able to asses the relative role of erosion and tectonic in each of the steps giving birth to the Taiwan mountain belt. Ultimately, I will be able to assess the potentiality of climatic forcing in the recent (i.e. Pleistocene) development of the belt.

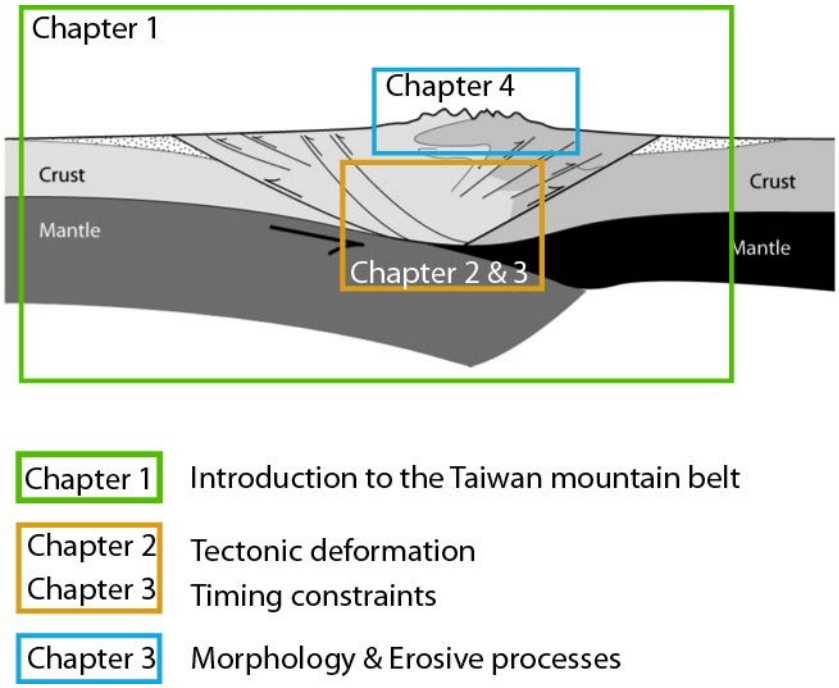

Fig.24*: Graphical representation of the organisation of this thesis. Schematic representation of the orogen modified from* [*Beaumont et al.*, 2000]*.*

Chapter 1: The Taiwan mountain belt

In this chapter I introduce the reader to the general geodynamic and geological setting of Taiwan to rise up the presently unanswered or controversial problematics concerning its geological history and the controlling geological processes involved.

I. Geodynamic setting

The island of Taiwan measures ~380km from north to south, and~140km from east to west. In spite of its small size, Taiwan topography reaches 3954m (Yushan) and has over 100 peaks over 3000m. The Taiwan strait, about ~150km wide, lies in between the continent and the island, and links the South China Sea (SCS) to the south, to the East China Sea to the North. The Pacific Ocean bounds Taiwan to the east.

A. The South China Sea margin and Philippine Sea plate in the geodynamic framework of SE Asia

At a first glance, Taiwan is the result of a relatively simple geodynamic configuration, characterized by the convergence between the oceanic Philippine Sea plate (PSP) and the SCS margin, which belongs to the Eurasian plate (Fig. 1.1). The present day motion of the PSP relatively to the Eurasian Plate is about ~8.2 cm/yr with an azimuth ~N309° [*Yu et al.*, 1997].

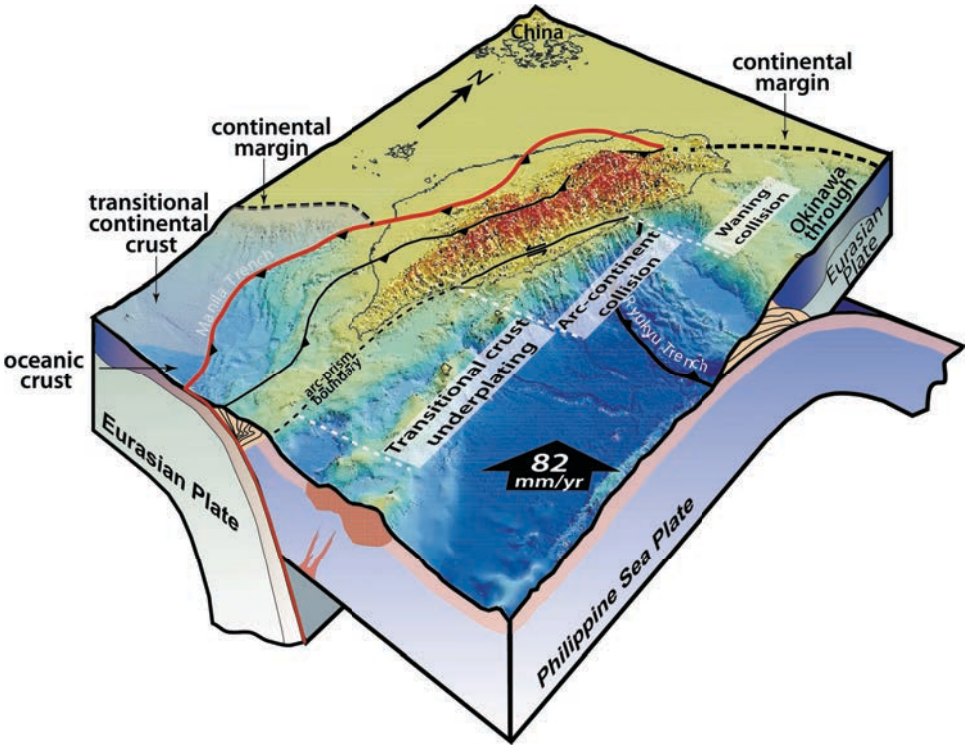

Fig. 1.1: Bloc diagram showing the double vergent subduction zone typical of Taiwan geodynamic setting. Red line = deformation front. Modified from [Ramsey, 2006].

In southern Taiwan, the northern SCS attached to the Eurasian plate is subducted below the PSP, while to the north, the Luzon volcanic arc collides with the Eurasian passive margin and creates the Taiwan mountain belt, a schoolbook living example of an arc-continent collision (Fig. 1.1). The departure from this simple tectonic setting is seen in northernmost Taiwan, where the Eurasian margin is not subducting, but overriding the Philippine plate. Opposite vergent subduction zones are usually linked by transform faults, and this was proposed to be the case before the total consumption of the northern South China sea [*Teng*, 1990; *Hall*, 1997, 2002; *Teng et al.*, 2000; *Hsu et al.*, 2004]. However, in the present-day configuration, since the contact with the Eurasian passive margin has occurred, the Taiwan mountain belt is the transfer zone between the E-directed and N-directed subduction zones.

In the following, I explore the current models concerning the formation of the SCS. The SCS is probably the most important element for understanding the regional context of the Taiwan orogenesis, as Taiwan was created by the accretion of oceanic and passive margin sediments together with Mesozoic continental basement of Eurasian affinity (Fig. 1.2). We will first see the different theories concerning the SCS inception and then try to understand the elements coming into play during this process.

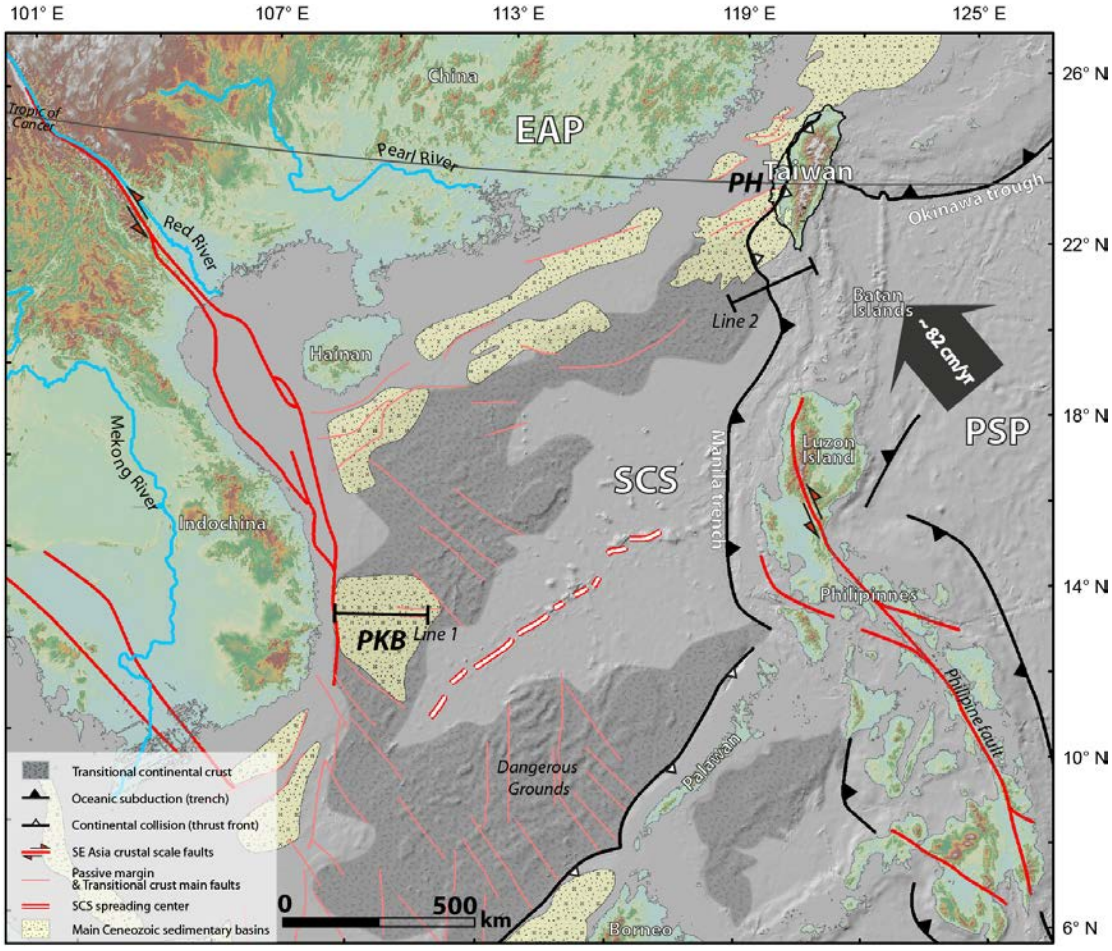

Fig. 1.2: *SE Asia physiography and tectonic context compiled from [Cullen et al., 2010; Hall, 2002; Li et al., 2009; Teng and Lin, 2004; Yan et al., 2006]. SCS = South China Sea; PSP= Philippine Sea Plate; EAP = Eurasian Plate; PH = Peikang high; PKB = Phu Khanh Basin. Line 1 and Line 2 indicate position of seismic reflection lines shown in Fig. 1.9. Arrow indicates motion of the PSP plate relatively to Eurasia. Note how the transition between ocean-continent boundary and the fully thick Eurasian continent is materialized by a wide band of transitional continental crust.*

1) The South China Sea margin and the Himalayan collision

The Himalayan collision has an important role in the Southeast Asia geodynamics, and in particular in the evolution of the SCS. First, it has been argued that the opening of the SCS and other east Asia marginal basins are a direct consequence of the Himalayan collision with the opening of pull-apart basins accommodates the strike-slip motion of extruded Asian crustal blocks [Fig. 1.3; *Tapponnier et al.*, 1986; *Peltzer and Tapponnier*, 1988; *Jolivet et al.*, 1994]. Secondly, almost the totality of sediment deposited in the SCS basin and passive margin are sourced in the Himalayan-Tibetan orogenic system and brought to the SCS by major rivers, such as the Mekong River, Red-River, Pearl River and Yellow River (Fig 1.2 and 1.3).

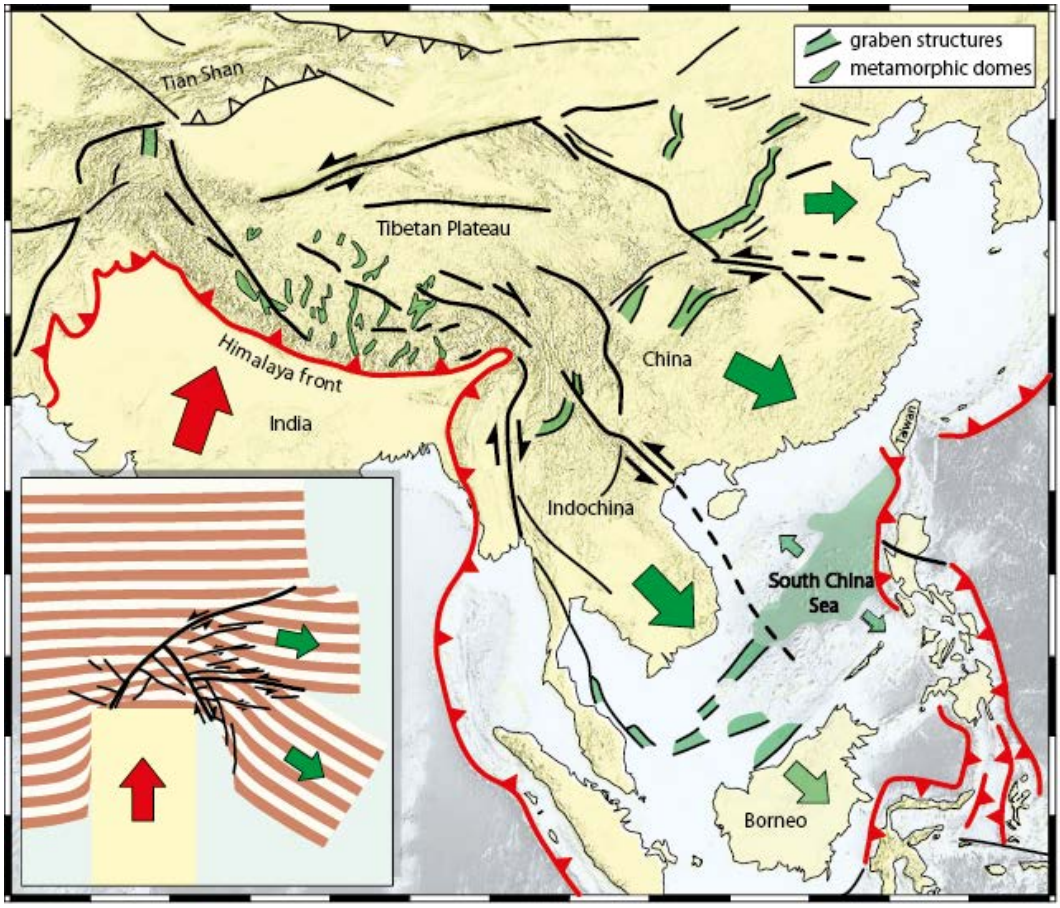

***Fig. 1.3**: Map of large-scale tectonic extrusion of Southeast Asia as proposed by* [*Tapponnier et al.*, 1986]*, modified from a redrawn version by* [*Frisch et al.*, 2011]*. Inset shows analog indentor experiments with plasticine reproducing the general structure of Southeast Asia.*

In the extrusion model, the Indochina block is extruded along the Red River sinistral strike-slip fault zone and would explain the opening of the SCS. The merit of such model is to give a geometrically elegant regional explanation to a tectonically complicated area, in a kinematic and mechanicaly viable way. Moreover the timing of rifting and India-Asia collision seem to correspond (i.e. ca. 50Ma; Fig.5; *Tapponnier et al.*, 1986).
However, the main weakness of this model as reviewed by *Cullen et al.* (2010) are the lack of paleomagnetic evidences of block rotation as expected for a pull-apart basin, the mismatch between the amount of extension and strike slip movement along the Red River Fault zone and the lack of unequivocal continuation of this same fault offshore in the SCS as required by the model. Yet another weakness is the assumption that subduction zones are purely passive agents accommodating continental extrusion, in an area where back-arc spreading plays a key role (as in present-day Japan Sea or Okinawa through, e.g. *Jolivet et al.*, 1994; or in the proto-SCS, e.g. *Hall*, 1997, 2002; *Hall et al.*, 2008).

2) The South China Sea margin and the geodynamics of the proto-SCS

Alternative models suggest the existence of long-lived subduction zones and drifting blocks, and argue for minor influence of Himalayan tectonics [*Hall*, 1997,

2002; *Hall et al.*, 2008]. According to these models, rifting of the SCS would initially be driven by the slab-pull of the subducted proto-SCS slab (Fig. 1.4, top right). Subduction of the proto-SCS oceanic crust under the proto-Manila trench would be totally consumed in the Early Miocene, as presently materialised in the northern Sabah (Borneo) - Palawan orogenic suture (Fig. 1.2 and 1.4, middle right panel). The existence of the proto-SCS is evidenced by the orgenic suture as well as by late Mesozoic shales and sandstones thought to be deposited in a shallow marine oceanic basin [e.g. *Hall*, 2002; *Wang and Li*, 2009]. It is worth noting that the role of the extruded Indochina crustal bloc is still argued to contribute to the SCS opening from the Middle Oligocene *[Fig. 1.4; Hall, 1997].* These models have the merit of taking into account most of the paleomagnetic data and the complicated subduction-collision geological histories of Southeast Asian numerous plates.

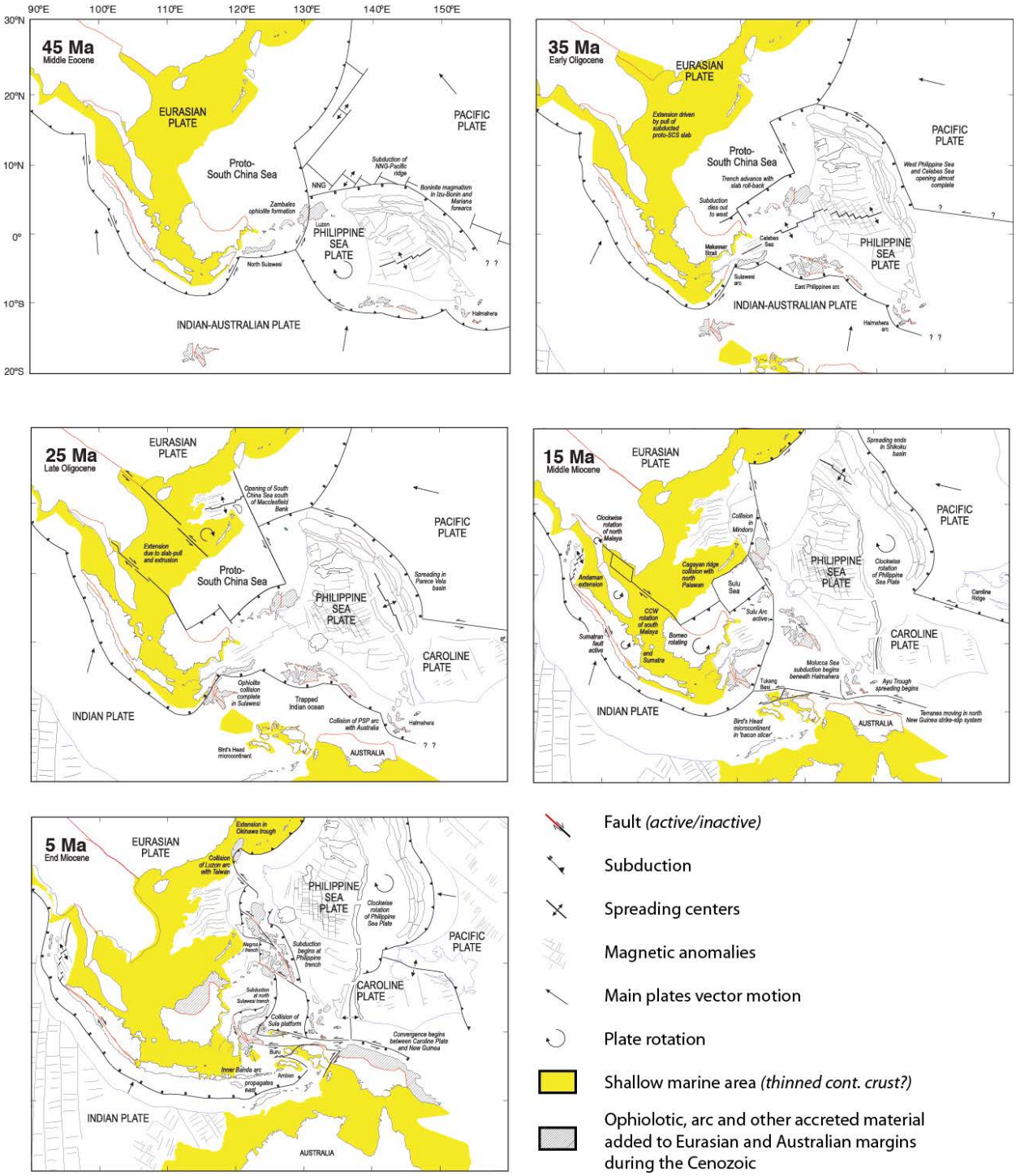

***Fig. 1.4**: Cenozoic geodynamical evolution of Southeast Asia. Modified from* [*Hall*, 1997].

Overall, an intermediate model of SCS genesis can be conceived, integrating the main actors in Southeast Asia geodynamics setting: ***1)*** The Himalayan collision through the extrusion of crustal blocks along major fault zones; ***2)*** The general setting in which India-Australian plate subduction and Pacific Eurasian plate subduction, give birth to a configuration where marginal basins, back-arc spreading, slab-pull and arc-continent collision are common features. In this framework, the Proto-SCS subduction and slab-pull triggered the opening of the SCS and allowed extrusion of the Indochinese bloc, enhancing extension and

plate rotation (Fig.1.4); ***3)*** The potential role of deep processes such as mantle upwelling (e.g. the Hainan hot spot; *Wang and Li*, 2009 and reference within it), or more local mantle convection cells developed under the nascent SCS [*Lin et al.*, 2003], cannot be excluded. ***4)*** Finally, the end of extension is argued to be the result of final consumption of the Proto-SCS and collision of Dangerous Grounds (Eurasian conjugate margin) with the Palawan-Borneo continental blocs [*Barckhausen et al.*, 2014] (Fig.1.2 and middle-right panel on Fig. 1.4).

If the original driving forces giving birth to the SCS remain somehow subject to discussion, the SCS spreading history is relatively well constrained by the sea-floor magnetic anomalies (Fig. 1.7) and stratigraphy (Fig. 1.4 and 1.6), and have been recently reviewed by a number of authors [e.g. *Cullen et al.*, 2010; *Huang et al.*, 2012; *Barckhausen et al.*, 2014]. Rifting initiated first in the North and Northeast of the SCS, the different phases based on the Taiwan strait and Southwest Taiwan stratigraphy are [*Lin et al.*, 2003]: ***1)*** Rifting phase between ca. 58 and ca. 37 Ma, creating a 200km wide rift zone formed by discrete rift depressions; ***2)*** at ca. 37Ma, a rift jump occurred focusing extension in the Northwestern part of the SCS, and led to ***3)*** initial continental break-up at ca. 30 Ma in the NW area positioned today offshore Southwest Taiwan; ***4)*** During the interval ca. 30-18 Ma post-break up thermal (inner margin) and tectonic, fault-related subsidence (outer-margin) occurred with deposition of well developed thick sedimentary series (Fig. 1.6); ***5)*** during the period between ca. 21 and ca. 12.5 Ma the whole margin experienced thermal subsidence; and ***6)*** rifting recommenced at ca. 12.5 Ma, ceasing its activity at ca. 6.5 Ma. It is worth noting that this last phase appear to be temporally linked to the initiation of the manila trench and subduction of SCS [*Teng*, 1990; *Huang et al.*, 2006] and may somehow be related to a far-field response of the subducting slab to initial subduction [*Lester et al.*, 2012].

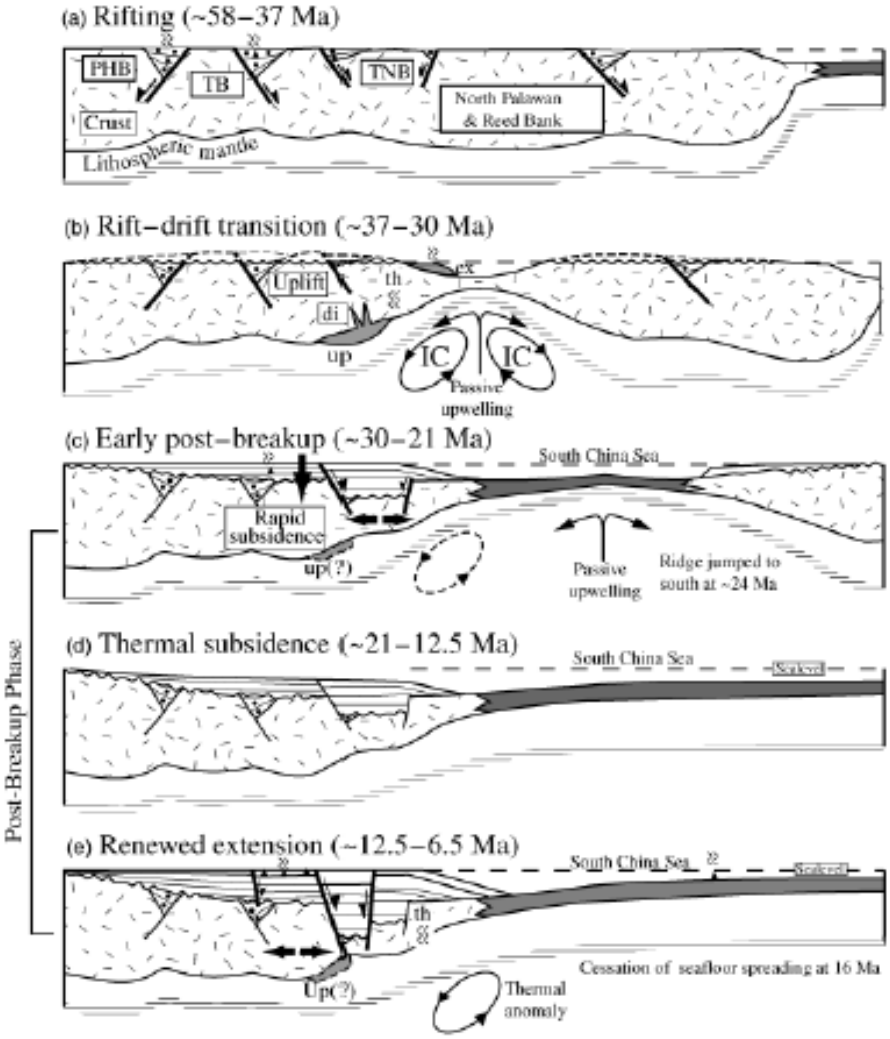

Fig. 1.6*: Reconstructed East-West cross sections in the Taiwan area showing the tectonic development of the northern South China Sea margin. See text for further discussion. PHB-Penghu Basin, TNB-Tainan Basin, TB-Taihsi Basin. Modified from [Lin et al., 2003].*

3) The Philippine Sea plate motion

After the general review of the Southeast Asia geodynamic setting and tectonic development of the SCS, we will now consider the third key actor for the understanding of the Taiwan setting, namely the Philippine Sea Plate (PSP). The Luzon Arc sits on the PSP and thus its motion during the recent geological past is of crucial importance for the Taiwan collision. Unfortunately the PSP is surrounded by subduction zones and is lacking of any obvious hot spot traces and consistent magnetic anomalies, which complicates further reconstruction of its past motion (e.g. *Hall*, 2002). The present-day rates and direction of the PSP motion relative to the Eurasian Plate are thought to have been established at about 6.5-5Ma [*Jolivet et al.*, 1994; *Hall*, 2002; *Sibuet and Hsu*, 2004; *Wang and Li*, 2009b] but later changes may have occurred.

The geology of the Philippines may bring some light to the more recent motion of the PSP. In particular, it has been argued that a major change in the PSP motion occurred at ca. 4 Ma from an essentially northward to a northwestward directed

motion [*Aurelio*, 1992, 2000]. The main evidence for such a change are the development of the central segment of the Philippine fault zone and Philippine Trench (Fig. 1.2 and 1.4), which accommodates most of the convergence in this area. Other evidences related to the volcanic development and deformation of the Bonin island, at the Northeastern edge of the PSP favour a recent change in the motion of the PSP (Francis Wu, 2013, personal communication).

The activation of the Manila trench where the SCS subducts below the PSP may have started in the Early [*Hall et al.*, 1995] or Middle Miocene [~16 Ma; *Huang et al.*, 2006], but the exact nature of the contact between the SCS and PSP plates before this time is not well known, and thus the northern extension of the Luzon magmatic arc is unsure.

B. Margins in the South-China Sea and inversion tectonics

Rifting events recorded within the South-China margin led to thermal and mechanical weakening of the passive margin lithosphere (Fig. 6). This inherited rheology and structure will be key elements in the later collisional history.

The relative importance of the processes intervening in the structuration of the SCS and its margin can be assessed by the role and nature of magmatism during the break-up process. Two end-members exist concerning the role of magmatism during rifting [*Yan et al.*, 2006; *Franke*, 2013]. On the one hand, volcanic continental margins are usually genetically associated to a nascent mantle plume and high volumes of volcanism or traps (e.g. Southern Atlantic with the Paraná traps), and to narrow rifts resulting in an abrupt continent-ocean transition. On the other hand, magma-poor margins present limited volcanism and highly strained continental lithosphere eventually leading to the exhumation of sub-continental mantle [e.g. Iberian margin; *Boillot et al.*, 1987; *Brun and Beslier*, 1996]. The SCS spreading is generally considered as belonging to magma-poor margins but presents a net break-up unconformity, characteristic of active volcanic rifts. Some consider the SCS as an intermediate form between volcanic and magma-poor margin end-members [*Franke*, 2013], but volcanism is generally post-spreading (i.e. late Miocene to recent igneous bodies), with very limited syn-extensional volcanism in its northern part [*Lin et al.*, 2003; *Yan et al.*, 2006], and the broad hyper-extended margin (Fig.1.2 and 1.9) indicate a typical passive-rift nature (i.e. magma-poor) driven by far-field stresses (e.g. Himalayan collision and proto-SCS slab-pull).

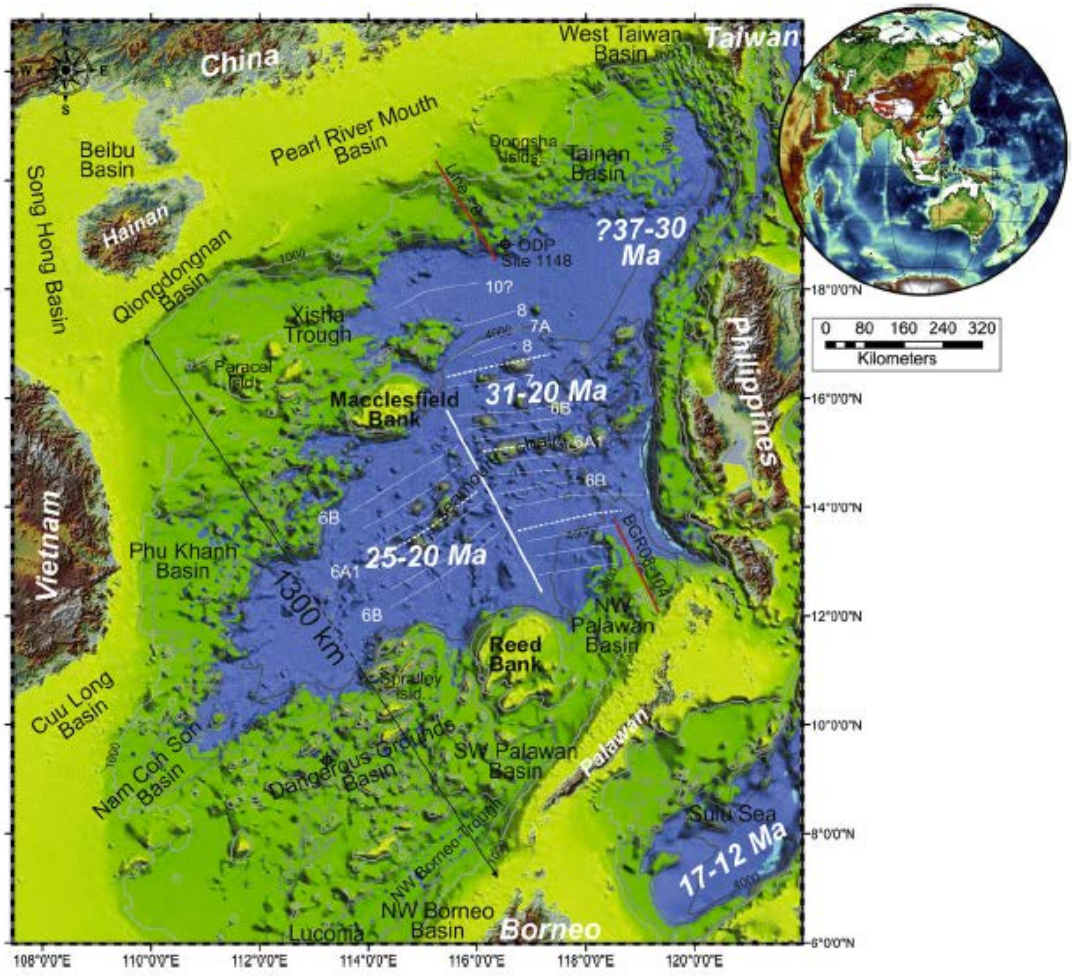

Fig. 1.7*: Topography and bathymetry of the South China Sea region with the location of the basins discussed. The area of highly attenuated continental crust is shown in yellow/light green. It exceeds 1000 km width. Bathymetric contours are shown every 1000 m. Age of break-up and magnetic anomalies of the oceanic crust (blue) is indicated. Seafloor spreading anomalies (white, dashed lines) and a major fracture zone (white, solid line). After Franke (2013).*

At distance from the South-China continental shelf and its proximal margin, there is a wide transitional continental crust surrounding the SCS basin, to the Northwest and Southwest passive margin as well as to the Southeast in the drifted terrains known as "Dangerous Grounds" (Fig. 1.2, Fig. 1.4 and Fig. 1.7). The successive rifting episodes have thinned the SCS passive margin to unusual crustal thickness for a continental crust: below ca. 12 km in the inner margin and reaching down to ca. 6km (i.e. hyper-extended continental crust; Fig. 1.9) in the outer margin [*Nissen et al.*, 1995a, 1995b; *Wang et al.*, 2006; *Zhao et al.*, 2010; *Lester et al.*, 2013; *McIntosh et al.*, 2013; *Eakin et al.*, 2014].

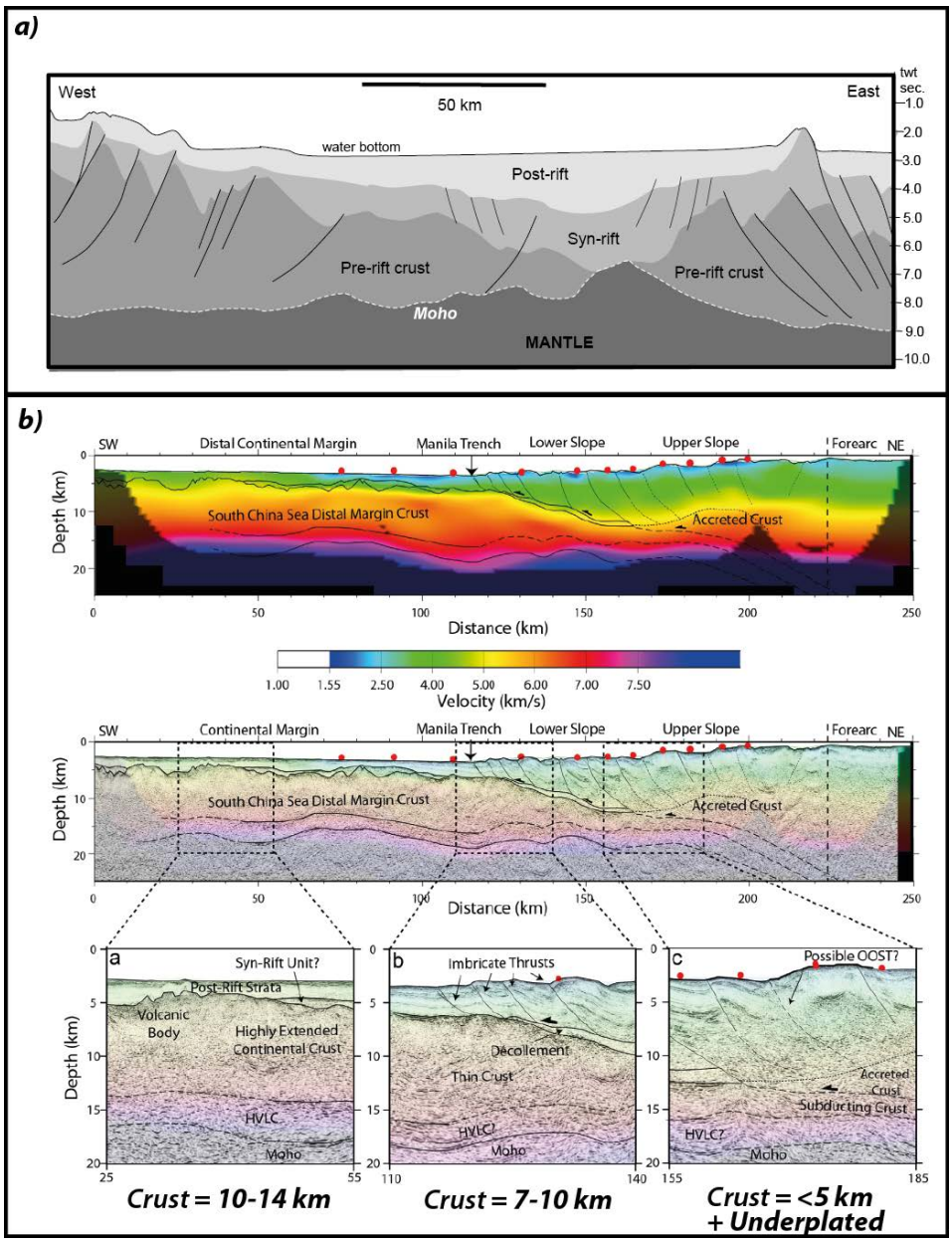

Fig. 1.9*: a) Interpretation of seismic reflection line 1(See Fig. 1.2 for location) of the eastern boundary of the Phu Khanh Basin (PKB, Fig. 1.2 and 1.7), offshore Vietnam. Modified from Cullen et al. (2010). Note how the syn-rift sediments lie directly on the sub-continental mantle. b) Seismic reflection profile and P-wave velocities indicating that SCS margin offshore soubTaiwan is largely composed by thin transitional crust. Below the accretionary wedge, duplexes suggest that the distal margin is accreted by underplating. Modified form* [*Lester et al.*, 2013]*.*

It has been argued that exhumed mantle is also present in the southwestern passive margin (Phu Khanh Basin, Fig. 1.2 and Fig. 1.9) and probably in the drifted continental terrains of the "Dangerous Grounds" [*Cullen et al.*, 2010; Fig. 1.9a], a feature increasingly described in other passive margins around the world and probably at the origin of many of the ophiolitic units in Alpine orogens [*Beltrando et al.*, 2014; *Mohn et al.*, 2014].

A well-described but poorly understood process is the presence of magmatism in the margin, indicated by both volcanism and plutonic underplating [e.g. *Yan et*

al., 2006; *Zhao et al.*, 2010b; *Lester et al.*, 2013], generally considered as post-spreading or inherited from the Eurasian continent pre-Cenozoic magmatic provinces. Whatsoever their origin, their influence on the distribution of topographic highs and lows in the margin and on basin development is widely accepted, in particular for the Taiwan collision [i.e. Peikang topographic high; e.g. *Lin et al.*, 2003; *Byrne et al.*, 2011; or in other parts of the SCS, e.g. *Barckhausen et al.*, 2014]

Some of the extensional faults in the proximal margin that developed during rifting were reactivated due to plate bending before collision [*Lester et al.*, 2012]. As the collision progressed, inversion of these normal faults on the proximal margin takes place and are at the origin large earthquakes [Fig. 1.10; e.g. *Mouthereau et al.*, 2001a, 2001b; *Rodriguez-Roa and Wiltschko*, 2010; *Ching et al.*, 2011a].

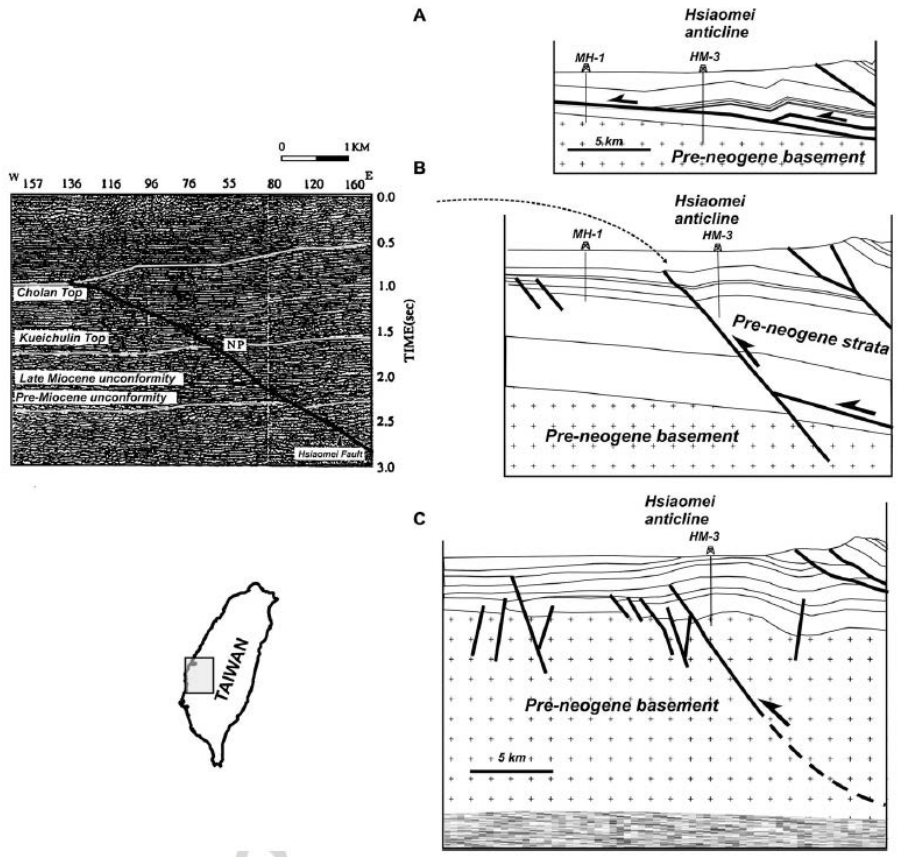

Fig. 1. 10*: Different structural interpretations of the same surface structure constrained by seismic reflection. a) Preliminary interpretation with a décollement in the Chinshui shale level (~3km depth)* [*Suppe and Namson*, 1979]*. b) Interpretation of the same seimic profile with a deeper décollement (~12km)* [*Hung et al.*, 1999]*. c) Due to the lack of evidences of a clear décollement a final interpretation roots surface faults down to the basement in agreement with deep crustal seismicity and focal mechanisms* [*Yang et al.*, 2001]*. Figure after* [*Mouthereau and Lacombe*, 2006]*.*

In Taiwan, the view that lower crust is involved in the deformation at thrust front is further confirmed by a recent analyses of the 2013 Nantou earthquake (M_L=6.2-6.5) and discovery of active crustal ramps below the shallow décollement at thrust front [*Chuang et al.*, 2013; Fig. 1.11].

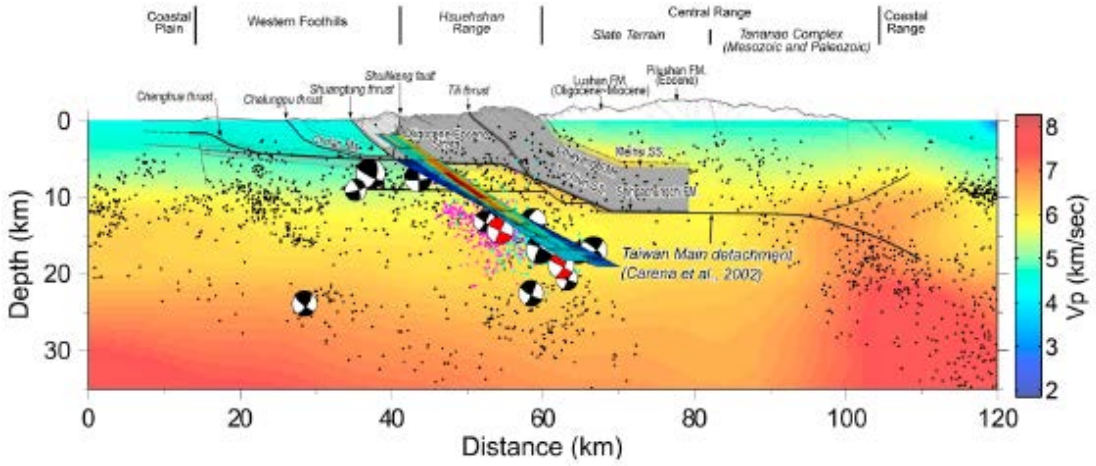

Fig. 1.11*: Central Taiwan cross-section showing the Nantou fault (Chuang et al. 2013). Structural profile is from Yue et al. [2005], and the P wave velocity tomography image from Kuo-Chen et al. [2012]. Black dots denote background seismicity from 1991 to 2009. After Chuang et al. (2013).*

II. Geology of Taiwan

A. Present-day kinematics and main active faults

The convergence rates between the Philippine Sea plate and the Eurasian continent have been estimated 82 mm/yr with a northwestward (~N309°) direction (Fig. 1.1 and 1.2; *Yu et al.*, 1997). Due to obliquity between the Philippine Sea Plate convergence vector, the geometry of the Eurasian margin trending N60°E, and the orientation of the Luzon arc, trending N11°E, (Fig. 1.2) the collision is considered to propagate southwards as the SCS is consumed below the Manila Trench (Fig. 1.2). Southward collision propagation rate have been estimated to between 60km/Myr [*Byrne and Liu*, 2002] and 84 mm/yr [*Suppe*, 1981]. This unique characteristic of the Taiwan orogen allows witnessing the mountain building processes at different maturity stages (i.e. relatively old collision in the north and younger collision in the southern part of the belt; Fig. 1.12).

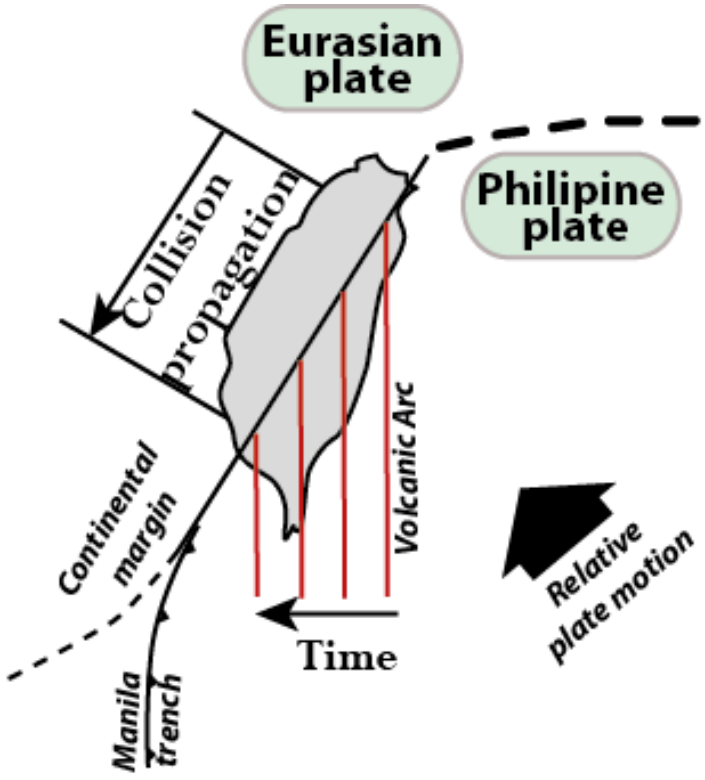

***Fig. 1.12**: Cartoon showing the southward propagation of collision and time-space equivalence along the length of the belt. Modified from [Byrne and Liu, 2002].*

Early papers [e.g. Barrier, 1985] distinguish distinct collisional stages resulting from these obliquities. A first stage resulting from the contact of the Manila accretionary wedge and the passive margin, and a second one resulting from the contact of the Luzon Arc with the passive margin. Each of these stages is materialised by two mélanges in east and the west. More recently *Shyu et al.* [2005b] conceptualise what they call "tandem suturing" in which the tectonic

framework involves three lithospheric elements, two continental (Continental to the west and Central Block – accretionary prism?) and one island-arc comprising the forearc basin.

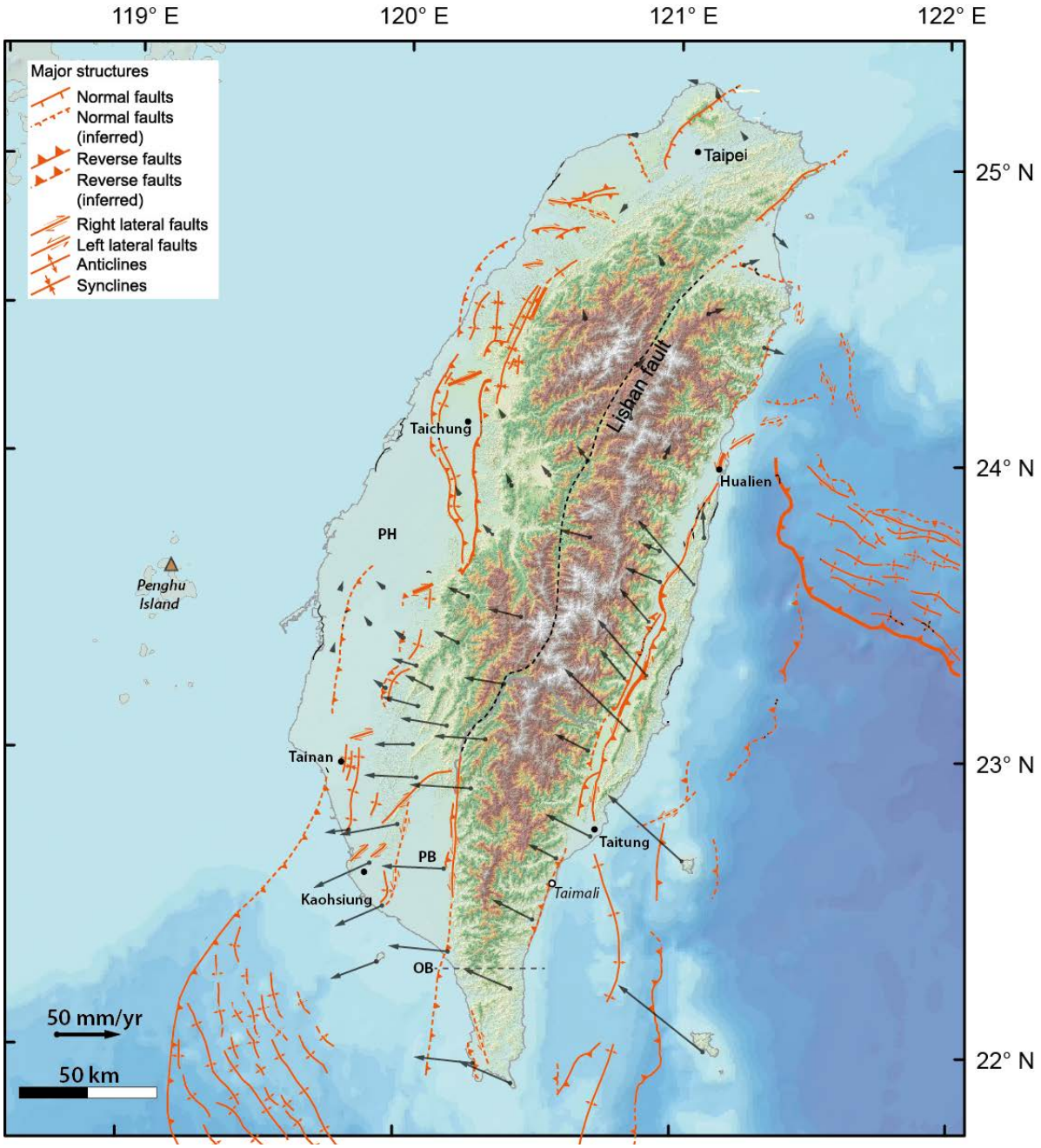

Fig. 1.13*: Map of the active fault of Taiwan map based on seismic activity (contemporaneous and historical) and morphological expression of active tectonics (Shyu et al., 2005], and selected GPS horizontal velocities* [*Yu et al.*, 1997] *relative to the Penghu island station (triangle). OB = Orocline bending (dashed grey line); PB = Pingtung Basin; PH = Peikang high.*

The southward propagation of the collision implies that different stages of orogenic construction can be seen along different profiles (Fig. 1.12) in the

island and offshore south (Fig. 1.2). From South to North these characteristics of the stages are:

- Offshore South Taiwan [*from the Luzon Island to ~21˚N*] is characterized by subduction of the South China Sea oceanic crust, with an undeformed forearc basin [*Chang et al.*, 2003]. At this latitude plate convergence is purely accommodated by the subduction and deformation of the subduction complex [e.g. *Eakin et al.*, 2014].

- **Offshore South Taiwan to Taitung** [*from ~21˚N to ~22˚40'N*]. The hyperextended continental margin starts to be underthrusted, leading to more intense deformation on the subduction complex through basal and frontal accretion [*Lester et al.*, 2013; *McIntosh et al.*, 2013]; on its eastern flank (i.e. Hengchung Peninsula and northwards, around Taimali draining basin; Fig. 1.13) and in its Western flank (i.e. Pingtung basin area), as well as in the forearc basin (Fig 1.14) [*Malavieille et al.,* 2009*; Chang et al.,* 2003]. In this region, plate convergence is absorbed by shortening onshore, but mainly offshore in forearc basin [*Malavieille et al.*, 2009] and by subduction, as the eastwards subducting slab can still be traced at depth under this area [e.g. *Wu et al.*, 2004, 2007]. It is worth noting that the northern boundary where continental accretion occurs through underthrusting of hyperextended continental margin may also be placed at the orocline bending (OB in Fig. 1.13) where a change in the trend of topography appears to be associated to the arrival of a thicker section of continental margin as proposed by *Byrne et al.* [2011].

- **From Taitung to Hualien** [from ~22.4˚N to ~24˚N]. This segment corresponds to the mature collision where the forearc has been reduced to the longitudinal valley. The convergence is accommodates mainly by shortening in the LV and Western Foothills and also probably in the upper plate offshore eastern Taiwan [*Malavieille and Trullenque*, 2009] (Fig. 1.13 and Fig. 1.14).

- **North of Hualien to the northern edge of the island** [*from ~24˚N to ~25˚5'N*]: the orogen is here in an extensional regime, partly due to the opening of the Okinawa trough and partly due to the probable collapse of the mountain belt [*Teng*, 1996]; the relative contribution of each of the processes is not yet well understood. Note that normal faulting is also seen in southern Taiwan as shown by current geodetic velocities (*Yu et al.,* 1997; Fig. 1.13) and structural studies [*Crespi et al.*, 1996].

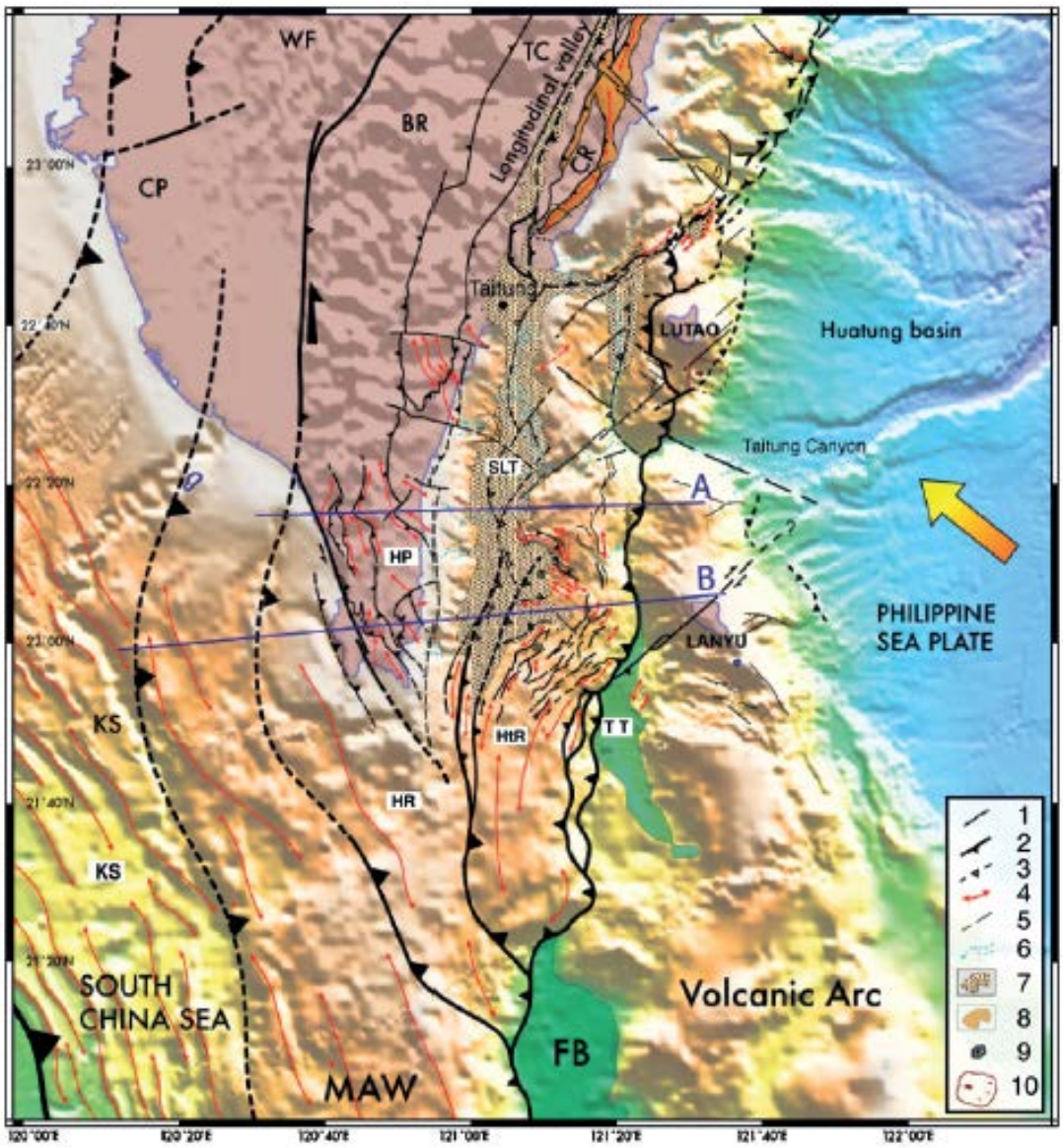

***Fig. 1.14**: Morphostructural map of southern Taiwan area. Onland and offshore structures and tectonic units are correlated. Symbols and patterns: 1 — fault, 2 — thrust, 3 — inactive thrust, 4 — fold axis, 5 — minor fault, 6 — drainage, 7 — recent collisional basin, 8 — volcanic rocks of the Coastal Range, 9 — mud volcano, 10 — mass wasting. CP, Coastal Plain; WF, Western Foothills; HSR, Hsueshan Range; LF, Lishan Fault; TC, Tananao Complex; BR, Backbone Range; CR, Coastal Range; SLT, "Southern Longitudinal Trough" orogenic basin; HP, Hengchun Peninsula; HR, Hengchun Ridge; HtR, Huatung Ridge; KS, Kaoping Slope; TT, Taitung Trough; MAW, Manila Accretionary Wedge; FB, Forearc Basin; OCT, inferred Ocean Continent Transition. After Malavieille and Trullenque (2009).*

B. Geological provinces

As a typical fold-and-thrust belt, Taiwan is built by the accretion of the Eurasian margin units of the lower plate. Here, we present the main geological units of Taiwan from East to west according to the classical nomenclature [*Ho*, 1986] (Fig. 1.15).

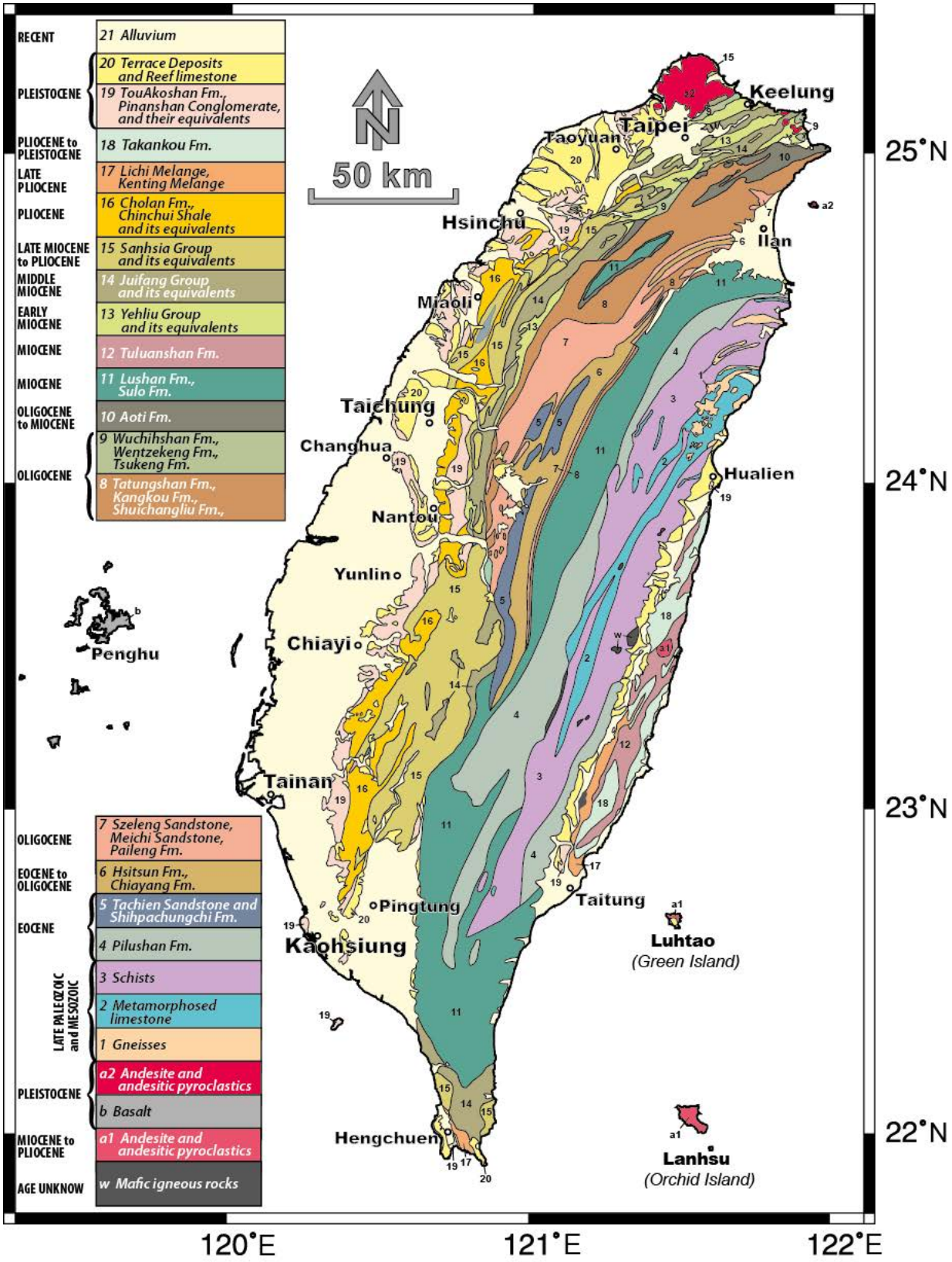

***Fig. 1.15**: Geological map of Taiwan. Modified from a geological map compiled by C.-P. Chang.*

The Coastal Range

The Coastal Range is part of the Luzon volcanic arc, and sits on top of the Philippine oceanic plate. In the north, the arc is accreted to the Eurasian plate

crust, but as we go south, beyond Taitung, the volcanic islands (Green island, Orchid island; Fig.1.15; and, further south, Batan and Luzon islands; Fig 1.2) are separated from the emerged (i.e. Southern Central Range and Hengchun peninsula) and submerged (underwater Hengchun ridge) by a forearc basin (Fig. 1.14 and Fig. 1.15). Thick sedimentary series deposited in a forearc and intra-arc tectonic settings overlie the Luzon volcanic and volcanoclastic basement with an ending of volcanic activity at 6 and 3.3 Ma in the north and south, respectively [*Huang et al.*, 2006]. Thickness of sediments reaches 6-8 km with extremely high sedimentation rates up to 2500 m/Ma (Fig. 1.16). Deposition mainly occurred in marine environment with variably coarse turbidites all along its thickness. Subaerial sedimentary conditions are only reached in the topmost Pleistocene sediments (Milun and Pinanshan conglomerates, Fig, 1.16). The basal, Early Pliocene Fanshuliao Fm. witnesses the first sub-aerial conditions of the Taiwan wedge with slightly metamorphosed clasts starting being deposited at ca. 5Ma. Widespread coarse marine conglomeratic deposits characterise the Late Pliocene to Pleistocene Paliwan Fm. (Fig. 1.16), marking the initiation of the Central Range mountains and thorough erosion at ca. 3.5 Ma [*Teng*, 1990].

The Longitudinal Valley

The Longitudinal Valley forms a ~50 km long and ~2 km wide depression between the Coastal Range and the Central Range, and drains most of the latter. The Longitudinal Valley Fault, considered as the plate boundary separating the Eurasian plate and the Philippine Sea plate, runs along it (Fig. 1.13). This valley presents mélange type lithologies (i.e. Lichi mélange) with ophiolites in a sheared muddy matrix [*Chang et al.*, 2009a]. The Longitudinal Valley fault is accommodating about 40% of the convergence [*Yu et al.*, 1997], through a shallow-dipping west verging fault, thrusting the arc on top of the fore-arc. Because the long-term rock uplift or exhumation of the Central Range occurred at rates higher than the Coastal Range, the existence of a west-dipping Central Range thrust fault has been postulated, and seems to be active only in the central and northern part of the valley, accommodating a small portion of the total shortening [*Yu*, 2001; *Shyu et al.*, 2006].

This depression propagates southwards offshore to the Southern longitudinal through (Fig. 1.14), a depression filled with syn-orogenic sediments on top of a deformed forearc deposits [*Malavieille and Trullenque*, 2009]. This continuity evidences the genetic relationship between the fore-arc basement and the fore-arc deposits, and the rocks forming the LV. Indeed, the sheared pelagic mudstone early Pliocene in age contains ophiolitic, sedimentary and andesitic rocks, with very in-homogenous size distribution (i.e. from decimetric to kilometric) and represents the deformed fore-arc deposits with remnants of the fore-arc oceanic basement [*Chang et al.*, 2000; *Huang et al.*, 2008a; *Malavieille and Trullenque*, 2009]. Thus, the Taiwan Lichi mélange results from the deformation of the fore-arc basement and deposits and therefore is opposed to the typical mélange described elsewhere (e.g. Franciscan mélange in the USA), where the lithology is characterized by a deformed subduction complex.

The Central Range

The Central Range is composed of a slightly metamorphosed Oligocene to Miocene passive margin sediment succession, and its pre-Cenozoic basement. The Central Range is divided into the Backbone Range and the Hsuehshan Range. In the latter, the syn-estensional Oligocene series are present, conversely to the hiatus observed in the Backbone Range. Indeed, the Hsueshan Range is considered to be an inverted passive margin half-graben acting as a sink for Oligocene sediments [*Teng et al.*, 1991]. Conversely, the Backbone is composed by Eocene to Miocene sediments slate and sandstone, with a tendency of more coarser material towards the Eocene series [*Ho*, 1988]. Paleozoic to Mesozoic rocks of Eurasian affinity compose the metamorphic core (Fig. 1.15 and Fig. 1.16).

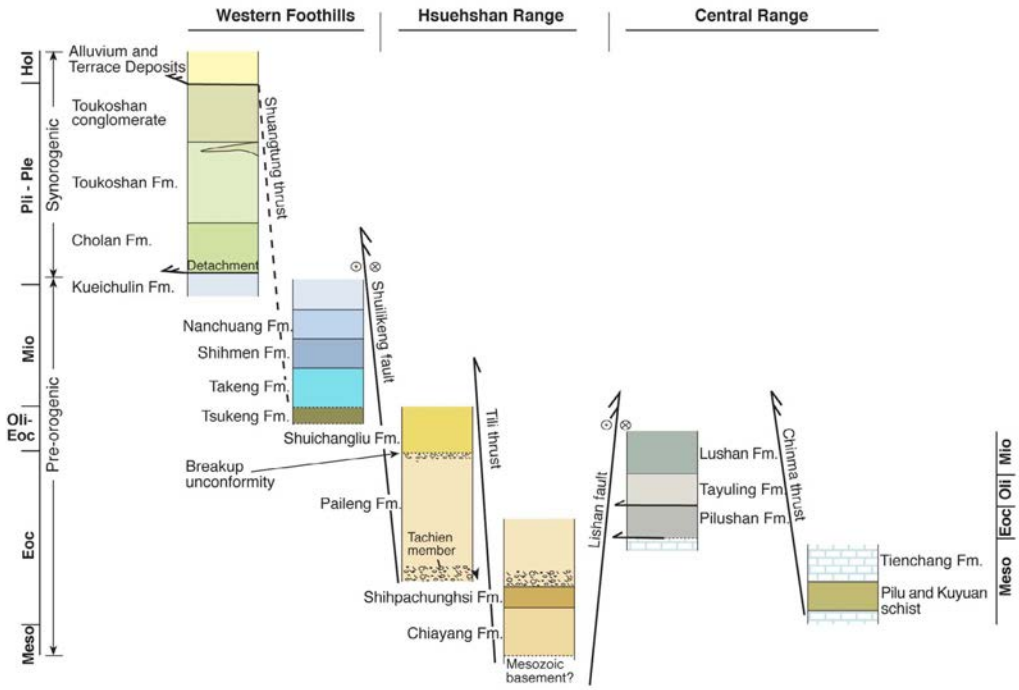

Fig. 1.16*: Tectonostratigraphy of the Central Range and Western Foothills of Taiwan. The preorogenic units are indicated for the Hsuehshan Range, as is the breakup unconformity. Ages of the formations in the Central Range are at a different scale. After Brown et al. (2012).*

The Central Range has undergone polyphased deformation and metamorphism. It shows at least two distinct sets of cleavage with a fan structure at the scale of the orogen [e.g. *Faure et al.*, 1991], either related to deeply rooted normal fault related rotation [*Crespi et al.*, 1996], to late stage backfolding [*Stanley et al.*, 1981; *Pelletier and Hu*, 1984] or as an inherent result of doubly-vergent wedge kinematics [*Fisher et al.*, 2007]. The eastern Central Range presents kinematic markers showing sinistral lateral extrusion as a result of the oblique convergence [*Fisher et al.*, 2002; *Pulver et al.*, 2002].
The current regime of the Central Range is extensional (cf. *Chapter 2*) mostly at shallow levels, while, at the same time, uplifting at rates up to 20 mm/yr [*Ching et al.*, 2011b]. Such apparent paradox is likely related to upper crustal level gravitational response to deeper, fast incorporation (i.e. underplating) of crustal material. Alternatively it can be an integral part of the orogenic development as

suggested by recent analog modelling of fold-and-thrust belts [*Haq and Davis*, 2008].

The Western Foothills and Coastal Plain

The Western Foothills are composed of west verging folded and faulted sediments ranging from Oligocene passive margin deposits to shallow-marine to fluvial Plio-Pleistocene syn-orogenic sediments. Stratigraphy is marked by the basal foreland unconformity dated to ca. 6.5 Ma, usually taken as the time of initiation of the orogenic loading and crustal thickening [*Lin et al.*, 2003]. The foreland sequence shows a gradual deepening followed by a rapid infill of the basin. Following initial loading, an overall transgressive sedimentary sequence was deposited (Kueichilun and Chinshui shale Fm; Fig. 1.17). From ca. 3.5 Ma a regressive phase marked by the appearance of the first slate clasts and reworked fossils, and rapid subsidence and sedimentation rates [*Chang and Chi*, 1983; *Lin et al.*, 2003] (Fig. 1.16) illustrates what is thought to be the main orogenic phase and a probable major topographic growth. The basin is then rapidly infilled until deposition of Pleistocene to sub-actual shallow marine to fluvial Toukoshan Fm. (Fig. 1.16). The thickness of the syn-orogenic Plio-Pleistocene series increases from North to South due to differential flexural response to the orogenic loading [*Lin and Watts*, 2002] and deposition is disrupted by a passive margin basement high (Peikang High; Fig. 1.2, Fig. 1.13 and Fig. 2.1) indenting the foreland and disrupting its stratigraphy [*Byrne et al.*, 2011; *Hu et al.*, 1997; *Lin et al.*, 2003] (Fig. 1.17).

The first structural studies in this area, giving birth to the fault-propagation folds and fault-bend fold deformations theories as well as the critical wedge theory [*Suppe*, 1981], considered the deformation as thin-skinned (i.e. not involving the pre-orogenic basement), but some quaternary and active faults associated with large earthquakes (M>6) in the Coastal Plain, and recent seismic data revealed the reactivation and inversion of old passive margin faults [*Wu et al.*, 1997; *Mouthereau et al.*, 2001a; *Rodriguez-Roa and Wiltschko*, 2010; *Ching et al.*, 2011a; *Chuang et al.*, 2013]. The implication of the basement in the foothills may suggest that the basement is also involved in the more pervasive deformation of the Central Range, as shown by the presence of Eurasian basement rocks in the metamorphic complex. The Western Foothills is currently accommodating about 50 to 60% of the total convergence [*Yu et al.*, 1997]. The Coastal Plain corresponds to the presently subsiding and non-tectonised passive margin and syn-orogenic sedimentary series corresponding to the lateral continuation of the offshore sedimentary series.

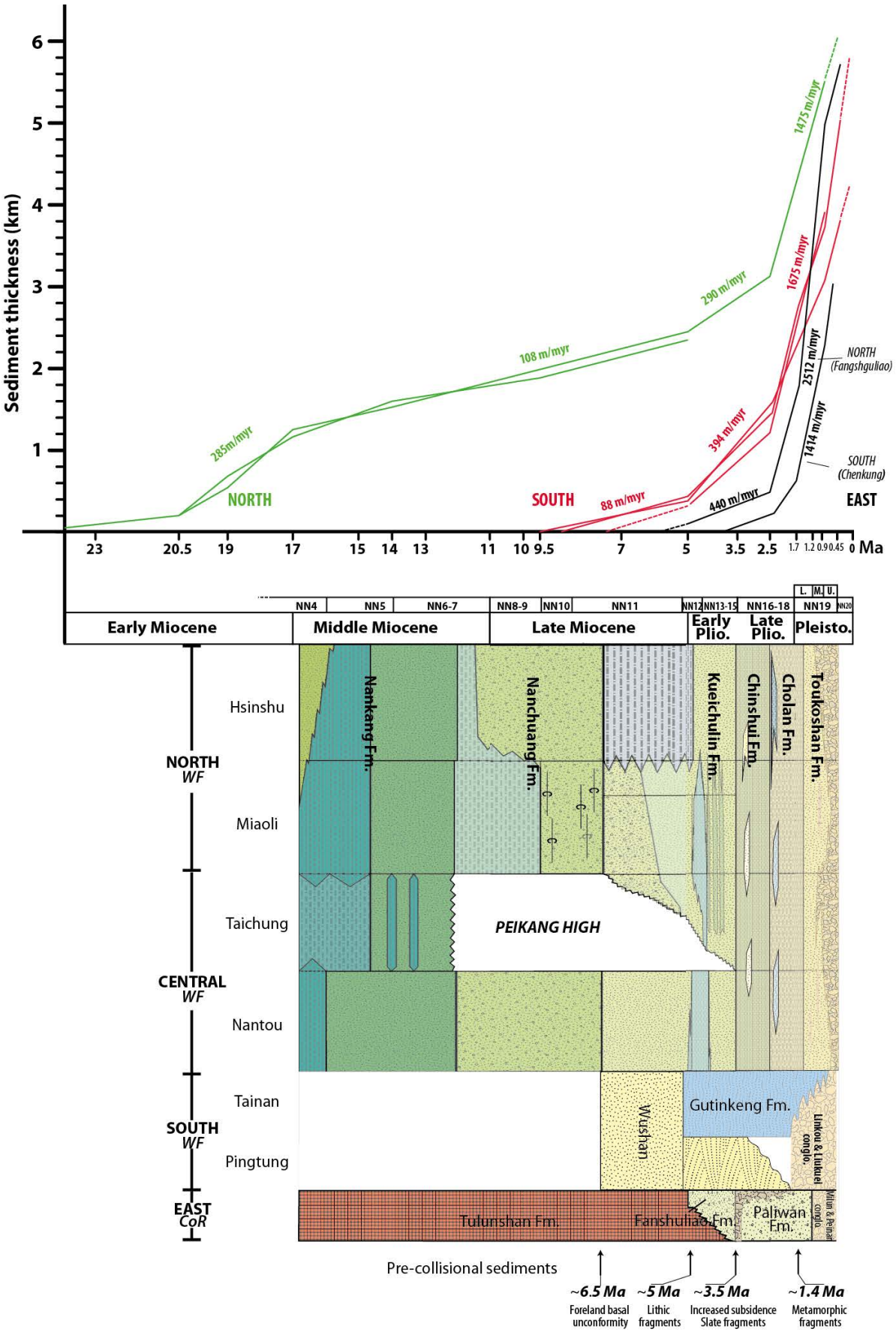

***Fig. 1.17**: Sedimentation rates and general chronostratigraphic chart as it is preserved in basins of the western foreland and Coastal Range. Sedimentation rates from* [*Chang and Chi*, 1983].

Stratigraphic chart partly based on a stratigraphic compilation kindly provided by Shao Pin from the Basin Research Group (principal researcher A. T.-S. Lin; National Central University).

The Kenting Mélange

In the western Hengchun Peninsula (Fig. 1.15), the southern tip of Taiwan, the Kenting ophiolitic mélange was emplaced onto the Eurasia margin after 10 Ma [*Pelletier and Stephan*, 1986a; *Chang et al.*, 2002, 2009a]. Recently acquired seismic velocities in southern offshore Taiwan show that the SCS is probably floored by a thin hyper-extended continental crust [Lester et al., 2013; McIntosh et al., 2013]. The Kenting mélange may therefore be viewed rather as a relic of the distal Chinese continental margin scraped off by tectonic inversion during collision, rather than a typical oceanic subduction mélange. In the east, adjacent to the Kenting mélange, post-rift sediments contain fragments of the pristine pre-collisional mantle (peridotites and serpentinized peridotites) associated with post-rift magmatism (plagiogranite and basalt) dated to 20 Ma (K-Ar dating; *Pelletier and Stephan, 1986*; Fig. 1.18). The same elements are present in the Kenting ophiolitic mélange, supporting the interpretation that it was formed as an olistostrome as the Miocene sediments were thrusted and then eroded [*Stephan and Pelletier,* 1986]. Its position in southern Taiwan, where transitional crust is observed, calls for a possible origin in the inversion of pre-collisional hyper-extended continental crust, in contradiction with inferences from past geochemical analyses, where oceanic affinity was inferred (*Pelletier and Stephan, 1986*) [see discussion in *Chapter 3*].

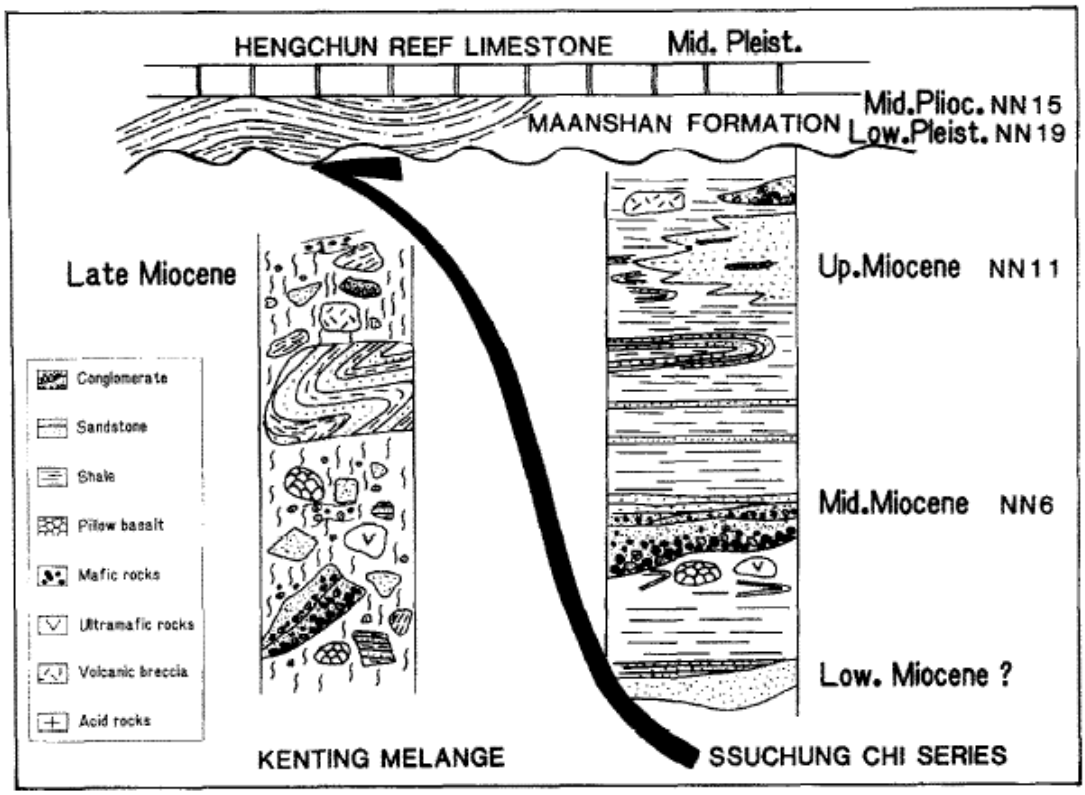

Fig. 1.18*: Stratigraphy and relationships between Kenting mélange (including nature of clasts) and post-rift Miocene sedimentation in Hengchung Peninsula. Conglomerates of the Ssuching Chi Series contain magmatic and ultramafic fragments that are found sheared in*

the Kenting Mélange. From Pelletier and Stephan [1986].

C. Exhumation and metamorphic history

1) Pre-Cenozoic metamorphism and deformation recorded in the Tananao metamorphic complex

The Tananao Metamorphic Complex (TMC) is the metamorphic and crystalline basement of the Taiwan orogen. It outcrops in the eastern divide (i.e. retro-wedge) and trends mostly North-Northeast, except in its northern part where the trend becomes East-West. Interestingly, the area where the metamorphic core outcrops in a North-South direction, corresponds to the area where the Luzon arc has been accreted (Fig 1.15), suggesting a link between arc accretion and basement exhumation. TMC is mainly composed of metasediments but plutonic rocks and ultra-basic rocks are also present mainly in its central and northern segments.

The Central Range's Eocene to Miocene sedimentary rocks are metamorphosed to the broad lower green-schist facies. This reflects both pre-orogenic conditions and collision overprint. Although, having undergone polyphased deformation and metamorphism related to the tectono-thermal history of the Eurasian continent before the Cenozoic, it presently displays Taiwan orogen's related deformation and metamorphism, with an overprinted greenschist facies and coherent schistosity with the sedimentary cover. Notably, prograde and retrograde P-T paths have been retrieved from the high-pressure rocks of Jiusui and Wanjung, recording subduction related metamorphism and subsequent collisional exhumation [*Beyssac et al.*, 2008].

In the following, we will review the geological characteristics of the TMC, its pre-Cenozoic and final collision related deformation and metamorphism.

The TMC has traditionally been subdivided into two metamorphic belts: The Yuli belt, which is in the easternmost part of the TMC, and the older Tailuko belt. Both are thought to be part of the Eurasian continental crust. The contact between these two units is not well defined [*Ho*, 1988], (Fig. 1.15) although the difference in metamorphic facies and structures suggests a faulted contact (i.e. Sofeng Fault; *Yen*, 1963]. For some authors, there is no clear difference between the two units and they consider them as a single bloc [*Wang Lee and Wang*, 1987]. However the presence of elongated (fault bounded?) ultra-basic rocks between the two units, particularly in the central part of the belt, may indeed indicate two independent units (Fig. 1.15).

The Taroko or **Tailuko belt** comprises the oldest rocks of the TMC , the marbles of the Changchun and Chiuchu formation. The protolith age is dated to late Permian using paleontological arguments or to 250 Ma using the Sr/Sr curve [*Jahn et al.*, 1986; *Jahn*, 2010]. The depositional environment was in an extensive continental platform and slope in a warm climate area permitting the deposition of thick carbonates. The same Permo/Triassic carbonates are well developed in mainland China coastal area and margin and have been found in drillings in the

Western Foothills [*Lan et al.*, 1996; *Jahn*, 2010], indicating its Eurasian affinity (Fig. 1.19). The metamorphism of these formation is dated to *193+/-15 Ma* and *242+/-22 Ma*, based on U-Pb isotope ages [*Jahn et al.*, 1986; *Jahn*, 2010], and may be the result of the Indosinian orogeny, well developed in SE Asia and South China [*Wang Lee and Wang*, 1987].

The Tienshiang mélange is presently overlying unconformably (i.e. deposited after the Indosinian cited above) on top of the Permian Taroko marbles. The protolith is interpreted as being mudstone and shale (now foliated quartz –mica schist) deposited in an oceanic basin, later accreted in a subduction accretionary prism where it was mixed to exotic blocs such as carbonates (now marbles), sandstones (now metasandstones), cherts (now metacherts), mafic rocks (now metabasites), and finally metamorphosed in the subduction accretionary complex. The depositional age of the matrix is thought to be Mid-Jurassic or older (Range between 175-200 Ma) [*Lan et al.*, 1996]. This mélange formation is interpreted as marking a Mesozoic suture.

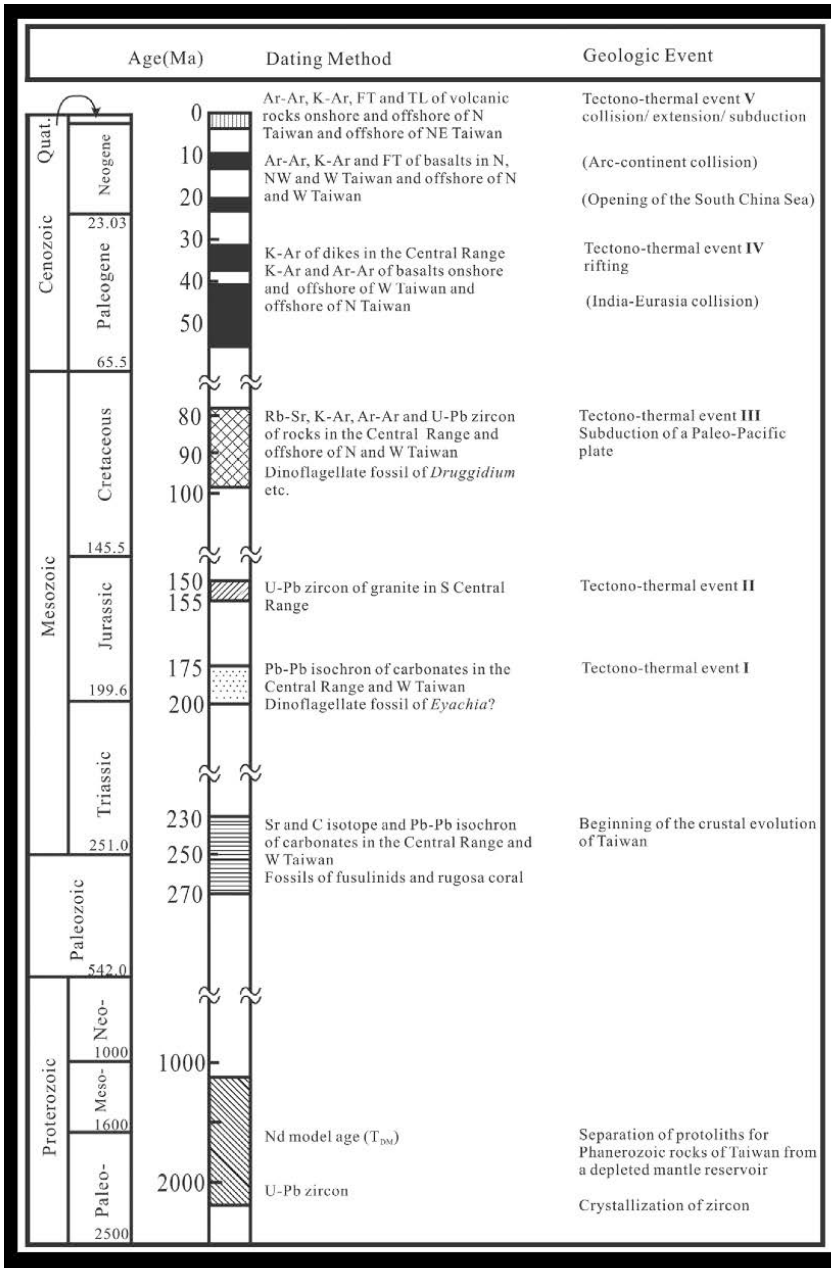

Fig. 1.19*: Tectono-termal events of the Taiwan metamorphic core* [*Lan et al.*, 1996, 2008].

Conversely to the Marbles, the Tienshiang Fm. has recorded polyphased deformation resulting in the development of several schistosities. Some authors recognize up to 6 deformational events within the TMC [e.g. *Stanley et al.*, 1981; *Wang*, 1979], however only two major events can extensively been recognized all along the TMC: a primary foliation, with crenulation locally developing S_2 schistosity (Fig. 1.20). The whole Tailuko sedimentary series were subjected to arc-type High T/P metamorphism in late Mesozoic times, around ~90 Ma [*Liou and Ernst*, 1984; *Ho*, 1988].

However this chronology seems to be in disagreement with the metamorphic chronology of the amphibolites and gneiss bodies in the northern Tailuko belt. Effectively, *Chen et al.* (1983) recognize an Early Mesozoic amphibolites facies

metamorphism (when the Tienshiang Fm. was not yet deposited?) followed by an upper amphibolite facies metamorphism due to granitic intrusion, and a final Cenozoic greenschist facies metamorphism related to the Taiwan orogenic event [*Chen et al.*, 1983]. Besides a more complex evolution of the gneiss and amphibolite units, the rest of the belt show 2 stages of green-schist metamorphism, pre-Cenozoic with a late Cenozoic overprinting.

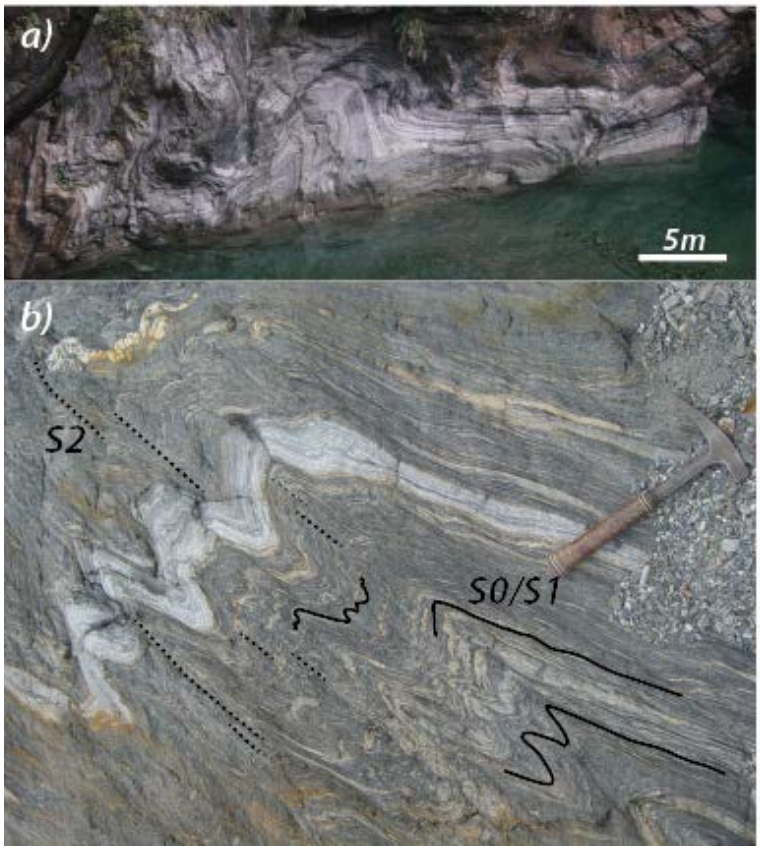

***Fig. 1.20**: a) Photo of the Tailuko marbles. Although the metamorphism is Early Mesozoic, the structures observed (here a plurimetric fold) and greenschist metamorphic facies are thought to result from the late Cenozoic collision. b) Photo of the Tienshiang mélange formation. We can recognize a primary foliation S1 (parallel to the elongated elements) and a secondary foliation S2 manifested here as crenulation folds and cleavage.*

The younger ***Yuli belt*** unit represents a mélange or Olistostrome, probably formed in a similar setting as the Tienshiang mélange. This similarity has led to amalgamate the two formations by some authors [e.g. *Wang Lee and Wang*, 1987]. The exotic blocs contained in the originally muddy-shaly mélange matrix (now black pelitic schists) are mainly of oceanic affinity [*Ho*, 1988]. Its depositional age is thought to be younger than the Tailuko belt, around middle Jurassic [*Ho*, 1988]. The age of the metamorphism has been dated to 78.8 Ma (Rb/Sr) and 94 Ma (Ar/Ar) [*Lan et al.*, 1996], roughly coeval to the late Mesozoic granitoid emplacement. The Yuli belt was subjected to accretionary trench high-pressure/low-temperature metamorphism leading to blue-schist metamorphism [*Ho*, 1988].

The pre-Cenozoic development of the TMC can be summarized in the following two stages:
1st stage: Deposition of the Tananao Schist from ca. 240-250 Ma.

2nd stage: Early Mesozoic metamorphism (193±15 Ma & 242±22 Ma) interpreted as the late expression of Variscan/Indosinian orogeny [*Jahn et al.*, 1986]. An accepted alternative chronology includes a Late Mesozoic

metamorphism high-T/low-P (Tailuko belt) and high-P/low-T (Yuli belt) associated to plutonic intrusions [*Ho*, 1988].

2) Cenozoic metamorphism

As mentioned earlier all the pre-Cenozoic metamorphism has been overprinted by more recent greenschist episodes. Subduction-related metamorphism is supported by the presence of ultra-basic ophiolitic exotic blocs in the Yuli formation and dated to 8-14 Ma [*Liou and Ernst*, 1984]. Prograde and retrograde P-T conditions have been recently retrieved from two exotic blocks within the serpetinized Yuli mélange indicating that the Yuli belt, and probably the Taroko belt, have been buried to depth ~35-40 km, before rapidly being exhumed to depth ~11 km at about ~15-10 Ma [*Beyssac et al.*, 2008] (Fig. 1.21). Independent evidences for continental subduction offshore southern Taiwan support such interpretation [*Eakin et al.*, 2014].

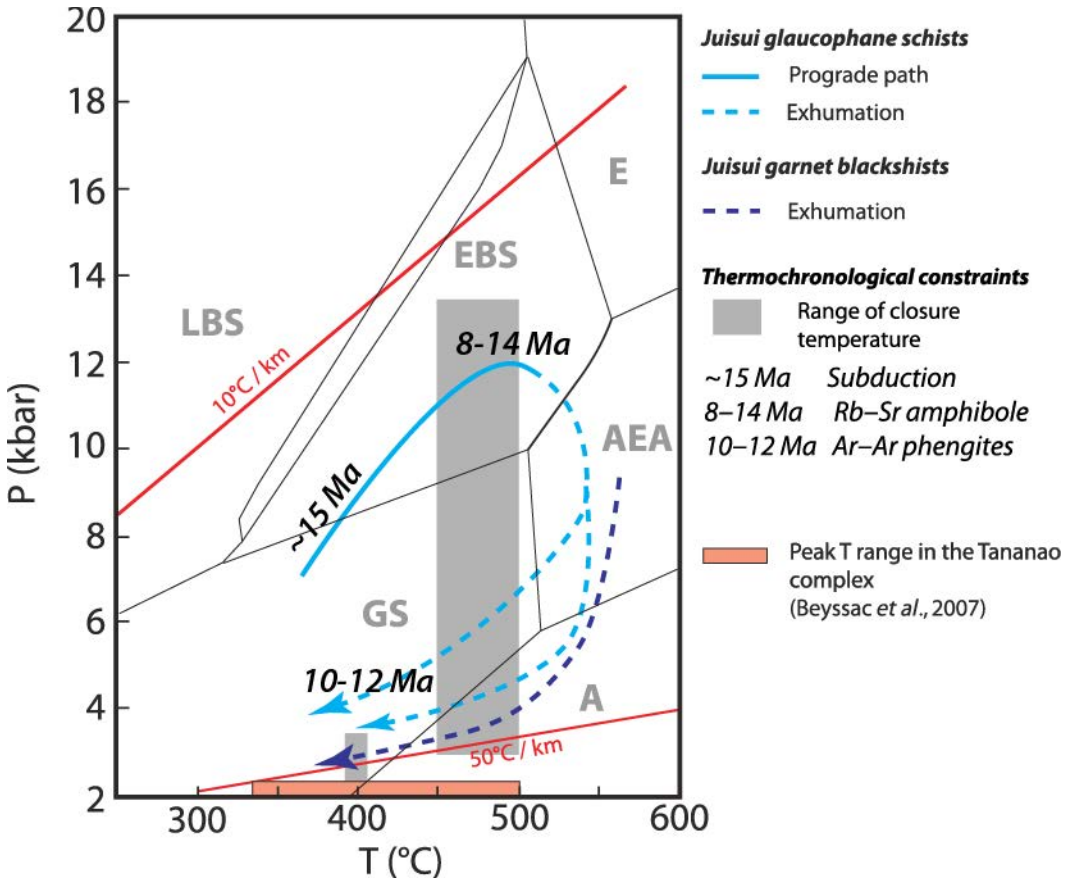

***Fig. 1.21**: Pressure-temperature-time path of the high-pressure rocks of the Juishui area belonging to the Yuli belt unit of the Tananao Metamorphic Complex. GS= greenschist; LBS = lawsonite blueschist; EBS= epidote blueschist; A= amphibolite; AEA = albite-amphibole amphibolite; E = eclogite. Red line indicates geothermal gradients potentially associated with prograde (10°C/km) and exhumational path (50°C/km) path of the high-pressure rocks of Juisui. Modified from Beyssac et al.* [2008].

The late Cenozoic greenschist metamorphism also affects the Eo-Oligo-Miocene passive margin series accreted into the Manila subduction complex, indicating a

common history with the TMC during the converging period. The eastern contact between the TMC basement and the cover seems to be sedimentary as highlighted by an erosional unconformity and the presence of basal conglomerates [*Suppe et al.*, 1976]. In the other hand, the western contact is mostly faulted, with the presence of elongated ultra-mafic bodies suggesting a deeply rooted structure (Fig. 1.15). These ultramafic bodies are the only subduction-related metamorphism. Otherwise, no obvious thermal discontinuity is found between the TMC and the sedimentary cover indicating that limited inherited metamorphism have been preserved [*Chen et al.*, 1983].

A penetrative cleavage is developed within both basement and cover, and exhibit a fan like structure [*Faure et al.*, 1991; *Fisher et al.*, 2007] in agreement with the double vergent orogenic model where topographic slope controls internal deformation in the wedge [*Willett et al.*, 1993]. Nevertheless, although locally coincident, the topographic divide and the apex of the schistose fan do not superpose all along the belt (Fig. 2.5), somehow disproving the inherent relation between topographic development and deformational pattern, or more likely precluding a more complex relationship. Moreover the cleavage apex appears to follow a structural contact in southern and central Taiwan (see *Chapter 3*) but is positioned within the TMC in northern Taiwan [*Lu et al.*, 2010a] (Fig. 2.5). More detailed aspects of the Cenozoic deformation of the Central Range are given in *Chapter 3*.

D. Models of mountain building

Since the birth of critical wedge theory in the 1980's Taiwan was considered the classical example of a thin-skinned accretionary wedge. Assuming the original critical wedge theory [*Davis et al.*, 1983] one may think that the thickening of the crust and subsequent creation of topography may be purely due to frontal accretion by thrusting. However, the Central Range presents the highest peaks and the deepest exhumed rocks of the whole island, while being currently in extensive regime, as shown by geological and geodetic evidences (*Crespi et al., 1996; Yu et al., 1997*). In the beginnings, the role of erosion although suggested, was still elusive. Analogue modeling (e.g. Malavieille*, 2010*) has shown that concomitant to the start of erosive processes, a deeper process comes into action, the so-called underplating (Fig. 1.22). Underplating basically consists in duplexing of material from the subducting plate at depth, and incorporation into the wedge across the décollement level. *Malavieille et al. (2009)* recall the main mechanism of wedge growth in Taiwan: frontal accretion in the Western Foothills, underplating in the Central Range (explaining the high exhumation rates in this area) and incorporation of the forearc into the wedge by backthrusting.

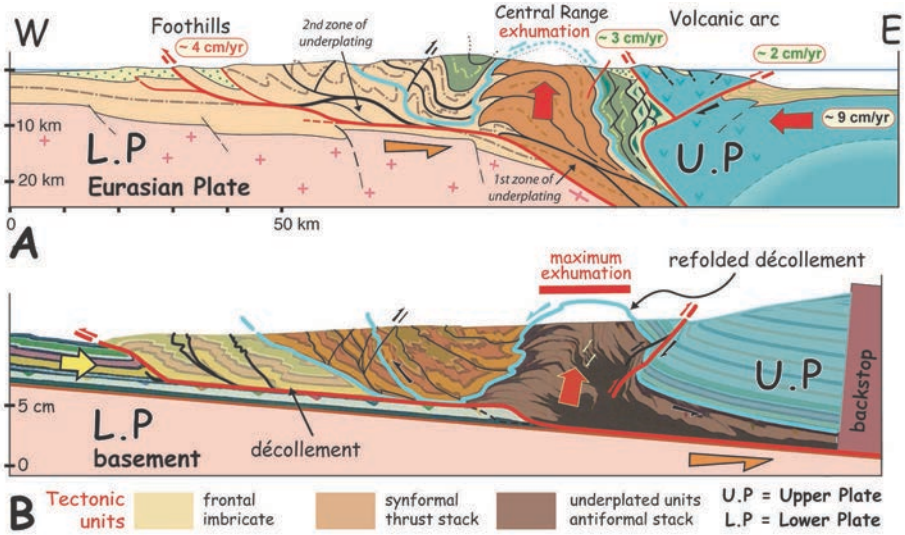

Fig. 1.22*: (A) interpretive geological section of Taiwan inspired by (B) analogue experiment with décollement and erosion. After Malavieille (2010).*

With the advent of low-temperature thermochronological techniques sensible to orogenic processes at different crustal depth, quantification of particle paths on the orogenic wedge became possible. Low-temperature thermochronology has been extensively applied to the Taiwan orogen, covering the Central Range [*Liu*, 1982; *Tsao et al.*, 1992; *Lo and Onstott*, 1995; *Tsao*, 1996; *Liu et al.*, 2000; *Willett et al.*, 2003; *Dadson et al.*, 2003; *Fuller et al.*, 2006; *Lee et al.*, 2006; *Beyssac et al.*, 2007; *Clift et al.*, 2008b; *Kirstein et al.*, 2010b], the Coastal Range intra-arc and forearc sediments [*Liu et al.*, 2001; *Huang et al.*, 2006; *Kirstein et al.*, 2010a, 2013], and the Western Foothills foreland sediments [*Liu et al.*, 2001; *Fellin et al.*, 2006, 2008, 2009, 2012; *Lock*, 2007; *Lock and Willett*, 2008; *Nagel et al.*, 2012a]. Additionally, data exist on the igneous rocks of the northern Luzon arc and Coastal Range [*Yang et al.*, 1995, 2003]. Most of the data (except the one published in conference proceedings) was recently compiled by [*Simoes et al.*, 2012].

Fig. 1.23 shows a compilation of reset zones for different thermochronometers. Reset zones delineate a nested pattern with higher temperature systems being included within lower temperature ones centred along the metamorphic core. Details on the existing thermochronological datasets in Taiwan are given in *Chapter 3.*

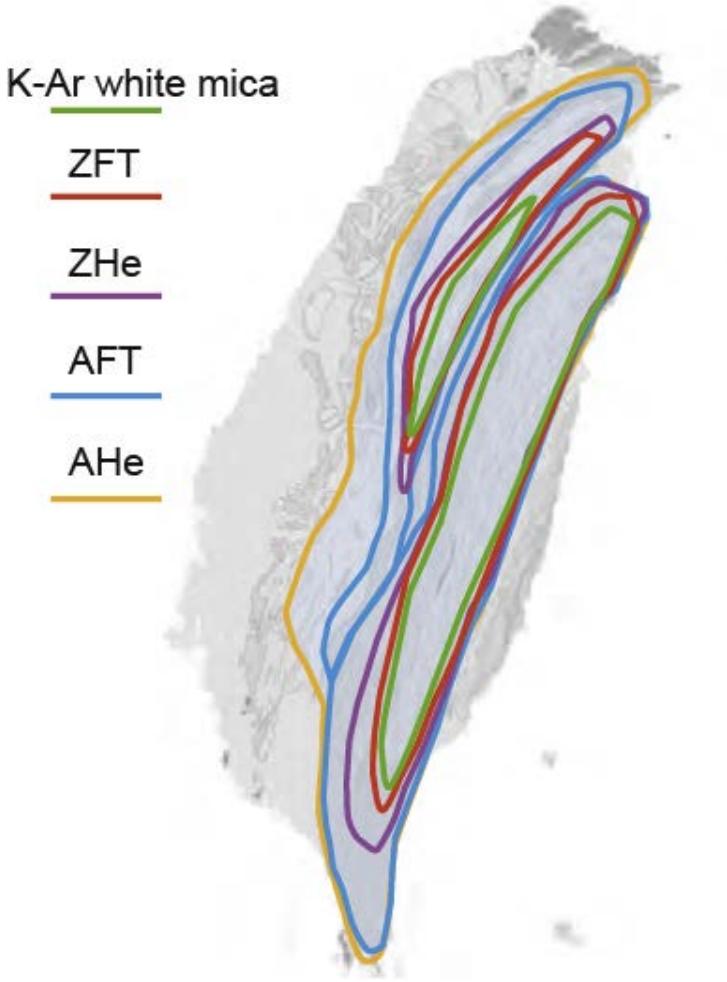

***Fig. 1.23**: Reset zone of the different low-temperature systems from Simoes et al. [2012]. A sample was considered as reset when cooling ages are younger than 5 Ma. Note that some of the zones are inferred from a few data points so that it has a nested pattern. AHe and ZHe= (U-Th)/He on apatite and zircon respectively; AFT & ZFT = apatite and zircon fission tracks, respectively. K-Ar = Potassium-Argon.*

1) Thermo-kinematic models with dominant subduction of the Chinese margin crust

Two main 2D thermo-kinematic forward model have been published to date [*Fuller et al.*, 2006; *Simoes and Avouac*, 2006 and *Simoes et al.*, 2007a]. Both approaches are based on the solution of the heat advection equation, but *Fuller et al.,* [2006] also integrates coulomb wedge properties so that the mechanics of brittle deformation are respected (Fig. 1.24). Both studies impose an *ad hoc* window in which vertical movements mimic the effect of underplating of the upper crust below the upper décollement, in order to fit surface deformation, thermochronological (Fig. 1.23) and metamorphic data. Underplating likely occurs as ductile duplexing, but ductile deformation is not explicitly taken into account in any of the modelling mentioned above. Underplating can represent up to 50% to 100% of the total accreted materials, which is significantly larger than the initially proposed 10-25% *(Barr and Dahlen, 1989*). One main assumption in this model is the subduction of the continental margin lower crust, a fact not proved by geophysical studies onland Taiwan where no subducting slab is imaged under the Central Range [e.g. *Wu et al.*, 2004, 2007].

The main virtue of these models it to highlight the role of deeper processes, as opposed to frontal accretion but do not take into account ductile deformation and the absence of lower crust subduction.

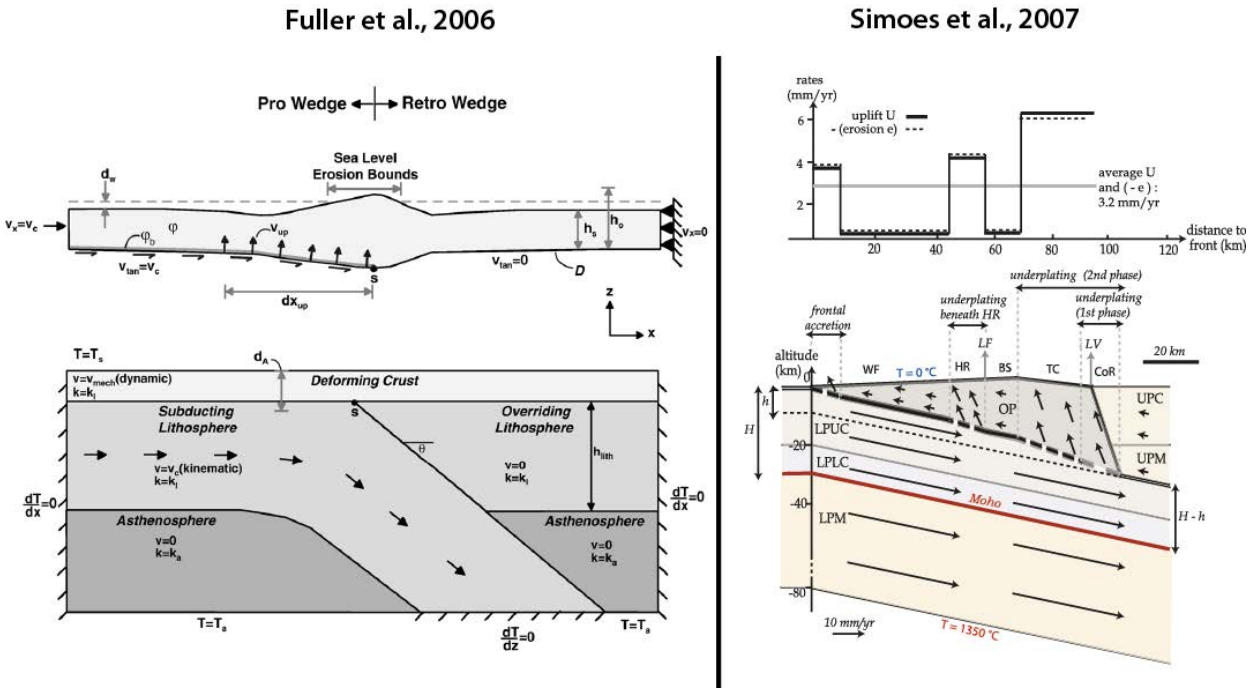

Fig. 1.24*: Geometry of two thermo-kinematic models, involving the upper crust in the collision and reproducing metamorphic and thermochronological data. Fuller et al. (2006) includes coulomb wedge rheological behaviour.*

2) A thermo-mechanical model with dominant accretion of the Chinese margin crust

A third fully-coupled thermo-mechanical model by *Yamato et al.* [2009] intends to account for the rheology of the Chinese margin without prescribing a kinematic field to reproduce the data (Fig. 1.25). They show that ductile thickening is required below the Central Range, and results from the accretion of the lower crust in the collision. Here, thermal advection in the orogen is simply the consequence of shortening of the originally deep, hot and ductile crust, and of the vergence of subduction. No underplating window is assumed to explain rapid heat advection and young cooling ages observed in the Central Range.

The model also considers that a significant part of the moderate greenschist metamorphism observed in Taiwan is inherited, thus limiting the effect of syn-orogenic burial, but favouring a key role played by the Chinese margin. In this model, decoupling between upper and lower crust occurred within the wedge as the material is advected to the east. This allows different accommodation of plate convergence that mimics the assumed underplating effects, i.e. low shortening at the surface and rapid exhumation in the Central Range. Evidences of a seismogenic deep crustal thrust ramp down to 20 km a the front seems to support the view that Taiwan can grow by accretion of the whole crust (*Chuang et al., 2013*). This also generally agrees with high erosion rates that promote rapid heat advection and the lack of present-day shortening across the Central Range.

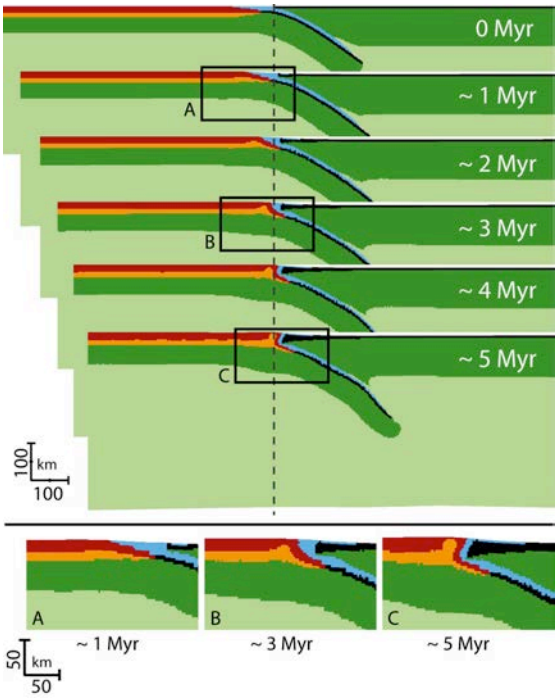

Fig. 1.25: Left panel: Evolution of the thermo-mechanical model during 5 Myr for the reference experiment of Yamato et al. (2009). The stage at 5 Myr is believed to correspond to the present-day configuration. Detailed view (left down) at the end of the model run. Metamorphic facies zones are calculated from the P-T conditions at final stage at 5 Myr. Note that the strain rates distribution indicates shear zones in the lower crust. Abbreviation: Amph., amphibolite facies; B.S., blueschist facies; Ecl., eclogite facies; Ecl.(c), eclogite with coesite; Gr., granulite facies; G.S., green schist facies; zpp, zeolithe-prehnyte-pumpellyite facies. Lower panels: Top - Predicted (blue line) and observed topography (white dots). Erosion rates as well as erosion/sedimentation fluxes are calculated over the last computed increment of deformation and is equivalent to the current erosion rates. Bottom – distribution of metamorphic facies and strain rates from the model.

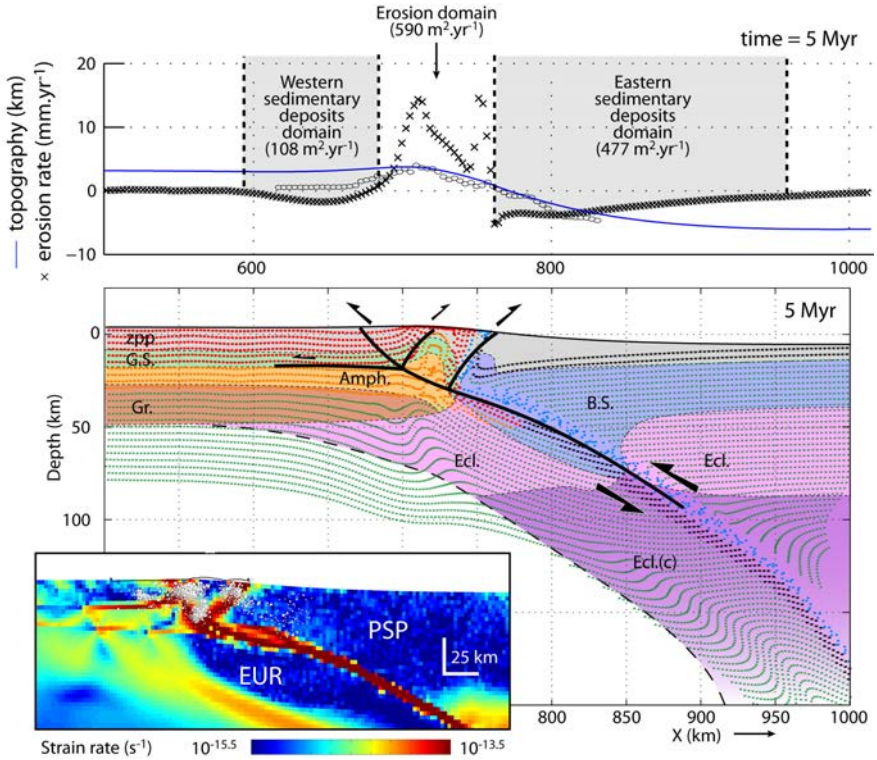

Altogether these models highlight that thermochronology and metamorphism can be reproduced with very different models, there is not a unique solution. Further geophysical constrains imaging the base of the crust in Taiwan and/or the geometry of the subducting slab, if any, may help to discern between a whole

crust and an upper crust involvement in deformation. Models incorporating geophysical evidences, rheologically plausible and thermochronological and metamorphic constrains may improve our knowledge on Taiwan orogen.

Chapter 2: Structure of the southern Taiwan Central Range

In this chapter, I first summarize the main structural features of the Central Range of Taiwan based on existing studies, then I present the geological and structural data collected during my own field expeditions in the southern part of the Central Range. Finally I propose a deformational sequence for the studied area and a regional geological cross-section.

I. Southern Taiwan: bridging the gap between oceanic subduction and arc collision

As described in the previous chapter, Southern Taiwan represents the onshore extension of the Manila trench accretionary wedge and the transition from oceanic subduction to arc-continent collision (Fig. 2.1). While in central and northern Taiwan the Eurasian pre-orogenic basement (i.e. Tananao Metamorphic complex - TMC) outcrops in the retro-wedge of the orogen, in southern Taiwan the whole passive margins cover series accreted in the Manila trench are well preserved. These sediments have recorded the early history of the wedge, from submarine deformation, associated with the early crustal thickening stages, to subaerial exposure and topographic development as the weakly-thinned crust and the volcanic arc started being involved in the deformation.

Straightforward first-order structural relationships can be made between the subaerial Taiwan wedge and its submarine counterpart. From west to east, the main ones are:

- The central Taiwan ***Peikang High*** (PK in Fig. 2.1) is in the continuity of the passive margin, basin bounding, offshore bathymetric high, as evidenced by sedimentological [e.g. *Chang and Chi*, 1983; *Lin et al.*, 2003] and gravimetric arguments (e.g. *Byrne et al. 2011*) and by simple bathymetric correlation.
- The southwestern ***Taiwan deformation front*** (DF in Fig. 2.1) is materialised onshore by the Tainan fault [e.g. *Mouthereau et al.*, 2001, 2002; *Lin et al.*, 2009] which is in continuity of the offshore deformation front [*Lin,* 2009].
- The ***Pingtung piggy-back basin*** (PB in Fig. 2.1) appears as the onshore extension of the Cenozoic Tainan basin (also known as Taixinan basin; Fig. 2.1), now partly incorporated and deformed into the wedge. The Pingtung basin west bounding fault, the Chishan fault (CF in Fig. 2.1), is the onshore extension of the underwater out-of-sequence thrust (OOST in Fig. 2.1 and Fig. 2.2.) bounding to the west the upper-slope of the submarine accretionary wedge [*Lin et al.*, 2009] (Fig. 2.2).

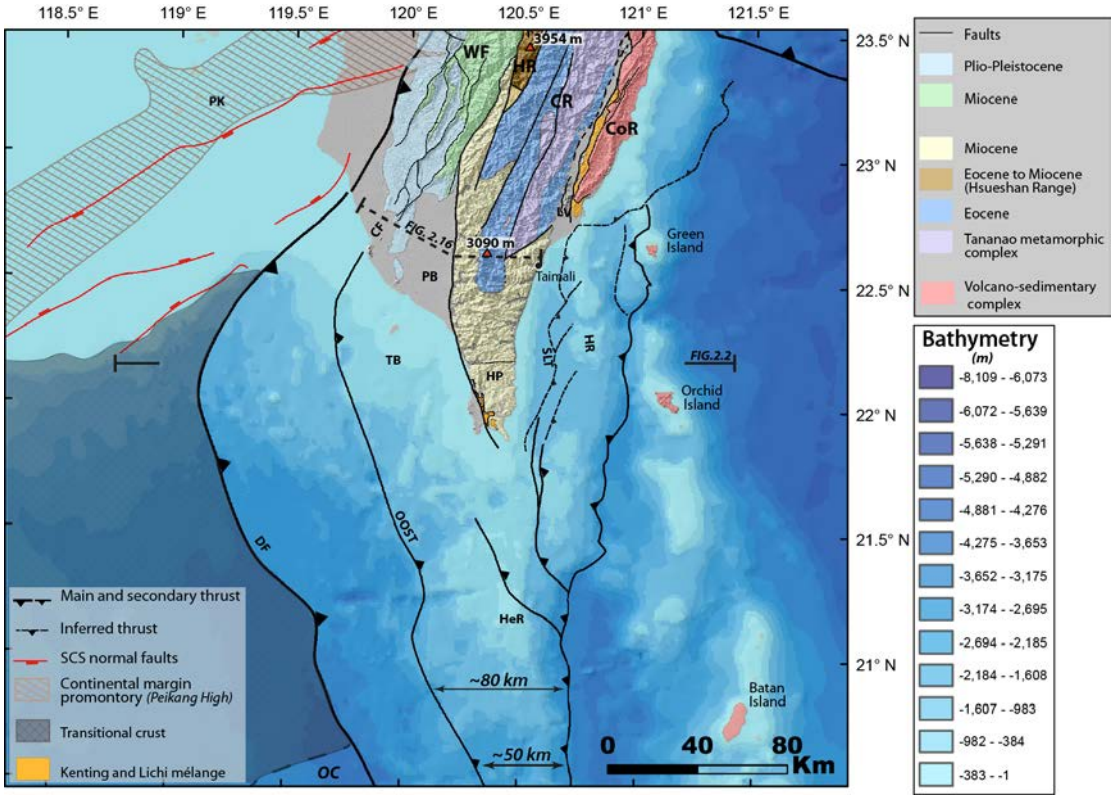

Fig. 2.1*: Onshore geology and submarine southward extension of the Taiwan orogen. The upper slope west-bounding fault (out-of-sequence thrust, OOST) is the prolongation of the Chishan fault (CF) onshore. The Huatung ridge (HR) is the prolongation of the Longitudinal Valley fault. The continental margin promontory (Peikang high, PK) is interpreted as the edge of the normal thickness continental crust (drawn after* [*Byrne et al.*, 2011]*). Note the early offshore developments of a backthrust deforming the upper plate forearc. The Hengchun Ridge (HeR) increases in width and bathymetry as the transitional continental crust starts to be incorporated into the wedge. Offshore faults based on* [*Lin et al.*, 2009; *Malavieille and Trullenque*, 2009]*. Transitional crust inferred from bathymetry in the NE. PK =Peikang High; DF= deformation front; OC= oceanic crust; HeR = Hengchun ridge; HR= Huatung Ridge; SLT = southern longitudinal through; PB = Pingtung basin; TB = Tainan basin; CF = Chishan fault; OOST = out-of-sequence thrust; WF = western Foothills; HR = Hsuehshan range; CR = Central range; CoR = coastal range.*

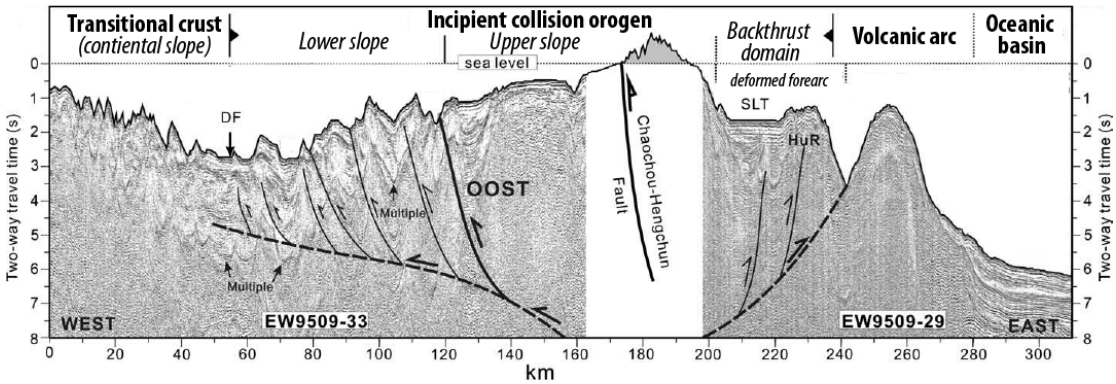

Fig. 2.2:*Seismic reflection line across the submarine accretionary wedge and Hengchun peninsula. Abbreviations are the same as in Fig. 2.1. Location shown in Fig. 2.1. Modified after Lin et al.*[2009].

- The submarine ***accretionary wedge*** (Hengchun Ridge, HeR in Fig. 2.1), can be followed from the Luzon island (Philippines) all along to the Hengchun peninsula (Fig. 1.2 and 1.8). We can remarkably recognise a discrete change in the submarine geometry of the inner wedge (comprising the upper-slope and backthrust domain, Fig. 2.2) in front of the Batan islands (~N20°, Fig. 2.1), where the wedge almost doubles its width and reduces to half its bathymetry: from ~50km width and -1.8km below sea level at latitude 20°N, to 80km and -0.8km at latitude 21.2°N. This change is interpreted as the initiation of collision by some authors [e.g. *Byrne et al, 2011*] as the transitional continental crust starts to be incorporated into the wedge *[McIntosh et al., 2013; Lester et al., 2013]*. Nevertheless, wedge growth may also be related to an increased terrigenous input from the approaching Taiwan and Chinese continent.
- The ***Longitudinal Valley*** (LV in Fig. 2.1) is the onshore extension of the southern longitudinal through (SLT in Fig. 2.1). The LV is associated to the Lichi mélange representing the shortened (subducted and/or accreted?) forearc basin [*Chang et al.*, 2002; *Malavieille and Trullenque*, 2009]. The longitudinal valley fault extends offshore as a distinct bathymetric high, the Huatung Ridge (HR in Fig. 2.1). Numerous west and east verging faults and folds [e.g. *Malavieille and Trullenque*, 2009] seismically active [e.g. *Wu et al.*, 1997] have been described in the fore-arc basins between the Taiwan island and the northernmost islands of the Luzon arc (i.e. Green and Orchid islands), indicating deformation of this domain (partly incorporated to the wedge?) before totally disappearing (Fig. 2.1 and 2.2).

Such onshore-offshore correlations highlight the importance of submarine, pre-subaerial exposure history of the accretionary wedge. In particular, the role of the rift-related heterogeneities (e.g. Peikang High and transitional crust), the development of backthrusting in the submarine sedimentary wedge and the processes through which the fore-arc basin and crust are deformed and overthrusted by the Luzon arc and probably partly incorporated into the wedge before the arc-continent collision occurs.

A related issue is the process sustaining Southern Taiwan topography, south of Taitung (~N22.7°, Fig. 2.1), where arc accretion/collision has not yet taken place. In this area the Luzon arc is still positioned at ~50-60km to the East but topography locally reaches 3090m (Peitawushan mountain, Fig. 2.1). Progressive underplating of the distal margin [*Lester et al.*, 2013; *McIntosh et al.*, 2013; *Eakin et al.*, 2014] and possibly the incorporation of forearc sediments and crust to the wedge [*Malavieille and Trullenque*, 2009] are the likely processes contributing to the early crustal thickening and subaerial topography before the Luzon volcanic arc is accreted onto the passive margin sedimentary series and crust.

In this chapter I focus on the southern Taiwan Central Range, an area where the Luzon volcanic arc has not yet collided. The southern Central Range preserves the pro- and retro-wedge passive margin sedimentary series conversely to the central and northern Central Range where only the pro-wedge sedimentary series are still outcropping. It is thus likely that the different stages of deformation of this area record good part of the orogenic development.

The issues I try to shade light in this chapter can be summarised in the following main points:

- Is the deformational style and kinematics thoroughly described in the central and northern part of the Central Range valid for the southern Central Range? Is there a decoupling between the sedimentary cover of southern Taiwan and the basement found further north?
- What are the processes involved in the early crustal thickening? Diffuse or more localised strain? What is the relative role of underplating, forearc closure, ductile strain and faulting?

In order to answer these questions I will first review the general characteristics of the Central Range and summarise the results of the existing studies. I will present my own study area, results and interpretation.

II. Active tectonics and long-term deformation of the southern Central Range

A. Seismological and geodetic observations in the Central Range: implications for crustal thickening

Seismicity in the whole Central Range is very shallow (<~12km) and with dominant extensional and strike-slip focal mechanism [e.g. *Wu et al.*, 2004; *Mouthereau et al.*, 2009; Fig. 2.3b and Fig. 2.3c]. The shallow seismogenic crust of the Central Range overlies a low-viscosity zone at depth [*Rousset et al.*, 2012] and is associated to high geothermal gradients [*Chi and Reed*, 2008] suggesting a relationship between the high exhumation rates of the Central Range (inducing heat advection) and a hypothetical extrusion of the ductile crustal levels (i.e. Eurasian basement). The cut-off depth of seismicity below ~12km has been attributed to a present day temperature of 350ºC at ~12km depth [*Wu et al.*, 1997; *Lin*, 2000; *Kuo-Chen et al.*, 2012a] but the geothermal gradients implied (i.e. ~30ºC/km; *Kuo-Chen et al.*, 2012a) are not consistent with the shallow geotherms from sub-surface measurements [*Chi and Reed*, 2008].
In any case, the inference of ductilly extruded lower crustal levels is supported by seismogenic derived strain rate orientation suggesting a top-to-the-east transport [*Mouthereau et al., 2009*] and by thermo-mechanical modelling of a rheologicaly-layered crust [*Yamato et al., 2009; Fig. 1.25*].

The Moho depth in the Central Range is relatively poorly constrained but some estimates exist. In the Western Foothills it reaches ~30km [*Ma and Song*, 1997], and reaches its maximum thickness of 50-70 km under the central part of the Central Range [*Wu et al.*, 1997; *Kuo-Chen et al.*, 2012b; *Ustaszewski et al.*, 2012]. In the southern Central Range Moho depth has been estimated to 40-50km and interestingly overlies mantellic high-velocities zones that may result from the eclogitization of oceanic or continental material as recently suggested [*Kuo-Chen et al.*, 2012b]. *Ustaszewski et al.* [2012] interpreted P-wave isovelocities of 7.5 km/s as the moho boundary (Fig. 2.3a).

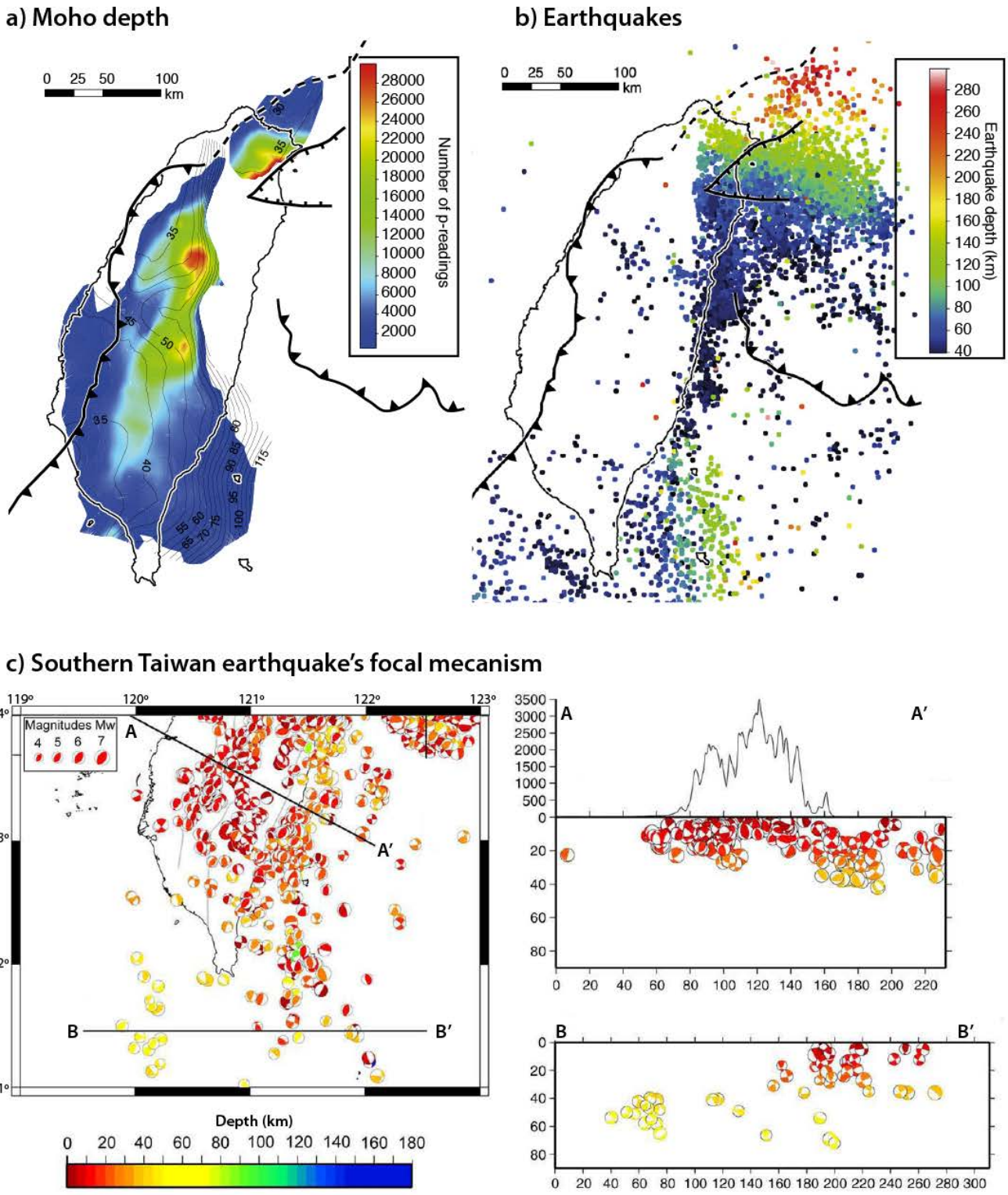

Fig. 2.3*:Moho depth, earthquakes depth and focal mechanism of Taiwan. a) Moho depth (contours) and number of p-wave counts (color) for the whole Taiwan island. Number of counts correspond to the ray coverage per cell and can be taken as the reliability of the Moho depth estimation. Modified from* [*Ustaszewski et al.*, 2012]*; b) earthquake depth an distribution for the whole Taiwan island. Modified from* [*Ustaszewski et al.*, 2012]*; c) Distribution of focal mechanisms of earthquakes in the southern half of Taiwan. The database covers events reported during 11 years (1995-2005) in the BATS (Broadband Array in Taiwan for Seismology) catalogue. Right panel shows distribution depth distribution along the two cross-sections positioned on the left panel. Modified from* [*Mouthereau et al.*, 2009].

GPS horizontal velocities display practically inexistent shortening in the Central Range. Instead, there is rather a significant left-lateral motion and extension (Fig.2.4) in agreement with seismicity. In the other hand, GPS vertical velocities and levelling indicate surface uplift rates reaching up to 18 mm/yr., with higher rates reached in the eastern Central Range (*Ching et al., 2011a*; Fig. 2.4). The lack of horizontal shortening in the Central Range contrasts with high shortening rates accommodated across the Longitudinal Valley to the east and the Western Foothills to the west (Fig. 2.4). The southern part of the Western Foothills presents a counter-clockwise rotation of the horizontal GPS vectors interpreted as the result of tectonic escape in this area [*Lacombe et al.*, 2001; *Ching et al.*, 2007a; *Hu et al.*, 2007]. This phenomenon has also been described to happen in the northeast part of the Taiwan island [e.g. *Angelier et al.*, 2009].
Somehow surprising is the dominant subsidence observed along the southeastern coast and the southern end of the Central Range (i.e. Hengchun peninsula) (Fig. 2.4). This probably reflects a transient signal and highlights the caution that needs to taken when extending geodetic values over longer, geological timescales.

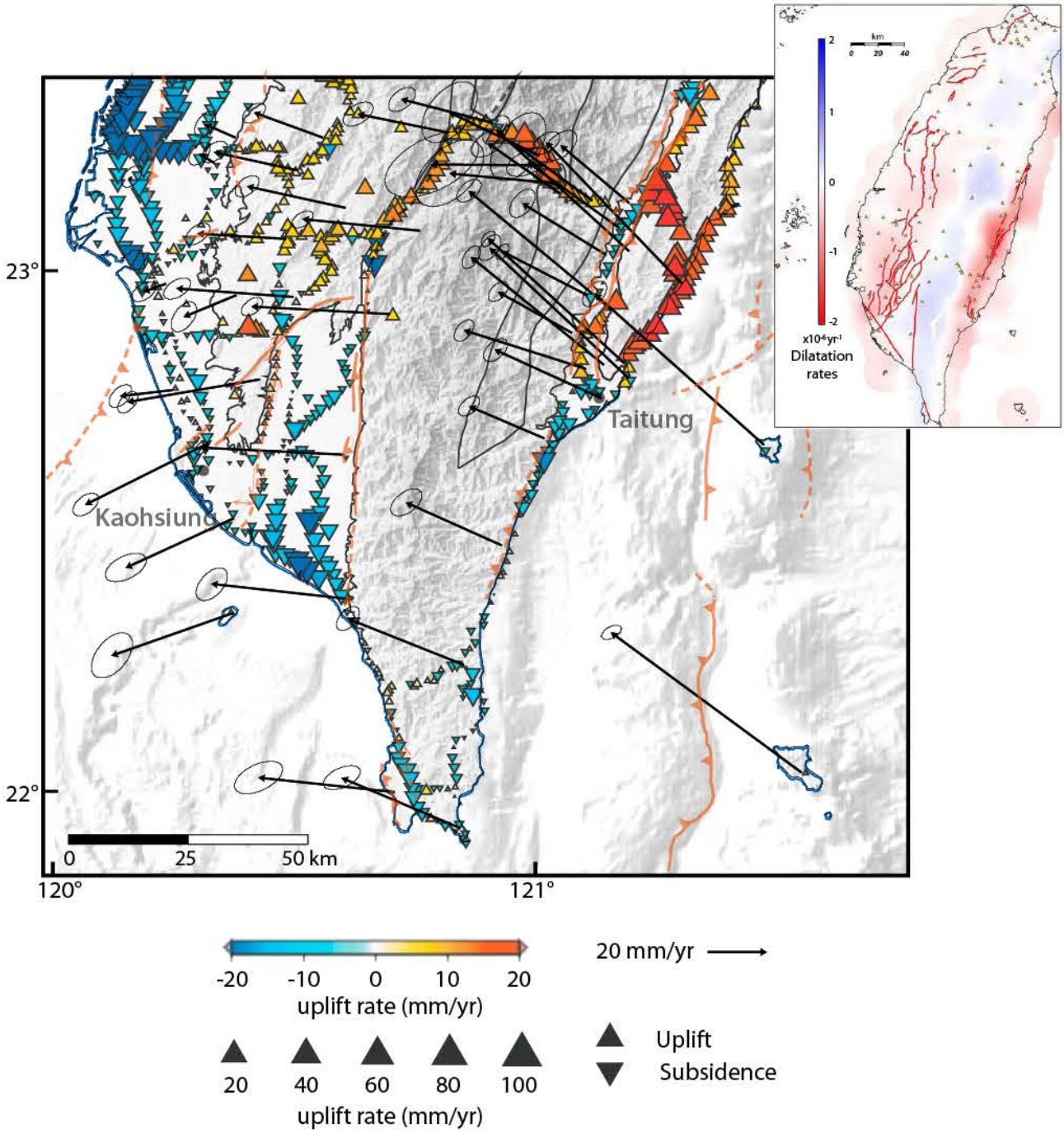

Fig. 2.4*: Present-day horizontal and vertical motion in the southern half of the Taiwan island. GPS horizontal velocities measured between 1995 and 1999 relative to Penghu island (Eurasian continent) with 95% confidence ellipses from [Yu et al., 1997]. Amalgamed GPS (199 continuous measurement) and levelling (1843 measurements) surface uplift rates between 2000 to 2008 after [Ching et al., 2011a]. Active faults from* [*Shyu et al.*, 2005a] *are shown in red. Top-right panel shows, dilatation calculated based on the strain rate field derived from the 1990-1995 GPS data for the whole Taiwan island. The red colour reveals area reduction (or 2D contraction) while the blue colour indicates area expansion (or 2D extension); modified from* [*Mouthereau et al.*, 2009].

Overall, seismicity and geodesy indicate that the brittle crust in the southern Central Range is shallow and currently in a dominant transtensive regime, while at the same time uplifting at very high rates. Both observations indicate that

shortening and crustal thickening is very likely taking place at deeper levels within the ductile crust. The presently high surface uplift rates and the higher long-term exhumation rates of the eastern Central Range [e.g. *Simoes et al.*, 2012] combined with the probable role ductile deformation in the building of the Central Range favour the idea of a ductile extrusion (ductile flow?) of the metamorphic units of the belt, as argued by a number of works [*Lin and Roecker*, 1998; *Yui and Chu*, 2000; *Lin*, 2002; *Yamato et al.*, 2007].

The mechanism behind this process remains to be unravelled, but one could imagine a similar mechanism as the one proposed for the Himalayas, namely the channel flow [*Beaumont et al.*, 2001]. The analogy needs to be taken with caution as difference in the tectonic setting and scale is significant (e.g. arc-continent vs. continent-continent collision; large vs. small orogen; absence of the Tibetan plateau weight in Taiwan). Nevertheless the comparison is still interesting to understand the processes. The main similarities are:

- Peak metamorphic temperatures increasing structurally upward (inverted metamorphic series; *Jamieson et al.*, 1996) with the oldest and originally deeper rocks of the Taiwanese metamorphic core (i.e. Taroko marbles) outcropping in the middle part of the Taroko belt (Fig. 1.15; *Yui and Chu*, 2000).
- The Taiwanese metamorphic core is bounded to the west by an oblique normal fault and to the east by a oblique thrust fault [*Gourley et al.*, 2007]. However in the central part of Taiwan, the east bounding fault (i.e. Central Range fault) is enigmatic and of limited seismic activity.
- The activation of the channel ductile flow in the Himalayas has been related to an increase monsoonal precipitation and erosion [*Clift et al.*, 2008a], but in Taiwan such an erosional asymmetry is not seen in present-day precipitation patterns (fig. 3.1). However other erosional processes such as glaciation may control long-term erosion (cf. *Chapter 3*).

B. Geology and deformation of the Central Range: a review

The following part aims to review the state of the knowledge on the geometry and play of the main faults and deformation style of the Central Range.

1) Major contacts: Crustal-scale faults and reactivated sedimentary contacts

In the southern Central Range, *four* main geological contacts are observed (Fig. 2.5):

- **Contact 1**: The west bounding contact juxtaposing the Central Range units with the Western Foothills (in central Taiwan), with the Pintung basin quaternary fill (in southern Taiwan) and with the coast and quaternary terrace (in the Hengchun Pensula).
- **Contact 2**: The east bounding contact juxtaposing the Central Range units with the Lichi Mélange and the Longitudinal valley quaternary fill.
- **Contact 3**: The contact between the Miocene Lushan Fm. and the Eocene Pilushan Fm.

- **Contact 4**: The contact between the Tananao Metamorphic Core (TMC) and the sedimentary cover (Eocene Pilushan Fm. and the Miocene Lushan Fm).

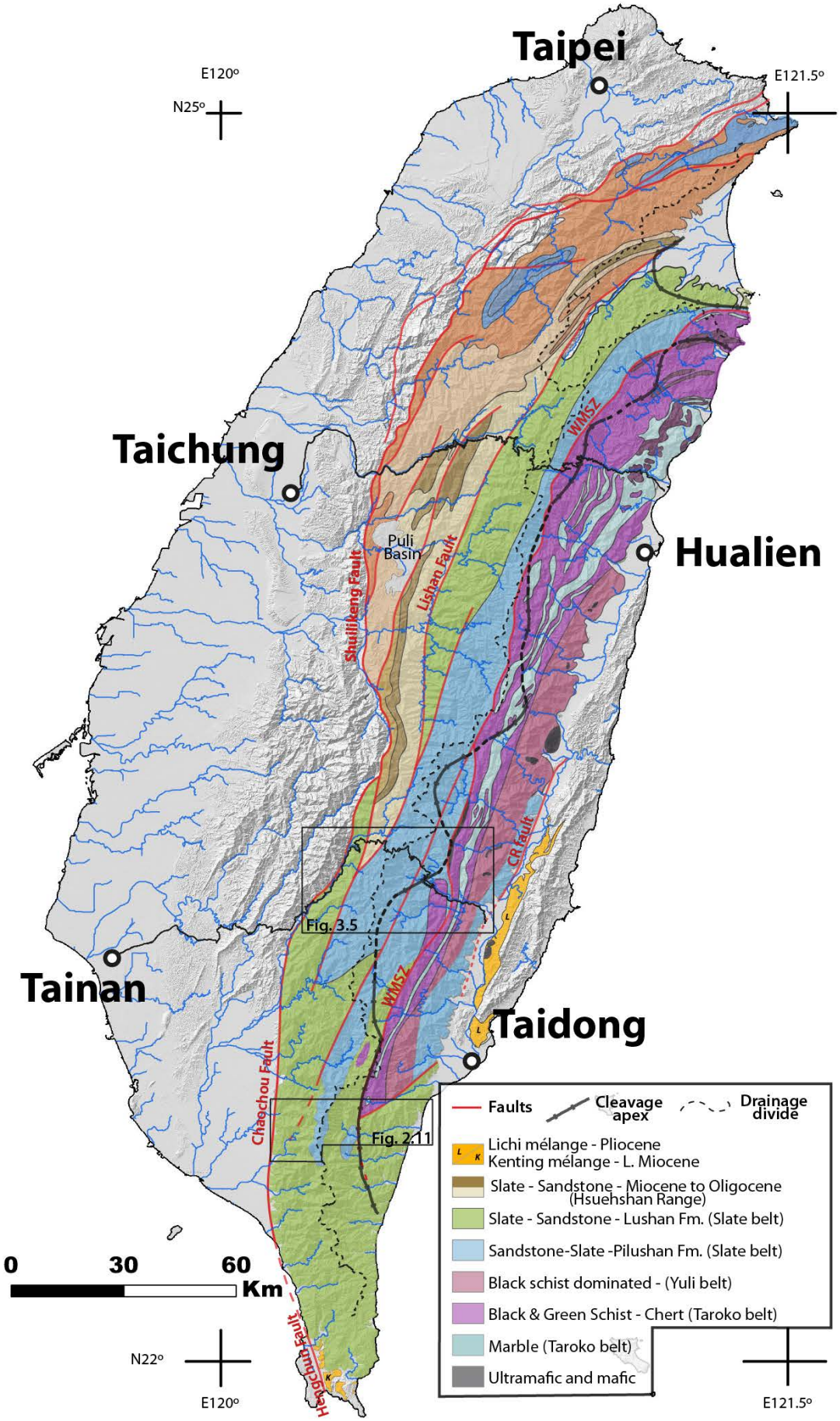

***Fig. 2.5**: Map with the geology of the Central Range and the location of the main transect*

crossing the Central Range of Taiwan, along which most of structural studies of the Central Range have been undertaken. Also shown are the topographic divide, the apex of the cleavage fan [*Lu et al.*, 2010a] *and the main contacts discussed in the text. Geology modified from* [*Chen et al.*, 2000].

Contact 1 corresponds to the Chaochou fault, a major crustal scale fault which is the southern extension of the Shuilikeng fault marking the border, in northern and central Taiwan, between the Hsuehshan and western foothills [*Camanni et al.*, 2013, 2014] (Fig. 2.5). In its southern tip, it becomes the Hengchun fault bounding the Kenting mélange (hanging wall) and quaternary marine terrace (footwall) [*Chang et al.*, 2003]. In the northern and central segment (Shuilikeng fault), the structure is seismically active, sub-vertical to west-dipping. In map view the Shuilikeng fault links the Lishan fault, which has been interpreted as an orogen backthrust [*Clark et al.*, 1993] with a relatively recent extensional play [*Crespi et al.*, 1996; *Lee et al.*, 1997] or a reactivated, deeply seated (~30 km depth) reactivated passive margin normal fault [*Brown et al.*, 2012]. In its southern segment (Chaochou fault), the structure is locked with no significant seismicity and is interpreted as a high-angle east-diping thrust separating the uplifting Central range and the subsiding Pintung basin with no-significant, geodetically measurable (i.e. interseismic), strike-slip motion [*Ching et al.*, 2007a; *Hu et al.*, 2007]. Similarly to the Shuilikeng and Lishan faults, the Chaochou fault is interpreted as a deeply rooted fault into pre-existing passive margin normal faults [*Lewis et al.*, 2004]. However, structural analysis of the surface expression of the Chaochou fault indicates a dominant transtensive regime [*Chan et al.*, 2001], in agreement with seismicity of the rest of the southern Central Range (Fig. 2.3) and implying that the sinistral motion observed in the GPS horizontal vectors (Fig. 2.4) is probably accommodated in the inner Central Range and not along the Chaochou fault as originally inferred by [*Yu et al.*, 1997]. In its southernmost segment (Hengchun fault), the structure keeps a similar geometry with structural measurements indicating an early compressional and late extensional regime [*Chang et al.*, 2003].

Contact 2 corresponds to the Central Range east-bounding fault, the Central Range fault (Fig. 2.5). Although clearly discernible in the landscape as it separates the high mountains of the Central Range and the low lying Longitudinal valley, the central Range fault is not a major seismic fault and recent activity is only discernable in its central and northern segment [*Shyu et al.*, 2006]. Geodesy shows no sharp discontinuity nor shallow creep along it [*Ching et al.*, 2011b; *Champenois et al.*, 2012], and indicates a diffuse boundary where the western block (Central Range) is slightly uplifting or even subsiding during the interseismic period. Although some interpret it as an east-dipping normal fault [*Crespi et al.*, 1996; *Lee*, 2003], the fault is believed to be steeply-dipping east-vergent with thrust motion at the long-term but presently locked at the surface [*Shyu et al.*, 2006; *Ching et al.*, 2007b, 2011c; *Lee et al.*, 2008; *Huang et al.*, 2010]. Some argue that is probably accomodating about ¼ of the total ~40mm/yr convergence in eastern Taiwan [*Shyu et al.*, 2006].

Contact 3 is the Eocene-Miocene sedimentary contact (Fig. 2.5). This contact is considered as sedimentary with the local occurrence of basal conglomerates (N-

conglomerates of *Chang*, 1972), revealing an Oligocene depositional hiatus. At the type locality near Nantawushan, on the western side of the southern Central Range, Eocene Discocyclina bearing limestone structurally overlies Miocene slates in an inferred inverted sequence [*Chu et al.*, 1995]. Nevertheless, field evidences of the N conglomerate and of the Miocene/Eocene hiatus are generally hard to find, as Eocene series are rich in intra-formational conglomeratic levels. Consistent with this proposal, a study of calcareous nannofossils [*Huang*, 1980a] along the southern cross-island highway yielded biostratigraphic data supporting an Eocene/Miocene hiatus in which late Oligocene transgressive strata unconformably overlies the Eocene Pilushan Fm.

Contact 4 is preserved as a sedimentary contact in the eastern contact between the metamorphic core and Eocene Pilushan Fm. [*Suppe et al.*, 1976]. In northern Taiwan the same east-metamorphic core bounding contact appears to be seismically active and playing through a steeply west-dipping thrust fault [*Gourley et al.*, 2007]. In the other hand, the southern and western contact between the metamorphic core and the Eocene and Miocene covers is consistently faulted. There the fault is likely steeply dipping to west dipping and probably normal [*Crespi et al.*, 1996; *Gourley et al.*, 2007], although often portrayed as an east-dipping thrust fault [e.g. *Malavieille and Trullenque*, 2009]. At the southern tip of the TMC a faulted contact has been inferred in the existing geological maps, however the geometry of the fault is unknown in this locality, although it may appear as a south dipping normal fault (or alternatively as a north dipping thrust fault).

Contact 3 and ***Contact 4*** are both two major sedimentary discontinuities that seem to have behaved as a mechanically weak units where faulting and/or ductile shearing preferentially accommodate differential movement, in agreement with analog modelling experiments including two mechanically weak sedimentary discontinuities and erosion [*Malavieille*, 2010; Fig. 1.22].

2) Existing structural studies of the Central Range

A table with the main existing structural studies of the Central Range and their interpreted phases and age (if provided) of deformation is enclosed in *Annexe 2*. Most of the existing publication focus on two transects the northern and southern cross-island highways (Fig.2.5). In the following, I summarise the main findings of the existing published works.
For the sake of clarity, I redefine the main geological provinces denomination of the Central Range as many names have ben used in the literature: The Central Range includes the Hsuehshan Range and the Backbone Range; the Backbone Range comprises the Eo-Miocene cover and the pre-Cenozoic basement; the Slate Belt refers to the Hsuehshan Range and Eo-Miocene cover of the Backbone Range. Although often referred as an independent unit, the Hengchun peninsula is taken here as the southern extension of the Central Range.

Ductile deformation in the Central Range is expressed through a well-developed fold-related schistosity affecting both the Cenozoic sedimentary cover and the pre-Cenozoic basement. The sedimentary cover is mainly affected by one

deformation event (D1) striking from N-S to NNE-SSW. The deformation styles differ between the Hsuehshan and Backbone Range.
The Hsuehshan Range presents up-right symmetrical folds with a sub-vertical schistosity containing a stretching lineation oriented downdip with no apparent shearing [*Clark et al.*, 1992, 1993; *Tillman and Byrne*, 1995], consistent with the interpretation where the Hsuehshan Range is a large pop-up structure resulting form the inversion of the Chinese passive margin half-graben [*Teng*, 1990; *Clark et al.*, 1993].
The sedimentary cover in the western Backbone Range presents west-vergent asymmetrical folds with an east-dipping schistosity; stretching lineation is oriented down-dip and indicates top-to-the-west shearing [*Clark et al.*, 1992; *Tillman and Byrne*, 1995]. The Tananao metamorphic core (TMC) displays, to the first order, a characteristic west dipping axial planar schistosity with a sub-horizontal, gently northeast plunging, stretching lineation [*Clark et al.*, 1992; *Fisher et al.*, 2002; *Pulver et al.*, 2002]. The oppositely dipping schistosity of the TMC and the sedimentary cover of the Backbone Range form the characteristic fan shape cleavage fan of the Backbone Range (Fig. 2.5 and Fig. 2.6).

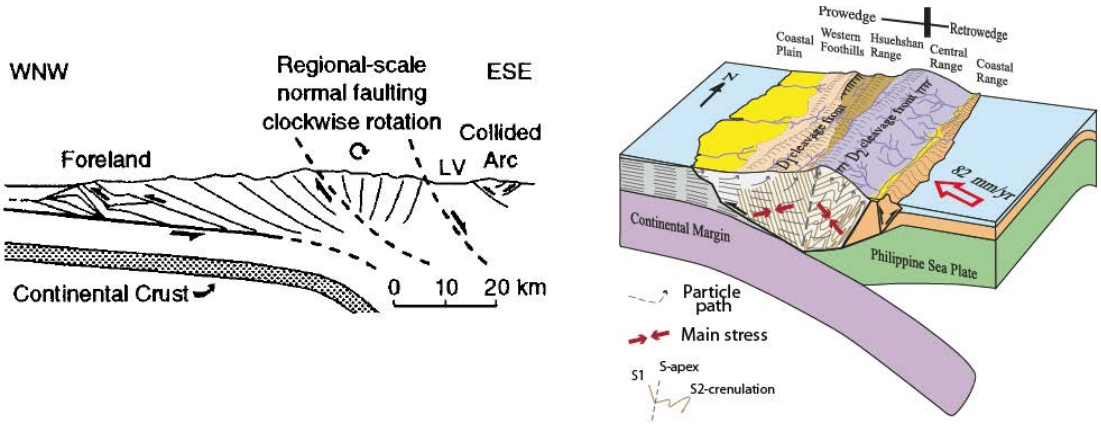

Fig. 2.6*: Two different models explaning the cleavage fan of the Central Range. Left: primary schistosity rotate clockwise through a normal fault.* From *Crespi et al., 1996; Right: topographically controlled stress state _brittle coulomb wedge_ (modified from Fisher et al., 2007). Note how continental crust is subducted in both models.*

Multiple generation of folds and cleavages in TMC have been described in the literature, interpreted either as ***(1)*** a succession of distinct deformation phases [*Stanley et al.*, 1981; *Wang Lee and Wang*, 1987] or ***(2)*** as a continuous progressive single phase [*Pulver et al.*, 2002].
In the former case ***(1)***, the west dipping schistosity is interpreted as resulting from a second generation of schistosity (S2) crenulating and locally transposing the initial east dipping schistosity observed in the structurally shallower western flank of the range. Usually the suggested mechanism implies the activation of a backfold/backthrust [*Stanley et al.*, 1981; *Pelletier and Hu*, 1984] or a result of coulomb wedge mechanics where the rock particle first goes through the west verging pro-wedge (D1) and then is exhumed in the retro-wedge (D2) [*Fisher et al.*, 2007] (Fig. 2.6). In the latter case ***(2)***, the structural geometry and kinematics of the TMC is controlled by lateral extrusion, a result of the partitioning of contractional strain into orogen perpendicular (orthogonal shortening, vertical

thickening in the Slate Belt) and orogen parallel (sinistral transpression where lateral extrusion dominates over vertical thickening in the TMC) [*Fisher*, 1999; *Fisher et al.*, 2002; *Pulver et al.*, 2002].
In the southern half of the Central Range TMC displays mainly west-dipping schistosity (Fig. 2.5) but some oval shaped outcrops of Eocene (underlied by TMC) and TMC appears to be in the east-dipping schistosity domain (Fig. 2.5). This implies that the west verging deformation affected the basement units. Moreover in the northern Central Range the cleavage apex crosses the TMC (Fig. 2.5). West-verging deformation affected both, basement and sedimentary cover.
East-verging deformation, as discussed below for my study area, affected also the sedimentary cover, prolonging the cleavage apex to the southern Central Range presumably Miocene cover (Fig. 2.5).
Surprisingly, the Eocene rocks in the elongated strip south-east of the TMC, although displaying the characteristic south-west verging folds and associated shictosity, appear as affected by north-south tectonic transport as evidenced by sub-horizontal mineral stretching lineation [*Clark et al.*, 1992; *Fisher*, 1999; *Yeh*, 2004].

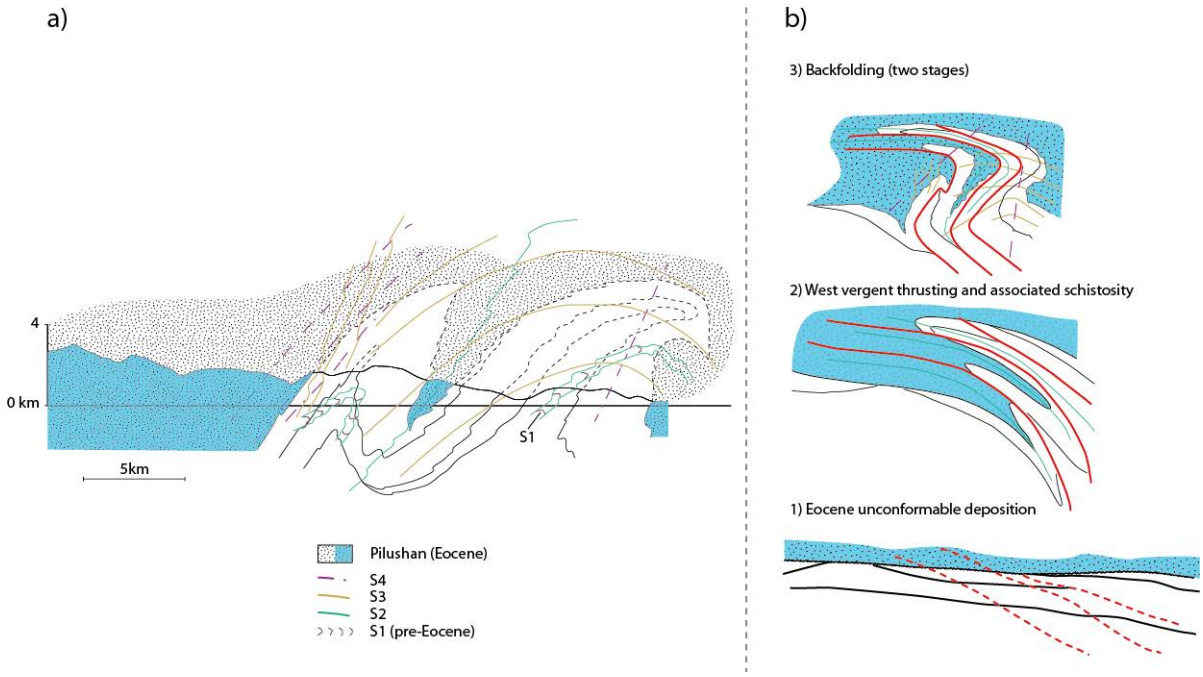

Fig. 2.7*: a) Metamorphic core cross-section along the eastern part of southern cross-island highway; b) evolutionary model as proposed by [Stanley et al., 1981]. Redrawn from the original figures.*

It is worth noting that first and most detailed study of the southern cross-island highway deformation by *Stanley* et al. (1981) (Fig. 2.7) invoked the backfolding and rotation of an initial east-dipping S1 schistosity to respect the paradigm of frontal accretion of material from the west [*Suppe*, 1980b]. However the authors only mapped west-dipping schistosity, with no evidences of west-verging structures. Subsequent works generally assumed the west-dipping schistosity as being a crenulated and transposed east-dipping schistosity, but little or no evidences were provided [e.g. *Fisher et al.*, 2007].

Brittle and ductile discontinuities of the Backbone Range have been relatively little studied, as evidenced by the poor knowledge and controversy existing on the geometry (east or west-verging and dipping of *Contact 4*, the west-bounding metamorphic core fault; as discussed above) and play of the main structural contacts. *Tillman and Byrne* [1996] partly based on the mapping of *Pelletier and Stephan* [1984] described thrust faults in the western Slate Belt along the southern cross-island highway, and interpreted them as being out-of-sequence thrust as they postdate peak-metamorphism and penetrative cleavage formation, and a jump in zircon fission-track ages occurred across it (Fig. 3.5). *Stanley et al.* [1981] mapped a shear zone within the TMC and interpreted early west verging thrust passively backfolded in his evolutionary model (Fig. 2.7). *Chang et al.* [2009] interpreted a major north-south, east-vergent thrust fault and minor east-west strike-slip faults in the eastern flank of the south-eastern Central Range, but little structural evidences were provided. In the same area, *Ramsey et al.* [2007], using geomorphic analysis, placed two sinistral, north-south, strike-slip faults, one in the same location as *Chang et al.* [2009] and the other along the south-eastern coast.

To summarize, the consensual main structural characteristics of the Central Range are:

- Pure shear deformation in the Hsuehshan Range, contrasting with simple shear deformation in the Backbone Range.
- Top-to-the-west deformation and vertical thickening [e.g. *Tillman and Byrne*, 1995] mostly limited to the Cenozoic sedimentary cover of the Backbone Range, and transpressional deformation with ductile lateral extrusion affecting principally the TMC [e.g. *Fisher et al.*, 2002; *Pulver et al.*, 2002].
- Cleavage fan in the backbone range with the apex partly coinciding with a major structural contact between the Cenozoic sedimentary cover and the pre-Cenozoic basement, and locally coinciding with the topographic divide (Fig. 2.5). Two different mechanism have been proposed to explain this geometry (Fig. 2.6):
    - Rotation of an initial east-dipping cleavage along the east-dipping, normal, west metamorphic bounding fault (contact 4) [*Crespi et al.*, 1996].
    - A result of the internal dynamics of a critical Coulomb wedge were the topographic divide controls the geometry of deformation [*Fisher et al.*, 2007].

III. Structure and geology of the Taimali-Taiwu area, southern Central Range

Field mapping and structural measurements were carried out intermittently during the period from 2010 to 2013, mainly within the Slate Belt of the Taimali valley (Fig. 2.8). To a lesser extent, the Zhiben and Jinlun valleys were also mapped mainly close to the river mouth. The western Central Range was also explored mostly during the hikes leading to the Beidawu peak (3094 m). Exposure and outcrops were numerous due to the recent Morakot typhoon (August 2009).

The southern Central Range has been relatively little studied compared to the Western foothills or to the transects along the northern and southern cross-island highways reviewed in the previous section. The steep topography, poor access and tropical vegetation cover may partly explain this fact. Nevertheless, a certain number of geological studies have produced geological and/or structural maps of part of the southern Central Range. Fig. 2.8 shows the main areas covered where field geological studies have been published, from the first maps produced by the Japanese colonizers [e.g *Usami and Matsumoto*, 1940] to more recent studies [e.g *Chang et al.*, 2009]. Although apparently well constrained by numerous maps, often detailed structural data and chronology is lacking.

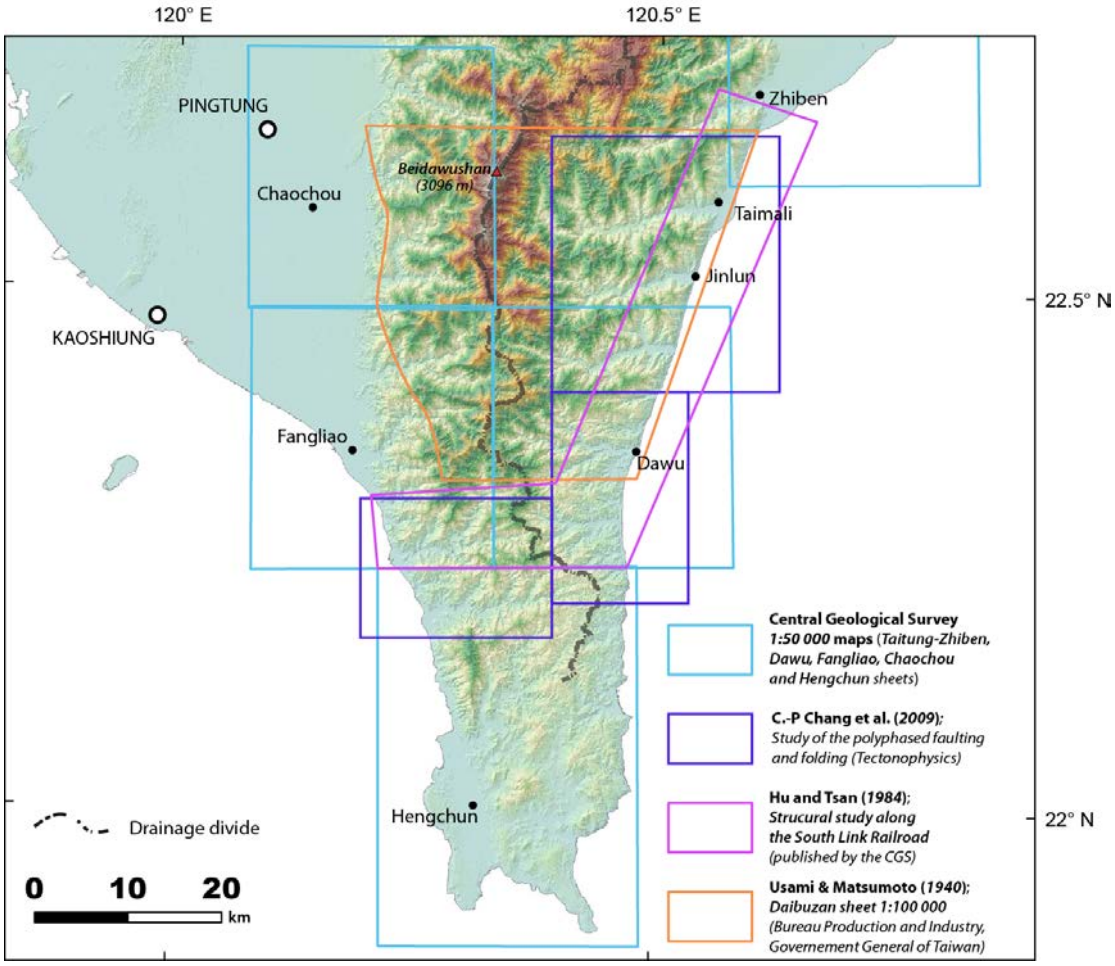

***Fig. 2.8**: Location of existing geological/structural maps on the topography of the Southern Central Range with the names of some of the main cities/villages of southern Taiwan. Note that the study and map Chang et al. (2009) mainly consider the structural elements of the considered areas; no geological or lithological correlations were contemplated. Other versions of the geological map of the Hengchun peninsula have been published; notably one by Chinese Petroleum Corporation, and by Huang et al.* (1997, 2006) and *Chang et al.* (2003)*. See Annex 1 for a reproduction of some of the old or historical original maps referred in this figure.*

A. General geology and structural units southern Central Range

Based on the existing paleontological, structural and geological data and my own field-work a structural map of the southern Central Range has been produced (Fig. 2.9). The main features can be summarised as follows:

- West vergent pro-wedge (mainly in western topographic flank) and east vergent retro-wedge (mainly in eastern topographic flank) resulting in a fan shaped geometry of the schistosity, or cleavage fan (see cleavage apex in Fig. 2.5). The west vergent structures appear to be limited to the Eo-Miocene sedimentary cover, while the east-vergent ones affect both, the sedimentary cover and basement rocks.
- The change from east to west dipping cleavage is very sharp, and probably faulted, at least in the Taimali area
- The Hengchun peninsula is the continuation of Central Range as attested by the continuity of the structures and sedimentary units (see discussion below).
- The TMC is fault bounded in its western and southern contacts. The western contact brings into contact the Eocene series and the metamorphic core through an enigmatic fault (Contact 4, above discussed) or shear zone rarely described but often pictured as west verging.

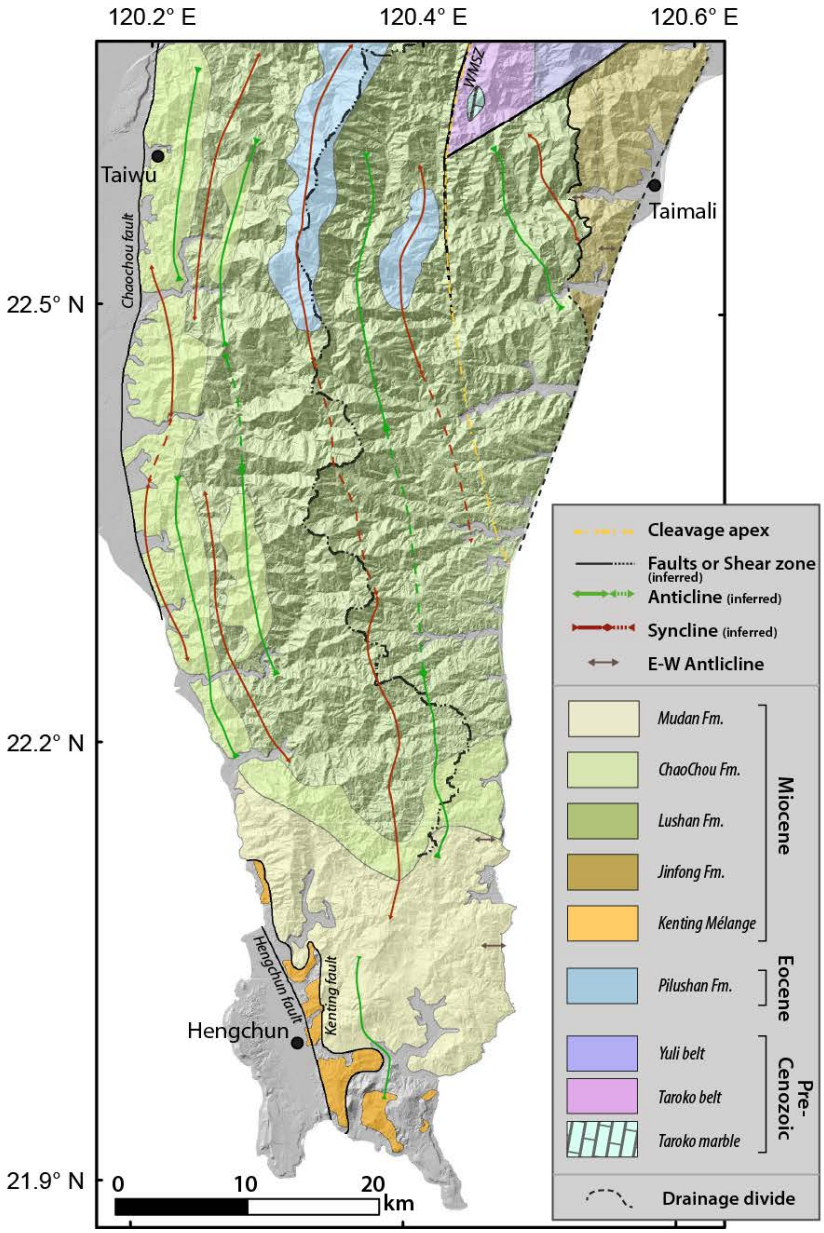

Fig. 2.9*: Geology and main structures of the Southern Central Range, from my own observations (detailed in the text), published maps from the Central Geological Survey (1/50000th Dawu, Chaochou, Fangliao and Hengchun sheets) and maps from published papers* [*Hu and Tsan*, 1984b; *Chang et al.*, 2003; *Huang et al.*, 2006]. *Cleavage apex drawn from* [*Lu et al.*, 2010a]. *The Jinfong Fm. is a newly baptised formation based on our own field observation (decribed below). WMSZ = west metamorphic shear zone.*

Although essentially based on the existing maps and my field-work, some disagreements may exist with the geological compilation of Fig. 2.9.
In particular the northern boundary of the Hengchun peninsula has been commonly interpreted as a faulted contact, based on the juxtaposition of the overturned (i.e. Mudan Fm. in the Hengchun peninsula) and normal polarity strata (i.e. Lushan Fm in the southern Central Range). However, some other studies and maps (e.g. Chinese Petroleum Corporation map of the Hengchun peninsula; *Pelletier and Stephan, 1984*) indicate a sedimentary contact questioning the overturned nature of the Mudan Fm. series. The Mudan Fm.

series are tightly folded with common isoclinal west-vergent folds, and thus the "overturned" interpretation could be biased by an over-measure of the inverted fold limb. I prefer the normal contact interpretation as no fault has ever been described (yet drawn), clustered seismicity is inexistent, and the continuity of lithologies and structures from the Central Range to the Hengchun peninsula favour a structural and lithological continuity. Further evidences of this continuity come from the correlation of the major overturned anticlined marking the topographic ridge in the north (Fig. 2.9) and the major anticline mapped by *Hu and Tsan* [1984] during the building of the south-link railroad (see Annexe 1 and Fig. 2.8).
Similarly, the northern extend of the Chaochou Fm. in the western Central Range is not depicted in the Chaochou sheet geological map, but is clearly mapped in the Fangliao sheet with an abrupt end at the northern edge of the map. Based on my field observation around Taiwu and the southern west flowing valleys and on the lithological similarities between the sedimentary series, the Chaochou Fm. is interpreted to cover the area depicted in Fig. 2.9.
The cleavage apex is defined by a fault zone mapped in the Taimali-Taiwu transect (see below). However the apex southernmost tip is shown as a post-cleavage syncline, with no evidence of structural discontinuity in the CGS-Dawu sheet geological map. Conversely to *Chang et al.* [2009] and *Ramsey et al.* [2007] I do not draw this fault all along the south-eastern Central Range as not much evidences exist besides the some morphological lineations observable mainly in the Taimali and Jinlun basins [*Ramsey et al.* 2007].
Finally, as will be discussed in the following a new formation has been defined (the Jinfong Fm.) for its structural and lithological characteristics.

B. Lithostratigraphic and structural units along the Taimali-Taiwu transect

1) Lithostratigraphy and depositional age constrains

The general tectono-stratigraphic units of the Central Range have been defined based on lithological and/or biostratigraphic correlations [*Chang*, 1970, 1971, 1972; *Huang*, 1979, 1980a, 1980b; *Chang and Chi*, 1983; *Yen and Yang*, 1991]. However, despite thorough attempts to precisely constrain depositional age, often the preservation of fossil assemblages in the deformed Slate Belt did not allow geographically dense age determination.
Yet three biostratigraphic studies in the Taimali-Taiwu area and suroundings exist. *Lee* [1984] constrains the Eocene age in the sandstone dominated series of the Beidawushan area and other sites north and south on the topographic divide; *Chu et al.* [1995] confirmed the Eocene on the Nantawushan area. *Chang* [1970], across a transect along Taimali and other the southern valleys, constraining the age to the foraminifera's biostratigraphic zone N7 to N8 (Ealry/Middle Miocene; Boudigalian/Early Langhian; 20.4 to ~15Ma; *Chang,* 1971) in the middle part of the Taimali valley and near the divide in the eastern slope, on the western slope of the Beidawu peak (Fig. 2.9 and 2.10).

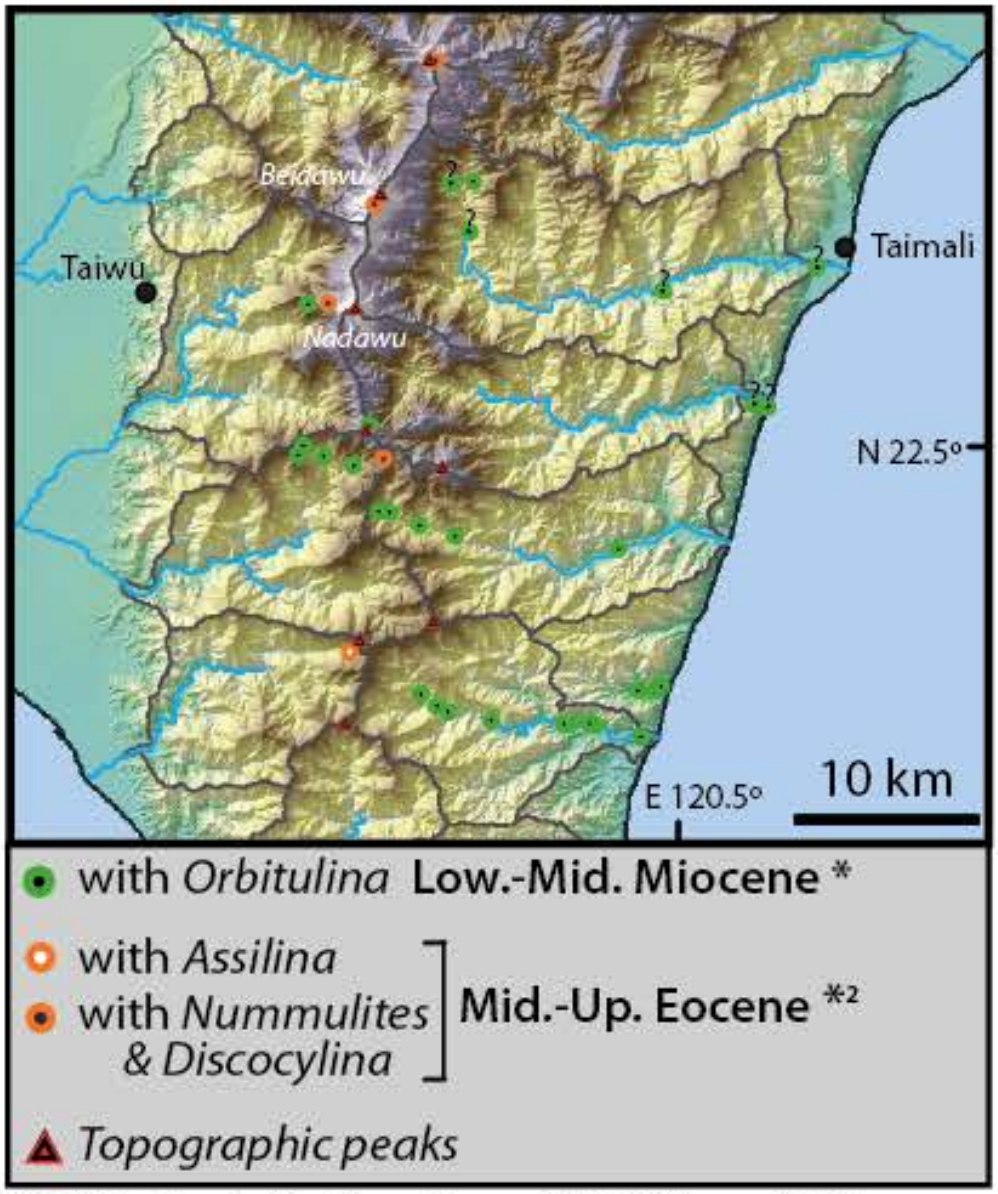

Fig. 2.10*: Map showing the existing age constrains biostratigraphy (i.e. foraminifera) the Taimali-Taiwu area and surroundings the study area. Data points compiled from* [*Chang*, 1970, 1972; *Lee*, 1984; *Chu et al.*, 1995]*. *Burdigalian/Langhian age Chang (1970). *2Chang (1972b), Lee (1984) and Chu et al. (1994). Note that the data point by Lee (1984) is not taken into account by the Central Geological maps, and the maps in this study. The question marks are questionable foraminifera identification from the original papers.*

To further constrain the depositional ages within a narrower time window, we tentatively produced nannofossils slides from samples collected all along the Taimali-Tawu section. The slides were made at the Basin Analysis Group laboratory (National Central University, Institute of Geophysics) with the help of Pr. Wen-Rong Chi and Andrew Tien-Shun Lin's students. Unfortunately, nannofossil preservation and yield of key/index nannofossil were very poor and did not allow attributing the samples to any established nannofossil zone.

In order to construct a geological map the Taimali-Taiwu area, I distinguished in the field five main lithostratigraphic units (LsU), as follows (Fig. 2.11):

- **LsU 1**: Grey to brown sandstone dominated series with minor interbedded fine-grained black mudstone. Sandstone is massif (50 to 100 cm thick), white-mica rich, and with millimetric angular crystalline quartz grains. Contains occasional oriented, bedding parallel, mudclasts. Groove and flute clasts and infrequent current ripples at the base of the sandstone beds are the only sedimentary figures observed (Plate 1). Mudstone beds (10 to 30 cm thick) are usually friable, organic rich with occasional unidentified carbonated fossils.
- **LsU 2**: Black mudstone dominated series with minor sandstone beds. Mudstone is massive and coherent, organic rich and with occasional carbonated fossils. Sandstone levels are thin (5 to 15 cm thick) and sometimes discontinuous as schistosity is well developed and often transposed. I have named this slaty association, the Jinfong Slates according to Jinfong a village located to the east of the Taimali catchment (Fig. 2.11); together with LsU1, it forms the Jinfong Fm.
- **LsU 3**: White to grey sandstone with no apparent internal structure. This unit is only found in the inner part of the Taimali valley (last tributary) as an isolated block/lens and in the Beidawu area on the crest. The contact with the surrounding black mudstone seems to be sedimentary but shows evidences of tectonic reactivation. The sandstone is mainly composed of quartz as opposed to unit 1's sandstone. These sandstones corresponds are exclusively found associated with the Pilushan Formation of Eocene age, as constrained by biostratigraphy in the Beidawu area (Fig.2.10).
- **LsU 4**: Brown to grey sandstone with minor black mudstone layers, and relatively common conglomerates and or breccias. They are interpreted as part of the Lower-Middle Miocene Lushan Formation, but could be part of the sandstone member of the Jinfong Formation.
- **LsU 5**: Black slates severely fractured and ductily sheared, particularly in the core of the synforms and antiforms in the middle part of the Taimali valley. They are also interpreted as lateral equivalent to the Miocene Lushan Formation.
- **LsU 6**: Alternating sandstone (30cm thick) and mudstone (20cm thick) tubiditic series with abundant syn-depostional deformation (e.g. slumps). This formation is interpreted as the Chaochou Formation for its similarities with the series found in the Hengchun peninsula.

The Jinfong Formation (LsU1 + LsU2) is inferred to be stratigraphically equivalent to the Lushan Formation, but it could be the southern extension of the Eocene strip found further north along the mountain front (Fig. 1.15), as discussed below.

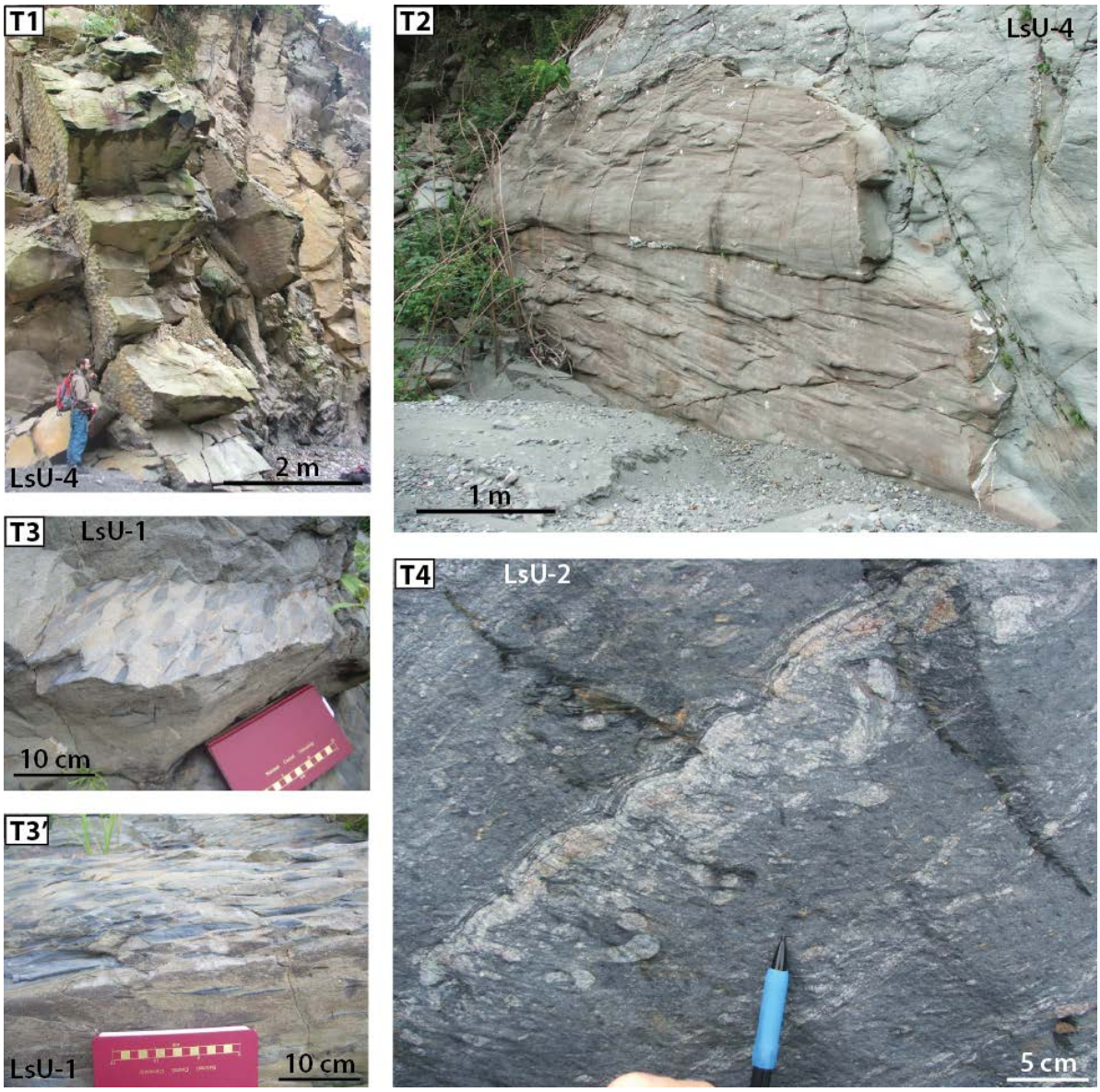

***Plate 1**: Photos with some examples of sedimentary features preserved in LsU 1and LsU 4, intepreted as Lower Miocene sandstones. T1: sandstone beds with wave current ripples. T2: flute casts at the base of a steeply dipping sandstone bed. Direction of flute casts indicates sediment transport from the south. T3 &T3': sandstones bearing stretched mudclats oriented N150°E in an overturned limbs striking N095°E 25N. T4: well-preserved burrows in alterning sandstones and clays locally indicating normal polarity.*

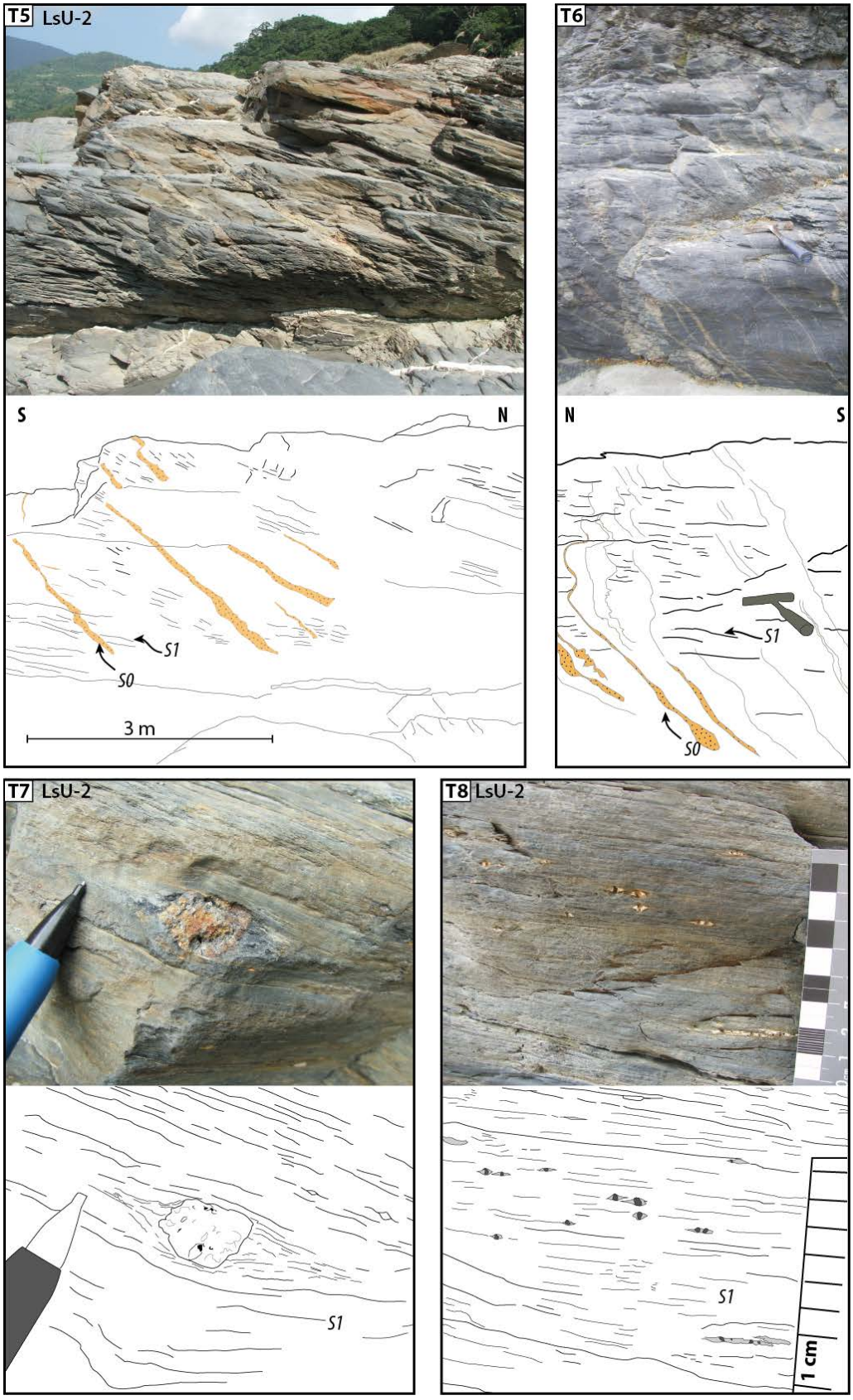

***Plate 2**: Photos taken in the eastern Taimali catchment close to Jin-Fong village and sketches. Photos T5 and T6 show the cross-cutting relationship between bedding (S0) and a sub-horizontal cleavage (S1), characteristic of StU-3. Photos T7 and T8 show detail on elements (probably fossils or burrows) within S1 cleavage of the same outcrop displaying no apparent or minor rotation and shear (T7 and T8 pictures oriented orthogonally).*

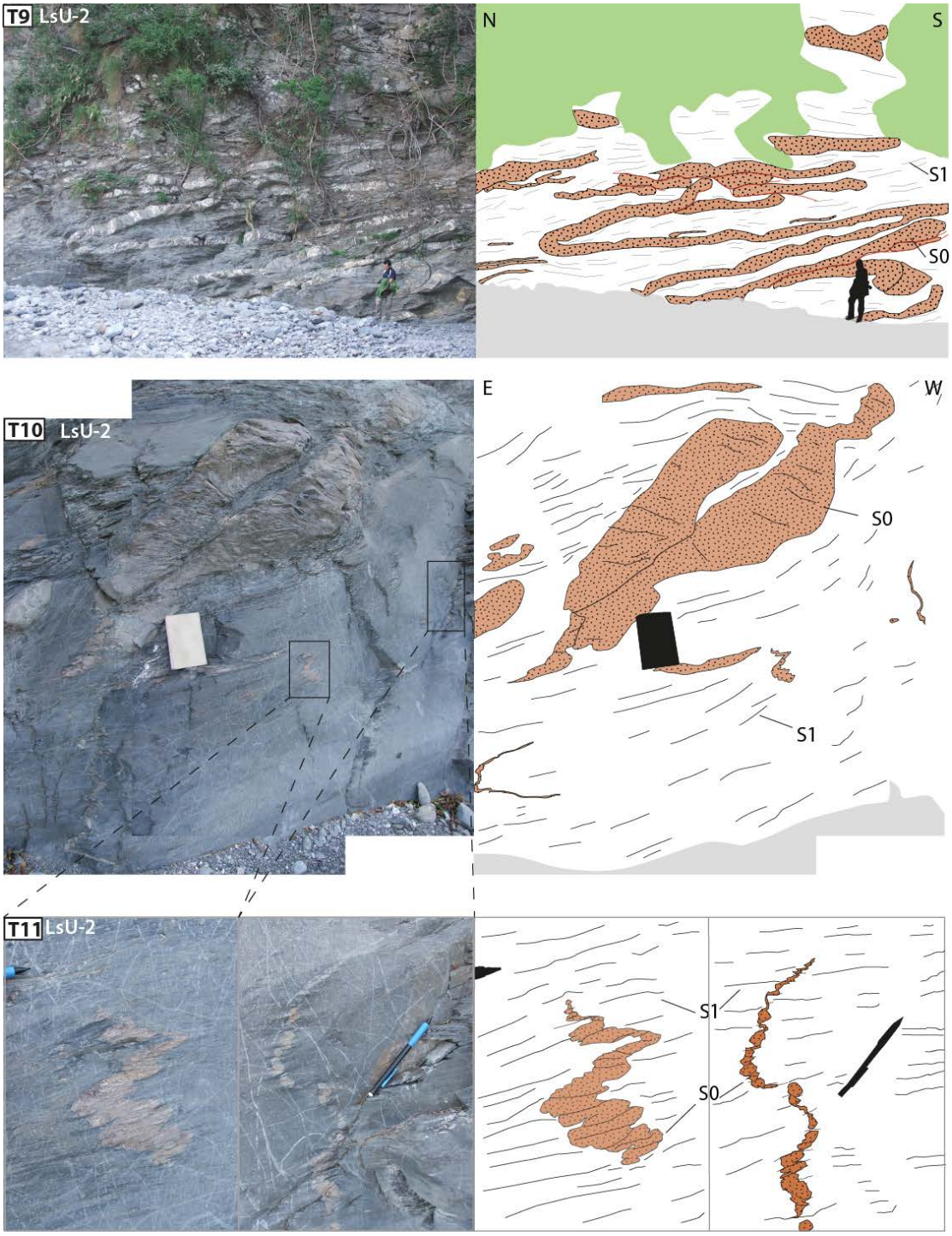

Plate 3: *Photos and sketches of the folded and flat lying series of LsU-2 in StU-3. T9 - slate dominated series tightly folded as witnessed by sandstone beds; T10- locally discontinuous, sandstone boudins; T11- detail on some discontinous sandstone beds.*

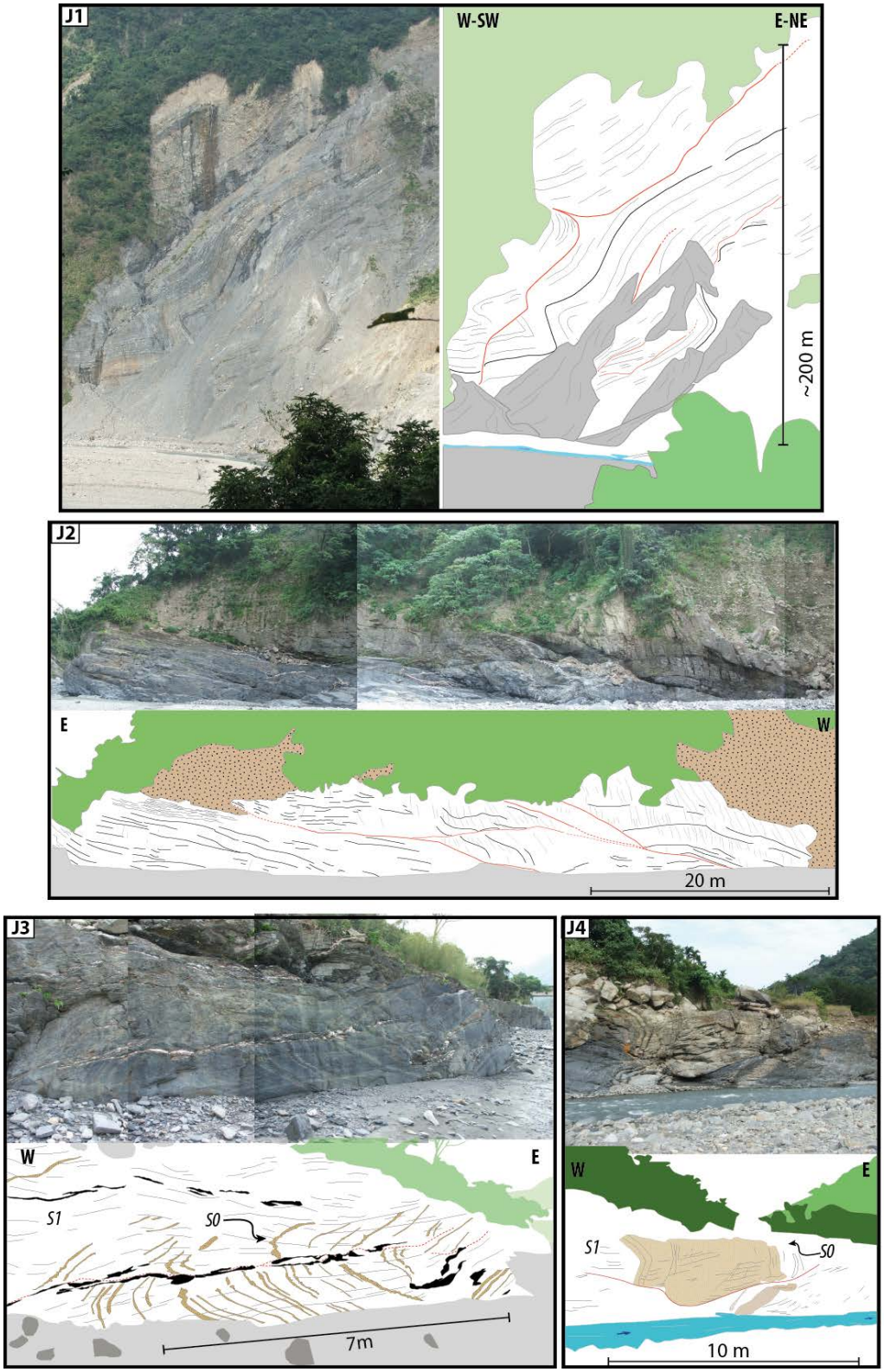

***Plate 4**: Photos taken in JinLuan valley, 8 km south of Taimali and sketches. This valley is very much like the Taimali valley, with west dipping S1 in the inner valley associated to regional scale folds (J1) similar to Taimali's StU 2. Photo J2 shows imbricated thrusts structures within the sub-horizontally lying slates piles. Photo J3-J4 depict sub-horizontal S1 in the outer valley similar to Taimali's StU 1. In J3, black indicates quartz veins, which appear to mainly develop along the axial plane of the observed fold.*

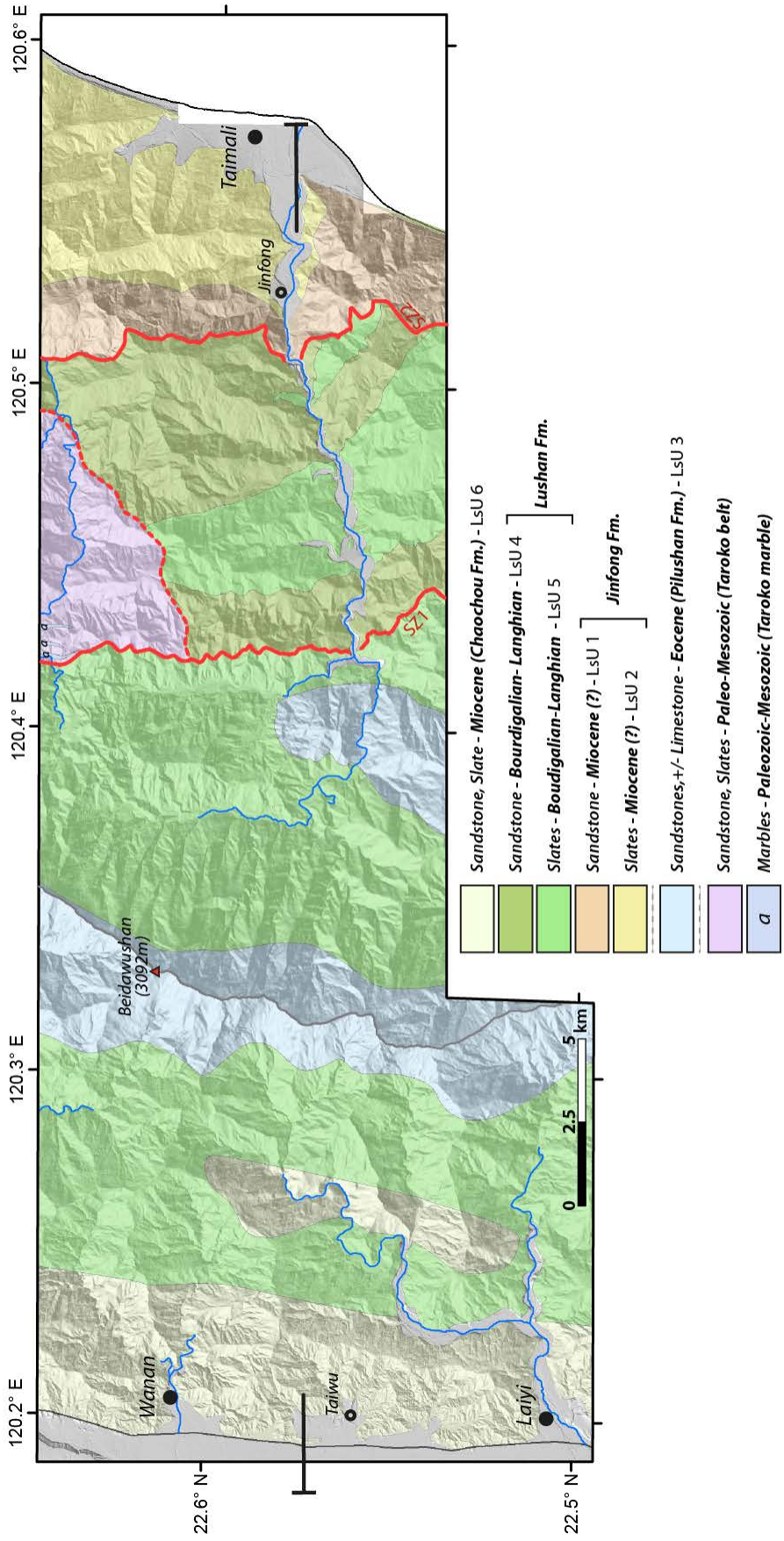

Fig. 2.11*: Main lithostratigraphic units Taimali-Taiwu area. Main shear zones observed in the field are shown in red. Position of the cross-section in Fig. 2.17 is shown.*

2) Characterisation of the main structural units and bounding faults

Hereafter, I describe the main structural units and their bounding faults on my field mapping. Metamorphism is limited and according to the official metamorphic map of Taiwan [*Chen*, 1994] is limited to prehnite-pumpellyite to lower green-schist facies. Deformation is mostly expressed through brittle fractures, multiscale folding, cleavage and shear zones. All throughout the study area only one set of cleavage with different orientation could be described and locally (large-scale fold hinges) a second schistosity (S2) was observed, usually with similar orientation. Based on the geometry of S1 ductile fabrics in Taiwu-Taimali area and its relation to S0 bedding, I identified three main shear-zone (SZ)-bounded structural units (StU) (Fig. 2.12):

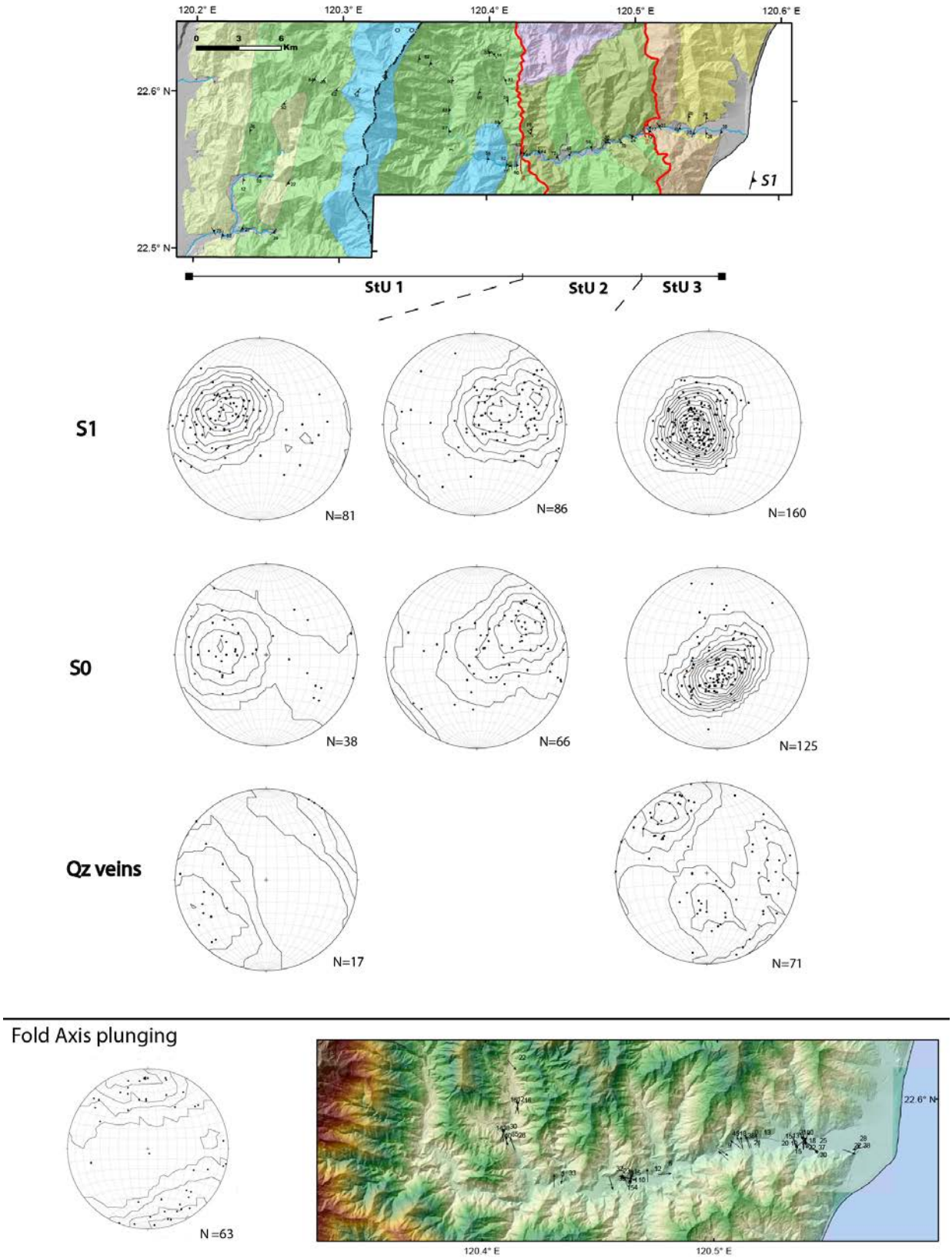

***Fig. 2.12**: Taimali valley structural data (S1 cleavage, S0 bedding plane and Quartz veins) plotted as poles on lower hemisphere equal area stereo plots for each of the different structural units. Density contours (kamp contour) with the lowest contour having a value of 2σ.*

StU-3: Bounded to the west by SZ1, newly baptised "meander fault" (Figs. 2.13), and to the east by the seacoast. This area is characterised by flat lying S1 (Fig. 2.15), and by consistent reverse polarity displaying an antiformal (domal?) structure at larger scale that fully agrees with earlier mapping along the south railroad [*Hu and Tsan*, 1984; Annex 1; Fig. 2.11]. Thick-bedded reverse polarity sandstones (LsU 1) outcrop in the east and west terminations of the domal structure, with below a dominant mudstone/black slate formation, displaying pervasive folding and horizontal S1 and S0 (LsU 2; T5 and T6 in Plate 2 and T9 in Plate 3). The surprising fact that no normal polarity limb is found implies recumbent folding. Boudinage and non-rotated element are common (Fig. 2.15 and photo T10 and T11 in Plate 3), suggesting important stretching associated with minor simple shear along S1 planes. Quatrz veins are mostly vertical but flat lying veins pare also common (Fig. 2.12 and Photo J3 in Plate 4).
Yet another characteristic feature is the presence of E-W trending folds, better exposed along the beach between Taimali and Jinluen (Fig. 2.9), already recognised by other researchers [*Pelletier and Hu*, 1984; *Chang et al.*, 2009b]. E-W folding verge towards the N-NW and is crosscut by flat-lying foliation and thus predates the foliation. This folding phase precedes thus recumbent folding and the now flat-lying schistosity. The large-scale domal structure (Fig. 2.11) seems to be a younger feature. Similarly, southwest verging folds, with fold axis plunging towards the northeast and mainly present towards the western end of StU 1, close to SZ1, deform (post-date) the schistosity.

SZ-2: This deformation zone, newly named "meander fault", separates the generally west-dipping cleavage zones StU-2 from the mostly flat-lying schistosity StU 3 (Fig. 2.9). This fault was not documented in any of the existing maps and was exposed by the 2009 Morakot Typhoon. The fault zone lies on a river meander 2 km upstream of Jin-Fong village, and lies exactly on top of documented and well-known hot springs. The fault planes are well defined and up to five embranchments can be recognised (Fig. 2.13). Fault slip data indicate a two-phased succession of stress regimes from transpressive regime to dip-slip normal faulting and N080°E extension (Fig. 2.13 and Fig. 2.16). The final extensive stage dominates all along the valley, where almost only normal faults are found, and overprints the early strike-slip regime.

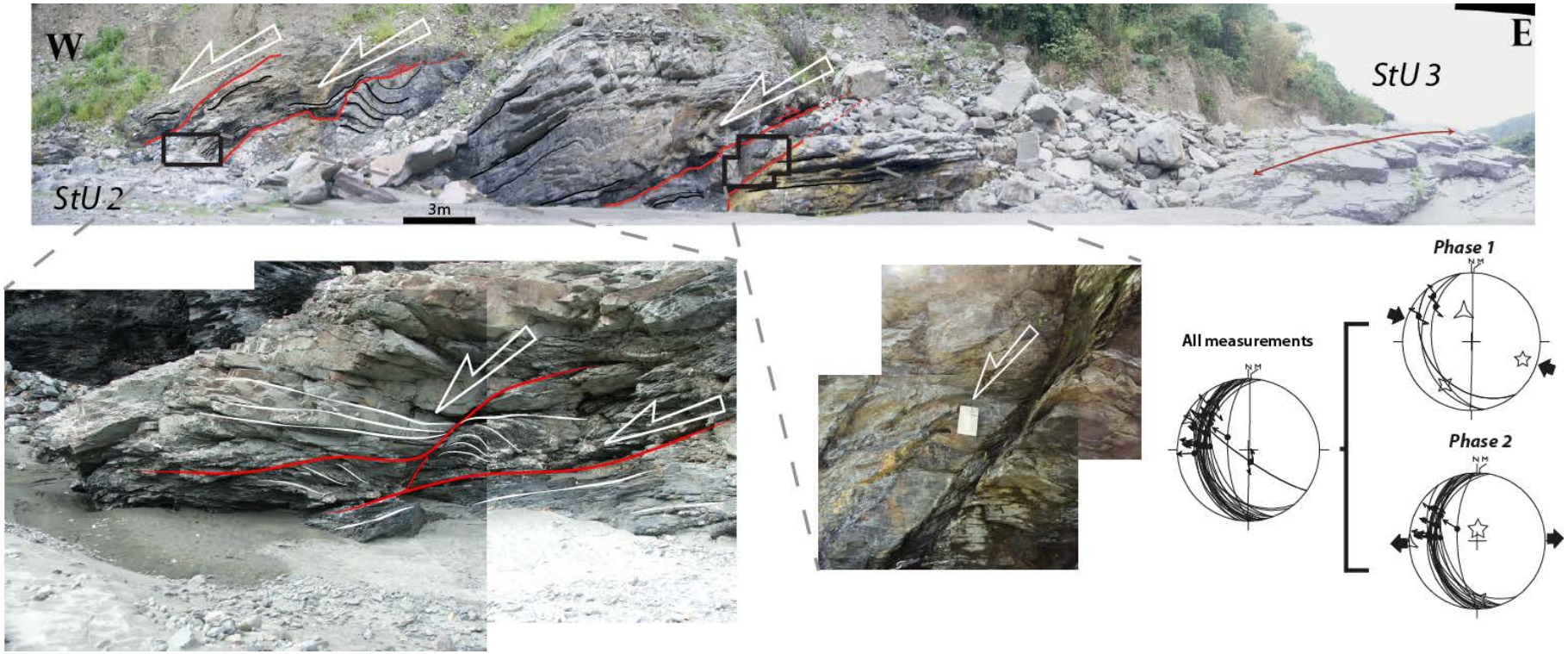

Fig. 2.13: Sheared boundary SZ2 between StU 2 and StU 3 units ("Meander fault zone").

StU 2: Includes the central portion of the Taimali valley and is characterised by a west dipping axial planar schistosity associated with a main regional-scale synform (Fig. 2.12and Photo J1 and J2 Plate 4). Outcrop-scale folds (5 to 50 m wavelength; Photo J1 Plate 4) are observed within the regional scale fold, and occasionally with vertical limbs (Photo T1 Plate 1) or overturned normal polarity. The synform is cored by black mudstone/slate (LsU 2) presenting numerous flat faults and shear zones and suggesting tightening during folding (photo J2 of Plate 4). To the west of the main dominant regional syncline follows an anticline similarly cored by sheared black mudstone/slate, but smaller in wavelength. The fold-axis of both the regional scale (Fig. 2.11) and the smaller scale (Fig. 2.12) folds appear to dip principally towards the north. No clear consistent crenulation cleavages was observed suggesting that the rocks in StU 2 have undergone only one major phase of deformation, or that the different phases had the similar stress directions. At its western boundary StU 2‘s bedding becomes progressively flatter.

SZ 1: This tectonic contact separates the east dipping schistosity of StU 1 with the west dipping schistosity of StU 2. In the field it is presented as a wide zone of ductile deformation within the blackschist-slates (between LsU 5 and LsU1-4). Additionally, abundant brittle faults can be found all along and around the deformation zone with a dominant normal sense of movement and dipping steeply towards the west (Fig. 2.14 and Fig. 2.16). An early transtensive movement although more rare because overprinted by the later normal play could also be recognised. Inversion of stresses of the fault striation and plane measurement highlight the evolution from a strike-slip regime (sinistral sense of shear) consistent with regional-scale compression oriented N100°E to a dominant extensive regime directed with extension N070-80°E (Fig. 2.14). This main structural boundary bounds the metamorphic core further to the north, as it is mapped in the 1:500 000 geological map. Although, we could not find the exact location of the contact between the metarmophic core and sedimentary cover, boulders of typical Tailuko marble were observed in the inner valley.
Overall, the transition from strike-slip to extensional faulting shows extension parallel or oblique to the main structural units. This finding is consistent with inferences from present-day deformation. For instance, the summation of seismic moment tensors has revealed that the Central Range is characterized by orogen-parallel extension under a regional-scale compression oriented N116°E [*Mouthereau et al*., 2009].

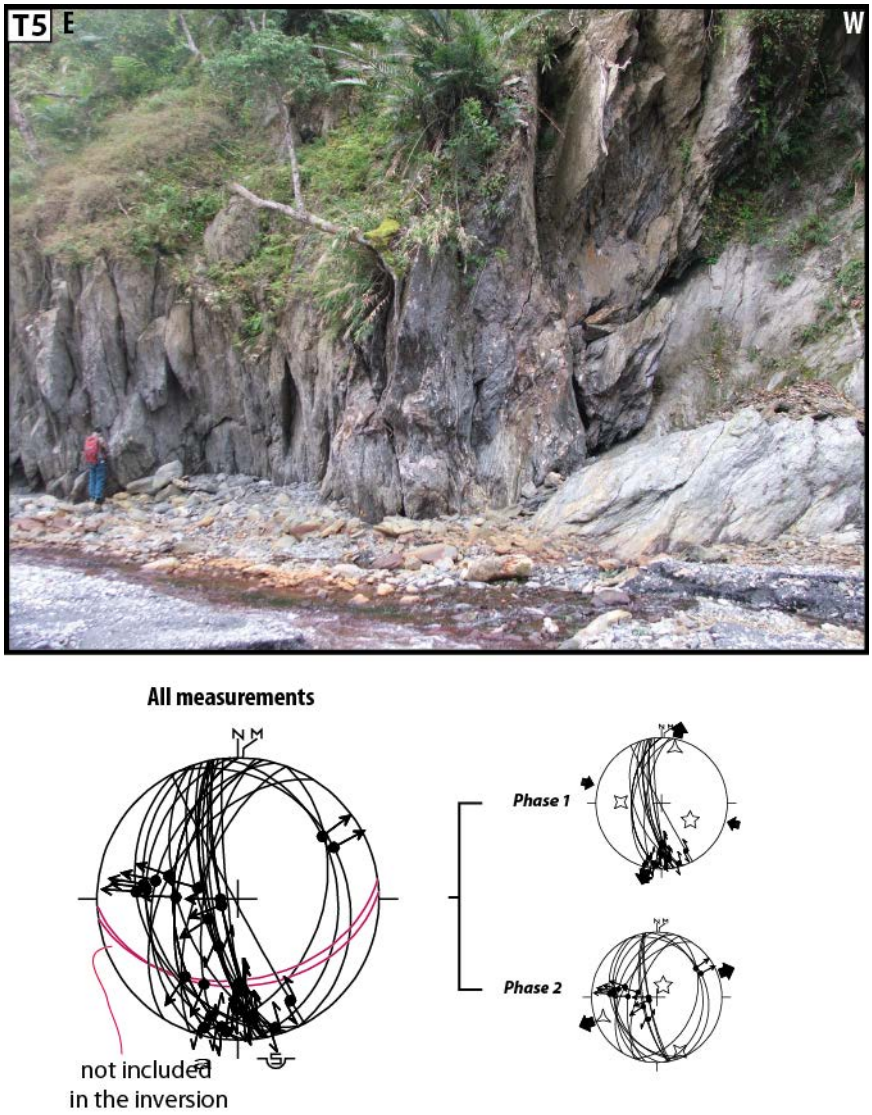

Fig. 2.14*: Photo of the shear zone SZ1. Lower hemisphere Schmidt projection, diagram plot of the fault slip data within and near the deformation zone. Stress inversion indicates a first strike-slip regime followed extensional phase, overall consistent with extension parallel or oblique to the main structural grain of the Central Range.*

StU 3: This unit includes all the western side of the divide (pro-wedge) until the southern prolongation of the Tananao metamorphic core west-bounding fault (Fig. 2.11 and Fig. 2.5), here expressed as a diffuse shear zone (Fig. 2.14). This structural unit is characterised by an east-dipping axial planar schistosity developed in association with regional-scale west vergent folds (3-5 km wavelength), locally overturned and with short western limbs. Outcrop scale folds (15 to 300 m wavelength) are observed within the regional scale folds, which is a common feature in the three StU's. The contact between Miocene and Eocene formations appears to be sedimentary, making difficult the distinction between both. The recognition of the Eocene is purely lithological and characterised by sandstone beds compared to the mostly slate-dominated Miocene. A sandstone lense in the Eastern divide is interpreted as belonging to the Eocene based on lithological resemblance only. Conglomeratic beds are common. Macroscale and thin-section observations support co-axial or minor

shearing along S1 planes (Fig. 2.15) conversely to what was described in the northern sections [e.g. *Tillman and Byrne*, 1995].

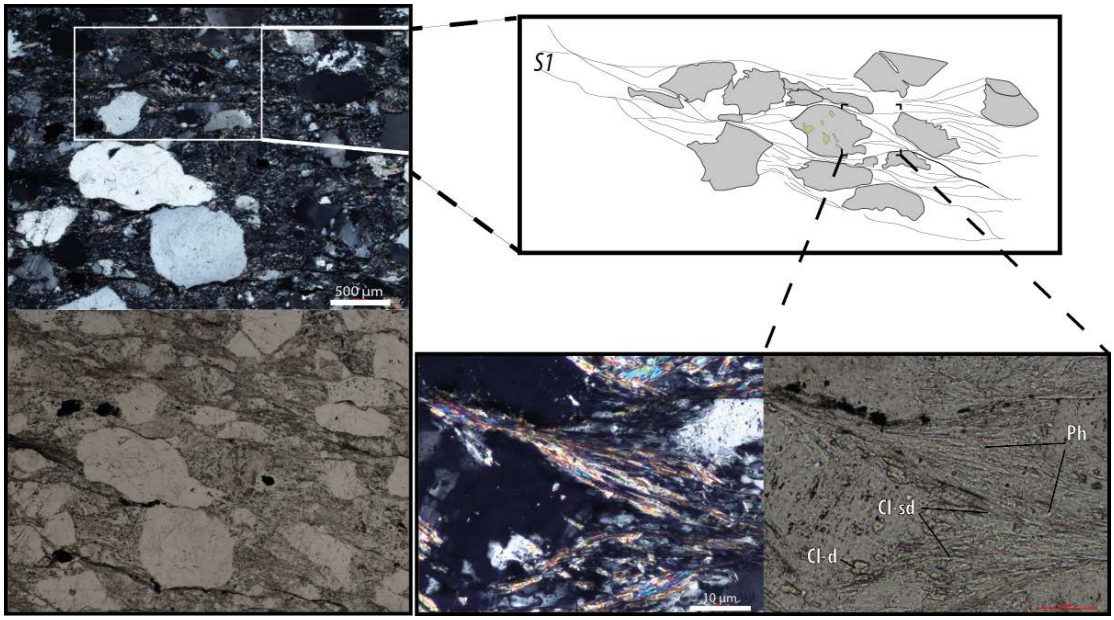

Fig. 2.15*: Natural (N) and polarised (P) photographs of polished thin-sections in the XZ plane (N002-52E) of sample Ph0 belonging to StU 1 in LsU 5 lithostratigraphic unit. East is to the left. Minor rotation of grains in S1 is displayed. Grains are mainly quartz. Deformation shadow displays syn-metamorphic Phengite (Ph) and Chlorite (Cl-sd). Also labelled probable detrital chlorite on the grains. Cl-d =detrital chlorite; Cl-sd = syn-deformation chlorite; Ph = Phengite.*

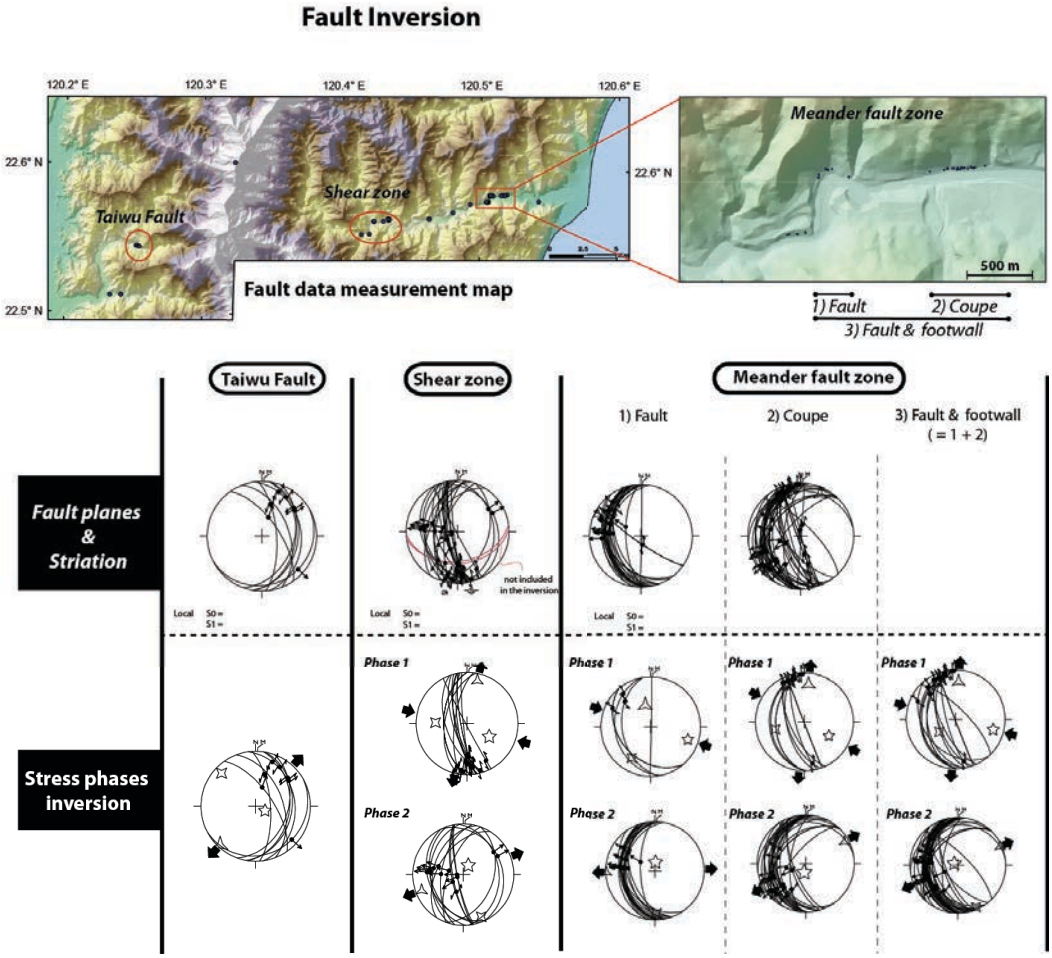

Fig. 2.16*: Synthesis of fault slip data and results of inversion along major shear zones observed in the study area. They all show consistent results that is shear zones are major sinistral strike-slip faults oriented ~N150°E reactivated as normal faults. Note that while SZ1 displays a first phase of trasnpression, SZ2's displays a trasntensive phase.*

IV. Cross-section, relative chronology of deformation and discussion

Based on the above lithostratigraphic and structural observations, Fig. 2.17 shows the cross-section along the Taimali-Taiwu transect. The large-scale folds in StU 2 have been drawn using the bedding (S0) – schistosity (S1) relationship and lithological correlations.

No vergence of the StU1 fold could be determined since no normal polarity bedding was found. In Fig. 2.17 I adopt an interpretation where StU1 is an alloctonous unit originated in the forearc but no unequivocal evidence exist for this interpretation, besides the probably shallow deposition of the lithostratigraphic units forming it (LsU1-LsU2). *Chang et al.* [2009] interpret the overturned attitude of StU1 as the down-going limb of a recumbent backfold originating in StU2, an interpretation as valid as mine. Interestingly StU-3 present similar fold geometries and mostly flat schistosity as the Eocene units found further north in the stripe east of the metamorphic core [*Clark et al.*, 1992; *Fisher et al.*, 2002; *Yeh*, 2004].

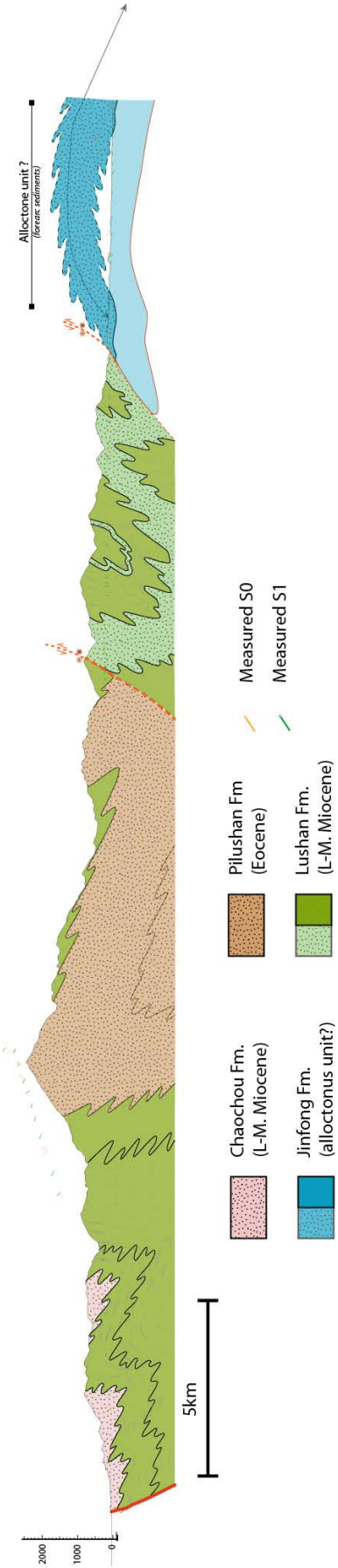

***Fig. 2.17**: Taimali-Taiwu cross-section based on the litostratigraphic and structural correlations of this study. Position of the cross-section is shown in figure 2.11.*

The relative chronology of deformation based on our field observation can be summarized as follow:

1) ***West-vergent deformation affecting the Eo-Miocene series of the Chinese continental margin***. This is consistent with the regional shear associated with the E-vergent subduction of the Eurasia plate. It therefore likely represents the first stage of deformation, as the underwater wedge starts incorporating the offscraped South China Sea sediments.
There is no evidence in our study area of major compressive thrust faults reactivating the Pilushan (Eocene)-Lushan (Miocene) sedimentary contact. However, decoupling between the Eocene and Miocene sedimentary cover and Eurasian basement (Metamorphic core) seems to exist. The northern prolongation of the main syncline of StU2 seems to correspond to the dome shaped culmination of the metarmophic core (i.e. outcropping of the Taroko marbles) so that cover and basement rock seem effectively decoupled; however we are limited here by the accuracy of the 1:500 000 geological map in the Zhiben valley. Mineral-lineations also seem to be different in the cover (downdip) compared to the basement (along-strike; *Fisher et al.,* 1999). Such decoupling may be true despite the lack of sharp metamorphic contact between the two (i.e. cover and basement), suggesting the decoupling may have occurred after peak metamorphism, in the late stages of exhumation, in agreement with mountain building models were the basement ductile extrusion is involved in the exhumational processes [e.g. *Yui and Chu*, 2000]. We therefore favour a structural model in which decoupling with the basement was limited to the retro-grade path of exhumation.
If the initial stage is related to the initiation of subduction and sediment accumulation in the accretionaey wedge along the Manila trench, the start of arc-volcanism at 16-15Ma [*Huang et al.*, 2006] could be considered as a lower bound constrain for the timing of deformation. Alternatively this phase can represent the initial involvement of continental crust and formation of the Kenting mélange at Middle to Late Miocene times (between NN11 and NN15) [*Pelletier and Hu*, 1984; *Pelletier and Stephan*, 1986b; *Chang et al.*, 2009a]. The fact that the basement rocks are locally involved in this phase favors the second interpretation.
Here, I interpret this initial stage with the east-dipping S1 cleavage to have occurred as the distal, hyperextended part of the Chinese continental margin started to be underthrusted, a recently imaged process seen on seismic reflection profiles offshore southern Taiwan [*McIntosh et al.*, 2013; *Lester et al.*, 2013; *Eakin et al.*, 2014], as discussed in *Chapter 3.* In this interpretation formation of the Kenting mélange could be the result of the closure of an hyperextended area of the margin where mantle is outcropping at the sea floor surface, an indeed mark the initiation of collision as postulated in earlier works [e.g. *Pelletier and Hu*, 1984; *Pelletier and Stephan*, 1986]. Initiation of the plate flexure in western Taiwan at ca. 6.5Ma [*Lin et al.*, 2003] dates the early stages of the collision and is a good approximation for initiation of ductile deformation in our study area. As further discussed in *Chapter 3*, cooling in our studied area is consistent with onset of inversion at this time.

2) ***East vergent phase and associated west-dipping cleavage.*** Although there may be some evidences in Taiwan that west-dipping cleavages occurred second as suggested to occure in the basement of the Tailuko and Yuli belts, some authors proposed that it results from rotation of S1 caused by synorogenic extension [*Crespi et al.,* 1996]. In my study the upper Eocene and Miocene units also show this W-dipping cleavage but there is less evidence of S2 crenulation cleavages cutting east-dipping S1. The underdeveloped crenulation schistosity in our study area may favour a contemporaneous development, as opposed to further north where crenulation of early schistosity east-dipping S1 may mark a clear change in the deformation regime.
This evolution overall illustrates a later stage of back-folding as the retro-wedge developed. This is associated in the field with the west-dipping S1 cleavages and generally flattening of the S1 to the east. Backthrusting of the rear of the accretionary wedge is a common feature of underwater wedges and is thought to develop very early in the sedimentary accretionary wedge development [*Silver and Reed*, 1988] or alternatively it can be interpreted as a marker of initital collision [*Beaumont et al.*, 1996]. Backthrusting was likely due to the combination of two effects. First, as convergence advances coupling between forearc region and thicker, positively buoyant, part of the Chinese margin produced stress transfer in the upper forearc crust. Second, the arrival of a weakly-thinned crust that have preserved a weak middle-lower crust, allows deformation to root in the deep crust, the lower crust being eventually squeezed in the course of increased indentation.

3*) Recumbent folding and normal brittle deformation*. During an advanced stage of back-folding and underplating, recumbent folds and nappes may develop, partly due to increasing gravitational effects. Moreover, main shear zones are clearly recent and extensional. The surprising fact of finding dominantly normal brittle structures may be also due to the underlying metamorphic core buoyant "push" as it is exhumed. Correlation of SZ1 with the Wester Metamorphic Shear Zone (WMSZ; Fig. 2.5) in the Zhiben valley to the north, indicates that WMSZ is likely steeply west dipping and normal in play. The southern bounding fault of the metarmophic core (Fig. 2.11) is probably south-dipping and also normal as advocated by the north-plunging axis of the regional and outcrop scale folds (Fig. 2.11 and Fig. 2.12) suggesting a northward tilt of the structures. This interpretation contrasts with geomorphologically inferred southward tilt by [*Ramsey et al.*, 2007].

V. Conclusive remarks

Based on the fieldwork carried out in the Taimali-Taiwu area we can conclude the following main points:

- The cleavage fan is observed also in the sedimentary cover, as opposed to the inference of previous works [*Fisher et al.*, 2007] and in agreement with recent publications [*Lu et al.*, 2010a]. The retro-wedge west-dipping schistosity does result from a crenulated former schistosity as inferred to

have happened in the northern sections, but is an axial planar schistosity developed from a single co-axial stress field.

- Brittle structures indicate that **1)** the WMSZ southern prolongation (SZ1) went through a transtensive phase followed by a dominant recent normal play; **2)** generally, the brittle regime is dominated by normal faulting all along the southern Central Range, in agreement with geodetic, seismic and other preliminary field work [*Chan et al.*, 2001].
- A flat lying, reversed polarity, structural unit (StU-3) have been identified with interestingly similar structural characteristics as the Eocene stripe preserved in the southeastern flank of the metarmophic core. Here we have interpreted this unit as an forearc alloctonous unit, but could well be the downgoing reversed limb of a large scale backfold, as interpreted by [*Chang et al.*, 2009b].

Chapter 3: Thermochronological constraints from southern Taiwan

In this chapter, I will first give a brief description of the general principles of thermochronology, and then describe the general analytical and sampling strategy for constraining the timing of the deformation phases described in the previous chapter. Next I present the dating and thermal modelling results. Finally, I discuss the first order implications of the data for the tectono-erosive events of the Taiwan mountain belt. The results and discussion is partly presented as a paper accepted for publication to *Geology*.

I. General thermochronological principles

Thermochronology provides constraints on the thermal history of dated rock samples. Similarly to other geochronological dating techniques, thermochronology is based on our capacity to measure parent elements and their daughter products, produced during nuclear decay reactions and accumulated since closure of the dating system. However, while geochronology dates crystallization time of a given mineral or rock, thermochronology integrates the thermal path of the mineral since it cooled below a certain temperature or range of temperatures [e.g. *Braun et al.*, 2006].
There is a wide variety of thermochronological systems, all sensible to specific temperatures ranges (Fig. 3.1), and thus can bring constraints on the processes taking place at different crustal depths, ranging from ~20 km depth to a few kilometers below the surface, given crustal thermal structure is known or can be modeled.

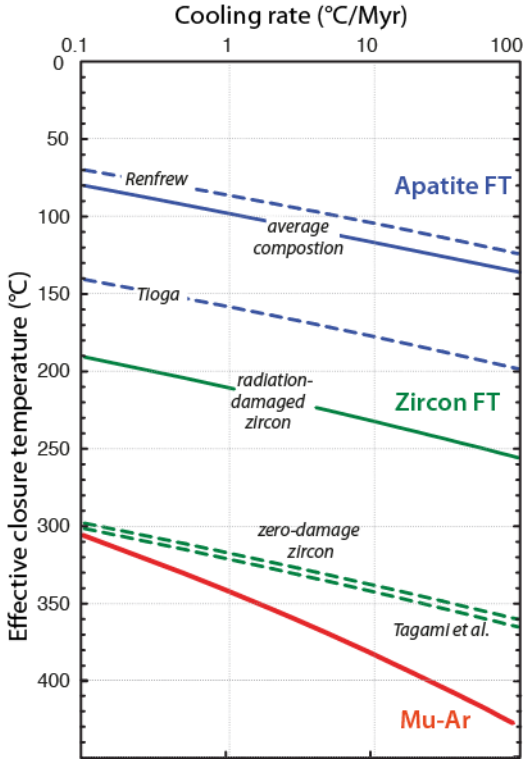

***Fig. 3.1**: Effective closure temperature vs. cooling rates for the main thermochronological systems for which extensive data sets exist in Taiwan. Note the dependence of closure temperature on cooling rate, composition (for AFT) and radiation damage (for ZFT). Modified from Reiners and Brandon [2006].*

In this study, we use fission-track (FT) dating on apatite and zircon (AFT & ZFT respectively). This method relies on the thermal dependence of preservation of FT in the mineral. FT is the result of ^{238}U decay by fission, which is the process of spontaneous nuclear splitting of ^{238}U into two more stable daughter atoms. Every single fission event is recorded as a linear damage zone (i.e. FT) in the crystal lattice and can be quantified to extract densities of tracks per unit surface, a value proportional to time and ^{238}U. The calculation of the fission track age is then obtained using a slightly modified form of the radioactive decay equation (*Braun et al.*, 2006b):

$$FTage = \frac{1}{\lambda}\ln\left(1 + \lambda\zeta\frac{\rho_s}{\rho_i}\rho_d\right)$$

where λ is the total constant decay of ^{238}U, ρ_s the counted spontaneous track density on the grain, ρ_i the induced track density in the external detector (i.e. remaining parent isotope) and ζ is the zeta-calibration factor specific to each analyst.

Provided that closure temperature of the system is known and an estimation of the thermal structure of the crust at the time of closure can be estimated, cooling rates can be converted to exhumation rates, defined as the spatially and temporally averaged unroofing rates of the dated rock sample.

For interpreting thermochronological ages into geological meaningful terms, two interacting factors need to be understood (Fig. 3.2): first the effect of temperature on a given thermochronological system; second the effect of tectonic and surficial processes on the thermal structure of the crust. In the following two sections I try to briefly summarize this two interacting factors.

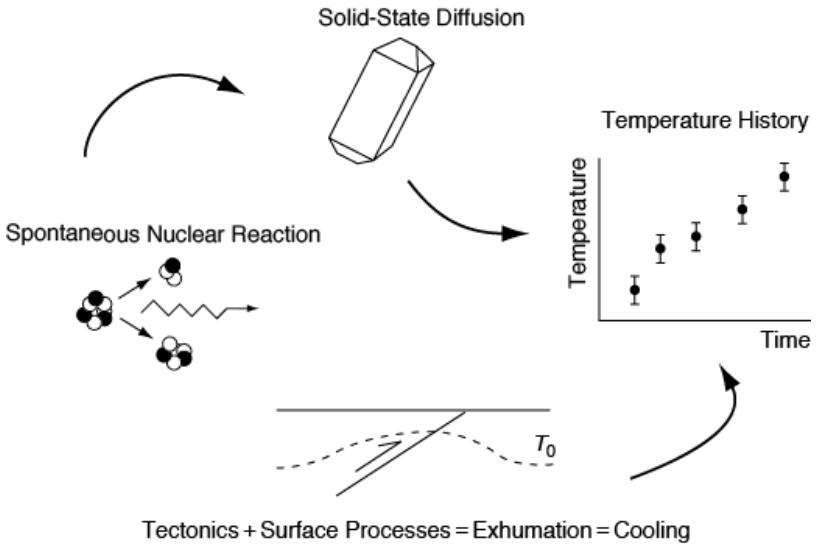

***Fig. 3.2**: Diagram synthetizing the two main effects on a thermochronological age: the effect of temperature on a thermochronological system and the effect of tectonics and surface processes on the thermal structure of the shallow crust. From [Braun et al., 2006].*

A. Closure temperature and partial annealing zone

In its simplest form, thermochronological ages can be considered as the time at which a thermochronological system has gone through the effective closure temperature isotherm (T_c) [*Dodson*, 1973]. However, closure of the system seems to occur in a broader depth range, where retention and annealing/diffusion are balanced. This depth range is called the partial retention zones (PRZ), and complicates the interpretation of a thermochronological age as the dating of a single tectonic/erosive event. The PRZ concept is central in the interpretation of thermochronological ages, particularly in slowly exhuming landscapes or in areas where complicated burial and exhumational events are integrated in a single thermochronological age. *Fitzgerald et al.* [1995] successfully documented exhumed paleo-PAZ through a vertically distributed set of samples (Fig. 3.3a) where the amount of annealing was monitored with track-length distributions, a proxy for quantifying partial annealing of a given grain.

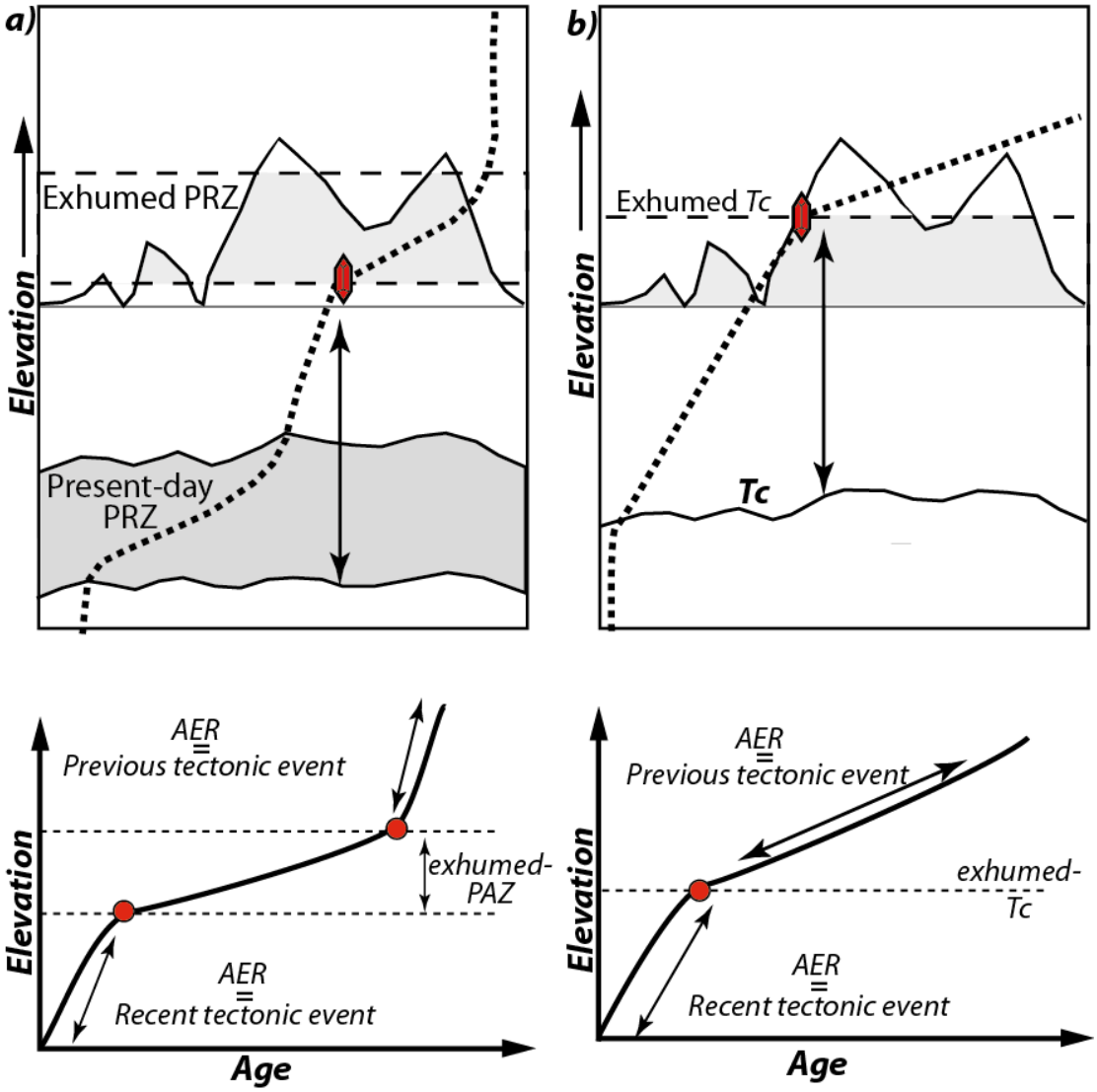

***Fig. 3.3**: Two opposing views of the annealing behavior of a thermochronometer in an active tectonic setting and its implications on the interpretation of a vertical profile. a) Schematic representation of the PAZ, exhumed PAZ concepts, and its effect on thermochronological ages (dotted curve and lower panel). b) Schematic representation of*

the closure temperature concept and its effect on thermochronological ages (doted curve and lower panel). In the lower panel of a) and b) is shown the expected age elevation relationship (AER) and what each portion of the AER records (current and previous tectonic event and paleo-PAZ). Red dots in the lower panels point the expected break-in-slope in the AER. Note that while in a) the lower break-in-slope separates the record between the recent AER and the "meaningless" PAZ AER, in b) the break-in-slope separates directly the recent and previous tectonic event AER. Modified from [*Fitzgerald et al.*, 1995; *Braun et al.*, 2006].

For other thermochronological systems, the existence of a PRZ is based on the variation of thermochronological ages with depth in deep boreholes [e.g. *House et al.*, 2002], mostly in stable cratonic areas. In areas where rapid monotonic cooling has occurred, the effective closure temperature concept can be applied, overlooking the PRZ effect on the final age [*Gallagher et al.*, 1998; *Braun et al.*, 2006; *Reiners and Brandon*, 2006] (fig. 3.3b).
Annealing temperatures of AFT are dependent on compositional factors [e.g. *Barbarand et al.*, 2003], while ZFT seem to depend on radiation damage [e.g. *Brandon et al.*, 1998] (Fig. 3.1). If the compositional effect on AFT can be easily quantifiable through elementary analytical measurement, radiation damage remains a largely unconstrained variable.
Radiation damage is the result of fission of Uranium and Thorium, and alpha (Helium)-recoil during radioactive decay. However alpha-recoil is the main radiation-damage producer due to its more frequent occurrence (4.468×10^9 for ^{238}U & 1.41×10^{10} for ^{232}Th *vs.* $\sim 1.3 \times 10^{16}$yr for FT decay of ^{238}U; *Donelick et al.*, 2005). Cristal lattice is distorted by both processes and induce changes in the annealing properties of Zircon. Highly damaged zircons anneal at lower temperatures than more crystalline zircons [*Garver et al.*, 2005; *Brandon et al.*, 1998].

B. Tectonics and topographic effects on thermochronological age

Various physical processes intervene to produce a thermochronological age, the main ones being (Fig. 3.2):

- Topographic effect on the shallow isotherms. This effect is dependent on the wavelength and amplitude of the topography and its depth (cf. Fig. 21 in Introduction) [e.g. *Stüwe et al.*, 1994; *Stüwe and Hintermüller*, 2000; *Braun*, 2002; *Braun et al.*, 2006; *Stüwe*, 2007].
- Advection of isotherm as erosion increases. Advection of rocks towards the surface leads to steeper geothermal gradient (Fig. 3.4). That is, closure depth becomes shallower [e.g. *Barr and Dahlen*, 1989; *Braun et al.*, 2006; *Reiners and Brandon*, 2006].
- Steeper thermal gradients lead to faster cooling. This effect leads to the increase of closure temperature. That is, closure depth becomes deeper [Fig. 3.4; e.g. *Reiners and Brandon*, 2006].

Additionally, we can recognize two other potential important effects perturbing the shallow isotherms.

- Faulting can perturb isotherms and control particle paths in the orogenic wedge [e.g. *Barr and Dahlen*, 1989; *Batt*, 2002]. This phenomenon is well described in subduction zones mega-thrusts, but the effect of single,

shallower, tectonic discontinuities is less well understood. Despite this, fault discontinuities are often used to explain variable thermochronological ages within a short distance.

- Effect of fluid circulations within the shallow crust is often largely ignored, as its effect has not been researched thoroughly. However it can potentially have important effects on the shallow isotherms.

The competing effects of isotherm advection and closure temperature increase at thermal steady-state are represented in Fig. 3.4. The downgoing part of the ZFT (green) and Ar-Ar on Muscovite (red) closure temperature profiles indicates a faster increase of closure temperature with increasing erosion rates, while the rising part display the dominance of isotherm advection. The trade-off appears to be somewhere around erosion rates of 0.5 km/Myr for muscovite Ar-Ar and below this value for ZFT (Fig. 3.4).

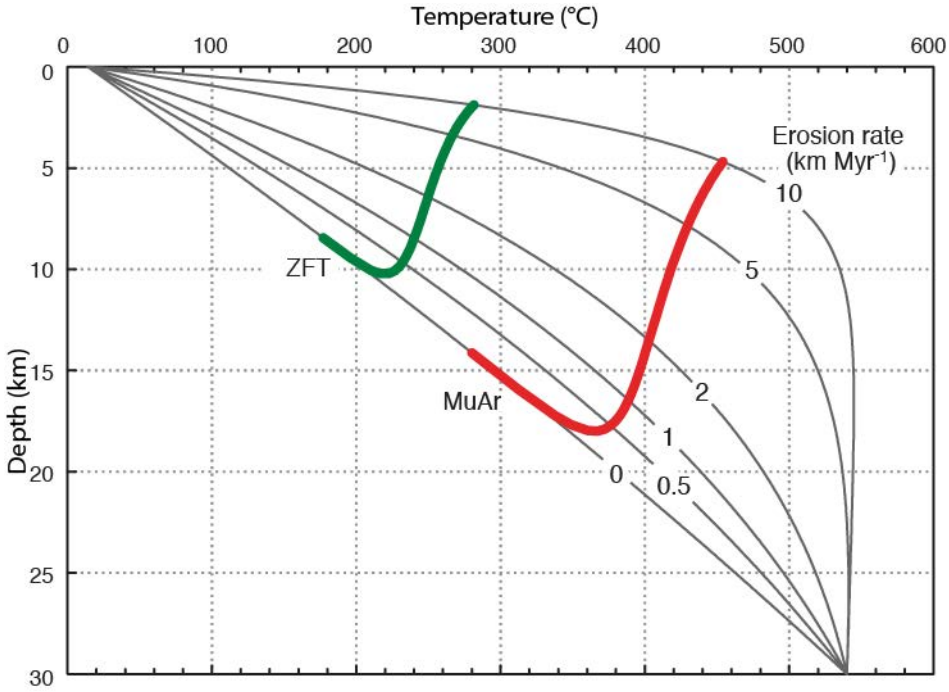

Fig. 3.4*: Closure depth and temperature of zircon fission track (ZFT in green) and Ar-Ar on muscovite (MuAr in red) for varying erosion rates. Modified from [Reiners and Brandon, 2006].*

II. Thermochronology in Taiwan

In the following section, I will briefly review the existing thermochronological studies of Taiwan. I divide the section in insitu thermochronology from the Central Range, detrital thermochronology of the western foreland and eastern forearc sediments, and thermochronology recording exhumation of the western fold-and-thrust belts.

A. *Insitu* thermochronology in the Central Range mountains

As for structural studies, an extensive thermochronological dataset exist for the northern and southern cross-island highways (Fig. 2.5), but other transects and

sparse samples along the Central Range low laying lands (i.e. river mouths) complete the coverage of the Central Range.
Higher closure temperature thermochronological systems have been applied on **1)** plutonic bodies of northern Taiwan [$^{39}Ar/^{40}Ar$ step-heating in hornblend, black and white mica, and microcline; *Lo and Onstott*, 1995]; **2)** backthrust (i.e. west-dipping shear zones) mylonites zones on the same plutonic rocks of northern Taiwan [$^{39}Ar/^{40}Ar$ on neoformed biotite*; Wang et al.*, 1998]; **3)** along several transects of the Central Range [K-Ar on fine fraction _ <2μm _ of white mica; *Tsao*, 1996]; and **4)** on two location in the slate belt and Tananao Metamorphic Belt [whole-rock and matrix ages $^{39}Ar/^{40}Ar$*; Yeh*, 2004]. The reader is referred to *Simoes et al.* [2012] for a comprehensive review.

The main results of high closure temperature system studies can be summarised as follows. Note that I focus the results form the studies yielding Late Cenozoic ages:

- The north-eastern Taiwan granitic bodies analysied by [*Lo and Onstott*, 1995] yield reset microcline $^{39}Ar/^{40}Ar$ ages [Tc~150-350°C; *Reiners et al.*, 2005] equal to ~1.6-1.7 Ma. In contrast, $^{39}Ar/^{40}Ar$ ages on muscovite and biotite $^{39}Ar/^{40}Ar$ [Tc~300-350 °C or 350-410 °C and 350-400°C or 300-330 °C, respectively, depending on the references; first values from *Reiners et al.*, 2005; second values reported in the original paper], while yielding integrated ages of ~25-83 Ma for muscovite and ~20-46Ma for biotite, presented "upward-convex" age spectra with fairly consistent young plateau ages of 6 to 9Ma for muscovite and ~7.7 Ma for biotite. This latter age are interpreted to reflect the age the latest metamorphic event (e.g. neoformation of phengite for the muscovite case). Mixing effect due to diferent generations of metamorphic minerals (i.e. phengite in muscovite and chlorite in biotite) appear to have limited influence in the young plateau ages. Additionally second-generation amphiboles [Tc~400-600°C; *Reiners et al.*, 2005] yield ages of 7.8 Ma.
- $^{39}Ar/^{40}Ar$ ages of biotites in mylonitic shear zones [*Wang et al.*, 1998] and of whole rock ages of the Tananao schists [*Yeh*, 2004], interpreted by the author to be dominated by the neoformed metamorphic mineral age, indicate that backthrusting started between ~3 and 4.1 Ma [*Wang et al.*, 1998] and is coeval to the formation of the west-dipping schistosity formation [~3.3-3.9 Ma; *Yeh*, 2004].
- The wider coverage by *Tsao* [1996] K-Ar ages on the fine fraction (neoformed?) muscovite [Tc~350°C or 250-280°C or 150-350°C; as reported in the original paper, in *Beyssac et al.*, 2007, and *Reiners et al.*, 2005, respectively] confirms the eastward youngening of ages with values as low as 1±0.19 Ma in the eastern Central Range, in agreement with metamorphic grade increase eastward. Ages in the Lushan Fm. are unreset in the southernmost section sampled (Fig. 3.5 and Fig. 3.6), in the southern tip of the Hsuehshan Range along the southern cross-island highway (Fig. 3.5) and the ages progressively degrease eastward in the Pilushan Fm. from or close of the drainage divide (Fig. 3.5) until reaching values equal to 1.5 Ma in the eastern limit of the Pilushan Fm. In the Taroko Belt K-Ar ages remain relatively constant ~1-1.5 Ma and increase again in Yuli Belt to a single value

of 3.9 Ma. The easternmost stripe of the Eocene Pilushan Fm. yields unreseted values >10Ma (Fig. 3.5).

Overall, higher temperature thermochronology indicates that the probable age of peak metamorphism is between 6-9Ma. Constrains on backthrusting-backfolding age, although scarce, are in the range of~3-4Ma. It is worth noting that the record of neoformed minerals probably dates crystallisation and not cooling, an important fact when considering the closure temperature of the thermochronological system.

Additionally, peak metamorphic temperatures have been constrained with Raman spectrometry along several transects of the Central Range [*Beyssac et al.*, 2007]. Maximum burial temperature are estimated to ~500 ^{o}C in the southern cross-island highway (Fig. 3.5). The temperatures are reached, somehow surprisingly, in the black and green schist series of the Taroko belt and not in the structurally depper and stratigraphically older marbles of the Taroko belt, as one would expect. No apparent major temperature jump can be observed along the major structural boundaries of the studied transects.

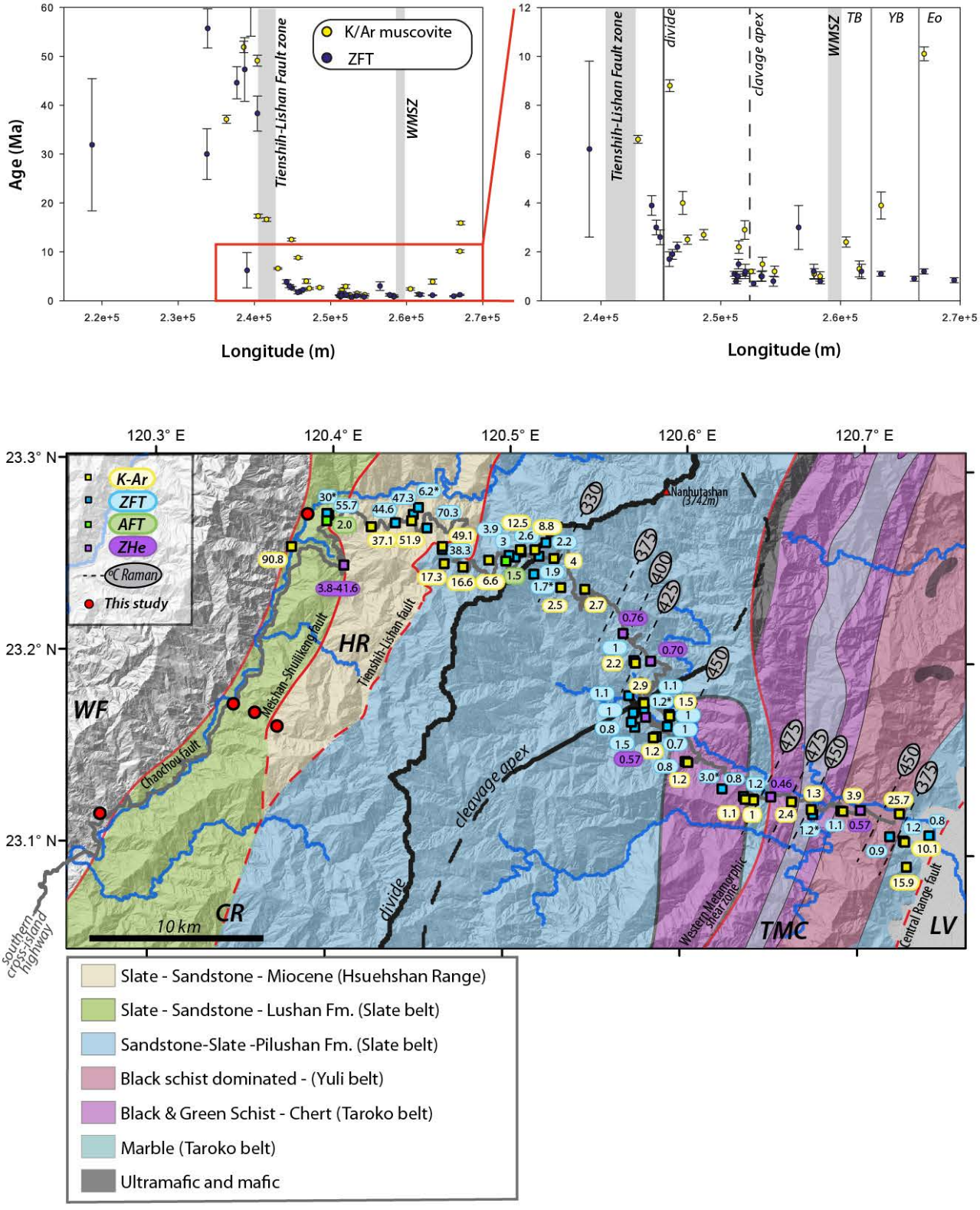

Fig. 3.5*: Southern cross island highway geology and thermochronological constrains (See location in Fig. 2.5).* ***Upper panels:*** *Plot of the horizontal position (x-axis is longitude of the local datum)* ***vs.*** *K-Ar and ZFT ages. TB= Taroko Belt; YB=Yuli Belt; Eo=Pilushan Fm (Eocene).* ***Lower panel:*** *Geological map and existing thermochronological constrains from the southern cross-island highway. Maximum burial temperatures derived from Raman spectroscopy of carbonaceous matter and U-Th/He on Zircon from* [*Beyssac et al.*, 2007]*; K-Ar on muscovite fine fraction from* [*Tsao*, 1996]*, note that the 25.7Ma age was sampled in the eastern Eocene Pilushan Fm.; ZFT pooled ages from* [*Tsao et al.*, 1996; *Willett et al.*, 2003] *and chi-square*

*ages (shown with an asterisk *) from [Liu et al.* 2001]*; AFT from* [*Fuller et al.*, 2006]*. Raman spectroscopy temperature in degrees Celsius. Thermochronological ages in Million years. The eastern sector's geology of the cross-island highway is based on* [*Stanley et al.*, 1981]*. The western sector, including fault trace of the Tienshih and Meishan faults based on* [*Pelletier and Hu*, 1984] *and on own structural observations for the southern portion of Meishan fault. Note that here we assume the Meishan and Tienshih faults to be the southern extension of the Shuilikeng and Lishan faults respectively given its geographic and structural position (i.e. Hsuehshan Range bounding faults), and the 1:500000th map of* [*Chen et al.*, 2000]*. However the geometries of the northern Shuikileng and Likuan faults appear to be steeply east-dipping* [*Camanni et al.*, 2011, 2014; *Brown et al.*, 2012] *while here the fault has been mapped as shallowly east-dipping by* [*Pelletier and Hu*, 1984]*. Cleavage apex position from* [*Lu et al.*, 2010; reported in *Byrne et al.,* 2011]*. WF= Western foothills; CR= Central Range; HR= Hsuehshan Range; TMC= Tananao Metamorphic Core; LV= Longitudinal Valley.*

Among lower thermochronological systems, ZFT and AFT are the systems that has being applied with the most densely coverage in the Central Range. For **ZFT**, *Tsao et al.* [1992] densely sampled the northern cross-island highway and *Tsao* [1996] the southern cross-island highway. Less dense coverage along the same and other cross-mountainous transects was completed by *Liu et al.* [2001]. Additionally, *Willett et al.* [2003] analysed punctual samples and *Lee et al.* [2006] a transect, both mainly in the southern Central Range. Finally, *Kirstein et al.*, [2010b] obtained ZFT ages from two sandstone bodies of the Hengchun peninsula. For **AFT**, *Liu* [1982] obtained ages in the northern Central Range and *Fuller et al.* [2006] all along the island including the southern Central Range and Hengchun peninsula. Finally *Huang et al.* [2008] obtained some extra ages at the southern end of the Central Range in the Hengchun peninsula. *Beyssac et al.* [2007] successfully applied **U-Th/ He on zircon** (ZHe) along the northern and southern cross-island highways and along another transect in the central Taiwan Central Range.

Somehow surprising is the fact that thermochronometric age-elevation-relationships (AER) have been largely unexploited, given the data coverage of the Central Range. The only exception is *Tsao et al.* [1992], the first and only published explicit age-elevation profile along the northern cross-island highway. *Simoes et al.*, [2012] argues that the ZFT age-elevation relationship of *Tsao et al.* [1992] in which an acceleration of exhumation rate of the eastern Central Range at ~1.5 Ma is observed for samples below ~1700m (Fig. 3.6b and detailed discussion below) is an artefact. A simple result of particle path through the orogen, where the low-lying lands of the eastern topographic front necessarily yield younger ages than the higher elevation samples. Although *Simoes et al.*, [2012] 's remarks may be appropriate, particularly given the large horizontal distance of *Tsao et al.* [1992] 's transect (~20km), the authors do not discuss the presence of the break-in-slope in the age-elevation relationship (underplating window?; backstop geometry?).

In the following I extract first-order observations from the thermochronological AER along the northern and southern cross-island highways. I emphasise on the relations between AER and some structural and geological characteristics of the two considered transects (Fig. 3.5 and Fig. 3.6).

Tsao et al. [1992] 's dataset in the northern cross-island highway, although sampled along large horizontal distances and yielding correlations with quite poor statistical significance, provides with some valuable information (Fig.3.6b). The ages reported are ZFT chi-squared ages, which can be defined as the pooled ages of the youngest ages population in a detrital sample [*Brandon*, 1992].

- ZFT reset ages are mostly present to the east of the drainage divide reaching values between ~0.8 and ~2.5 Ma (if considering *Tsao* [1996] data, the range in the eastern divide increase to ~2.9 Ma, and one extra sample yields ~4.6 Ma in the western divide, close to the topographic crest).
- The break-in-slope, although not net and within a region less densely sampled, lies between ~1500m and ~1900m within the Tananao Metamorphic Core (TMC). The timing of the exhumation rate change lies between ~0.8-1.4 Ma, corresponding to the age-range of the lower profile. (~1.5 Ma in the original publication).
    - The lower profile yields generally younger ages with low variation with altitude. Linear regression provides an estimation of exhumation rates of 446m/Myr (r^2=0.14) between ~0.8 and ~1.4 Ma. Mean age of the lower profile samples is 1.1 ± 0.2 Ma (uncertainty is one standard deviation),
    - The higher profile regression indicates exhumation rates of 265m/Myr (r^2=0.12) between ~1 and 2.5Ma.
- Samples from the lower profile pertain to the west-dipping schistosity structural domain while the higher profile samples are in the east-dipping schistosity domain.
- When considering separately the different geological domains (Fig.3.6b and Fig.3.6c):
    - The Slate Belt appears to be exhuming at lower rates of 126m/Myr (r^2=0.31) than the TMC exhuming at 882m/Myr (r^2=0.55; all TMC's data regression).
    - Within the TMC (here the Taroko Belt), the overall two-phased trend is reproduced. Lower profile samples with ages <~1.5Ma exhume at 1255m/Myr (r^2=0.27) and samples >~1.5Ma exhume at 445m/Myr (r^2=0.22) (Fig. 3.6-a2). If regressing together the samples >~1500m, the obtained exhumation of the high TMC samples becomes 118m/Myr (regression equation y = 1764 + 118x; r^2=0.04), a similar value to the one extracted from the regression of the Slate Belt, but with less statistical significance (not in Fig. 3.6).
    - Within the east-dipping schistosity domain (higher profile), although the TMC and Slate Belt yield similar age-elevation trends (i.e. parallel in the age-elevation plot), the age-elevation relationship is not continuous, suggesting a role of the west-dipping West Metarmophic Shear Zone (WMSZ) structural discontinuity in the exhumation of the two distinct geological units. Different exhumation processes (e.g. erosional, ductile flow dominated unroofing) in the distinct geological and structural units may explain the difference.

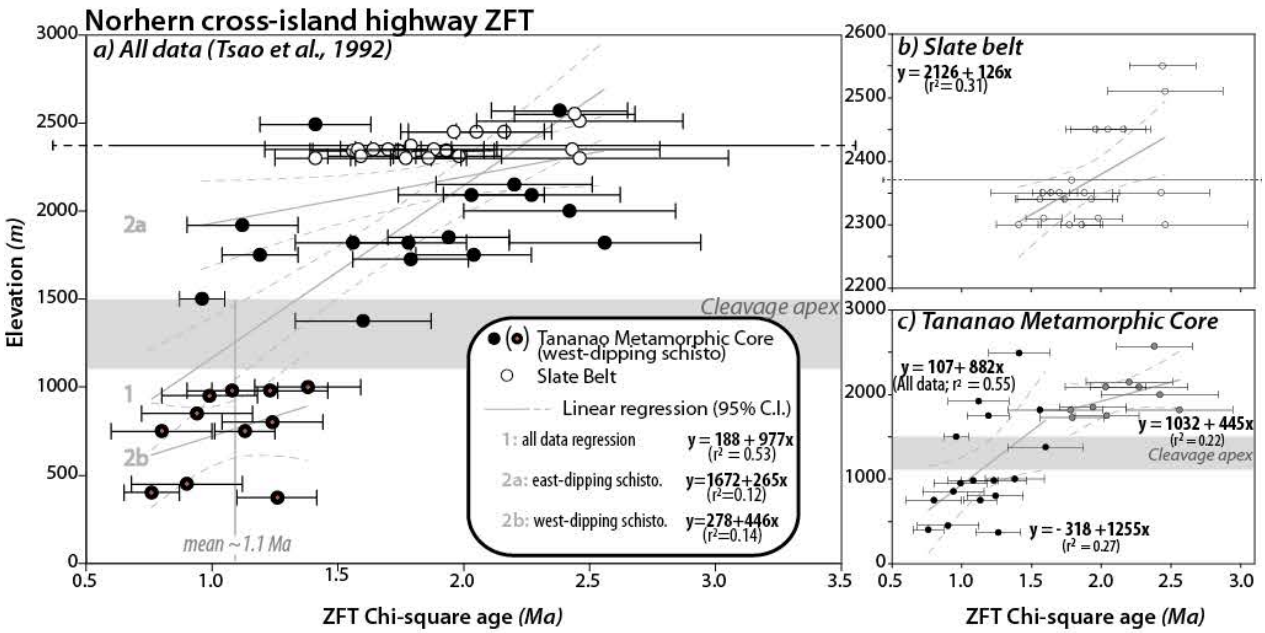

Fig. 3.6: a) *ZFT age-elevation-relationship collected along the eastern part of the northern cross-island highway by* [*Tsao et al.*, 1992]*. Linear regression and 95% confidence interval of all samples (curve 1) and of the two-schistosisty domains (curve 2a and 2b) are shown. Note that all the samples plotted were collected on the eastern divide of the Central Range, the western divide samples being unreset. ZFT ages are chi-square ages that are mostly concordant with pooled ages (see original publication for comparison).* ***b)*** *Detail and regression of the Slate Belt samples.* ***c)*** *Detail and regression of the Tananao Metamorphic Core samples with a two-phased exhumation as proposed in the original paper. Note that the all-data regression is not plotted for clarity just the equation is given.*

For the southern cross-island highway, I consider all the existing thermochronological data along the transect, including the data in the western divide and topographic front (Fig.3.5, Fig. 3.7 and Table 3.1).

- Structural and stratigraphic discontinuities appear to separate distinct exhumational domains (Fig. 3.5):
  - The Tienshih-Lushan fault neatly separates reset, in the east, and unreset, in the west, K-Ar and ZFT ages.
  - The Chaochou fault's hanging wall AFT ages are reset with ages ~3Ma (Fig.3.7).
  - The Central Range fault's hanging wall ages present the youngest ages of the transect.
  - The easternmonst stripe of Eocene Pilushan Fm. yield reset ages for all thermochronometers except for K-Ar on muscovite, suggesting a role in exhumation of the stratigraphic contact with the TMC at depths higher than K-Ar's closure (crystallisation?) temperature.

- Generally, younger ages are found to the east of the drainage divide, with ages ranging from 0.4 Ma to 8.8 Ma for all thermochronometers (Table 3.1).
- AER for decreasing closure temperature systems indicates a general increase of exhumation rates with time. When regressing linearly all the data points for each system together, exhumation rates evolve through time as follows (Fig. 3.7):
  - ~280 m/Myr between ~8.8 Ma and ~1.2 Ma (K-Ar muscovite).

- ~760 m/Myr between ~2.2 Ma and ~1 Ma (ZFT).
- ~2240 m/Myr between ~1.5 Ma and ~0.4 Ma (AFT).
- ~5440 m/Myr between ~0.8 Ma and ~0.5 Ma (ZHe).

Note that AFT and ZHe exhumation rates and ages are not concordant considering closure temperature of both systems (cf. Table 3.1). This is probably due to lack of data points in the AER and to the use of one data-point (i.e. 1.5 Ma at 2558m, only point in the higher profile) belonging to the western divide, but close to the crest (Fig. 3.5), in the AFT's AER.

- For the ZFT and K-Ar on muscovite systems, the AER displays a relatively well defined break-in-slope probably lying between at ~1400-1800 m, roughly coincident with the cleavage fan apex (Fig. 3.7):
  - For ZFT, the lower profile ages remain relatively constant (mean of ~1± 0.2 Ma). For K-Ar on muscovite, the AER in the lower profile is less marked and ages have a wider range (3.9 to 1 Ma with a mean value of 1.8 ± 1; Table 3.1); however a cluster with a mean age of 1.2 Ma is observed.
  - The higher profile linear regression indicate exhumation rates of ~1440 m/Myr between ~2.2 and ~1 (ZFT) and a of ~200m/Myr between ~8.8 Ma and ~2 Ma (K-Ar).

Numerical modelling of age-elevation profiles [e.g. *Braun et al.*, 2012; *Gallagher*, 2012; *Willett and Brandon*, 2013] of the northern and southern cross-island highways would yield more reliable exhumation rates evolution through time, given the poor statistical reliability of some of the linear regressions as well as the large horizontal distance span of the transects.

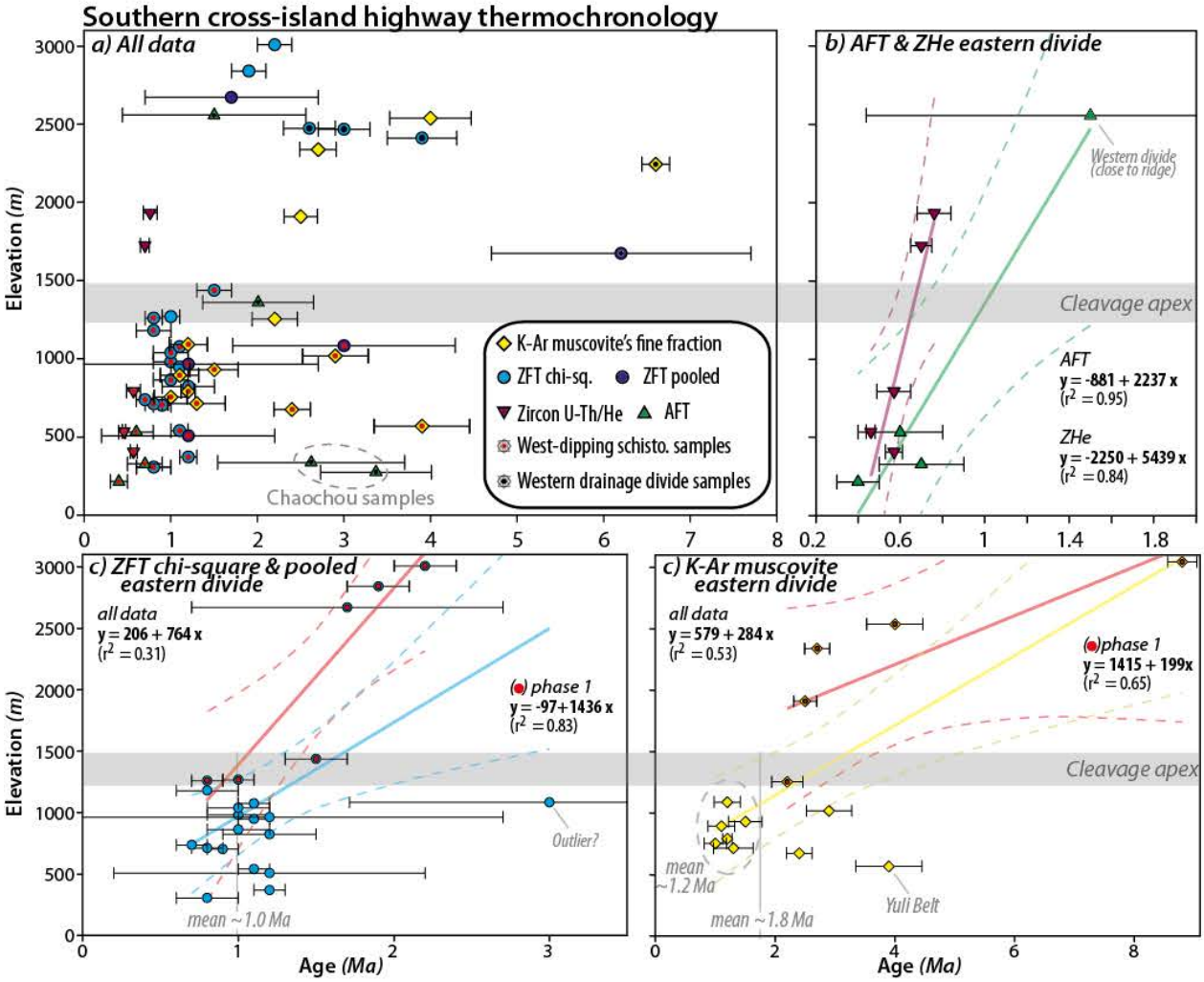

Fig. 3.7: a) *Thermochronometric age-elevation relationship for all data along the southern cross-island highways. ZFT data from Liu et al. [2001] (chi-square age), Tsao [1996] (pooled age) and Willet 2003] (pooled ages). Note that the outlier in a2) is a pooled age from Liu et al.* [2001]. *Some of the lower altitude AFT samples do not belong to the southern cross-island highway but have been sampled further south in the eastern Eocene-Pilushan Fm. stripe (x2) and further to the north in the TMC (x1) by Fuller et al. [2006] and Willett et al.* [2003]. *Similarly, Chaochou samples include samples that do not appear in Fig. 3.5 (positioned further south along the Laonung river sides). See Fig. 3.5 for references.* ***b)*** *AER for AFT and ZHe of the eastern Central Range. One AFT age from the western divide is included as it is the only available AFT age at high altitudes.* ***c)*** *AER for ZFT of the eastern Central Range. ZFT ages include chi-square ages of Liu et al. [2001] which are mostly concordant with pooled ages, except for the sample marked as "outlier".* ***d)*** *AER for K-Ar on muscovite's fine fraction for the eastern Central Range*

System (T_c)	**K-Ar** *300-350 °C (250-280 °C)*	***1σ***	**ZFT** 230 °C *(260 °C)*	***1σ***	**ZHe** *160-200°C*	***1σ***	**AFT** *90-120°C*	***1σ***
***Mean* west-dip. schisto.**	1.83	*1.01*	0.99	*0.22*	0.53	*0.06*	0.57	*0.15*
***Mean* eastearn divide**	2.62	*2.04*	1.12	*0.39*	0.61	0.12	0.88*	0.48
Range west-dip. schisto.	3.9-1		1.5-0.7		0.57-0.46		0.7-0.4	

Range eastern divide	8.8-1	2.2 (3.9)-0.7	0.76-0.46	0.7 (1.5)-0.4
Range reset	8.8-1	3.9-0.7	*idem*	3.4-0.4

Table 3.1: *Mean and range of the thermochronological ages within the distinct structural and physiographic domains at the southern cross-island highway. Ages in brackets for AFT and ZFT indicate ages in the western divide but close to the topographic ridge. For muscovite K-Ar ages, the choice of reset vs. unreset is done following Lo and Onstott* [1995] *criteria (i.e age >~10Ma taken as mixed age). In the range and mean calcualtion for K-Ar, the unreset ages from the eastern Eocene stripe are not considered. ZHe is U-Th/He on zircon. Ages are in million years. 1σ corresponds to the standard deviation. Closure temperature (Tc) of the system from* [*Reiners et al.*, 2005] *with additional estimation for K-Ar and ZFT, in brackets from Beyssac et al. [2006] and Liu et al.* [2001] respectively. **Mean considering 1.5Ma ages close to the divide.*

An additional unpublished age-elevation profile was presented during the Tectonics of Taiwan International Meeting (Taoyuan, Taiwan, 2013) by [*Byrne and Lee*, 2013]. The age-elevation profile was sampled along the Hsuehshan Range reaching the highest point of Taiwan (Yushan mountain, 3960m), although the exact sample sites were not shown. ZFT and ZHe were applied to most of the profile samples. The AER are linear without any unequivocal break-in-slope and indicate exhumation rates of ~500-800 m/Myr between ~5 and ~2 Ma and of 3000 m/Myr between ~2 and ~1Ma. The timing and rates are of the same order of magnitude as the ones extracted in the southern (Fig. 3.7b and Fig. 3.7c) and northern cross-islands highways (Fig. 3.6c).

Taken together, the existing thermochronological ages and the general structure of the Central Range, we can assert the following:
1) From AER in the eastern divide:

- Different schistose structural domain exhume at different rates as shown by bi-phased exhumational trends with a break-in-slope generally coincident with the cleavage apex and lying at altitudes between 1400-1900m. AER display a consistent acceleration of exhumation of the west-dipping schistosity TMC at ~1-1.5 Ma to exhumation rates exceeding ~2000m/Myr. Exhumation before ~1-1.5 Ma exhumation may still be high but probably at lower rates.
- Structural and geological discontinuities seem to separate differently exhuming structural domains:
    - The Eastern Metamorphic Shear Zone separates two similarly exhuming but discontinuous domains in the northern cross-island highway. In the southern cross-island highway the same structural discontinuity is less evident.
    - The Tienshih-Lishan fault is a major structural discontinuity probably active since ~6.6 Ma (based on muscovite´s K-Ar) or ~3-4 Ma (based on ZFT). This observation was invoked as supporting an out-of-sequence activity by *Tillman and Byrne* [1996].
    - The Chaochou fault seems to be active since ~2-3Ma as recorded by AFT samples close to the fault.

- The eastern Eocene Pilushan Fm. stripe found in the southern cross-island highway has not been buried below the muscovite's closure temperature. The stratigraphic boundary between this formation and the TMC either corresponds to the muscvite's K-Ar closure temperature isotherm or was active before closure of the muscovite's K-Ar system. This same discontinuity is not apparent in the lower closure temperature thermochronometers datasets.

A subsidiary observation is that for the ZFT system the oldest reset ages are not in the topographic crest but slightly further west. This may be the result of long-term orogen kinematics as prediced by critical wedge models [e.g. *Dahlen and Barr*, 1989; *Willett*, 1999] or, alternatively, may be indicative of a more recent physiographic changes in the orogen (i.e. divide migration).

B. Detrital thermochronology of the syn-orogenic sediments

Thermochronological studies of sediments derived from the Central Range are not numerous. Published data is mainly concentrated in the forearc and intraarc sediments of the Coastal Range [*Liu et al.*, 2000; *Huang et al.*, 2006; *Kirstein et al.*, 2010a, 2013]. Scattered samples from the Western Foothills sedimentary series exist [*Liu et al.*, 2001] and other unpublished studies of present day river sediments and older foreland series have been presented in international conferences [*Fellin et al.*, 2006, 2008, 2009, 2012; *Willett et al.*, 2008; *Nagel et al.*, 2012a]. Finally, *Lock* [2007] applied AFT and U-Th/He on apatite along various sections in the Western Foothills but, although mainly focusing on the post-depositional thrust and fold related exhumation of the western fold-and-thrust belt, obtained some pre-depositional ages related to the exhumation of the Central Range.

Forerarc stratigraphy preserves the whole orogenic record due to the limited post-depositional erosion. This contrast with the western foreland stratigraphy, which has undergone significant erosion and reworking [*Chang and Chi*, 1983] during the fold-and-thrust belt development, erasing the proximal sedimentary record of the Central Range structuration. Moreover, because the metamorphic core and east verging formations outcrops in the eastern divide of the central range, its exhumational history is well recorded in the forearc sediments [*Teng*, 1987; *Dorsey*, 1988], and thus provide with an excellent setting to understand back-thrust/back-fold development in the Central Range.

Liu et al. [2000] worked on the northern Coastal Range Plio-Pleistocene Shuilien conglomeratic Fm. along the Shuilien and Chimei transects (depositional age of ~2.5-3.4Ma and ~1-1.7M respectively). The authors applied ZFT dating on a limited number of zircon grains from metasandstone boulders finding ZFT grain-ages ranging from 1.4 to 8.5 Ma and ZFT pooled ages of 3.8 ±0.4 Ma (13 grains) and 3.3 ±0.3 Ma (19 grains) for the Shuilien conglomerate at the Shulien and Chimei sections, respectively. Although of doubtful meaning given the small number of grains dated, reported lag-times of ~1.8-0.9Myr and ~2.8-2.1Myr respectively may be indicative of a sedimentary source positioned in the now at higher-altitude east-dipping schistosity domain for the Shuilien conglomerate at

the Shuilien section, as opposed to a dominant source at the low lying west-dipping domain for the Shuilien conglomerate at the Chimei section (Fig. 3.6).

Kirstein et al. [2010, 2013] carried out a more comprehensive study of the Plio-Pleistocene stratigraphic sections along northern, central and southern parts of the Coastal Range (Fig. 3.9). The authors applied ZFT and U-Pb double-dating with additional limited constraints from AFT and U-Th/He on zircon. Their main findings include **1)** Input of ZFT grains with ages <~ 3Ma starts at the Plio-Pleistocene boundary (~1.9 Ma) in the northern and central section and start later (~1.2 Ma) in the southern sections. **2)** In both the northern and southern sections the appearance of ZFT ages < ~10 Ma start in the Pliocene (Fig. 3.9), conclusion in agreement with more limited data by *Liu et al.* [2000] and *Huang et al.* [2006]. While *Kirstein et al.* [2010] interpret as orogenic only the ZFT ages < ~3 Ma and as partially reset ZFT ages <~10Ma, *Kirstein et al.* [2013] favour an interpretation where all ZFT ages <~10Ma reflect the orogenic history, and pinpoint the importance of sediment transfer pathway and sedimentary centres fractionation in the sedimentary record of the Coastal Range.

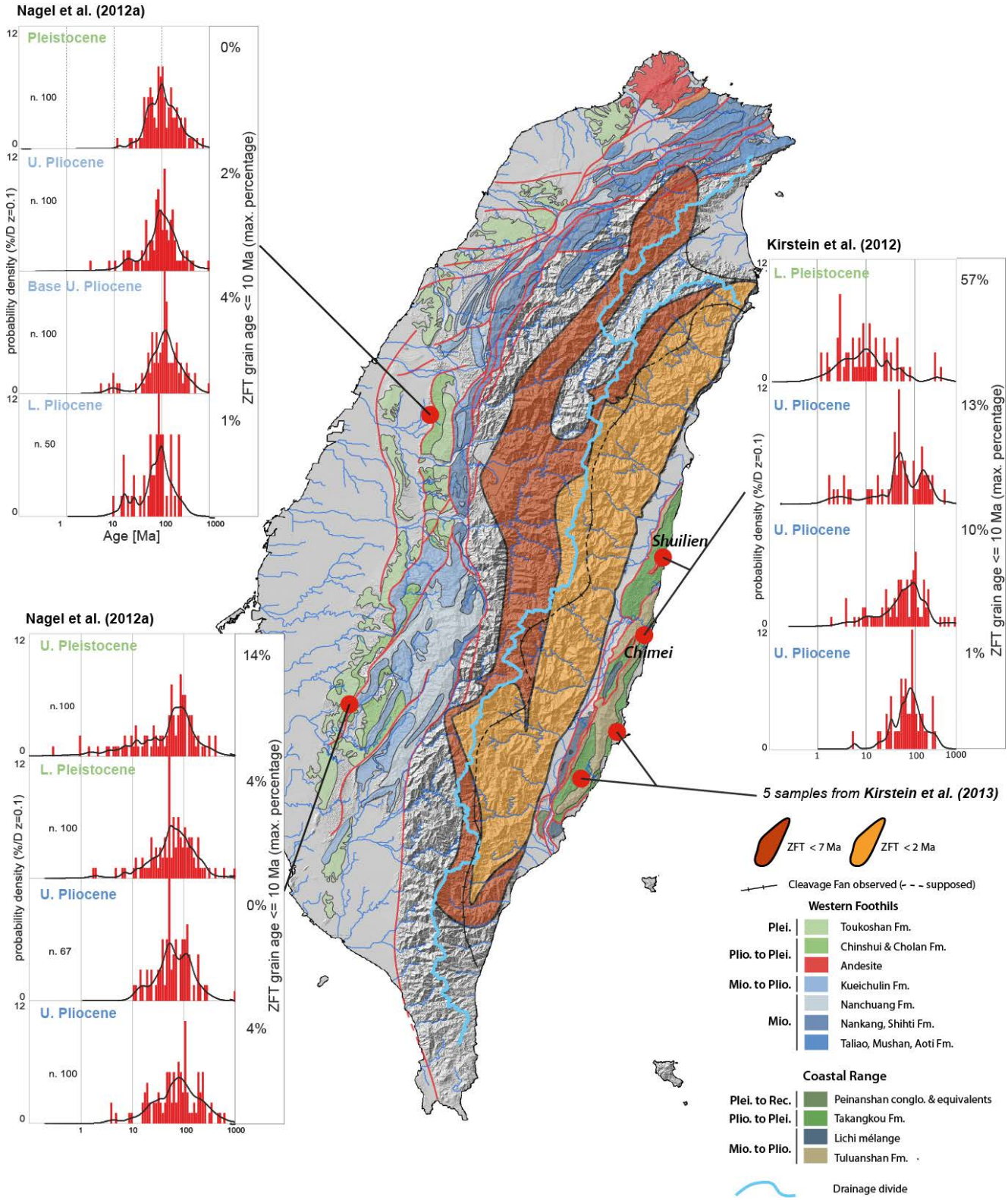

Fig. 3.9: *Existing ZFT detrital studies from foreland (west) and forearc and intraarc (east) studies in Taiwan. The results from Kirstein et al. (2013) are not shown in this figure, only the position of the studied transects; see text for discussion including Kirstein et al. (2013). The Central Range reset zones (i.e. ZFT age isochrones) are an updated version comprising the results presented in this chapter. Graphic representation of the detrital data from* [*Nagel et al.*, 2012a]. *Cleavage fan modified 2from* [*Lu et al.*, 2010b].

Liu et al. [2001] sparsely sampled Miocene series of the Western Foothills and dominantly found pre-orogenic ages related to the eastern China sedimentary

sources cooling history. More detailed thermochronological investigation was done by [*Fellin et al.*, 2006, 2008, 2009, 2012; *Willett et al.*, 2008; *Nagel et al.*, 2012a] but has been published only in conference proceeding abstract. Conversely to the Coastal Range sections, the western foothills do not present a net timing where orogenic ages start to be eroded in the Central Range. The studied sections rather reflect probable fluctuation of the drainage divide position variably exposing the reset areas (<~7Ma and <2Ma; Fig. 3.9) to erosion since the Pliocene.

C. Exhumation of the western fold-and-thrust belt

Lock [2007] applied AFT and U-Th/He on apatite along various sections in the Western Foothills (WF). The author undertook 2-D thrust motion modelling to reproduce the aged. The main results can be summarized in the following main points:

1) Overall, thrust-related cooling ages of the WF are older in the west and younger towards the west. Rather than reflecting out-of-sequence thrusting, ages record vertical advection of material above a thrust ramp crossing the closure temperature of thermochronological system, and subsequent horizontal transport on the upper flat décollement. Indeed, the youngest ages are systematically in the core of fold-bend-fold anticlines forming U-shaped distribution of thermochronological ages in distance vs. age plots within thrust sheets, and older ages towards the west indicates longer post-clusure transport along the shallowly dipping décollement above closure temperature of the system. The rate of westward deformation propagation calculated with age gradients is ~12mm/yr in central and southern WF, and appear to be constant since the onset of thrust activity in the WF.

2) The oldest AFT ages interpreted as collision related thrust faulting in the WF is ~3.5 Ma in the central and northern WF and ~1Ma in the southern WF. Nevertheless ~3.5 Ma ages are also found in the southern WF but 2-D numerical models of fault propagation do not manage to reproduce this ages. The onset of thrusting and exhumation of the northern and central WF at ~3.5Ma is coincident with a major increase in sedimentation rates and subsidence [*Chang and Chi*, 1983; *Lin et al.*, 2003] and coincident with similar AFT ages in the Hsuehshan Range and southern Central Range including the Hengchun Peninsula [*Fuller et al.*, 2006]. *Lock* [2007] interpreted this age cluster in the Central Range as marking the onset of erosion of the subaerial part of the subduction accretionary wedge, not relating the arc-continent collision.

3) The youngest cooling ages indicate thrust activity at ~0.5Ma in the southern and central WF and ~1.2Ma in the northern WF, interpreted as recording a steady southward shift of fault activity, with the northern WF no longer accommodating convergence. However ages ~0.5Ma are also found in the southern Taiwan WF mainly on the Chishan thrust-sheet, but are interpreted as partially reset samples.

4) The Chaochou fault is interpreted as not accommodating significant thrust motion since 3Ma on the basis of similar ages on both sides of the faults, implying that the sharp topographic jump across this fault to be depositional. Nevertheless the author considers the possibility of an activity at ~2.5-3Ma due to a slight mismatch of the ages. This suggests the thrust motion of the Chaochou

fault geodetically measured today [*Ching et al.*, 2007a] to be a very recent feature.

III. Adopted approach

After this review of the existing thermochronological studies, I present the adopted approach in my study and the main strategy and goals, followed by a brief analytical and laboratory techniques description.

A. Sampling strategy in southern Taiwan

Three areas (fig. 3.10) where sampled for thermochronological analysis intended to constrain exhumation at different temporal and spatial scales in the orogen (fig. 3.11).

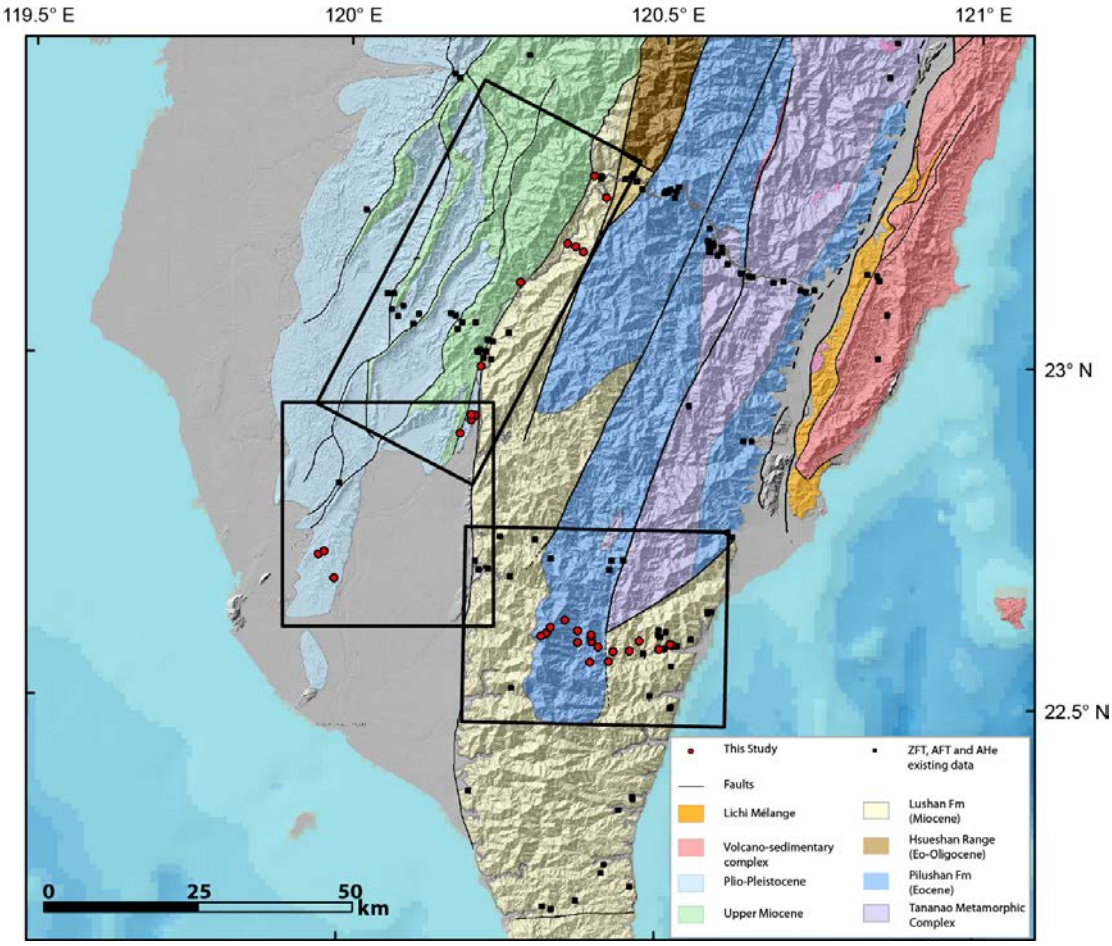

Fig. 3.10: *Map of Southern Taiwan with the sampled areas and the existing ZFT, AFT, and U-Th/He (AHe) on apatite. Existing data points from* [*Tsao*, 1996; *Willett et al.*, 2003; *Fuller et al.*, 2006; *Huang et al.*, 2006; *Lee et al.*, 2006; *Lock*, 2007] *and from this study (Mesalles et al., 2014, pending minor corrections).*

We used four different approaches (fig. 3.11):

- A vertically distributed transect across a high relief area and along a short horizontal distance in the eastern Central Range to constrain the exhumation history of the Central Range.

- A horizontal profile along the eastern Central Range intended to record a potentially the activity of faulting in the retro-wedge (e.g. SZ1from previous chapter).
- Foreland detrital sediments from Plio-Pleistocene syn-tectonic conglomeratic deposits of the western and northern Pingtung basin. This was aimed to improve the understanding of the ~2Ma major erosive phase (tectonic vs. climatic origin).
- Localised bedrock samples on the western Central Range along the Laonung catchment, main drainage basin running into the Pingtung Basin. This was carried out for three main reasons: 1) Obtain cooling age constraints on the main source of the Plio-Pleistocene conglomeratic deposits; 2) Improve the geographical coverage in the pro-wedge area and resolve as the area has been interpreted as partially-reset samples despite containing young ZFT & AFT ages (i.e. 3-6 Ma) [*Fuller et al.*, 2006; *Lock*, 2007].

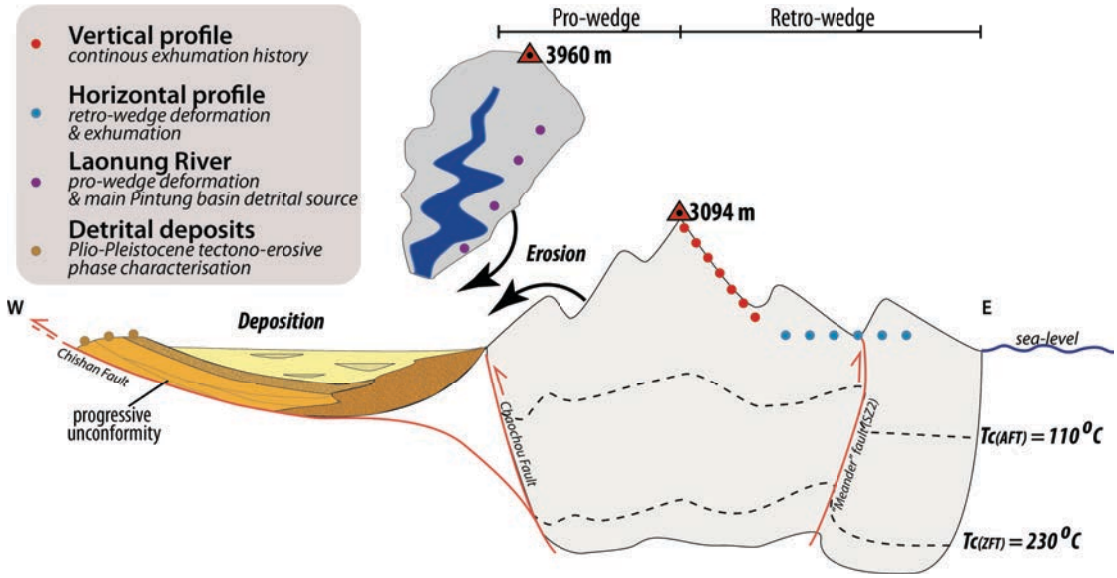

Fig. 3.11: *Schematic representation of the sampling strategy. Tc is the closure temperatures for apatite (110°C) and zircon (230°C)* [*Reiners et al.*, 2005]. *Triangles represent the highest local topographic peaks, Yushan (3960 m) and Beitawushan (3094 m). Note how detrital samples were collected in a syn-orogenic conglomeratic deposit with the formation of a progressive unconformity and are thus likely reflecting a major tectono-erosive phase starting at Plio-Pleistocene times. The Laonung river samples are bedrock samples exposed along the riversides.*

For the sake of clarity, from here on, I will refer as "detrital" the ages or samples recording the pre-depostional history of foreland sediments, and as "insitu" or "bedrock" the ages or samples mainly recording the post-depostional (i.e. exhumational) thermal history of the sampled Central Range sediments.

1) Eastern Central Range: vertical profile and horizontal transect along the retro-wedge

19 samples were collected along the Taimali valley (Fig. 2.24) including one vertical profile and one horizontal profile (i.e. iso-altitude transect) within the Miocene and Eocene passive margin sedimentary series. The vertical profile was sampled in upstream of the Taimali river on the eastern flank of the Peitawu mountain and reaching the highest peak in the area (Peitawushan, 3096 m). The sampled formations range in depositional age from Miocene to Eocene. The profile spans an altitude between ~465 m to ~3096 m and was sampled sub-parallel to the structural trend and in the same structural unit (i.e. StU1 defined in the previous section). The horizontal profile was sampled along most of the tributaries of the Taimali river at an altitude of ~465 m except for two of the easternmost samples that were collected at ~274 m due to inaccessibility. The horizontal transect crosses the main fault bounded structural units described in the previous chapter.

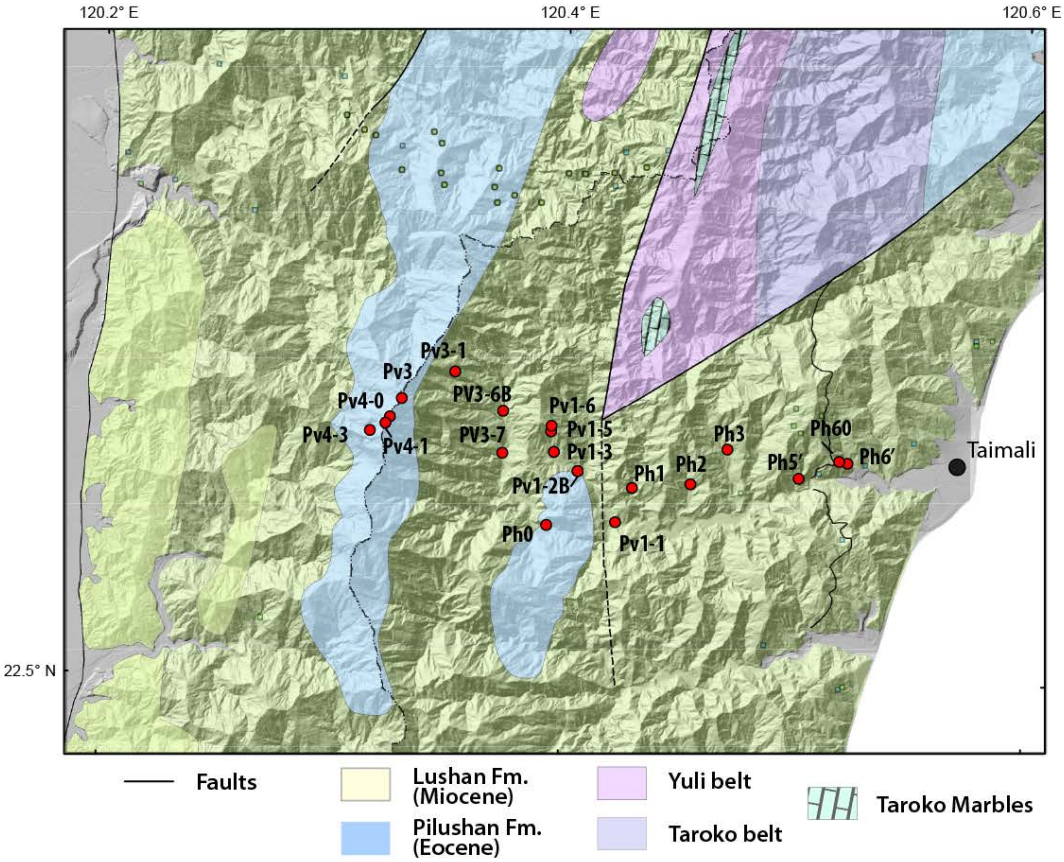

Fig. 3.12: *Geology map of the southern Central Range, with the position and names of the samples collected (red circles). Existing thermochronological data is depicted in green dots.*

The thermochronological vertical profile approach has been extensively used in orogenic settings [e.g. *Fitzgerald et al.*, 1995; *Valla et al.*, 2011] and assumes that present day altitude along a steep vertical profile corresponds to different crustal depth presently exhumed to the surface. Thus, thermochronological age-elevation relationships (AER) correspond to the exhumation rates of the given crustal block at a given time range without need of any assumption on the

geothermal gradient at the time of closure. Any change on the AER trend indicates a change in exhumation rates at the age of the AER break-in-slope [Fig. 3.3; e.g. *Reiners and Brandon*, 2006].
On the other hand, the horizontal profile has as a main aim to constrain the timing of the activity and offset of mapped faults in the Taimali area and exhumation of each of the structural units, without the need to consider the topographic effect on geotherms. For instance, if samples on each sides of the fault display different ages, it could mean that the fault was active such that the age of the younger samples gives a minimum age bound for the fault activity. Combining more than one thermochronometer per sample could further constrain the timing, although we did not manage to do so. If no age offset is observed, it could mean that the fault offset is not enough to significantly offset the ages or simply that the fault is not active.
The literature is not abundant for the horizontal, iso-altitude transect. Most of it is from sampling along tunnels [*Foeken et al.*, 2007; *Glotzbach*, 2008] where thermochronological age disparities were attributed to topographic development, not to the activity of single structures. However, it is common to invoke fault activity to explain age disparities of relatively close samples, but the exact effect of faults on the thermal structure of the shallow crust is not well known, particularly the effect of fluids circulating along the fault, which possibly counteract or accentuate the thermal effect of thrust and normal faults, respectively.
As discussed in the previous section, *Lock* [2007] constrained the areas of maximum exhumation within single thrust sheets in western Taiwan fold-and–thrust belt. The author agrees in that a jump across a fault may be indicative of the activity of the fault at the time of the youngest cooling age. However in foreland normal propagating sequence, or in closely spaced faults settings, one fault may record slip along a younger fault but the timing in which each fault was active may be preserved. However, in our case the structural context is not as simple as in the WF, and the geometry of the faults at depth is not well constrained. Moreover given the probable young age of most of the deformation observed in the area, the lag-time to expose material from below the closure temperature of the thermochronometric system needs to be considered, although this may be not be as important given the high convergence and deformation rates. Additionally, a jump in ages across the fault depends on how much offset and cycling of material has occurred on the structure, so rather than capturing the initiation of activity as expected, we could get a record of steady-state or decline of activity.

2) Plio-Pleistocene foreland sediments: record of a recent tectonic-erosive phase

A total of six samples were collected along two Plio-Pleistocene sections of the southern Western Foothills (WF) and one sample was taken from an older Pliocene clastic formation (Fig. 3.13).
The Plio-Pleistocene sections are mainly formed by conglomeratic series, the Linkou conglomerate (*嶺口礫岩 not to be confused with 林口礫岩_ Linkou conglomerate of Northern Taiwan, with the same English Romanization*) and the Liukuei conglomerates (*六龜礫岩*). Both are thought to be local members and lateral equivalent of the widespread coarsening upwards, shallow marine to

fluvial, Toukoshan formation (cf. Fig. 1.16 of Chapter 1), a stratigraphic level marking the emergence of the WF.
The additional sample was taken from below an angular unconformity in the Linkou section and belongs to the Nanshihlun sandstone, a member of the Pliocene Wushan formation.

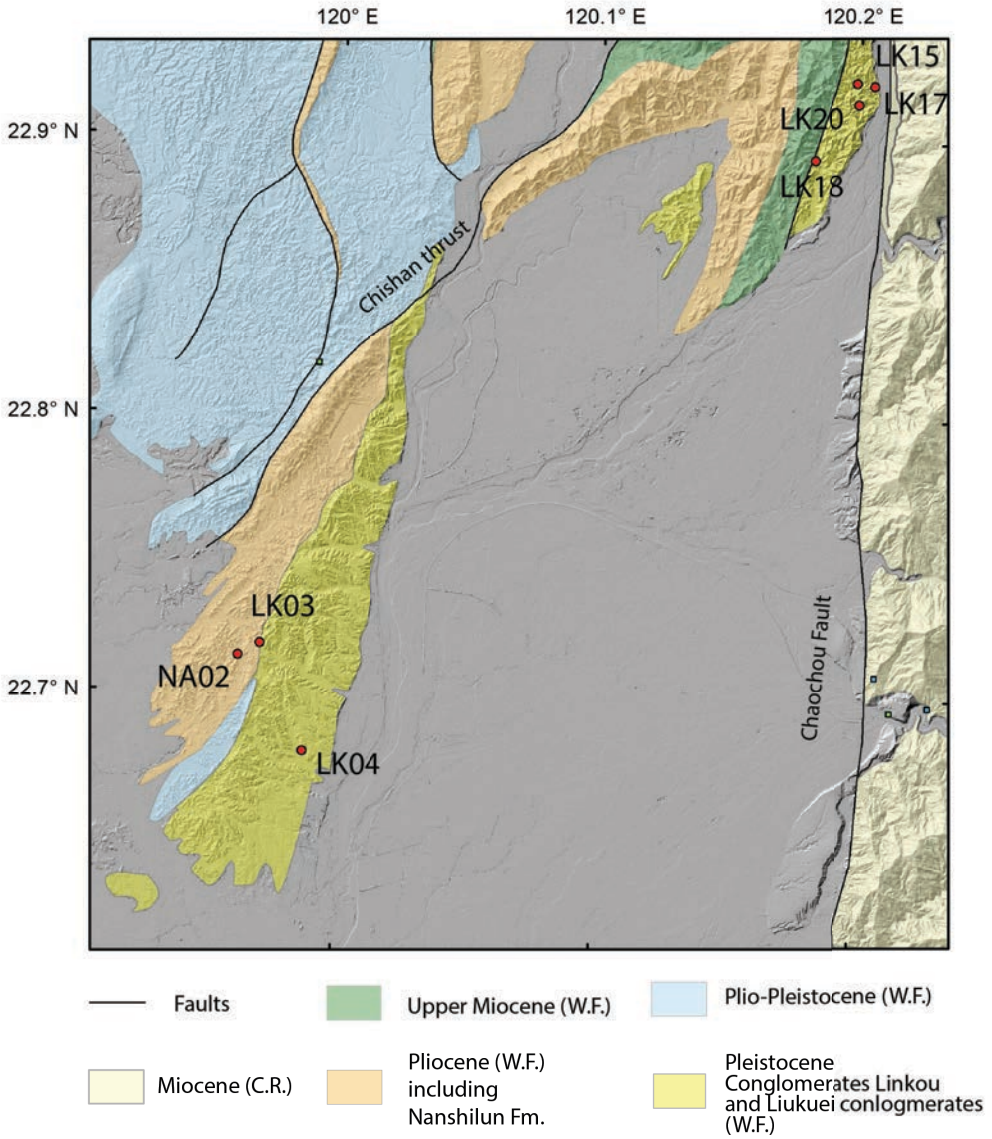

Fig. 3.13: *Geology map of southern south Western Foothills, Pingtung Basin and Central Range. Samples collected are shown as red circles (LK for Linkou and Liukuei Fm. and NA for Nanshihlun Fm.).*

The depositional age of the shallow-marine base of the Linkou conglomerates is constrained by nanofossil biostratigraphy, giving an age between 1.96 and 1.7 Ma (base of nanofossil zone NN19; *Chi*, 1979). The upper sections are inferred to belong to the middle Pleistocene (upper NN19; *W.-R. Chi*, 2012, *personal communication*). The age of the Liukuei member is unconstrained but was originally thought to be older than the Linkou member due to its more competent and consolidated lithology [*Ho*, 1988]. This seems to have been confirmed by unpublished magnetostratigraphic data [*Horng et al.*, 2007], although the results of the study are not conclusive.

For the sample below the angular unconformity in the Nanshilun sandstone, the depositional age is constrained by calcareous nanofossil biostratigraphy to ~3.7-3.9 Ma (NN15; *Chi*, 1979).



***Fig. 3.14**: Linkou and Nanshihlun Formations as seen in the Western Foothills, few kilometers north of Pingutng. Note the typical ruined morphology of the Linkou conglomerate in the back, and the relative steep dip attitude of the Nanshihlun Fm.*



***Fig. 3.15**: Folded Liukuei conglomerates as they appear below fluvial terrace along the Laonung river.*

Depositional environment of Linkou member is interpreted to be similar to the present Laonung-Kaoping river presently running southward on the Pingtung plain. Sedimentary facies in the Linkou member show discrete pebble filled channels and bars surrounded by thick overbank deposits (Fig. 3.12). The ratio of channel fill and overbank deposits indicates rapid subsidence and frequent avulsion during deposition. High subsidence rates are in agreement with the great thickness of the deposits locally reaching more than 2000m thick [*Chi*, 1979]. Additionally, the angular unconformity with the underlying Pliocene and Pleistocene series and the decreasing dipping of the sedimentary beds as we go upsection highlights a probable progressive unconformity reflecting the

syndepositional activity of the Chishan fault. This interpretation is in agreement with the geographical distribution of the conglomeratic formations, limited to the Pingtung depression, with no conglomeratic depostis overbridging the Chishan fault escarpment, which arguably started or reactivated its activity at Plio-Pleistocene times.

The Liukuei member presents more relief-proximal facies with no fine sediments or overbank depostis. It is interepreted as deposited in a mountain front alluvial fan. In the field, a reddish patine and a slightly more consolidated matrix characterize it. Close to the Chishan backthrust the Liukuei pebbles are fractured and the whole comglomeratic serie is folded indicating a postdepostional activity of the fault.

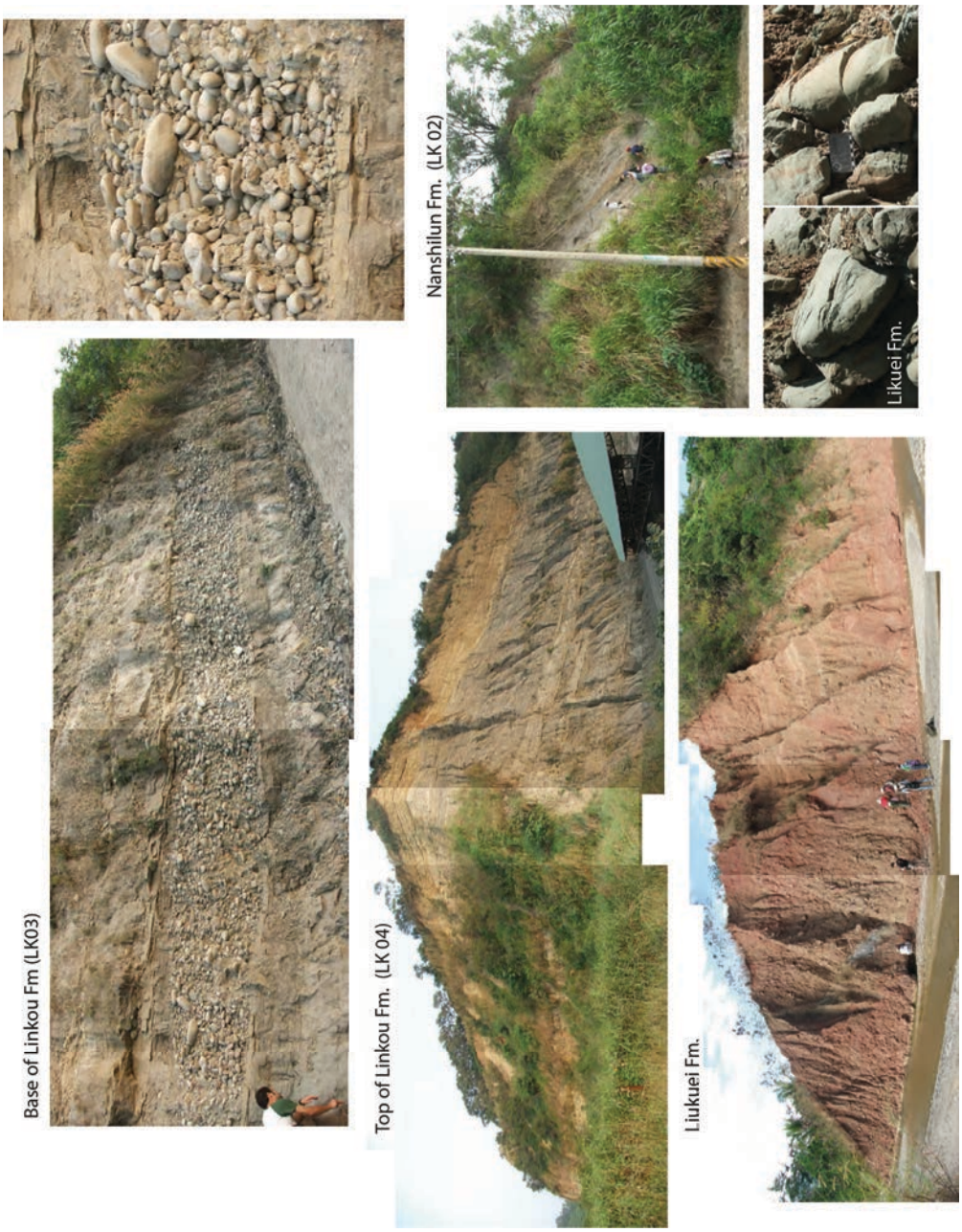

Fig. 3.16: *Field exposures of the sampling sites of conglomerates of the Linkou and Liukuei Formations . Note the tipical braided river fluvial facies of the Linkou Fm, with localized channels and bars surrounded by thick overbank muddy deposits. The deposit architecture suggest rapid subsidence and frequent channel avulsion, very much like preent day Laonung river. Lower right detail photo of the Liukeui pebbles, show fractured pebbels due to postdepositional tectonism.*

Detrital thermochronology of foreland sediments provides the thermochronological ages of the sediment source areas at the time of sedimentation. If the detrital sample preserves its pre-depositional thermal history and the stratigraphic age is well constrained along the sampled section, lag-times evolution through stratigraphic time can be extracted [*Bernet and Spiegel*, 2004]. Lag-time corresponds to the time taken by the sample from the closure of the thermochronological system in the source area to its deposition (i.e. detrital age minus stratigraphic age); shorter lag-times imply faster exhumation rates and longer lag-times imply slower exhumation rates of the sediment's source area. Given the significance of the coarse deposits of the

Toukoshan formation and its apparently synchronous deposition in the Western Foothills, detrital thermochronology can shed light on the nature of this major erosive event.

3) Western Central Range: pro-wedge exhumation and source rocks of the western foreland sediments.

Finally, 6 bedrock samples were collected along the Laonung river catchment (Fig. 3.17) for AFT and ZFT dating. The Laonung catchment drains the highest peak in Taiwan (Yushan, 3954m; Fig. 3.3) and most of the >3000m peaks of southern Taiwan (Fig. 3.17) and is a major sediment source for the Pingtung basin where the Linkou and Liukuei conglomerates were deposited likely in a similar geomorphic configuration as the present day one (*cf.* section 2 above).
Along most of its course, the river follows the western Central Range bounding fault, the northern continuation of the Chaochou fault, known as Laonung fault or Tulugwun fault, a major crustal scale fault linked further north to the Shuilikeng fault. Although little discussion exist in the English-written literature [*Pelletier and Hu*, 1984; *Ho*, 1988] and with the existing maps consistently placing the fault along the Laonung river (e.g. Chinese Petroleum Corporation geological map, Chiayi Sheet,1:100000), the trace of the Laonung fault is not apparent in the field and the stratigraphic offset (Lower Miocene in the footwall and Middle Miocene in the hangingwall) and thermochronological ages (*Lock*, 2007; as discussed previously) indicates a limited thrust activity, in contradiction with present-day geodetic motion of the Chaochou fault further south [*Ching et al.*, 2007a].To the west of this structural boundary the Upper Miocene series outcrop along the inner WF fold and thrust belt. To the east lies the Low to Middle Miocene and Eocene series of the Slate Belt.

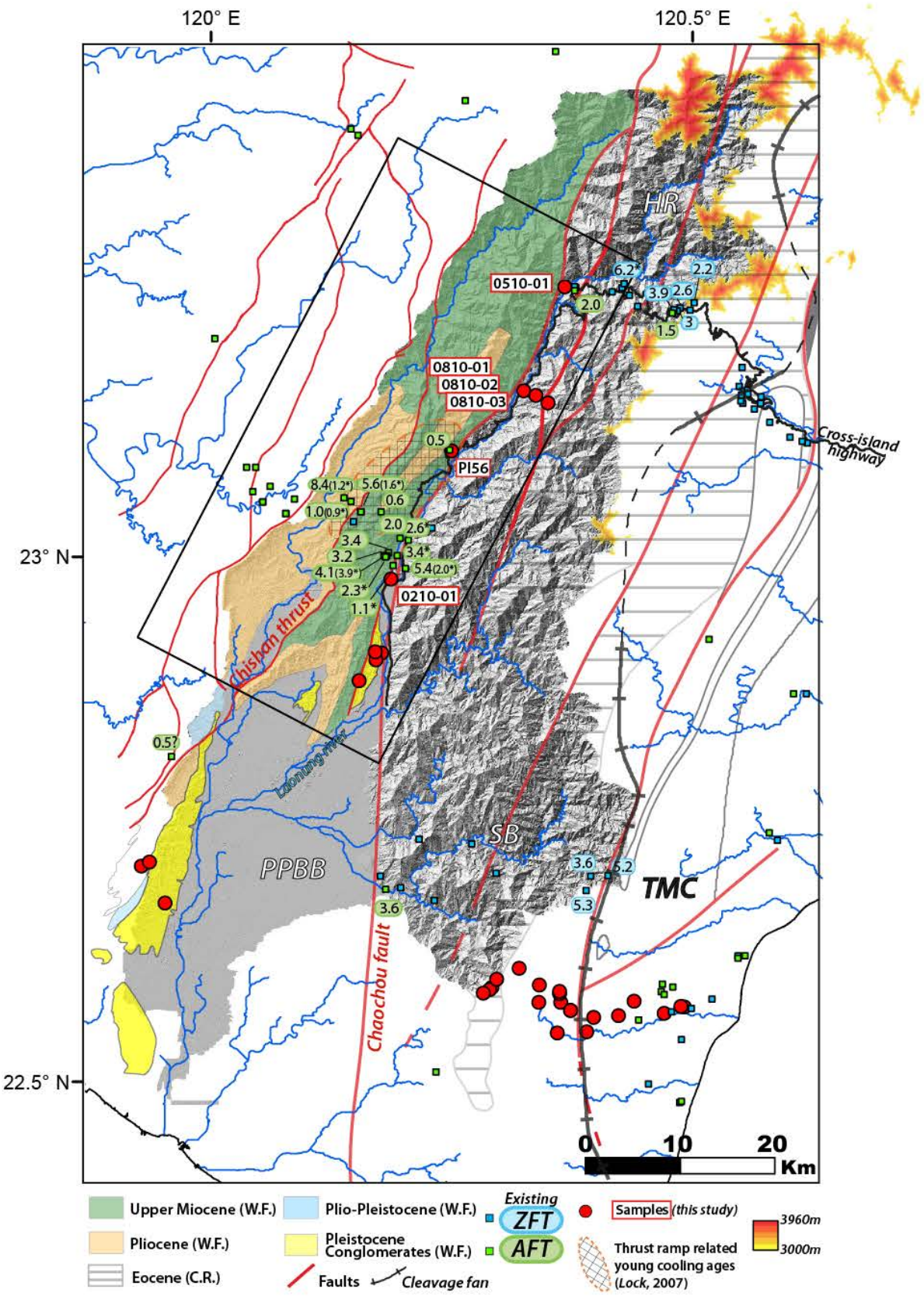

Fig. 3.17*: Hillshade relief of the Laonung basin, areas with elevations greater than 3000m, existing reset AFT and ZFT ages (<10Ma) within the Laonung basin and samples collected in this study including the six samples along the Laonung valley (with names). Pooled age is provided and when available (Lock, 2007; Liu et al., 2001) and younger than 10Ma. Young-peak age (*asterisk) is also shown. Data from shown from* [*Tsao et al.*, 1992; *Tsao*, 1996; *Liu et al.*, 2001; *Willett et al.*, 2003;

Fuller et al., 2006; *Lee et al.*, 2006]. *Note that some of the WF samples may indicate exhumation of the fold-and-thrust belt not the CR cooling. The two AFT ages equal to 0.5 Ma are plotted twice becasue the original source (Lock, 2007) present some inconsistencies in in the coordinates and heights of the samples (0.5 with question mark is plotted with the coordinates from original source; 0.5 without question mark is plotted as in the maps provided in the original source). Rectangle indicates position of Fig. 3.32. SB= Slate Belt; HR= Hsuehshan Range; TMC = Tananao Metamorphic Core; PPBB=Pingtung piggy-back basin.*

We sampled an incomplete three-sample vertically distributed profile ranging in altitude between 640-1097m in the hangingwall of the Laonung fault (0810-01, 0810-02 and 0810-03) and three other samples, two in the hanging wall (0510-01 and 0210-01) and one in the footwall (PI56) of the Laonung fault.. The samples consisted of sandstone interbeds in domaintly fine grained black shale on the lower greenschist facies (Fig. 3.18).
While sampling the vertical profile we identified a fault zone inbetween the two highest samples (0810-02 and 0810-03). I interpret this fault as the southern continuation of the Meishan fault identified along the southern cross-island highway by *Pelletier and Hu* [1984] (Fig. 3.5 and Fig 3.17) although it could also be the southern extension of the Meishan-Tienshih fault after their union further to the north.



***Fig. 3.18**: Photograph of the kind of lithology sampled along the Laonung river: Slate-dominated sedimentary series with thin sandstone beds of the Middle Miocene Lushan Fm.*

The main aims for sampling along the Laonung valley are:

1. The existing AFT samples in this area have been interpreted as a partially reset [*Dadson et al.*, 2003; *Fuller et al.*, 2006; *Lock*, 2007] although yielding younger cooling ages than depositional ages (Fig. 3.17).
2. The geological boundary marked by the Laonung fault is supposedly a major structural boundary limiting the WF and the CR. However the stratigraphic offset, cooling age offset and structural manifestation in the field is limited (Fig. 3.17). Interestingly a young cooling ages (AFT and AHe) zone in the footwall of the Laonung fault in the Chishan thrust sheet (Fig. 3.17) has been interpreted as an area overlying a ramp [*Lock,* 2007].

Defining the extent of this young ages area can confirm or dismiss this interpretation.

3. The Laonung catchment represents a major contributor of the present-day sediment deliver of the Pintung basin where the Linkou and Liukuei conglomerates were deposited (Fig. 3.17).

➔ Given the patchy coverage of cooling ages along this structure with a well-defined gap in its middle part (Fig. 3.17), a better coverage along the fault trace may contribute to a better understanding on the significance of this supposedly major geological boundary. As a major source of the Pingtung basin (Fig. 3.17), the Laonung catchment cooling ages may help understand the potential changes in detrital ages recorded in the Linkou and Liukuei conglomerates.

B. Analytical methods

AFT and ZFT sample processing and dating was performed in Institute of Earth Sciences (ISTerre) at Joseph Fourier University, Grenoble. Some samples were processed in the Institute of Earth Science, Academia Sinica. For thermal neutron irradiation, samples were sent to FRM-II reactor in Garching (Munich, Germany).
A total of 44 samples (7 in Laonung, 30 in Taimali and 7 Linkou-Liukuei) were initially sampled, 33 were mounted for AFT and ZFT, for the final obtention of 10 apatite fission track (without considering 6 samples that were counted but resulting in very low data-quality due to low spontaneous tracks) and 33 zircon fission track ages.

Processing of the bulk samples, summarized as follows (Fig. 3.19):

1) Crushing of bulk sample with a jaw crusher.

2) Dry sieving to obtain the fraction between 80 and 200 μm.

3) Shaking table for cleaning from the dust and concentrate heavier grains.

4) Heavy liquor mineral separation in two steps, first Sodium Polytungstate (density = 3.1) and then tetrabromoethane (density = 3.3) to obtain at each step apatite (3.1<d<3.3) and zircon (density >3.3).

5) Franz magnetic separator to withdraw all magnetic grains.

Generally, apatites were very scarce in the final heavy, non-magnetic fraction. The morphology of the rare apatites was sub-rounded to completely round and with opaque-milky surface. Zircons were more abundant but diluted within mica (not magnetized), tourmaline (?), abundant pyrite and other translucent unidentified grains.
For both apatite and zircon, we had thus to manually purify the fraction under an optical microscope, for most of the studied samples. This step allowed selection of zircon grains for (U-Th)/He zircon dating (not presented in this work, due to low-quality and inconsistent data).

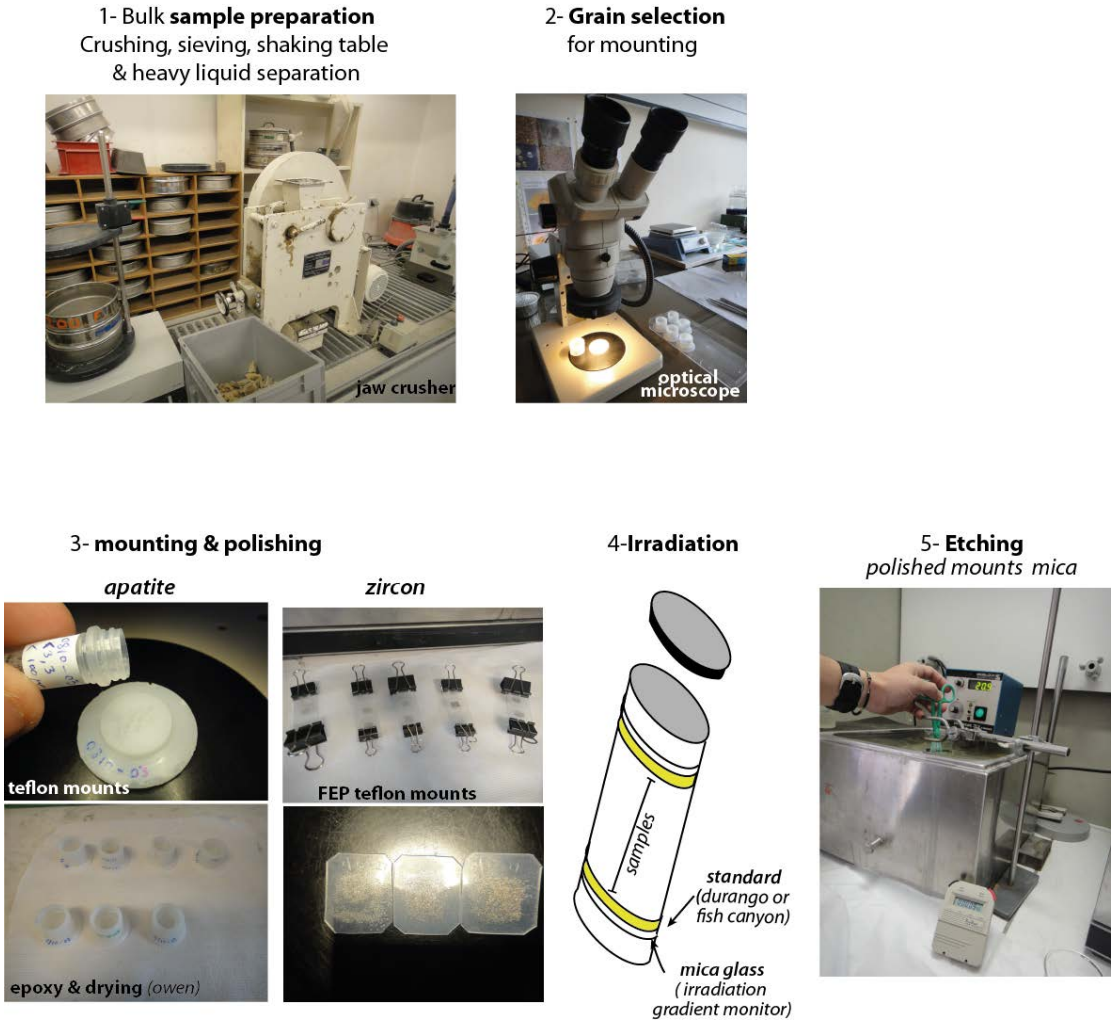

Fig. 3.19*: Sample preparation and treatment for FT dating.*

Etching of apatites was done within an acidic solution of 5.5 mol/l of HNO_3 (pH=1-2) for 20 seconds at a temperature of 21°C, then rinsed in sodium hydroxide NaOH (pH=14) and water. Etching of zircons was performed in a basic solution done from 11.2g potassium hydroxide KOH, added to 8 grams of sodium hydroxide NaOH at 228°C. Various mounts were produced for a single sample, with varying etching time (from 5 to 56 hours). Etching of the mica external detector was completed in a solution containing fluoric acid (40-48% reagent grade), deionized water and 2 grams of sodium hydroxide NaOH for 18 minutes at 21°C, then rinsed in sodium hydroxide NaOH and water.

Fission-track dating was performed using the external detector method of white mica [*Hurford and Green*, 1982] summarized in Fig. 3.20, using a personal zeta ζ factor of 135.42±15.20 for ZFT and 268.37±7.61 for AFT.

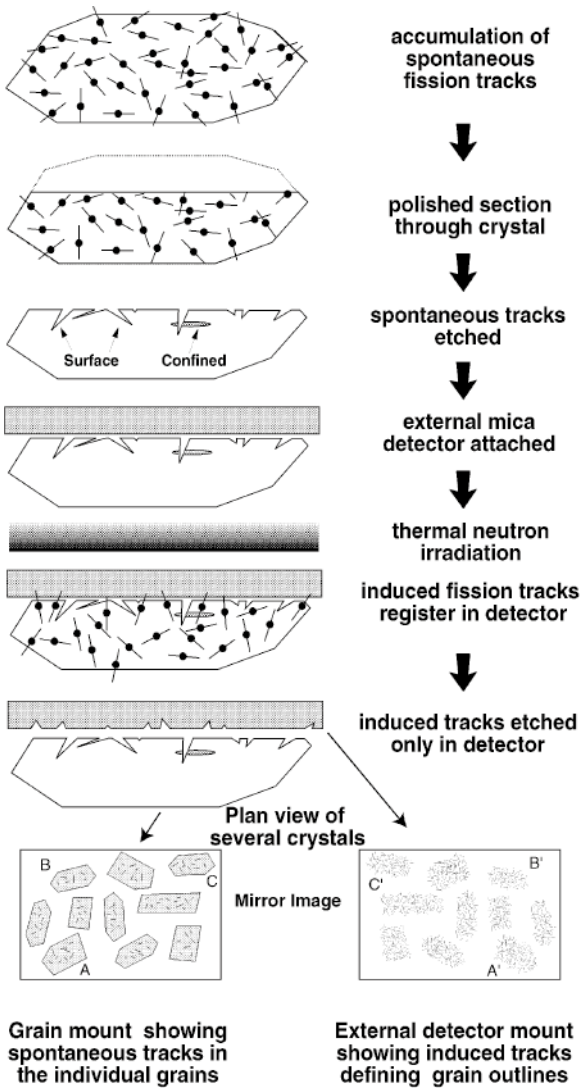

***Fig. 3.20**: External detector analytical steps* [*Gallagher et al.*, 1998]

IV. Results

All the raw counting data files are provide in Annex 4.

A. Age-elevation profile in the Taimali valley

1) ZFT ages and age-elevation relationship

The sampled sedimentary formations range in depositional age from Miocene to Eocene (Fig. 3.21). The ZFT vertical profile shows a younging trend of the ages from the topmost sample at 3090 m aged 7.1 ± 1.3 Ma (from now on, errors are given as 1σ) to the samples at about 1500 m. From about 1500 m to the base of the profile the ages range from 2.8 ± 0.6 to 3.6 ± 0.7 Ma with mean age of equal to ~3.2±0.2 Ma and can be considered constant within the error bar.

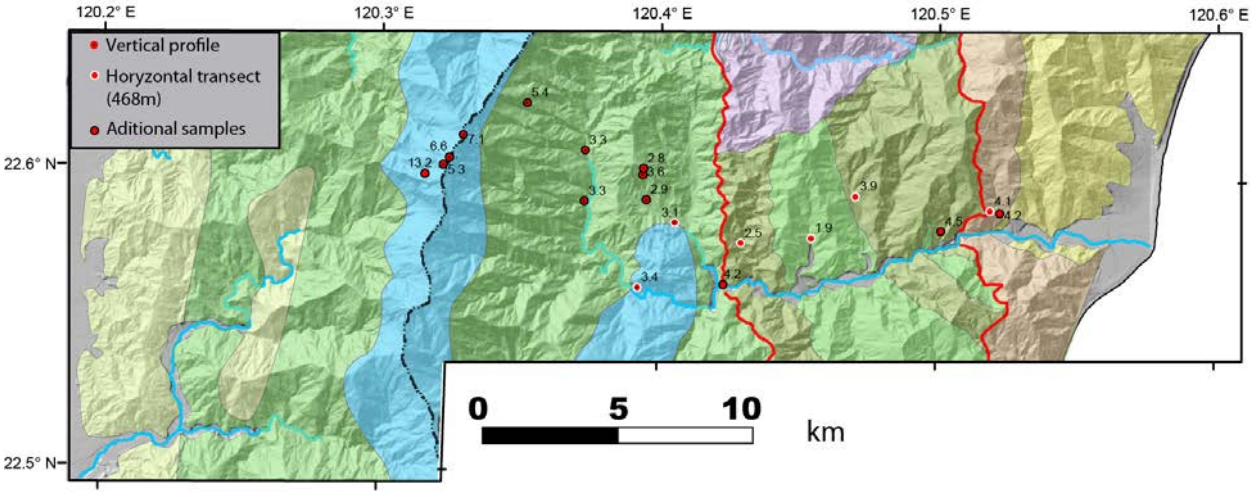

Fig. 3.21*: Geological map at the latitude of Taimali area and data sampled for vertical profile and horizontal profile. Geological units caption as in Fig. 2.11.*

The topmost samples mostly present discordant ages with a young post-depositional and an old pre-depositional age populations. (Fig. 3.22). The high error bars in the younger component mean age (black circles in Fig. 3.22; Fig. 3.23) of the two of the three topmost samples discordant ages is due to the fact that grains representing the younger population in the uppermost samples are only constrained by about 20% of the 24 total grains counted (Fig. 3.22, Fig. 3.23 and Tables 3.2 and Table 3.3). Nevertheless, the topmost young peak age is well constrained with 61% of the counted grains.

Interestingly, discordant ages are not limited to the upper part of the profile. One sample near the base of the profile (sample PV3-6B) presents a young-peak age of 3.3 ± 0.6 and an older population of 8.6 ± 2.6 Ma (Fig. 3.22 and Fog. 3.23), rising the question whether this zircons grains also recorded the early stages of cooling recorded by the higher samples or whether this grains are partially reset. It could be that all lower altitude samples record the early event and a counting bias where young ages (i.e. low spontaneous track-density) are preferentially counted, prevented from characterising this phase in the other low altitude samples.

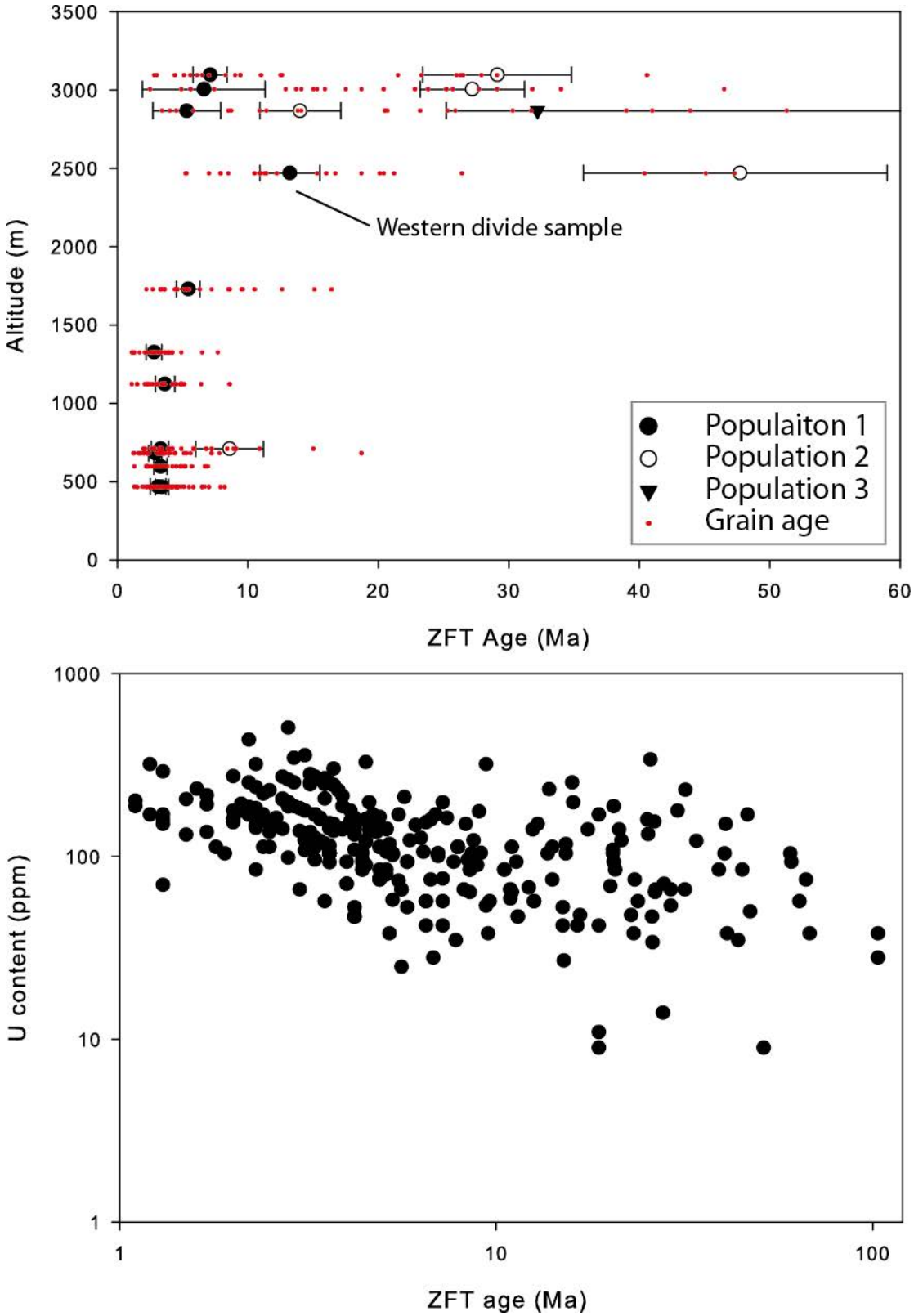

Fig. 3.22: *Top panel: Grain ZFT age vs. elevation. Also shown are the different populations ages extracted with the Gaussian peak fitting method in Binonfit 1.2.62* [*Brandon*, 1992]. *Lower Panel: Uranium content vs. ZFT grain age for the age-elevation profile samples. Note that the relationaship in the U-contant vs. age is to be expected since U-content intervenes in the calculation of ZFT ages; the trend is probably also the result of the etching properties of zircons were young low-uranium zircons need longer etching times.*

Despite the high error, the trend for the upper samples appears quite clearly (Fig. 3.23). Regression of the topmost samples, including the highest sample of the constant-age lower profile (i.e. sample PV1-6), gives a statistically significant linear regression equation of *y=456x + 229* (R^2=0.74). Implying exhumation rates of 456 ± 120 m/Myr between ~7.1±1.3 (age of topmost sample) and ~3.2±0.2 Ma (mean age of the lower samples). No linear fit could be extracted from the lower profile since the ages are nearly constant, within the error bars, with variable elevation.

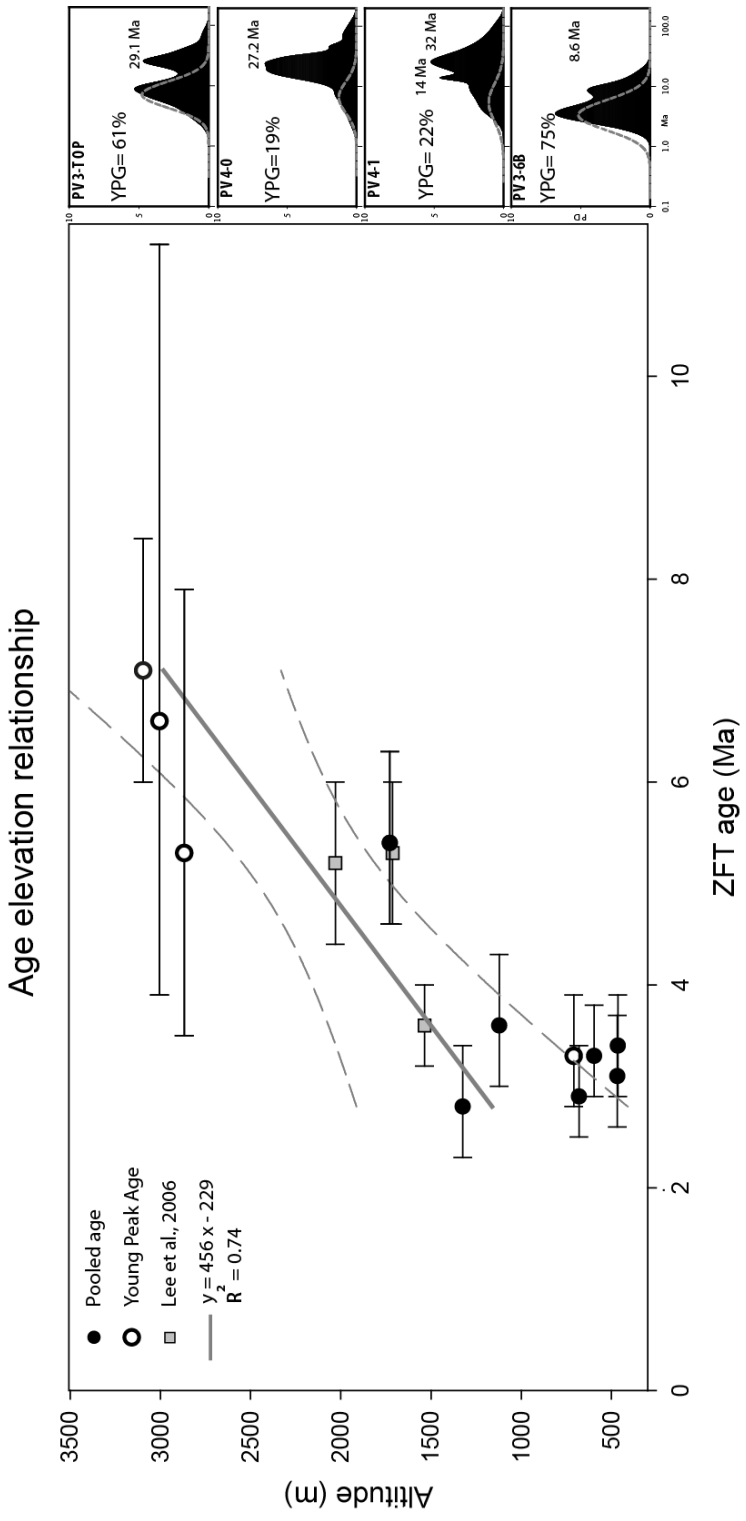

Fig. 3.23: *Age elevation relationship of the Taimali vertical profile with fitted regression and 95% confidence interval for the top-most 8 samples including samples from Lee et al. (2006). Right panels show the probability density plots for the discordant ages, x-axis in Ma (logarithmic) and y-axis probability density (%/Dz =0.1). Also shown is the percentage of young pick grains and the age of the older populations. YPG = young peak grains.*

Name	Long.	Lat.	Position	Alt. (m)	ρ_s (10^5 tracks . cm^{-2})	Ns (tracks)	ρ_i (10^6 tracks .cm^{-2})	Ni (track)	U±2s (ppm)	N	Gain-age Range (Ma)	Pooled age ±1σ (Ma)
Ph0	120.8238	22.576	LT	465	6.83	151	3.72	823	181±39	24	1.7-8.7	**3.4 ±0.5**
PV1-2B	120.837	22.597	TT	467	3.98	83	2.39	497	129±12	24	1.4-7.2	**3.1±0.6**
PV3-7	120.804	22.604	LT	596	5.92	169	3.34	955	181±12	24	1.4-7.1	**3.3±0.5**
PV1-3	120.827	22.605	TT	680	4.13	123	2.7	804	147±11	38	1.4-18.7	**2.9±0.5**
PV1-5	120.825	22.613	TT	1122	4.86	81	2.51	419	136±14	24	1.4-8.7	**3.6±0.7**
PV1-6	120.826	22.615	TT	1324	3.79	54	2.51	358	136±15	23	1.4-8	**2.8±0.6**
PV3-1	120.784	22.637	LT	1728	5.92	107	2.06	372	112±12	24	2.5-26.5	**5.4±0.9**
PV3-6B ♪	120.805	22.621	LT	709	5.60	131	2.49	582	135±12	24	2.2-15.1	**4.2±0.7 ♪**
PV4-3 ♪	120.747	22.614	WD	2468	16.8	298	1.56	277	85±10	25	5.6-59.5	**20.1±3.0♪**
PV4-1 ♪	120.754	22.617	Crest	2867	20.0	337	1.98	334	108±12	24	3.7-96.9	**18.8±2.8♪**
PV4-0 ♪	120.756	22.619	Crest	3004	26.3	549	2.04	427	111±11	24	2.8-97.0	**24.0±3.3♪**
PV3 ♪	120.761	22.627	Peak	3095	13.2	264	1.90	381	103±11	24	3.2-64.2	**12.9±1.9♪**

Table 3.2*: Pooled age of concordant and discordant (musical note ♪**) ZFT ages (east of main drainage divide) interpreted as fully reset samples. N: Total number of counted grains. LT = last Taimali tributary; TT= Turituri tributary (penultimate tributary); WD = Western divide. Discordant samples (♪**) are presented in Table 3.3. Coordinates in WGS-84. Pooled ages extracted with Binomfit 1.1.60.*

						ZFT age components ±1σ		
Name	Position	Alt. (m)	N	Gain-age Range (Ma)	F test (%)	P1 (Ma)	P2 (Ma)	P2 (Ma)
PV3-6B	Eastern Divide	709	24	2.2-15.1	0	**3.3±0.6 (75%)**	**8.6±2.6 (25%)**	
PV4-3	Western divide	2468	25	5.6-59.5	0	**13.2±2.3 (77%)**	**47.7±12 (23%)**	
PV4-1	Close to crest-Western divide	2867	24	3.7-96.9	0	**5.3±2.2 (19%)**	**14±2.7 (28%)**	**32.2±6.2 (53%)**
PV4-0	Crest	3004	24	2.8-97.0	0	**6.6±4.7 (19%)**	**27.2±4 (81%)**	
PV3	Crest-Peak	3095	24	3.2-64.2	0	**7.1±1.3 (61%)**	**29.1±5.7 (39%)**	

Table 3.3*: Discordant ZFT ages in which P1 is interpreted as a reset low-retention zircon grains population. N: Total number of counted grains; binomial peak fitting are given ± 1s. Also*

given is the percentage of grains in a specific peak. All samples ages including concordant samples (Table 3.2) using a zeta factor of 135.42 ± 15.20. The probability based on F-test evaluates how significant is the number of peaks. A F-test probability of 0% indicates that the introduction of additional peak would result in the decrease of the best-fitting solution. Note that all discordant samples were collected in the last tributary of the Taimali valley, in the Beidawu crest/peak or in the western divide. Coordinates in WGS-84. Populations extracted with Binomfit 1.1.60.

ZFT ages from *Lee et al.* [2006] sampled 10 km to the north (Fig. 3.24) fit relatively well the AER in the Taimali area (Fig. 3.23). However, it is worth noticing that the location and altitude of their samples as well as the raw data was not provided in the original paper, nor by the author when requested, so we cannot know further about the quality and approach used (e.g. young-peak-age approach?). I extracted location and altitude from digitalization of their published maps.

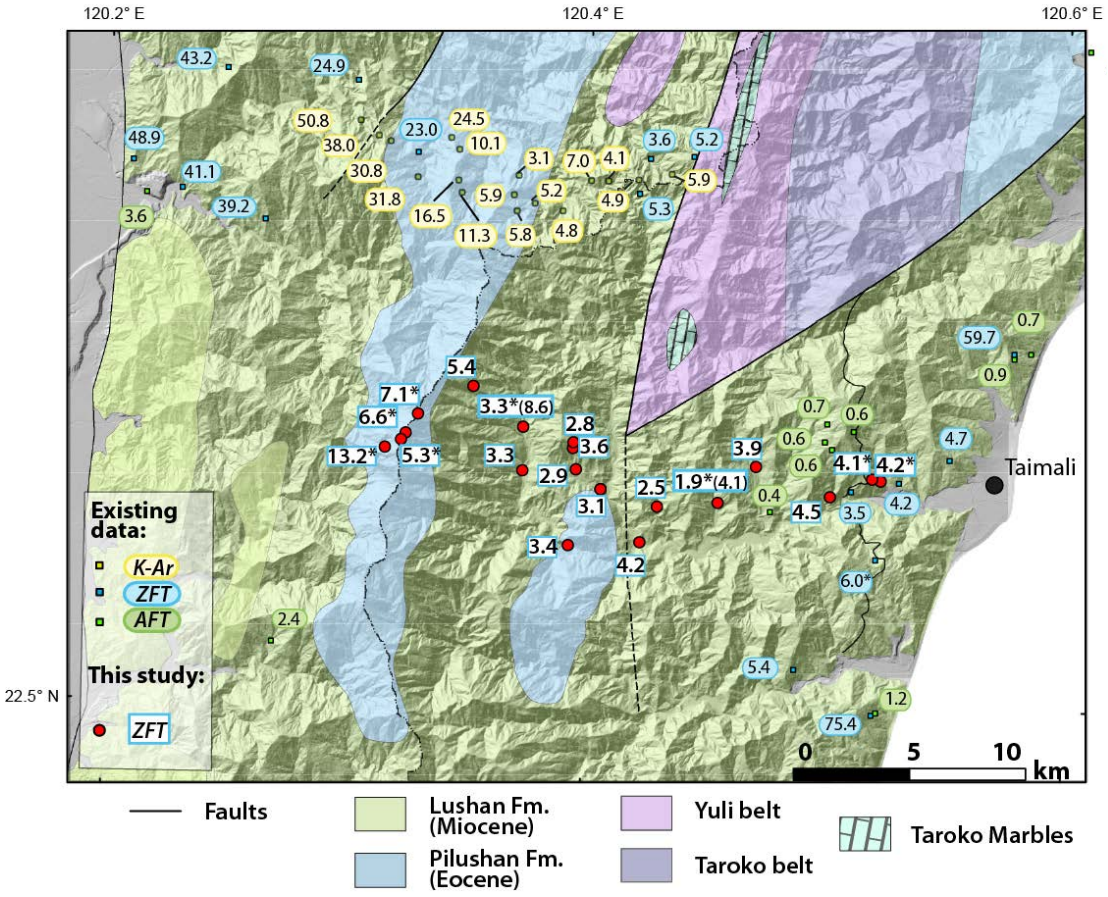

***Fig. 3.24**: Sampled localities and ZFT ages in the Taimali valley. Also shown are the existing AFT (Fuller et al., 2006), ZFT (Liu et al., 2001; Lee et al., 2006; Willett et al., 2003) and K-Ar ages on muscovite's clay fraction (Tsao, 1996). Asterisk (*) indicates young-peak ages and a second population is indicated in brackets if younger than 10Ma. Ages are given in million years.*

One additional sample from the western divide had an age of 13.2 ± 2.3 Ma, which did not fit with the general trend of the eastern divide AER (Fig. 3.22;

Table 3.3). However, this sample is consistent with progressively older existing ages in the western divide (Fig. 3.24).

2) Thermal modelling of the vertical profile

To gain a better understanding of the effects of advection of heat due to cooling rate changes, and dependence of closure temperature to cooling rates we performed inverse modelling of our ZFT age-elevation profile data. To capture this aspect in the data, I adopted the analytical solution proposed by Willett and Brandon (2013) that use the time-dependant eroding half-space thermal model solution. This solution is particularly useful to extract exhumation rates in the lower part of the profile (from 465 to 1324 m) where the ages remain constant and no age-elevation relationship can be extracted directly from the age-elevation plot (Fig.3.23). I also modelled the upper profile to compare the results with the linear fitting curve while considering the influence of exhumation rates on geotherms and on closure temperature of the ZFT system (Fig. 3.26, Fig. 3.27 and Table 3.5).

The geothermal gradient is taken as dependent on time and erosion rate and no steady-state can be attained. With *Willett and Brandon* [2013] code we are able to visualize each sample as a curve on a graph plotting geothermal gradient as a function of exhumation rates (Fig. 3.25, Fig. 3.26 and Fig. 3.27). One strong assumption in the model is that geotherm is linear, which is inconsistent with stepwise exhumation as transient effects may become dominant. Because assumption of constant exhumation rates to the present does not take into account the effect of potential younger exhumation phases, independent constraints on the exhumation history are ultimately needed to quantify exhumation rates. Yet another limitation is that in input ages do not take into account the error bars which are considerable particularly in the upper part of the profile (Fig. 3.23). Moreover, It is worth noting that an inherent limitation that our data has on the model results is the use of young-peak ages. This is due to the fact that models assume a total resetting of the samples and thus assume fixed closure temperature or partial annealing zones when modelling the vertical profiles samples and that the understanding of variable annealing behaviour of differently radiation-damaged grains is not well known. This aspect is further discussed in the following.

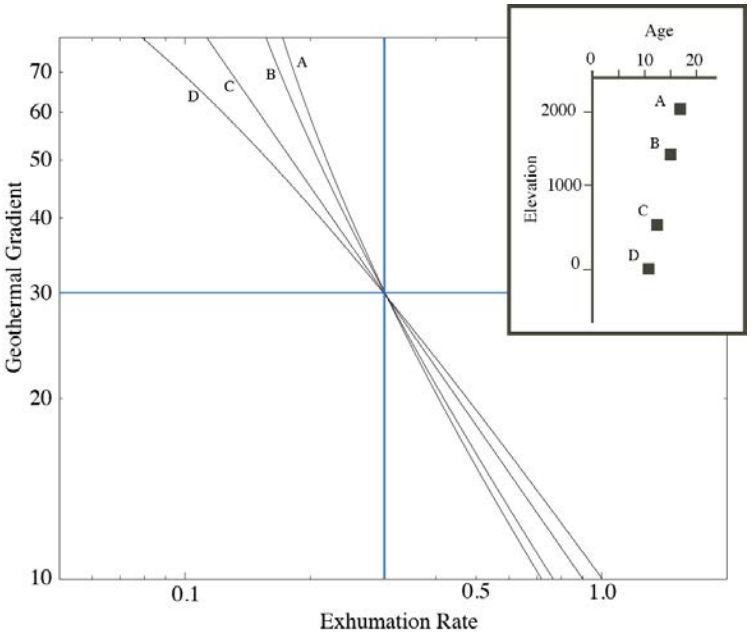

***Fig. 3.25**: Idealized analytical solution for a perfectly linear age-elevation relationship. The convergence into a single point of each sample's curve (A,B,C and D) indicates the geothermal gradient and exhumation rate fitting the data. From* [*Willett and Brandon*, 2013].

A surface temperature of 15°C and a mean elevation of 939 m at sample vicinity (mean elevation at a 20km radius of the sampled area) were adopted, using the annealing parameters of Brandon et al. (1998).

As shown in the Fig. 3.27, the results are highly sensitive to the geothermal gradient, and in a lesser degree to the initiation of exhumation of the studied phase, respectively (Tables 3.4 and 3.5).

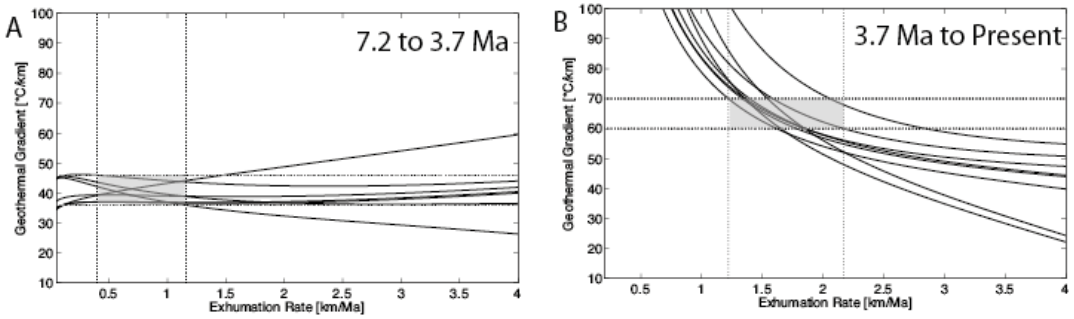

***Fig. 3.26**: Results of our half space inverse modeling. Here is presented our preferred geotherms accounting for all the data. Left panel samples from the upper profile and right panel samples form the lower profile. Each line represents a sample. The crossing point of all samples is the best-fit solution.*

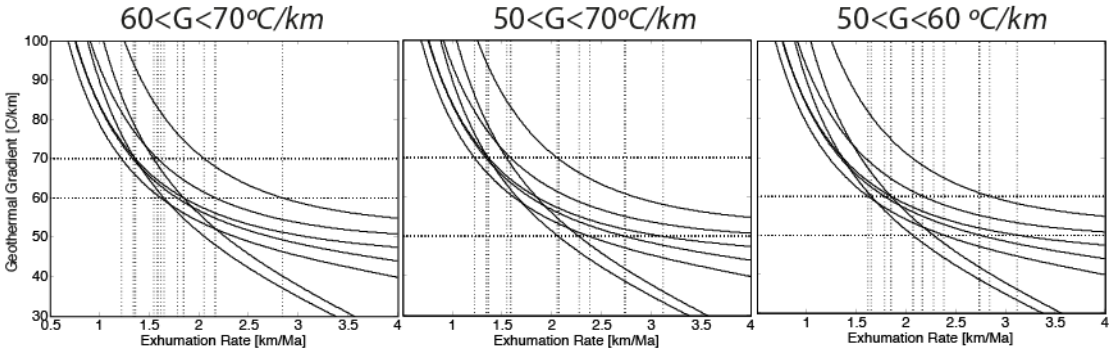

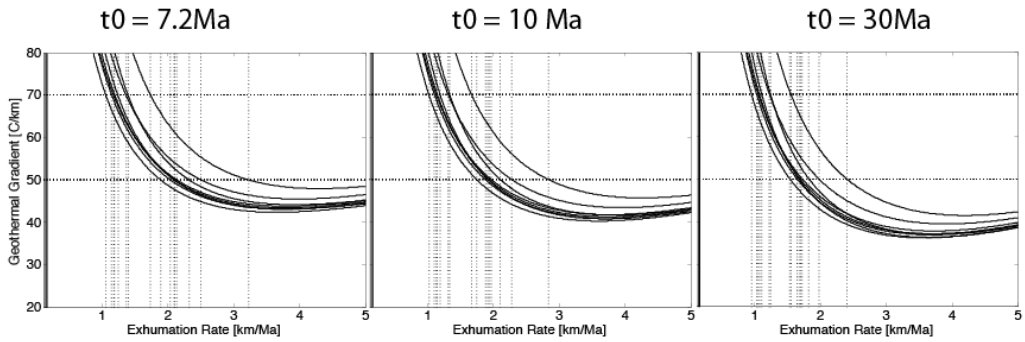

Fig. 3.27*: Results of half space inverse modeling models for the lower profile considering different geothermal gradients and starting time of the exhumation. The best fit of our data is obtained for exhumation rates of 1.2 to 2.84 km/m.y. (1.75 km/m.y. on average), for exhumation starting at 3.7 Ma with geothermal gradients of 60 to 70ºC/km (Fig. 2.38).*

Although there is no single crossing point of all the age-curves in the age-function plot (Fig. 3.27), as expected for a linear AER (fig. 3.25), the models show convergence in an area supporting exhumation rates of 1.2 to 2.84 km/m.y. (1.75 km/m.y. on average), for exhumation starting at 3.7 Ma with geothermal gradients of 60 to 70ºC/km for the lower section of the profile, and of 0.4 to 1.16 km/Myr (0.78 km/m.y. on average) with geothermal gradients of 36 to 46°C/km, for the upper section of the profile (Tables 3.4 and 3.5). The choice of the best fitting initial geotherms was done based on the range that provided the less widespread exhumation rates (Fig. 3.27 and Table3.4 and Table 3.5) as should be expected for a column of rocks undergoing the same thermal history.

Geothermal gradient *(°C/km)*	60-70	50-60	50-70
Exhumation range *(km/Myr)*	1.22-2.84	1.62 - 3.12	1.22-3.12
Mean exhumation *(km/Myr)*	1.71	2.15	1.99
Total exhumation since 3.7Ma *(km)*	6.35	7.94	7.37
Total exhumation since 3.2Ma *(km)*	5.49	6.87	6.38

Table 3.4: *Output values from the inverse modeling of the lower profile assuming start of exhumation at 3.7 Ma, that is right before the age of the oldest modeled sample. Two different total exhumation values are reported. The first one assumes initiation of this tectonic phase at 3.7 Ma and the second one assumes initiation at 3.2 Ma. Note that although modeling assumed initiation at 3.7 Ma, considering the cluster of ages at around 3.2 Ma, the second value may be more accurate. Annealing parameters used are from* [*Brandon et al.*, 1998]*.*

Geothermal gradient *(°C/km)*	40-50	36-46	35-50
Exhumation range *(km/Myr)*	0.31 - 1.46	0.44- 1.16	0.26 - 3.21
Mean exhumation *(km/Myr)*	0.87	0.78	1.13
Total exhumation from 7.1 Ma to 3.2Ma *(km)*	3.41	4.78	4.41

Table 3.5*: table of the output values from the inverse modeling of the upper profile assuming start of exhumation at 7.2 Ma, right before the age of the oldest modeled sample). To model exhumation before the start of the 3 Ma phase, we subtracted 3.2 Ma to the ages (mean age of the lower profile) and substracted the exhumation during that time (=3.2 Myr x 1.75km/Myr=5.44km) of rock column.*

The geothermal gradient values seem to be in agreement with present day geotherms for the younger phase, and with present-day offshore southern Taiwan geotherms for the older phase (Chi and Reed, 2008; fig. 3.36), as further discussed later on (Section V.B). It is worthnoting that the exhumation values inverse modelled for the upper are of the same order of magnitude that the ones extracted by simple regression of the age- elevation relationship (Fig. 3.23) but significantly higher (0.78 *vs.* 0.46 km/myr).

B. Horizontal iso-altitude profile in the Taimali valley

The iso-altitude profile had as main aim to constrain the exhumational history of the different structural domains (StU1, StU2 and StU3) observed in the field so that the development of the east-verging deformation (i.e west-dipping schistosity) could be assessed. Likewise, I expected being able to constrain the devlepment of the the structural domain bounding faults (i.e. SZ1 and SZ2). Additionally to the eleven samples of the vertical profile, I obtained seven ZFT ages on samples in different tributaries of the Taimali main course (Fig.3.24 and Fig. 3.29). I originally planed to perform multiple thermochronometers on each sample so that the time-span covered would be longer, and the iso-altitude nature of the transect would allow the dismiss of an altitudinal effect on the ages. However AFT and U-Th/He on zircon did not yield reproducible results due to the lack of apatite for AFT dating and the young age of the samples for both AFT and ZHe dating.

Similarly to the vertical profile samples, three samples in the transect yielded discordant ages (Ph2, ph6' and Ph60; Fig. 3.12 and 3.24; Table 3.7). However while sample Ph2 yielded two populations younger than 10 Ma (1.9±2.3 and 4.1±1.0Ma), Ph60 and Ph6' yielded only one orogenic young-peak population (4.1±0.8 and 4.3±0.8 Ma respectively) with an older detrital population (31.6±5.0 and 53.1±12.2 Ma respectively). Likewise the discordant samples in the vertical profile, whether this is a result of a counting bias, a result of a specific characteristic of the zircons in this particular samples (e.g. wider range in uranium content and/or crystallization age of zircons) or rather a real reflection of the cooling histories of the samples, particularly for sample Ph2, remains to be further explored.

Indeed, sample's Ph2 older population appears to be in agreement with the ages measured along the transect, while the younger young-peak age, although not well constrained and with large error bars, yields ages more similar to the existing AFT in the same structural unit (StU-2) of the Taimali valley (Fig. 3.24). Treating this samples as detrital sample where ~100 grains are counted would have helped for a better systematic characterization of the all the sample's populations.

Name	Long.	Lat.	Position (StU)	Alt (m)	ρ_s (10^5 tracks . cm^{-2})	Ns (tracks)	ρ_i (10^6tracks . cm^{-2})	Ni (track)	U±2s (ppm)	N	Gain-age Range (Ma)	Pooled age ±1σ (Ma)
Ph0	120.823	22.576	3	465	6.83	151	3.72	823	181±39	24	1.7-8.7	***3.4 ±0.5***
PV1-2B	120.837	22.597	3	467	3.98	83	2.39	497	129±12	24	1.4-7.2	***3.1±0.6***
Pv1-1	120.853	22.577	2	304	4.28	144	1.92	644	104±9	24	2.6-11.8	**4.2±0.7**
Ph1*	120.861	22.590	2	469	3.42	43	3.21	404	174±18	22	0.5-7.2	**2±0.4**
Ph3	120.902	22.606	2	466	3.62	61	1.75	296	95±11	24	1.6-18.7	**±0.7**
Ph5'	120.933	22.5947	2	264	5.16	62	1.71	255	93±12	24	2.0-13.3	**±0.5**
Ph2 ♪	120.886	22.592	2	466	4.04	64	2.09	331	113±13	24	1.4-11.2	**3.6±0.7 ♪**
Ph60 ♪	120.950	22.601	1	458	15.5	430	2.11	584	115±10	43	1.6-73.4	**13.8±1.9 ♪**
Ph6' ♪	120.954	22.600	1	284	11.3	248	1.96	430	106±11	32	1.8-109.2	**10.8±1.6 ♪**

Table 3.6*: Pooled ZFT counting values and ZFT ages of samples in the Taimali transect. Spontaneous track densities, ρ_s, and counts, Ns; Induced track densities, ρ_i, and counts, Ni; uranium content, U; and total number of counted grains, N. StU is the structural unit the sample belongs to. Musical note (♪) indicates discordant samples presented in Table 3.7. Asterisk (*) indicates sample in which one grain-age outlier with an age of 1130Ma was removed. Bold italic names indicate samples also used in the vertical profile. Coordinates in WGS-84. Pooled age extracted with Binomfit 1.1.60.*

					ZFT age components ±1σ	
Name	Elevation (m)	N	Gain-age Range (Ma)	F test (%)	P1 (Ma)	P2 (Ma)
Ph2	466	24	1.4-11.2	5	**1.9 ±2.3 (10%)**	**4.1±0.8 (90%)**
Ph60	458	43	1.6-73.4	0	**4.1±1.0(64%)**	**36±4.3 (36%)**
Ph6'	284	32	1.8-109.2	0	**4.2±0.8 (73%)**	**53.1 ±12.2(27%)**

Table 3.7*: Discordant ZFT ages in which P1 (and probably P2 for sample Ph2) is interpreted as a reset low-retention zircon grains population. Coordinates in WGS-84. Populations extracted with Binomfit 1.1.60.*

To the first order, there is no major age variation along strike the Taimali transect, with an average age and one standard deviation of 3.5 ±0.9 Ma (Fig. 3.29). The bounding structural domain faults (SZ1 and SZ2) seem to have a minor affect on the ZFT system as almost all ages are within the average plus or minus one standard deviation.

Samples Ph1 and Ph2 yield ages lying in the lower bound of the average plus or minus one standard deviation, in particular the young-peak age of Ph2; but Ph2 young-peak age is loosely constrain with high error bars making this observation a weak one.

However the fact that the discordant samples yielding older detrital population are limited to the StU-1 (table 3.7) may indicate a lower total exhumation in this unit, since older population (i.e. high-retentive/low radiation damaged zircon populations) have remained unreset.

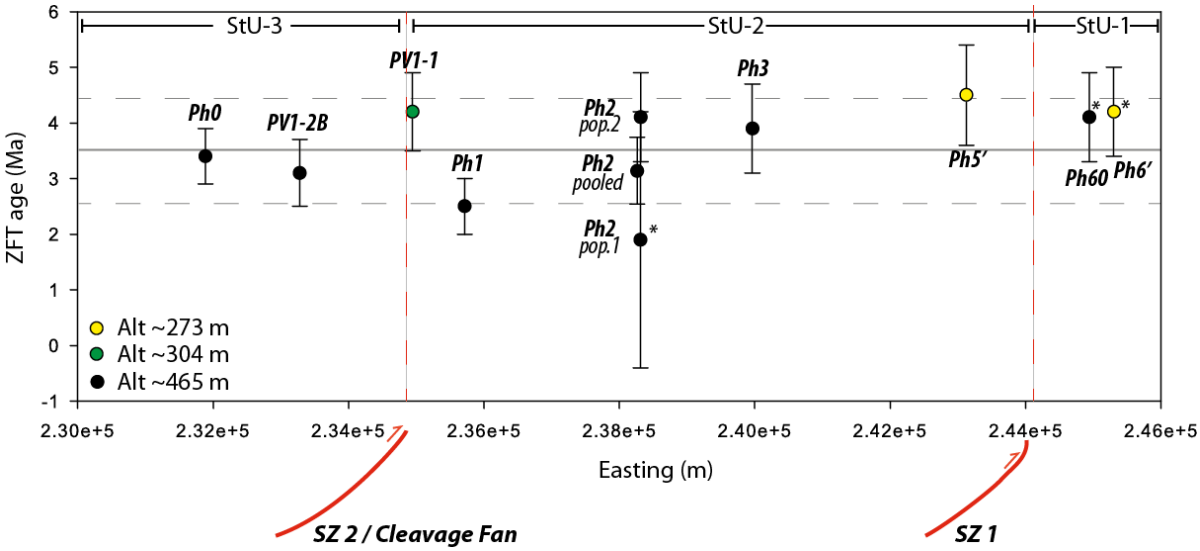

***Fig. 3.29**: Horizontal transect in the Taimali valley. Asterisk (*) indicates young-peak age. For sample Ph2 the two obtained age population and the pooled age are shown. Horizontal plane line and two dashed lines in dicate the average age and standard deviation (3.5±0.9Ma) of the whole transect data.*

Our ZFT ages are in agreement with ZFT pooled ages of *Lee et al.* [2006] and ZFT chi-squared ages of *Liu et al.* [2001] in the same area (Fig. 3.24) but contrast with the completely unreset ages of *Willett et al.* [2003] (ZFT ages of 59.7 Ma and 75.4 Ma) obtained ~10km to the north and to the south (Fig. 3.24).
It is interesting to note that AFT ages in the Taimali valley obtained by *Fuller et al.* [2006] are the youngest ages found in Central Range (<1Ma) together with the ages in the eastern Central Range front (i.e. hanging wall of the Central Range fault in both north and south), indicating high cooling rates for the last ~1Ma and an acceleration between 3.5 ±0.9 Ma and 1Ma, maybe related to the weak lithologies, high relief and ersion rates of the area.

C. Fission-track detrital record from Plio-Pleistocene foreland sediments

Hereafter, I present fission-track analysis from six samples that were collected for AFT and ZFT analyses from the Linkou and Liukuei formations of Plio-Pleistocene wedge-top basin deposits between the Western Foothills and the CR and one sample from an older Pliocene clastic formation (Fig. 3.30 and Fig. 3.31). These results were combined with the results of the age-elevation profile in the Taimali valley to assess the time-temperature history of southern Taiwan (*Mesalles et al.*, 2014; minor corrections) as presented in the next section. Understanding the nature of the erosive event resulting in the deposition of the widespread conglomerates of the Toukoshan Fm. was also one of the main objectives.

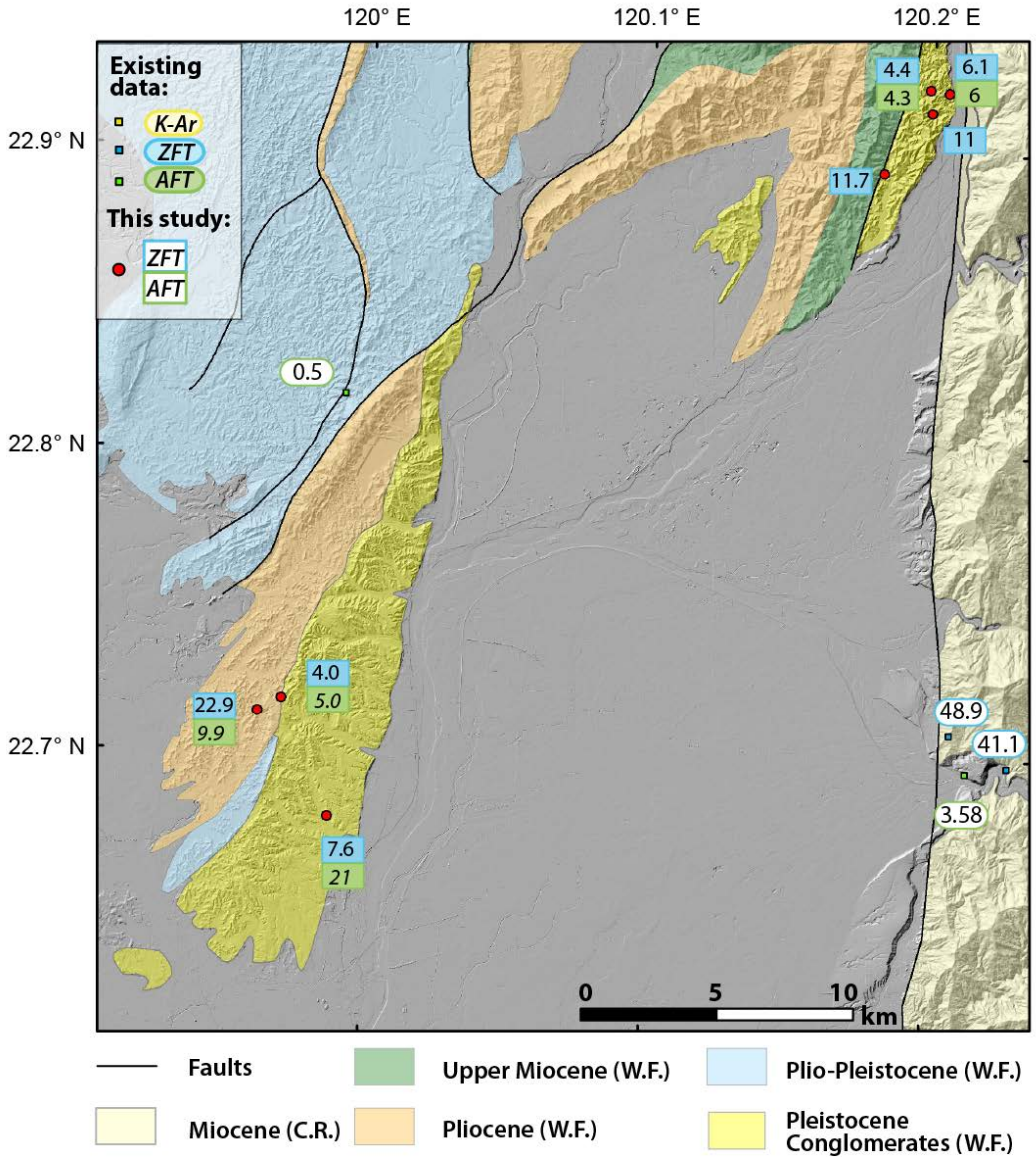

Fig. 3.30*: Geological map with the obtained ZFT and AFT younger population ages interpreted to record the exhumation of the Central Range during Plio-Pleistocene times. Italic AFT age indicates ages constrained by less than 20 grains. See Tables 3.8 and 3.9 for the original data.*

As detailed previously, the Linkou and Liukuei formations are the youngest studied conglomerates, with depositional ages younger than 2 Ma (Base of the Linkou member dated to the base of nannofossil biozone NN19; ~1.96-1.70Ma; Chi, 1979). The conglomerates are separated by an angular unconformity from the underlying shallow-marine Nanhsihlun sandstone dated to ~3.7-3.9Ma (nannofossil biozone NN15; Chi, 1979, Fig. 3.31), representing the oldest sampled strata. We collected non-metamorphic to very low-grade metamorphic sandstone cobbles in two localities interpreted to represent lateral equivalents of the same coarsening-upward succession of a fluvial-dominated fan fed by the paleo-Laonung river catchment (Fig. 3.17) draining the highest peaks of southern Taiwan. The sampled sandstones pebbles represent the pre-orogenic

Paleogene to Miocene cover of the CR, although a dominant source Eocene rocks particularly in the upper conglomeratic member [Huoyenshan member of *Chou*, 1977].

All samples had a good zircon yield allowing to count over 600 zircon grains with al least 80 grains counted per sample (Table 3.8 and Table 3.10). Zircon colour varied from colourless, dark red to black with considerable metamicted grains.
All the samples analysed contain ZFT populations older than ~20Ma (Table 3.8) not related to the cooling history of the Taiwan orogen. The older pre-Taiwan orogeny ages are found in the Nanshihlun sandstone sample (NA02) with one age population older than 150Ma, all other samples contain at least one age population with an age between ~50Ma and ~70Ma in age. Both pre-Taiwan orogeny age are in agreement with tectono-thermal events in SE China as discussed in *Kistein et al.* [2010]. An additional age peak with ages between ~15Ma and ~20 Ma is present in at least one sample per each sedimentary formation studied, but is not evident when merging the ZFT within each formation (Table 3.8).
The jump from a source without orogenic ages to a source yielding Taiwan orogen related ages is net and occurs between samples NA02 and sample LK03 (between the depositional hiatus between ~4.1 and ~1.9Ma; Fig. 3.30 and Fig. 3.31; Table 3.8). Orogenic ages are present in all the samples from the Linkou and Liukuei formation conglomerates except for two samples of the Liukuei conglomerate (LG17-LG18; Table 3.8) yielding both young population of ~11Ma. However this population disappear when performing binomial peak fitting in the all Liukuei samples together (Table 3.8). Orogenic ages (<~10Ma) in the conglomerates have ages between ~4Ma and ~7 Ma when considering all samples, or between ~4Ma ~6Ma when dismissing the baldy constrained young population of sample LK04. The Liukuei samples present generally older young population when compared to the Linkou young population. However, in the younger peaks ages do not show a clear shift when comparing both formations.

									ZFT age components ±1σ			
Sample	Lat.	Long.	Formation	Depositional age	Alt (m)	N (grains)	Age range (Ma)	F test (%)	P1 (Ma)	P2 (Ma)	P3 (Ma)	P4 (Ma)
NA02	120.395	22.734	Nanshihlun sandstones	NN15 (~4.1-4.3Ma)	124	84	21.1-781.3	3	22.9±6.5 (3%)	59.0±8.3 (42%)	136.8±21.6 (47%)	395.7±213 (8%)
								0	22.9±6.5 (3%)	61.3±8.6 (46%)	159.3±23.3 (51%)	
LK03	120.404	22.738	Linkou Fm (base Lower member)	NN19 (~1.96-1.7 Ma)	119	83	1.2-186.8	4	4.0±0.6 (61%)	15.3±3.9 (14%)	74.6±10.5 (25%)	
								0	5.1±0.7 (73%)	72.6±10.3 (27%)		
LK04	120.420	22.699	Linkou Fm (top Upper member)	n.a.	53	108	6.2-179.4	0	7.6±4.8 (2%)	44.8±7.1 (41%)	85.9±12.2 (57%)	
LK grouped						191	1.2-186.8	0	**4.6±0.7 (32%)**	**66±8.2 (68%)**		
LG15	120.642	22.938	Liukuei Fm	n.a.	203	88	0,8-462.9	0	6.1±0.8 (59%)	67.0±8.4 (41%)		
LG17	120.636	22.931	Liukuei Fm	n.a	250	78	5.3-311.2	0	11.0±1.8 (28%)	65.8±8.4 (72%)		
LG18	120.619	22.911	Liukuei Fm	n.a	155	82	11.5-599.7	0	11.7±4.9 (1%)	37.2±11.4 (19%)	59.4±10.7 (51%)	116.3±18.3 (29%)
LG20	120.635	22.939	Liukuei Fm	n.a.	227	84	2.3-282.6	3	4.4±0.7 (24%)	22.2±3.7 (15%)	79.4±10.3 (61%)	
								0	5.5±0.8 (30%)	68.0±8.6 (70%)		
LG grouped						332	0.8-599.8	0	**6.3±0.8 (28%)**	**47.5±6.2 (41%)**	**102.9±14.9 (31%)**	

Table 3.8*: Individual samples and grouped by formation ZFT ages from the Plio-Pleistocene orogenic sediments. For samples where F-test was >0% a second binomial fitting is shown below the respective samples so that fitting passes the F-test (i.e. equal to 0%). Binomial peak fitting are given ± 1σ. Also given is the percentage of grains in a specific peak. N: Total number of counted grains. All samples were counted using a zeta of 135.42 ± 15.20.*

The analysed samples had very poor apatite yield. Apatite were rounded with a milky surface and almost every sample presented some zero-spontaneous track grains, and one sample (LK04) presented zero-indiced tracks grains, implying

very low uranium content or misidentified grains with track-like features. Thus, the number of counted apatite grain was very limited with a total of 69 grains counted (Table 3.9 and Table 3.10; Annex 4).
Pre-Taiwan orogen age populations are rare and not well constrained. The Pliocene sample from the Nanshihlun sandstone (NA02) yielded two old grains yielding an age >300Ma, while one sample in the Liukuei conglomerate (LG20) yielded one grain >100Ma. Similarly to the ZFT dataset but less well constrained, the shift from unreset to reset AFT ages populations in the sedimentary record appear to have occurred in the sedimentary hiatus between the samples NA02 and LK03, although the young population of NA02 has large error bars and could also be related to cooling of the Central Range. The two counted grains in sample LK04 yielded very disparate ages apparently unreseted, but not significant given the few number of grains.
Grouping the samples of each conglomeratic formation together produce a relatively concordant young population age of 4.4±0.5Ma and 5.5±1.3Ma in the Liukuei and Linkou conglomerates respectively (Table 3.9).

						AFT age components ±1σ	
Sample	Formation	Depositional age	N	Age range (Ma)	F test (%)	P1 (Ma)	P2 (Ma)
NA02	Nanshihlun sandstones	NN15 (~4.1-4.3Ma)	8	4.9-335	0	9.9±3.0 (75%)	365.3±1217 (25%)
LK03	Linkou Fm (base Lower member)	Base of lower NN19 (~1.96-1.7 Ma)	17	1.9-56.6	0	5.0±1.2 (100%)	
LK04	Linkou Fm (top Upper member)	n.a.	2	20.6-56.8	0	21.9±19.6 (100%)	
LK grouped			19	1.9-56.8	0	**5.5±1.3 (100%)**	
LG15	Liukuei Fm	n.a.	18	0.6-30.6	4	0.0±~∞ (11%)	5.8 ±1.3 (89%)
					0	4.8±1.0 (100%)	
LG20	Liukuei Fm	n.a.	32	1.6-144.1	0	4.3±0.6 (96%)	127.9±186.8 (4%)
LG grouped			50	0.6-144.1	0	**4.4±0.5 (98%)**	**139.1±169.5 (2%)**

Table 3.9 *Individual samples and grouped by formation AFT ages from the Plio-Pleistocene orogenic sediments. For samples where F-test was >0% a second binomial fitting is shown below the respective samples so that fitting passes the F-test (i.e. equal to 0%). Binomial peak fitting are given ± 1σ. Also given is the percentage of grains in a specific peak. N: Total number of counted grains. All samples were counted using a zeta of 268.37±7.61.*

Although generally concordant (i.e. AFT-age<ZFT-age), AFT and ZFT age populations extracted from the Linkou and Liukuei conglomerates present some inconsistencies. Particularly in the Linkou conglomerate where an AFT age of 5.5±1.3 Ma is older than the younger ZFT population of 4.6±0.7Ma (Fig. 3.31; Table.3.8 and 3.9), but the large error bar of the AFT age allows some overlap. Similarly when combining all samples from the Linkou and Liukuei

conglomerates together (Table 3.10), the AFT and ZFT young population are strikingly similar, which can be interpreted as an effect of very high exhumation rates or a complexe mixture of ages difficult to deconvolve with the binomial peak fitting method, which may tend to add an excessive number of population to reproduce the data. Indeed, the F-test probability may succeed with a less number of populations as proven for individual samples (Table 3.8 and Table 3.9) and for all the samples grouped (Table 3.10). When reducing the peaks to two, the ZFT younger population goes from 4.8±0.6Ma to 6.1±0.8Ma, the latter value seems more plausible and concordant with the AFT age population (Table 3.10). However we should keep in mind that grouping samples might be mixing likely similar ages, particularly if age-elevation relationships exist in the source areas (although no such age-elevation relationship has been reported in the western divide), or if changes in exhumation and/or sources occurred during deposition of the sediments.

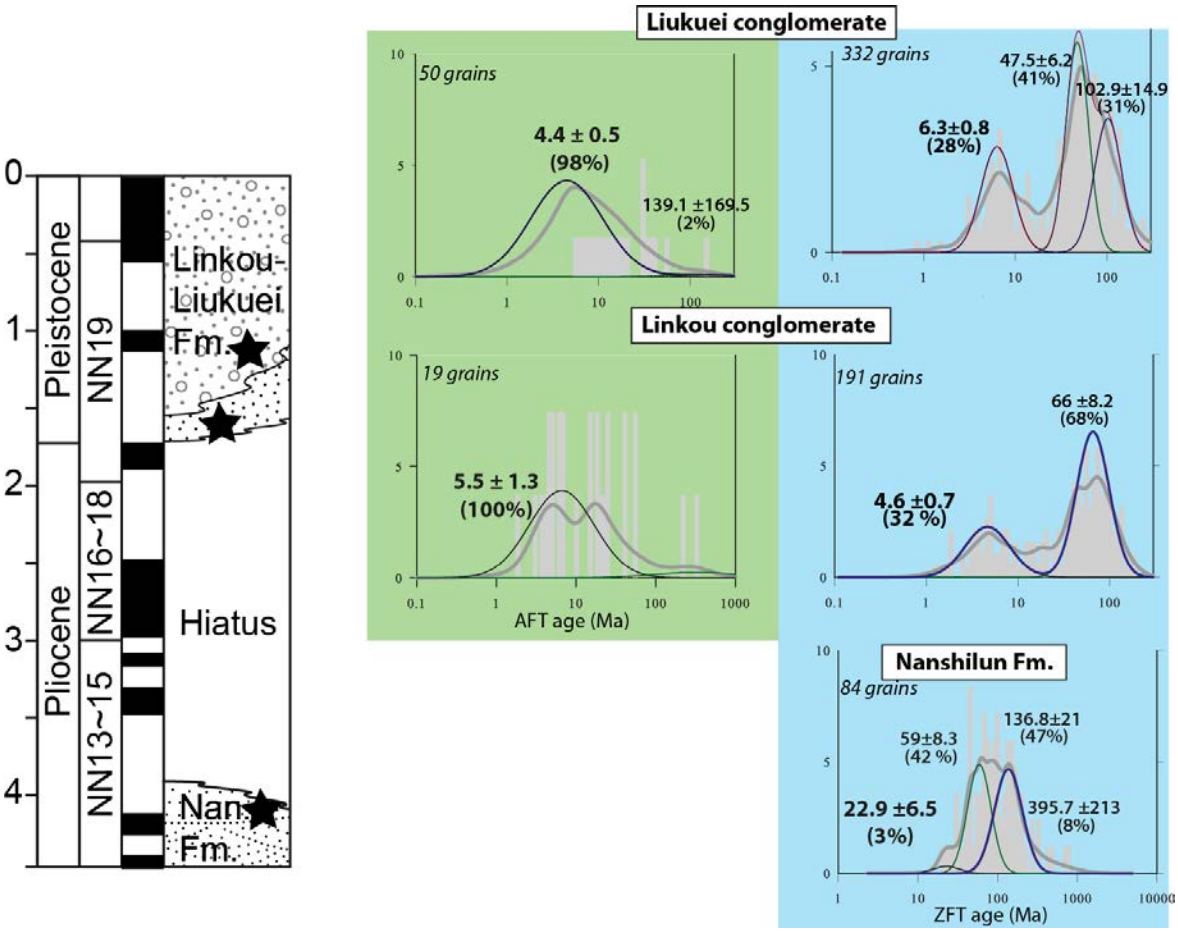

Fig. 3.31*: Depositional age and calcareous nannofossil bio-zones of the Linkou (LK), Liukuei (LG) Formation and Nanhsihlun sandstone with the position of detrital fission-track samples and corresponding AFT (green) and ZFT (blue) grain-age probability-density plot with binomial fitted peaks and distribution histograms.*

				ZFT age components ±1σ							AFT age components ±1σ	
Sample	N	Gain-age range (Ma)	F test (%)	P1 (Ma)	P2 (Ma)	P3 (Ma)	P4 (Ma)	N	Gain-age range (Ma)	F test (%)	P1 (Ma)	P2 (Ma)
LK03 LK04 LKG15	523	0.8-599.8	0	4.8±0.6 (23%)	14.6±2.7 (9%)	51±6.3 (39%)	104.0±13.2 (28%)	69	0.6-144.8	0	4.7±0.5 (98%)	134.6±167 (2%)
LKG17 LKG18 LKG20			0	6.1±0.8 (30%)	65.9±7.9 (70%)							

***Table 3.10**: Linkou (LK) and Liukuei (LG) combined ZFT and AFT data. For ZFT data, two sets of age population are given, both passing the F-test. N: Total number of counted grains; binomial peak fitting are given ± 1s. Also given is the percentage of grains in each population.*

Finally, because the depositional age of the studied stratigraphic section is poorly constrained, I was not able to extract lag-time (i.e. cooling age minus depositional age) evolution along the conglomeratic deposits, to test the inference of increasing tectonism up-section the Toukoshan Fm. (which includes the Linkou and Liukuei local members) inferred from sedimentological arguments [*Chou*, 1977]. Nevertheless the LK03 sample belongs to the lower member of the Linkou conglomerate and its depositional age has been well constrained to base of nannofossil biozone NN19 [*Chi*, 1979] equivalent to absolute ages between ~1.96 and 1.70Ma. LK03 has ZFT age of 4.0±0.6Ma or 5.1±0.7Ma (depending on the number of peaks chosen during binomial fitting; Table 3.8) and an AFT age of 5.0±1.2Ma. Resulting lag-times for ZFT and AFT are between 2.3±0.6Ma and 3.4±0.7Ma, and between 3.3±1.2 Ma and 3.0±1.2, respectively.

D. Laonung fault samples

Seven samples were sampled along the Laonung river (Fig. 3.17 and Fig. 3.32), but only five ZFT and five AFT ages obtained. Sample Ba3 was mounted for ZFT and AFT dating but not counted due to lack of time. Sample PI56 was mounted for AFT and ZFT dating but only AFT dating was performed.

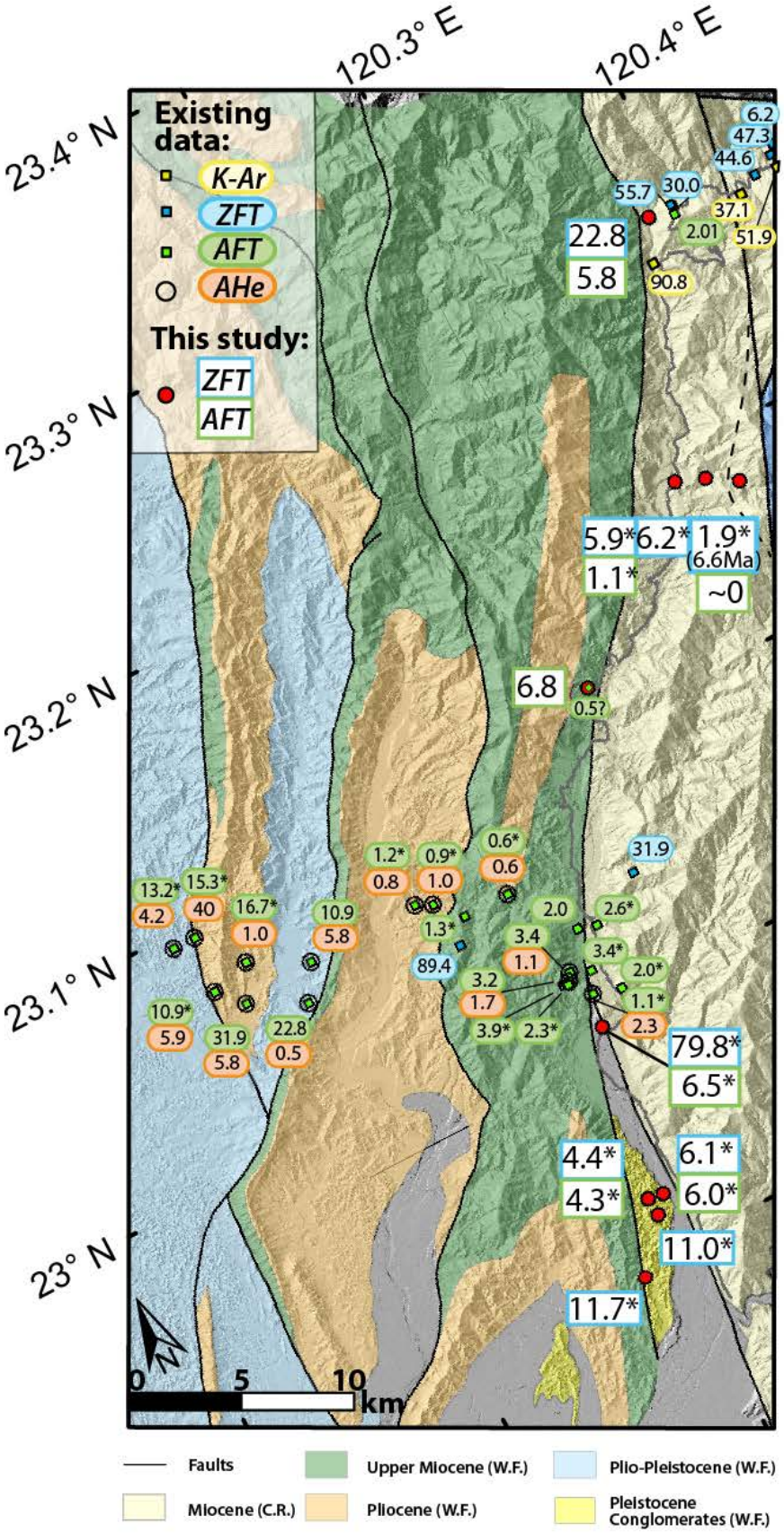

***Fig. 3.32**: Map showing the obtained AFT and ZFT data in the Laonung area including young-peak-ages of the Liukuei conglomerate. Also shown is the existing data in the area. K-Ar ages on muscovite (Tsao, 1996). AHe ages are from Lock (2007) are the average age of all the grains dated (usually 3 but up to 6 grains for 6 of the samples shown). AFT data*

from Lock [2007] and Fuller et al. [2006]. ZFT from Liu et al. [2006], Willett et al. [2003] Asterisk (*) indicates young peak age in my data and in the AFT existing data. Ages in million years. Age in parenthesis below the 1.9Ma ZFT age indicates the young peak population when performing binomial peak fitting on two age populations (sample 0810-03 in Table 3.13). Note that the ages shown are a mixture between exhumation on the fold-and-thrust belt thrust sheets, detrital ages derived form the cooling history of the Central Range and pre-orogenic detrital ages not related to the Taiwan orogeny.

Generally, zircon yield was good allowing a large number of grains to be counted (Table 3.11) so that young-peak population could be well characterized. All counted samples presented were discordant with a recurrent old population with an age between ~70Ma and ~110Ma, and some samples presented an additional old population between ~13Ma and ~20Ma (Table 3.13).
Young orogenic population are present only in the attempt of vertical profile samples (0810-01, 0810-02 and 0810-03) ranging in age between ~1.9Ma and ~6.6Ma. The youngest age population belongs to sample 0810-03, the highest sample (1097m) in the vertical profile attempt, and although not well characterized (~5 grains), it is possible that this population witness of the reseting of the lowermost –retention zircon population of this samples. The age jump from age ~6Ma in the lower elevation sample to the young age population of this sample is attributed to the fault observed in the field between the two localities (Fig. 3.17 and Fig. 3.32). However, because the age-elevation relationship appears to be concordant (positive correlation between age and elevation) when extracting two population instead of three (second row of sample 0810-03 in Table 3.13), it could also be that the young population (~1.9Ma) is an artifact of binomial peak fitting used to extract the age populations. The other analyzed ZFT samples (0510-01 and 0210-01) present only pre-Taiwan orogen ages in both the footwall and hangingwall of the Laonung fault.

Name	Long.	Lat.	Position	Alt (m)	ρ_s (10^5 tracks . cm^{-2})	Ns (tracks)	ρ_i (10^6tracks . cm^{-2})	Ni (track)	U±2s (ppm)	N	Gain-age Range (Ma)	Pooled ZFT age ±1σ (Ma)
0810-01 ♪	120.789	23.189	HW	642	82.5	2660	1.67	540	118±11	45	4.3-424.2	**70.3±9.1 ♪**
0810-02 ♪	120.801	23.184	HW	850	76.3	3569	2.31	1081	164±11	73	4.5-211.3	**47.1±5.9 ♪**
0810-03 ♪	120.813	23.177	HW	1097	55.7	3300	1.24	735	88±7	73	1.2-402.3	**63.9±8.1 ♪**
0210-01 ♪	120.652	23.009	FW	269	116	2510	1.81	392	127±13	23	52.7-189.9	**92.0±12.2 ♪**
0510-01 ♪	120.831	23.287	HW	833	109	1258	2.41	278	170±21	15	9.7-150.1	**64.6±9.0 ♪**

Table 3.11*: Pooled age of concordant and discordant (musical note ♪) ZFT from the Laonung area. N: Total number of counted grains. HW = Hangingwall of Laonung fault; FW= Footwall of Laonung fault. Discordant samples (♪) are presented in Table 3.13. Coordinates in WGS-84. Values extracted with Binomfit 1.1.60.*

The attempt of vertical profile allowed extracting a ZFT age-elevation relationship (AER) with 3 samples with constraints from AFT in the lowermost and highermost samples (Fig. 3.33). The variation of ZFT age with elevation is low and not significant given the error bars. Nevertheless, linear regression of the AER imply exhumation rates of ~648m/Myr between 5.9±1.9Ma and 6.6±1.5Ma (Fig.3.33). If the 1.9±0.8 ZFT age population of the topmost sample is really reflecting cooling and resetting of the low-retention zircons population, it may be indicative of a play along the fault observed in the field (Meishan fault), in agreement with the AFT age of ~0Ma inferred from the topmost sample (0810-03, AFT with no counted spontaneous tracks).

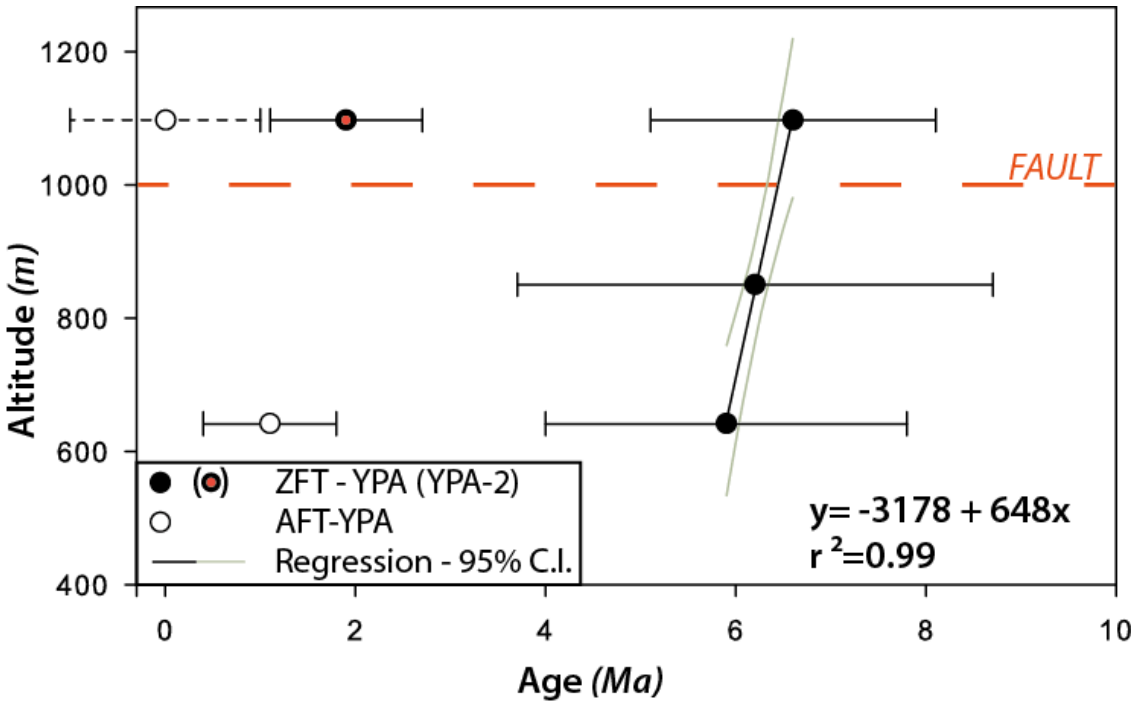

***Fig. 3.33**: Age-elevation relationship in the attempt of vertical profile in the hangingwall of the Laonung fault (samples 081901, 0810-02 and 0810-03 Table 3.13). Note that AFT age of sample 0810-03 (1097m) is here plotted as if its age was 0±1Ma. The age elevation linear regression is obtained using the second binomial fitting young-peak age (YPA) for samples 0810-03 (Table 3.13). See Fig. 3.32 for location of the profile and Table 3.13 for the original data.*

Apatite yield was relatively poor preventing to count a large number of grains (Table 3.12). Counted grain-ages range from 1.1Ma to 303Ma and two samples presented discordant ages, with poorly characterized old age populations of ~40Ma and ~300Ma (Table 3.13). Young age population range from 1.1±0.7Ma to 6,8±1.8Ma. All samples presented zero spontaneous tracks grains and one sample (0810-03) did not yield apatites with spontaneous track preventing from extracting an age. The latter sample reflect a very young cooling age, in agreement with the ZFT young population age of the same sample (as discussed above), and likely confirming the potential important role in cooling and exhumation of the observed fault between samples 0810-02 and 0810-03. The lowermost sample fromteh vertical profile attempt (0810-01) also yield a very

young age of 1.1±0.7Ma indicating high cooling rates in this area for the last ~1Myr. The other samples along the Laonung valley presented realtively consistent ages converging to ~6Ma in both the footwall and hangingwall of the Laonung fault.

PI56 was sampled very close to sample 33_01 of *Lock* [2007] according to the maps provided and interpretation in the text (Fig. 3.17). However the geographic coordinates provided place the 33_01 sample in the footwall of the Chishan thrust further southwest (AFT 0.5Ma age in Fig. 3.30) close to the Linkou conglomerate samples presented above. Considering *Lock* [2007] wrongly reported the coordinates in the datatables and that the maps were rightly drawn, the age discrepancy would be considerable (0.535±0.220Ma pooled age of 40 grains with 6 tracks counted and U-content obtained with LA-ICPMS *vs.* 6.8±1.8Ma obtained hereon 20 grains). However, it seems more likely that *Lock* [2007] misplaced the 33_01 sample.

Name	Position (Laonung F.)	Alt (m)	ρ_s (10^4 tracks . cm^{-2})	Ns (tracks)	ρ_i (10^6tracks . cm^{-2})	Ni (track)	U±2s (ppm)	N	Gain-age Range (Ma)	Pooled AFT age ±1σ (Ma)
0810-01♪	HW	642	1.84	6	1.11	362	24±3	15	1.1.-51.6	***1.5±0.8*** ♪
0810-03*	HW	1097	-	-	-	-	-	17	0.9-31-1	**0***
0210-01 ♪	FW	269	14.5	73	1.82	916	40±3	23	3.0-303.3	**7.3±1.0** ♪
0510-01	HW	833	4.46	4	0.703	63	15±4	7	5.2-39.2	**5.8 ±3.9**
PI56	FW	532	7.05	20	0.993	282	21±3	20	1.9-56.9	**6.8±1.8**

Table 3.12: *Asterisk (*) indicates a sample in which no spontaneous tracks could be counted equivalent to an age equal to 0Ma. See Annex 5 for original counting data of this sample. Discordant samples (**♪**) are presented in Table 3.13.*

					AFT age components ±1σ					ZFT age components ±1σ		
Name	Alt. (m)	N	Gain-age Range (Ma)	F-test (%)	P1 (Ma)	P2 (Ma)	N	Gain-age Range (Ma)	F test (%)	P1 (Ma)	P2 (Ma)	P3 (Ma)
0810-01 ♪		15	1.1-51.6	0	**1.1±0.7 (93%)**	42.6±64.8 (7%)	45	4.3-424.2	0	**5.9±1.9 (10%)**	77.9±10.2 (90%)	
				0	**1.5±0.8 (100%)**							
0810-02 ♪	No AFT data for this sample						73	4.5-211.3	1	**6.2±2.5 (3%)**	14.6±3.2 (22%)	70.5±9.6 (75%)
									0	**13.1±2.0 (23%)**	69.4 ±9.0 (77%)	
0810-03 ♪	Sample with no induced AFT counts						73	1.2-402.3	0	**1.9±0.8 (7%)**	19.9±6.4 (12%)	83.5 ±11.2 (81%)
									0	**6.6±1.5 (13%)**	77.7 ±20.8 (87%)	
0210-01 ♪		23	3.0-303.3	0	**6.5±0.9 (96%)**	354.6±405 (4%)	23	52.7-189.9	0	**79.8±17.3 (49%)**	110.2±26.6 (51%)	
0510-01 ♪							15	9.7-150.1	0	**22.8±4.3 (31%)**	93.0±14.2(69%)	

Table 3.13: *Binomial peak fitting of AFT and ZFT discordant samples. For some samples two d*

V. Discussion and implications

In the following I first present a succinct discussion on the young-peak age approach, then present the first order interpretation of part of the results as published in *Mesalles et al.* 2014 (minor revisions), to finally briefly discuss other implications the results right discussed have on the Taiwan mountain building processes and timing. In the last section I try to make the link between the deformation phases observed in the field and described in the literature (Chapter 2) and the thermochronological age constraints presented in this chapter.

A. Young-peak age approach

The effect of radiation damage in ZFT annealing behaviour is critical when interpreting ZFT ages, however not much literature in the subject exists. This effect needs to be considered from the initial steps of zircon mounting and track revealing since revealing behaviour has been empirically correlated to the amount of radiation damage, where higher radiation damaged zircons etch more easily than more crystalline, less radiation damaged zircons [*Bernet et al.*, 2004; *Bernet and Garver*, 2005]. The effect radiation damage during interpretation of ZFT ages is crucial since closure/annealing temperature has also been empirically correlated to the amount of radiation damage with high radiation damaged zircons annealing at lower temperatures [Fig. 3.1; *Bernet and Garver*, 2005; *Tagami and O'Sullivan*, 2005; *Reiners and Brandon*, 2006; and reference within it]. Zircons in detrital suites are known to have a wide range of radiation damage due to the varied source thermal history and Uranium and Thorium content. This implies different closure temperature for the different radiation damaged populations, with low-retentive zircons (i.e. with high radiation damage) annealing at low temperature of about 180-200˚C and high retentive zircons (i.e. with low radiation damage) annealing at higher temperature of about 280-300˚C [*Garver et al.*, 2005].

In this study I used a combination of FT dating in the Central Range and of sediments derived from it. Because the source rocks (Central Range) presented partially annealed samples (not necessarily form a partial retention zone, or with a dominant component of partially annealed grains), in the sense that not all zircon grains population were annealed, the identification of areas where the young-peak age (YPA) were present in the Central Range was a critical step to understand sedimentary source and infer source rock exhumation. Additionally, assigning to YPA as resulting from particular tectonic events (onset of collision) or the YPA-AER as exhumation rates goes through the assumption that they are the result from genuine cooling through a given closure temperature and not from a meaningless mixture of partially reset grains.

The use of the vertical profile approach (Fig. 3.3 and Fig. 3.34) allows for an assessment of zircon annealing behaviour of a pseudo-vertical column of rocks at depth. *Liu et al.* [2001] derived the total annealing temperature of zircons in Taiwan to 260±20ºC based on a spatial correlation between prehnite-pumpellite/lowergreenshist boundary [illite-smectite to 2M-mica; *Chen*, 1994] and the reset/partially-reset distribution of chi-square and central ZFT ages. One could place the exhumed, paleo-260ºC isotherm above our ~3.2Ma group of samples (break-in-slope) if assuming our concordant sample of 5.4±0.9Ma (PV2-

1; Table 3.2) age was counted with a bias towards young easily countable grains, with the same arguments towards Lee et al. [2006] samples at the same altitude. Alternatively we could place the paleo-260ºC isotherm above this samples (Fig. 3.34). Assuming the acceleration of exhumation rates at ~3.2Ma is responsible for the exhumation of totally reset samples, the former option can be assumed. In this case, a geothermal gradient with an upper bound of 50ºC/km can be extracted (Fig. 3.34). This estimate is in agreement with the estimates 36-46ºC/km extracted in the numerical inversion of the upper profile and suggests that the topmost sample was probably very close to the 180-200ºC isotherm and thus record the timing of initiation of cooling. .

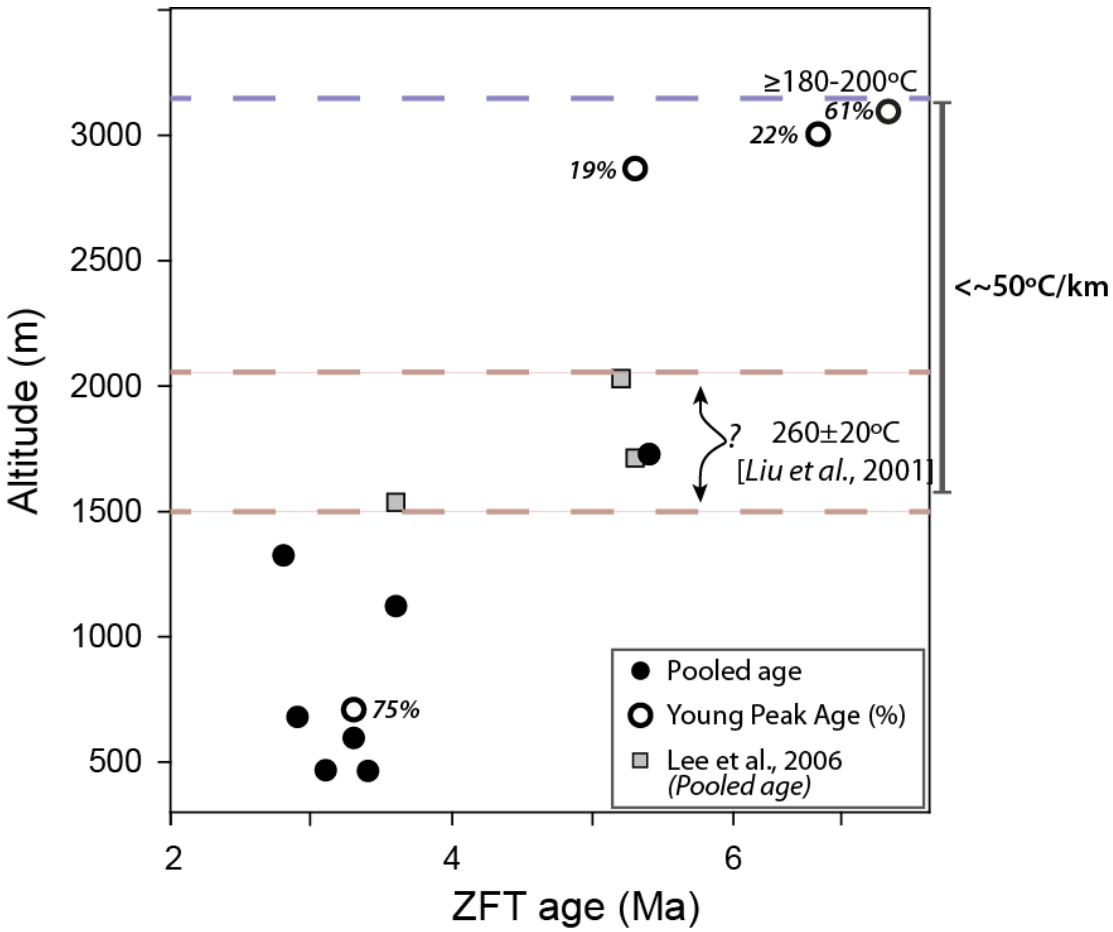

Fig. 3.34*: Vertical profile of the Taimali area with young-peak ages (discordant ages) with percentage of young-peak grains in the sample and totally annealed (concordant ages). Total annealing of zircons on Taiwan has been estimated to 260±20ºC by Liu et al. [2001] and annealing of the less retentive zircon grains is estimated to 180-200ºC by Grarver et al. [2005]. The estimate of a maximum geothermal in the upper profile is estimate by dividing 80ºC (260-180ºC) by the elevation offset between the break-in-slope and the highest samples (~1600m). It is worth noting that Lee et al [2006] did not mention if the samples used were concordant or discordant, but we assume they were concordant.*

In our study we observed that most of the higher altitude samples present a YPA younger than the depositional age, and we interpret it as a reset low-retention

zircon population having reached 180-200˚C. In the other hand, most of the lower altitude (<~1500m) samples present a single young population, thus they are fully reset and have reached temperatures of about 260±20˚C. The young peak populations are interpreted to record the last thermal event and, thus, the age-elevation trend observed in the profile reflects cooling rate. Hence the ZFT partial annealing zone concept is not appropriate in our case. The low retentive grains have been totally annealed and thus have not kept any record of its previous history as implied by the partial annealing zone concept (Fig. 3.3).

To illustrate the effect of radiation damage on zircon retentivity, we have plotted ZFT age versus Uranium content (Fig. 3.35). A trend can be observed between uranium content and ZFT age, with younger ZFT ages for high uranium content samples, suggesting the YPA approach adopted in this work is appropriate.
This is true not only for zircon grains in our vertical profile but also for detrital ZFT grain ages in the foreland, for zircon grains of the Laonung valley and for the horizontal profile in the Taimali catchment as well as for detrital zircons from Kirstein et al. (2009, 2010). This trend may be partly due to a counting bias where low-uranium young ZFT age and high-uranium old ZFT age are not counted due to the lack of tracks in the former or to metamictisaton in the latter, but it could also be a retentivity related correlation.

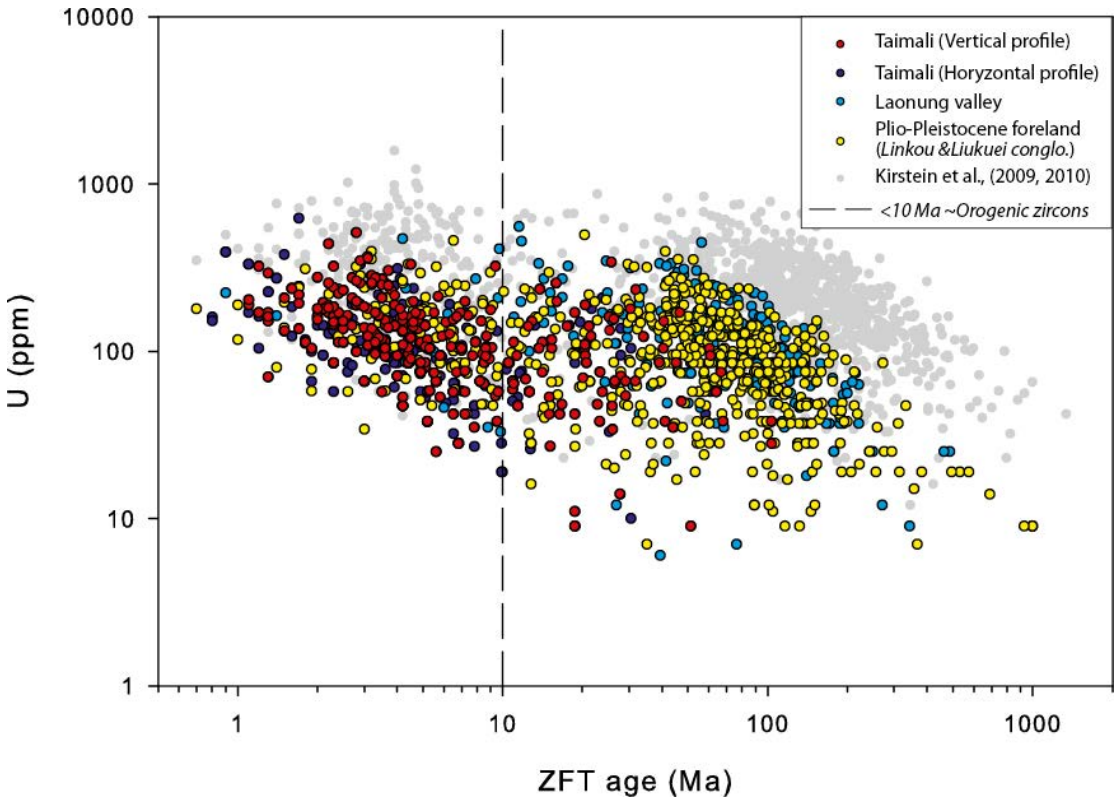

Fig. 3.35*: Uranium content vs. ZFT grain age, for our vertical profile, our Plio-Pleistocene foreland sediments data and unpublished data, and ZFT data from Kirstein et al. (2009, 2010). Note the trend with increasing Uranium content for younger orogenic ages (i.e. ~<10Ma), suggesting that nuclear decay 's radiation damage is one of the factors controlling ZFT annealing properties and closure temperature.*

To further explore the effect of radiation damage we used *Kirstein et al.* [2010a, 2010b] ZFT and U-Pb double dated data from the Plio-Pleistocene sediments of the eastern forearc and from sandstone bodies of southern Taiwan (Fig. 3.36). A first order observation of this data indicated that orogenic ZFT aged grains (<10Ma) yield old U-Pb ages and high uranium content (Fig. 3.36, upper panel). A more detailed look into the only double dated sample containing orogenic ZFT ages (HK3 sample of *Kirstein et al.* 2010a) indicates the almost systematically (grain HK19 appears as the probable only exception; Fig. 3.36, lower panel) orogenic ZFT grains yield either a high uranium content and relatively young U-Pb ages or low uranium content and old U-Pb ages (Fig. 3.35, lower panel).

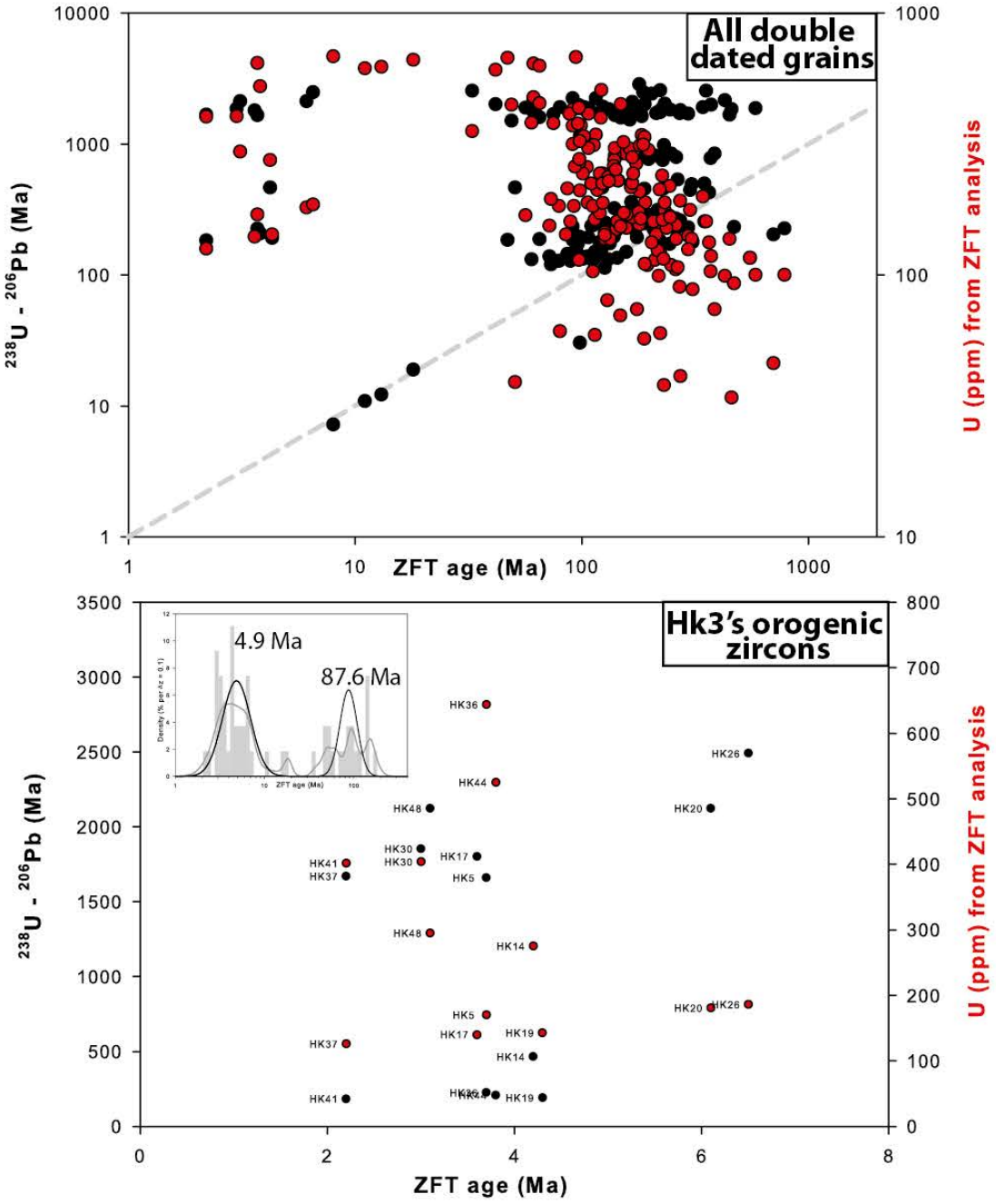

***Fig. 3.36**: Double-dated ZFT and U-Pb grains from Kirstein et al.* [2010a, 2010b].
Upper panel: plot of all double dated grains (black dots, left axis) and uranium content of the same grains from ZFT analysis (red dots, right axis) versus ZFT age. 1:1 line indicates grains with same U-Pb and ZFT age (i.e. rapidly cooled, volcanic zircons). Note how orogenic (i.e. ZFT ~<10Ma) grains have relatively old U-Pb age and high Uranium content, compared to older ZFT grains, which some have lower uranium content
Lower panel: Same plot for young ZFT grains from Hk3's sample from Pleistocene sediments (Kirstein et al., 2009). Hk3 sample is the only double-dated sample with orogenic (i.e. reset) zircon grains. Inset is the probability density plot of Hk3 with binomial peak fit. Labels indicate grain reference for comparing Uranium content and U-Pb age of a given zircon crystal. Note that the orogenic grains present systematically_ except Hk19_, either an old U-Pb age and low Uranium content or high Uranium content and a relatively young U-Pb age.

A way to extract more rigorously the annealing behaviour of zircon from the Taimali vertical profile could imply:

- Counting a higher number of grains (~100 grains) so that each population is better characterised.
- Quantifying the presence of metamicted grains while counting.
- Quantify grains containing old and young tracks, distinguishable by their width (zircon's Dpar?), with fine tracks being the "young" ones and "fat-chubby" (and shorter?) tracks being the old ones (personal observation during counting and personal communication with J. Garver during the Thermo 2012 meeting, Guilin, China).
- Double date with U-Pb the young ZFT age grains to assess the relation between uranium content, crystallisation age and radiation damage and ZFT age. Alternatively, a qualitative observations of zircon colour and use it as a proxy for radiation damage as suggested by *Garver and Kamp* [2002]. Potentially this could lead to the extraction of uranium-content/U-Pb age range grain groups behaving the same way to the same temperature ranges.

→ Although often seen as a problem, the different annealing behaviour of radiation damage zircons could give birth to a new multi-temperature (180ºC to 260ºC) sensitive thermochronometer, solely based on the well established ZFT dating technique. Indeed, as stated by *Garver et al.* [2005]: " *[…] there is probably an infinite number of partial annealing zones for a suite of heated detrital grains that have accumulated radiation damage*". If the mentioned "infinity" became finite and well constrained, the ZFT-YPA approach applied in slightly metamorphosed terrains (below low greenschist metamorphic facies) could provide priceless thermal constraints. However field test as the one presented here need to be further exploited for a reliable temperature calibration.

B. The thermal record of a two-phased collision in the Taiwan mountain belt

1) From underwater continental crust underthrusting to arc-continent collision

Based on the results presented above, a paper has been accepted to *Geology* pending correction.

With this paper, I show that low-temperature thermochronological data are able to provide constraints on the timing of initial collision when offshore distal continental margin are tectonically inverted.

Moreover, time-temperature history shows changes that reflect transition from onset of inversion at distal margin to rapid growth of the Taiwan orogenic wedge as it became subaerial.

Our data support models in which the inherited margin architecture controls the tectono-thermal evolution of mountain belts.

Innovative and solid dataset:

We provide the first age-elevation relationship in the Taiwan belt sampled within a single structural domain and with a clear break-in-slope reflecting a major change in the processes governing orogenic evolution.

We provide the first orogenic related detrital record in the western foreland.

We use newly developed inversion models (i.e. Willett and Brandon, 2013) taking into account various processes not considered in standard thermal models. We further double-check the inverted results with more widely used thermal models (HeFTy).

Provocative implications and wide impact conclusions:

Our thermochronological data dates the onset of continental crust involvement in the submarine accretionary wedge, and thus dates collision in Taiwan. It further constrain what is probably the major phase of mountain building of Taiwan (i.e. 3.2 Ma phase), well described in the geological record of the adjacent basins (e.g. increase in subsidence and sedimentation rates of the foreland and forearc), but poorly described in the Central Range mountains.

Our data implies rock cooling in the submarine accretionary wedge. To our knowledge, we are the first to report a record of early underwater rock cooling.

Given the particular geodynamic setting of Taiwan, we are able to relate the observed early cooling with a recently described process, namely underplating of hyper-extended continental margin crust (McIntosh at al., *Geology,* 2013; Lester et al., *EPSL,* 2013; Eakin et al., *JGR,* 2014).

Our geological model for the early phase is consistent with a wide range of existing data, including the time of initiation of orogenic load related subsidence, underwater surface heat-flow, the above-mentioned underplating and with the more general expected rheological behavior of an

hyperextended crust, where the whole crust is implied in the collision with no or little continental crust subduction (Mouthereau et al., *Nat. Geo*, 2013).

Methodological implications:

To our knowledge, we present the first ZFT elevation profile using the young-peak approach. The application of the young-peak-age in a vertical profile extends the potential use of such approach in slightly metamorphosed orogenic settings not having reached total annealing of zircons. It appears to be an adequate methodological strategy (i.e. multiple zircon mountings for track counting) for the study of the early collisional evolution of orogenic wedges. Although much still needs to be done to understand and quantify the radiation damage effect on closure temperature, our study confirms the potentially successful future of this approach.

The text of the paper is presented as it was accepted, without the corrections required for final publications.

From submarine continental accretion to arc-continent orogenic evolution: the thermal record in the Taiwan mountain belt

Lucas Mesalles[1,2,3], Frédéric Mouthereau[2,3,4], Matthias Bernet[5], Chung-Pai Chang[1,4,6], Andrew Tien-Shun Lin[1], Charlotte Fillon[7], Xavier Sengelen[8]

[1] Institute of Geophysics, National Central University, Chungli 320, Taiwan.
[2] Sorbonne Universités. UPMC Univ Paris 06, UMR 7193, Institut des Sciences de la Terre Paris (iSTeP), 4 Place Jussieu, F-75005 Paris, France
[3] CNRS, UMR 7193, Institut des Sciences de la Terre Paris (iSTeP), 4 Place Jussieu, F-75005 Paris, France
[4] Laboratoire International Associé ADEPT, CNRS-NSC
[5]ISTerre, Université Joseph Fourier, CNRS, 1381 rue de la piscine, 38041 Grenoble, France
[6]Geological Remote Sensing Laboratory, Center for Space and Remote Sensing Research, National Central University, Chungli 320, Taiwan
[7]Instituto de Ciencias de la Tierra Jaume Almera (ICTJA-CSIC), Solé i Sabarís s/n, 08028 Barcelona, Spain
[8]Formerly at [1], now at CEREGE, Aix-Marseille Université, Technopole Environnement Arbois, Mediterranée BP80, 13545 Aix en Provence, Cedex 04, France

ABSTRACT
Constraining the timing of initial collision is critical for understanding how long-term plate convergence is partitioned at collisional plate boundaries. Reevaluation of the age of collision from orogenic thermal evolution requires distinguishing the onset of submarine continental accretion, from earlier oceanic subduction and subsequent subaerial orogenic evolution. We present new thermochronological constraints from the first age-elevation relationship (AER) transect in Taiwan and zircon and apatite fission-track ages from orogen derived detrital sediments in the western foreland. Our data reveal onset of cooling from ca. 7.1 ± 1.3 Ma Ma at a minimum rate of 21°C/m.y. in the submarine sedimentary wedge followed by a marked acceleration of subaerial exhumation after ca. 3.2 ± 0.6 Ma at an average rate of 1.7 km/m.y. Our data reflect the thermal record of initial collision stages as Taiwan evolved from submarine accretion of the distal extremely thinned continental margin to crustal thickening of the proximal margin and orogenic development.

Key words: *Taiwan, thermochronology, age-elevation relationship, subduction, underthrusting, collision*.

INTRODUCTION
Dating the onset of collision and subsequent stages of crustal thickening provide first-order constraints for assessing how plate convergence is partitioned to form mountain belts. Inherited passive margins are major actors in the collisional process as their first arrival at the subduction zone marks the initiation of continental accretion. Increasing evidence suggests passive margins to be constituted of wide areas, up to ~200 km, of extremely thinned continental crust rather than narrow transition zones (e.g. Reston, 2009). This suggests that in orogenic settings, continental crust involvement may have started earlier than previously thought. However, such early collisional stages have seldom been described in the literature due to the difficulty of deconvolving the incipient stages from the subsequent orogenic evolution.
Taiwan is a classical example of an active arc-continent collision. Its study gave birth to the first critical wedge approach on orogenic evolution (Davis et al., 1983). Because the Taiwan orogen results from oblique plate convergence between the Philippine Sea and Eurasian plates, the transition from oceanic subduction to collision of the Eurasian margin is presently observed underwater 80 km south of the southern tip of the island (Fig. 1A). Recent seismic data from offshore of southern Taiwan documents underthrusting and accretion of the distal, hyperextended 10 km thick Eurasian continental crust, below the submarine accretionary prism (McIntosh et al., 2013).

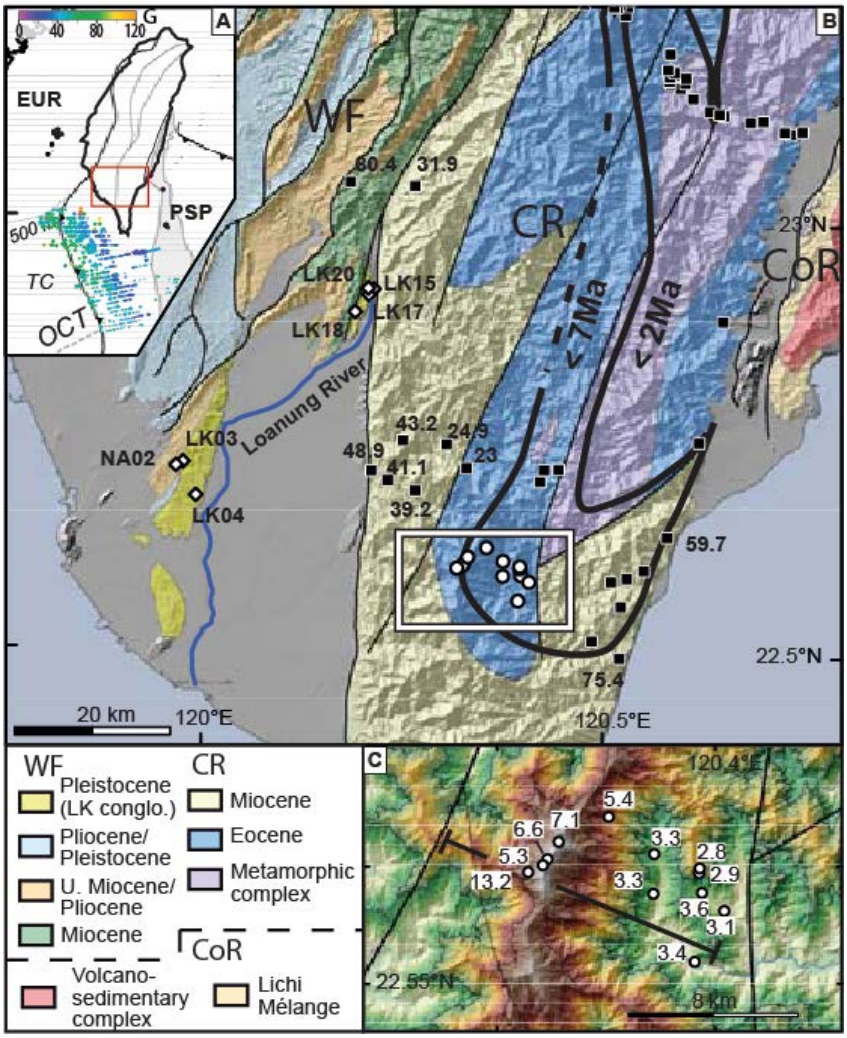

Figure 1. ***A****: Tectonic features of the Taiwan area. EUR-Eurasian plate; PSP-Philippine sea plate; TC-Transitional crust; and OCT-Ocean/Continent Transition. Submarine shallow geothermal gradients (G) from Chi and Reed (2006) are depicted in colors.* ***B****: Geologic map of southern Taiwan and location of samples for fission-track analyses (white circles and diamonds). Thick black lines show contour of ZFT ages <7Ma and <2Ma (black squares) based on published data (Tsao et al., 1992; Liu et al., 2001; Willett et al., 2003; Lee et al., 2006). For ZFT ages older than 7 Ma, age is indicated.* ***C****: ZFT ages from the age-elevation profile in Fig. 2 plotted on digital elevation model with the main structural boundaries and location of cross-section in Fig. 2 (black line). Lines on topography depict 1000 and 2000m contour lines (thin black line). Geology based on Chen et al. (2000).*

Nevertheless, the record of incipient continental crust involvement on land in Taiwan is poorly documented. One key constraint is the orogenic loading-related plate flexure dated to 6.5 Ma in the Western Taiwan foreland (Lin et al., 2003), but little is recognized in the Central Range (CR) mountains.

For defining the orogenic cooling history and resolving the earliest stages of collision, we extracted the first thermochronological age-elevation relationship in Taiwan from samples collected in the southern CR mountains. This is aimed to retrace the thermal and exhumational history of rocks from initial accretion in the sedimentary wedge, as the transitional crust started to be underthrusted, to the final stages of crustal thickening. The vertical profile was combined with thermochronologic analyses of Plio-Pleistocene detrital pro-foreland deposits, which recorded exhumation of the CR.

The results lead to a reevaluation of the timing of the first collision related thermal perturbation affecting the rifted South China Sea (SCS) margin and subsequent major orogenic growth.

GEOLOGICAL BACKGROUND AND COOLING AGE CONSTRAINTS

Accumulation and deformation of continentally derived sediments have continuously been taking place in the subduction accretionary wedge since the start of SCS subduction (~15 Ma, e.g. Huang et al., 2006). Initiation of collisional processes in Taiwan started with the first arrival of Eurasian continental crust to the Manila trench. Following the initial involvement of highly extended passive margin crust, progressive arrival of thicker continental crust onshore in northern Taiwan coincided with the closure of the forearc basin, and accretion of the northernmost Luzon volcanic arc of the Philippine Sea Plate (Fig.1A-B). The CR results from the stacking of pre/syn-rift Eocene to Miocene post-rift SCS margin sediments, and its Eurasian Mesozoic-Paleozoic basement. The Western Foothills represents the western fold and thrust belt composed of west-propagating thrust slices of pre-orogenic and syn-orogenic foreland sediments. The active suture between the two plates is represented by the Lichi mélange along the Longitudinal Valley (Fig. 1A).

Apatite fission-track (AFT) ages show that the CR exhumed over the last 1-2 Ma at rates of 4 to 6 km/m.y. (Willett et al., 2003). Consistently, Dorsey (1988) found the first metamorphic core clasts, and Kirstein et al. (2010) the first unequivocal orogenic zircon fission-track (ZFT) ages, in the <2 Ma deposits of the eastern retro-foredeep basin, implying relatively recent exhumation and exposure of the metamorphic core.

Liu et al. (2001) described slightly older ZFT age populations of 5-6 Ma in the northwestern and southern parts of the CR and interpreted them as reset ages, consistent with cooling from temperatures in excess of 260°C. In southern Taiwan, where exhumation is considered the most recent, Willett et al. (2003) interpreted AFT ages of 1.2 to 5.5 Ma and ZFT ages older than 3 Ma as not related to the collisional history, despite being younger than the depositional age (Fig. 1B), arguing for a high geothermal gradient during burial. By contrast, ZFT ages of 3.6-5.3 Ma from the same Miocene slates of the southern CR were interpreted as fully reset by Lee et al. (2006), who concluded that collision dates back to about 6 Ma, although no consistent thermochronological model was proposed to reproduce these data.

METHODS

General approach

In this study, we use fission-track dating which provides information on the time-temperature history of rocks that have cooled in the shallow (<10 km) crust (see DR for analytical procedures and data treatment). Our aim is to constrain the cooling history of the orogenic wedge since (1) the first stages of collisional accretion of the thin continental crust and (2) its later evolution as the wedge became subaerial and thicker continental crust was involved. To solve this, we first applied the vertically distributed samples approach (e.g. Reiners and Brandon, 2006) within the Eo-Miocene series in the CR, to retrace the cooling history of this series since they were accreted in the orogenic wedge to the more recent tectonic events creating present day topography. Secondly, we sampled Plio-Pleistocene shallow-marine to fluvial sediments derived from the Taiwan orogen, now deformed and exposed in the southern Western Foothills fold and thrust belt. The sampled stratigraphic sections includes syn-orogenic deposits resulting from a major Pleistocene tectonic/erosive event as evidenced by a major increase of sedimentation rates and coarsening Early

Pleistocene (Chang and Chi, 1983), and thus intend to improve the understanding of the subaerial evolution of the belt.

Vertical profile sampling and modeling

Twelve samples of very low-grade metamorphic Eocene and Miocene sandstone were collected for ZFT analyses. Sampling sites range in elevation from 465 to 3097 m and include Peitawu Shan, the highest point of southern Taiwan (Fig. 1C and 2B). The geological structure of the study area indicates that sampled sandstones are tightly folded with penetrative cleavages but no major faults or shear zones exist, consistent with the Geologic Map of Taiwan (Chen et al., 2000) (Fig. 1B and 2B). For samples with over-dispersed age distributions and one age population younger than the depositional age (Fig. 2 and Table DR2), we used the young-peak age approach where only the youngest age peak is considered to record the last thermal event (Brandon et al., 1998; Garver et al., 2005). Young peak ages indicate resetting of the least retentive population of zircons, more retentive zircons remaining unreset (e.g. Garver et al., 2005). While resetting of all zircon populations in a given sample implies closure of the system at 280-300ºC. Resetting low retentive zircon populations may entail closure temperature as low as 180-200ºC (Brandon et al., 1998; Garver et al. 2005).

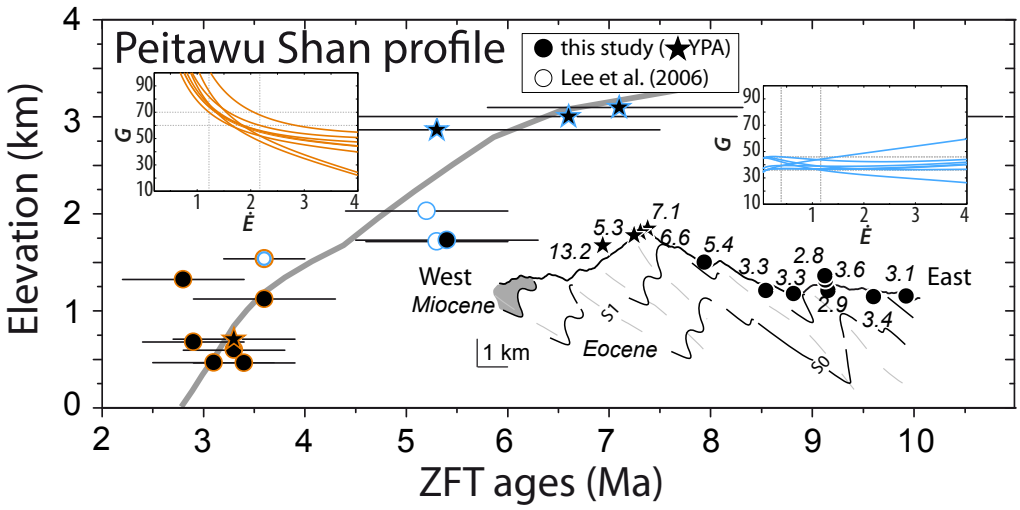

Figure 2. *ZFT age-elevation profile from Peitawu Shan compared with prediction of a forward thermal model (gray line), reproducing timing and cooling rates inferred from inverse modeling. Graphic representation of exhumation rate (Ė in km/Myr) vs. geothermal gradients (G in ºC/km) from the inverse models for the upper (blue) and lower (orange) part of the vertical profile are shown; each modeled sample is represented by one curve. Our ZFT cooling ages are positioned along an E-W geologic section (see location on Fig. 1C) drawn based on Chen et al. (2000) and our own field observations, with S0 and S1 depicting bedding and cleavages, respectively. Samples from Lee et al. (2006) at the vicinity of our sample location are also plotted and modeled. YPA is shown for samples where the young-peak age approach was applied.*

To derive geothermal gradients and exhumation rates our ZFT vertical profile results were modeled using the analytical solution of Willett and Brandon (2013) that accounts for advection of heat and the dependence of closure temperature to cooling rates. We then entered the inverted values into a forward HeFTy model (Ketcham, 2005) to independently test the fit of the data (see Data Repository).

Western foreland samples

Seven samples were collected for AFT and ZFT analyses from Plio-Pleistocene wedge-top foreland basin deposits between the Western Foothills and the CR (Fig. 1B). The Linkou and Liukuei conglomeratic formations are the youngest studied sediments, with depositional ages younger than 2 Ma (base of nannofossil biozone NN19, Chi (1979), Fig. 1B and Fig. 3). The conglomerates are separated by an angular unconformity from the underlying shallow-marine Nanhsihlun sandstone dated to ca. 4 Ma (nannofossil biozone NN15, Chi, 1979; Fig. 3), representing the oldest sampled strata. We collected non-metamorphic to very low-grade metamorphic sandstone cobbles in two localities interpreted to represent lateral equivalents of the same coarsening-upward succession of a fluvial-dominated fan fed by the paleo-Laonung River catchment (Fig 1B). The sampled sandstones represent the pre-orogenic Miocene to Paleogene pre-erosional cover of the CR.

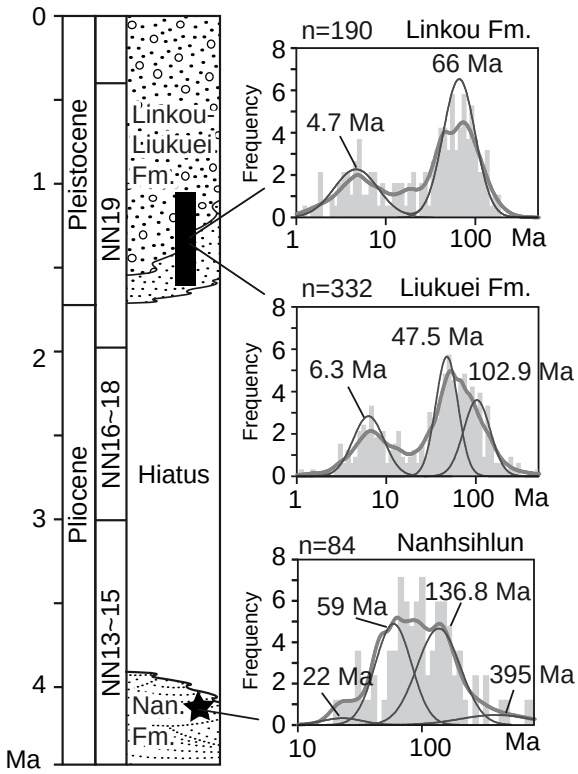

Figure 3. Depositional age and calcareous nannofossil bio-zones of the Linkou (LK), Liukuei (LG) Formation and Nanhsihlun sandstone with the position of detrital ZFT samples and corresponding ZFT grain-age probability-density plot with binomial fitted peaks and distribution histograms (see Fig. DR1 for AFT grain-age probability density plot and tables DR3 – DR4 for fission-track data).

RESULTS

ZFT analyses from the topographic profile (Fig. 2) have minimum ages ranging from 2.8 to 7.1 Ma for samples to the east of the drainage divide and display a well-defined AER with a break-in-slope at ~1500 m (Fig. 2). Samples above the break-in-slope have ZFT ages that consistently increase with elevation revealing onset of cooling by ca. 7.1 ± 1.3 Ma. Samples below the break-in-slope have ages that remain invariant with altitude with an average age of ca. 3.2±0.6 Ma. An additional sample west of the divide has an age of 13.2 Ma that does not correlate with the AER defined east of the divide (Fig. 2), but is consistent with the spread of older (>20 Ma), unreset or partially reset zircons within the stratigraphically younger Miocene Lushan Formation (e.g. Lee et al., 2006) (Fig. 1B).

The fact that discordant cooling ages are not only limited to the higher elevation samples, but are also present and consistent with cooling ages in the lower part of the transect, validate our minimum age approach (Fig.2A).

Inversion of the upper part of the profile (ages between 7.1±1.3 and 3.6±0.7 Ma) gives a best fit model for cooling starting at 7.2 Ma. We obtain apparent exhumation rates of 0.4 to 1.16 km/m.y. (0.8 km/m.y. on average) with geothermal gradients of 36 to 46ºC/km, equivalent to cooling rates of 21°C/m.y. to 37°C/m.y. For the lower part of the profile cooling initiated at 3.7 Ma (older age in the lower profile). We obtain exhumation rates of 1.2 to 2.2 km/m.y. (1.7 km/m.y. on average) with geothermal gradients of 60 to 70ºC/km, equivalent to cooling rates of 102 to 119°C/m.y. (Fig. 2).

Figure 2 shows the fit with the age-elevation data using inverted values on timing and geothermal gradients. We infer that after a period of isothermal holding since 30 Ma, cooling of the rocks that are exposed at the surface today started at ca. 7.2 Ma and accelerated after 3.7 Ma.

ZFT dating of ~600 detrital zircon grains shows ages older than the depositional age, indicating no significant post-depositional resetting. The 2 Ma conglomerates display slightly different age components (Fig. 3; Table DR3), with the youngest population of 6.3±0.8 and 4.7±0.7 Ma, for the Linkou and Liukuei conglomerates respectively. These ages are the first record of mountain building in the western foreland and are similar to the ZFT ages from the upper part of the vertical profile. Older populations of 47.5±6.2 and 66±8.2 Ma represent pre-orogenic zircons. ZFT analyses in the 4 Ma Nanhsihlun sandstone yielded the same pre-orogenic age population at 59±8.3 Ma and a distinctive older age peak at 136.8±21.6 Ma. AFT dating of ~70 apatites in the Linkou and Liukuei samples combined confirm the appearance of young grains from 2 Ma with a young peak population of 4.7±0.5 Ma (Table DR4).

DISCUSSION AND CONCLUSIONS

Our data document an initial phase of rapid cooling from ca. 7.2 to 3.2 Ma, as recorded in the vertical profile (Fig. 2) and in the <2 Ma sediments (Fig. 3), followed by a drastic increase in average exhumation rates from ca. 3.2 Ma (Fig. 2). Older ZFT populations (>20 Ma) in both sets of samples record the pre-depositional Jurassic-Cretaceous tectono-magmatic events in the Chinese margin source areas (e.g. Kirstein et al., 2010). Early orogenic zircon populations start appearing in the southern pro-foreland basin from ca. 2 Ma, similarly to the post-2 Ma retro-foredeep sediments yielding distinctive zircon populations from 7.9 Ma to 4.9 Ma (Kirstein et al., 2010).

Conversely to the retro-foredeep record, our 2 Ma western foreland sediments do not bear ~3 Ma ZFT ages. These observations suggest that while the early cooling phase from ca. 7.2 Ma appears to have affected the whole Central Range equally, the latter phase at ca. 3.2 Ma exhumed principally the retro-wedge and is possibly responsible for the rapid exhumation of the metamorphic core.

An early phase of rapid cooling contrasts with interpretations where ZFT ages older than 3 Ma are not considered being related to the collision evolution (Fuller et al., 2006, Willett et al., 2003). Indeed, as the Taiwan wedge emerged at ca. 5 Ma (Teng, 1990), it may seem difficult to conceive collision related cooling in a submarine accretionary prism, as we usually associate cooling with subaerial exhumation of rocks. Processes other than erosion may explain such contradiction, namely, underwater exhumation through normal faulting and/or cooling from above (i.e. fluid circulation) and/or cooling from below (i.e. underplating of 'cold' passive margin continental crust) characteristics of subduction zones.
The latter process appears to be the most likely and dominant given the analogy with the ongoing continental underplating observed offshore southern Taiwan (McIntosh et al., 2013). Published data indicate a reduction (i.e. cooling) of the present-day geothermal gradients offshore Taiwan from the undeformed distal margin (70-80°C/km) to the accretionary wedge (30-40°C/km) (inset in Fig.1, Chi and Reed, 2006). The latter values are remarkably consistent with our inverted gradients of 36-46°C/km for the early stage of cooling. We infer that the studied margin-derived sediments recorded the earliest stage of continental accretion on top of the underthrusted distal margin of the SCS. This supports onset of foreland flexure at 6.5 Ma as a result of submarine accretion of the transitional hyperextended margin crust, a process that was inferred from numerical experiments (Lester et al., 2012).

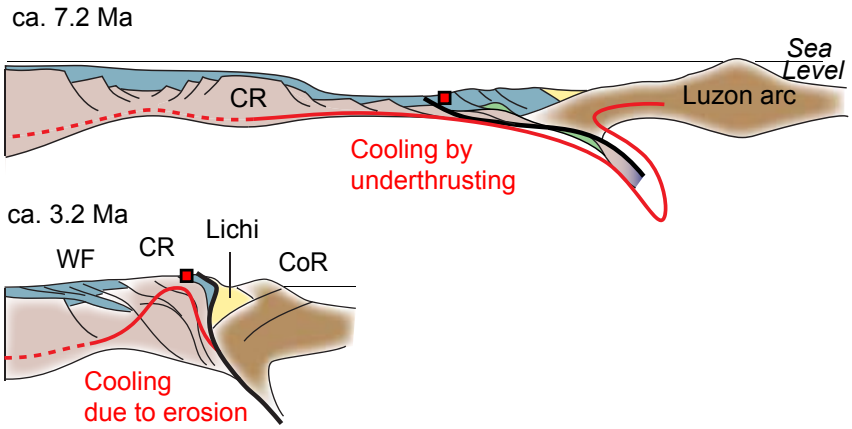

Figure 4*. Tectonic evolution of the Taiwan arc-continent collision that integrates our results on initial cooling at ca. 7.2 Ma related to inversion of the distal Eurasian margin and subsequent accelerated exhumation after ca. 3.2 Ma associated with Luzon arc collision. Red line presents isotherms deflected downward during initial underthrusting of the distal margin and upward as the proximal margin is thickened and erosion rate increases. Approximate location of the age-elevation profile is shown as a square.*

Accelerated exhumation documented at ca. 3.2 Ma, occurred coevally with formation of an ubiquitous angular unconformity (Fig. 3) and increased tectonic subsidence in the foreland (e.g. Chang and Chi, 1983; Lin et al., 2003). This is temporally correlated with the Luzon arc collision as recorded by the development of the Lichi ophiolitic mélange at 3.7-3.5 Ma (Chang et al., 2009). Fast heat advection due to increasing erosion is consistent with higher gradients of ~60°C/km reconstructed for this period. It remarkably agrees with currently observed gradients in the CR (Chi and Reed,

2008). All together our results confirm that the Taiwan collision started at ca. 7.1 ± 1.3 Ma as the accretion of the extremely-thinned distal margin of SCS started. A stepwise increase of exhumation starting at ca. 3.2 ± 0.6 Ma recorded the transition towards shortening of a thicker margin section and accretion of the volcanic arc, which eventually led to major topographic growth and erosion, and probably contemporaneous eastward exhumation of the metamorphic core. This study shows that cooling processes recorded at accreted distal margins help resolving the onset of collision prior to initiation of widespread subaerial exhumation and foreland development associated with mountain building.

ACKNOWLEDGMENTS

S. Willett is thanked for his advice during handling of inverse modeling. E. Hardwick is thanked for help during sample preparation. W.-R. Chi is thanked for discussion on stratigraphy of Taiwan. S., O. and H. Giletycz are acknowledged for their assistance in the field and hosting. LM was supported by LIA ADEPT between National Science Council (Taiwan) and French CNRS, and University Pierre and Marie Curie. FM benefited from a PHC Orchid grant provided by the French Ministry of Foreign Affairs.

REFERENCES

Brandon, M. T., Roden-Tice M. K., and Garver J. I., 1998, Late Cenozoic exhumation of the Cascadia accretionary wedge in the Olympic Mountains, northwest Washington State: GSA Bulletin, v. 110(8), p. 985–1009.

Chang, S.S.L., and Chi, W.-R., 1983, Neogene nannoplankton biostratigraphy in Taiwan and the Tectonic implications: Petroleum Geology of Taiwan, v. 19, p. 93-147.

Chen, C.-H., Ho, H.-C., Shea, K.-S., Lo, W., Lin, W.-H., Chang, H.-C., Huang, C.-W., Chen , C.-H., Yang, C.-N., and Lee, Y.-H., 2000, Geological map of Taiwan.1:500,000 scale, Central Geological Survey, Taiwan.

Chi, W.-R.,1979, A biostratigraphic study of the Late Neogene sediments in the Kaoshiung area based on calcareous nannofossils: Proceedings of the Geological Society of China, v. 22, 121–144.

Chi, W.-C., and Reed, D. L., 2008, Evolution of shallow, crustal thermal structure from subduction to collision: An example from Taiwan: Geological Society of America Bulletin, v. 120, p. 679–690.

Davis, D., Suppe J., and Dahlen F. A., 1983, Mechanics of Fold-and-Thrust Belts and Accretionary Wedges: Journal of Geophysical Research, v. 88(B2), p. 1153–1172.

Dorsey, R.J., 1988, Provenance evolution and unroofing history of a modern arc-continent collision: evidence from petrography of Plio-Pleistocene sadnstones, eastern Taiwan: Journal of Sedimentary Petrology, v. 58, p. 208-218.

Fuller, C., Willett, S.D., Fischer, D., and Lu, C.-Y., 2006, A thermomechanical wedge model of Taiwan constrained by fission-track thermochronometry: Tectonophysics, v. 425, p. 1-24.

Garver, J. I., Reiners P. W., Walker L. J., Ramage J. M., and Perry S. E., 2005, Implications for Timing of Andean Uplift from Thermal Resetting of Radiation-Damaged Zircon in the Cordillera Huayhuash, Northern Peru: The Journal of Geology, v. 113, p. 117–138.

Huang, C.-Y., Yuan, P. B., and Tsao, S.-J., 2006, Temporal and spatial records of active arc-continent collision in Taiwan: A synthesis: Geological Society of America Bulletin, v. 118(3-4), p. 274–288.

Ketcham, R.A., 2005 Forward and inverse modeling of low-temperature thermochronometry data: Reviews in Mineralogy & Geochemistry, v. 58, p. 275–314.

Kirstein, L.A., Fellin, M.G., Willett, S., Carter, A., Chen, Y.-G., Garver, J.I., and Lee, D.C., 2010, Pliocene onset of rapid exhumation in Taiwan during arc-continent collision: new insights from detrital thermochronometry: Basin Research, v. 22, p. 1-16.

Lee, Y.-H., Chen, C.-C., Liu, T.-K., Ho, H.-C., Lu, H.-Y., and Lo, W., 2006, Mountain building mechanisms in the Southern Central Range of the Taiwan Orogenic Belt -- From accretionary

wedge deformation to arc-continental collision: Earth and Planetary Science Letters, v. 252, p. 413-422.
Lester, R., Lavier L. L., McIntosh K., Van Avendonk H. J. A., and Wu F., 2012, Active extension in Taiwan's precollision zone: A new model of plate bending in continental crust: Geology, v. 40(9), p. 831–834.
Lin, A.T., Watts, A.B., and Hesselbo, S.P., 2003, Cenozoic stratigraphy and subsidence history of the South China Sea margin in the Taiwan region: Basin Research, v. 15, p. 453-478.
Liu, T.-K., Hsieh, S., Chen, Y.-G., & Chen, W.-S., 2001, Thermo-kinematic evolution of the Taiwan oblique-collision mountain belt as revealed by zircon fission track dating: Earth and Planetary Science Letters, v. 186, p. 45–56.
McIntosh, K., van Avendonk, H., Lavier, L., Lester, W.R., Eakin, D., Wu, F., Liu, C.-S., and Lee, C.-S., 2013, Inversion of a hyper-extended rifted margin in the southern Central Range of Taiwan: Geology, v. 41, p. 871-874.
Reiners, P. W., and Brandon, M. T., 2006, Using thermochronology to understand orogenic erosion: Annual Review of Earth and Planetary Sciences, v. 34(1), p. 419–466.
Reston, T. J. 2009, The structure, evolution and symmetry of the magma-poor rifted margins of the North and Central Atlantic: A synthesis, Tectonophysics, 468(1-4), 6–27.
Suppe, J., 1984, Kinematics of arc-continent collision, flipping of subduction, and back-arc spreading near Taiwan: Memoir of the Geological Society of China, v. 4, p. 67-90.
Teng, L.-S., 1990, Geotectonic evolution of late Cenozoic arc-continent in Taiwan: Tectonophysics, v. 183, p. 67-76.
Tsao, S.-J., Li, T.-C., Tien, J.-L., Chen, C.-H. , Liu, T.-K, and Chen, C.-H., 1992, Illite cristallinity and fission-track ages along the East Central cross-ilsland highway of Taiwan: Acta Geologica Taiwanica, v. 30, p. 45–64.
Willett, S.D., and Brandon, M.T., 2013, Some analytical methods for converting thermochronometric age to erosion rate: Geochemistry, Geophysics, Geosystems, v. 14, p. 209-222.
Willett, S.D., Fischer, D., Fuller, C., Yeh, E.-C., and Lu, C.-Y., 2003, Erosion rates and orogenic-wedge kinematics in Taiwan inferred from fission-track thermochronometry: Geology, v. 31, p. 945-948.

Data repository
Mesalles et al.

Zircon fission-track method and data

Sampling processing and ZFT analysis were performed at the thermochronology laboratory of ISTerre (Université Joseph Fourier). We used standard ZFT preparation procedures (Bernet and Garver, 2005). In addition, for each sample two to three different Teflon mounts were prepared and etched for different lengths of time, ranging from 15h to 56h, ensuring proper etching for variable radiation damage zircon populations.

In contrast to other studies we use young-peak ages (YPA) in the vertical profiles when more than one population instead of central ages (Table DR1 and DR2). The reason behind this choice lies on the thermal stability of ZFT which is dependent on single grain radiation damage. Zircons in detrital suites are known to have a wide range of radiation damage due to the varied source thermal history and Uranium and Thorium content. This implies different closure temperature for the different radiation damaged populations, with low-retentive zircons (i.e. high radiation damage) annealing at low temperature of about 180-200°C and high retentive zircons (i.e. with low radiation damage) annealing at higher temperature of about 280-300°C (Garver et al., 2005). In our study we observed that most of the higher altitude samples present a young peak younger than the depositional age, and we interpret it as a reset low-retention zircon population having reached 180-200°C. In the other hand, most the lower samples present a single young population, thus they are fully reset and may have reached temperatures of about 280-300°C. The young peak populations are interpreted to record the last thermal event and, thus, the age-elevation trend observed in the profile reflects cooling rate. Hence, the ZFT partial annealing zone concept is not appropriate in our case. The low retentive zircon grains have been totally annealed and thus have not kept any record of its previous history as implied by the partial annealing zone concept.

Age populations deconvolution was extracted using Binomfit 1.2.62 (Brandon, 1992).

Apatite fission-track method and data

We used standard AFT preparation procedures (Donelick et al., 2005). Results were obtained from the conglomeratic samples of the Linkou and Liukuei formations and presented very low spontaneous and induced track counts with some grains presenting up to zero effective uranium content (Figure DR2 and Table DR4). Conversely to the ZFT ages presented in Fig.3, AFT samples from the Linkou and Liukuei were merged together as the number of counted grains did not allow to reliably extract detrital age population for the two conglomerates separately.

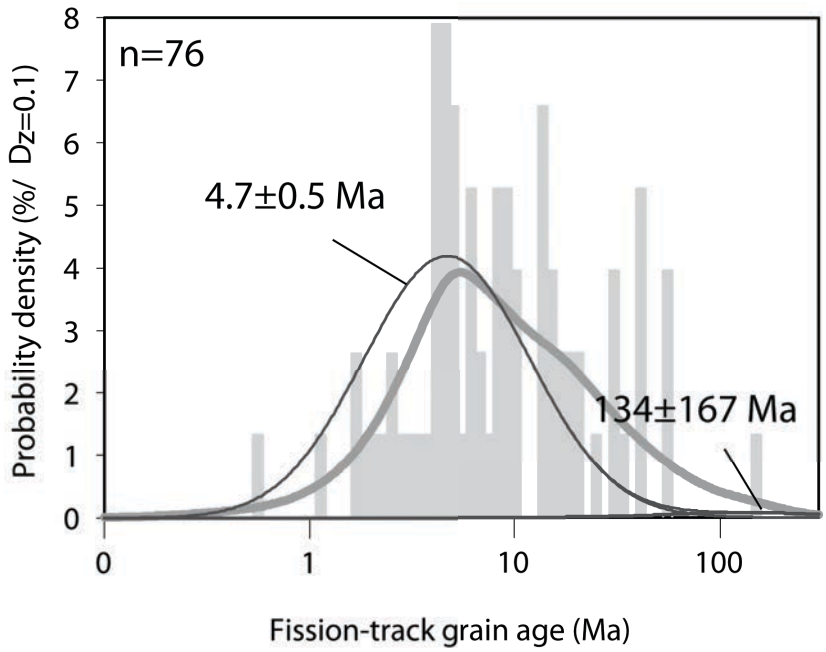

Figure DR1 : AFT grain-age probability-density plot and distribution histogram with binomial fitted peaks of the Linkou and Liukuei samples all together (see also Table DR4).
Age populations deconvolution was extracted using Binomfit 1.2.62 (Brandon, 1992).

Inverse modeling approach

To gain a better understanding of the effects of advection of heat due to erosion rate changes, and dependence of closure temperature to cooling rates we performed inverse modelling of our ZFT age-elevation profile data presented in Figure 2. To capture this aspect in our data we adopted the analytical solution proposed by Willett and Brandon (2013) that uses the time-dependant eroding half-space thermal model solution. In our case, this solution is particularly useful to extract exhumation rates in the lower part of the profile (from 465 to 1324 m) where the ages remain constant and no age-elevation relationship (AER) can be extracted directly from the age-elevation plot, or through classical thermal models (Gallagher, 2012; Braun et al., 2012).
The results are highly sensitive to the initial geothermal gradients and in a lesser degree to the time of initiation of exhumation of the studied phase. The model requires choosing a time of initiation of exhumation slightly older than the oldest modelled sample. We choose 7.2 Ma and 3.7 Ma as the time for initiation of cooling for the upper and lower parts of the profile respectively. Although there is no single crossing point of all the age-curves in the age-function plots, as expected for perfectly linear AER, the models show convergence in an area supporting exhumation rates of 1.22 to 2.17 km/m.y. (1.7 km/m.y. on average) with geothermal gradients of 60 to 70ºC/km for the lower section of the profile (Figure 2), and of 0.4 to 1.16 km/Myr (0.78 km/m.y. on average) with geothermal gradients of 36 to 46ºC/km, for the upper section of the profile (Figure 2). A surface temperature of 15°C and a mean elevation of 939 m at sample vicinity (mean elevation at a 20km radius of the sampled area) were adopted, using the annealing parameters of Brandon et al. (1998). The geothermal gradient values seem to be in agreement with present day geotherms for the younger phase, and with present-day offshore southern Taiwan geotherms for the older phase (Chi and Reed, 2008), as discussed in the main text.

Forward modeling

To independently represent the cooling history inferred from inverse modeling and test the fit with ZFT age variations from the age-elevation profile, we forward modeled time-Temperature history and calculated synthetic profiles of age versus elevation using HeFTy v.1.8.0 (Ketcham, 2005). In the new release of the HeFTy software, ZFT annealing models of (Rahn et al., 2004; Yamada et al., 2007) and Ketcham et al. (unpublished) are incorporated. During modeling we tested different annealing parameters and finally retained the fanning model (Yamada et al., 2007), for its best fit for our data, probably due to the high cooling rate involved, and therefore the high closure temperature necessary to reproduce our data.

To explore the time-temperature space, using the prescribed scenario of exhumation given by the inverse model, all samples positioned at different elevation, or paleo-depth in a column of rocks, were subjected to the same thermal history. We ran forward models offset by 10°C increment to simulate time-temperature history and obtain ZFT age at different depths. To obtain the final age-elevation plot of Figure 2 we converted time-temperature paths obtained for intervals at 30-7.2 Ma, 7.2-3.7 and 3.7-0 Ma to time-elevation using geothermal gradients of 36°C/km before 3.7 Ma and 70°C/km after, in agreement with inverse modeling. The initial gradient of 36°C/km is consistent with current values reported in the accretionary prism offshore southern Taiwan (Chi and Reed, 2008). After 3.7 Ma, the geothermal gradient of 70°C/km reflects efficient advection of heat enhanced by coupling between tectonics and surface processes and it also consistent with current values determined in central Taiwan (Chi and Reed, 2008).

Our preferred forward model, as shown in Fig. 2, was established for three successive cooling periods at 30-7.2 Ma, 7.2-3.7 Ma and 3.7-0 Ma. Slow cooling from Oligocene to Late Miocene is intended to reproduce post-break-up thermal evolution recognized offshore Taiwan in the SCS margin, which is associated with thermal subsidence (Lin et al., 2003).

Name	Lon(°E)	Lat(°N)	Alt (m)	ρ_s (10^5 tracks . cm^{-2})	Ns (tracks)	ρ_i (10^6 tracks . cm^{-2})	Ni (track)	U±2s (ppm)	N	Gain-age Range (Ma)	Pooled age ±1σ (Ma)
Ph0	120.8238544	22.5761057	465	6.83	151	3.72	823	181±39	24	1.7-8.7	**3.4 ±0.5**
PV1-2B	120.8373659	22.5977135	467	3.98	83	2.39	497	129±12	24	1.4-7.2	**3.1±0.6**
PV3-7	120.8048601	22.6049834	596	5.92	169	3.34	955	181±12	24	1.4-7.1	**3.3±0.5**
PV1-3	120.8271145	22.6053973	680	4.13	123	2.7	804	147±11	38	1.4-18.7	**2.9±0.5**
PV1-5	120.8258882	22.6137317	1122	4.86	81	2.51	419	136±14	24	1.4-8.7	**3.6±0.7**
PV1-6	120.8260995	22.6158633	1324	3.79	54	2.51	358	136±15	23	1.4-8	**2.8±0.6**
PV3-1	120.7843633	22.637686	1728	5.92	107	2.06	372	112±12	24	2.5-26.5	**5.4±0.9**

Table DR1: Concordant ZFT ages (east of main drainage divide) interpreted as fully reset zircon grains. N: Total number of counted grains

								ZFT age components ±1σ		
Name	Position	Lon(°E)	Lat(°N)	Elevation (m)	N	Gain-age Range (Ma)	F test (%)	P1 (Ma)	P2 (Ma)	P2 (Ma)
PV3-6B	Eastern Divide	120.8051961	22.6219263	709	24	2.2-15.1	0	**3.3±0.6 (75%)**	**8.6±2.6 (25%)**	

PV4-3	Western divide	120.747465	22.6141513	2468	25	5.6-59.5	0	**13.2±2.3 (77%)**	**47.7±12 (23%)**	
PV4-1	Western divide	120.7541618	22.617142	2867	24	3.7-96.9	0	**5.3±2.2 (19%)**	**14±2.7 (28%)**	**32.2±6.2 (53%)**
PV4-0	Crest	120.7562781	22.6196287	3004	24	2.8-97.0	0	**6.6±4.7 (19%)**	**27.2±4 (81%)**	
PV3	Crest-Peak	120.7613627	22.6270509	3095	24	3.2-64.2	0	**7.1±1.3 (61%)**	**29.1±5.7 (39%)**	

Table DR2: Discordant ZFT ages in which P1 is interpreted as a reset low-retention zircon population. N: Total number of counted grains; binomial peak fitting are given ± 1σ. Also given is the percentage of grains in a specific peak. All samples were counted by Lucas Mesalles using a zeta of 135.42 ± 15.20. The probability based on F-test evaluates how significant is the number of peaks. A probability of 0% indicates that the introduction of additional peak would result in the decrease of the best-fitting solution.

									ZFT age components ±1σ			
Sample	Formation	Depositional age	Lon(°E)	Lat(°N)	Alt (m)	N	age range (Ma)	F test (%)	P1 (Ma)	P2 (Ma)	P3 (Ma)	P4 (Ma)
NA02	Nanshihlun sandstones	NN15 (~3.8-4Ma)	120.3957062	22.7341431	124	84	21.1-781.3	0	**22.9±6.5 (3%)**	**59±8.3 (42%)**	**136.8±21.6 (47%)**	**395.7±213 (8%)**
LK03	Linkou Fm (base Lower member)	NN19 (~1.8-2 Ma)	120.4042457	22.7383202	119	190	1.2-186.8	0	**4.7±0.7 (32.2%)**	**66±8.2 (67.8%)**		
LK04	Linkou Fm (top Upper member)	n.a.	120.4204844	22.6992047	53							
LG15	Liukuei Fm	n.a.	120.6424799	22.9383224	203	332	0.8-599.8	0	**6.3±0.8 (28.4%)**	**47.5±6.2 (40.6%)**	**102.9±14.9 (31%)**	
LG17			120.6365015	22.9315449	250							
LG18			120.6192217	22.911682	155							
LG20			120.6357397	22.9393456	227							

Table DR3: Detrital zircon fission-track data in Nanhsihlun Sandstones (NA) and Linkou (LK) and Liukuei (LG) conglomerates. N: Total number of counted grains; binomial peak fitting are given ± 1σ. Also given is the percentage of grains in a specific peak. All samples were counted by Lucas Mesalles using a zeta of 135.42 ± 15.20. In the text we refer only to populations that are close or above 30%.

				AFT age components ±1σ	
Sample	N	Gain-age range (Ma)	Prob F test (%)	P1 (Ma)	P2 (Ma)
LK03	76	0.6-144	0	**4.7±0.5 (98%)**	**134.6±167 (2%)**
LK04					
LG15					
LG17					
LG18					
LG20					

Table DR4: Detrital apatite fission-track data from the Linkou (LK) and Liukuei (LG) conglomerates. N: Total number of counted grains; binomial peak fitting are given ± 1σ. Also given is the percentage of grains in a specific peak. All samples were counted by Lucas Mesalles using a zeta of 268.37 ± 7.61. In the text we refer only to populations that are close or above 30%.

References

Bernet, M., and Garver, J.I., 2005, Fission-track analysis of detrital zircon, Low-temperature thermochronology: techniques, interpretations, and applications Volume 58: Reviews in mineralogy & geochemistry, Mineralogical Society of America, p. 205-237.

Brandon, M.T., 1992, Decomposition of fission-track grain-age distributions: American Journal of Science, v. 292, p. 535-564.

Brandon, M.T., Roden-Tice, M.K., and Garver, J.I., 1998, Late Cenozoic exhumation of the Cascadia accretionary wedge in the Olympic Mountains, northwest Washington State: Geological Society of America Bulletin, v. 110, p. 985-1009.

Braun, J., van der Beek, P. Valla, P., Robert, X., Herman, F., Glotzbach, C., Pedersen, V., Perry, C., Simon-Labric, T. and Prigent, C., 2012, Quantifying rates of landscape evolution and tectonic processes by thermochronology and numerical modeling of crustal heat transport using PECUBE, Tectonophysics, v. 524-525, p. 1–28, doi:10.1016/j.tecto.2011.12.035.

Chi, W.-C., and Reed, D. L., 2008. Evolution of shallow, crustal thermal structure from subduction to collision: An example from Taiwan. Geological Society of America Bulletin, v.120(5-6), p. 679–690.

Donelick, R. A., O'Sullivan, P. B., and Ketcham, R. A., 2005. Apatite Fission-Track Analysis. Reviews in Mineralogy and Geochemistry, v. 58(1), p. 49–94.

Gallagher, K., 2012, Transdimensional inverse thermal history modeling for quantitative thermochronology, Journal of Geophysical Research, v. 117(B2), p. 1–16, doi:10.1029/2011JB008825.

Garver, J., Reiners, P., Walker, L.J., Ramage, J., and Perry, S., 2005, Implications for timing of Andean uplift from thermal resetting of radiation damaged zircon in the Cordillera Huayhuash, Northern Peru: The Journal of Geology, v. 113, p. 117-138.

Ketcham, R.A., 2005 Forward and inverse modeling of low-temperature thermochronometry data: Reviews in Mineralogy & Geochemistry, v. 58, p. 275–314.

Kirstein, L. A., M. G. Fellin, S. D. Willett, A. Carter, Y.-G. Chen, J. I. Garver, and D. C. Lee , 2009, Pliocene onset of rapid exhumation in Taiwan during arc-continent collision: new insights from detrital thermochronometry, Basin Research, v. 22(3), p. 270–285.

Kirstein, L. A., A. Carter, and Y.-G. Chen, 2010, Testing inferences from palaeocurrents: application of zircon double-dating to Miocene sediments from the Hengchun Peninsula, Taiwan, Terra Nova, 22(6), p. v. 483–493.

Lin, A.T., Watts, A.B., and Hesselbo, S.P., 2003, Cenozoic stratigraphy and subsidence history of the South China Sea margin in the Taiwan region: Basin Research, v. 15, p. 453-478.

Rahn, M.K., Brandon, M.T., Batt, G.E., and Garver, J.I., 2004, A zero-damage model for fission-track annealing in zircon: American Mineralogist, v. 89, p. 473-484.

Willett, S.D., and Brandon, M.T., 2013, Some analytical methods for converting thermochronometric age to erosion rate: Geochemistry, Geophysics, Geosystems, v. 14, p. 209-222, 10.1029/2012gc004279.

Yamada, R., Murakami, M., and Tagami, T., 2007, Statistical modelling of annealing kinetics of fission tracks in zircon; Reassessment of laboratory experiments: Chemical Geology, v. 236, p. 75-91.

Yamato, P., Mouthereau, F., and Burov, E., 2009, Taiwan mountain building: insights from 2D thermo-mechanical modelling of a rheologically-stratified lithosphere: Geophysical Journal International, v. 176, p. 307-326.

2) Relationship between mélange formations and the two-phased collisional events.

As mentioned in *Mesalles et al.* (2014, minor corrections) the net exhumation rate increase at 3.2±0.6Ma is very likely correlated to the closure of the forearc and formation of the Lichi mélange in eastern Taiwan. I interpret this tectonic events as resulting from the arrival of normal thickness continental crust in western Taiwan materialized by the Peikang high continental promontory leading to collisional tightening, major crustal thickening and forearc closure, in agreement with some recent interpretations [e.g. *Byrne et al.*, 2011].

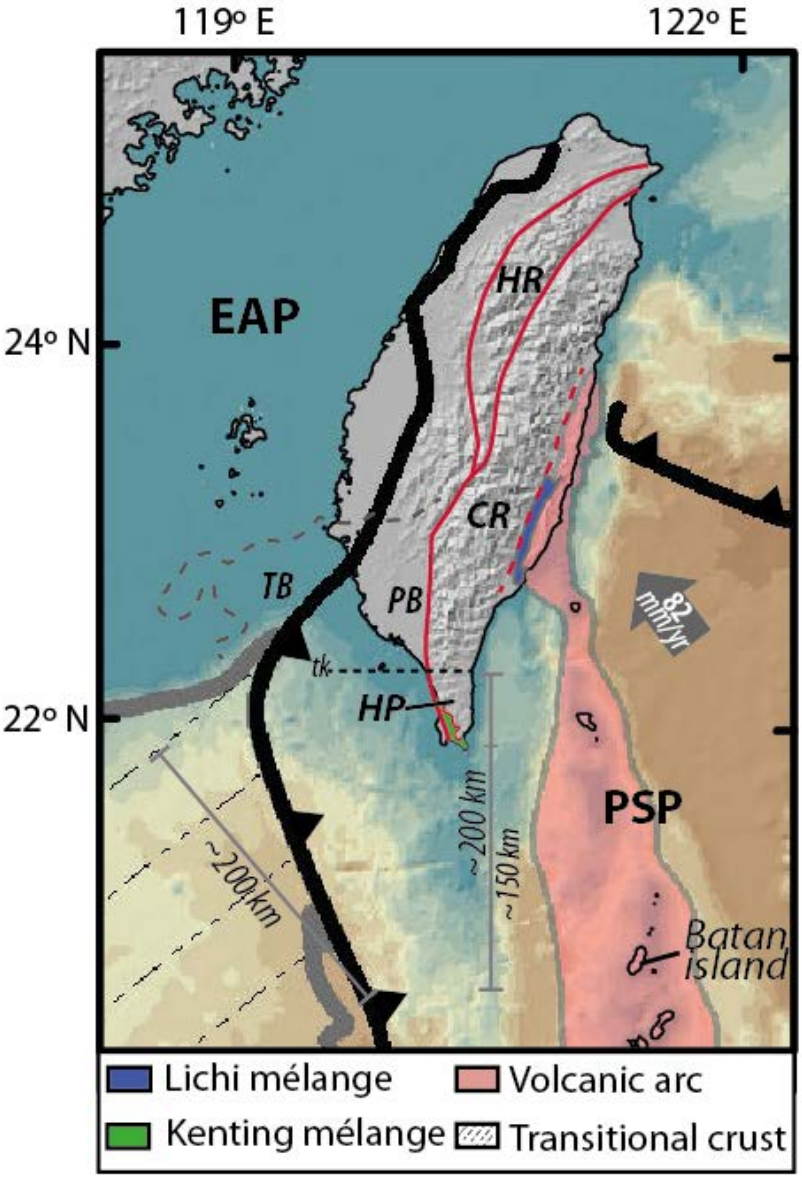

***Fig. 3.34**: Bathymetric map and position of the ophiolitic mélanges in Taiwan. The western boundary of the transitional continental crust is approximate and is here based on bathymetry. EAP – Eurasian plate; PSP – Philippine sea plate; HR- Hsuehshan range; CR- Central Range; HP- Hengchun peninsula; PB – Pingtung basin; TB- position of the precollisional Tainan basin from*[*Lin and Watts*, 2002]*; tk- topographic kink. Dashed horizontal line to the north of HP indicates the approximate position of the orocline bending*

A longstanding enigmatic feature of the Taiwan orogen is the second mélange in Taiwan, the Kenting mélange. The existence of a second mélange led some authors to argue for a two-stage collision [*Pelletier and Stephan*, 1986a, 1986b].

Two main characteristic features distinguish this mélange:

- Its structural position in the Central Range western front between a vertical fault (Kenting fault) and a shallowly east dipping fault (Hengchun fault) (Fig. 3.34) [*Chang et al.*, 2003].
- A formation age constrained by nannofossil biostratigraphy to the Late Miocene to Middle Pliocene, probably between Late Miocene to Early Pliocene when considering the dominant age in the matrix and blocks [*Chang et al.*, 2009a].
- Include ultrabasic rocks but no volcanic blocks (as opposed to the Lichi mélange) [*Chang et al.*, 2009a].
- Often considered an olistrostomal formation rather than a strictly speaking tectonic mélange with exotic elements of SCS affinity [*Biq*, 1977; *Pelletier and Stephan*, 1986a, 1986b; *Chang et al.*, 2009a].

Here, I interpret the Kenting mélange as resulting of the first phase of collision recorded in the ZFT vertical profile. The main arguments supporting this interpretation are:
1) Coincidence in the timing of cooling related to underthrusting at 7.1±1.3Ma, and mélange emplacement in the Late Miocene.
2) Emplacement along west verging structures is in agreement with the kinematics inferred to be associated to the initial phase of underwater orogenic development, as discussed in the next section.

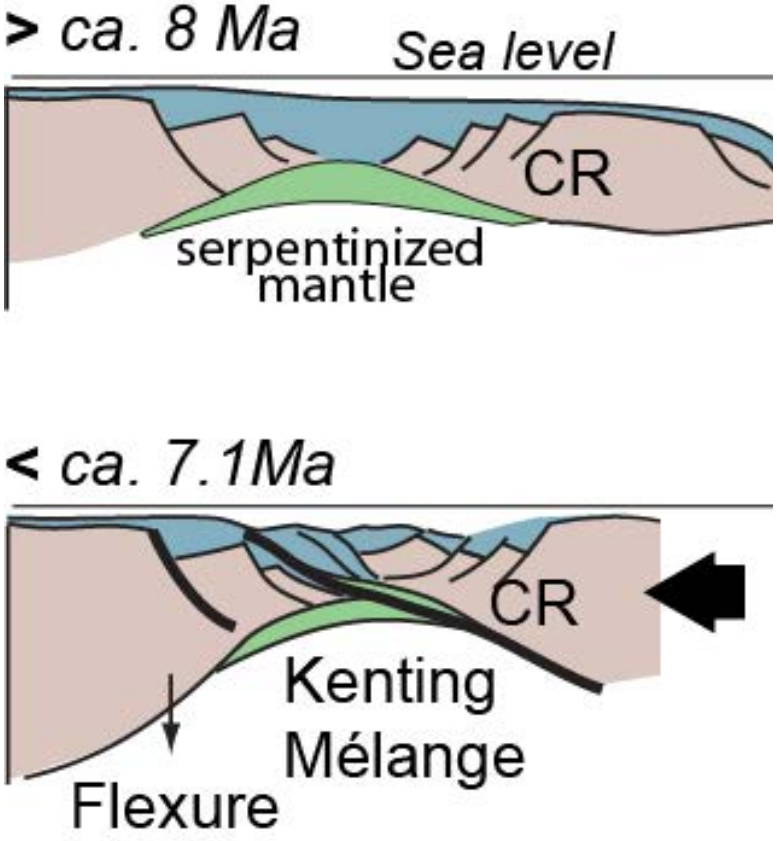

***Fig. 3.35**: Sketch diagram showing how the Kenting may have resulted from closure and shortening of an hyperextended passive margin domain with exhumed mantle bounded to the east by the Central Range continental bloc. Black arrow in the lower panel indicates the far-field stress coming from the adjacent subduction zone where the first involvement of continental crust marks the end of subduction and start of the deformation of the lower-plate.*

The initial involvement of continental crust in the subduction wedge lead to far-field reactivation and inversion of a hyperextended domain in the inner passive

margin (Fig. 3.35). Such hyperextended domains are relatively well described in the outer margin offshore southern Taiwan [Fig.1.2 and Fig. 1.9; *Lester et al.*, 2013; *Eakin et al.*, 2014] and the presence exhumed mantle has been described elsewhere in the southern SCS margin (Phu Khanh Basin) and in the conjugate margin (Dangerous Grounds) in the soutern SCS [Fig. 1.9*; e.g. Cullen et al.*, 2010]. Moreover, in the island of Palawan and in main islands of the Luzon archipelago multiple ophiolitic belts have been described, although most are Mesozoic, Cenozoic ophiolites are also present [*Rangin*, 1991] , and some have been interpreted as been emplaced along continental margins [*Yumul*, 2007].
The structural position of the Kenting mélange in the western Central Range along the southern extension of one of the main crustal scale faults of Taiwan (Kenting-Chaochou faults) implies that the Central Range was bounded to the west by an hyperextended domain (passive margin necking zone), later obducted during the first stage of collision. This may explain the Airy and Bouger negative gravity anomalies of these areas, including the Pingtung basin, of these area [e.g. *Lin and Watts*, 2002; *Hwang et al.*, 2007] and is in agreement with the position of syn-rift pre-collisional lows comprising this domain [Fig. 3.34; *Lin and Watts*, 2002; *Lin et al.*, 2003]. Such interpretation implies that the Central Range was a thicker isolated block drifted away to the outer margin, as supported by sedimentological observations in the Taimali area where the Miocene coarse sediments (LsU-1 and LsU-2 in StU-3) suggest a more proximal source as opposed to the general view of this sediments as distal lower-slope fine deposits.
My interpretation contrast with the traditional view of the Kenting mélange as materializing a paleo-manila trench now inactive, containing SCS affinity blocks [*Chang et al.,* 2009]. A critical clue that needs to be further explored is the nature of the ultrabasic rocks so that their continental mantle *vs.* oceanic mantle nature can be revealed.

C. Constraints on the timing of tectonic events of the Central Range

The initial phase of underthrusting-related cooling comprised underwater conditions (~7Ma to 5Ma) and the beginning of subaerial exposure of the orogenic wedge (~5Ma to 3.2Ma). The later phase of exhumation-related cooling at ~3.2Ma was exclusively subaerial, likely related to a major phase of crustal growth and topographic development.

Here I discuss some general concepts about deformation in Taiwan and the draw correlation between the deformation phases observed in the Taimali area (Chapter 2) and the cooling histories extracted form the ZFT vertical profile and the AFT and ZFT data from foreland sediments.

1) General considerations

An analogy with present-day configuration in southern Taiwan allows the following considerations:

- The early stage of collision is currently occuring from ~150km south of the southern tip of Taiwan until the northern edge of the Hengchun peninsula where a kink the topographic grain of the range shifts from a N-S trend in the

Hengchun peninsula to a N-NE trend in the rest of the Central Range (oroclinal bend of *Byrne et al.,* 2011). Such configuration implies the consumption of ~200km of transitional continental crust during the initial underthrusting-related cooling (Fig. 3.34).

- The second stage of collision comprises the whole Central Range from the northern edge of the Henghun peninsula to probably the northern Central Range or at least comprises the whole southern and central part of the Central Range.

This interpretation contrast with the generally assumed and widely used southward propagation of collision and '*deformation-age per space equivalence*' along the orogen (Fig. 1.12), a view getting increasing acceptance among the scientist working on Taiwan [e.g. *Lee et al.*, 2006; *Byrne et al.*, 2011; *Nagel et al.*, 2012b]. The southward propagating orogen is used to explain a wide range of features in Taiwan from topographic development and steady state [e.g. *Davis et al.*, 1983; *Willett and Brandon*, 2002; *Willett et al.*, 2003; *Stolar et al.*, 2007] to seismological and geophysical characteritics [e.g. *Kao et al.*, 1998; *Hsu et al.*, 2008]. For istance, *Huang et al.* (2006) compiled a large amount of data mainly in the Coastal Range all indicating the younging of deformation towards the south, and concluded that the arc-continent collision has been steadily propagating since waning of volcanism in the northern Coastal range at ~6-5Ma in the north and ~3.3Ma in the south.

More importantly, the main arguments favouring a punctuated mountain building contemporaneous along the orogen are:

(1) *In the foreland basin*

- North to south contemporaneous foreland development [*Lin et al.*, 2003].
- Minor north-south sedimentary facies migration in foreland [*Nagel et al.*, 2012b]

(2) In the fold and thrust belt:

- No unequivocal evidence that northern faults are less active than southern ones.
- No unequivocal evidence that initiation of frontal propagation in the north started earlier than in the southern Western Foohtills.
- Overall structural geometry of the Western Foothills appears to be more related to the Peikang High than to a southward propagating deformation front.

(3) In the Central Range

- Similar peak metarmophic condition and timing [*Lo and Onstott*, 1995; *Tsao*, 1996; *Beyssac et al.*, 2007].
- Orogenic thermochronometric ages as old in the North as in the South implying similar time of initiation of crustal thickening, *but* with higher magnitudes of total exhumation in the north maybe due to the complexe setting due to the Ryukyu trench extension on land (Yilan plain) or to early forearc closure (arc-accretion).

2) Southern Taiwan deformation

The ZFT-age elevation profile of this study was sampled on the eastern flank of a regional scale west verging anticline with its axis running along the topographic crest of the area (Fig. 3.12). The samples section although mostly sampled along two structure-parallel profiles (Taimali last tributary and Turitury tributary; Fig. 3.21; Table 3.2), ran along progressively older sedimentary series (Middle Miocene to Eocene) and structurally deeper units (Fig. 3.21). Because no evidence of major structural discontinuity or reactivated stratigraphic boundary were observed in the field or mapped in existing geological maps, this configuration implies that the initial phase of cooling from ~7.1 Ma to ~3.2 Ma post-dated west-verging, east-dipping schistosity-forming deformation. Thus, one may argue that west verging deformation corresponds to the initial deformation in the lower slope area of the underwater orogenic wedge (Fig.2.2 and Fig. 3.36).

The east-verging deformation domain in the Taimali area and basement rocks found to the north may have only undergone the (easternmost) upper-slope, east verging deformation, implying that underthrusting affected the basement but also part of the sedimentary cover. This last statement is based on the absence of an obvious S2 deformation in the east-verging structural units (Stu-2 and StU-3; Fig. 2.12), which would prove that the sediments were incorporated from the deformation front and then crenulated in the upper slope. In any case the basement rocks, although presenting multiple phases of deformation appear to have undergone mainly east-vergent deformation (Fig. 2.7).

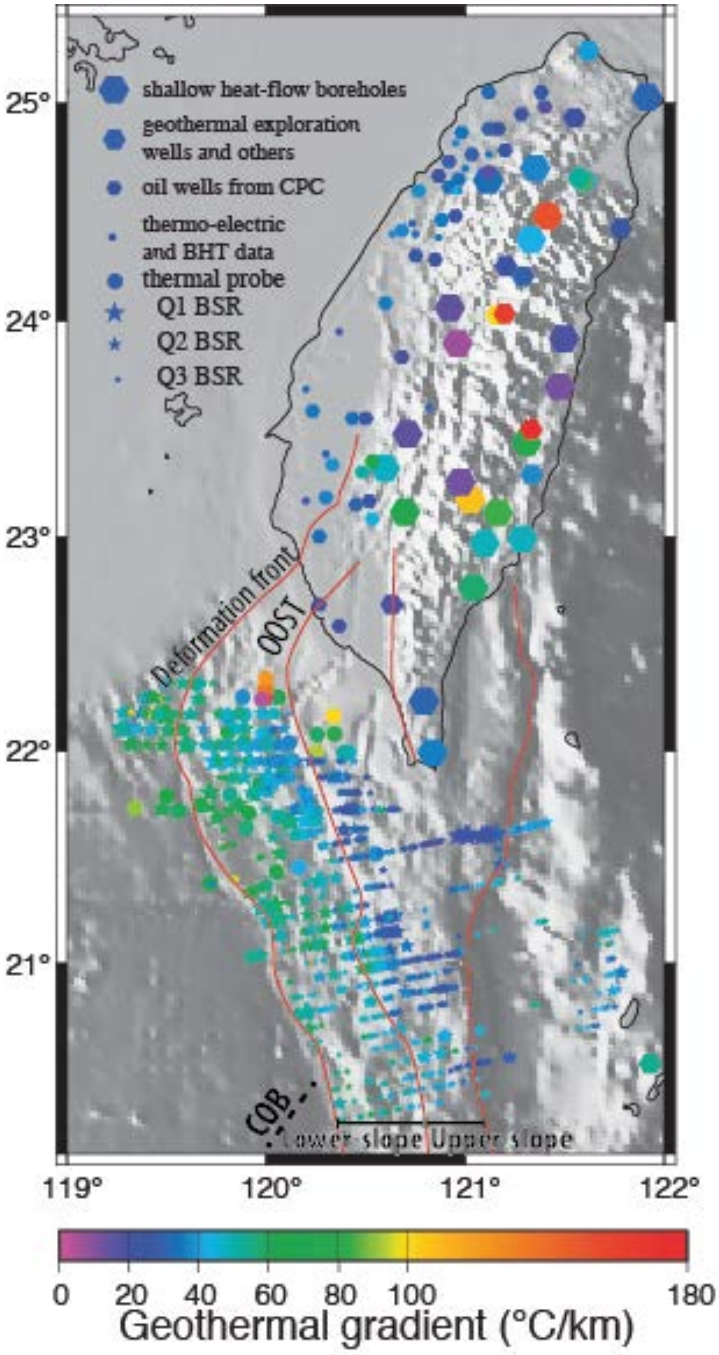

Fig.3.36: *Geothermal gradients onshore and offshore southern Taiwan [modified from Chi and Reed, 2008] with main tectonic features of offshore and in southern Taiwan [red-lines; from Lin et al., 2009]. COB = Continent-Ocean boundary (approximate); OOST = out-of-sequence thrust.*

A plausible scenario could be:
1) As the passive margin sediments entered the toe of the accretionary wedge west-vergent deformation and slight heating occurred arguably reseting the low-retention zircons.
2) When underplating start occurring in the upper-slope domain, cooling and closure of the ZFT-YPA zircon population of the samples in the upper part of the vertical profile followed, probably without further deformation of the sediments (e.g. passive rock uplift as underplated material is added form below).
3) Cooling due to underplating kept occurring until the arrival of a thicker section of the passive margin and subsequent collision of the Luzon volcanic arc, both leading to a major topographic growth, collisional tightening and high exhumation rates at ~3.2Ma.

The 3.2±0.6Ma phase is probably the most unequivocal and clear event in age-elevation profile presented in this work (Fig. 3.23). This age is well described in the literature as a major tectonic phase in Taiwan. It is contemporaneous to increased foreland subsidence, deepening of sedimentary facies (Hsinshui shale deposition) and increased sedimentation in the foreland and forearc/intra-arc (Fig.1.17) [*Chang and Chi*, 1983; *Lin et al.*, 2003]. It is also the start of forward thrust propagation in the northern and central Western Foothills fold-and-thrust belt and probably in the southern Western Foothills [*Lock,* 2007]. It also corresponds to the end of volcanism in the southern Coastal Range [*Huang et al.,* 2006]. The most consistent thermochronological record of the the ~3Ma phase is found in the detrital record in the eastern forearc-intraarc basins where dominant ZFT-age population of ~3Ma were obtained in the post-2Ma sediments with pre-2Ma sediments not yielding any significant reset age [Fig. 3.9; *Kirstein et al.*, 2010a]. This is in agreement with the relatively stationary (~3.5±0.9Ma; Fig. 3.29) found in the Taimali valley ages. The eastern basin detrital record contrast with the record of the western forland where limited ~3Ma ZFT age population were found in this study (Table 3.9), in agreement with limited exposure of ~3Ma ZFT ages in the present-day Laonung basin (Fig. 3.17 and Fig. 3.32). Taken together, all these evidences suggest that the ~3.2Ma phase mainly affected the retro-wedge and was responsible for the exposure of both, the ZFT record of initial collision and the initial rapid unroofing of the retro-wedge at rates of 1.7km/Myr.

Finally, ZFT-ages obtained along the Laonung river appear to record the initial phase as seen in the attempt of vertical profile yielding similar exhumation rates as our initital phase in the Taiwnali area; and a recent activity of the Chaochou-Laonung fault since ~2Ma as recroded by the AFT ages (Fig. 3.33 and Fig. 3.32). Similarly, the Meishan fault appears to mark an age- break in out attempt of AFT vertical profile (Fig. 3.33) and further north along the southern cross-island highway where it marks the shift from reset to unreset ZFT ages (Fig. 3.5). Both observation appear to challenge that the view in which the Western Foothills are steadily forward propagating in sequential manner, favouring an interpretation where thrusting occurs in an out-of-sequence fashion, in agreement with other studies [*Byrne and Tillman*, 1996; *Mouthereau et al*., 2001; *Ching et al*., 2007].

VI. Conclusions

The main conclusions of this chapter can be summarized as follow:

- Initiation of collision at 7.1±1.3Ma after sedimentary cover accretion and deformation, and coeval to initial underthrusting of the hyper-extended South China Sea outer margin. This timing of initial collisional related cooling is in agreement with Ar-Ar dating of neo-formed metamorphic minerals to ~7.8±0.2Ma for biotite and between 6 and 9Ma for phengite in the northern Taiwan granitic bodies [*Lo and Onstott*, 1995]. This implies contemporaneous initiation of underwater collisional processes along the island, and not the commonly assumed southern steady propagation of

collision [e.g. Suppe, 1981]. Present day convergence obliquity and southward propagation might be a more recent geodynamical feature.

- Collisional tightening and eastward extrusion of the metamorphic core at 3.2±0.6Ma as thicker passive margin section start being deformed. This phase probably corresponds to the major phase topographic growth of the Central Range.
- Probable out-of-sequence thrusting in the western front as shown by the recent activity of the inner Laonung fault and Meishan fault.

Chapter 4: Morphological elements of southern Taiwan

Erosion can be considered as the major agent leading to rock exhumation, particularly in the sub-tropical island of Taiwan where crustal thickening is counteracted by a very efficient erosive system with one of the highest erosion rates on earth [*Li*, 1975; *Dadson et al.*, 2003]. Change in erosion efficiency, whatever its nature (i.e. fluvial, hillslope, glacial), should thus be recorded in the exhumational histories. Erosion rates in active orogens are dependent on topography, lithology and on climatically controlled factors, such as weathering, climate variability and glaciation [*Milliman and Syvitski*, 1992; *Montgomery and Brandon*, 2002; *Dadson et al.*, 2003]. Indeed, erosion is the dynamic link between tectonically created topography and the local and regional climatic conditions. For instance, it has been argued that long term exhumation rates in the tectonically active Washington Cascades mountains is dependent on presently observable orographicaly controlled precipitation [*Reiners et al.*, 2003], somehow confirming theoretical links between erosion and deformation in active orogens. Controversy exists around this spatial link as it assumes present-day precipitation patterns extend back into geological time, which is largely unconstrained. Nevertheless, in a young active orogen like Taiwan, it may be sensible to consider presently running geomorphic processes to be operating in the close geological past.

In the previous chapter, I have documented a one order of magnitude increase in exhumation rates at ca. 3.2 Ma. The timing is strikingly coincident with the start of northern hemisphere glaciation at ca. 3.2 Ma [*Zachos et al.*, 2001], with monsoon intensification since ca. 3.6 Ma [*An et al.*, 2001; *Ge et al.*, 2013], and greater monsoonal seasonality since ca. 3 Ma [*Clift and Plumb*, 2008]. Although tempting, a causal relation between this major climatic change and increased exhumation has, at the time being, been discarded. Well documented tectonic events seem a more reasonable cause for the increased exhumation, the main ones are: *1)* increased foreland basin subsidence from ca. 3.5 Ma [*Chou et al.*, 1994; *Lin et al.*, 2003; *Nagel et al.*, 2012]; and, *2)* waning of volcanism in the southern Coastal Range at 3.3 Ma and beginning of forearc deformation and formation of the Lichi mélange at 3.7-3.5 Ma (calcareous nannofossil biozone NN15; *Chang and Chi*, 1983; *Huang et al.*, 2006]. Moreover, considering the continental platform geometry and the present-day convergent rates, it seems sensible to associate this phase with the first contact of the weakly thinned Eurasian margin continental crust.

If the ultimate cause behind this major exhumational phase can be tectonic in origin, crustal thickening is necessarily associated with erosion to unroof and expose formerly buried rocks. Isostatic compensation of a thickening crust builds topography, either underwater or subaerial. In the Taiwan case, we have seen that the initial contact with a transitional, extremely thin continental crust and its ensuing underplating [*Lester et al.*, 2013] probably occurred at ca. 7.1 Ma and

gave birth to a major bathymetric high (Fig. 2.1). As previously discussed, cooling of the accretionary wedge from below produced an "apparent exhumation" but real effective exhumation did not occur until subaerial exposure at ca. 5Ma as witnessed by the first lithic fragments in the forearc basin [e.g. *Teng*, 1990]. Consequently, the inferred tectonic phase at ca. 3.2 Ma likely indicates major topographic growth of the subaerial orogen, leading to increased erosion and exhumation. The added effect of the global and regional climatic shift towards the glacial-interglacial periods and monsoonal climatic conditions has certainly favored erosional efficiency, eventually leading to high altitude glacial development when topography reached snowline altitudes. Glaciation of high peaks in Taiwan is likely to have been a widespread phenomenon since snow-line altitude for the last glacial maximum is estimated be at about ~3000m [e.g. *Böse and Hebenstreit*, 2008] and literally hundred of peaks exceeding this altitude are present all along the central part of the Central Range (Fig. 3.5).

An additional younger tectonic phase has been suggested to have occurred at 1-2 Ma based on syntectonic sedimentation and fault development in the Western foothills and on thermo-mechanical modeling of the orogen [e.g. *Chang and Chi*, 1983; *Chi*, 1979; *Simoes et al.*, 2007a, 2007b]. The deposition of the early Pleistocene conglomeratic deposits of the Toukoshan Fm. (Fig. 1.16) have traditionally been interpreted to mark the paroxysm of a major orogenic phase [e.g. *Ho*, 1986] in agreement with orogenic ZFT ages of 1-2Ma in the metamorphic core in the eastern Taiwan Central Range (Fig. 3.5, Fig. 3.6 and Fig. 3.7). The thermochronological data presented in the *Chapter 3* support such interpretation. If initiation of fast exhumation at ~3.2Ma was synchronous along the Central Range at rates of 1.7km/Myr, after 1.6Ma only the ~2.72 km of exhumation occurred; an observation inconsistent with the appearance of the first metamorphic clasts in the 1.6Ma sediments [*Dorsey,* 1988]. Indeed, the deformed sedimentary cover of the metamorphic core was certainly thicker than this value, thus a more recent acceleration of exhumation rates is needed.

However, the traditional interpretation of Plio-Pleistocene coarse, molassic, sedimentation in ranges' foreland basins as indicative of recent rock uplift has alternatively been interpreted as a global climatic signal [*Molnar and England*, 1990; *Zhang et al.*, 2001; *Cederbom et al.*, 2004; *Molnar*, 2004; *Willett*, 2010]. Indeed, a worldwide orogenic phase is difficult to conceive while an erosional response to global climatic change seems more sensible. In this context, the coarse sedimentation observed in western Taiwan could actually be the response to the passage to a more erosive climate: stronger monsoonal seasonality or glacial-interglacial periods, for instance. The widespread extent of this coarse unit and apparently contemporaneous deposition along the Western Foothills and Coastal plane island favour its climatic origin, rather than tectonic. Additionally, the deposition seems to predate deformation in the central Western Foothills [Pakuashan fault-related-fold; *Mouthereau et al.*, 1999; *Simoes et al.*, 2007b], and thus precedes deformation and topographic development in this area.

In the following I will explore the possibility of a climatic origin of the upper Toukoshan Fm. and the potential effect of such climatic shift can have on

deformation. First I review present-day erosion rates and how they shape the landscape. Then, I will present the preliminary results of the mapping of low-relief surfaces in southern Taiwan and discuss their significance and origin. And finally present the preliminary results of the application of morphometric analysis to extract the dominant process shaping the landscape.

I. Erosion in the Taiwan orogeny: questioning steady-state in Taiwan

A. Climate and sediment discharge in Taiwan

Taiwan is a subtropical island reaching tropical climate in its southern part with average precipitation of 2.5 m/yr. As such, the island is subject to three main seasonal climatic events: Summer monsoon, winter monsoon and typhoons. The monsoon is characterized by large rainfalls and a seasonal cycle, and is part of a planetary scale circulation of the tropical atmosphere, the Inter-tropical convergence zone. In Taiwan, summer monsoon hits the island from the SW, as it comes from the South China Sea. Winter monsoon, comes form the N-NE from the East China Sea. Typhoons are a common feature of Taiwan, with an average of almost 4 typhoons per year, bringing up to 80% of the total precipitation between June and October [*Central Weather Bureau website, accessed* Dec. 2013]. Typhoons are characterised by strong winds and short heavy rains. Typhoons can reach the base of the stratosphere (~8km) and thus are less affected by topographic barriers, but often loose they strength as they enter the continent. About 75 % of Typhoons hit Taiwan from its eastern side, leading to a slightly assymetrical precipitation distribution with a wetter eastern divide in the north and a more distributed average precipitation in the southern part (Fig. 4.1).

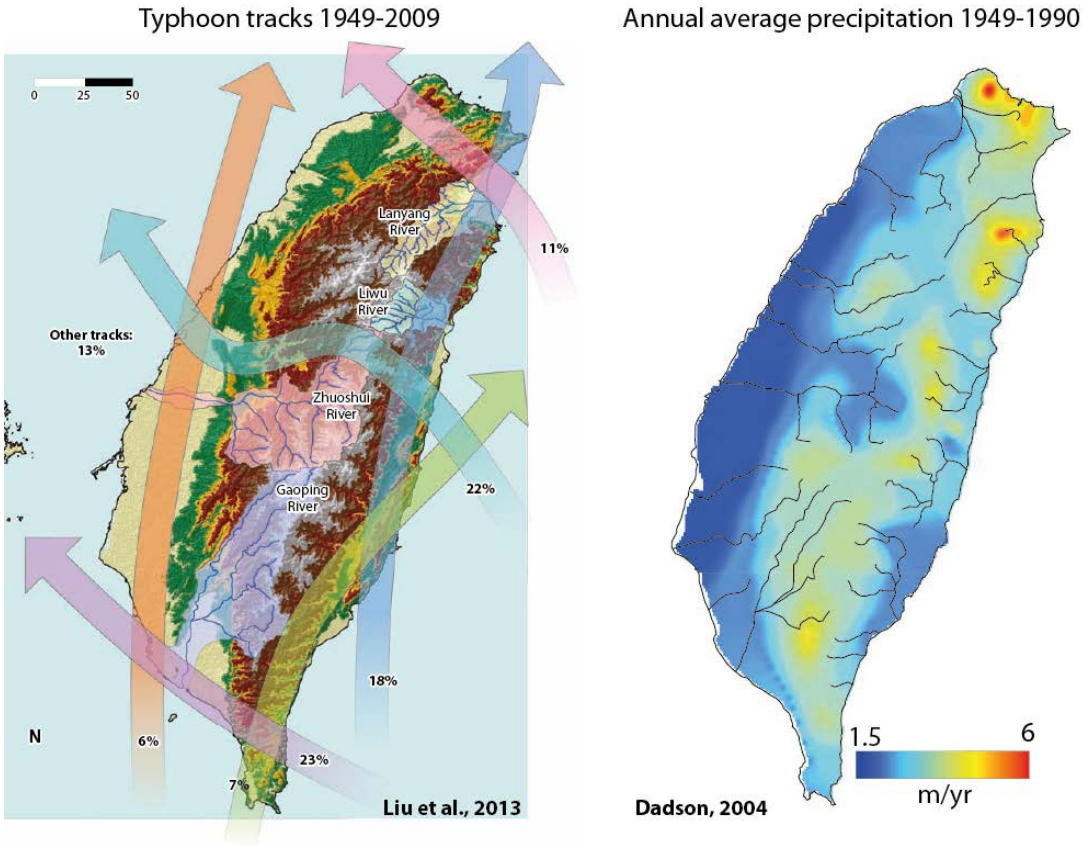

Fig. 4.1*: Left panel: Main typhoon tracks and percentage between 1949 and 2009; modified from* [*Liu et al.*, 2013]. *Right panel: Annual average precipitation between 1949-1990 in mm/year (right panel); modified from* [*Dadson*, 2004; based on the record of Water Resource Agency of Taiwan].

The importance of small mountainous islands to the global sediment discharge to the oceans was described more than two decades ago [*Milliman and Syvitski*, 1992; *Milliman and Farnsworth*, 2011]. The importance of islands such as Taiwan representing 0.024% of the earths subaerial surface, with 1.9% of the global sediment discharge to the ocean has been emphasized more recently [*Dadson et al.*, 2003; *Dadson*, 2004], highlighting the relative importance of highly tectonic and erosive settings in global sediment input into the oceans, comparable to much larger basins draining well developed orogens such as the Himalayas. Indeed sediment discharge for the Pearl, Mekong and Red rivers have all sediment discharge values below the ones found in Taiwan, in spite of draining greater areas and relief (Fig. 4.2).

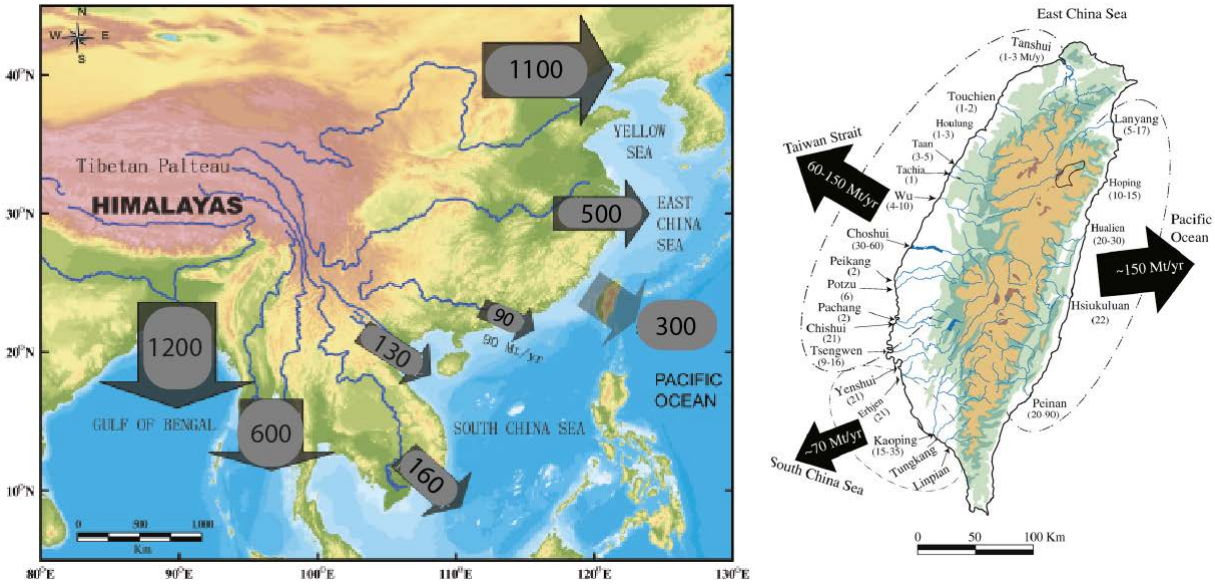

***Fig. 4.2**: Present-day Southeast Asian [Liu et al., 2009] and Taiwan [Liu et al., 2009] suspended sediment discharge to the oceans in Mt/yr. Note how Taiwan island deliver is comparable to many of the Southeast Asian rivers draining the Himalayas.*

B. Recent erosion rates: Suspended sediment load and Holocene incision rates in Southern Taiwan

The main catchments of Taiwan are monitored since the 1970's with more than 150 hydrometric stations all around the island. Daily measurements of water discharge and intermittent measurements of suspended sediment discharge were carried out by the Water Resource Agency of Taiwan (Fig.4.3).

Analysis of present-day, Holocene (incision rates) and long-term (AFT) erosion rates by [*Dadson et al.*, 2003; *Dadson*, 2004] found correlation between long and short term erosion rates and 1) runoff variabily, 2) cumulative seismic moment of historical earthquake and 3) substrate strength. Indicating for instance that the southwestern foreland presents one of the highest erosion rates of the orogen (Fig. 4.3) due to its loose substrate, high seismicity and high runoff variability. These results implied that neither pdischarge nor relief were the main controlling factors of present erosion and long-term exhumation, as implicitly assumed by stream power laws of erosion.

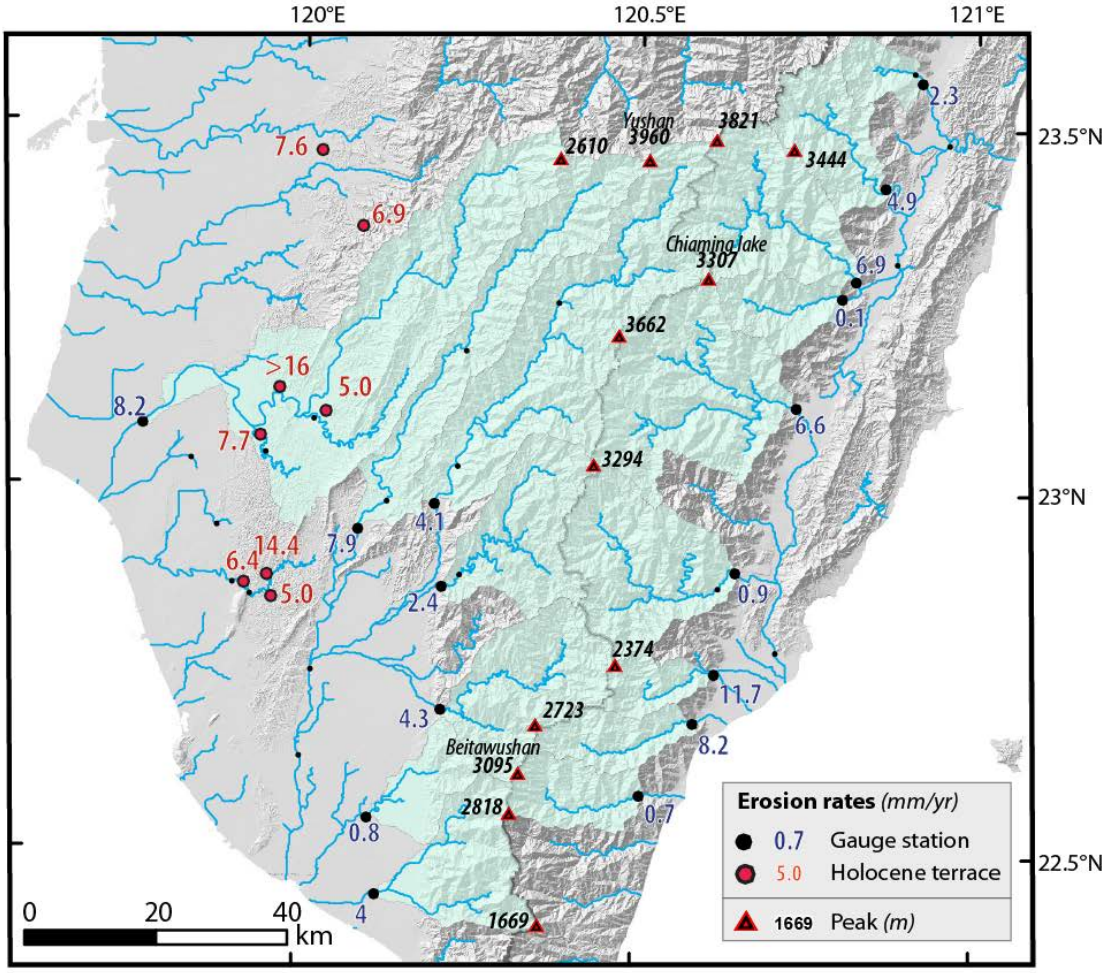

***Fig. 4.3**: Erosion rates from river sediment load (assuming 30% of bed-load) draining the Central Range mountains and existing Holocene strath terraces dating. All hydrometric stations in south Taiwan are shown (black circles). Contributing drainage area is highlighted in blue for the selected stations (big black circles). Existing incision rates from Holocene terraces dating from Dadson et al. (2003). Dated terraces from the coastal range are not shown..*

Orogenic systems, and landscape in general, have been argued to reach a dynamical steady state after some time of a given perturbation. Because of its effective erosive engine and time-space equivalence (Fig. 1.13), Taiwan has been argued to have reached various of the steady-state forms defined by *Willett and Brandon* [2002]: exhumational steady-state (i.e. nested pattern of reset thermochronological ages, [*Willett and Brandon*, 2002; *Fuller et al.*, 2006]) and topographic steady-state (invariant topographic characteristics with time; [*Suppe*, 1981; *Stolar et al.*, 2006; *Cheng et al.*, 2012] and in most of the numerical models of orogenic wedges, flux steady-state is assumed [e.g. *Dahlen*, 1990; *Hilley and Strecker*, 2004].

In the previous chapter have seen that exhumational steady-state is probably not attained in Southern Taiwan and likely in the rest of the orogen given the recent tectonic and exhumational changes that have occurred. Topographic steady-state was the first to be recognised by early researchers on Taiwan [*Suppe*, 1981], and further characterised using modern morphometric measurements such as regional and local topographic slope and hypsometry [*Stolar et al.*, 2007; *Cheng et al.*, 2012]. Stolar et al. (2007) estimated the time to

topographic steady-state to 1.8-2.3 Ma in agreement with more general assessment of landscape response to perturbation [*Allen*, 2008b]. Topographic steady-state may be atained for one morphometric parameter, but not necessarily by all of them.

Topographic steady-state ultimately relies on the assumption that topographic evolution and landscape maturation is controlled by the geodynamic scale oblique collision. There are evidences that more punctuated events have affected the orogen rather than a simply steady southward propagation [e.g. *Byrne et al.*, 2011], thus questioning the validity of the steady-state assumtion.

II. Morphometry and landscape development

The relation between erosion rates and topography are not linear as initially theorized by *Ahnert* [1970]. For inactive tectonic areas, slope and local topographic relief appear to correlate linearly with erosion rates at different scales (fig. 4.4). The linearity is broken for active, rapidly eroding landscape with threshold values of ~25-30 ° and ~1500 m of mean local slope and local relief areas [Fig. 4.4; *Montgomery and Brandon*, 2002]. Above these values, topographic relief and slopes appear to be decoupled from erosion rates. Hillslope mass wasting is argued to be behind this decoupling, and has been demonstrated to be a major factor governing reach lowering and erosion in the river channels [e.g. *Montgomery*, 2001; *Larsen et al.*, 2010]. Taiwan is a landslide-dominated mountain belt and landslides appear to occur mainly during and shortly after stochastic events such as earthquakes and typhoons [*Hovius et al.*, 2000; *Lin et al.*, 2008; *Meunier et al.*, 2008; *Huang and Montgomery*, 2013].

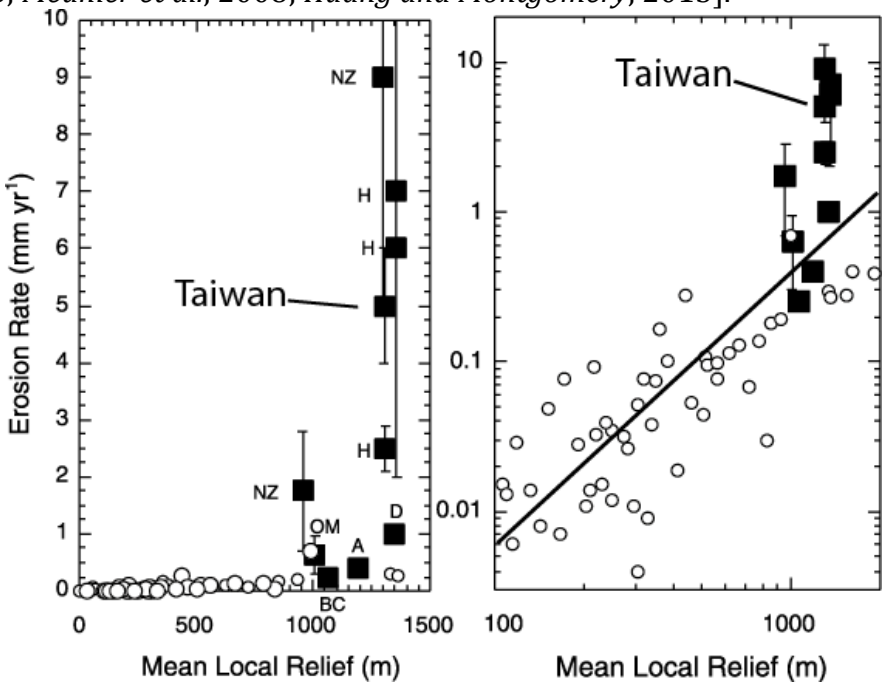

Fig. 4.4*: Long to short term erosion rates vs. mean local relief in active tectonic areas (Black square) and inactive areas (circle) plot with a linear and logarithmic axis. Note the non-linear relationship in in active tectonic areas. Erosion rates a derived from a compilation of river suspended, river-strath terraces and thermochronology. For Taiwan the values come from* [*Li*, 1975] *who combined river sediment yield with Pleistocene*

estimates of erosion/deposition rates, in agreement with recent estimates of long and short term erosion/exhumation rates [e.g. Fuller et al., 2003, 2006; Lee et al., 2006]. NZ = New Zealand; H = Himalayas; D = Denali-Alaska; OM = Olympic mountains; A =Andes; BC = British Colombia. Modified from Montgomery and Brandon [2002].

In the present study I explore recently demonstrated unsteady nature of the landscape [*Willett et al.*, 2014] and to correlate it to specific features of the landscape, such as low relief areas preserved in the Central Range mountains. I then argue for a potential role of glacial or peri-glacial erosive processes in the morphogenesis of such features and test it with published paleoclimatic reconstruction.

A. Low relief areas as evidenced by relief and slopes maps

The founding geomorphic monograph of *Davies (1899)* defined peneplains (i.e. ancient planation surfaces) as the last evolutive stage of landscape, and thus invoking vertical movements when found at height. Today, a preserved relic landscape is known to be the result of various processes and thus to potentially have various origins and ages, and is conservatively interpreted as the marker of ancient erosive phase [*Widdowson*, 1997].

.

The aim of this section is to map and characterize a pervasive low relief surface described in the old Taiwanese literature as "高山平地面 " ("high mountains flat surface"). To my knowledge, it was firstly described by [*Lin*, 1957], but probably early Japanese publications exist, notably by Yoshiro Tomita (富田芳郎撰) (1937 ?) in a monograph on Taiwan geomorphology, not available to me at this date. Surprisingly, to my knoweledge, not much published work exist on this surfaces, with the exception of [*Ouimet et al.*, 2012] and the more spatially restrained studies of glaciated landscape in the high mountains [e.g. *Cui et al.*, 2000; *Böse*, 2004; *Chu et al.*, 2007; *Siame et al.*, 2007; *Hebenstreit*, 2012].

1) Methods

Topographic relief and slope maps of the southern Central Range were extracted from a 40m DEM using ArcGIS environment for the purpose of localizing low-relief areas in the Central Range. I first extracted topographic local relief and average slope within a given focal circular window. Different focal radii were tested, from 100 m to 8 km to qualitatively evaluate the resulting maps and the potential geological controls at different focal scales. An altitudinal threshold above which the low relief surface were considered was chosen low enough to include all ridges and high enough to exclude river beds. Then we selected three focal radii for the extraction of the low relief (LR) zones based on a the following query:

LR = (TR < mean TR) & (MS < mean MS) & (T > threshold)

With LR = low relief, TR = local topographic relief, MS = mean slope and T = topography, mean TR and mean MS refer to the whole southern Central Range mean.

This query extracts the low relief and slopes areas of the landscape but not necessarily a lower relict-landscape as defirned by *Clark et al.*, [2006] where she defines thresholds of 600m and 10º for local relief and slope, respectively. However, as seen in the following, the areas satisfying both low relief and low slopes are not that bumerous and the method captures well the anomalies in the landscape. Moreover when checked in detailed with satellite images and precise digital elevation models, the method manage to identify landscapes already described in the literature as glacial and/or areas where distinctive features such as lakes or arguable wide U-shaped valleys are found.

2) General morphology of southern Taiwan

The southernmost tip of the metamorphic core starts to outcrop in the Taimali as evidenced by metamorphic boulders seen upstream of the valley. We have mapped a broad deformation zone (SZ 1), which appears to be the west-bounding fault of the metamorphic core. In the Zhiben drainage basin, right to the north of the Taimali valley (Fig. 4.6) the Tananao metamorphic core already crosses the entire width of the valley and occupies most of the upstream area of the drainage basin. This coincides with a main drainage divide anomaly that bends towards the east to end up near the top of the northward extension of SZ1 and the metamorphic core 's deeper rocks (Taroko marbles; Fig. 4.6). This is the only place in southern Central Taiwan where the metamorphic core is drained towards the west. In this manner, the divide goes from being on top of the Eocene Pilushan Fm to the top of the metamorphic core (Fig. 4.6). The divide decreases in topography from 3090 m in the Taimali up waters (Beitawushan) to about 2100 m in the Zhiben (Fig. 4.6).

As the divide migrates towards the east and shrinks the eastern divide basins, the western divide basins (Sandimen basin, Fig. 4.6) become wider and progressively north-south directed. It ultimately becomes north south directed as it gets caught by the western Central Range frontal thrusts (Choachou-Laonung fault) and the first thrust sheets and related anticlines of the western-foothills.
At a broader geological scale, this geomorphic transition zone with a drainage divide anomaly, and changing of draining direction of the western divide basins coincides with the southernmost tip of the longitudinal valley where the Luzon Arc has already overthrusted most of the fore-arc basin and starts entering in contact with the Central Range units.

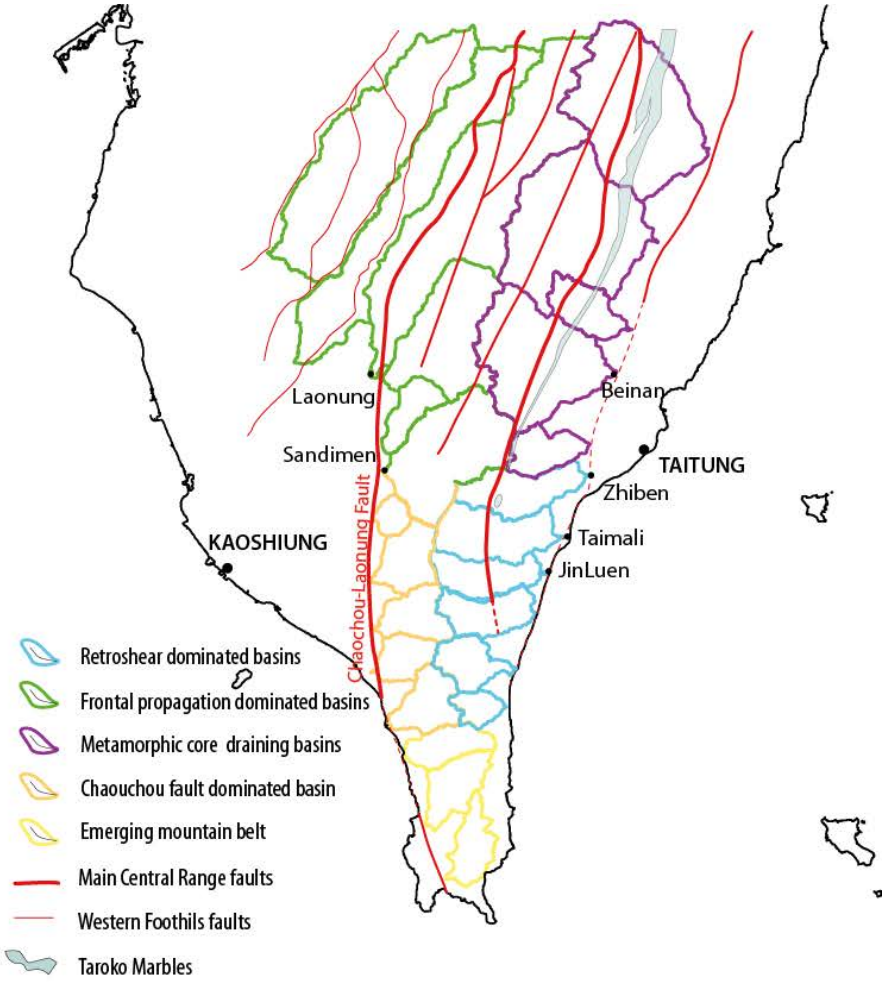

Fig. 4.6*: Drainage basin of southern Taiwan and classification depending on the geological controls on drainage morphology. Based on our own observations and on existing published interpretation [Ramsey et al., 2007; Wiltschko et al., 2010]. Also shown the main faults and the location of the deepest rocks exhumed in the orogen (Taroko marbles).*

Morphological studies of the central Range are sparse. *Ramsey et al.* [2007] characterized the south-eastern basins, including the Taimali catchment, and based on geomorphic observations delineated a sinistral fault, in close geographic correspondence with our SZ1 shear zone. The authors also developed a conceptual model invoking tilting of the region to the north to explain the drainage asymmetry (northern tributaries longer than southern ones) in the Zhiben-Taimaly-Jinluan area (Fig.6). However, recent numerical model results applied to transpressional settings manage to reproduce drainage basin asymmetry with the involvement of transpresional faults and surface processes only, implying that the landscape records long-term deformation at plate boundaries [*Castelltort et al.*, 2012; *Goren et al.*, 2012]. For south-eastern Taiwan and the Taimali area, these results imply that drainage-basin morphology is controlled by the long-term sinistral shearing observed in the field, and not by the recent normal faulting that seems to dominate recent brittle deformation (see Chapter 2; e.g. Fig. 2.11).

A study along the southwestern Central Range drainage basins show the increase of activity of the Chaochou fault towards the north [*Wiltschko et al.* 2010], consistent with our new ZFT and AFT ages in the hanging wall of the Laonung fault (Fig. 3.32). The eastern Central Range has been studied by a certain number of researchers [*Knuepfer and Willemin*, 1992; *Willemin and Knuepfer*, 1994; *Stolar et al.*, 2007]. Topographic steady-state has been inferred from the relatively constant values of morphometric parameters [*Stolar et al.*, 2007]. Interestingly, they describe high hypsometric integrals values (up to 0.5 for the smaller basins and ~0.4 for the bigger ones), relative to the low hyspometric integrals found further south in the Central Range (down to ~0.2), for all the inferred at steady-state basins.

3) Results

a) Local topographic relief and mean slope: mapping of low-relief domains

A selection of the computed local relief and slope using different moving window radii are shown in Fig. 4.8 (a, b, c) and Fig. 4.9 (a, b, c). To extract the areas were the local relief and slope are low we extracted two other maps where values are below the southern Central Range mean at a given radius, and where values are below mean minus one standard deviation (Fig. 4.10). The later give us the extremes were relief and slopes are markedly low.

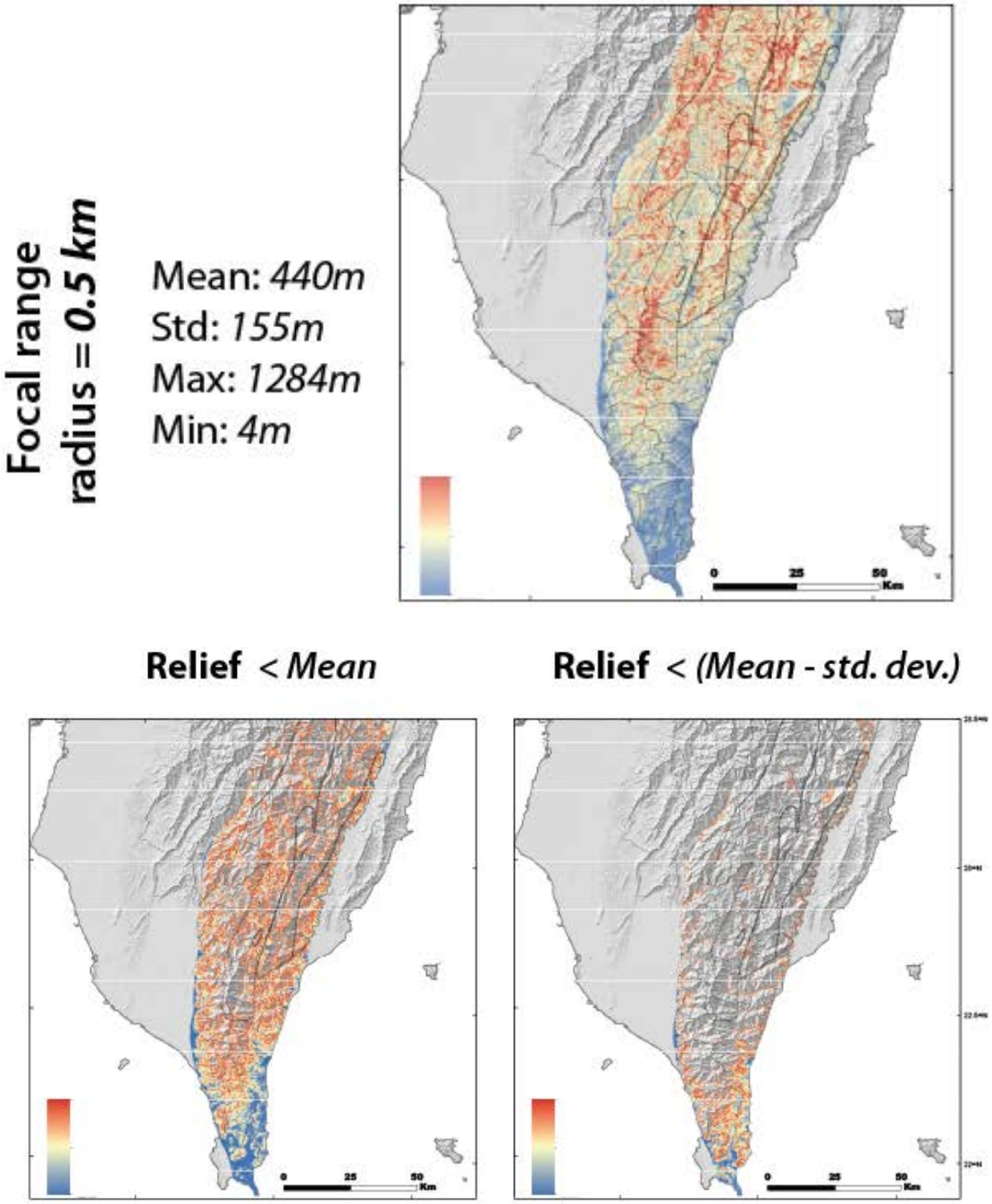

Fig. 4.8a: *Relief map and areas below the Central Range mean and the Central Range mean minus one standard deviation for a focal radius of 0.5km. Colour bar values correspond to the values reported in the top figure.*

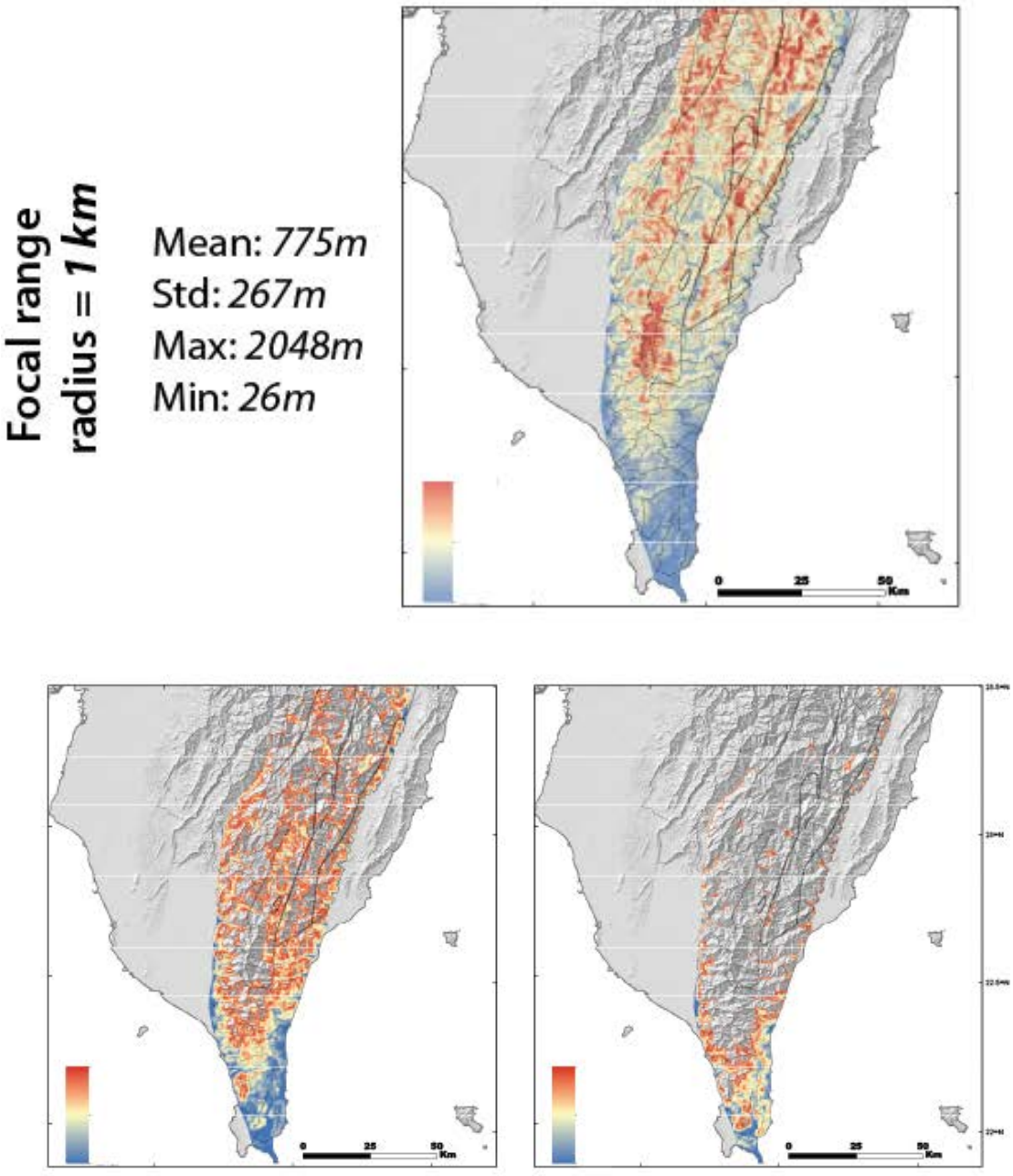

Fig. 4.8b *(continued): Relief map and areas below the Central Range mean and the Central Range mean minus one standard deviation for a focal radius of 1km. Colour bar values correspond to the values reported in the top figure.*

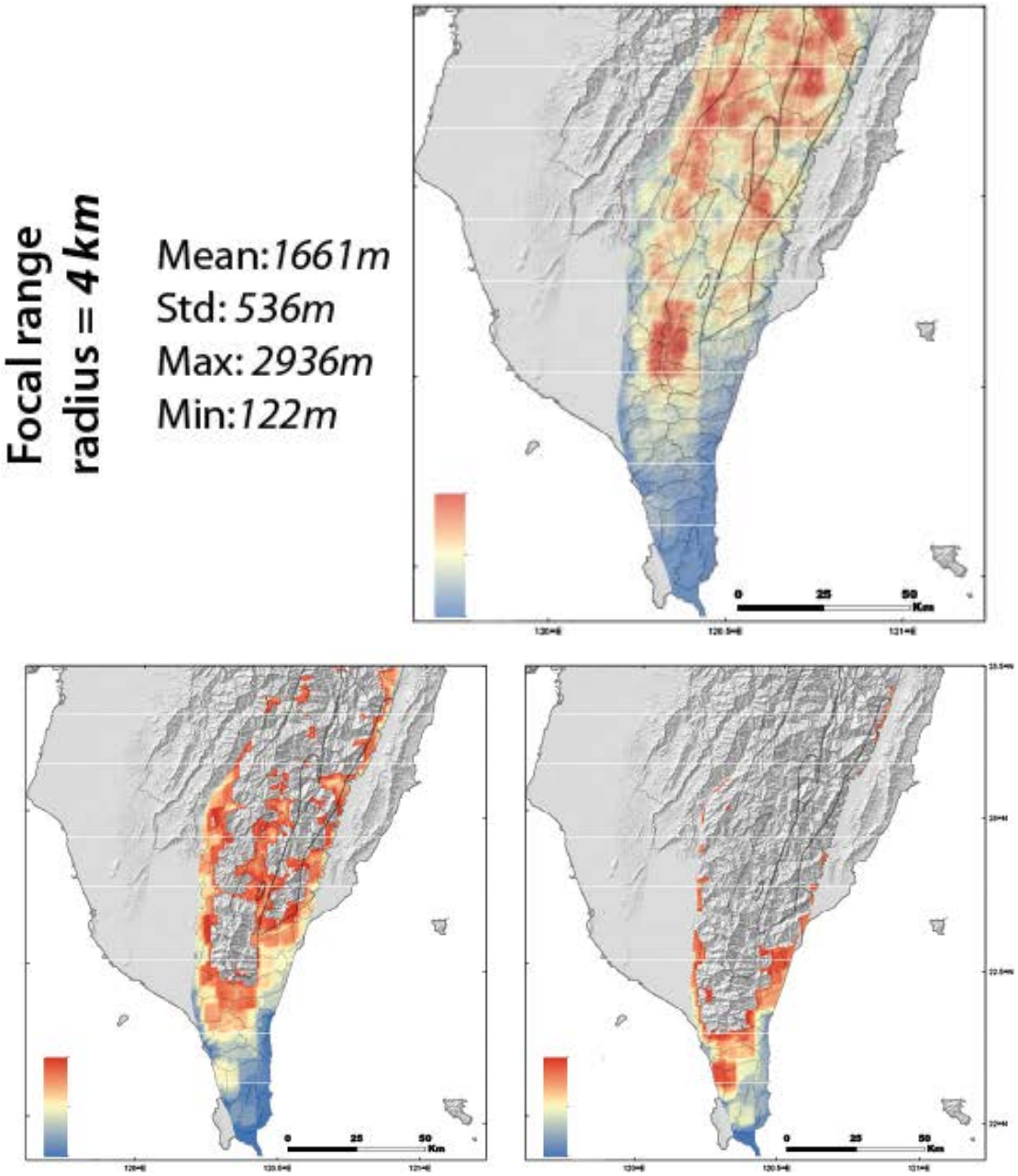

Fig. 4.8c *(continued): Relief map and areas below the Central Range mean and the Central Range mean minus one standard deviation for a focal radius of 4km. Colour bar values correspond to the values reported in the top figure.*

Some first order observation can be made from the local relief map of Fig. 4.8. As we increase the moving window radius, maximum, minimum and the mean relief increase (Fig. 4.8). Note that the width of the southern central range is about 40 km, meaning that 10 windows of 4 km would cover it.

For the largest radius focal range, equal to 4 km (Fig. 4.8c), relief is very smoothed and values below the mean are limited to southernmost area, to the outlets of the basins and to a central belt going from the shear zone (SZ1) described in the Taimali valley towards the inner mountains. This belt includes the drainage divide anomaly and the upstream area of the large eastern drainage

basin. It corresponds to the upstream part of the Beinan (Xinwulu) river drainage basin, as well as some parts of the western draining upstream areas.
This low relief belt in the inner mountains is also observed for the lower radius moving window radii. Lowering the radius allows to identify very specific areas in the topography with low relief. They appear to be mainly positioned either on the top of the drainage divide or along the drainage basin ridges as well as in some upstream alluvial rivers.

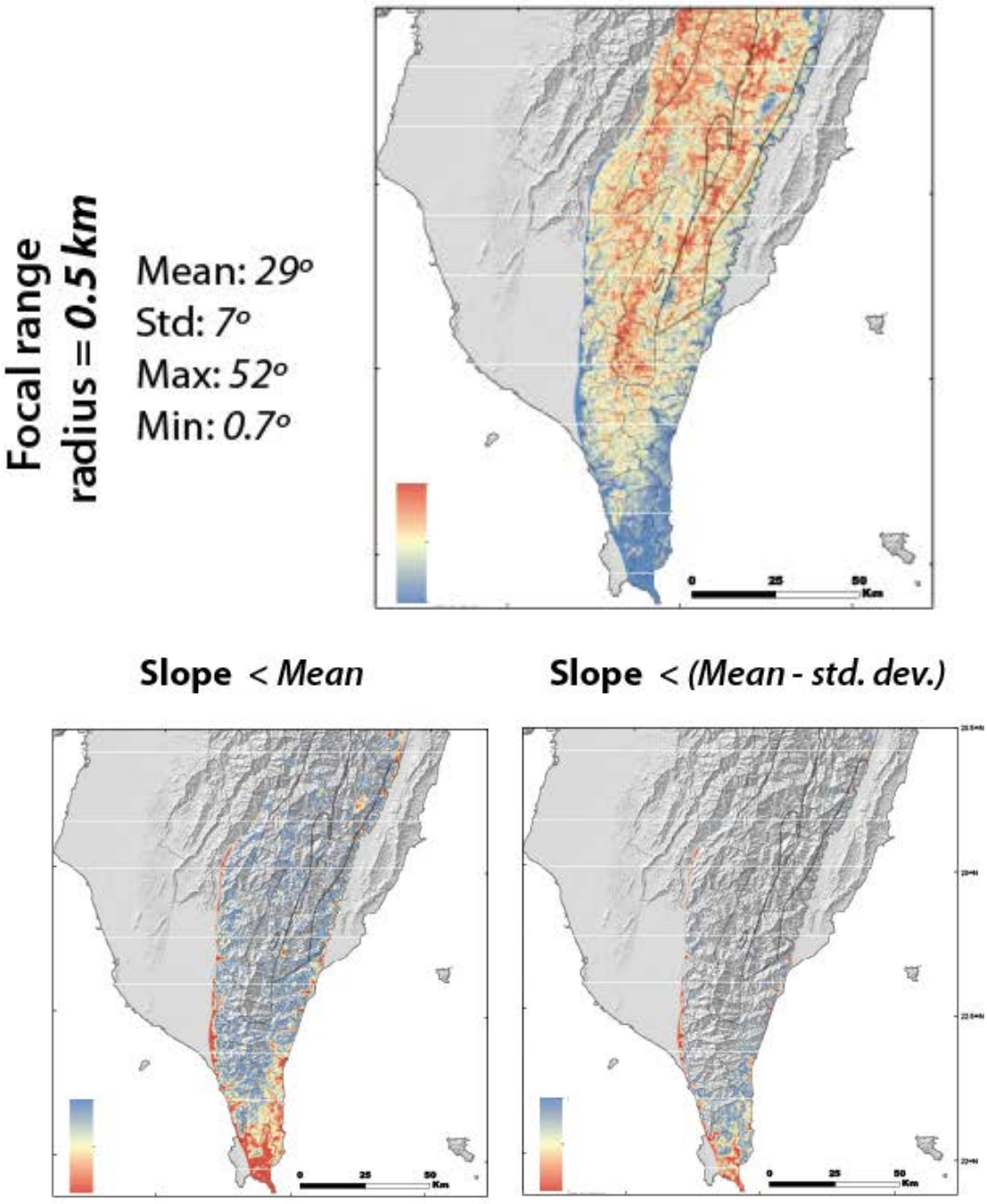

Fig. 4.9 a*: Slope maps, and slopes map of areas below mean and the mean minus one standard deviation for a focal radius of 0.5km. Colour bar values correspond to the values reported in the top figure.*

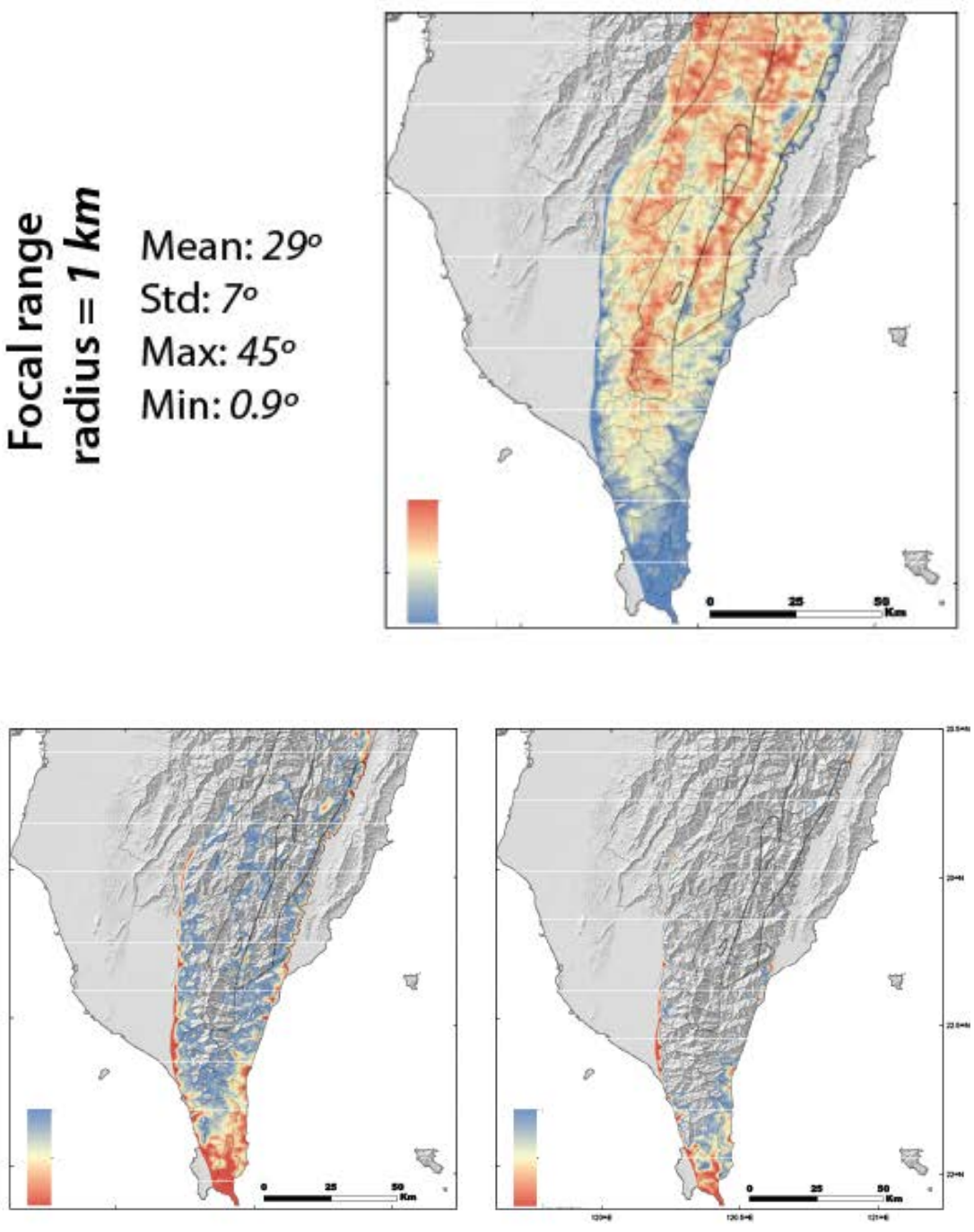

Fig. 4.9 b *(continued): Slope maps, and slopes map of areas below mean and the mean minus one standard deviation for a focal radius of 1km. Colour bar values correspond to the values reported in the top figure.*

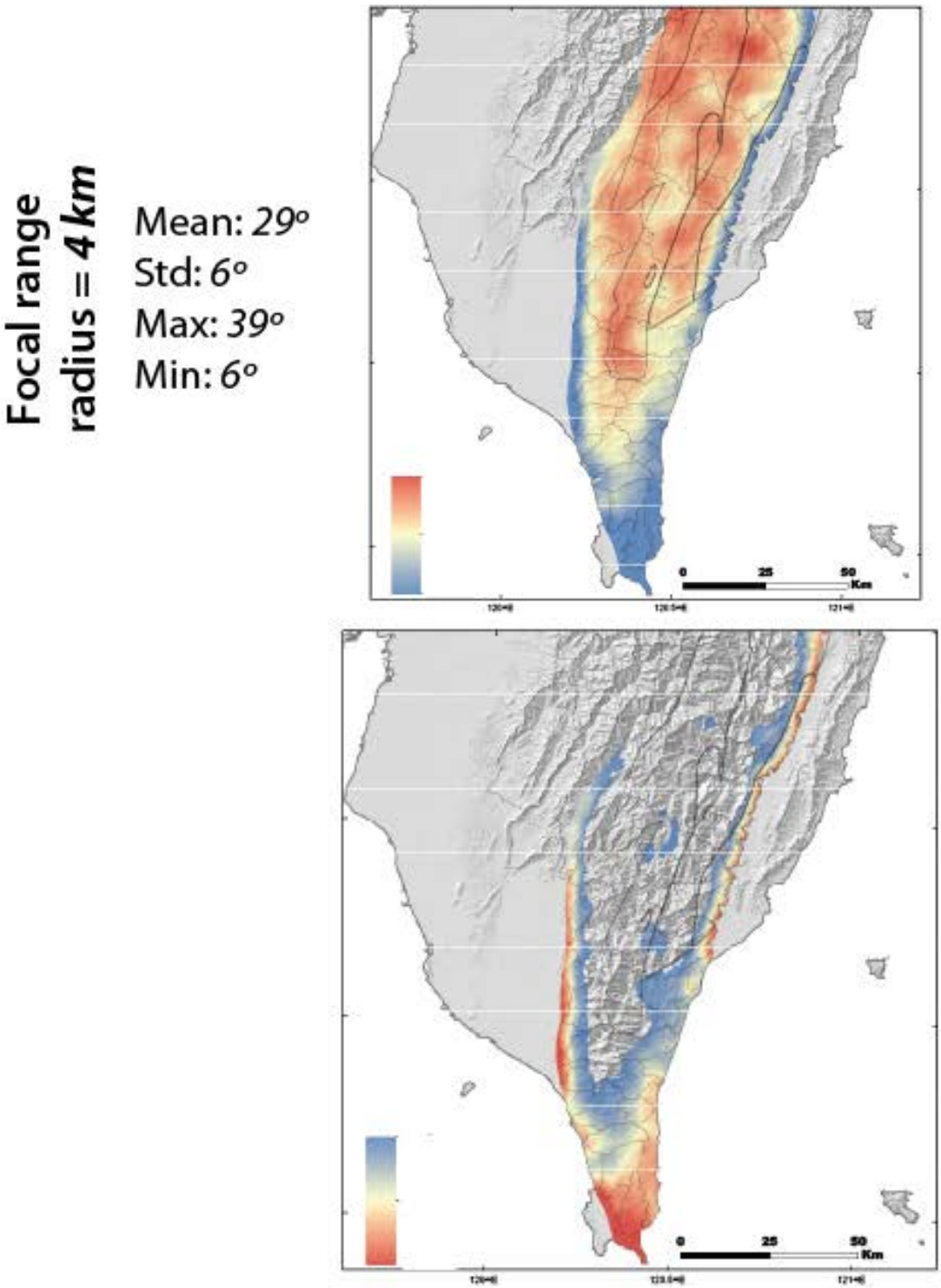

Fig. 4.9 c *(continued): Slope maps, and slopes map of areas below mean for a focal radius of 4km. Colour bar values correspond to the values reported in the top figure.*

Low slope (<mean) maps follow the same general trend as the relief map with low slope areas concentrated in the southern Central Range and at the mouth of

the rivers (Fig. 4.9). They highlight, similarly to the low relief maps, low slope areas in an inner discontinuous belt.

In order to map the localization of the low relief areas, we combined together the above maps using the low relief and slope (<mean) of the 500 m and 1 km radius maps, adding an extra condition on the altitude. This was done to avoid low relief and slope on the alluvial channels and river mouths. The resulting maps are shown in Fig. 4.10.

Low relief areas extracted from slope and relief map of southern Taiwan are characterized by the following:

- The drainage divide anomaly (Fig. 4.6; DA in Fig. 4.10), appears as the most prominent and south-most low relief area in southern Taiwan. This area correspond to the only place in southern Taiwan where the drainage divide sits on top of the metamorphic core.

- They are mainly positioned on the drainage divide mainly on top of the Pilushan sandstones, or to the east of the drainage divide on top of the metamorphic core. Two quite distinct low relief belts can be distinguished:
    - The first is positioned on the drainage divide, starting from the drainage divide anomaly and then moving west further north. Besides in the drainage divide anomaly, the bedrocks covered are mainly the Eocene rocks of the Pilushan Fm.
    - The second start at the drainage divide anomaly as well, but remains sitted on top of the metamorphic core, as patchy dissected low-relief zones.
- Known LGM glaciated landscapes are comprised in the low relief areass; particularly the southern Chia Ming lake (blue squares in Fig. 4.10)

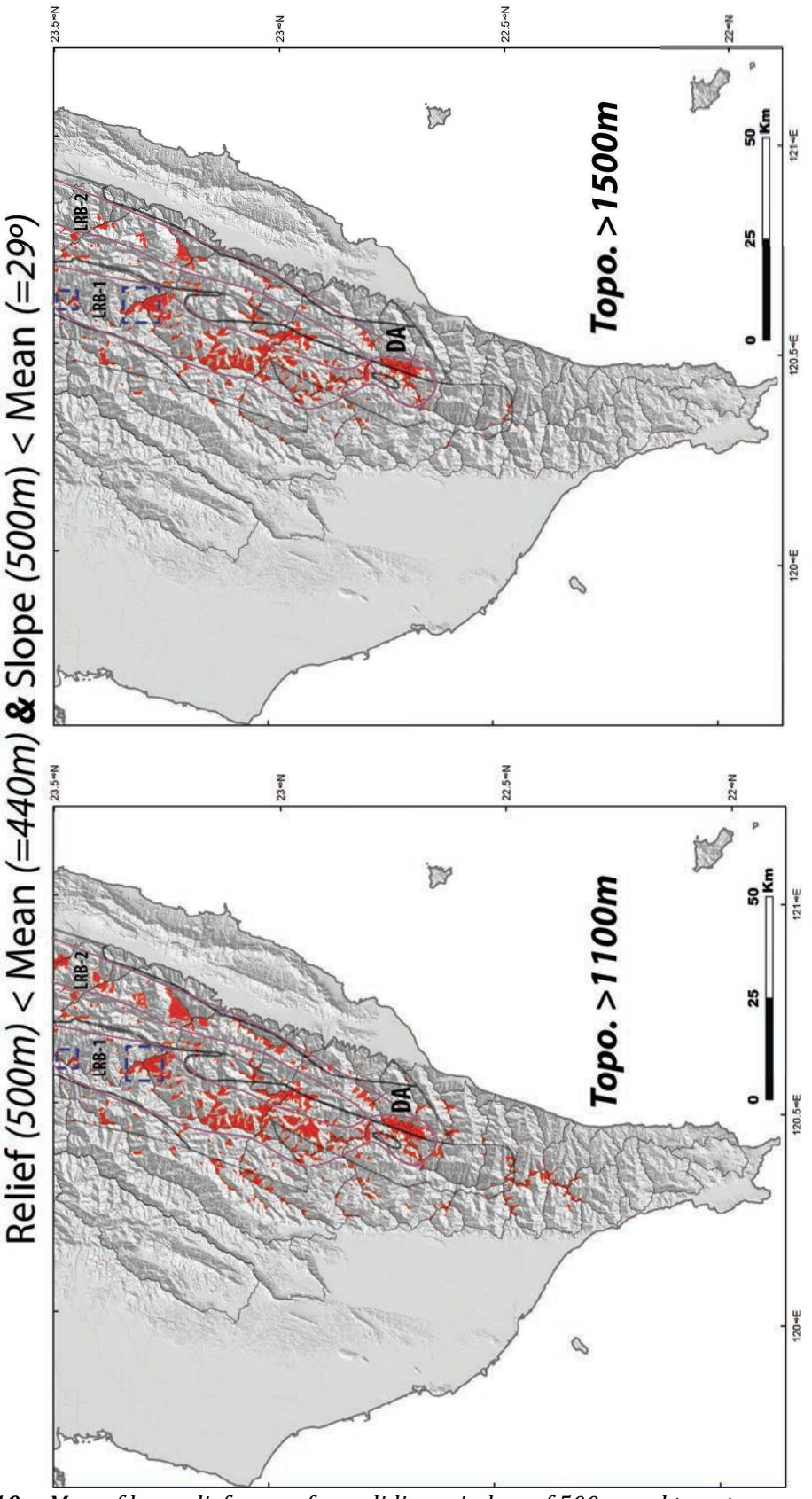

***Fig. 4.10a**: Map of low relief areas, for a sliding window of 500m and two topographic height trade off. Blue-dashed square indicate glacial morphologies described in the literature. DA = drainage divide anomaly. LRB = low-relief belt.*

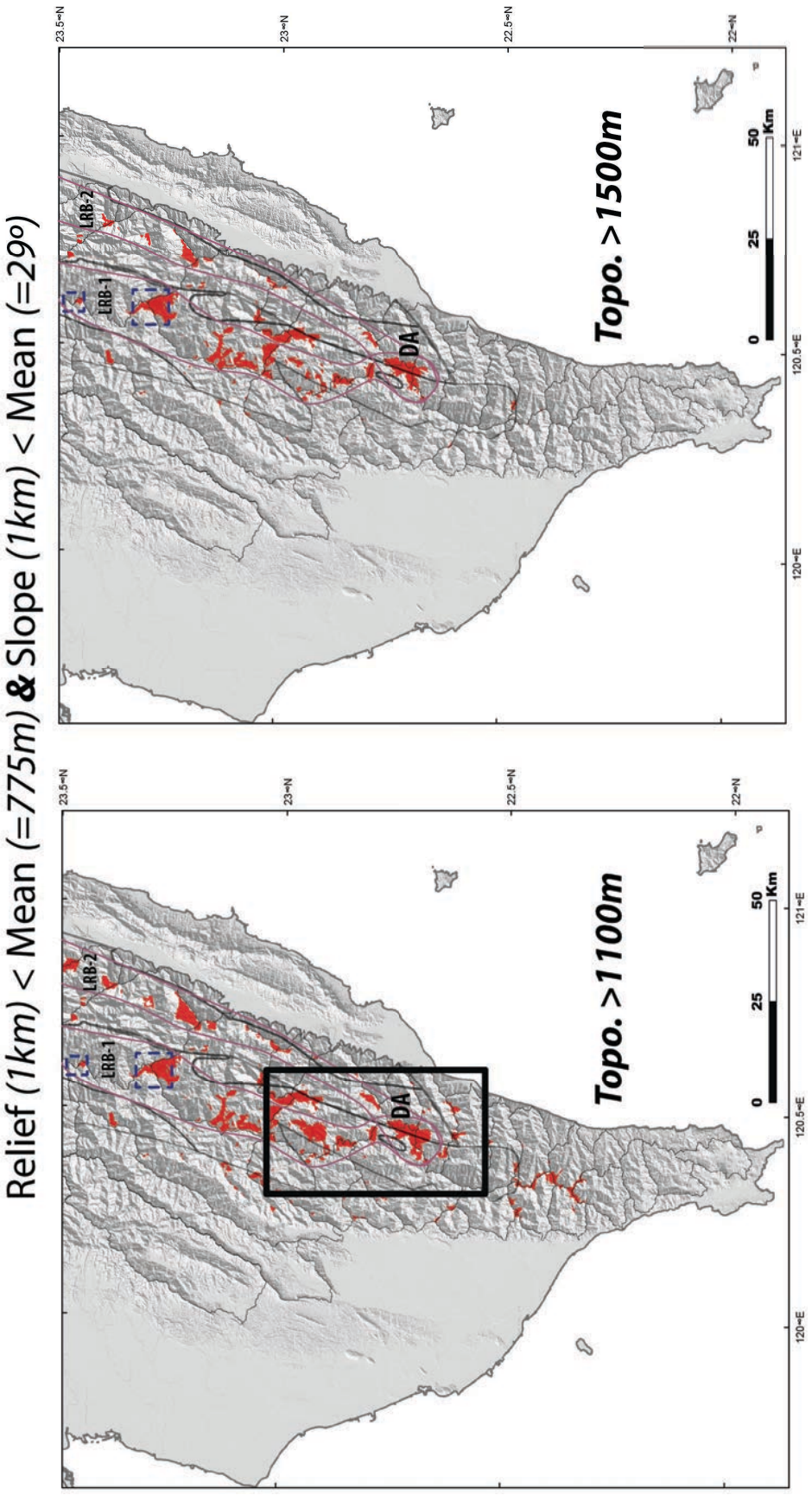

Fig. 4.10b *(continued): Map of low relief areas, for a sliding window of 1km and two topographic height trade off and topographic height trade off. Blue-dashed square indicate glacial morphologies described in the literature. DA = drainage divide anomaly. LRB = low-relief belt*

b) Some morphological characteristics of the low relief areas

A closer look on the morphology of the low relief areas (4.11) reveals they are usually associated to:
- Round shaped lakes (potholes?), linear erosive troughs (basal scour?) (Fig. 4.12 and Fig. 4.13);
- Bounded by knick-points (in most cases waterfalls);
- Some of the downstream valleys are U-shaped (Fig. 4.13 and 4.14);
- Grasslands (periglacial vegetation?) surrounded by red-ceder forests;
- Lobal sedimentary deposits with no upstream sediment source (solifluction figures?) (Fig. 4.12).

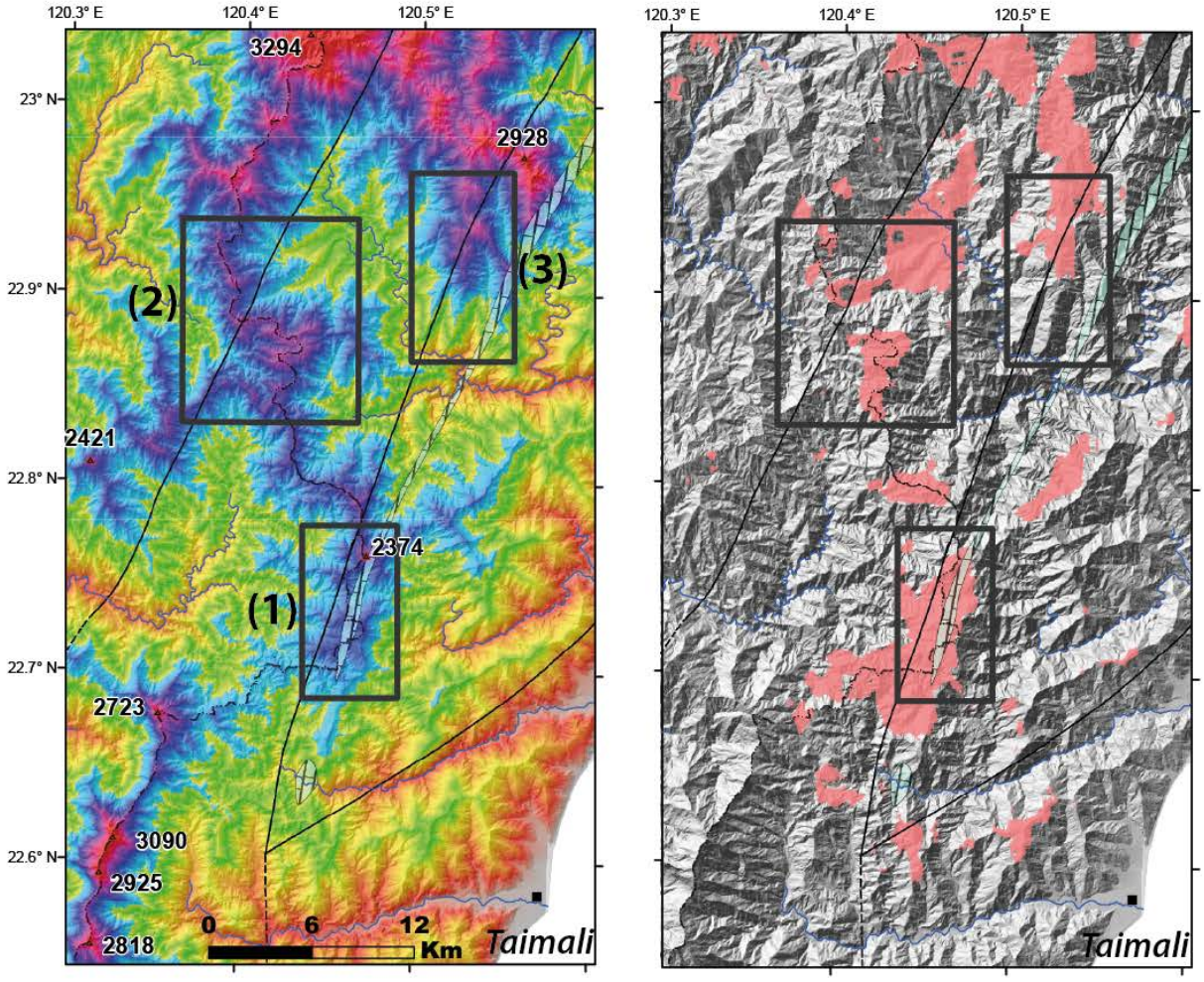

Fig. 4.11*: Detail topography and shaded relief with low relief area (relief <775m, slope <29º topography >1100m) of the low relief areas north of Taimali (see location in Fig. 4.10b. Square shows location of Fig. 4.12 (1), Fig. 4.13 (2) and 4.14 (3).*

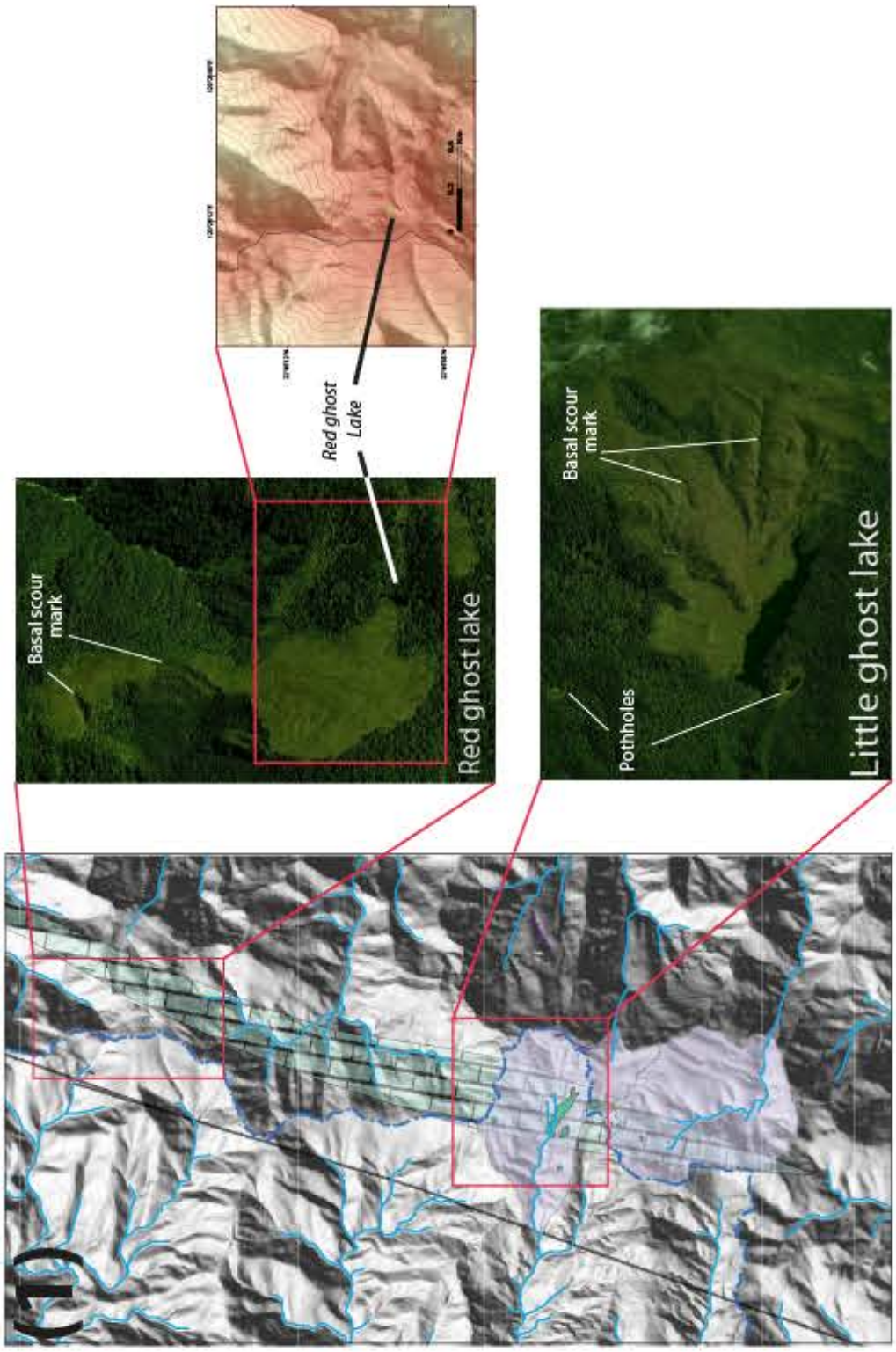

***Fig. 4.12**: Geomorphic elements of the low relief areas at the drainage divide anomaly, southern Taiwan. Note the almost systematic presence of lakes and grassland vegetation, and the underlying basement, the Taroko marbles (light blue). See Fig. 4.11 for location. Satellite images from Google Earth.*

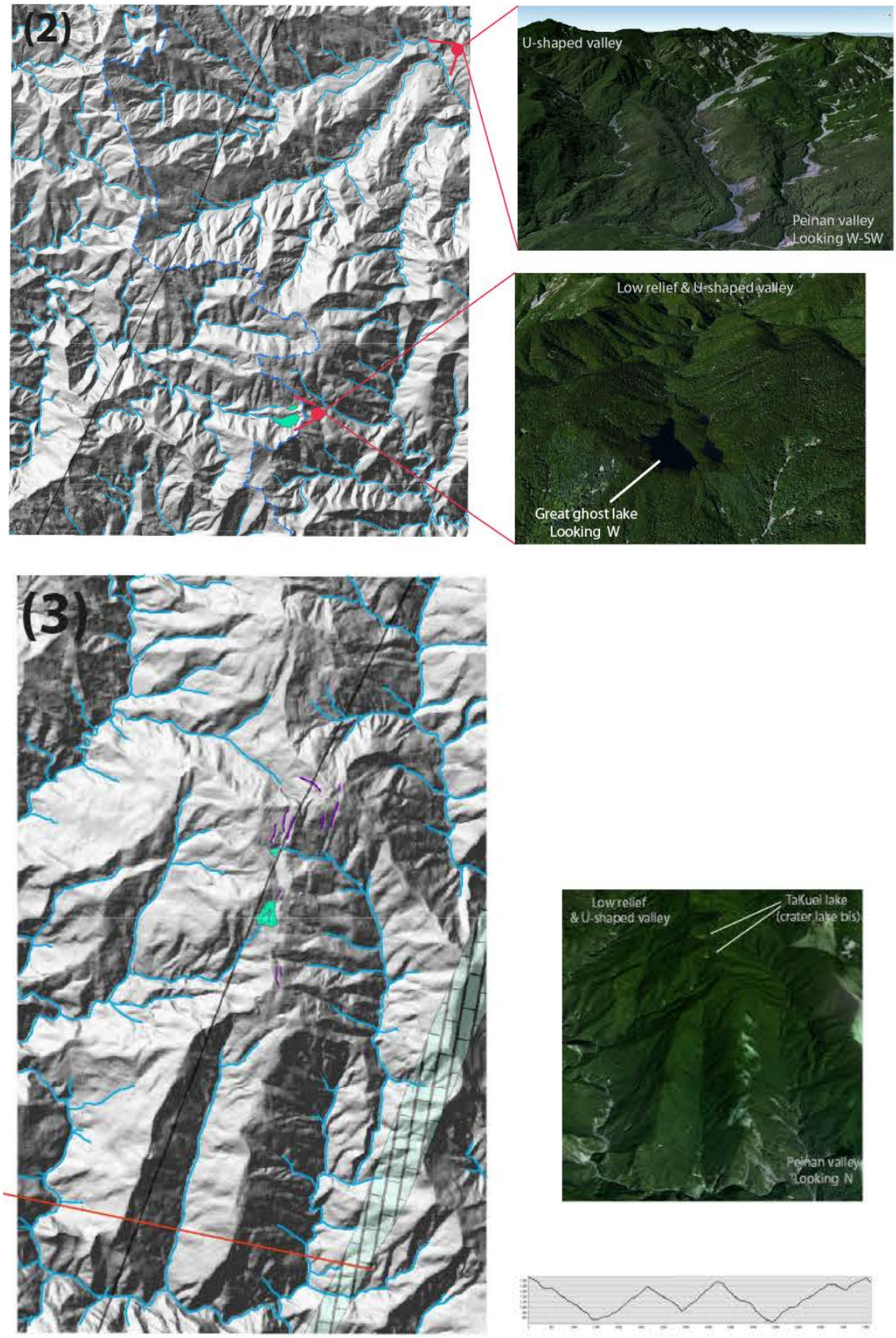

Fig. 4.13: *Upper panel: Great ghost lake and upstream part of the Peinan valley. Note the alluviated rivers in and wide valley. Lower panel: Takuei lake and downstream area. Note the very particular V-shape and over-elevated (see topographic profile) of the downstream*

valley. See Fig. 4.11 for location. Satellite images from Google Earth.



***Fig. 4.14**: Photography of the low-relief areas in the central Central Range, alonghte souterh cross island highway. No photogrpahs of our low-relief areas could be taken due to lack of access and time.*

4) Discussion: potential glacial imprint on low-relief areas

Low relief areas in southern Taiwan yield some similarities with glaciogenic landforms. Particularly the presence of scour marks, oval-shaped lakes and lobal depostis without upstream source argue. Nonetheless definite assignation of a glacial process to the low relief areas need field verification, and ideally dating of the surfaces.
Keeping this in mind I do still explore the possibility of a glacial origin of this surfaces. However some problems arise, the main ones being:

- Last glacial maximum (LGM) elevation line altitude (ELA) has been estimated to ~3500 m [*Cui et al.*, 2000, 2002] or ~3000 m [*Böse*, 2004; *Hebenstreit et al.*, 2006; *Siame et al.*, 2012].
- Lakes below 3000 m have been attributed either to meteoritic impact, or to structural/lithological controlled depression [*Chen*, 2001; *Chen et al.*, 1997].

In the following I discuss the current knowledge on Late Pleistocene paleo-climate to evaluate the possibility of a lower ELA in the recent past and on the different theories about lake genesis in the high mountains of Taiwan.

a) ELA and climatic record in Taiwan

The present-day ELA is theoretically estimated to 3950 m [*Hebenstreit*, 2006], this is about the height of the highest peak of Taiwan (Yushan, 3952 m). Most of the glacial landforms described in Taiwan are found at altitudes above 3000 m and mainly in the northern and central part of the Central Range mountains (Fig. 4.15). Reported deposition or exposure dating of the same landforms is predominantly of Holocene age and estimates of LGM ELA's range from 2950 to 3500 m [*Cui et al.*, 2002; *Siame et al.*, 2007; *Hebenstreit et al.*, 2011].

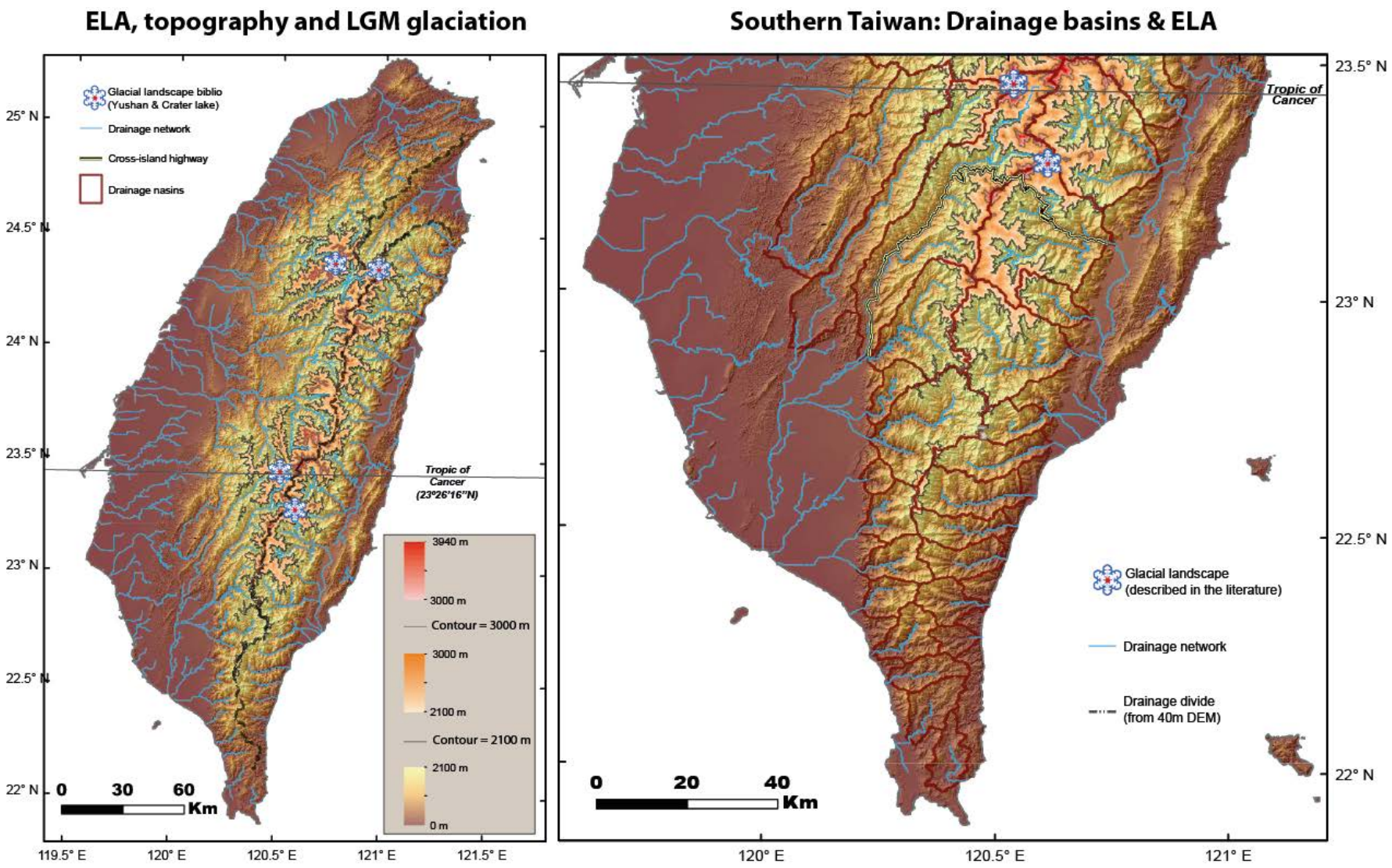
ELA, topography and LGM glaciation
Glacial landscape biblio (Yushan & Crater lake)
Drainage network
Cross-island highway
Drainage nasins
Tropic of Cancer (23°26'16"N)
3940 m
3000 m
Contour = 3000 m
3000 m
2100 m
Contour = 2100 m
2100 m
0 m
0 30 60 Km
25° N
24.5° N
24° N
23.5° N
23° N
22.5° N
22° N
119.5° E
120° E
120.5° E
121° E
121.5° E
Southern Taiwan: Drainage basins & ELA
Tropic of Cancer
Glacial landscape (described in the literature)
Drainage network
Drainage divide (from 40m DEM)
0 20 40 Km
23.5° N
23° N
22.5° N
22° N
120° E
120.5° E
121° E

***Fig. 4.15**: Topography, drainage basins and documented LGM glacial landforms. Note that all documented LGM landforms are above 3000 m. Also shown are the areas above 2100 m, minimum altitude where I find the low relief areas and lakes described in this study. The two southernmost decribed glaciated areas are Yushan (right under the tropic of Cancer) and JiaMing Lake (to the SE).*

However, glacial deposits at lower altitudes, down to 2250 m [*Böse and Hebenstreit*, 2008; *Hebenstreit*, 2012, p.109] and older ages going back to ~50 kyr (corresponding to Marine Isotope Stage MIS 3-4) have also been reported [*Hebenstreit*, 2006; *Cui et al.*, 2002]. Pre-LGM Pleistocene glaciations are not well constrained due to the lack of terminal deposits and thus maximum glacial extend during Pleistocene times remains unknown [e.g. *Böse and Hebenstreit*, 2008].

Glaciation in the tropics appears to be more dependent on temperature than moisture [*Hastenrath*, 2009] and to follow solar radiation variation [*Liew et al.*, 2006a, 2013], conversely to higher latitude climatic regions. In East Asia, mountain glaciations were stronger in the pre-LGM than during the global LGM [*Ono and Naruse*, 1997; cited in *Böse and Hebenstreit*, 2008].

Detailed local paleo-climatic reconstructions of Taiwan go back to early Pleistocene time and are mainly based on palinological studies of foreland stratigraphic sections or low-altitude lake coring. Two important findings are evidenced from palinological studies: ***1)*** the period between 73.9 kyr and 59.0 kyr, corresponding to MIS-4, is the colder phase during the last glacial cycle with an altitudinal shift of 1500 m and 8-10°C [*Liew and Huang*, 1994; *Liew et al.*, 2006b]; ***2)*** Cold/warm cycles can be traced back to Lower Pleistocene times and Pleistocene conglomeratic deposits (i.e. northern Linkou tableland) are associated to glacial periods with lateritic weathering during the warm interglacial periods [*Liew*, 1991].

Finally, some strong evidence for a cold perdiod during MIS-4 come from the IODP Leg-95 in the IODP site 1202 [Fig. 4.16; *Wei*, 2006]. Oxygene isotopic composition indicates that temperatures were at least as cold as the LGM during the MIS-4 period. Interestingly deposition of a turbidites (TL in Fig. 4.16) with dominant slate and mica-flakes (S and M in Fig. 4.16) elements coming from the Taiwan mountain belt [*Huang et al.*, 2005] occurred during the relatively warmer period between MIS4 and MIS2.

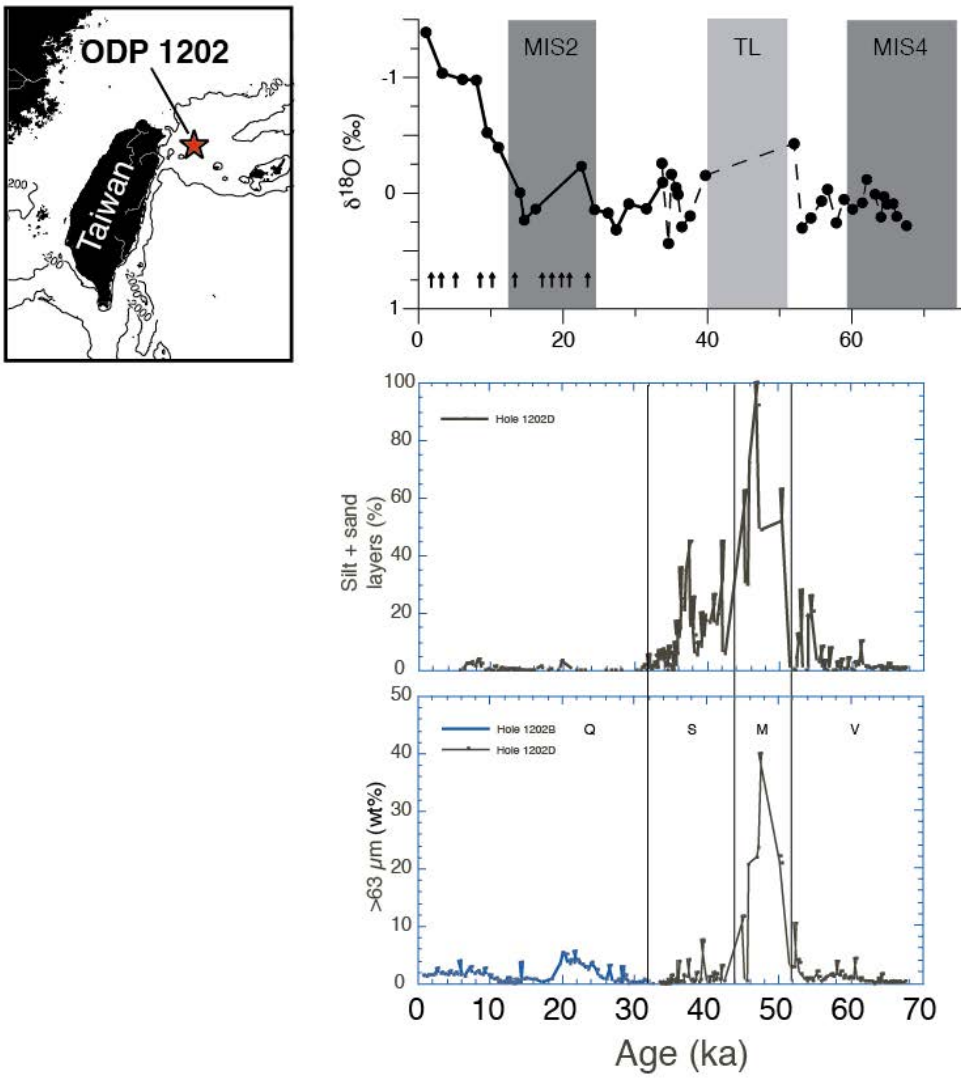

Fig. 4.16*: IODP leg-95 climatic and erosive record from [Wei, 2006] partly using data of* [*Huang et al.*, 2005]*. Inset: Position of the IODP drilling site. Upper panel: Planktonic foraminifera δ¹⁸O. TL=interval containing turbidites. Middle panels: percentage of silt-sandstone layer thickenes in total length of the core. Lower panel: weight percent in coarse fraction in bulk sediment. (Q), slate (S), metamorphic grains (M) and volcanic grains (V) indicate the dominat mineralogy of the perdiod. Note that what in the originalpaer is called "metamorphic" refers to mica flakes.*

One of the most convincing evidence of a glacial origin of these surfaces come from the PhD thesis of Robert Hebenstreit (Freien Universität Berlin, 2006) entitled "*Geomorphological studies on the late Pleistocene and early Holocene glaciation in selected high mountain ranges in Taiwan*". I report in the following the author's concluding remarks as in the original publication (p.117):

1- The high mountains of Taiwan were subject to repeated glaciations during the last glacial cycle.
2- Large scale glacio-erosional landforms indicate a last glacial ELA below 3000 m with an ELA depression of about 1000 m and a possible glacier extent down to 2000 m probably during the MIS 4.
3- No reliable glacial evidence from Taiwan can be clearly attributed to the global LGM.

4- Small scale glacial sediments yielded independently derived and reliable OSL and 10Be exposure ages in Nanhuta Shan from a Lateglacial to Holocene stage with two possible sub-stages at 12 - 15 ka and 9.5 ka and ELA depressions of 610 m and 510 m, respectively.

b) Lakes

High-altitude lakes in Taiwan are referred to as sub-alpine lakes. When above 3000 m they are considered as LGM related, but when below, they are usually attributed to some nebulous lithological, or structurally controlled depression, or, even to meteoritic impact related depressions (Central Geological Survey of Taiwan has apparently found impactites in Jia Ming lake, fig. 3,15). Some works exist on the lake water geochemistry and some lakes have been cored for paleo-climatology and environmental purposes [*Chen et al.*, 1997, 2004; *Chen*, 2001]. In these publications lake genesis is not well described, but the authors of the work assert that "most of subalpine lakes in Taiwan were formed from the blocked fault fractures". [*C.-T A. Chen personal comunication,* 2013]. Renowned field geologists also argue for a strucural control on its formation [*H.-T Chu*, Central Geological Survey of Taiwan, *personal comunication,* 2013], arguing that during last glacial cycle the Taiwan strait was dry and available moisture limited, thus a glacial origin should be discarded. However, as described above, moisture appears not to be a limiting factor, but insolation and temperature are. Moreover pre-LGM glacial depostis and paleo-climatic reconstruction in Taiwan argue for a larger extent of glacier at MIS-4 times.

As mentioned early, high altitude low-relief areas have been recognized since very long in Taiwan, their preservation is guaranteed by low erosion rates as witnessed by the sedimentation rates of 0.06-0.16 cm/yr (^{210}Pb dating, *Chen et al.*, 1997) in the Great ghost lake (Fig. 4.14) and of 0.075-0.12 cm/yr (^{14}C dating, *Chen et al.*, 1997) in Little Ghost Lake (Fig. 4.12). Although mostly surrounded by knick-points, the low-relief areas present often downstream alluviated and low-gradient valleys, certainly favouring its preservation (Fig. 4.14).

As right discussed, although our observation of low relief surfaces are at much lower altitudes (about 2100m), there are strong evidences for a lower ELA during Marine Isotopes Stage 4 (MIS 4) when ELA depression was probably lower than the during the LGM with a wider glacier extend [*Liew*, 1991; *Liew and Huang*, 1994; *Cui et al.*, 2000; *Böse*, 2004; *Hebenstreit*, 2012].

B. Hypsometry and hypsokyrtome: markers of glaciated landscape

In the following, I will assess the possibility of a glaciation reaching southern Taiwan. For this task, I will use two morphometric parameters that have been used to characterize glaciated landscapes, hypsometry (Fig. 4.16) [e.g *Brocklehurst and Whipple*, 2004; *Egholm et al.*, 2009] and the recently developed hypsokyrtome [*Sternai et al.*, 2011].

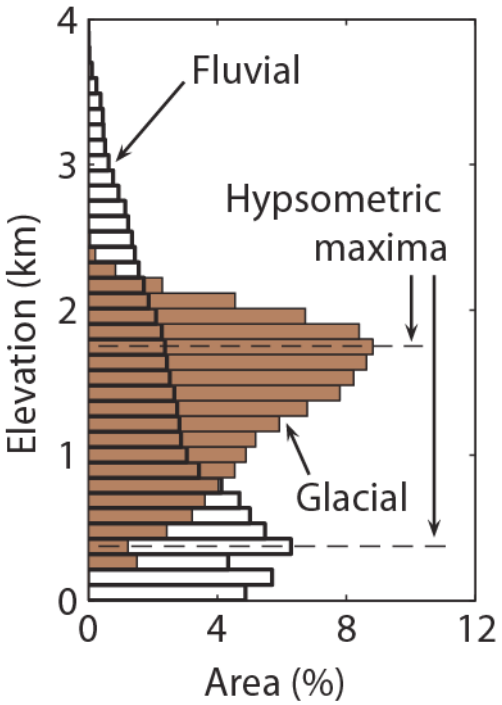

***Fig. 4.16**: Hypsometric distribution from a fluvial (northern Andes) and a glacial (Cascade Range, USA) mountainous landscape. Note how hypsometric maxima are different for the two areas. After Egholm et al. (2009).*

Hypsometry is defined as the areal frequency distribution of altitudes and has frequently been used to assess the degree of landscape development and maturity [e.g. *Stolar et al.*, 2007; *Strahler*, 1952] and/or the role of the processes behind landscape development [e.g. *Brozovic et al.*, 1997; *Montgomery et al.*, 2001]. The hypsometric integral (HI) is a commonly associated value and is defined as the area lying under the normalized hypsometric curve. It is defined as [*Strahler*, 1952]:

$$HI = \int_0^1 h' da'$$

$$with\ h' = \frac{h - Hmin}{Hmax - Hmin}$$

where h is the elevation, $Hmax$ and $Hmin$ are the maximum and minimum altitudes respectively, and a' is the normalized area.

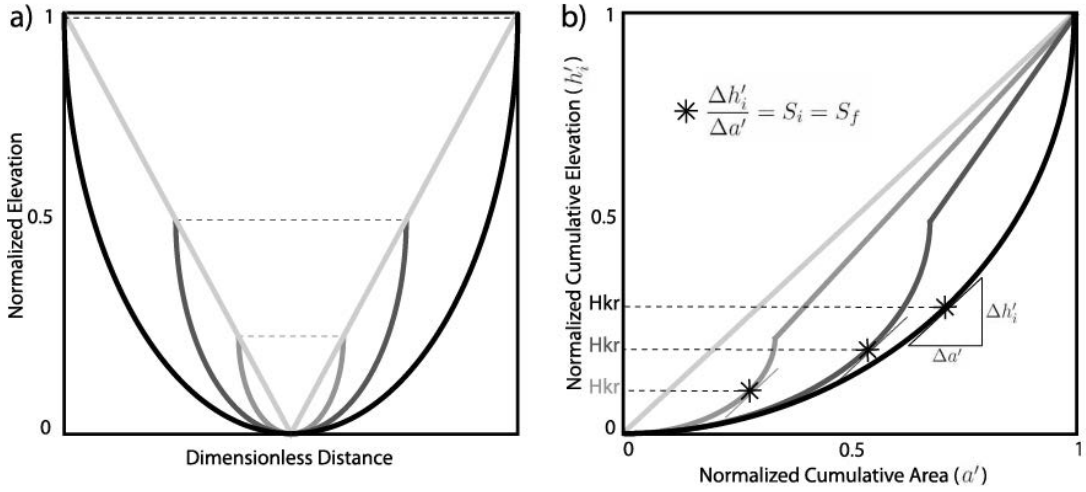

Fig. 4.18*: Conceptual sketches illustrating the principle behind. a) evolution of the cross-section of a valley from V-shaped (fluvial) to U-shaped (glacial). b) Evolution of the respective H_{kr}. hypsokyrtome. As fluvial valley (grey line in a) is carved by a glacier, its hypsometry decreases and H_{kr} increases*

Hypsokyrtome (H_{kr}) uses the curvature of the hypsometric curve to assess the degree of glacial landscape imprint in the landscape (Fig. 4.18). It takes advantage of the U-shaped character of glaciated valleys, which is reflected on the slope (S) of lower portion of hypsometric curves. H_{kr} is defined as minimum relative altitude (h') at which S is greater or equal to a reference value (S_f) [*Sternai et al.*, 2011].

$$H_{kr} = min[(h'(S \geq S_f)\ ]$$

High valules of H_{kr} imply stronger imprint of glaciers in the valleys, while low H_{kr} indicate that there is no significant departure from a fluvial dominated landscape.
In the next section, I first describe the methodology and validation of the technique, in particular relative to the hypsokyrtome. I then will discuss the significance of the obtained results.

Because hypsometry is the histogram representation of the distribution of altitudes, the choice of bin-size is a critical parameter for extracting the underlying dominant "true" probability density [*Scott*, 1979; *Knuth*, 2006]. As stated by *Sternai et al.* [2011] "*Potential trends within a DEM can be better recognized when the elevation values are binned [e.g., Strahler, 1952; Lifton and Chase, 1992]".* In practical terms, the bin-size corresponds to the number by which I divide the total range of altitudes to build the hypsometric histogram. If the bin-size is too large the obtained hypsometric curve will be too rough and will miss the real distribution. Indeed, bin-size needs to be sufficiently large to capture the major features of the data ignoring the random sampling fluctuation, but not too large to avoid an excessively rough hypsometric curve. Too small bin-size can result in a noisy signal with no clear trends. Surprisingly, there is not a well-established procedure for obtaining an optimal bin-size for a given distribution.

Scott (1979) proposed an optimal data-based formula, assuming normal distribution, for extracting the bin-size b_s:

$$b_s = \frac{R}{3.49s} n_p^{\frac{1}{3}}$$

with R = data range (relief), n_p = the number of data points (pixels) and s= variance (standard deviation).

Bin-size values ranging from 30m to 500m can be found in the literature [*Brozovic et al.*, 1997; *Brocklehurst and Whipple*, 2004; *Egholm et al.*, 2009], with a relative dominance for values between 30m and 100m. Given the disagreement for obtaining an optimal bin-size I will assume that the most satisfactory bin-size is in between 30 and 100, as found in the literature. Later in this section we will discuss the effect of the choice of bin-size on the different parameters extracted from the hypsometric curve.

1) Method and validation

A distinctive parameter critical for the obtention of the hypsokyrtome is S_f, the reference hypsometric curve slope that will ultimately define if the dominant process shaping the landscape is fluvial or glacial. Assuming that mountain ranges can be divided into glacial dominated and fluvial dominated, S_f is defined as the reference curvature value of the fluvial dominated landscape hypsometric curve. Given the variety of fluvial landforms depending on climate and tectonics, S_f must be evaluated for the given tectono-climatic context of each study area. In a glaciated landscape, erosion has been empirically demonstrated to be maximized around and above the equilibrium line altitude (ELA) [*Brozovic et al.*, 1997; *Brocklehurst and Whipple*, 2004; *Egholm et al.*, 2009]. Thus, the characteristic reference value S_f must be computed in the area below the presumed ELA altitude, where fluvial processes dominate.. The departure between the S_f value and the slope of the hypsometric curve will provide de degree of glacial imprint of the landscape.

I calculated S_f as the mean curvature (derivative) of the lower half of the hypsometric curve for three different DEMs reflecting the three different ELA estimates: 3500 m [*Cui et al.*, 2002], 3000 m [*Böse*, 2004] and 2100 m (this study). The extraction of the hypsometric curve was made for the whole DEM of Taiwan below each of the ELA estimates. This method for extracting S_f differs from the one described in *Sternai et al.* (2011), as instead of extracting the value from a certain number of hypsometric curves extracted with a given window size running on the DEM, I extracted it from a single hypsometric curve from the whole DEM below the ELA. This method has been validated by the author of the paper describing the method (P. Sternai, personal communication 2013). S_f values using the original and my method differ from each (Compare the S_f value of 1.58 given in the original paper for an ELA of 3500m and the values from Table 4.2), and both will be used in the final computation of H_{kr}.

Evaluation of the effect of the choice of bin-size and ELA on the value of S_f is shown in Table 4.2 and Fig. 4.12. Table 4.2 also shows the values calculated for the inferred glaciated part of the orogen, above the each of the ELA estimates. S_f for the areas below the ELA varies from 0.88 to 1.10 for bins between 1 to 100. Higher values are generally found for small bin size (i.e. values equal to 1 and 10), and for lower ELA's (Fig. 4.12). However, overall the variability for different ELA is quite low.

		ELA=3500 m *(Cui et al., 2002)*		***ELA=3000 m*** *(Bose et al, 2004)*		***ELA=2100 m*** *(This study)*	
		<*ELA*	>ELA	<ELA	>ELA	<ELA	>ELA
	Relief (m)	3500	454	3000	954	2100	1854
bin=1	***Sf***	**0.99**	**0.70**	**1.05**	**0.77**	**1.09**	**0.62**
	HI	0.22	0.23	0.25	0.203	0.27	0.25
	~HI	0.22	0.23	0.25	0.203	0.27	0.25
Bin =5	***Sf***	*n.a.*	**0.73**	*n.a.*	**0.79**	*n.a.*	**0.63**
	HI	*n.a.*	0.22	*n.a.*	0.20	*n.a.*	0.25
	~HI	*n.a.*	0.22	*n.a.*	0.20	*n.a.*	0.25
bin=10	***Sf***	**0.99**	**0.77**	**1.05**	**0.82**	**1.10**	**0.63**
	HI	0.22	0.21	0.25	0.20	0.27	0.24
	~HI	0.22	0.22	0.25	0.20	0.27	0.25
bin=30	***Sf***	**0.89**	**0.92***	**0.94**	**0.91***	**0.99**	**0.65**
	HI	0.25	0.18*	0.28	0.18*	0.31	0.23
	~HI	0.21	0.22*	0.24	0.18*	0.26	0.24
bin=50	***Sf***	**0.88**	**1.39***	**0.94**	**1.11***	**1.00**	**0.70**
	HI	0.25	0.16*	0.28	0.17*	0.31	0.23
	~HI	0.21	0.17*	0.24	0.18*	0.26	0.24
bin=100	***Sf***	**0.91**	*n.a.*	**1.00**	*n.a.*	**1.06**	*n.a.*
	HI	0.24	*n.a.*	0.27	*n.a.*	0.29	*n.a.*
	~HI	0.21	*n.a.*	0.24	*n.a.*	0.25	*n.a.*

Table 4.2*: Extracted parameters values from whole DEM values below 3 different estimates of ELA.* ***S_f*** *(gradient of the lower half of the hypsometric curve),* ***HI*** *(hypsometric integral), and* ***~HI*** *(common approximation to the hypsometric integral equal to (hmean-hmin)/(hmax-hmin).* indicates bin-size value giving very rough and imprecise hypsometric curves, insufficient points. Relief is indicated so that the relation between bin-size and "roughnes" or accuracy of the extracted values can be assessed.*

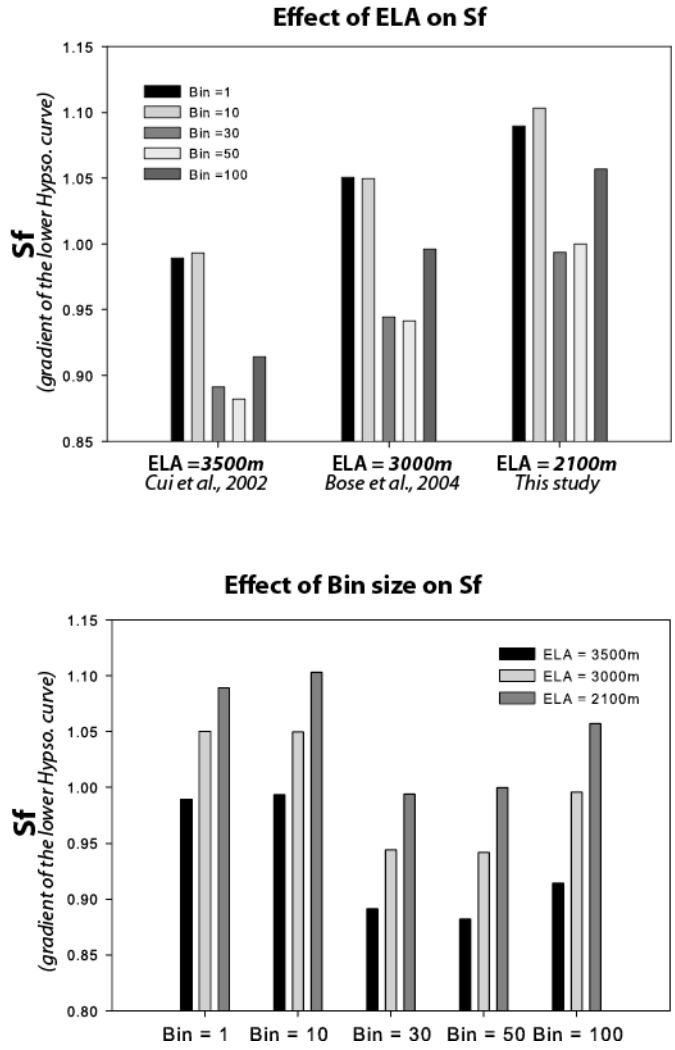

Fig. 4.18*: Graphic representation of Sf values for the DEM below the ELA form Table 4.2.*

Hypsometric integral (HI) for the areas below the ELA has values between 0.22 and 0.31 (Table 4.2). Lower values are generally for bins equal to 30 and 50, and low elevation ELA (e.g. 2100m). Overall the values show low variability with varying ELA and bin.

When comparing HI and Sf values obtained for the inferred supposed fluvial (<ELA) and glaciated (>ELA), we can see that systematically Sf and HI values are lower for the inferred glaciated part (Table 4.2). This observation either confirms the validity of the approach or shows that other processes may imprint the landscape with glacial like high curvature valleys (landslides? high altitude alluvial channels?).

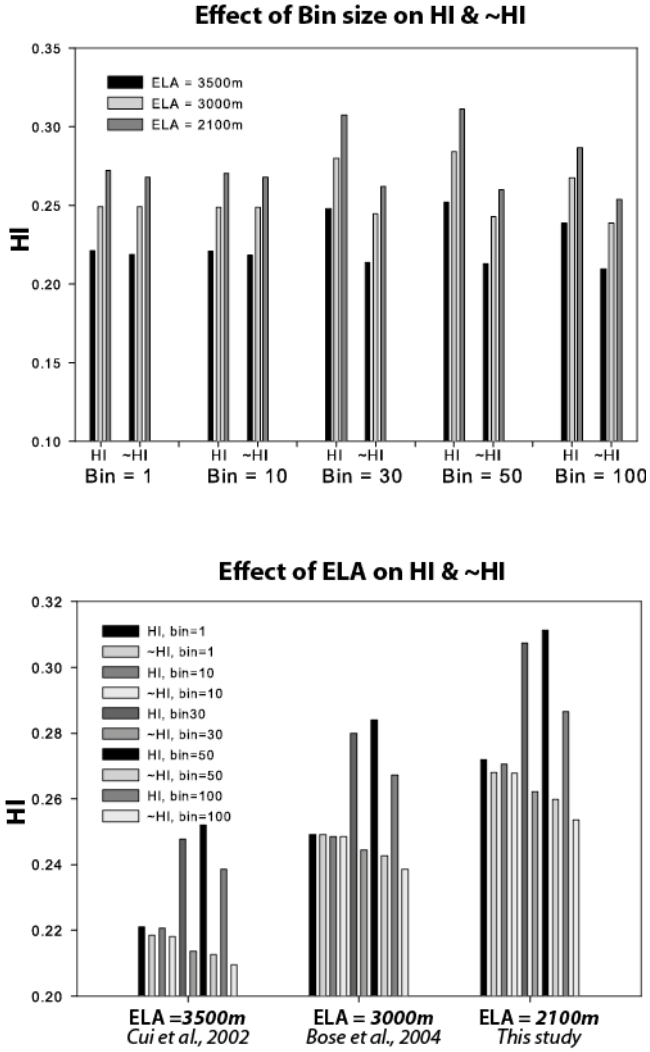

Fig. 4.19*: Sf is defined as the gradient of the lower half of the hypsometric curve. HI is the hypsometric integral and ~HI is a common approximation of the hypsometric integral defined as (hmean – hmin)/(hmax-hmin), h been altitude.*

In this approach I extract hypsometric curves form a grid of squared cells rather than extracting it from basins. This eliminates the effect of basin outlet geometry on the lower part of hypsometric curves. I need thus to choose an optimal cell size, or window, where the hypsometric curve, its integral and Hkr will be calculated. Here I use the methodology suggested by *Sternai et al*. (2009), the empirical variogram 2γ indicating correlation between the data, and defined as the expected square variance of the observation at different measurements; defined as follows (*Sternai et al*., 2011):

$$2\gamma_k = \frac{\sum_{i=1}^{N}(H_{kr}{}_{(i)}^{(c+k)} - H_{kr}{}_{(i)}^{(c)})^2}{N}$$

where k is the increment in pixels (=1; 2;3;...), n is the increment on the length of the cell, c is the minimum cell length and N the total number of pixels. Fig. 4.20 shows the resulting semivariograms for different values of S_f and bin-size.

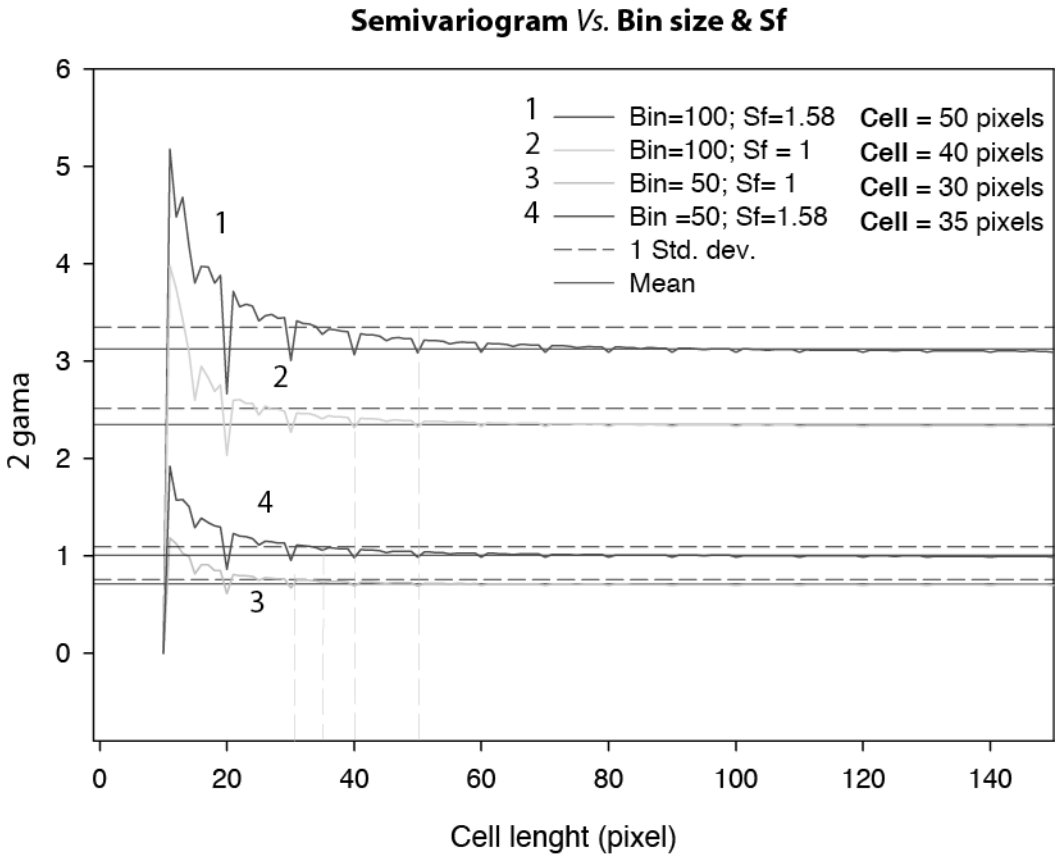

***Fig. 4.20**: Semivariogram showing the ideal output cell size for different bin sizes and Sf. Computed on a 40m DEM of the whole island of Taiwan.*

In practice, the semivariogram allows extracting the minim optimal cell size (or window size) used to extract H_{kr} so that the general topographic signature is preserved without sampling biases. I choose the cell size from the semivariogram when the curve becomes relatively constant, below the 1 standard deviation (Fig. 4.20). From Fig. 4.20 we can see that lower bin size implies lower optimal cells, and that lower S_f values for a same bin-size gives also lower optimal cell values.

2) Results

a) Basin Hypsometry

Grouped basin hypsometry show very different values area/altitude distribution for the different geological and hydrological areas of Taiwan (Fig. 4.6). I tested different groups of basins, either related to the lithology drained by the basins, or related to their relative position in the mountain belt (i.e. eastern-western divide). All the resulting elevation-area distributions are presented in fig. A4.1 (Annexe 3), here I present a representative selection.

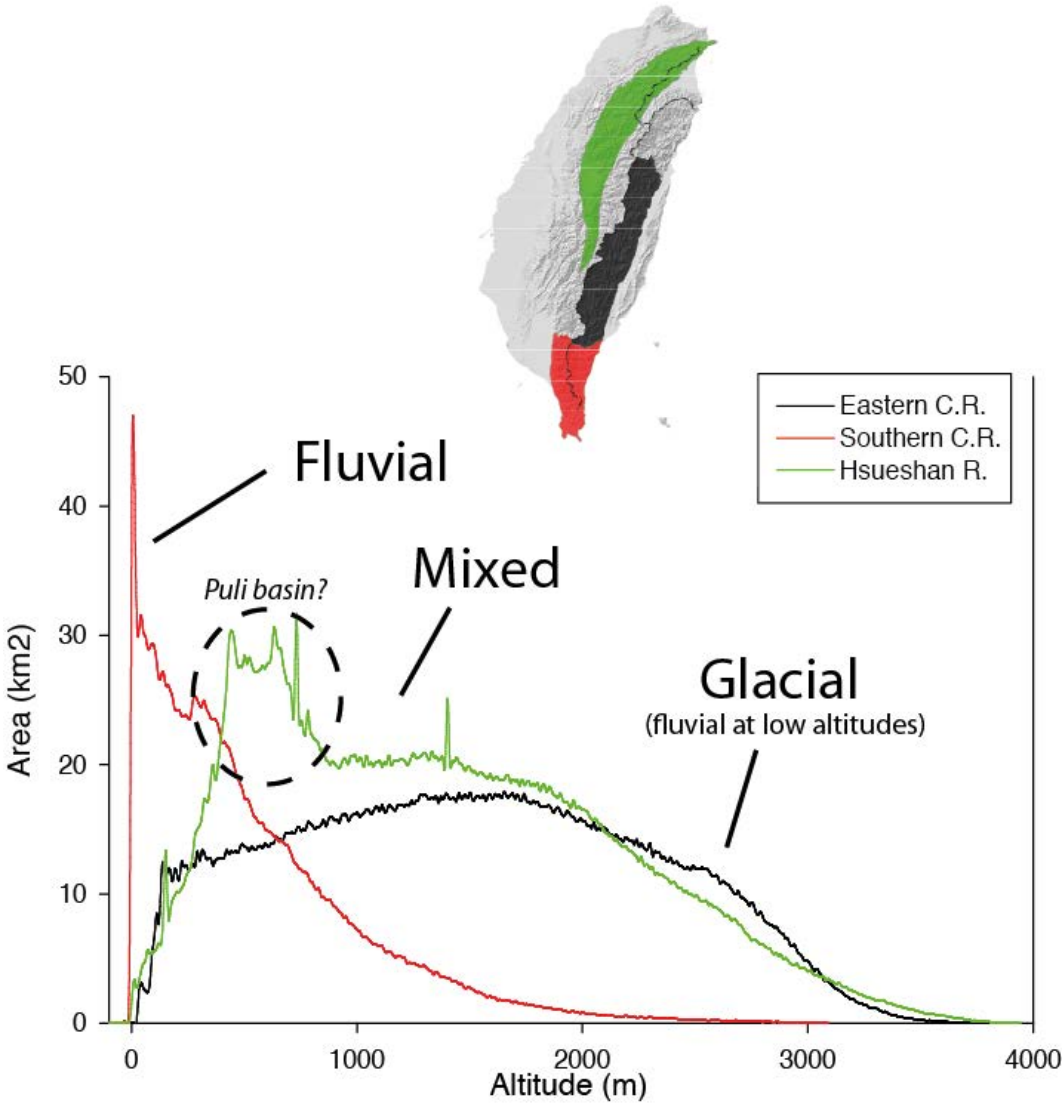

Fig. 4.21 *: Representative hyspmetric curves of the three regions of the Central Range. A tentative interpretation of the processes behind the distribution is also shown. Note that here interpreted as fluvial dominated hypsometric curve corresponds to areas with weak lithologies dominated by unmetamorphised or slightly metamorphosed (prehnellite-pumpelite facies) sedimentary cover areas.*

The three selected regions present very different hypsometric area altitude distribution (fig, 4.21). The southern Central range is dominated by low altitudes and skewed towards the higher altitudes. The Hhsueshan Range presents an overall domal shaped distribution with an anomalously high area between 500 m and 800 m. The central basin from the eastern Central range presents a distribution close to binomial (fig. 4.22) with a mean altitude of 1512 m and a mode height 1546 m (Fig. 4.22). The hypsometric distribution departs from the binomial distribution at low altitudes and also at altitude between 2500 m and 2900 m.

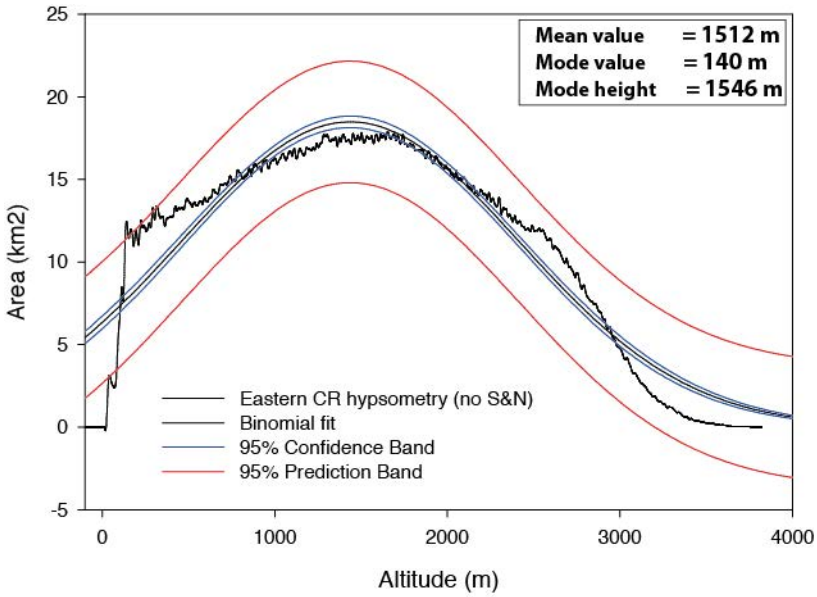

***Fig. 4.22**: binomial fit of the eastern Central Range basins hyspometry.*

b) Hypsokyrtome

A selection of the resulting maps of hypsokyrtome is shown in Fig. 4.23 and 4.24. The general pattern of high H_{kr} values can be seen form larger bin-sizes and cell-size although smaller bin-size and cell-size appear to delineate more precisely patterns of grouped high- H_{kr} . Generally, high H_{kr} values follow the topographic crest in the southern part with some patches in areas where we recognised low-relief zones.

The method appear to recognise areas where glaciated landscape has been described in the literature, as in the Chia Ming lake and Yushan where high values of H_{kr} are found (white-dashed square in Fig. 4.23). Conversely, rivers are relatively well delineated with quite systematically low values of H_{kr}.
High H_{kr} are also found in many other areas mainly along the crests and drainage divide or the upstream parts of drainage basins and alluviated channels. Patches of particularly high H_{kr} coincide if some the low-relief areas indentified earlier. However extracting a clear trend from the raw maps is quite difficult. A neighbourhood interpolation allows more visually exploitable identification of areas with particularly high value of H_{kr} (Fig. 4.24)

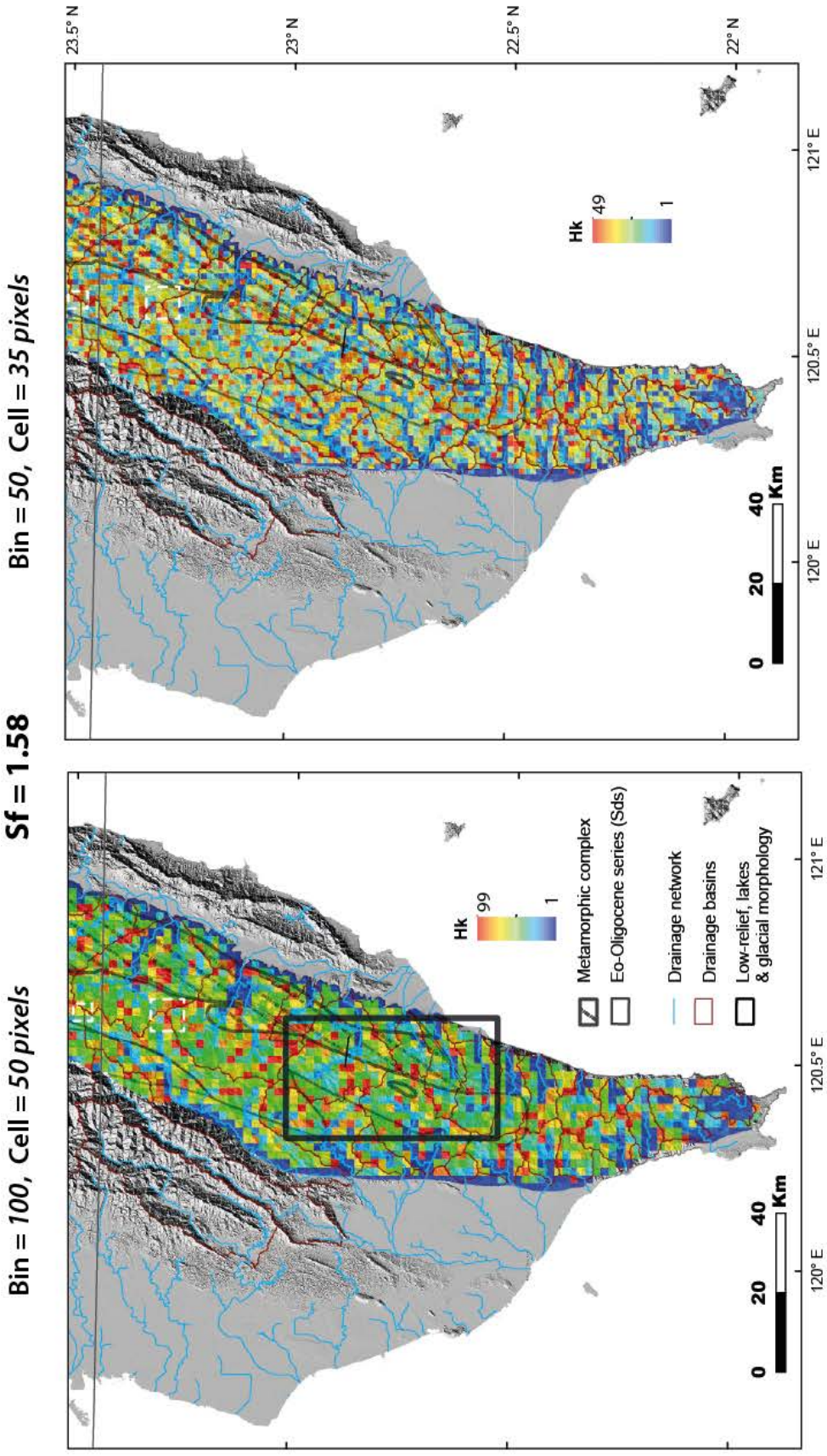

Fig. 4.23: *a) Hypsokyrtome maps for Sf = 1.58 (value given by Sternai et al., 2011) for two different bin and cell size. Black square indicates location of Fig. 4.24. White dashed square indicate location of glaciated landscape described in the literature.*

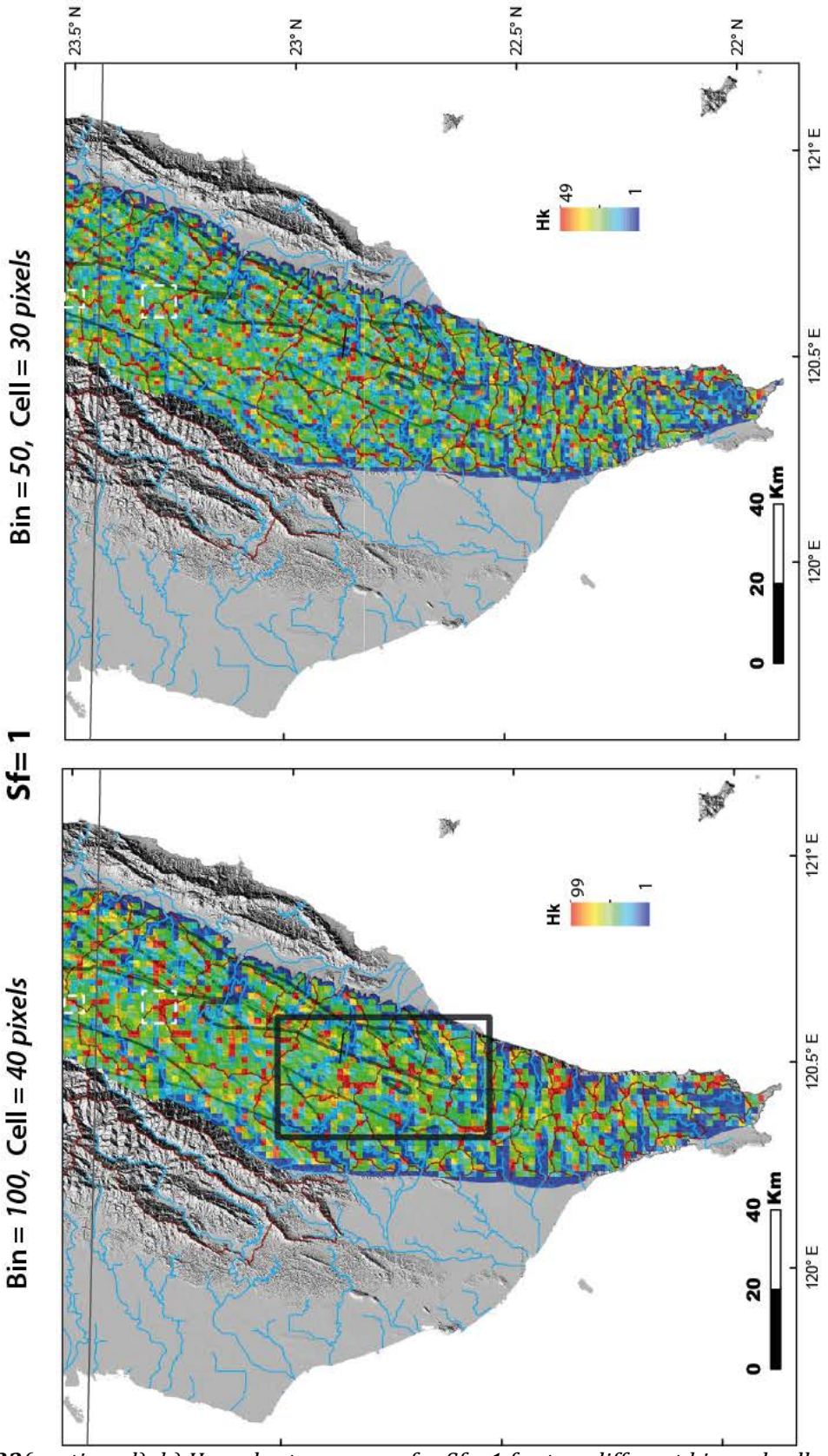

Fig. 4.23*(continued): b) Hypsokyrtome maps for Sf = 1 for two different bin and cell size. Black square indicates location of Fig. 4.24. White dashed square indicate location of glaciated landscape described in the literature*

When giving a closer look to the areas where lakes and presumable glacial morphologies were observed in the previous section (Fig. 4.24), we can see that our described postulated glacial morphologies correspond to high values of H_{kr} (~50 to 70) including the U-shaped valleys (fig. 4.13) and lake areas. Particularly the drainage divide anomaly and the Great ghost lake areas (Fig. 4.12 and Fig. 4.13) yield very high values of H_{kr}.

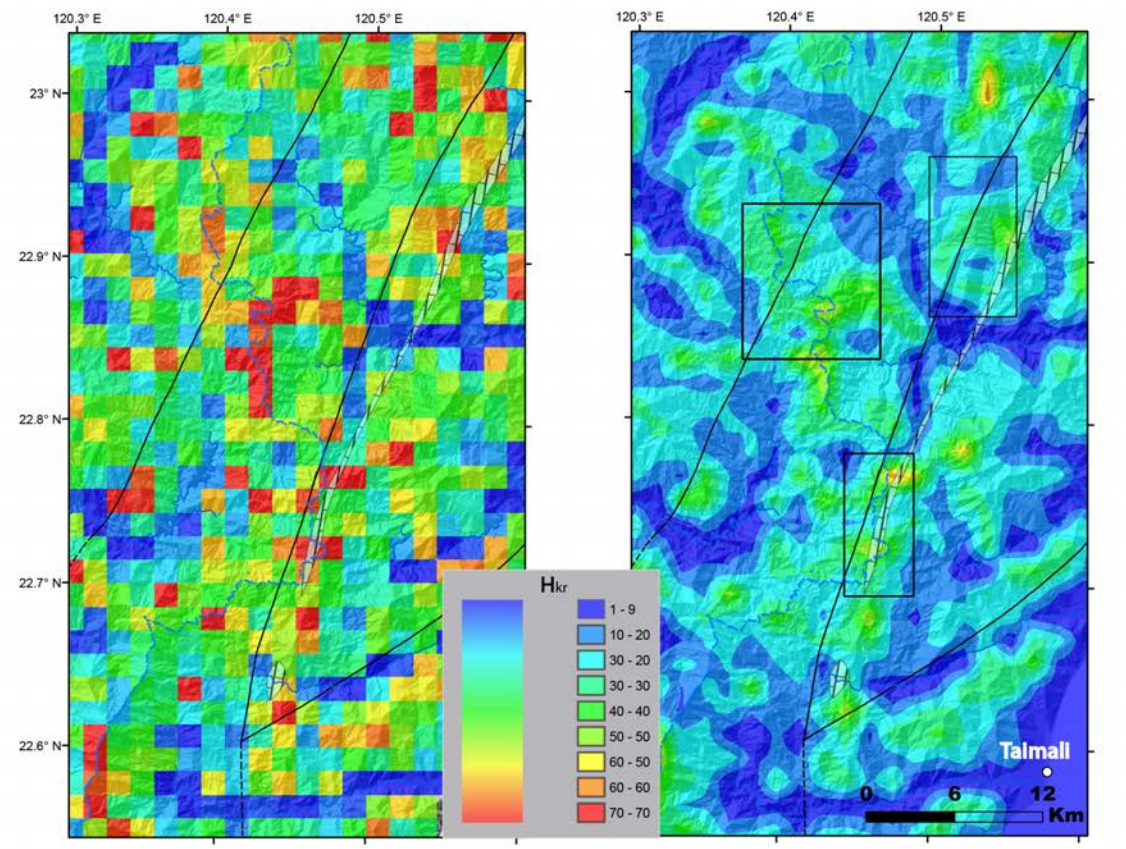

Fig. 4.24*: Hypsokyrtome for Sf =1, bin = 100 and cell = 40pixels, at the drainage anomaly where glacial landscape was described in the previous section. On the left panel, the output H_{kr} values, on the right panel a natural neighborhood interpolation of the same H_{kr} map. Squares on the right panel show the low relief areas shown in Fig. 4.12 and 4.13.*

Overall, high H_{kr} values appear to match our low relief areas and glacial morphologies described in the previous section. However the signal is quite noisy and many other areas yield high H_{kr} values. Further evidences andmore detailed field-based studies are needed to confirm the extent of glacial imprint in Taiwan and the glacial origin of low-relief areas.

III. Conclusions

The presence of relic landscape eroding at very low rates in southern Taiwan is a quite surprising result of this study. Morphologies appear to yield significant similarities with glacial landscapes, and the presence of lakes is difficult to explain otherwise. U-shape valleys downstream the low-releif areas and lakes

also support a glacial inception. The review of the paleo-climatic record of Taiwan allows for lower ELA in the past glacial cycle, probably in the MIS-4. Because ground-truthing was not possible due to inaccessibility and lack of time, the use of morphometric analysis offered the opportunity to test the glaciogenic origin of the low-relief areas. I found a binomial distribution of hypsometric integral in the eastern Central Range were the metamorphic core is outcropping. Wheter this results from lithological differential strength or that the binomial distribution is really centrered around the MIS-4 paleo ELA, as suggested by a number of studies in glaciated areas [*Brocklehurst and Whipple*, 2004; *Brozovic et al.*, 1997; *Egholm et al.*, 2009], remains an unanswered question to be further tested. High hypsokyrtome values were found to correspond relatively well with the low-relief areas. However some other areas such as alluvial rivers, appear to present high values and, thus, the results need to be taken with caution. Field evidences are needed to further confirm the glacial origin of the low-relief areas.

Glacial or not, the preservation of such ancient landforms tends to dismiss the topographic steady state usually assumed in Taiwan. The original argument leading to this assumption was the relatively constant height of the drainage divide in its central part (*Suppe,* 1984) and the constant width of the Central range along different "time" sections in the orogen. Assuming that erosion is maximized at ELA altitude as argued by numerous authors (*Brozovic et al.*, 1997; *Egholm et al.*, 2009), the relative constant height could be a result of the glacial buzzsaw.

GENERAL CONCLUSIONS

In the attempt to provide new clues to understand the development of southern Taiwan mountain belt, this work was divided into three main chapters, of which I summarize the main results below.

1) Structure of southern Taiwan

Structural analysis of southern Taiwan indicates a general doubly-vergent fan-shaped structure delineated by a penetrative, mainly coaxial deformation that probably witness deformation at temperature above 240-300°C. The apex of the fan-shaped schistosity is outlined by a main structural boundary (SZ-1), characterized by an early transpressive phase, and late, mostly brittle, dominant normal sense of shear.

I suggest that this main boundary corresponds to the western boundary of the southern extension of the metamorphic core structure (Fig. 2.11). Its geometry and movement both suggest that this main tectonic boundary accompanied the exhumation of the metamorphic core, although further study on its prolongation at depth needs to be done.

A structural unit to the East is characterized by a flat-lying schistosity and some East-West folds, and may either be related to a west-vergent incorporation of forearc cover sediments, or to the continuation of the tightly folded wedge sediments.

Southern Taiwan therefore maybe viewed as the place where east-vergent backfolding is incipient. Although, partly related to the indentation by the upper forearc crust, exhumation by extrusion of deeper crustal units may be an important element controlling the recent tectonic pattern in the area.

Southern Taiwan was initially thought to represent the transition from oceanic subduction to arc-continental collision. Based on my own observations and inferences from thermochronological data, it should be better view as to be situated at the transition between extremely-thinned margin collision and arc/weakly-thinned margin collision.

2) Low-temperature thermochronological constraints: dating collisional processes

From a methodological point of view, we have confirmed the use of young-peak-ages for the ZFT system, and the potential use of ZFT as a "multi" thermochronometer, with variably alpha-damaged zircon populations recording different events. Quantification of radiation damage is probably the big step hampering this potentiality.

Low-temperature thermochronolgical analyses from southern Taiwan suggest that collision initiated at ~7.1±1.3 Ma and is related to the arrival of the South China Sea hyper-extended distal parts of the margin. This phase may be linked to the inversion of the distal margin and formation of the Kenting mélange in south Taiwan. The thermochronological record of this initial phase is still preserved in the Central Range, mainly in the western divide, as we documented in the southwestern foreland detrital record.

A major phase of topographic growth and exhumation occurs at ~3.2±0.6Ma after subaerial exposure. This marks the onset of fore-arc closure (Lichi mélange formation) to the east, and the contact with a weakly thinned proximal margin to the west. This phase is associated with the initiation of (or accentuation of a pre-existing) east vergent back-folding and west dipping schistosity development in the Central Range. This phase ultimately leads to a preferential exhumation of the eastern divide (retro-wedge), as shown in the detrital record in the central Coastal Range basins where orogenic zircon starts at 1.9 Ma [*Kirstein et al.*, 2010]. No such reset grains are seen in the same age sediments of the western foreland.

Although not directly constrained by our data, an additional phase of frontal propagation and increased exhumation since ~2 Ma is evidenced by post-depositional foreland sediments apatite U-Th/He reset ages [*Lock*, 2007] and by 1-2Ma ZFT ages in the metamorphic core

3) Morphology of southern Taiwan: arguments for a glaciated landscape

Low-relief surfaces are preserved in the southern Central Range. They are mainly positioned on the drainage divide and on top of the metamorphic complexes. Preservation of this surfaces is guaranteed by very low-erosion rates in those areas (~0.01 cm/yr for the last 2000 yrs, *Chen et al.*, 1997), as opposed to the adjacent landslide dominated areas.

GIS analysis and existing publications on the low relief areas indicate the presence of 1) lateritic, clay rich soils, 2) multiple round to ellipsoidal-shaped lakes, 3) rectilinear trough depressions, 4) peri-glacial morphologies (e.g. solifluction figures); overall, quite typical glacial morphology. However stronger field evidences are needed to confirm the glacial origin.

Finally, the spatial coincidence of the relic glacial landscape and the deepest exhumed rocks, suggest a potential role of glaciation in the exhumation of the Central Range, although it needs to be confirmed by stronger field evidences. This raises the question of whether present-day erosion rates from suspended sediments measurements can be extended to times larger than a glacial cycle (~10's kyr). This morphological configurations appears to be in agreement with published numerical models where glacial erosion controls the location of the maximum erosion and deformation and the coincidence of maximum erosion with the topographic divide for areas where topography is close to the ELA [*Tomkin*, 2007; *Tomkin and Roe*, 2007]. Elswhere, the presence of a systematic-break-slope in ZFT age-altitude profile at ~1500m all alonghte island, within

different geological units, and at different ages hint for some geomorphologicallly-controlled process having probably strong influences on long-term exhumation.

Extrapolation of present-day erosion rates to geological times, especially considering that glacial periods are long-lasting compared to interglacial, and thus could potentially dominate the long term exhumational signal. Although, very vigorous at present-day, fluvial erosion may have contributed realtively less than previously assumed to the long-term erosion, and its role may possibly consist more into exporting the glacially eroded material, as suggested by the timing of increased Taiwan derived sediment export to the oceans right after Taiwan's major glacial period (MIS4; Fig. 4.16). Another hypothesis is that glacially derived sediments could have provided the "tools" to carve the depply inced valleys observed in Taiwan. This may partly explain the apparent inconsistency between the location of long-term and short-term erosion rates documented in Taiwan, despite similar values [*Dadson et al.*, 2003; *Dadson*, 2004].

The extension of widespread glaciation into the tropics may explain the worldwide increase in erosion/sedimentation in low latitude areas, and may come as a factual prove confirming glaciers as being major erosive agents, and major contributors to long term exhumation in mountain belts, as recently suggested by other studies [*Herman et al.*, 2013].

The predicted behaviors for a climatically-forced wedge are not met. Frontal propagation seems to have taken place since ~2 Ma as evidenced by deformed Plio-Pleistocene foreland conglomeratic deposits all along western Taiwan. Nevertheless, subsidence in the foreland has increased and out-of sequence thrusting occurred in southern Taiwan (e.g. the Chishan thrust; Chaochou-Laonung fault; Meishan fault). Dating the initiation of out-of-sequence thrusting remains difficult and is probably the main issue to be solved to confirm or dismiss a climatic forcing. The effective field test by *Whipple* (2009) may not be totally adapted to the Taiwan case, as changing essentially fast convergence rates probably triggered punctuated frontal propagation. It could also be that the basic assumption of a steady-state wedge is not met in Taiwan. The Taiwan orogen has very likely not reached topographic steady-state as shown by the presence of relic landscape and confirmed by other recent stuides [*Willett et al.,* 2014]. The original reason based on which topographic steady-state is based on (constant divide height, *Suppe*, 1981) may just be a results of the glacial buzzsaw [*Brozovic et al.*, 1997; *Egholm et al.*, 2009], if the low relief areas came to be confirmed as glacial in origin. Similarly, the relatively constant morphometric parameters along the eastern Central Range [*Stolar et al.*, 2007] may just indicate a constant and widespread glacial imprint in this areas instead of a steady-state topography.

All together, this study brings important insights on the long-to-short term evolution of the Taiwanese mountain belt, from the first incorporation of thinned continental crust into the wedge to the Late Cenozoic climatic shift to glacial-interglacial periods.

Bibliography

Ahnert, F. (1970), Functional relationships between denudation, relief, and uplift in large, mid-latitude drainage basins, *Am. J. Sci.*, *268*(3), 243–263.

Allen, P. (2005), Striking a chord., *Nature*, *434*(7036), 961, doi:10.1038/434961a.

Allen, P. a (2008a), From landscapes into geological history., *Nature*, *451*(7176), 274–6, doi:10.1038/nature06586.

Allen, P. A. (2008b), Time scales of tectonic landscapes and their sediment routing systems, in *Landscape Evolution: Denudation, Climate and Tectonics Over Different Times and Space scales*, edited by K. Gallagher, S. Jones, and J. Wainwright, pp. 7–28, Geological Society, London, Special Publications.

An, Z., J. E. Kutzbach, W. L. Prell, and S. C. Porter (2001), Evolution of Asian monsoons and phased uplift of the Himalaya-Tibetan plateau since Late Miocene times, *Nature*, *411*(May), 62–66.

Angelier, J., T.-Y. Chang, J.-C. Hu, C.-P. Chang, L. Siame, J.-C. Lee, B. Deffontaines, H.-T. Chu, and C.-Y. Lu (2009), Does extrusion occur at both tips of the Taiwan collision belt? Insights from active deformation studies in the Ilan Plain and Pingtung Plain regions, *Tectonophysics*, *466*(3-4), 356–376, doi:10.1016/j.tecto.2007.11.015.

Aurelio, M. A. (1992), Tectonique du segment central de la faille philippine: Etude structurale, cinématique et évolution géodynamique = Tectonics of the central segment of the Philippine Fault: structures, kinematics, geodynamic evolution, 500 pp., Université de Paris 06, Paris, FRANCE.

Aurelio, M. A. (2000), Shear partitioning in the Philippines: Constraints from Philippine Fault and global positioning system data, *Isl. Arc*, *9*, 584–597.

Avouac, J.-P., and E. Burov (1996), Erosion as a driving mechanism of intracontinental mountain growth, *J. Geophys. Res.*, *101*(B8), 17747–17769.

Barbarand, J., A. Carter, I. Wood, and A. J. Hurford (2003), Compositional and structural control of fission-track annealing in apatite, *Chem. Geol.*, *198*(1-2), 107–137, doi:10.1016/S0009-2541(02)00424-2.

Barckhausen, U., M. Engels, D. Franke, S. Ladage, and M. Pubellier (2014), Evolution of the South China Sea: Revised ages for breakup and seafloor spreading, *Mar. Pet. Geol.*, doi:10.1016/j.marpetgeo.2014.02.022.

Barr, T. D., and F. A. Dahlen (1989), Brittle Frictional Mountain Building 2. Thermal Structure and Heat Budget, *J. Geophys. Res.*, *94*(88), 3923–3947.

Barr, T. D., F. A. Dahlen, and D. C. McPhail (1991), Brittle Frictional Mountain Building 3. Low-Grade Metamorphism, *J. Geophys. Res.*, *96*(B6), 10319–10338, doi:10.1029/91JB00295.

Barrier, E. (1985), The two stage collision of Taiwan: an active orogen, *Tectonophysics*, *115*, 167–175.

Batt, G. E., and M. T. Brandon (2002), Lateral thinking: 2-D interpretation of thermochronology in convergent orogenic settings, *Tectonophysics*, *349*(1-4), 185–201, doi:10.1016/S0040-1951(02)00053-7.

Batt, G. E., and J. Braun (1997), On the thermomechanical evolution of compressional orogens, *Geophys. J. Int.*, *128*(2), 364–382, doi:10.1111/j.1365-246X.1997.tb01561.x.

Beaumont, C., P. Fullsack, and J. Hamilton (1992), Erosional control of active compressional orogens, in *Thrust Tectonics*, edited by K. McClay, pp. 1–18., Chapman and Hall, London.

Beaumont, C., S. Ellis, J. Hamilton, and P. Fullsack (1996), Mechanical model for subduction-collision tectonics of Alpine-type compressional orogens, *Geology*, *24*(8), 675–678, doi:10.1130/0091-7613(1996)024<0675.

Beaumont, C., H. Kooi, and S. D. Willett (2000), Coupled tectonic-surface process models with applications to rifted margins and collisional orogens, in *Geomorphology and Global Tectonics*, edited by M. A. Summerfield, pp. 29–55, John Wiley & Sons Ltd,.

Beaumont, C., R. A. Jamieson, M. H. Nguyen, and B. Lee (2001), Himalayan tectonics explained by extrusion of a low-viscosity crustal channel coupled to focused surface denudation., *Nature*, *414*(6865), 738–42, doi:10.1038/414738a.

Beltrando, M., G. Manatschal, G. Mohn, G. V. Dal Piaz, A. Vitale Brovarone, and E. Masini (2014), Recognizing remnants of magma-poor rifted margins in high-pressure orogenic belts: The Alpine case study, *Earth-Science Rev.*, *131*, 88–115, doi:10.1016/j.earscirev.2014.01.001.

Berger, A. L. et al. (2008), Quaternary tectonic response to intensified glacial erosion in an orogenic wedge, *Nat. Geosci.*, *1*(11), 793–799, doi:10.1038/ngeo334.

Bernet, M., and J. I. Garver (2005), Fission-track Analysis of Detrital Zircon, in *Low-Temperature Thermochronology: Techniques, Interpretations, and Applications*, vol. 58, edited by P. W. Reiners and T. A. Ehlers, pp. 205–237, Reviews in Mineralogy and Geochemistry.

Bernet, M., and C. Spiegel (2004), Introduction: detrital thermochronology, in *Detrital thermochronology—Provenance analysis, exhumation, and landscape evolution of mountain belts*, vol. 378, edited by M. Bernet and C. Spiegel, pp. 1–6, Geological Society of America.

Bernet, M., M. T. Brandon, J. I. Garver, and B. Molitor (2004), Fundamentals of detrital zircon fission-track analysis for provenance and exhumation studies with examples from the European Alps, *Geol. Soc. Am. Spec. Pap.*, *378*, 25–36.

Beyssac, O., M. Simoes, J.-P. P. Avouac, K. a. Farley, Y.-G. Chen, Y.-C. Chan, and B. Goffé (2007), Late Cenozoic metamorphic evolution and exhumation of Taiwan, *Tectonics*, *26*(6), 1–32, doi:10.1029/2006TC002064.

Beyssac, O., F. Negro, M. Simoes, Y. C. Chan, and Y. G. Chen (2008), High-pressure metamorphism in Taiwan: from oceanic subduction to arc-continent collision?, *Terra Nov.*, *20*(2), 118–125, doi:10.1111/j.1365-3121.2008.00796.x.

Biq, C. (1977), The Kenting Mélange and the Manila Trench., *Proc. Geol. Soc. China*, *20*, 119–122.

Boillot, G. et al. (1987), Tectonic denudation of the upper mantle along passive margins : a model based on drilling results (ODP leg 103, western Galicia margin, Spain), *Tectonophysics*, *132*(2).

Bonnet, S., and A. Crave (2003), Landscape response to climate change: Insights from experimental modeling and implications for tectonic versus climatic uplift of topography, *Geology*, *31*(2), 123, doi:10.1130/0091-7613(2003)031<0123:LRTCCI>2.0.CO;2.

Böse, M. (2004), Traces of glaciation in the high mountains of Taiwan, *Dev. Quat. Sci.*, (1983).

Böse, M., and R. Hebenstreit (2008), Late Pleistocene and Early Holocene Glaciations in the Taiwanese High Mountain Ranges, in *Quaternary Glaciations - Extent and Chronology*, edited by J. Ehlers, P. Gibbard, and P. Hughes, pp. 1003–1012.

Brandon, M. T. (1992), Decomposition of fission-track grain-age distribution, *Am. J. Sci.*, (October), 535–564.

Brandon, M. T. (1996), Probability density for fission-track grain-age samples, *Radiat. Meas.*, *26*(5), 663–676.

Brandon, M. T., M. K. Roden-Tice, and J. I. Garver (1998), Late Cenozoic exhumation of the Cascadia accretionary wedge in the Olympic Mountains, northwest Washington State, *GSA Bull.*, *110*(8), 985–1009.

Braun, J. (2002), Quantifying the effect of recent relief changes on age–elevation relationships, *Earth Planet. Sci. Lett.*, *200*(3-4), 331–343, doi:10.1016/S0012-821X(02)00638-6.

Braun, J. (2006), Recent advances and current problems in modelling surface processes and their interaction with crustal deformation, in *Analogue and Numerical Modelling of Crustal-Scale Processes*, edited by S. J. H. Buiter and G. Schreurs, pp. 307–325, Spec. Publ. Geol. Soc. Lond. 253.

Braun, J., P. Van der Beek, and G. E. Batt (2006), *Quantitative Thermochronology: Numerical Methods for the Interpretation of Thermochronological Data*, Cambridge University Press, Cambridge.

Braun, J., F. Herman, and G. E. Batt (2010), Kinematic strain localization, *Earth Planet. Sci. Lett.*, *300*(3-4), 197–204, doi:10.1016/j.epsl.2010.08.018.

Braun, J., P. van der Beek, P. Valla, X. Robert, F. Herman, C. Glotzbach, V. Pedersen, C. Perry, T. Simon-Labric, and C. Prigent (2012), Quantifying rates of landscape evolution and tectonic processes by thermochronology and numerical modeling of crustal heat transport using PECUBE, *Tectonophysics*, *524-525*, 1–28, doi:10.1016/j.tecto.2011.12.035.

Brocklehurst, S. H., and K. X. Whipple (2004), Hypsometry of glaciated landscapes, *Earth Surf. Process. Landforms*, *29*(7), 907–926, doi:10.1002/esp.1083.

Brown, D., J. Alvarez-Marron, M. Schimmel, Y.-M. Wu, and G. Camanni (2012), The structure and kinematics of the central Taiwan mountain belt derived from geological and seismicity data, *Tectonics*, *31*(5), TC5013, doi:10.1029/2012TC003156.

Brozovic, N., D. W. Burbank, and A. J. Meigs (1997), Climatic Limits on Landscape Development in the Northwestern Himalaya, *Science (80-.).*, *276*(5312), 571–574, doi:10.1126/science.276.5312.571.

Brun, J. P., and M. O. Beslier (1996), Mantle exhumation at passive margins, *Earth Planet. Sci. Lett.*, *142*(1-2), 161–173, doi:10.1016/0012-821X(96)00080-5.

Burchfiel, B. C., L. H. Royden, R. D. van der Hilst, B. H. Hager, Z. Chen, R. W. King, C. Li, J. Lü, H. Yao, and E. Kirby (2008), A geological and geophysical context for the Wenchuan earthquake of 12 May 2008, Sichuan, People's Republic of China, *GSA Today*, *18*(7), 4, doi:10.1130/GSATG18A.1.

Bürgmann, R., and G. Dresen (2008), Rheology of the Lower Crust and Upper Mantle : Evidence from Rock Mechanics , Geodesy , and Field Observations, *Annu. Rev. Earth Planet. Sci.*, *36*, 531–567, doi:10.1146/annurev.earth.36.031207.124326.

Burov, E. B. (2011), Rheology and strength of the lithosphere, *Mar. Pet. Geol.*, *28*(8), 1402–1443, doi:10.1016/j.marpetgeo.2011.05.008.

Burov, E. B., and A. B. Watts (2006), The long-term strength of continental lithosphere:" jelly sandwich" or" crème brûlée"?, *GSA today*, *16*(1), 4, doi:10.1130/1052-5173(2006)016<4.

Byrne, T. B., and Y.-H. Lee (2013), Not available, in *Tectonics of Taiwan International Meeting*.

Byrne, T. B., and C.-S. Liu (2002), Preface: introduction to the geology and geophysics of Taiwan., in *Geology and Geophysics of an Arc- continent Collision, Taiwan*, Geological Society of America.

Byrne, T. B., Y.-C. Chan, R.-J. Rau, C.-Y. Lu, Y.-H. Lee, and Y.-J. Wang (2011), The Arc–Continent Collision in Taiwan, in *Arc-Continent Collision*, edited by D. Brown and P. D. Ryan, pp. 213–246, Springer.

Camanni, G., D. Brown, J. Alvarez-Marron, M. Shcimmel, and Y.-M. Wu (2011), Deformation partitioning in Central Taiwan : new insights from surface geology , earthquake focal mechanisms , seismic energy

release and GPS measurements along the Shuilikeng Transpressive Fault System, *Rend. online Soc. Geol. It.*, *15*, 17–19.

Camanni, G., D. Brown, J. Alvarez-Marron, Y.-M. Wu, and H. -a. Chen (2013), The Shuilikeng fault in the central Taiwan mountain belt, *J. Geol. Soc. London.*, *171*(1), 117–130, doi:10.1144/jgs2013-014.

Camanni, G., C.-H. Chen, D. Brown, J. Alvarez-Marron, Y.-M. Wu, H.-A. Chen, H.-H. Huang, H.-T. Chu, M.-M. Chen, and C.-H. Chang (2014), Basin inversion in central Taiwan and its importance for seismic hazard, *Geology*, *42*(2), 147–150, doi:10.1130/G35102.1.

Castelltort, S., L. Goren, S. D. Willett, J.-D. Champagnac, F. Herman, and J. Braun (2012), River drainage patterns in the New Zealand Alps primarily controlled by plate tectonic strain, *Nat. Geosci.*, *5*(10), 744–748, doi:10.1038/ngeo1582.

Cederbom, C. E., H. D. Sinclair, F. Schlunegger, and M. K. Rahn (2004), Climate-induced rebound and exhumation of the European Alps, *Geology*, *32*(8), 709, doi:10.1130/G20491.1.

Champenois, J., B. Fruneau, E. Pathier, B. Deffontaines, K. Lin, and J. Hu (2012), Monitoring of active tectonic deformations in the Longitudinal Valley (Eastern Taiwan) using Persistent Scatterer InSAR method with ALOS PALSAR data, *Earth Planet. Sci. Lett.*, *338*, 144–155, doi:10.1016/j.epsl.2012.05.025.

Chan, Y. C., J. C. Lee, C. Y. Lu, and H. T. Chu (2001), Transtensional tectonics along a major north–south trending fault in the active convergent Taiwan mountain belt, in *EOS Trans. AGU Fall Meet. Suppl. 82(47) F1179.*

Chang, C.-P., J. Angelier, and C.-Y. Huang (2000), Origin and evolution of a mélange: the active plate boundary and suture zone of the Longitudinal Valley, Taiwan, *Tectonophysics*, *325*(1-2), 43–62, doi:10.1016/S0040-1951(00)00130-X.

Chang, C.-P., J. Angelier, C. Huang, and C. S. Liu (2002), Structural evolution and significance of a mélange in a collision belt: the Lichi Mélange and the Taiwan arc–continent collision, *Geol. Mag.*, *138*(06), 633–651, doi:10.1017/S0016756801005970.

Chang, C.-P., J. Angelier, T. Q. Lee, and C.-Y. Huang (2003), From continental margin extension to collision orogen: structural development and tectonic rotation of the Hengchun peninsula, southern Taiwan, *Tectonophysics*, *361*(1-2), 61–82, doi:10.1016/S0040-1951(02)00561-9.

Chang, C.-P., J. Angelier, and C.-Y. Huang (2009a), Evolution of Subductions Indicated by Mélanges in Taiwan, in *Subduction Zone Geodynamics*, edited by S. Lallemand and F. Funiciello, pp. 207–225, Springer-Verlag, Berlin Heidelberg.

Chang, C.-P., J. Angelier, and C.-Y. Lu (2009b), Polyphase deformation in a newly emerged accretionary prism: Folding, faulting and rotation in the southern Taiwan mountain range, *Tectonophysics*, *466*(3-4), 395–408, doi:10.1016/j.tecto.2007.11.002.

Chang, L.-S. (1970), A biostratigraphic study of the so-called Slate Formation on the east flank of the Central Range between Tawu and Taimali, southeastern Taiwan, based on smaller foraminifera, *Proc. Geol. Soc. China*, *13*, 129–142.

Chang, L.-S. (1971), A boistratigraphic study of the so-called slate formation in Taiwan based on smaller foraminifera: the E-W cross-mountain highway, *Proc. Geol. Soc. China*, *14*, 45–61.

Chang, L.-S. (1972), Eocene/Miocene hiatus and N conglomerate in the Central Range of Taiwan, *Proc. Geol. Soc. China*, (15), 93–98.

Chang, S. S. L., and W.-R. Chi (1983), Neogene Nannoplankton Biostratigraphy in Taiwan and the Tectonic Implications, *Pet. Geol. Taiwan*, *19*, 93–147.

Chen, C. H., H. T. Chu, J. G. Liou, and W. G. Ernst (1983), Explanatory notes for the metamorphic facies map of Taiwan, *Spec. Pub. Cent. Geol. Surv.*, (2).

Chen, C.-H. (1994), *Metamorphic Facies Map of Taiwan (1/500 000)*, CGS Specia., Central Geological Survey, The Ministry of Economic Affairs, Republic of China.

Chen, C.-H., H.-C. Ho, K.-S. Shea, W. Lo, W.-H. Lin, H.-C. Chang, C.-W. Huang, C.-N. Yang, and Y.-H. Lee (2000), Geological map of Taiwan. 1:500,000 scale, *Cent. Geol. Surv. Taipei, Taiwan*.

Chen, C.-T. A. (2001), Unveiling secrets locked in the great ghost lake in Taiwan, in *Paradoxes in Geology*, edited by U. Briegel and W. Xiao, pp. 389–409.

Chen, C.-T. A., J.-Y. Lou, J.-M. Lin, and C.-C. Chen (1997), Sedimentation rates of lakes and reservoirin Taiwan, *Oceanol. Limnol. Sin.*, *28*(6), 389–409.

Chen, C.-T. A., J.-T. Wu, B.-J. Wang, and K.-M. Huang (2004), Acidification and Trace Metals of Lakes in Taiwan, *Aquat. Geochemistry*, *10*(1/2), 33–57, doi:10.1023/B:AQUA.0000038956.17279.ff.

Cheng, K.-Y., J.-H. Hung, H.-C. Chang, H. Tsai, and Q.-C. Sung (2012), Scale independence of basin hypsometry and steady state topography, *Geomorphology*, *171-172*, 1–11, doi:10.1016/j.geomorph.2012.04.022.

Chi, W.-C., and D. L. Reed (2008), Evolution of shallow, crustal thermal structure from subduction to collision: An example from Taiwan, *Geol. Soc. Am. Bull.*, *120*(5-6), 679–690, doi:10.1130/B26210.1.

Chi, W.-R. (1979), A biostratigraphic study of the Late Neogene sediments in the Kaoshiung area based on calcareous nannofossils, *Proc. Geol. Soc. China*, *22*, 121–144.

Ching, K.-E., R.-J. Rau, J.-C. Lee, and J.-C. Hu (2007a), Contemporary deformation of tectonic escape in SW Taiwan from GPS observations, 1995–2005, *Earth Planet. Sci. Lett.*, *262*(3-4), 601–619, doi:10.1016/j.epsl.2007.08.017.

Ching, K.-E., R.-J. Rau, and Y. Zeng (2007b), Coseismic source model of the 2003 M w 6.8 Chengkung earthquake, Taiwan, determined from GPS measurements, *J. Geophys. Res.*, *112*(B6), 1–31, doi:10.1029/2006JB004439.

Ching, K.-E., K. M. Johnson, R.-J. Rau, R. Y. Chuang, L.-C. Kuo, and P.-L. Leu (2011a), Inferred fault geometry and slip distribution of the 2010 Jiashian, Taiwan, earthquake is consistent with a thick-skinned deformation model, *Earth Planet. Sci. Lett.*, *301*(1-2), 78–86, doi:10.1016/j.epsl.2010.10.021.

Ching, K.-E., M.-L. Hsieh, K. M. Johnson, K.-H. Chen, R.-J. Rau, and M. Yang (2011b), Modern vertical deformation rates and mountain building in Taiwan from precise leveling and continuous GPS observations, 2000–2008, *J. Geophys. Res.*, *116*(B8), 2000–2008, doi:10.1029/2011JB008242.

Ching, K.-E., R.-J. Rau, K. M. Johnson, J.-C. Lee, and J.-C. Hu (2011c), Present-day kinematics of active mountain building in Taiwan from GPS observations during 1995–2005, *J. Geophys. Res.*, *116*(B9), 1–22, doi:10.1029/2010JB008058.

Chou, J.-T. (1977), Sedimentology and Paleogeography of the Pleistocene Toukoshan Formation in Western Taiwan, *Pet. Geol. Taiwan*, *14*, 25–36.

Chou, S.-C., L. S. Teng, H.-S. Chung, and T.-W. Shiao (1994), Geohistory Analysis of West Taiwan Foreland Basin: A preliminary Study, *Pet. Geol. Taiwan*, *29*(Dec), 289–323.

Chu, H. T., H. N. Hu, H. Liew, and T. Chuang (1995), The geology of the western slope of the Nantawushan, southern Taiwan, *Bull. Cent. Geol. Surv*, *10*, 1–21.

Chu, H.-T., L. L. Siame, S. W. Lu, and C. Y. Wei (2007), The Preservation of Glacial Erosional Forms and Landscapes of the last Glaciations in subtropical area : Example from the High Mountains of Taiwan, in *Geophysical Research Abstracts*, vol. 9.

Chuang, R. Y., K. M. Johnson, Y. Wu, K. Ching, and L. Kuo (2013), A midcrustal ramp-fault structure beneath the Taiwan tectonic wedge illuminated by the 2013 Nantou earthquake series, *Geophys. Res. Lett.*, *40*, 5080–5084, doi:10.1002/grl.51005.

Clark, M. B., D. M. Fisher, and C.-Y. Lu (1992), Strain variations in the Eocene and older rocks exposed along the Central and Southern cross-island highways, Taiwan, *Acta Geol. taiwanica*, *30*, 1–10.

Clark, M. B., D. M. Fisher, C. Lu, and C.-H. Chen (1993), Kinematic analyses of the Hsueshan range, Taiwan: a large-scale pop-up strucure, *Tectonics*, *12*(1), 205–217.

Clark, M. K., M. A. House, L. H. Royden, K. X. Whipple, B. C. Burchfiel, X. Zhang, and W. Tang (2005), Late Cenozoic uplift of southeastern Tibet, *Geology*, *33*(6), 525–528, doi:10.1130/G21265.1.

Clark, M. K., L. H. Royden, K. X. Whipple, B. C. Burchfiel, X. Zhang, and W. Tang (2006), Use of a regional , relict landscape to measure vertical deformation of the eastern Tibetan Plateau, *J. Geophys. Res.*, *111*(F03002), 1–23, doi:10.1029/2005JF000294.

Clift, P. D., and R. A. Plumb (2008), *The Asian monsoon: causes, history and effects*, Cambridge University Press.

Clift, P. D., K. V. Hodges, D. Heslop, R. Hannigan, H. Van Long, and G. Calves (2008a), Correlation of Himalayan exhumation rates and Asian monsoon intensity, *Nat. Geosci.*, *1*(12), 875–880, doi:10.1038/ngeo351.

Clift, P. D., A. T.-S. Lin, A. Carter, F. T. Wu, A. E. Draut, T. H. Lai, L. Y. Fei, H. Schouten, and L. S. Teng (2008b), Post-collisional collapse in the wake of migrating arc-continent collision in the Ilan Basin, Taiwan, in *Formation and Applications of the Sedimentary Record in Arc Collision Zones*, vol. 80301, edited by A. E. Draut and P. D. Clift, pp. 257–278, Geological Society of America Special Paper 436.

Cloetingh, S., P. Ziegler, F. Beekman, P. Andriessen, L. Matenco, G. Bada, D. Garciacastellanos, N. Hardebol, P. Dezes, and D. Sokoutis (2005), Lithospheric memory, state of stress and rheology: neotectonic controls on Europe's intraplate continental topography, *Quat. Sci. Rev.*, *24*(3-4), 241–304, doi:10.1016/j.quascirev.2004.06.015.

Cowie, P. A., C. H. Scholz, G. P. Roberts, J. P. F. Walker, and P. Steer (2013), Viscous roots of active seismogenic faults revealed by geologic slip rate variations, *Nat. Geosci.*, (November), 10–14, doi:10.1038/ngeo1991.

Crespi, J., Y. C. Chan, and M. S. Swaim (1996), Synorogenic extension and exhumation of the Taiwan hinterland, *Geology*, *24*(3), 247–250, doi:10.1130/0091-7613(1996)024<0247.

Cui, Z., J. Yang, G. Liu, X. Wang, and G. Song (2000), Discovery of Quaternary glacial evidence of Snow Mountain in Taiwan, China, *Chinese Sci. Bull.*, *45*(6), 566–571, doi:10.1007/BF02887108.

Cui, Z., C. Yang, G. Liu, W. Zhang, S. Wang, and Q. Sung (2002), The Quaternary glaciation of Shesan Mountain in Taiwan and glacial classification in monsoon areas, *Quat. Int.*, *98*, 147–153.

Cullen, A., P. Reemst, G. Henstra, S. Gozzard, and A. Ray (2010), Rifting of the South China Sea: new perspectives, *Pet. Geosci.*, *16*(3), 273–282, doi:10.1144/1354-079309-908.

Dadson, S. (2004), Erosion of an active mountain belt, 191 pp., The University of Cambridge.

Dadson, S. J. et al. (2003), Links between erosion, runoff variability and seismicity in the Taiwan orogen., *Nature*, *426*(6967), 648–51, doi:10.1038/nature02150.

Dahlen, F. A. (1984), Noncohesive Critical Coulomb Wedges: An Exact Solution, *J. Geophys. Res.*, *89*(B12), 10125–10133, doi:10.1029/JB089iB12p10125.

Dahlen, F. A. (1990), Critical taper model of fold-and-thrust belts and accretionary wedges, *Annu. Rev. Earth Planet. Sci.*, *18*, 55.

Dahlen, F. A., and T. D. Barr (1989), Brittle Frictional Mountain Building 1. Deformation and Mechanical Energy Budget, *J. Geophys. Res.*, *94*(B4), 3906–3922, doi:10.1029/JB094iB04p03906.

Dahlen, F. A., J. Suppe, and D. . Davis (1984), Mechanics of Fold-and-Thrust Belts and Accretionary Wedges' Cohesive Coulomb Theory, *J. Geophys. Res.*, *89*(B12), 10087–101.

Davis, D., J. Suppe, and F. a. Dahlen (1983), Mechanics of Fold-and-Thrust Belts and Accretionary Wedges, *J. Geophys. Res.*, *88*(B2), 1153–1172, doi:10.1029/JB088iB02p01153.

Davis, W. M. (1899), The Geographical Cycle, *R. Geogr. Soc. (with Inst. Br. Geogr.*, *14*(5), 481–504.

DeCelles, P. G., and K. a. Giles (1996), Foreland basin systems, *Basin Res.*, *8*(2), 105–123, doi:10.1046/j.1365-2117.1996.01491.x.

Dodson, M. H. (1973), Closure temperature in cooling geochronological and petrological systems, *Contrib. to Mineral. Petrol.*, *40*, 259–274.

Donelick, R. A., P. B. O'Sullivan, and R. A. Ketcham (2005), Apatite Fission-Track Analysis, *Rev. Mineral. Geochemistry*, *58*(1), 49–94, doi:10.2138/rmg.2005.58.3.

Dorsey, R. J. (1988), Provenance evolution and unroofing history of a modern arc-continent collision; evidence from petrography of Plio-Pleistocene sandstones, eastern Taiwan, *J. Sediment. Res.*, *58*(2), 208.

Dunlap, W. J., G. Hirth, and C. Teyssier (1997), Thermomechanical evolution of a ductile duplex, *Tectonics*, *16*(6), 983–1000.

Eakin, D. H., K. D. McIntosh, H. J. a. Van Avendonk, L. Lavier, R. Lester, C.-S. Liu, and C.-S. Lee (2014), Crustal-scale seismic profiles across the Manila subduction zone: The transition from intraoceanic subduction to incipient collision, *J. Geophys. Res. Solid Earth*, *119*(1), 1–17, doi:10.1002/2013JB010395.

Egholm, D. L., S. B. Nielsen, V. K. Pedersen, and J.-E. Lesemann (2009), Glacial effects limiting mountain height., *Nature*, *460*(7257), 884–7, doi:10.1038/nature08263.

Von Elverfeldt, K. (2012), *System Theory in Geomorphology: Challenges, Epistemological Consequences and Practical Implications*, Springer.

Faccenna, C., and T. W. Becker (2010), Shaping mobile belts by small-scale convection, *Nature*, *465*, 602–606.

Faure, M., C.-Y. Lu, and H.-T. Chu (1991), Ductile deformation and Miocene nappe-stacking in Taiwan related to motion of the Philippine Sea Plate, *Tectonophysics*, *198*(1), 95–105, doi:10.1016/0040-1951(91)90134-E.

Fellin, M. G., S. D. Willett, and J. I. Garver (2006), Plio-Pleistocene erosion rates in Taiwan inferred from detrital zircon fission-track and (U-Th)/ He thermochronometry, *Geophys. Res. Abstr. Vol. 8*, *8*.

Fellin, M. G., S. D. Willett, and Y. Chen (2008), Spatial and temporal variations of erosion rates in Taiwan from detrital zircon-fission-track dating ., *Geophys. Res. Abstr.*, *10*(EGU2008-A-07624), 8–9.

Fellin, M. G., S. D. Willett, R. C. Thiede, and Y. Chen (2009), Topographic and Exhumational History of Taiwan Based on Detrital Zircon Fission-Track Thermochronometry, *Am. Geophys. Union, Fall Meet. 2009*, 3.

Fellin, M. G., S. D. Willett, and M. T. Brandon (2012), Zircon fission-track dating of modern river sands and exhumational patterns in Taiwan, *13th Int. Conf. Thermochronology, Abstr.*

Fillon, C., R. S. Huismans, and P. van der Beek (2013), Syntectonic sedimentation effects on the growth of fold-and-thrust belts, *Geology*, *41*(1), 83–86, doi:10.1130/G33531.1.

Fisher, D. M. (1999), Orogen parallel extension Eastern Central range of Taiwan, *J. Geol. Soc. China-Taiwan*, *42*(2), 41–58.

Fisher, D. M., C. Lu, and H.-T. Chu (2002), Taiwan Slate Belt: Insights into the ductile interior of an arc-continent collision, in *Geology and Geophysics of an Arc-Continent Collision, Taiwan*, edited by T. B. Byrne and C.-S. Liu, pp. 93–106, Geological Society of America Special Paper 358, Boulder, Colorado.

Fisher, D. M., S. D. Willett, E.-C. Yeh, M. B. Clark, and Y. En-Chao (2007), Cleavage fronts and fans as reflections of orogen stress and kinematics in Taiwan, *Geology*, *35*(1), 65, doi:10.1130/G22850A.1.

Fitzgerald, P. G., R. B. Sorkhabi, T. F. Redfield, and E. Stump (1995), Uplift and denudation of the central Alaska Range: A case study in the use of apatite fission track thermochronology to determine absolute uplift parameters, *J. Geophys. Res.*, *100*(B10), 20175–20191, doi:10.1029/95JB02150.

Foeken, J. P. T., C. Persano, F. M. Stuart, and M. ter Voorde (2007), Role of topography in isotherm perturbation: Apatite (U-Th)/He and fission track results from the Malta tunnel, Tauern Window, Austria, *Tectonics*, *26*(3), 1–15, doi:10.1029/2006TC002049.

Fossen, H. (2010), *Structural Geology*, Cambridge University Press.

Franke, D. (2013), Rifting, lithosphere breakup and volcanism : Comparison of magma-poor and volcanic rifted margins, *Mar. Pet. Geol.*, *43*, 63–87, doi:10.1016/j.marpetgeo.2012.11.003.

Frisch, W., M. Meschede, and R. Blakey (2011), *Plate Tectonics: Continental Drift and Mountain Building*, Springer-Verlag.

Fuller, C. W., S. D. Willett, N. Hovius, and R. Slingerland (2003), Erosion Rates for Taiwan Mountain Basins: New Determinations from Suspended Sediment Records and a Stochastic Model of Their Temporal Variation, *J. Geol.*, *111*(1), 71–87, doi:10.1086/344665.

Fuller, C. W., S. D. Willett, D. M. Fisher, and C. Y. Y. Lu (2006), A thermomechanical wedge model of Taiwan constrained by fission-track thermochronometry, *Tectonophysics*, *425*(1-4), 1–24, doi:10.1016/j.tecto.2006.05.018.

Fusseis, F., M. R. Handy, and C. Schrank (2006), Networking of shear zones at the brittle-to-viscous transition (Cap de Creus , NE Spain), , *28*, 1228–1243, doi:10.1016/j.jsg.2006.03.022.

Gallagher, K. (2012), Transdimensional inverse thermal history modeling for quantitative thermochronology, *J. Geophys. Res.*, *117*(B2), 1–16, doi:10.1029/2011JB008825.

Gallagher, K., R. Brown, and C. Johnson (1998), Fission Track Analysis and Its Applications To Geological Problems, *Annu. Rev. Earth Planet. Sci.*, *26*(1), 519–572, doi:10.1146/annurev.earth.26.1.519.

Garver, J. I., and P. J. J. Kamp (2002), Integration of zircon color and zircon fission-track zonation patterns in orogenic belts: application to the Southern Alps, New Zealand, *Tectonophysics*, *349*(1-4), 203–219, doi:10.1016/S0040-1951(02)00054-9.

Garver, J. I., P. W. Reiners, L. J. Walker, J. M. Ramage, and S. E. Perry (2005), Implications for Timing of Andean Uplift from Thermal Resetting of Radiation-Damaged Zircon in the Cordillera Huayhuash, Northern Peru, *J. Geol.*, *113*, 117–138.

Ge, J., Y. Dai, Z. Zhang, D. Zhao, Q. Li, Y. Zhang, L. Yi, and H. Wu (2013), Major changes in East Asian climate in the mid-Pliocene : Triggered by the uplift of the Tibetan Plateau or global cooling ?, *J. Asian Earth Sci.*, *69*, 48–59, doi:10.1016/j.jseaes.2012.10.009.

Glotzbach, C. (2008), Low-temperature thermochronology from tunnel and surface samples in the Central and Western Alps, der Geowissenschaftlichen Fakultät der Eberhard-Karls-Universität Tübingen.

Goren, L., S. Castelltort, S. D. Willett, J.-D. Champagnac, F. Herman, and J. Braun (2012), Passive advection and dynamic reorganization of mountainous bedrock rivers : A landscape evolution modeling approach, in *Geophysical Research Abstracts*, vol. 14, pp. Vol.14, EGU2012–10441.

Gourley, J., T. B. Byrne, Y. Chan, F. T. Wu, and R.-J. Rau (2007), Fault geometries illuminated from seismicity in central Taiwan: Implications for crustal scale structural boundaries in the northern Central Range, *Tectonophysics*, *445*(3-4), 168–185, doi:10.1016/j.tecto.2007.08.013.

Hall, R. (1997), Cenozoic plate tectonic reconstructions of SE Asia, in *Petroleum Geology of Southeast Asia*, vol. 126, edited by A. J. Fraser, S. J. Mattehs, and R. W. Murphy, pp. 11–23, Geological Society, London, Special Publications 126.

Hall, R. (2002), Cenozoic geological and plate tectonic evolution of SE Asia and the SW Pacific: computer-based reconstructions, model and animations, *J. Asian Earth Sci.*, *20*(4), 353–431, doi:10.1016/S1367-9120(01)00069-4.

Hall, R., M. Fuller, J. R. Ali, and C. D. Anderson (1995), The Philippine Sea Plate: Magnetism and Reconstruction, in *Active Margin and Marginal Basins of the Western Pacific, Geophysical Monograph 88*, pp. 371–404, American Geophysical Union.

Hall, R., M. W. A. van Hattum, and W. Spakman (2008), Impact of India–Asia collision on SE Asia: the record in Borneo, *Tectonophysics*, *451*, 366–369.

Haq, S. S. B., and D. M. Davis (2008), Extension during active collision in thin-skinned wedges: Insights from laboratory experiments, *Geology*, *36*(6), 475, doi:10.1130/G24718A.1.

Hastenrath, S. (2009), Past glaciation in the tropics, *Quat. Sci. Rev.*, *28*(9-10), 790–798, doi:10.1016/j.quascirev.2008.12.004.

Hay, W., E. Soeding, R. DeConto, and C. Wold (2002), The Late Cenozoic uplift - climate change paradox, *Int. J. Earth Sci.*, *91*(5), 746–774, doi:10.1007/s00531-002-0263-1.

Hebenstreit, R. (2006), Present and former equilibrium line altitudes in the Taiwanese high mountain range., *Quat. Int.*, *147*, 70–75.

Hebenstreit, R. (2012), Geomorphological studies on the late Pleistocene and early Holocene glaciation in selected high mountain ranges in Taiwan, Freien Universität Berlin.

Hebenstreit, R., M. Böse, and A. Murray (2006), Late Pleistocene and early Holocene glaciations in Taiwanese mountains, *Quat. Int.*, *147*(1), 76–88, doi:10.1016/j.quaint.2005.09.009.

Hebenstreit, R., S. Ivy-Ochs, P. W. Kubik, C. Schlüchter, and M. Böse (2011), Lateglacial and early Holocene surface exposure ages of glacial boulders in the Taiwanese high mountain range, *Quat. Sci. Rev.*, *30*(3-4), 298–311, doi:10.1016/j.quascirev.2010.11.002.

Herman, F., D. Seward, P. G. Valla, A. Carter, B. Kohn, S. D. Willett, and T. A. Ehlers (2013), Worldwide acceleration of mountain erosion under a cooling climate, *Nature*, *504*, 423–426, doi:10.1038/nature12877.

Hilley, G. E., and M. R. Strecker (2004), Steady state erosion of critical Coulomb wedges with applications to Taiwan and the Himalaya, *J. Geophys. Res.*, *109*(B1), 1–17, doi:10.1029/2002JB002284.

Ho, C. S. (1986), A synthesis of the geologic evolution of Taiwan, *Tectonophysics*, *125*(1-3), 1–16, doi:10.1016/0040-1951(86)90004-1.

Ho, C. S. (1988), *An introduciton to the geology of Taiwan: Explanatory text of the geologic map of Taiwan (2nd edition)*, Second Edi., Central Geological Survey, The Ministry of Economic Affairs, Taipei, Taiwan, Republic of China.

Horng, C.-S., K. Shea, K.-H. Chen, and C.-Y. Kao (2007), Magnetobiostratigraphy of the Liukuei and Linkou Conglomerates and the Tashe Formation in the Kaohsiung Area, in *XIth Symposium on Quaternary of Taiwan, 21-22 September*, pp. 79–80.

House, M., B. P. Kohn, K. A. Farley, and A. Raza (2002), Evaluating thermal history models for the Otway Basin, southeastern Australia, using (U-Th)/He and fission-track data from borehole apatites, *Tectonophysics*, *349*(1-4), 277–295, doi:10.1016/S0040-1951(02)00057-4.

Hovius, N., C. Stark, H.-T. Chu, and L. Jiun-Chuan (2000), Supply and Removal of Sediment in a Landslide-Dominated Mountain Belt: Central Range, Taiwan., *J. Geol.*, *108*(1), 73–89.

Hsu, S.-K., Y. C. Yeh, W. B. Doo, and C. H. Tsai (2004), New bathymetry and magnetic lineations identifications in the northernmost South China Sea and their tectonic implications, *Mar. Geophys. Res.*, *25*, 29–44.

Hsu, S.-K., Y.-C. Yeh, C.-L. Lo, A. T.-S. Lin, and W.-B. Doo (2008), Link between Crustal Magnetization and Earthquakes in Taiwan, *October*, *19*(5), 445–450, doi:10.3319/TAO.2008.19.5.445(T)1.

Hu, H. N., and S. Tsan (1984a), Structural Study of the Slate formation along the South link railroad, Taiwan, *Spec. Pub. Cent. Geol. Surv.*, 25–44.

Hu, H.-N., and S. F. Tsan (1984b), Strucural Study of the slate formation along the Sout link railroad, Taiwan, *Spec. Pub. Cent. Geol. Surv.*, *3*(December), 25–43.

Hu, J. et al. (2007), Fault activity and lateral extrusion inferred from velocity field revealed by GPS measurements in the Pingtung area of southwestern Taiwan, *J. Asian Earth Sci.*, *31*(3), 287–302, doi:10.1016/j.jseaes.2006.07.020.

Huang, A. Y., and D. R. Montgomery (2013), Topographic locations and size of earthquake- and typhoon generated landslides, tachia river, Taiwan, *Earth Surf. Process. Landforms*, doi:10.1002/esp.3510.

Huang, C. Y., C. W. Chien, B. Yao, and C.-P. Chang (2008a), The Lichi Melange: A collision melange formation along early arcward backthrust during forearc basin closure, Taiwan arc-continent collision, in *Formation and applications of the sedimentary record in arc collision zones*, vol. 436, edited by A. E. Draunt, P. D. Clift, and D. W. Scholl, pp. 127–154, Geological Society of America Special Paper 436.

Huang, C.-Y., W.-Y. Wu, C.-P. Chang, S. Tsao, P. B. Yuan, C.-W. Lin, and K.-Y. Xia (1997), Tectonic evolution of accretionary prism in the arc-continent collision terrane of Taiwan, *Tectonophysics*, *281*(1-2), 31–51, doi:10.1016/S0040-1951(97)00157-1.

Huang, C.-Y., Y.-L. Chiu, and M. Zhao (2005), Core Description and a Preliminarily Sedimentology Study of Site 1202D, Leg 195, in the Southern Okinawa Trough, *Terr. Atmos. Ocean. Sci.*, *16*(1), 19–44.

Huang, C.-Y., P. B. Yuan, and S.-J. Tsao (2006), Temporal and spatial records of active arc-continent collision in Taiwan: A synthesis, *Geol. Soc. Am. Bull.*, *118*(3-4), 274–288, doi:10.1130/B25527.1.

Huang, C.-Y., C. C. W. Chien, B. Yao, and C. Chang (2008b), The Lichi Mélange: A collision mélange formation along early arcward backthrusts during forearc basin closure, Taiwan arc-continent collision, in *The Geological Society of America Special Paper 436*, vol. 2436, edited by A. E. Draunt, P. D. Clift, and D. W. Scholl, pp. 127–154, Geological Society of America Special Paper 436.

Huang, C.-Y., Y. Yen, Q. Zhao, and C. Lin (2012), Cenozoic stratigraphy of Taiwan : Window into rifting , stratigraphy and paleoceanography of South China Sea, *Chinese Sci. Bull.*, *57*(24), 3130–3149, doi:10.1007/s11434-012-5349-y.

Huang, T.-C. (1979), The Oligocene/Miocene boundary in Taiwan, *Mem. Geol. Soc. China*, (3), 103–123.

Huang, T.-C. (1980a), A calcareous nannofossil biostratigraphic study of the Assilia-bearing section, Chunkengchi, Nantou, *Proc. Geol. Soc. China*, (23), 7–15.

Huang, T.-C. (1980b), Calcareous Nannofossils from the slate terrane west of Yakou , Southern Cross-Island Highway, *Pet. Geol. Taiwan*, *17*, 59–74.

Huang, W.-J., K. M. Johnson, J. Fukuda, and S.-B. Yu (2010), Insights into active tectonics of eastern Taiwan from analyses of geodetic and geologic data, *J. Geophys. Res.*, *115*(B3), 1–18, doi:10.1029/2008JB006208.

Hung, J.-H., D. V. Wiltschko, H.-C. Lin, J. B. Hickman, P. Fang, and Y. Bock (1999), Structure and motion of the southwestern Taiwan fold and thrust belt., *Terr. Atmos. Ocean. Sci.*, *10*(3), 543–568.

Hurford, A. J., and P. F. Green (1982), A users' guide to fission track dating calibration Anthony J. Hurford, , *59*, 343–354.

Hwang, C., Y.-S. Hsiao, H.-C. Shih, M. Yang, K.-H. Chen, R. Forsberg, and A. V. Olesen (2007), Geodetic and geophysical results from a Taiwan airborne gravity survey: Data reduction and accuracy assessment, *J. Geophys. Res.*, *112*(B4), 1–14, doi:10.1029/2005JB004220.

Jahn, B., J. Martineau, J. Peucat, and J. Cornichet (1986), Geochronology of the Tananao schist complex and crustal evolution of Taiwan: Mem, *Geol. Soc. China*, (7), 383–404.

Jahn, B.-M. (2010), CHECK IT OUT, in *Taiwan Tectonics Workshop, Institute of Earth Science, Academia Sinica, Taiwan.*

Jamieson, R. A., C. Beaumont, J. Hamilton, and P. Fullsack (1996), Tectonic assembly of inverted metamorphic sequences, *Geology*, *24*, 839–842, doi:10.1130/0091-7613(1996)024<0839.

Jammes, S., and R. S. Huismans (2012), Structural styles of mountain building : Controls of lithospheric rheologic stratification and extensional inheritance, , *117*(October), 1–22, doi:10.1029/2012JB009376.

Jolivet, L., K. Tamaki, and M. Fournier (1994), Japan Sea, opening history and mechanism: A synthesis, *J. Geophys. Res.*, *99*(B11), 22237–22259.

Kao, H., S. J. Shen, and K. Ma (1998), Transition form oblique subduction to collision: earthquakes in the southermost Ryukyu arc-Taiwan region, *J. Geophys. Res.*, *103*(B4), 211–229.

Kirstein, L. A., M. G. Fellin, S. D. Willett, A. Carter, Y.-G. Chen, J. I. Garver, and D. C. Lee (2010a), Pliocene onset of rapid exhumation in Taiwan during arc-continent collision: new insights from detrital thermochronometry, *Basin Res.*, *22*(3), 270–285, doi:10.1111/j.1365-2117.2009.00426.x.

Kirstein, L. A., A. Carter, and Y.-G. Chen (2010b), Testing inferences from palaeocurrents: application of zircon double-dating to Miocene sediments from the Hengchun Peninsula, Taiwan, *Terra Nov.*, *22*(6), 483–493, doi:10.1111/j.1365-3121.2010.00970.x.

Kirstein, L. A., A. Carter, and Y. Chen (2013), Impacts of arc collision on small orogens: new insights from the Coastal Range detrital record, Taiwan, *J. Geol. Soc. London.*, doi:10.1144/jgs2013-046.

Knuepfer, P. L. K., and J. H. Willemin (1992), Geomorphic evidence for axial tilting of teh longitudinal valley, Taiwan, *Acta Geol. taiwanica*, *30*, 89–100.

Knuth, K. (2006), Optimal data-based binning for histograms, *arXiv Prepr. physics/0605197*, (3), 1–27.

Koons, P. (1990), Two-sided orogen : Collision and erosion from the sandbox to the Southern Alps, New Zealand, *Geology*, *18*, 679–682, doi:10.1130/0091-7613(1990)018<0679.

Koppes, M. N., and D. R. Montgomery (2009), The relative efficacy of fluvial and glacial erosion over modern to orogenic timescales, *Nat. Geosci.*, *2*(9), 644–647, doi:10.1038/ngoe616.

Kuo-Chen, H., F. T. Wu, D. M. Jenkins, J. Mechie, S. W. Roecker, C. Wang, and B. Huang (2012a), Seismic evidence for the a-b quartz transition beneath Taiwan from Vp/Vs tomography, *Geophys. Res. Lett*, *39*(L22302), 1–6, doi:10.1029/2012GL053649.

Kuo-Chen, H., F. T. Wu, and S. W. Roecker (2012b), Three-dimensional P velocity structures of the lithosphere beneath Taiwan from the analysis of TAIGER and related seismic data sets, *J. Geophys. Res.*, *117*(B06306), 1–19, doi:10.1029/2011JB009108.

Lacombe, O., F. Mouthereau, J. Angelier, and B. Deffontaines (2001), Structural, geodetic and seismological evidence for tectonic escape in SW Taiwan, *Tectonophysics*, *333*(1-2), 323–345, doi:10.1016/S0040-1951(00)00281-X.

Lan, C.-Y., C.-H. Chen, C.-H. Chen, S.-L. Chung, T. Lee, C.-M. Wang Lee, and T.-F. Yui (1996), The crustal evolution of continental Taiwan, *J. Geol. Soc. China*, *39*(3), 337–353.

Lan, C.-Y., C.-S. Lee, T.-F. Yui, H.-T. Chu, and B.-M. Jahn (2008), The tectono-thermal events of Taiwan and their relationship with SE China, *Terr. Atmos. Ocean. Sci.*, *19*(3), 257–278, doi:10.3319/TAO.2008.19.3.257(TT)1.

Larsen, I. J., D. R. Montgomery, and O. Korup (2010), Landslide erosion controlled by hillslope material, *Nat. Geosci.*, *3*(4), 247–251, doi:10.1038/ngeo776.

Law, R. D., M. P. Searle, and L. Godin (Eds.) (2006), *Channel flow, ductile extrusion and exhumation in continental collision zones*, Geological Society, London, Special Publications, 268.

Lee, C. (1984), Systematics of Assilina formosensis Hanzawa from the slate terrain of Taiwan, *Mem. Geol. Soc. China*, (6), 335–344.

Lee, J.-C. (2003), Active fault creep variations at Chihshang, Taiwan, revealed by creep meter monitoring, 1998–2001, *J. Geophys. Res.*, *108*(B11), 1998–2001, doi:10.1029/2003JB002394.

Lee, J.-C., J. Angelier, and H.-T. Chu (1997), Polyphase history and kinematics of a complex major fault zone in the northern Taiwan mountain belt: the Lishan Fault, *Tectonophysics*, *274*(1-3), 97–115, doi:10.1016/S0040-1951(96)00300-9.

Lee, Y.-H., C.-C. Chen, T.-K. Liu, H.-C. Ho, H.-Y. Lu, and W. Lo (2006), Mountain building mechanisms in the Southern Central Range of the Taiwan Orogenic Belt — From accretionary wedge deformation to arc–continental collision, *Earth Planet. Sci. Lett.*, *252*(3-4), 413–422, doi:10.1016/j.epsl.2006.09.047.

Lee, Y.-H., G.-T. Chen, R.-J. Rau, and K.-E. Ching (2008), Coseismic displacement and tectonic implication of 1951 Longitudinal Valley earthquake sequence, eastern Taiwan, *J. Geophys. Res.*, *113*(B4), 1–13, doi:10.1029/2007JB005180.

Leighly, J. (1940), Walter Penck's contribution to Geomorphology, *Ann. Ass. Am. Geogr.*, *30*, 223–32.

Lester, R., L. L. Lavier, K. McIntosh, H. J. a. Van Avendonk, and F. T. Wu (2012), Active extension in Taiwan's precollision zone: A new model of plate bending in continental crust, *Geology*, *40*(9), 831–834, doi:10.1130/G33142.1.

Lester, R., K. McIntosh, H. J. A. Van Avendonk, L. Lavier, C.-S. Liu, and T. K. Wang (2013), Crustal accretion in the Manila trench accretionary wedge at the transition from subduction to mountain-building in Taiwan, *Earth Planet. Sci. Lett.*, *375*, 430–440.

Lewis, C., S.-W. Chen, and P.-C. Yen (2004), Magnetic Surveying of the Chaochou Fault of Southern Taiwan: Culmination of Basement-Involved Surface Thrusting in Arc-Continent Collision, *Int. Geol. Rev.*, *46*(5), 399–408, doi:10.2747/0020-6814.46.5.399.

Li, Q., G. Zhong, and J. Tian (2009), Stratigraphy an sea level changes, in *The South China Sea*, edited by P. Wang and Q. Li, pp. 55–133, Springer, Dordrecht, The Netherlands.

Li, Y. H. (1975), Denudation of Taiwan island since Pliocene epoch, *Geology*, *4*(2), 105–107.

Liew, P.-M. (1986), Palynological stratigraphy and climatic implications of pleistocene sediments in western Taiwan, *Acta Geol. taiwanica*, *24*, 165–177.

Liew, P.-M. (1991), Pleistocene cool stage and geological changes of western Taiwan based on palynological study, *Acta Geol. Taiwanica*, *29*, 21–32.

Liew, P.-M., and S.-Y. Huang (1994), Pollen analysis and their paleoclimatic implication in the Middle Pleistocene lake deposits of ilan district, northeastern Taiwan, *J. Geol. Soc. China*, *37*(1), 115–124.

Liew, P.-M., C. Y. Lee, and C. M. Kuo (2006a), Holocene thermal optimal and climate variability of East Asian monsoon inferred from forest reconstruction of a subalpine pollen sequence, Taiwan, *Earth Planet. Sci. Lett.*, *250*(3-4), 596–605, doi:10.1016/j.epsl.2006.08.002.

Liew, P.-M., S.-Y. Huang, and C.-M. Kuo (2006b), Pollen stratigraphy, vegetation and environment of the last glacial and Holocene—A record from Toushe Basin, central Taiwan, *Quat. Int.*, *147*(1), 16–33, doi:10.1016/j.quaint.2005.09.003.

Liew, P.-M., B.-C. Chen, M.-L. Hsieh, S.-Y. Huang, and C.-Y. Lee (2013), Decreasing intensity of the last glacial stadials in low latitude terrestrial East Asia inferred by a new observation of pollen records in central Taiwan, *J. Asian Earth Sci.*, *69*, 159–165, doi:10.1016/j.jseaes.2012.05.027.

Lin, A. T.-S., and A. B. Watts (2002), Origin of the West Taiwan basin by orogenic loading and flexure of a rifted continental margin, *J. Geophys. Res.*, *107*(B9), doi:10.1029/2001JB000669.

Lin, A. T.-S., A. B. Watts, and S. P. Hesselbo (2003), Cenozoic stratigraphy and subsidence history of the South China Sea margin in the Taiwan region, *Basin Res.*, *15*(4), 453–478, doi:10.1046/j.1365-2117.2003.00215.x.

Lin, A. T.-S., B. Yao, S.-K. Hsu, C.-S. Liu, and C.-Y. Huang (2009), Tectonic features of the incipient arc-continent collision zone of Taiwan: Implications for seismicity, *Tectonophysics*, *479*(1-2), 28–42, doi:10.1016/j.tecto.2008.11.004.

Lin, C., and S. W. Roecker (1998), Active Crustal Subduction and Exhumation in Taiwan, in *When Continents Collide : Geodynamics and Geochemistry of Ultrahigh-Pressure Rocks*, edited by B. Hacker and J. G. Liou, pp. 1–16, Chapman Hall.

Lin, C. C. (1957), *Geomorphology of Taiwan*, Taiwan Literature Commitee.

Lin, C.-H. (2000), Thermal modeling of continental subduction and exhumation constrained by heat flow and seismicity in Taiwan, *Tectonophysics*, *324*(3), 189–201, doi:10.1016/S0040-1951(00)00117-7.

Lin, C.-H. (2002), Active continental subduction and crustal exhumation: the Taiwan orogeny, *Terra Nov.*, *14*(4), 281–287, doi:10.1046/j.1365-3121.2002.00421.x.

Lin, G., G. Lin, H. Chen, N. Hovius, M. Horng, S. Dadson, P. Meunier, and M. Lines (2008), Effects of earthquake and cyclone sequencing on landsliding and fluvial sediment transfer in a mountain catchment, *Earth Surf. Process. Landforms*, *33*, 1354–1373, doi:10.1002/esp.

Liou, J. G., and W. G. Ernst (1984), Summary of Phanerozoic Metamorphism in Taiwan, *Mem. Geol. Soc. China*, (6), 133–152, doi:10.1089/aid.2011.0096.

Liu, J., C. Liu, K. Xu, J. Milliman, J. Chiu, S. Kao, and S. Lin (2008), Flux and fate of small mountainous rivers derived sediments into the Taiwan Strait, *Mar. Geol.*, *256*, 65–76, doi:10.1016/j.margeo.2008.09.007.

Liu, J., Z. Xue, K. Ross, H. Wang, Z. Yang, A. Li, and S. Gao (2009), Fate of sediments delivered to the sea by Asian large rivers: Long-distance transport and formation of remote alongshore clinothems, *SEPM-The Sediment. Rec.*, *7*(4), 4–9.

Liu, J. T., S.-J. Kao, C.-A. Huh, and C.-C. Hung (2013), Gravity flows associated with flood events and carbon burial: Taiwan as instructional source area., *Ann. Rev. Mar. Sci.*, *5*, 47–68, doi:10.1146/annurev-marine-121211-172307.

Liu, T.-K. (1982), Tectonic implication of fission track ages from the Central Range, Taiwan, *Proc. Geol. Soc. China*, *25*, 22–37.

Liu, T.-K., Y.-G. Chen, W.-S. Chen, and S.-H. Jiang (2000), Rates of cooling and denudation of the Early Penglai Orogeny, Taiwan, as assessed by fission-track constraints, *Tectonophysics*, *320*(1), 69–82, doi:10.1016/S0040-1951(00)00028-7.

Liu, T.-K., S. Hsieh, Y.-G. Chen, and W.-S. Chen (2001), Thermo-kinematic evolution of the Taiwan oblique-collision mountain belt as revealed by zircon fission track dating, *Earth Planet. Sci. Lett.*, *186*(1), 45–56, doi:10.1016/S0012-821X(01)00232-1.

Lo, C.-H., and T. C. Onstott (1995), Rejuvenation of K-Ar systems for minerals in the Taiwan Mountain Belt, *Earth Planet. Sci. Lett.*, *131*(1-2), 71–98, doi:10.1016/0012-821X(95)00011-Z.

Lock, J. (2007), Interpreting Low-Temperature Thermochronometric Data in Fold-and-Thrust Belts: An Example from the Western Foothills, Taiwan, 196 pp., University of Washington.

Lock, J., and S. D. Willett (2008), Low-temperature thermochronometric ages in fold-and-thrust belts, *Tectonophysics*, *456*(3-4), 147–162, doi:10.1016/j.tecto.2008.03.007.

Lu, C., Y. Chan, L. Kuo, K. Chang, J. Lee, and C. Chen (2010a), TI: Geohazards in Related to Neotectonic Patterns of Taiwan Based on Recent Multi-Source Data, *AGU Fall Meet. Abstr.*, B2071.

Lu, C.-Y., Y.-C. Chan, L.-C. Kuo, K. Chang, and J.-C. Lee (2010b), Geo-hazards in related to neotectonic patterns of taiwan based on recent multi-source data., in *AGU Fall Meeting Abstracts, presented at the EOS Trans. AGU, Taipei, Taiwan*, p. B2071.

Ma, K. F., and D. R. Song (1997), Pn velocity and Moho depth in Taiwan, *J. Geol. Soc. China*, *40*, 167–184.

Malavieille, J. (2010), Impact of erosion, sedimentation, and structural heritage on the structure and kinematics of orogenic wedges: Analog models and case studies, *GSA Today*, (1), 4–10, doi:10.1130/GSATG48A.1.

Malavieille, J., and G. Trullenque (2009), Consequences of continental subduction on forearc basin and accretionary wedge deformation in SE Taiwan: Insights from analogue modeling, *Tectonophysics*, *466*(3-4), 377–394, doi:10.1016/j.tecto.2007.11.016.

McIntosh, K., H. van Avendonk, L. Lavier, W. R. Lester, D. Eakin, F. T. Wu, C.-S. Liu, and C.-S. Lee (2013), Inversion of a hyper-extended rifted margin in the southern Central Range of Taiwan, *Geology*, *41*(8), 871–874, doi:10.1130/G34402.1.

Meunier, P., N. Hovius, and J. A. Haines (2008), Topographic site effects and the location of earthquake induced landslides, *Earth Planet. Sci. Lett.*, *275*(3-4), 221–232, doi:10.1016/j.epsl.2008.07.020.

Milliman, J. D., and K. L. Farnsworth (2011), *River Discharge to the Coastal Ocean: A Global Synthesis*, Cambridge University Press.

Milliman, J. D., and J. P. M. Syvitski (1992), Geomorphic/Tectonic Control of Sediment Discharge to the Ocean: The Importance of Small Mountainous Rivers, *J. Geol.*, *100*(5), 525–544, doi:10.1086/629606.

Mohn, G., G. Manatschal, M. Beltrando, and I. Haupert (2014), The role of rift-inherited hyper-extension in Alpine-type orogens, *Terra Nov.*, doi:10.1111/ter.12104.

Molnar, P. (2004), Late Cenozoic increase in accumulation rates of terrestrial sediments: How Might Climate Change Have Affected Erosion Rates?, *Annu. Rev. Earth Planet. Sci.*, *32*(1), 67–89, doi:10.1146/annurev.earth.32.091003.143456.

Molnar, P., and P. England (1990), Late Cenozoic uplift of mountain ranges and global climate change: chicken or egg?, *Nature*, *346*(6279), 29–34.

Molnar, P., and P. Tapponnier (1975), Cenozoic Tectonics of Asia: Effects of a Continental Collision, *Science*, *189*(4201), 419–26, doi:10.1126/science.189.4201.419.

Montgomery, D. (2002), Valley formation by fluvial and glacial erosion, *Geology*, *30*, 1047–1050, doi:10.1130/0091-7613(2002)030<1047.

Montgomery, D. R. (2001), Slope distributions, threshold hillslopes, and steady-state topography, *Am. J. Sci.*, *301*(4-5), 432–454, doi:10.2475/ajs.301.4-5.432.

Montgomery, D. R., and M. T. Brandon (2002), Topographic controls on erosion rates in tectonically active mountain ranges, *Earth Planet. Sci. Lett.*, *201*(3-4), 481–489, doi:10.1016/S0012-821X(02)00725-2.

Montgomery, D. R., G. Balco, and S. D. Willett (2001), Climate, tectonics, and the morphology of the Andes, *Geology*, *29*(7), 579, doi:10.1130/0091-7613(2001)029<0579:CTATMO>2.0.CO;2.

Mouthereau, F., and O. Lacombe (2006), Inversion of the Paleogene Chinese continental margin and thick-skinned deformation in the Western Foreland of Taiwan, *J. Struct. Geol.*, *28*(11), 1977–1993, doi:10.1016/j.jsg.2006.08.007.

Mouthereau, F., O. Lacombe, B. Deffontaines, J. Angelier, H.-T. Chu, and C. T. Lee (1999), Quaternary transfer faulting and belt front deformation at Pakuashan (western Taiwan), *Tectonics*, *18*(2), 215, doi:10.1029/1998TC900025.

Mouthereau, F., O. Lacombe, B. Deffontaines, J. Angelier, and S. Brusser (2001a), Deformation history of the southwestern Taiwan foreland thrust belt: insights from tectono-sedimentary analyses and balanced cross-sections, *Tectonophysics*, *333*(1-2), 293–318, doi:10.1016/S0040-1951(00)00280-8.

Mouthereau, F., J. Angelier, and J.-C. Lee (2001b), Le séisme du 21 septembre 1999 : influence de l'héritage structural et implication du socle au front de la chaîne de Taiwan, *Comptes Rendus l'Académie des Sci. - Ser. IIA - Earth Planet. Sci.*, *333*(1), 93–103, doi:10.1016/S1251-8050(01)01616-0.

Mouthereau, F., B. Deffontaines, O. Lacombe, and J. Angelier (2002), Variations along the strike of the Taiwan thrust belt : Basement control on structural style , wedge geometry , and kinematics, in *Geology and Geophysics of an Arc-Continent Collision, Taiwan*, vol. 358, edited by T. B. Byrne and C.-S. Liu, pp. 35–58, Geological Society of America Special Paper 358.

Mouthereau, F., C. Fillon, and K.-F. Ma (2009), Distribution of strain rates in the Taiwan orogenic wedge, *Earth Planet. Sci. Lett.*, *284*(3-4), 361–385, doi:10.1016/j.epsl.2009.05.005.

Mouthereau, F., O. Lacombe, and J. Vergés (2012), Building the Zagros collisional orogen : Timing, strain distribution and the dynamics of Arabia/Eurasia plate convergence, *Tectonophysics*, *532-535*, 27–60, doi:10.1016/j.tecto.2012.01.022.

Mouthereau, F., A. B. Watts, and E. Burov (2013), Structure of orogenic belts controlled by lithosphere age, *Nat. Geosci.*, *6*(8), 1–5, doi:10.1038/ngeo1902.

Mouyen, M., M. Simoes, F. Mouthereau, F. Masson, C. Hwang, and C.-C. Cheng (2014), Investigating possible gravity change rates expected from long-term deep crustal processes in Taiwan, *Geophys. J. Int.*, doi:10.1093/gji/ggu133.

Nagel, S., M. G. Fellin, S. Castelltort, W. Sean, F. Mouthereau, and A. T. Lin (2012a), Provenance evolution of the Western foreland basin in Taiwan and its relationship to the exhumation of source rocks during arc-continent collision, in *European Geological Union Meeting*, p. 464.

Nagel, S., S. Castelltort, A. Wetzel, S. D. Willett, F. Mouthereau, and A. T.-S. Lin (2012b), Sedimentology and foreland basin paleogeography during Taiwan arc continent collision, *J. Asian Earth Sci.*, doi:10.1016/j.jseaes.2012.09.001.

Nemcok,, M., S. Schamel, and R. Gayer (2005), *Thrust-belts. Structural Architecture, Thermal Regimes, and Petroleum Systems*, Cambridge University Press, Cambridge, New York, Melbourne.

Nilfouroushan, F., R. Pysklywec, A. Cruden, and H. Koyi (2013), Thermal-mechanical modeling of salt-based mountain belts with pre-existing basement faults : Application to the Zagros fold and thrust belt , southwest Iran, , *32*, 1–15, doi:10.1002/tect.20075.

Nissen, S. S., D. E. Hayes, P. Buhl, J. Diebold, Y. Bochu, Z. Weijun, and C. Yongqin (1995a), Deep penetration seismic soundings across the northern margin of the South China Sea, *J. Geophys. Res.*, *100*(B11), 22407–22.

Nissen, S. S., D. E. Hayes, B. Yao, W. Zeng, Y. Chen, and X. Nu (1995b), Gravity, heat flow, and seismic constraints on the process of crustal extension: Northern margin of the South China sea, *J. Geophys. Res.*, *100*(B11), 447–483.

Ono, Y., and T. Naruse (1997), Snowline elevation and eolian dust flux in the Japanese Islands during Isotope Stages 2 and 4, *Quat. Int.*, *37*(0), 45–54, doi:http://dx.doi.org/10.1016/1040-6182(96)00003-1.

Ouimet, W. B., T. B. Byrne, and C. Huang (2012), Non-Equilibrium Topography in the southern Central Range of Taiwan, in *EP13B-0846 : presented at the 2012 Fall Meeting, AGU, San Francisco, Calif., 3-7 Dec.*

Pelletier, B., and H. N. Hu (1984), New structural data along two transects across the southern half of the Central Range of Taiwan, *Mem. Geol. Soc. China*, *6*, 1–19.

Pelletier, B., and J. Stephan (1986a), Middle Miocene obduction and Late Miocene beginning of collision registered in the Hengchun peninsula: Geodynamic implications for the evolution of Taiwan, *Mem. Geol. Soc. China*, *7*, 301–324, doi:10.1016/0040-1951(86)90011-9.

Pelletier, B., and J. F. Stephan (1986b), Middle Miocene obduction and Late Miocene beginning of collision registered in the Hengchun peninsula: Geodynamic implications for the evolution of Taiwan, *Tectonophysics*, *125*, 133–160.

Peltzer, G., and P. Tapponnier (1988), Formation and evolution of strike-slip faults, rifts, and basins during the India-Asia collision: an experimental approach, *J. Geophys. Res.*, *93*(B12), 15085–15117.

Phillips, J. D. (1992), The end of equilibrium?, *Geomorphology*, *5*(3-5), 195–201, doi:10.1016/0169-555X(92)90002-6.

Porter, S. (1989), Some geological implications of average Quaternary glacial conditions., *Quat. Res.*

Pulver, M. H., J. M. Crespi, and T. B. Byrne (2002), Lateral extrusion in a transpressional collision zone : An example from the pre-Tertiary metamorphic basement of Taiwan, in *Geology and Geophysics of an Arc-Continent Collision, Taiwan*, vol. 358, edited by T. B. Byrne and C.-S. Liu, pp. 107–120, Geological Society of America Special Paper 358, Boulder, Colorado.

Ramsey, L. A. (2006), Topographic evolution of emerging mountain belts, University of Cambridge.

Ramsey, L. a., R. T. Walker, and J. Jackson (2007), Geomorphic constraints on the active tectonics of southern Taiwan, *Geophys. J. Int.*, *170*(3), 1357–1372, doi:10.1111/j.1365-246X.2007.03444.x.

Ranalli, G., and D. C. Murphy (1987), Rheological stratification of the lithosphere, *Tectonophysics*, *132*(4), 281–295, doi:10.1016/0040-1951(87)90348-9.

Rangin, C. (1991), The Philippine Mobile Belt: a complex plate boundary, *J. Southeast Asian Earth Sci.*, *6*(3), 209–220.

Raymo, M., and W. F. Ruddiman (1992), Tectonic forcing of late Cenozoic climate, *Nature*, *359*(6391), 117–122.

Reiners, P. W., and M. T. Brandon (2006), Using Thermochronology To Understand Orogenic Erosion, *Annu. Rev. Earth Planet. Sci.*, *34*(1), 419–466, doi:10.1146/annurev.earth.34.031405.125202.

Reiners, P. W., T. a Ehlers, S. G. Mitchell, and D. R. Montgomery (2003), Coupled spatial variations in precipitation and long-term erosion rates across the Washington Cascades., *Nature*, *426*(6967), 645–7, doi:10.1038/nature02111.

Reiners, P. W., T. A. Ehlers, and P. K. Zeitler (2005), Past, present and future of thermochronology, in *Low-Temperature Thermochronology: Techniques, Interpretations, and Applications*, vol. 58, pp. 1–18, Reviews in Mineralogy & Geochemistry 58.

Reston, T. J., and G. Manatchal (2011), Rifted Margins: Building Blocks of Later Collision, in *Arc-Continent Collision*, edited by D. Brown and P. D. Ryan, pp. 3–21, Springer-Verlag.

Ring, U., M. T. Brandon, S. D. Willett, and G. S. Lister (1999), Exhumation processes, in *Exhumation Processes: Normal Faulting, Ductile Flow and Erosion*, vol. 154, edited by U. Ring, M. T. Brandon, G. S. Lister, and S. D. Willett, pp. 1–27, Geological Society, London, Special Publications 154.

Rodriguez-Roa, F. A., and D. V. Wiltschko (2010), Thrust belt architecture of the central and southern Western Foothills of Taiwan, in *Hydrocarbons in Contractional Belts*, vol. 348, edited by G. P. Goffey, J. Craig, T. Needham, and R. Scott, pp. 137–168, Geological Society, London, Special Publications.

Roe, G. (2009), Feedbacks, Timescales, and Seeing Red, *Annu. Rev. Earth Planet. Sci.*, *37*, 93–115, doi:10.1146/annurev.earth.061008.134734.

Roe, G. H., K. X. Whipple, and J. K. Fletcher (2008), Feedbacks among climate, erosion, and tectonics in a critical wedge orogen, *Am. J. Sci.*, *308*(7), 815–842, doi:10.2475/07.2008.01.

Rousset, B., S. Barbot, J.-P. Avouac, and Y.-J. Hsu (2012), Postseismic deformation following the 1999 Chi-Chi earthquake , Taiwan : Implication for lower-crust rheology, *J. Geophys. Res.*, *117*(B12405), 1–16, doi:10.1029/2012JB009571.

Royden, L. (1996), Coupling and decoupling of crust and mantle in convergent orogens: Implications for strain partitioning in the crust, *J. Geophys. Res.*, *101*(B8), 17,679–17,705.

Royden, L. H., B. C. Burchfiel, R. W. King, E. Wang, Z. Chen, F. Shen, and Y. Liu (1997), Surface Deformation and Lower Crustal Flow in Eastern Tibet, *Science (80-.).*, *276*(5313), 788–790, doi:10.1126/science.276.5313.788.

Ruddiman, W., and W. Prell (1997), Introduction to the uplift-climate connection, in *Tectonic uplift and climate change*, edited by W. Ruddiman, pp. 3–15, Plenum Press, New York.

Scott, D. (1979), On Optimal and Data-Based Histograms, *Biometrika*, *66*(3), 605–610.

Seilacher, A. (2007), *Trace Fossil Analysis*, Springer-Verlag.

Shyu, J. B. H., K. Sieh, Y.-G. Chen, and C.-S. Liu (2005a), Neotectonic architecture of Taiwan and its implications for future large earthquakes, *J. Geophys. Res.*, *110*(B8), 1–33, doi:10.1029/2004JB003251.

Shyu, J. B. H., K. Sieh, and Y. Chen (2005b), Tandem suturing and disarticulation of the Taiwan orogen revealed by its neotectonic elements, *Earth Planet. Sci. Lett.*, *233*(1-2), 167–177, doi:10.1016/j.epsl.2005.01.018.

Shyu, J. B. H., K. Sieh, Y.-G. Chen, and L.-H. Chung (2006), Geomorphic analysis of the Central Range fault, the second major active structure of the Longitudinal Valley suture, eastern Taiwan, *Geol. Soc. Am. Bull.*, *118*(11-12), 1447–1462, doi:10.1130/B25905.1.

Siame, L., H.-T. Chu, J. Carcaillet, D. Bourlès, R. Braucher, W.-C. Lu, J. Angelier, and P. Dussouliez (2007), Glacial retreat history of Nanhuta Shan (north-east Taiwan) from preserved glacial features: the cosmic ray exposure perspective., *Quat. Sci. Rev.*, *26*(17-18), 2185–2200, doi:10.1016/j.quascirev.2007.04.016.

Siame, L. L., H.-T. Chu, D. L. Bourlès, F. Derrieux, L. Léanni, and R. Chen (2012), Preservation of glacial landforms in the high mountains of Taiwan : Insights from in situ cosmogenic 10Be, in *Geophysical Research Abstracts Vol. 14, EGU2012-3573, 2012*, vol. 14, p. 3573.

Sibuet, J.-C., and S.-K. Hsu (2004), How was Taiwan created?, *Tectonophysics*, *379*(1-4), 159–181, doi:10.1016/j.tecto.2003.10.022.

Silver, E. A., and D. L. Reed (1988), Backthrusting in accretionary wedges, *J. Geophys. Res.*, *93*(B4), 3116–3126.

Simoes, M., and J.-P. Avouac (2006), Investigating the kinematics of mountain building in Taiwan from the spatiotemporal evolution of the foreland basin and western foothills, *J. Geophys. Res.*, *111*(B10), 1–25, doi:10.1029/2005JB004209.

Simoes, M., J.-P. Avouac, Y.-G. Chen, A. K. Singhvi, C.-Y. Wang, M. Jaiswal, Y.-C. Chan, and S. Bernard (2007a), Kinematic analysis of the Pakuashan fault tip fold, west central Taiwan: Shortening rate and age of folding inception, *J. Geophys. Res.*, *112*(B3), 1–30, doi:10.1029/2005JB004198.

Simoes, M., J.-P. Avouac, O. Beyssac, B. Goffé, K. a. Farley, and Y.-G. Chen (2007b), Mountain building in Taiwan: A thermokinematic model, *J. Geophys. Res.*, *112*(B11), 1–25, doi:10.1029/2006JB004824.

Simoes, M., O. Beyssac, and Y.-G. Chen (2012), Late Cenozoic metamorphism and mountain building in Taiwan: A review, *J. Asian Earth Sci.*, *46*(November), 92–119, doi:10.1016/j.jseaes.2011.11.009.

Stanley, R. S., L. B. Hill, H. C. Chang, and H. N. Hu (1981), A transect through the metamorphic core of the central mountains, southern Taiwan, *Mem. Geol. Soc. China*, *4*(4), 443–473.

Sternai, P., F. Herman, M. R. Fox, and S. Castelltort (2011), Hypsometric analysis to identify spatially variable glacial erosion, *J. Geophys. Res.*, *116*, 1–17, doi:10.1029/2010JF001823.

Stiiwe, K., and T. D. Barr (2000), On the relationship between surface uplift and gravitational extension, *Tectonics*, *19*(6), 1056–1064.

Stolar, D. B., S. D. Willett, and G. H. Roe (2006), Climatic and tectonic forcing of a critical orogen, in *Tectonics, Climate, and Landscape Evolution*, vol. 398, pp. 241–250.

Stolar, D. B., S. D. Willett, and D. R. Montgomery (2007), Characterization of topographic steady state in Taiwan, *Earth Planet. Sci. Lett.*, *261*(3-4), 421–431, doi:10.1016/j.epsl.2007.07.045.

Storti, F., and K. McClay (1995), Influence of syntectonic sedimentation on thrust wedges in analogue models, *Geology*, *23*(11), 999, doi:10.1130/0091-7613(1995)023<0999.

Strahler, A. (1952), Hypsometric (area-altitude) analysis of erosional topography, *Geol. Soc. Am. Bull.*, *63*, 1117–1142.

Stüwe, K. (2007), *Geodynamics of the Lithosphere: Quantitative decription of geological problems*, 2nd ed., Springer-Verlag.

Stüwe, K., and M. Hintermüller (2000), Topography and isotherms revisited: the influence of laterally migrating drainage divides, *Earth Planet. Sci. Lett.*, *184*(1), 287–303, doi:10.1016/S0012-821X(00)00315-0.

Stüwe, K., L. White, and R. Brown (1994), The influence of eroding topography on steady-state isotherms. Application to fission track analysis, *Earth Planet. Sci. Lett.*, *124*, 63–74.

Suppe, J. (1980a), A retrodeformable cross section of northern Taiwan, *Proceedings, Geol. Soc. China*, *23*, 46–55.

Suppe, J. (1980b), Imbricated structure of the western Foothills Belt, Central Taiwan, *Pet. Geol. Taiwan*, *17*, 1–16.

Suppe, J. (1981), Mechanics of mountain building and metamorphism in Taiwan, *Mem. Geol. Soc. China*, *4*, 67–89.

Suppe, J. (1984a), Kinematics of arc-continent collision, flipping of subduction, and back-arc spreading near Taiwan, *Mem. Geol. Soc. China*, *6*, 21–33.

Suppe, J. (1984b), *Principles of Structural Geology*, Prentice-Hall, Inc., Englewood Cliffs, New Jersey.

Suppe, J., and J. Namson (1979), Fault-bend origin of frontal folds of the Western Taiwan fold-and-thrust belt., *Pet. Geol. Taiwan*, *16*, 1–18.

Suppe, J., Y. Wang, J. Liou, and W. G. Ernst (1976), Observation of some contacts between the basement and Cenozoic cover in the Central Mountains, Taiwan, *Proc. Geol. Soc. China*, *19*, 59–70.

Tagami, T., and P. B. O'Sullivan (2005), Fundamentals of Fission-Track Thermochronology, *Rev. Mineral. Geochemistry*, *58*(1), 19–47, doi:10.2138/rmg.2005.58.2.

Tapponnier, P., G. Peltzer, and R. Armijo (1986), On the mechanism of collision between India and Asia., in *Collision Tectonics*, edited by M. P. Coward and A. C. Ries, pp. 115–157, Geological Society, London, Special Publications, 19,.

Teng, L. S. (1987), Stratigraphic records of the late Cenozoic Penglai orogeny of Taiwan, *Acta Geol. Taiwanica*, (25), 205–224.

Teng, L. S. (1990), Geotectonic evolution of late Cenozoic arc-continent in Taiwan, *Tectonophysics*, *183*, 57–76.

Teng, L. S. (1996), Extensional collapse of the northern Taiwan mountain belt, *Geology*, *24*(10), 949–952, doi:10.1130/0091-7613(1996)024<0949.

Teng, L. S., and A. T.-S. Lin (2004), Cenozoic tectonics of the China continental margin: insights from Taiwan, in *Aspects of Tectonic evolution of China*, vol. 226, edited by J. Malpas, C. J. N. Fletcher, J. Ali, and J. Aitchison, pp. 313–332, Geological Society, London, Special Publications 226.

Teng, L. S., Y. Wang, C. H. . Tang, C.-Y. Huang, T. . C. Huang, M. . S. Yu, and A. Ke (1991), Tectonic aspects of the Paleogene depositional basin of Northern Taiwan, *Proc. Geol. Soc. China*, *34*, 313–336.

Teng, L. S., C. T. Lee, Y. B. Tsai, and L.-Y. Hsiao (2000), Slab breakoff as a mechanism for flipping of subduction polarity in Taiwan, *Geology*, *28*(2), 155–158, doi:10.1130/0091-7613(2000)028<0155:SBAAMF>2.3.CO;2.

Tillman, K. S., and T. B. Byrne (1995), Kinematic analysis of the Taiwan Slate Belt, *Tectonics*, *14*(2), 322–341, doi:10.1029/94TC02451.

Tillman, K. S., and T. B. Byrne (1996), Out-of-sequence thrusting in the Taiwan slate belt, *J. Geol. Soc. China*, *39*(2), 189–208.

Tomita, Y. (1939), On the correlation of the topographical planes in Taiwan., *Rep. Japanese Assoc. Adv. Sci.*, *13*(3), 395–399.

Tomkin, J. H. (2007), Coupling glacial erosion and tectonics at active orogens: A numerical modeling study, *J. Geophys. Res.*, *112*(F2), F02015, doi:10.1029/2005JF000332.

Tomkin, J. H., and G. H. Roe (2007), Climate and tectonic controls on glaciated critical-taper orogens, *Earth Planet. Sci. Lett.*, *262*(3-4), 385–397, doi:10.1016/j.epsl.2007.07.040.

Tsao, S.-J. (1996), The geological significance of illite critallinity, zircon fission-track ages and K–Ar ages of metasedimentary rocks of the Central Range., 272 pp., National Taiwan University, Taipei, ROC.

Tsao, S.-J., T.-C. Li, J.-L. Tien, C.-H. Chen, T.-K. Liu, and C.-H. Chen (1992), Illite cristallinity and fission-track ages along the East Central cross-ilsland highway of Taiwan, *Acta Geol. Taiwanica*, (30), 45–64.

Usami, M., and T. Matsumoto (1940), Geologic map of Taiwan: Daibuzan sheet, *Beaureu Prod. Indus., Governement Gen. Taiwan*, (Scale 1: 100 000).

Ustaszewski, K., Y.-M. Wu, J. Suppe, H.-H. Huang, C.-H. Chang, and S. Carena (2012), Crust–mantle boundaries in the Taiwan–Luzon arc-continent collision system determined from local earthquake tomography and 1D models: Implications for the mode of subduction polarity reversal, *Tectonophysics*, *578*, 31–49, doi:10.1016/j.tecto.2011.12.029.

Valla, P. G., P. a. van der Beek, and J. Braun (2011), Rethinking low-temperature thermochronology data sampling strategies for quantification of denudation and relief histories: A case study in the French western Alps, *Earth Planet. Sci. Lett.*, *307*(3-4), 309–322, doi:10.1016/j.epsl.2011.05.003.

Wang Lee, C., and Y. Wang (1987), Tananao Terrane of Taiwan: its relation to the late mesozoic collision and accretion of the Southeast China margin, *Acta Geol. Taiwanica*, (25), 225–239.

Wang, P., and Q. Li (2009a), Oceanographic and geological backgrounds, in *The South China Sea*, edited by P. Wang and Q. Li, pp. 13–53, Springer, Dordrecht, The Netherlands.

Wang, P., and Q. Li (2009b), *The South China Sea*, Springer.

Wang, P.-L., L.-H. Lin, and C.-H. Lo (1998), 40Ar/39Ar dating of mylonitization in the Tananao schist, eastern Taiwan, *J. Geol. Soc. China*, *2*, 159–183.

Wang, T. K., M.-K. Chen, C.-S. Lee, and K. Xia (2006), Seismic imaging of the transitional crust across the northeastern margin of the South China Sea, *Tectonophysics*, *412*(3-4), 237–254, doi:10.1016/j.tecto.2005.10.039.

Wang, Y. (1979), Some strucural characyeristics of the Tertiary basement on Taiwan, *Mem. Geol. Soc. China*, *3*, 139–145.

Wegener, A. (1912), Die Entstehung der Kontinente, *Geol. Rund.*, *3*, 276–292.

Wei, K. (2006), Leg 195 synthesis: Site 1202 - Quaternary sedimentation and paleogeography in the southern Okinawa through, in *Proceedings of the Ocean Drilling Program, Scientific Results Volume 195*, vol. 195, edited by M. Shinohara, M. H. Salisbury, and C. Richter.

Whipple, K. X. (2009), The influence of climate on the tectonic evolution of mountain belts, *Nat. Geosci.*, *2*(2), 97–104, doi:10.1038/ngeo413.

Whipple, K. X., and B. Meade (2006), Orogen response to changes in climatic and tectonic forcing, *Earth Planet. Sci. Lett.*, *243*(1-2), 218–228, doi:10.1016/j.epsl.2005.12.022.

Widdowson, M. (1997), The geomorphological and geological importance of palaeosurfaces, *Geol. Soc. London, Spec. Publ.*, *120*, 1–12, doi:10.1144/GSL.SP.1997.120.01.01.

Willemin, J. H., and P. L. K. Knuepfer (1994), Kinematics of arc-continent collision in the eastern Central Range of Taiwan inferred from geomorphic analysis, *J. Geophys. Res.*, *99*(B10), 20267–20.

Willenbring, J. K., and F. von Blanckenburg (2010), Long-term stability of global erosion rates and weathering during late-Cenozoic cooling., *Nature*, *465*(7295), 211–4, doi:10.1038/nature09044.

Willett, S. D. (1999), Orogeny and orography: The effects of erosion on the structure of mountain belts, *J. Geophys. Res.*, *104*(B12), 28.957–28.981.

Willett, S. D. (2010), Late Neogene Erosion of the Alps: A Climate Driver?, *Annu. Rev. Earth Planet. Sci.*, *38*(1), 411–437, doi:10.1146/annurev-earth-040809-152543.

Willett, S. D., and M. T. Brandon (2002), On steady states in mountain belts, *Geology*, *30*(2), 175, doi:10.1130/0091-7613(2002)030<0175:OSSIMB>2.0.CO;2.

Willett, S. D., and M. T. Brandon (2013), Some analytical methods for converting thermochronometric age to erosion rate, *Geochemistry Geophys. Geosystems*, *in press*(14), 209–222, doi:10.1029/2012GC004279.

Willett, S. D., C. Beaumont, and P. Fullsack (1993), Mechanical model for the tectonics of doubly vergent compressional orogens, *Geology*, *21*(4), 371, doi:10.1130/0091-7613(1993)021<0371.

Willett, S. D., R. Slingerland, and N. Hovius (2001), Uplift, shortening, and steady state topography in active mountain belts, *Am. J. Sci.*, *301*, 455– 485.

Willett, S. D., D. M. Fisher, C. W. Fuller, Y. En-Chao, and L. Chia-Yu (2003), Erosion rates and orogenic-wedge kinematics in Taiwan inferred from fission-track thermochronometry, *Geology*, *31*(11), 945, doi:10.1130/G19702.1.

Willett, S. D., N. Hovius, M. T. Brandon, and D. M. Fisher (2006a), Introduction, in *Tectonic, Climate, and Landscape evolution*, vol. 398, edited by S. D. WIllett, N. Hovius, M. T. Brandon, and D. M. Fisher, pp. vii–xi, The Geological Society of America Special Paper.

Willett, S. D., F. Schlunegger, and V. Picotti (2006b), Messinian climate change and erosional destruction of the central European Alps, *Geology*, *34*(8), 613, doi:10.1130/G22280.1.

Willett, S. D., M. G. Fellin, and Y. G. Chen (2008), Detrital zircon fission track thermochronometry with implications for the topographic and exhumational history of Taiwan., in *Geochimica et Cosmochimica Acta 72, 12S (Goldschmidt Conference Abstracts)*, vol. 72, p. A1021.

Willett, S. D., S. W. McCoy, J. T. Perron, L. Goren, and C.-Y. Chen (2014), Dynamic Reorganization of River Basins, *Science (80-.).*, *343*(6175), doi:10.1126/science.1248765.

Wiltschko, D. V., L. Hassler, J.-H. Hung, and H.-S. Liao (2010), From accretion to collision: Motion and evolution of the Chaochou Fault, southern Taiwan, *Tectonics*, *29*(2), 1–23, doi:10.1029/2008TC002398.

Wu, F. T., R.-J. Rau, and D. Salzberg (1997), Taiwan orogeny: thin-skinned or lithospheric collision?, *Tectonophysics*, *274*(1-3), 191–220, doi:10.1016/S0040-1951(96)00304-6.

Wu, F. T., C. S. Chang, and Y.-M. Wu (2004), Precisely relocated hypocentres, focal mechanisms and active orogeny in Central Taiwan, *Geol. Soc. London, Spec. Publ.*, *226*(1), 333–353, doi:10.1144/GSL.SP.2004.226.01.18.

Wu, Y.-M., C.-H. Chang, L. Zhao, J. B. H. Shyu, Y.-G. Chen, K. Sieh, and J.-P. Avouac (2007), Seismic tomography of Taiwan: Improved constraints from a dense network of strong motion stations, *J. Geophys. Res.*, *112*(B8), 1–14, doi:10.1029/2007JB004983.

Yamato, P., P. Agard, E. Burov, L. Le Pourhiet, L. Jolivet, and C. Tiberi (2007), Burial and exhumation in a subduction wedge: Mutual constraints from thermomechanical modeling and natural P-T-t data (Schistes Lustrés, western Alps), *J. Geophys. Res.*, *112*(B7), 1–28, doi:10.1029/2006JB004441.

Yamato, P., F. Mouthereau, and E. Burov (2009), Taiwan mountain building: insights from 2D thermomechanical modelling of a rheologically stratified lithosphere, *Geophys. J. Int.*, *176*(1), 307–326, doi:10.1111/j.1365-246X.2008.03977.x.

Yan, P., H. Deng, H. Liu, Z. Zhang, and Y. Jiang (2006), The temporal and spatial distribution of volcanism in the South China Sea region, *J. Asian Earth Sci.*, *27*(5), 647–659, doi:10.1016/j.jseaes.2005.06.005.

Yang, K.-M., S.-T. Huang, J.-C. Wu, M. Lee, H.-H. Ting, and W.-W. Mei (2001), The characteristics of subsurface structure and evolution of the Tachien- shaneChukou thrust system., in *Annual Meeting of the Geological Society of China*, pp. 82–84.

Yang, T. F., J. Tien, C. Chen, T. Lee, and R. S. Punongbayang (1995), Fission-track dating of volcanics in the northern part of the Taiwan-Luzon Arc : eruption ages and evidence for crustal contamination, *J. Asian Earth Sci.*, *11*(2), 81–93.

Yang, T. F., C. Chen, R. L. Tien, S. R. Song, and T. K. Liu (2003), Remnant magmatic activity in the Coastal Range of East Taiwan after arc – continent collision : fission-track data and 3He/4He ratio evidence, *Radiat. Meas.*, *36*, 343–349, doi:10.1016/S1350-4487(03)00149-5.

Yeh, E.-C. (2004), Structural evolution of slates belts: examples from Tawain and eastern Pennsylvania., 207 pp., The Pennsylvania State University.

Yen, T. P. (1963), The metamorphic belts within the Tananao schist terrain of Taiwan, *Proc. Geol. Soc. China*, *6*, 72–74.

Yen, T. P., C. H. Wu, and T. Y. Chuang (1984), Geology along the Southern Taiwan east-west cross-mountain highway, *Spec. Pub. Cent. Geol. Surv.*, (3), 11–23.

Yen, T.-P., and Y.-T. Yang (1991), Miocene series and its basement strata in Taimali-Taiwu arera Southeastern Taiwan, *Proc. Geol. Soc. China*, *34*(1), 3–16.

Yu, S. (2001), Present-day crustal motion along the Longitudinal Valley Fault, eastern Taiwan, *Tectonophysics*, *333*(1-2), 199–217, doi:10.1016/S0040-1951(00)00275-4.

Yu, S., H.-Y. Chen, and L.-C. Kuo (1997), Velocity field of GPS stations in the Taiwan area, *Tectonophysics*, *274*(1-3), 41–59, doi:10.1016/S0040-1951(96)00297-1.

Yui, T.-F., and H.-T. Chu (2000), "Overturned" marble layers: evidence for upward extrusion of the Backbone Range of Taiwan, *Earth Planet. Sci. Lett.*, *179*(2), 351–361, doi:10.1016/S0012-821X(00)00119-9.

Yumul, G. P. (2007), Westward younging disposition of Philippine ophiolites and its implication for arc evolution, *Isl. Arc*, *16*(2), 306–317, doi:10.1111/j.1440-1738.2007.00573.x.

Zachos, J., M. Pagani, L. Sloan, E. Thomas, and K. Billups (2001), Trends , Rhythms , and Aberrations in Global Climate 65 Ma to Present, *Science (80-.).*, *292*(2001), 600–603, doi:10.1126/science.1059412.

Zhang, P. Z., P. Molnar, and W. R. Downs (2001), Increased sedimentation rates and grain sizes 2-4 Myr ago due to the influence of climate change on erosion rates., *Nature*, *410*(6831), 891–7, doi:10.1038/35073504.

Zhao, M., X. Qiu, S. Xia, H. Xu, P. Wang, T. K. Wang, C.-S. Lee, and K. Xia (2010), Seismic structure in the northeastern South China Sea: S-wave velocity and Vp/Vs ratios derived from three-component OBS data, *Tectonophysics*, *480*(1-4), 183–197, doi:10.1016/j.tecto.2009.10.004.

Ahnert, F. (1970), Functional relationships between denudation, relief, and uplift in large, mid-latitude drainage basins, *Am. J. Sci.*, *268*(3), 243–263.

Allen, P. (2005), Striking a chord., *Nature*, *434*(7036), 961, doi:10.1038/434961a.

Allen, P. a (2008a), From landscapes into geological history., *Nature*, *451*(7176), 274–6, doi:10.1038/nature06586.

Allen, P. A. (2008b), Time scales of tectonic landscapes and their sediment routing systems, in *Landscape Evolution: Denudation, Climate and Tectonics Over Different Times and Space scales*, edited by K. Gallagher, S. Jones, and J. Wainwright, pp. 7–28, Geological Society, London, Special Publications.

An, Z., J. E. Kutzbach, W. L. Prell, and S. C. Porter (2001), Evolution of Asian monsoons and phased uplift of the Himalaya-Tibetan plateau since Late Miocene times, *Nature*, *411*(May), 62–66.

Angelier, J., T.-Y. Chang, J.-C. Hu, C.-P. Chang, L. Siame, J.-C. Lee, B. Deffontaines, H.-T. Chu, and C.-Y. Lu (2009), Does extrusion occur at both tips of the Taiwan collision belt? Insights from active

deformation studies in the Ilan Plain and Pingtung Plain regions, *Tectonophysics*, *466*(3-4), 356–376, doi:10.1016/j.tecto.2007.11.015.

Aurelio, M. A. (1992), Tectonique du segment central de la faille philippine: Etude structurale, cinématique et évolution géodynamique = Tectonics of the central segment of the Philippine Fault: structures, kinematics, geodynamic evolution, 500 pp., Université de Paris 06, Paris, FRANCE.

Aurelio, M. A. (2000), Shear partitioning in the Philippines: Constraints from Philippine Fault and global positioning system data, *Isl. Arc*, *9*, 584–597.

Avouac, J.-P., and E. Burov (1996), Erosion as a driving mechanism of intracontinental mountain growth, *J. Geophys. Res.*, *101*(B8), 17747–17769.

Barbarand, J., A. Carter, I. Wood, and A. J. Hurford (2003), Compositional and structural control of fission-track annealing in apatite, *Chem. Geol.*, *198*(1-2), 107–137, doi:10.1016/S0009-2541(02)00424-2.

Barckhausen, U., M. Engels, D. Franke, S. Ladage, and M. Pubellier (2014), Evolution of the South China Sea: Revised ages for breakup and seafloor spreading, *Mar. Pet. Geol.*, doi:10.1016/j.marpetgeo.2014.02.022.

Barr, T. D., and F. A. Dahlen (1989), Brittle Frictional Mountain Building 2. Thermal Structure and Heat Budget, *J. Geophys. Res.*, *94*(88), 3923–3947.

Barr, T. D., F. A. Dahlen, and D. C. McPhail (1991), Brittle Frictional Mountain Building 3. Low-Grade Metamorphism, *J. Geophys. Res.*, *96*(B6), 10319–10338, doi:10.1029/91JB00295.

Barrier, E. (1985), The two stage collision of Taiwan: an active orogen, *Tectonophysics*, *115*, 167–175.

Batt, G. E., and M. T. Brandon (2002), Lateral thinking: 2-D interpretation of thermochronology in convergent orogenic settings, *Tectonophysics*, *349*(1-4), 185–201, doi:10.1016/S0040-1951(02)00053-7.

Batt, G. E., and J. Braun (1997), On the thermomechanical evolution of compressional orogens, *Geophys. J. Int.*, *128*(2), 364–382, doi:10.1111/j.1365-246X.1997.tb01561.x.

Beaumont, C., P. Fullsack, and J. Hamilton (1992), Erosional control of active compressional orogens, in *Thrust Tectonics*, edited by K. McClay, pp. 1–18., Chapman and Hall, London.

Beaumont, C., S. Ellis, J. Hamilton, and P. Fullsack (1996), Mechanical model for subduction-collision tectonics of Alpine-type compressional orogens, *Geology*, *24*(8), 675–678, doi:10.1130/0091-7613(1996)024<0675.

Beaumont, C., H. Kooi, and S. D. Willett (2000), Coupled tectonic-surface process models with applications to rifted margins and collisional orogens, in *Geomorphology and Global Tectonics*, edited by M. A. Summerfield, pp. 29–55, John Wiley & Sons Ltd,.

Beaumont, C., R. A. Jamieson, M. H. Nguyen, and B. Lee (2001), Himalayan tectonics explained by extrusion of a low-viscosity crustal channel coupled to focused surface denudation., *Nature*, *414*(6865), 738–42, doi:10.1038/414738a.

Beltrando, M., G. Manatschal, G. Mohn, G. V. Dal Piaz, A. Vitale Brovarone, and E. Masini (2014), Recognizing remnants of magma-poor rifted margins in high-pressure orogenic belts: The Alpine case study, *Earth-Science Rev.*, *131*, 88–115, doi:10.1016/j.earscirev.2014.01.001.

Berger, A. L. et al. (2008), Quaternary tectonic response to intensified glacial erosion in an orogenic wedge, *Nat. Geosci.*, *1*(11), 793–799, doi:10.1038/ngeo334.

Bernet, M., and J. I. Garver (2005), Fission-track Analysis of Detrital Zircon, in *Low-Temperature Thermochronology: Techniques, Interpretations, and Applications*, vol. 58, edited by P. W. Reiners and T. A. Ehlers, pp. 205–237, Reviews in Mineralogy and Geochemistry.

Bernet, M., and C. Spiegel (2004), Introduction: detrital thermochronology, in *Detrital thermochronology—Provenance analysis, exhumation, and landscape evolution of mountain belts*, vol. 378, edited by M. Bernet and C. Spiegel, pp. 1–6, Geological Society of America.

Bernet, M., M. T. Brandon, J. I. Garver, and B. Molitor (2004), Fundamentals of detrital zircon fission-track analysis for provenance and exhumation studies with examples from the European Alps, *Geol. Soc. Am. Spec. Pap.*, *378*, 25–36.

Beyssac, O., M. Simoes, J.-P. P. Avouac, K. a. Farley, Y.-G. Chen, Y.-C. Chan, and B. Goffé (2007), Late Cenozoic metamorphic evolution and exhumation of Taiwan, *Tectonics*, *26*(6), 1–32, doi:10.1029/2006TC002064.

Beyssac, O., F. Negro, M. Simoes, Y. C. Chan, and Y. G. Chen (2008), High-pressure metamorphism in Taiwan: from oceanic subduction to arc-continent collision?, *Terra Nov.*, *20*(2), 118–125, doi:10.1111/j.1365-3121.2008.00796.x.

Biq, C. (1977), The Kenting Mélange and the Manila Trench., *Proc. Geol. Soc. China*, *20*, 119–122.

Boillot, G. et al. (1987), Tectonic denudation of the upper mantle along passive margins : a model based on drilling results (ODP leg 103, western Galicia margin, Spain), *Tectonophysics*, *132*(2).

Bonnet, S., and A. Crave (2003), Landscape response to climate change: Insights from experimental modeling and implications for tectonic versus climatic uplift of topography, *Geology*, *31*(2), 123, doi:10.1130/0091-7613(2003)031<0123:LRTCCI>2.0.CO;2.

Böse, M. (2004), Traces of glaciation in the high mountains of Taiwan, *Dev. Quat. Sci.*, (1983).

Böse, M., and R. Hebenstreit (2008), Late Pleistocene and Early Holocene Glaciations in the Taiwanese High Mountain Ranges, in *Quaternary Glaciations - Extent and Chronology*, edited by J. Ehlers, P. Gibbard, and P. Hughes, pp. 1003–1012.

Brandon, M. T. (1992), Decomposition of fission-track grain-age distribution, *Am. J. Sci.*, (October), 535–564.

Brandon, M. T. (1996), Probability density for fission-track grain-age samples, *Radiat. Meas.*, *26*(5), 663–676.

Brandon, M. T., M. K. Roden-Tice, and J. I. Garver (1998), Late Cenozoic exhumation of the Cascadia accretionary wedge in the Olympic Mountains, northwest Washington State, *GSA Bull.*, *110*(8), 985–1009.

Braun, J. (2002), Quantifying the effect of recent relief changes on age–elevation relationships, *Earth Planet. Sci. Lett.*, *200*(3-4), 331–343, doi:10.1016/S0012-821X(02)00638-6.

Braun, J. (2006), Recent advances and current problems in modelling surface processes and their interaction with crustal deformation, in *Analogue and Numerical Modelling of Crustal-Scale Processes*, edited by S. J. H. Buiter and G. Schreurs, pp. 307–325, Spec. Publ. Geol. Soc. Lond. 253.

Braun, J., P. Van der Beek, and G. E. Batt (2006), *Quantitative Thermochronology: Numerical Methods for the Interpretation of Thermochronological Data*, Cambridge University Press, Cambridge.

Braun, J., F. Herman, and G. E. Batt (2010), Kinematic strain localization, *Earth Planet. Sci. Lett.*, *300*(3-4), 197–204, doi:10.1016/j.epsl.2010.08.018.

Braun, J., P. van der Beek, P. Valla, X. Robert, F. Herman, C. Glotzbach, V. Pedersen, C. Perry, T. Simon-Labric, and C. Prigent (2012), Quantifying rates of landscape evolution and tectonic processes by thermochronology and numerical modeling of crustal heat transport using PECUBE, *Tectonophysics*, *524-525*, 1–28, doi:10.1016/j.tecto.2011.12.035.

Brocklehurst, S. H., and K. X. Whipple (2004), Hypsometry of glaciated landscapes, *Earth Surf. Process. Landforms*, *29*(7), 907–926, doi:10.1002/esp.1083.

Brown, D., J. Alvarez-Marron, M. Schimmel, Y.-M. Wu, and G. Camanni (2012), The structure and kinematics of the central Taiwan mountain belt derived from geological and seismicity data, *Tectonics*, *31*(5), TC5013, doi:10.1029/2012TC003156.

Brozovic, N., D. W. Burbank, and A. J. Meigs (1997), Climatic Limits on Landscape Development in the Northwestern Himalaya, *Science (80-.).*, *276*(5312), 571–574, doi:10.1126/science.276.5312.571.

Brun, J. P., and M. O. Beslier (1996), Mantle exhumation at passive margins, *Earth Planet. Sci. Lett.*, *142*(1-2), 161–173, doi:10.1016/0012-821X(96)00080-5.

Burchfiel, B. C., L. H. Royden, R. D. van der Hilst, B. H. Hager, Z. Chen, R. W. King, C. Li, J. Lü, H. Yao, and E. Kirby (2008), A geological and geophysical context for the Wenchuan earthquake of 12 May 2008, Sichuan, People's Republic of China, *GSA Today*, *18*(7), 4, doi:10.1130/GSATG18A.1.

Bürgmann, R., and G. Dresen (2008), Rheology of the Lower Crust and Upper Mantle : Evidence from Rock Mechanics , Geodesy , and Field Observations, *Annu. Rev. Earth Planet. Sci.*, *36*, 531–567, doi:10.1146/annurev.earth.36.031207.124326.

Burov, E. B. (2011), Rheology and strength of the lithosphere, *Mar. Pet. Geol.*, *28*(8), 1402–1443, doi:10.1016/j.marpetgeo.2011.05.008.

Burov, E. B., and A. B. Watts (2006), The long-term strength of continental lithosphere:" jelly sandwich" or" crème brûlée"?, *GSA today*, *16*(1), 4, doi:10.1130/1052-5173(2006)016<4.

Byrne, T. B., and Y.-H. Lee (2013), Not available, in *Tectonics of Taiwan International Meeting*.

Byrne, T. B., and C.-S. Liu (2002), Preface: introduction to the geology and geophysics of Taiwan., in *Geology and Geophysics of an Arc- continent Collision, Taiwan*, Geological Society of America.

Byrne, T. B., Y.-C. Chan, R.-J. Rau, C.-Y. Lu, Y.-H. Lee, and Y.-J. Wang (2011), The Arc–Continent Collision in Taiwan, in *Arc-Continent Collision*, edited by D. Brown and P. D. Ryan, pp. 213–246, Springer.

Camanni, G., D. Brown, J. Alvarez-Marron, M. Shcimmel, and Y.-M. Wu (2011), Deformation partitioning in Central Taiwan : new insights from surface geology , earthquake focal mechanisms , seismic energy release and GPS measurements along the Shuilikeng Transpressive Fault System, *Rend. online Soc. Geol. It.*, *15*, 17–19.

Camanni, G., D. Brown, J. Alvarez-Marron, Y.-M. Wu, and H. -a. Chen (2013), The Shuilikeng fault in the central Taiwan mountain belt, *J. Geol. Soc. London.*, *171*(1), 117–130, doi:10.1144/jgs2013-014.

Camanni, G., C.-H. Chen, D. Brown, J. Alvarez-Marron, Y.-M. Wu, H.-A. Chen, H.-H. Huang, H.-T. Chu, M.-M. Chen, and C.-H. Chang (2014), Basin inversion in central Taiwan and its importance for seismic hazard, *Geology*, *42*(2), 147–150, doi:10.1130/G35102.1.

Castelltort, S., L. Goren, S. D. Willett, J.-D. Champagnac, F. Herman, and J. Braun (2012), River drainage patterns in the New Zealand Alps primarily controlled by plate tectonic strain, *Nat. Geosci.*, *5*(10), 744–748, doi:10.1038/ngeo1582.

Cederbom, C. E., H. D. Sinclair, F. Schlunegger, and M. K. Rahn (2004), Climate-induced rebound and exhumation of the European Alps, *Geology*, *32*(8), 709, doi:10.1130/G20491.1.

Champenois, J., B. Fruneau, E. Pathier, B. Deffontaines, K. Lin, and J. Hu (2012), Monitoring of active tectonic deformations in the Longitudinal Valley (Eastern Taiwan) using Persistent Scatterer InSAR method with ALOS PALSAR data, *Earth Planet. Sci. Lett.*, *338*, 144–155, doi:10.1016/j.epsl.2012.05.025.

Chan, Y. C., J. C. Lee, C. Y. Lu, and H. T. Chu (2001), Transtensional tectonics along a major north–south trending fault in the active convergent Taiwan mountain belt, in *EOS Trans. AGU Fall Meet. Suppl. 82(47) F1179.*

Chang, C.-P., J. Angelier, and C.-Y. Huang (2000), Origin and evolution of a mélange: the active plate boundary and suture zone of the Longitudinal Valley, Taiwan, *Tectonophysics*, *325*(1-2), 43–62, doi:10.1016/S0040-1951(00)00130-X.

Chang, C.-P., J. Angelier, C. Huang, and C. S. Liu (2002), Structural evolution and significance of a mélange in a collision belt: the Lichi Mélange and the Taiwan arc–continent collision, *Geol. Mag.*, *138*(06), 633–651, doi:10.1017/S0016756801005970.

Chang, C.-P., J. Angelier, T. Q. Lee, and C.-Y. Huang (2003), From continental margin extension to collision orogen: structural development and tectonic rotation of the Hengchun peninsula, southern Taiwan, *Tectonophysics*, *361*(1-2), 61–82, doi:10.1016/S0040-1951(02)00561-9.

Chang, C.-P., J. Angelier, and C.-Y. Huang (2009a), Evolution of Subductions Indicated by Mélanges in Taiwan, in *Subduction Zone Geodynamics*, edited by S. Lallemand and F. Funiciello, pp. 207–225, Springer-Verlag, Berlin Heidelberg.

Chang, C.-P., J. Angelier, and C.-Y. Lu (2009b), Polyphase deformation in a newly emerged accretionary prism: Folding, faulting and rotation in the southern Taiwan mountain range, *Tectonophysics*, *466*(3-4), 395–408, doi:10.1016/j.tecto.2007.11.002.

Chang, L.-S. (1970), A biostratigraphic study of the so-called Slate Formation on the east flank of the Central Range between Tawu and Taimali, southeastern Taiwan, based on smaller foraminifera, *Proc. Geol. Soc. China*, *13*, 129–142.

Chang, L.-S. (1971), A boistratigraphic study of the so-called slate formation in Taiwan based on smaller foraminifera: the E-W cross-mountain highway, *Proc. Geol. Soc. China*, *14*, 45–61.

Chang, L.-S. (1972), Eocene/Miocene hiatus and N conglomerate in the Central Range of Taiwan, *Proc. Geol. Soc. China*, (15), 93–98.

Chang, S. S. L., and W.-R. Chi (1983), Neogene Nannoplankton Biostratigraphy in Taiwan and the Tectonic Implications, *Pet. Geol. Taiwan*, *19*, 93–147.

Chen, C. H., H. T. Chu, J. G. Liou, and W. G. Ernst (1983), Explanatory notes for the metamorphic facies map of Taiwan, *Spec. Pub. Cent. Geol. Surv.*, (2).

Chen, C.-H. (1994), *Metamorphic Facies Map of Taiwan (1/500 000)*, CGS Specia., Central Geological Survey, The Ministry of Economic Affairs, Republic of China.

Chen, C.-H., H.-C. Ho, K.-S. Shea, W. Lo, W.-H. Lin, H.-C. Chang, C.-W. Huang, C.-N. Yang, and Y.-H. Lee (2000), Geological map of Taiwan. 1:500,000 scale, *Cent. Geol. Surv. Taipei, Taiwan*.

Chen, C.-T. A. (2001), Unveiling secrets locked in the great ghost lake in Taiwan, in *Paradoxes in Geology*, edited by U. Briegel and W. Xiao, pp. 389–409.

Chen, C.-T. A., J.-Y. Lou, J.-M. Lin, and C.-C. Chen (1997), Sedimentation rates of lakes and reservoirin Taiwan, *Oceanol. Limnol. Sin.*, *28*(6), 389–409.

Chen, C.-T. A., J.-T. Wu, B.-J. Wang, and K.-M. Huang (2004), Acidification and Trace Metals of Lakes in Taiwan, *Aquat. Geochemistry*, *10*(1/2), 33–57, doi:10.1023/B:AQUA.0000038956.17279.ff.

Cheng, K.-Y., J.-H. Hung, H.-C. Chang, H. Tsai, and Q.-C. Sung (2012), Scale independence of basin hypsometry and steady state topography, *Geomorphology*, *171-172*, 1–11, doi:10.1016/j.geomorph.2012.04.022.

Chi, W.-C., and D. L. Reed (2008), Evolution of shallow, crustal thermal structure from subduction to collision: An example from Taiwan, *Geol. Soc. Am. Bull.*, *120*(5-6), 679–690, doi:10.1130/B26210.1.

Chi, W.-R. (1979), A biostratigraphic study of the Late Neogene sediments in the Kaoshiung area based on calcareous nannofossils, *Proc. Geol. Soc. China*, *22*, 121–144.

Ching, K.-E., R.-J. Rau, J.-C. Lee, and J.-C. Hu (2007a), Contemporary deformation of tectonic escape in SW Taiwan from GPS observations, 1995–2005, *Earth Planet. Sci. Lett.*, *262*(3-4), 601–619, doi:10.1016/j.epsl.2007.08.017.

Ching, K.-E., R.-J. Rau, and Y. Zeng (2007b), Coseismic source model of the 2003 M w 6.8 Chengkung earthquake, Taiwan, determined from GPS measurements, *J. Geophys. Res.*, *112*(B6), 1–31, doi:10.1029/2006JB004439.

Ching, K.-E., K. M. Johnson, R.-J. Rau, R. Y. Chuang, L.-C. Kuo, and P.-L. Leu (2011a), Inferred fault geometry and slip distribution of the 2010 Jiashian, Taiwan, earthquake is consistent with a thick-skinned deformation model, *Earth Planet. Sci. Lett.*, *301*(1-2), 78–86, doi:10.1016/j.epsl.2010.10.021.

Ching, K.-E., M.-L. Hsieh, K. M. Johnson, K.-H. Chen, R.-J. Rau, and M. Yang (2011b), Modern vertical deformation rates and mountain building in Taiwan from precise leveling and continuous GPS observations, 2000–2008, *J. Geophys. Res.*, *116*(B8), 2000–2008, doi:10.1029/2011JB008242.

Ching, K.-E., R.-J. Rau, K. M. Johnson, J.-C. Lee, and J.-C. Hu (2011c), Present-day kinematics of active mountain building in Taiwan from GPS observations during 1995–2005, *J. Geophys. Res.*, *116*(B9), 1–22, doi:10.1029/2010JB008058.

Chou, J.-T. (1977), Sedimentology and Paleogeography of the Pleistocene Toukoshan Formation in Western Taiwan, *Pet. Geol. Taiwan*, *14*, 25–36.

Chou, S.-C., L. S. Teng, H.-S. Chung, and T.-W. Shiao (1994), Geohistory Analysis of West Taiwan Foreland Basin: A preliminary Study, *Pet. Geol. Taiwan*, *29*(Dec), 289–323.

Chu, H. T., H. N. Hu, H. Liew, and T. Chuang (1995), The geology of the western slope of the Nantawushan, southern Taiwan, *Bull. Cent. Geol. Surv*, *10*, 1–21.

Chu, H.-T., L. L. Siame, S. W. Lu, and C. Y. Wei (2007), The Preservation of Glacial Erosional Forms and Landscapes of the last Glaciations in subtropical area : Example from the High Mountains of Taiwan, in *Geophysical Research Abstracts*, vol. 9.

Chuang, R. Y., K. M. Johnson, Y. Wu, K. Ching, and L. Kuo (2013), A midcrustal ramp-fault structure beneath the Taiwan tectonic wedge illuminated by the 2013 Nantou earthquake series, *Geophys. Res. Lett.*, *40*, 5080–5084, doi:10.1002/grl.51005.

Clark, M. B., D. M. Fisher, and C.-Y. Lu (1992), Strain variations in the Eocene and older rocks exposed along the Central and Southern cross-island highways, Taiwan, *Acta Geol. taiwanica*, *30*, 1–10.

Clark, M. B., D. M. Fisher, C. Lu, and C.-H. Chen (1993), Kinematic analyses of the Hsueshan range, Taiwan: a large-scale pop-up strucure, *Tectonics*, *12*(1), 205–217.

Clark, M. K., M. A. House, L. H. Royden, K. X. Whipple, B. C. Burchfiel, X. Zhang, and W. Tang (2005), Late Cenozoic uplift of southeastern Tibet, *Geology*, *33*(6), 525–528, doi:10.1130/G21265.1.

Clark, M. K., L. H. Royden, K. X. Whipple, B. C. Burchfiel, X. Zhang, and W. Tang (2006), Use of a regional , relict landscape to measure vertical deformation of the eastern Tibetan Plateau, *J. Geophys. Res.*, *111*(F03002), 1–23, doi:10.1029/2005JF000294.

Clift, P. D., and R. A. Plumb (2008), *The Asian monsoon: causes, history and effects*, Cambridge University Press.

Clift, P. D., K. V. Hodges, D. Heslop, R. Hannigan, H. Van Long, and G. Calves (2008a), Correlation of Himalayan exhumation rates and Asian monsoon intensity, *Nat. Geosci.*, *1*(12), 875–880, doi:10.1038/ngeo351.

Clift, P. D., A. T.-S. Lin, A. Carter, F. T. Wu, A. E. Draut, T. H. Lai, L. Y. Fei, H. Schouten, and L. S. Teng (2008b), Post-collisional collapse in the wake of migrating arc-continent collision in the Ilan Basin, Taiwan, in

Formation and Applications of the Sedimentary Record in Arc Collision Zones, vol. 80301, edited by A. E. Draut and P. D. Clift, pp. 257–278, Geological Society of America Special Paper 436.

Cloetingh, S., P. Ziegler, F. Beekman, P. Andriessen, L. Matenco, G. Bada, D. Garciacastellanos, N. Hardebol, P. Dezes, and D. Sokoutis (2005), Lithospheric memory, state of stress and rheology: neotectonic controls on Europe's intraplate continental topography, *Quat. Sci. Rev.*, *24*(3-4), 241–304, doi:10.1016/j.quascirev.2004.06.015.

Cowie, P. A., C. H. Scholz, G. P. Roberts, J. P. F. Walker, and P. Steer (2013), Viscous roots of active seismogenic faults revealed by geologic slip rate variations, *Nat. Geosci.*, (November), 10–14, doi:10.1038/ngeo1991.

Crespi, J., Y. C. Chan, and M. S. Swaim (1996), Synorogenic extension and exhumation of the Taiwan hinterland, *Geology*, *24*(3), 247–250, doi:10.1130/0091-7613(1996)024<0247.

Cui, Z., J. Yang, G. Liu, X. Wang, and G. Song (2000), Discovery of Quaternary glacial evidence of Snow Mountain in Taiwan, China, *Chinese Sci. Bull.*, *45*(6), 566–571, doi:10.1007/BF02887108.

Cui, Z., C. Yang, G. Liu, W. Zhang, S. Wang, and Q. Sung (2002), The Quaternary glaciation of Shesan Mountain in Taiwan and glacial classification in monsoon areas, *Quat. Int.*, *98*, 147–153.

Cullen, A., P. Reemst, G. Henstra, S. Gozzard, and A. Ray (2010), Rifting of the South China Sea: new perspectives, *Pet. Geosci.*, *16*(3), 273–282, doi:10.1144/1354-079309-908.

Dadson, S. (2004), Erosion of an active mountain belt, 191 pp., The University of Cambridge.

Dadson, S. J. et al. (2003), Links between erosion, runoff variability and seismicity in the Taiwan orogen., *Nature*, *426*(6967), 648–51, doi:10.1038/nature02150.

Dahlen, F. A. (1984), Noncohesive Critical Coulomb Wedges: An Exact Solution, *J. Geophys. Res.*, *89*(B12), 10125–10133, doi:10.1029/JB089iB12p10125.

Dahlen, F. A. (1990), Critical taper model of fold-and-thrust belts and accretionary wedges, *Annu. Rev. Earth Planet. Sci.*, *18*, 55.

Dahlen, F. A., and T. D. Barr (1989), Brittle Frictional Mountain Building 1. Deformation and Mechanical Energy Budget, *J. Geophys. Res.*, *94*(B4), 3906–3922, doi:10.1029/JB094iB04p03906.

Dahlen, F. A., J. Suppe, and D. . Davis (1984), Mechanics of Fold-and-Thrust Belts and Accretionary Wedges' Cohesive Coulomb Theory, *J. Geophys. Res.*, *89*(B12), 10087–101.

Davis, D., J. Suppe, and F. a. Dahlen (1983), Mechanics of Fold-and-Thrust Belts and Accretionary Wedges, *J. Geophys. Res.*, *88*(B2), 1153–1172, doi:10.1029/JB088iB02p01153.

Davis, W. M. (1899), The Geographical Cycle, *R. Geogr. Soc. (with Inst. Br. Geogr.*, *14*(5), 481–504.

DeCelles, P. G., and K. a. Giles (1996), Foreland basin systems, *Basin Res.*, *8*(2), 105–123, doi:10.1046/j.1365-2117.1996.01491.x.

Dodson, M. H. (1973), Closure temperature in cooling geochronological and petrological systems, *Contrib. to Mineral. Petrol.*, *40*, 259–274.

Donelick, R. A., P. B. O'Sullivan, and R. A. Ketcham (2005), Apatite Fission-Track Analysis, *Rev. Mineral. Geochemistry*, *58*(1), 49–94, doi:10.2138/rmg.2005.58.3.

Dorsey, R. J. (1988), Provenance evolution and unroofing history of a modern arc-continent collision; evidence from petrography of Plio-Pleistocene sandstones, eastern Taiwan, *J. Sediment. Res.*, *58*(2), 208.

Dunlap, W. J., G. Hirth, and C. Teyssier (1997), Thermomechanical evolution of a ductile duplex, *Tectonics*, *16*(6), 983–1000.

Eakin, D. H., K. D. McIntosh, H. J. a. Van Avendonk, L. Lavier, R. Lester, C.-S. Liu, and C.-S. Lee (2014), Crustal-scale seismic profiles across the Manila subduction zone: The transition from intraoceanic subduction to incipient collision, *J. Geophys. Res. Solid Earth*, *119*(1), 1–17, doi:10.1002/2013JB010395.

Egholm, D. L., S. B. Nielsen, V. K. Pedersen, and J.-E. Lesemann (2009), Glacial effects limiting mountain height., *Nature*, *460*(7257), 884–7, doi:10.1038/nature08263.

Von Elverfeldt, K. (2012), *System Theory in Geomorphology: Challenges, Epistemological Consequences and Practical Implications*, Springer.

Faccenna, C., and T. W. Becker (2010), Shaping mobile belts by small-scale convection, *Nature*, *465*, 602–606.

Faure, M., C.-Y. Lu, and H.-T. Chu (1991), Ductile deformation and Miocene nappe-stacking in Taiwan related to motion of the Philippine Sea Plate, *Tectonophysics*, *198*(1), 95–105, doi:10.1016/0040-1951(91)90134-E.

Fellin, M. G., S. D. Willett, and J. I. Garver (2006), Plio-Pleistocene erosion rates in Taiwan inferred from detrital zircon fission-track and (U-Th)/ He thermochronometry, *Geophys. Res. Abstr. Vol. 8*, *8*.

Fellin, M. G., S. D. Willett, and Y. Chen (2008), Spatial and temporal variations of erosion rates in Taiwan from detrital zircon-fission-track dating ., *Geophys. Res. Abstr.*, *10*(EGU2008-A-07624), 8–9.

Fellin, M. G., S. D. Willett, R. C. Thiede, and Y. Chen (2009), Topographic and Exhumational History of Taiwan Based on Detrital Zircon Fission-Track Thermochronometry, *Am. Geophys. Union, Fall Meet. 2009*, 3.

Fellin, M. G., S. D. Willett, and M. T. Brandon (2012), Zircon fission-track dating of modern river sands and exhumational patterns in Taiwan, *13th Int. Conf. Thermochronology, Abstr.*

Fillon, C., R. S. Huismans, and P. van der Beek (2013), Syntectonic sedimentation effects on the growth of fold-and-thrust belts, *Geology*, *41*(1), 83–86, doi:10.1130/G33531.1.

Fisher, D. M. (1999), Orogen parallel extension Eastern Central range of Taiwan, *J. Geol. Soc. China-Taiwan*, *42*(2), 41–58.

Fisher, D. M., C. Lu, and H.-T. Chu (2002), Taiwan Slate Belt: Insights into the ductile interior of an arc-continent collision, in *Geology and Geophysics of an Arc-Continent Collision, Taiwan*, edited by T. B. Byrne and C.-S. Liu, pp. 93–106, Geological Society of America Special Paper 358, Boulder, Colorado.

Fisher, D. M., S. D. Willett, E.-C. Yeh, M. B. Clark, and Y. En-Chao (2007), Cleavage fronts and fans as reflections of orogen stress and kinematics in Taiwan, *Geology*, *35*(1), 65, doi:10.1130/G22850A.1.

Fitzgerald, P. G., R. B. Sorkhabi, T. F. Redfield, and E. Stump (1995), Uplift and denudation of the central Alaska Range: A case study in the use of apatite fission track thermochronology to determine absolute uplift parameters, *J. Geophys. Res.*, *100*(B10), 20175–20191, doi:10.1029/95JB02150.

Foeken, J. P. T., C. Persano, F. M. Stuart, and M. ter Voorde (2007), Role of topography in isotherm perturbation: Apatite (U-Th)/He and fission track results from the Malta tunnel, Tauern Window, Austria, *Tectonics*, *26*(3), 1–15, doi:10.1029/2006TC002049.

Fossen, H. (2010), *Structural Geology*, Cambridge University Press.

Franke, D. (2013), Rifting, lithosphere breakup and volcanism : Comparison of magma-poor and volcanic rifted margins, *Mar. Pet. Geol.*, *43*, 63–87, doi:10.1016/j.marpetgeo.2012.11.003.

Frisch, W., M. Meschede, and R. Blakey (2011), *Plate Tectonics: Continental Drift and Mountain Building*, Springer-Verlag.

Fuller, C. W., S. D. Willett, N. Hovius, and R. Slingerland (2003), Erosion Rates for Taiwan Mountain Basins: New Determinations from Suspended Sediment Records and a Stochastic Model of Their Temporal Variation, *J. Geol.*, *111*(1), 71–87, doi:10.1086/344665.

Fuller, C. W., S. D. Willett, D. M. Fisher, and C. Y. Y. Lu (2006), A thermomechanical wedge model of Taiwan constrained by fission-track thermochronometry, *Tectonophysics*, *425*(1-4), 1–24, doi:10.1016/j.tecto.2006.05.018.

Fusseis, F., M. R. Handy, and C. Schrank (2006), Networking of shear zones at the brittle-to-viscous transition (Cap de Creus , NE Spain), , *28*, 1228–1243, doi:10.1016/j.jsg.2006.03.022.

Gallagher, K. (2012), Transdimensional inverse thermal history modeling for quantitative thermochronology, *J. Geophys. Res.*, *117*(B2), 1–16, doi:10.1029/2011JB008825.

Gallagher, K., R. Brown, and C. Johnson (1998), Fission Track Analysis and Its Applications To Geological Problems, *Annu. Rev. Earth Planet. Sci.*, *26*(1), 519–572, doi:10.1146/annurev.earth.26.1.519.

Garver, J. I., and P. J. J. Kamp (2002), Integration of zircon color and zircon fission-track zonation patterns in orogenic belts: application to the Southern Alps, New Zealand, *Tectonophysics*, *349*(1-4), 203–219, doi:10.1016/S0040-1951(02)00054-9.

Garver, J. I., P. W. Reiners, L. J. Walker, J. M. Ramage, and S. E. Perry (2005), Implications for Timing of Andean Uplift from Thermal Resetting of Radiation-Damaged Zircon in the Cordillera Huayhuash, Northern Peru, *J. Geol.*, *113*, 117–138.

Ge, J., Y. Dai, Z. Zhang, D. Zhao, Q. Li, Y. Zhang, L. Yi, and H. Wu (2013), Major changes in East Asian climate in the mid-Pliocene : Triggered by the uplift of the Tibetan Plateau or global cooling ?, *J. Asian Earth Sci.*, *69*, 48–59, doi:10.1016/j.jseaes.2012.10.009.

Glotzbach, C. (2008), Low-temperature thermochronology from tunnel and surface samples in the Central and Western Alps, der Geowissenschaftlichen Fakultät der Eberhard-Karls-Universität Tübingen.

Goren, L., S. Castelltort, S. D. Willett, J.-D. Champagnac, F. Herman, and J. Braun (2012), Passive advection and dynamic reorganization of mountainous bedrock rivers : A landscape evolution modeling approach, in *Geophysical Research Abstracts*, vol. 14, pp. Vol.14, EGU2012–10441.

Gourley, J., T. B. Byrne, Y. Chan, F. T. Wu, and R.-J. Rau (2007), Fault geometries illuminated from seismicity in central Taiwan: Implications for crustal scale structural boundaries in the northern Central Range, *Tectonophysics*, *445*(3-4), 168–185, doi:10.1016/j.tecto.2007.08.013.

Hall, R. (1997), Cenozoic plate tectonic reconstructions of SE Asia, in *Petroleum Geology of Southeast Asia*, vol. 126, edited by A. J. Fraser, S. J. Mattehs, and R. W. Murphy, pp. 11–23, Geological Society, London, Special Publications 126.

Hall, R. (2002), Cenozoic geological and plate tectonic evolution of SE Asia and the SW Pacific: computer-based reconstructions, model and animations, *J. Asian Earth Sci.*, *20*(4), 353–431, doi:10.1016/S1367-9120(01)00069-4.

Hall, R., M. Fuller, J. R. Ali, and C. D. Anderson (1995), The Philippine Sea Plate: Magnetism and Reconstruction, in *Active Margin and Marginal Basins of the Western Pacific, Geophysical Monograph 88*, pp. 371–404, American Geophysical Union.

Hall, R., M. W. A. van Hattum, and W. Spakman (2008), Impact of India–Asia collision on SE Asia: the record in Borneo, *Tectonophysics*, *451*, 366–369.

Haq, S. S. B., and D. M. Davis (2008), Extension during active collision in thin-skinned wedges: Insights from laboratory experiments, *Geology*, *36*(6), 475, doi:10.1130/G24718A.1.

Hastenrath, S. (2009), Past glaciation in the tropics, *Quat. Sci. Rev.*, *28*(9-10), 790–798, doi:10.1016/j.quascirev.2008.12.004.

Hay, W., E. Soeding, R. DeConto, and C. Wold (2002), The Late Cenozoic uplift - climate change paradox, *Int. J. Earth Sci.*, *91*(5), 746–774, doi:10.1007/s00531-002-0263-1.

Hebenstreit, R. (2006), Present and former equilibrium line altitudes in the Taiwanese high mountain range., *Quat. Int.*, *147*, 70–75.

Hebenstreit, R. (2012), Geomorphological studies on the late Pleistocene and early Holocene glaciation in selected high mountain ranges in Taiwan, Freien Universität Berlin.

Hebenstreit, R., M. Böse, and A. Murray (2006), Late Pleistocene and early Holocene glaciations in Taiwanese mountains, *Quat. Int.*, *147*(1), 76–88, doi:10.1016/j.quaint.2005.09.009.

Hebenstreit, R., S. Ivy-Ochs, P. W. Kubik, C. Schlüchter, and M. Böse (2011), Lateglacial and early Holocene surface exposure ages of glacial boulders in the Taiwanese high mountain range, *Quat. Sci. Rev.*, *30*(3-4), 298–311, doi:10.1016/j.quascirev.2010.11.002.

Herman, F., D. Seward, P. G. Valla, A. Carter, B. Kohn, S. D. Willett, and T. A. Ehlers (2013), Worldwide acceleration of mountain erosion under a cooling climate, *Nature*, *504*, 423–426, doi:10.1038/nature12877.

Hilley, G. E., and M. R. Strecker (2004), Steady state erosion of critical Coulomb wedges with applications to Taiwan and the Himalaya, *J. Geophys. Res.*, *109*(B1), 1–17, doi:10.1029/2002JB002284.

Ho, C. S. (1986), A synthesis of the geologic evolution of Taiwan, *Tectonophysics*, *125*(1-3), 1–16, doi:10.1016/0040-1951(86)90004-1.

Ho, C. S. (1988), *An introduciton to the geology of Taiwan: Explanatory text of the geologic map of Taiwan (2nd edition)*, Second Edi., Central Geological Survey, The Ministry of Economic Affairs, Taipei, Taiwan, Republic of China.

Horng, C.-S., K. Shea, K.-H. Chen, and C.-Y. Kao (2007), Magnetobiostratigraphy of the Liukuei and Linkou Conglomerates and the Tashe Formation in the Kaohsiung Area, in *XIth Symposium on Quaternary of Taiwan, 21-22 September*, pp. 79–80.

House, M., B. P. Kohn, K. A. Farley, and A. Raza (2002), Evaluating thermal history models for the Otway Basin, southeastern Australia, using (U-Th)/He and fission-track data from borehole apatites, *Tectonophysics*, *349*(1-4), 277–295, doi:10.1016/S0040-1951(02)00057-4.

Hovius, N., C. Stark, H.-T. Chu, and L. Jiun-Chuan (2000), Supply and Removal of Sediment in a Landslide-Dominated Mountain Belt: Central Range, Taiwan., *J. Geol.*, *108*(1), 73–89.

Hsu, S.-K., Y. C. Yeh, W. B. Doo, and C. H. Tsai (2004), New bathymetry and magnetic lineations identifications in the northernmost South China Sea and their tectonic implications, *Mar. Geophys. Res.*, *25*, 29–44.

Hsu, S.-K., Y.-C. Yeh, C.-L. Lo, A. T.-S. Lin, and W.-B. Doo (2008), Link between Crustal Magnetization and Earthquakes in Taiwan, *October*, *19*(5), 445–450, doi:10.3319/TAO.2008.19.5.445(T)1.

Hu, H. N., and S. Tsan (1984a), Structural Study of the Slate formation along the South link railroad, Taiwan, *Spec. Pub. Cent. Geol. Surv.*, 25–44.

Hu, H.-N., and S. F. Tsan (1984b), Strucural Study of the slate formation along the Sout link railroad, Taiwan, *Spec. Pub. Cent. Geol. Surv.*, *3*(December), 25–43.

Hu, J. et al. (2007), Fault activity and lateral extrusion inferred from velocity field revealed by GPS measurements in the Pingtung area of southwestern Taiwan, *J. Asian Earth Sci.*, *31*(3), 287–302, doi:10.1016/j.jseaes.2006.07.020.

Huang, A. Y., and D. R. Montgomery (2013), Topographic locations and size of earthquake- and typhoon generated landslides, tachia river, Taiwan, *Earth Surf. Process. Landforms*, doi:10.1002/esp.3510.

Huang, C. Y., C. W. Chien, B. Yao, and C.-P. Chang (2008a), The Lichi Melange: A collision melange formation along early arcward backthrust during forearc basin closure, Taiwan arc-continent collision, in *Formation and applications of the sedimentary record in arc collision zones*, vol. 436, edited by A. E. Draunt, P. D. Clift, and D. W. Scholl, pp. 127–154, Geological Society of America Special Paper 436.

Huang, C.-Y., W.-Y. Wu, C.-P. Chang, S. Tsao, P. B. Yuan, C.-W. Lin, and K.-Y. Xia (1997), Tectonic evolution of accretionary prism in the arc-continent collision terrane of Taiwan, *Tectonophysics*, *281*(1-2), 31–51, doi:10.1016/S0040-1951(97)00157-1.

Huang, C.-Y., Y.-L. Chiu, and M. Zhao (2005), Core Description and a Preliminarily Sedimentology Study of Site 1202D, Leg 195, in the Southern Okinawa Trough, *Terr. Atmos. Ocean. Sci.*, *16*(1), 19–44.

Huang, C.-Y., P. B. Yuan, and S.-J. Tsao (2006), Temporal and spatial records of active arc-continent collision in Taiwan: A synthesis, *Geol. Soc. Am. Bull.*, *118*(3-4), 274–288, doi:10.1130/B25527.1.

Huang, C.-Y., C. C. W. Chien, B. Yao, and C. Chang (2008b), The Lichi Mélange: A collision mélange formation along early arcward backthrusts during forearc basin closure, Taiwan arc-continent collision, in *The Geological Society of America Special Paper 436*, vol. 2436, edited by A. E. Draunt, P. D. Clift, and D. W. Scholl, pp. 127–154, Geological Society of America Special Paper 436.

Huang, C.-Y., Y. Yen, Q. Zhao, and C. Lin (2012), Cenozoic stratigraphy of Taiwan : Window into rifting , stratigraphy and paleoceanography of South China Sea, *Chinese Sci. Bull.*, *57*(24), 3130–3149, doi:10.1007/s11434-012-5349-y.

Huang, T.-C. (1979), The Oligocene/Miocene boundary in Taiwan, *Mem. Geol. Soc. China*, (3), 103–123.

Huang, T.-C. (1980a), A calcareous nannofossil biostratigraphic study of the Assilia-bearing section, Chunkengchi, Nantou, *Proc. Geol. Soc. China*, (23), 7–15.

Huang, T.-C. (1980b), Calcareous Nannofossils from the slate terrane west of Yakou , Southern Cross-Island Highway, *Pet. Geol. Taiwan*, *17*, 59–74.

Huang, W.-J., K. M. Johnson, J. Fukuda, and S.-B. Yu (2010), Insights into active tectonics of eastern Taiwan from analyses of geodetic and geologic data, *J. Geophys. Res.*, *115*(B3), 1–18, doi:10.1029/2008JB006208.

Hung, J.-H., D. V. Wiltschko, H.-C. Lin, J. B. Hickman, P. Fang, and Y. Bock (1999), Structure and motion of the southwestern Taiwan fold and thrust belt., *Terr. Atmos. Ocean. Sci.*, *10*(3), 543–568.

Hurford, A. J., and P. F. Green (1982), A users' guide to fission track dating calibration Anthony J. Hurford, , *59*, 343–354.

Hwang, C., Y.-S. Hsiao, H.-C. Shih, M. Yang, K.-H. Chen, R. Forsberg, and A. V. Olesen (2007), Geodetic and geophysical results from a Taiwan airborne gravity survey: Data reduction and accuracy assessment, *J. Geophys. Res.*, *112*(B4), 1–14, doi:10.1029/2005JB004220.

Jahn, B., J. Martineau, J. Peucat, and J. Cornichet (1986), Geochronology of the Tananao schist complex and crustal evolution of Taiwan: Mem, *Geol. Soc. China*, (7), 383–404.

Jahn, B.-M. (2010), CHECK IT OUT, in *Taiwan Tectonics Workshop, Institute of Earth Science, Academia Sinica, Taiwan.*

Jamieson, R. A., C. Beaumont, J. Hamilton, and P. Fullsack (1996), Tectonic assembly of inverted metamorphic sequences, *Geology*, *24*, 839–842, doi:10.1130/0091-7613(1996)024<0839.

Jammes, S., and R. S. Huismans (2012), Structural styles of mountain building : Controls of lithospheric rheologic stratification and extensional inheritance, , *117*(October), 1–22, doi:10.1029/2012JB009376.

Jolivet, L., K. Tamaki, and M. Fournier (1994), Japan Sea, opening history and mechanism: A synthesis, *J. Geophys. Res.*, *99*(B11), 22237–22259.

Kao, H., S. J. Shen, and K. Ma (1998), Transition form oblique subduction to collision: earthquakes in the southermost Ryukyu arc-Taiwan region, *J. Geophys. Res.*, *103*(B4), 211–229.

Kirstein, L. A., M. G. Fellin, S. D. Willett, A. Carter, Y.-G. Chen, J. I. Garver, and D. C. Lee (2010a), Pliocene onset of rapid exhumation in Taiwan during arc-continent collision: new insights from detrital thermochronometry, *Basin Res.*, *22*(3), 270–285, doi:10.1111/j.1365-2117.2009.00426.x.

Kirstein, L. A., A. Carter, and Y.-G. Chen (2010b), Testing inferences from palaeocurrents: application of zircon double-dating to Miocene sediments from the Hengchun Peninsula, Taiwan, *Terra Nov.*, *22*(6), 483–493, doi:10.1111/j.1365-3121.2010.00970.x.

Kirstein, L. A., A. Carter, and Y. Chen (2013), Impacts of arc collision on small orogens: new insights from the Coastal Range detrital record, Taiwan, *J. Geol. Soc. London.*, doi:10.1144/jgs2013-046.

Knuepfer, P. L. K., and J. H. Willemin (1992), Geomorphic evidence for axial tilting of teh longitudinal valley, Taiwan, *Acta Geol. taiwanica*, *30*, 89–100.

Knuth, K. (2006), Optimal data-based binning for histograms, *arXiv Prepr. physics/0605197*, (3), 1–27.

Koons, P. (1990), Two-sided orogen : Collision and erosion from the sandbox to the Southern Alps, New Zealand, *Geology*, *18*, 679–682, doi:10.1130/0091-7613(1990)018<0679.

Koppes, M. N., and D. R. Montgomery (2009), The relative efficacy of fluvial and glacial erosion over modern to orogenic timescales, *Nat. Geosci.*, *2*(9), 644–647, doi:10.1038/ngoe616.

Kuo-Chen, H., F. T. Wu, D. M. Jenkins, J. Mechie, S. W. Roecker, C. Wang, and B. Huang (2012a), Seismic evidence for the a-b quartz transition beneath Taiwan from Vp/Vs tomography, *Geophys. Res. Lett*, *39*(L22302), 1–6, doi:10.1029/2012GL053649.

Kuo-Chen, H., F. T. Wu, and S. W. Roecker (2012b), Three-dimensional P velocity structures of the lithosphere beneath Taiwan from the analysis of TAIGER and related seismic data sets, *J. Geophys. Res.*, *117*(B06306), 1–19, doi:10.1029/2011JB009108.

Lacombe, O., F. Mouthereau, J. Angelier, and B. Deffontaines (2001), Structural, geodetic and seismological evidence for tectonic escape in SW Taiwan, *Tectonophysics*, *333*(1-2), 323–345, doi:10.1016/S0040-1951(00)00281-X.

Lan, C.-Y., C.-H. Chen, C.-H. Chen, S.-L. Chung, T. Lee, C.-M. Wang Lee, and T.-F. Yui (1996), The crustal evolution of continental Taiwan, *J. Geol. Soc. China*, *39*(3), 337–353.

Lan, C.-Y., C.-S. Lee, T.-F. Yui, H.-T. Chu, and B.-M. Jahn (2008), The tectono-thermal events of Taiwan and their relationship with SE China, *Terr. Atmos. Ocean. Sci.*, *19*(3), 257–278, doi:10.3319/TAO.2008.19.3.257(TT)1.

Larsen, I. J., D. R. Montgomery, and O. Korup (2010), Landslide erosion controlled by hillslope material, *Nat. Geosci.*, *3*(4), 247–251, doi:10.1038/ngeo776.

Law, R. D., M. P. Searle, and L. Godin (Eds.) (2006), *Channel flow, ductile extrusion and exhumation in continental collision zones*, Geological Society, London, Special Publications, 268.

Lee, C. (1984), Systematics of Assilina formosensis Hanzawa from the slate terrain of Taiwan, *Mem. Geol. Soc. China*, (6), 335–344.

Lee, J.-C. (2003), Active fault creep variations at Chihshang, Taiwan, revealed by creep meter monitoring, 1998–2001, *J. Geophys. Res.*, *108*(B11), 1998–2001, doi:10.1029/2003JB002394.

Lee, J.-C., J. Angelier, and H.-T. Chu (1997), Polyphase history and kinematics of a complex major fault zone in the northern Taiwan mountain belt: the Lishan Fault, *Tectonophysics*, *274*(1-3), 97–115, doi:10.1016/S0040-1951(96)00300-9.

Lee, Y.-H., C.-C. Chen, T.-K. Liu, H.-C. Ho, H.-Y. Lu, and W. Lo (2006), Mountain building mechanisms in the Southern Central Range of the Taiwan Orogenic Belt — From accretionary wedge deformation to arc–continental collision, *Earth Planet. Sci. Lett.*, *252*(3-4), 413–422, doi:10.1016/j.epsl.2006.09.047.

Lee, Y.-H., G.-T. Chen, R.-J. Rau, and K.-E. Ching (2008), Coseismic displacement and tectonic implication of 1951 Longitudinal Valley earthquake sequence, eastern Taiwan, *J. Geophys. Res.*, *113*(B4), 1–13, doi:10.1029/2007JB005180.

Leighly, J. (1940), Walter Penck's contribution to Geomorphology, *Ann. Ass. Am. Geogr.*, *30*, 223–32.

Lester, R., L. L. Lavier, K. McIntosh, H. J. a. Van Avendonk, and F. T. Wu (2012), Active extension in Taiwan's precollision zone: A new model of plate bending in continental crust, *Geology*, *40*(9), 831–834, doi:10.1130/G33142.1.

Lester, R., K. McIntosh, H. J. A. Van Avendonk, L. Lavier, C.-S. Liu, and T. K. Wang (2013), Crustal accretion in the Manila trench accretionary wedge at the transition from subduction to mountain-building in Taiwan, *Earth Planet. Sci. Lett.*, *375*, 430–440.

Lewis, C., S.-W. Chen, and P.-C. Yen (2004), Magnetic Surveying of the Chaochou Fault of Southern Taiwan: Culmination of Basement-Involved Surface Thrusting in Arc-Continent Collision, *Int. Geol. Rev.*, *46*(5), 399–408, doi:10.2747/0020-6814.46.5.399.

Li, Q., G. Zhong, and J. Tian (2009), Stratigraphy an sea level changes, in *The South China Sea*, edited by P. Wang and Q. Li, pp. 55–133, Springer, Dordrecht, The Netherlands.

Li, Y. H. (1975), Denudation of Taiwan island since Pliocene epoch, *Geology*, *4*(2), 105–107.

Liew, P.-M. (1986), Palynological stratigraphy and climatic implications of pleistocene sediments in western Taiwan, *Acta Geol. taiwanica*, *24*, 165–177.

Liew, P.-M. (1991), Pleistocene cool stage and geological changes of western Taiwan based on palynological study, *Acta Geol. Taiwanica*, *29*, 21–32.

Liew, P.-M., and S.-Y. Huang (1994), Pollen analysis and their paleoclimatic implication in the Middle Pleistocene lake deposits of ilan district, northeastern Taiwan, *J. Geol. Soc. China*, *37*(1), 115–124.

Liew, P.-M., C. Y. Lee, and C. M. Kuo (2006a), Holocene thermal optimal and climate variability of East Asian monsoon inferred from forest reconstruction of a subalpine pollen sequence, Taiwan, *Earth Planet. Sci. Lett.*, *250*(3-4), 596–605, doi:10.1016/j.epsl.2006.08.002.

Liew, P.-M., S.-Y. Huang, and C.-M. Kuo (2006b), Pollen stratigraphy, vegetation and environment of the last glacial and Holocene—A record from Toushe Basin, central Taiwan, *Quat. Int.*, *147*(1), 16–33, doi:10.1016/j.quaint.2005.09.003.

Liew, P.-M., B.-C. Chen, M.-L. Hsieh, S.-Y. Huang, and C.-Y. Lee (2013), Decreasing intensity of the last glacial stadials in low latitude terrestrial East Asia inferred by a new observation of pollen records in central Taiwan, *J. Asian Earth Sci.*, *69*, 159–165, doi:10.1016/j.jseaes.2012.05.027.

Lin, A. T.-S., and A. B. Watts (2002), Origin of the West Taiwan basin by orogenic loading and flexure of a rifted continental margin, *J. Geophys. Res.*, *107*(B9), doi:10.1029/2001JB000669.

Lin, A. T.-S., A. B. Watts, and S. P. Hesselbo (2003), Cenozoic stratigraphy and subsidence history of the South China Sea margin in the Taiwan region, *Basin Res.*, *15*(4), 453–478, doi:10.1046/j.1365-2117.2003.00215.x.

Lin, A. T.-S., B. Yao, S.-K. Hsu, C.-S. Liu, and C.-Y. Huang (2009), Tectonic features of the incipient arc-continent collision zone of Taiwan: Implications for seismicity, *Tectonophysics*, *479*(1-2), 28–42, doi:10.1016/j.tecto.2008.11.004.

Lin, C., and S. W. Roecker (1998), Active Crustal Subduction and Exhumation in Taiwan, in *When Continents Collide : Geodynamics and Geochemistry of Ultrahigh-Pressure Rocks*, edited by B. Hacker and J. G. Liou, pp. 1–16, Chapman Hall.

Lin, C. C. (1957), *Geomorphology of Taiwan*, Taiwan Literature Commitee.

Lin, C.-H. (2000), Thermal modeling of continental subduction and exhumation constrained by heat flow and seismicity in Taiwan, *Tectonophysics*, *324*(3), 189–201, doi:10.1016/S0040-1951(00)00117-7.

Lin, C.-H. (2002), Active continental subduction and crustal exhumation: the Taiwan orogeny, *Terra Nov.*, *14*(4), 281–287, doi:10.1046/j.1365-3121.2002.00421.x.

Lin, G., G. Lin, H. Chen, N. Hovius, M. Horng, S. Dadson, P. Meunier, and M. Lines (2008), Effects of earthquake and cyclone sequencing on landsliding and fluvial sediment transfer in a mountain catchment, *Earth Surf. Process. Landforms*, *33*, 1354–1373, doi:10.1002/esp.

Liou, J. G., and W. G. Ernst (1984), Summary of Phanerozoic Metamorphism in Taiwan, *Mem. Geol. Soc. China*, (6), 133–152, doi:10.1089/aid.2011.0096.

Liu, J., C. Liu, K. Xu, J. Milliman, J. Chiu, S. Kao, and S. Lin (2008), Flux and fate of small mountainous rivers derived sediments into the Taiwan Strait, *Mar. Geol.*, *256*, 65–76, doi:10.1016/j.margeo.2008.09.007.

Liu, J., Z. Xue, K. Ross, H. Wang, Z. Yang, A. Li, and S. Gao (2009), Fate of sediments delivered to the sea by Asian large rivers: Long-distance transport and formation of remote alongshore clinothems, *SEPM-The Sediment. Rec.*, *7*(4), 4–9.

Liu, J. T., S.-J. Kao, C.-A. Huh, and C.-C. Hung (2013), Gravity flows associated with flood events and carbon burial: Taiwan as instructional source area., *Ann. Rev. Mar. Sci.*, *5*, 47–68, doi:10.1146/annurev-marine-121211-172307.

Liu, T.-K. (1982), Tectonic implication of fission track ages from the Central Range, Taiwan, *Proc. Geol. Soc. China*, *25*, 22–37.

Liu, T.-K., Y.-G. Chen, W.-S. Chen, and S.-H. Jiang (2000), Rates of cooling and denudation of the Early Penglai Orogeny, Taiwan, as assessed by fission-track constraints, *Tectonophysics*, *320*(1), 69–82, doi:10.1016/S0040-1951(00)00028-7.

Liu, T.-K., S. Hsieh, Y.-G. Chen, and W.-S. Chen (2001), Thermo-kinematic evolution of the Taiwan oblique-collision mountain belt as revealed by zircon fission track dating, *Earth Planet. Sci. Lett.*, *186*(1), 45–56, doi:10.1016/S0012-821X(01)00232-1.

Lo, C.-H., and T. C. Onstott (1995), Rejuvenation of K-Ar systems for minerals in the Taiwan Mountain Belt, *Earth Planet. Sci. Lett.*, *131*(1-2), 71–98, doi:10.1016/0012-821X(95)00011-Z.

Lock, J. (2007), Interpreting Low-Temperature Thermochronometric Data in Fold-and-Thrust Belts: An Example from the Western Foothills, Taiwan, 196 pp., University of Washington.

Lock, J., and S. D. Willett (2008), Low-temperature thermochronometric ages in fold-and-thrust belts, *Tectonophysics*, *456*(3-4), 147–162, doi:10.1016/j.tecto.2008.03.007.

Lu, C., Y. Chan, L. Kuo, K. Chang, J. Lee, and C. Chen (2010a), TI: Geohazards in Related to Neotectonic Patterns of Taiwan Based on Recent Multi-Source Data, *AGU Fall Meet. Abstr.*, B2071.

Lu, C.-Y., Y.-C. Chan, L.-C. Kuo, K. Chang, and J.-C. Lee (2010b), Geo-hazards in related to neotectonic patterns of taiwan based on recent multi-source data., in *AGU Fall Meeting Abstracts, presented at the EOS Trans. AGU, Taipei, Taiwan*, p. B2071.

Ma, K. F., and D. R. Song (1997), Pn velocity and Moho depth in Taiwan, *J. Geol. Soc. China*, *40*, 167–184.

Malavieille, J. (2010), Impact of erosion, sedimentation, and structural heritage on the structure and kinematics of orogenic wedges: Analog models and case studies, *GSA Today*, (1), 4–10, doi:10.1130/GSATG48A.1.

Malavieille, J., and G. Trullenque (2009), Consequences of continental subduction on forearc basin and accretionary wedge deformation in SE Taiwan: Insights from analogue modeling, *Tectonophysics*, *466*(3-4), 377–394, doi:10.1016/j.tecto.2007.11.016.

McIntosh, K., H. van Avendonk, L. Lavier, W. R. Lester, D. Eakin, F. T. Wu, C.-S. Liu, and C.-S. Lee (2013), Inversion of a hyper-extended rifted margin in the southern Central Range of Taiwan, *Geology*, *41*(8), 871–874, doi:10.1130/G34402.1.

Meunier, P., N. Hovius, and J. A. Haines (2008), Topographic site effects and the location of earthquake induced landslides, *Earth Planet. Sci. Lett.*, *275*(3-4), 221–232, doi:10.1016/j.epsl.2008.07.020.

Milliman, J. D., and K. L. Farnsworth (2011), *River Discharge to the Coastal Ocean: A Global Synthesis*, Cambridge University Press.

Milliman, J. D., and J. P. M. Syvitski (1992), Geomorphic/Tectonic Control of Sediment Discharge to the Ocean: The Importance of Small Mountainous Rivers, *J. Geol.*, *100*(5), 525–544, doi:10.1086/629606.

Mohn, G., G. Manatschal, M. Beltrando, and I. Haupert (2014), The role of rift-inherited hyper-extension in Alpine-type orogens, *Terra Nov.*, doi:10.1111/ter.12104.

Molnar, P. (2004), Late Cenozoic increase in accumulation rates of terrestrial sediments: How Might Climate Change Have Affected Erosion Rates?, *Annu. Rev. Earth Planet. Sci.*, *32*(1), 67–89, doi:10.1146/annurev.earth.32.091003.143456.

Molnar, P., and P. England (1990), Late Cenozoic uplift of mountain ranges and global climate change: chicken or egg?, *Nature*, *346*(6279), 29–34.

Molnar, P., and P. Tapponnier (1975), Cenozoic Tectonics of Asia: Effects of a Continental Collision, *Science*, *189*(4201), 419–26, doi:10.1126/science.189.4201.419.

Montgomery, D. (2002), Valley formation by fluvial and glacial erosion, *Geology*, *30*, 1047–1050, doi:10.1130/0091-7613(2002)030<1047.

Montgomery, D. R. (2001), Slope distributions, threshold hillslopes, and steady-state topography, *Am. J. Sci.*, *301*(4-5), 432–454, doi:10.2475/ajs.301.4-5.432.

Montgomery, D. R., and M. T. Brandon (2002), Topographic controls on erosion rates in tectonically active mountain ranges, *Earth Planet. Sci. Lett.*, *201*(3-4), 481–489, doi:10.1016/S0012-821X(02)00725-2.

Montgomery, D. R., G. Balco, and S. D. Willett (2001), Climate, tectonics, and the morphology of the Andes, *Geology*, *29*(7), 579, doi:10.1130/0091-7613(2001)029<0579:CTATMO>2.0.CO;2.

Mouthereau, F., and O. Lacombe (2006), Inversion of the Paleogene Chinese continental margin and thick-skinned deformation in the Western Foreland of Taiwan, *J. Struct. Geol.*, *28*(11), 1977–1993, doi:10.1016/j.jsg.2006.08.007.

Mouthereau, F., O. Lacombe, B. Deffontaines, J. Angelier, H.-T. Chu, and C. T. Lee (1999), Quaternary transfer faulting and belt front deformation at Pakuashan (western Taiwan), *Tectonics*, *18*(2), 215, doi:10.1029/1998TC900025.

Mouthereau, F., O. Lacombe, B. Deffontaines, J. Angelier, and S. Brusser (2001a), Deformation history of the southwestern Taiwan foreland thrust belt: insights from tectono-sedimentary analyses and balanced cross-sections, *Tectonophysics*, *333*(1-2), 293–318, doi:10.1016/S0040-1951(00)00280-8.

Mouthereau, F., J. Angelier, and J.-C. Lee (2001b), Le séisme du 21 septembre 1999 : influence de l'héritage structural et implication du socle au front de la chaîne de Taiwan, *Comptes Rendus l'Académie des Sci. - Ser. IIA - Earth Planet. Sci.*, *333*(1), 93–103, doi:10.1016/S1251-8050(01)01616-0.

Mouthereau, F., B. Deffontaines, O. Lacombe, and J. Angelier (2002), Variations along the strike of the Taiwan thrust belt : Basement control on structural style , wedge geometry , and kinematics, in *Geology and Geophysics of an Arc-Continent Collision, Taiwan*, vol. 358, edited by T. B. Byrne and C.-S. Liu, pp. 35–58, Geological Society of America Special Paper 358.

Mouthereau, F., C. Fillon, and K.-F. Ma (2009), Distribution of strain rates in the Taiwan orogenic wedge, *Earth Planet. Sci. Lett.*, *284*(3-4), 361–385, doi:10.1016/j.epsl.2009.05.005.

Mouthereau, F., O. Lacombe, and J. Vergés (2012), Building the Zagros collisional orogen : Timing, strain distribution and the dynamics of Arabia/Eurasia plate convergence, *Tectonophysics*, *532-535*, 27–60, doi:10.1016/j.tecto.2012.01.022.

Mouthereau, F., A. B. Watts, and E. Burov (2013), Structure of orogenic belts controlled by lithosphere age, *Nat. Geosci.*, *6*(8), 1–5, doi:10.1038/ngeo1902.

Mouyen, M., M. Simoes, F. Mouthereau, F. Masson, C. Hwang, and C.-C. Cheng (2014), Investigating possible gravity change rates expected from long-term deep crustal processes in Taiwan, *Geophys. J. Int.*, doi:10.1093/gji/ggu133.

Nagel, S., M. G. Fellin, S. Castelltort, W. Sean, F. Mouthereau, and A. T. Lin (2012a), Provenance evolution of the Western foreland basin in Taiwan and its relationship to the exhumation of source rocks during arc-continent collision, in *European Geological Union Meeting*, p. 464.

Nagel, S., S. Castelltort, A. Wetzel, S. D. Willett, F. Mouthereau, and A. T.-S. Lin (2012b), Sedimentology and foreland basin paleogeography during Taiwan arc continent collision, *J. Asian Earth Sci.*, doi:10.1016/j.jseaes.2012.09.001.

Nemcok,, M., S. Schamel, and R. Gayer (2005), *Thrust-belts. Structural Architecture, Thermal Regimes, and Petroleum Systems*, Cambridge University Press, Cambridge, New York, Melbourne.

Nilfouroushan, F., R. Pysklywec, A. Cruden, and H. Koyi (2013), Thermal-mechanical modeling of salt-based mountain belts with pre-existing basement faults : Application to the Zagros fold and thrust belt , southwest Iran, , *32*, 1–15, doi:10.1002/tect.20075.

Nissen, S. S., D. E. Hayes, P. Buhl, J. Diebold, Y. Bochu, Z. Weijun, and C. Yongqin (1995a), Deep penetration seismic soundings across the northern margin of the South China Sea, *J. Geophys. Res.*, *100*(B11), 22407–22.

Nissen, S. S., D. E. Hayes, B. Yao, W. Zeng, Y. Chen, and X. Nu (1995b), Gravity, heat flow, and seismic constraints on the process of crustal extension: Northern margin of the South China sea, *J. Geophys. Res.*, *100*(B11), 447–483.

Ono, Y., and T. Naruse (1997), Snowline elevation and eolian dust flux in the Japanese Islands during Isotope Stages 2 and 4, *Quat. Int.*, *37*(0), 45–54, doi:http://dx.doi.org/10.1016/1040-6182(96)00003-1.

Ouimet, W. B., T. B. Byrne, and C. Huang (2012), Non-Equilibrium Topography in the southern Central Range of Taiwan, in *EP13B-0846 : presented at the 2012 Fall Meeting, AGU, San Francisco, Calif., 3-7 Dec.*

Pelletier, B., and H. N. Hu (1984), New structural data along two transects across the southern half of the Central Range of Taiwan, *Mem. Geol. Soc. China*, *6*, 1–19.

Pelletier, B., and J. Stephan (1986a), Middle Miocene obduction and Late Miocene beginning of collision registered in the Hengchun peninsula: Geodynamic implications for the evolution of Taiwan, *Mem. Geol. Soc. China*, *7*, 301–324, doi:10.1016/0040-1951(86)90011-9.

Pelletier, B., and J. F. Stephan (1986b), Middle Miocene obduction and Late Miocene beginning of collision registered in the Hengchun peninsula: Geodynamic implications for the evolution of Taiwan, *Tectonophysics*, *125*, 133–160.

Peltzer, G., and P. Tapponnier (1988), Formation and evolution of strike-slip faults, rifts, and basins during the India-Asia collision: an experimental approach, *J. Geophys. Res.*, *93*(B12), 15085–15117.

Phillips, J. D. (1992), The end of equilibrium?, *Geomorphology*, *5*(3-5), 195–201, doi:10.1016/0169-555X(92)90002-6.

Porter, S. (1989), Some geological implications of average Quaternary glacial conditions., *Quat. Res.*

Pulver, M. H., J. M. Crespi, and T. B. Byrne (2002), Lateral extrusion in a transpressional collision zone : An example from the pre-Tertiary metamorphic basement of Taiwan, in *Geology and Geophysics of an Arc-Continent Collision, Taiwan*, vol. 358, edited by T. B. Byrne and C.-S. Liu, pp. 107–120, Geological Society of America Special Paper 358, Boulder, Colorado.

Ramsey, L. A. (2006), Topographic evolution of emerging mountain belts, University of Cambridge.

Ramsey, L. a., R. T. Walker, and J. Jackson (2007), Geomorphic constraints on the active tectonics of southern Taiwan, *Geophys. J. Int.*, *170*(3), 1357–1372, doi:10.1111/j.1365-246X.2007.03444.x.

Ranalli, G., and D. C. Murphy (1987), Rheological stratification of the lithosphere, *Tectonophysics*, *132*(4), 281–295, doi:10.1016/0040-1951(87)90348-9.

Rangin, C. (1991), The Philippine Mobile Belt: a complex plate boundary, *J. Southeast Asian Earth Sci.*, *6*(3), 209–220.

Raymo, M., and W. F. Ruddiman (1992), Tectonic forcing of late Cenozoic climate, *Nature*, *359*(6391), 117–122.

Reiners, P. W., and M. T. Brandon (2006), Using Thermochronology To Understand Orogenic Erosion, *Annu. Rev. Earth Planet. Sci.*, *34*(1), 419–466, doi:10.1146/annurev.earth.34.031405.125202.

Reiners, P. W., T. a Ehlers, S. G. Mitchell, and D. R. Montgomery (2003), Coupled spatial variations in precipitation and long-term erosion rates across the Washington Cascades., *Nature*, *426*(6967), 645–7, doi:10.1038/nature02111.

Reiners, P. W., T. A. Ehlers, and P. K. Zeitler (2005), Past, present and future of thermochronology, in *Low-Temperature Thermochronology: Techniques, Interpretations, and Applications*, vol. 58, pp. 1–18, Reviews in Mineralogy & Geochemistry 58.

Reston, T. J., and G. Manatchal (2011), Rifted Margins: Building Blocks of Later Collision, in *Arc-Continent Collision*, edited by D. Brown and P. D. Ryan, pp. 3–21, Springer-Verlag.

Ring, U., M. T. Brandon, S. D. Willett, and G. S. Lister (1999), Exhumation processes, in *Exhumation Processes: Normal Faulting, Ductile Flow and Erosion*, vol. 154, edited by U. Ring, M. T. Brandon, G. S. Lister, and S. D. Willett, pp. 1–27, Geological Society, London, Special Publications 154.

Rodriguez-Roa, F. A., and D. V. Wiltschko (2010), Thrust belt architecture of the central and southern Western Foothills of Taiwan, in *Hydrocarbons in Contractional Belts*, vol. 348, edited by G. P. Goffey, J. Craig, T. Needham, and R. Scott, pp. 137–168, Geological Society, London, Special Publications.

Roe, G. (2009), Feedbacks, Timescales, and Seeing Red, *Annu. Rev. Earth Planet. Sci.*, *37*, 93–115, doi:10.1146/annurev.earth.061008.134734.

Roe, G. H., K. X. Whipple, and J. K. Fletcher (2008), Feedbacks among climate, erosion, and tectonics in a critical wedge orogen, *Am. J. Sci.*, *308*(7), 815–842, doi:10.2475/07.2008.01.

Rousset, B., S. Barbot, J.-P. Avouac, and Y.-J. Hsu (2012), Postseismic deformation following the 1999 Chi-Chi earthquake , Taiwan : Implication for lower-crust rheology, *J. Geophys. Res.*, *117*(B12405), 1–16, doi:10.1029/2012JB009571.

Royden, L. (1996), Coupling and decoupling of crust and mantle in convergent orogens: Implications for strain partitioning in the crust, *J. Geophys. Res.*, *101*(B8), 17,679–17,705.

Royden, L. H., B. C. Burchfiel, R. W. King, E. Wang, Z. Chen, F. Shen, and Y. Liu (1997), Surface Deformation and Lower Crustal Flow in Eastern Tibet, *Science (80-.).*, *276*(5313), 788–790, doi:10.1126/science.276.5313.788.

Ruddiman, W., and W. Prell (1997), Introduction to the uplift-climate connection, in *Tectonic uplift and climate change*, edited by W. Ruddiman, pp. 3–15, Plenum Press, New York.

Scott, D. (1979), On Optimal and Data-Based Histograms, *Biometrika*, *66*(3), 605–610.

Seilacher, A. (2007), *Trace Fossil Analysis*, Springer-Verlag.

Shyu, J. B. H., K. Sieh, Y.-G. Chen, and C.-S. Liu (2005a), Neotectonic architecture of Taiwan and its implications for future large earthquakes, *J. Geophys. Res.*, *110*(B8), 1–33, doi:10.1029/2004JB003251.

Shyu, J. B. H., K. Sieh, and Y. Chen (2005b), Tandem suturing and disarticulation of the Taiwan orogen revealed by its neotectonic elements, *Earth Planet. Sci. Lett.*, *233*(1-2), 167–177, doi:10.1016/j.epsl.2005.01.018.

Shyu, J. B. H., K. Sieh, Y.-G. Chen, and L.-H. Chung (2006), Geomorphic analysis of the Central Range fault, the second major active structure of the Longitudinal Valley suture, eastern Taiwan, *Geol. Soc. Am. Bull.*, *118*(11-12), 1447–1462, doi:10.1130/B25905.1.

Siame, L., H.-T. Chu, J. Carcaillet, D. Bourlès, R. Braucher, W.-C. Lu, J. Angelier, and P. Dussouliez (2007), Glacial retreat history of Nanhuta Shan (north-east Taiwan) from preserved glacial features: the cosmic ray exposure perspective., *Quat. Sci. Rev.*, *26*(17-18), 2185–2200, doi:10.1016/j.quascirev.2007.04.016.

Siame, L. L., H.-T. Chu, D. L. Bourlès, F. Derrieux, L. Léanni, and R. Chen (2012), Preservation of glacial landforms in the high mountains of Taiwan : Insights from in situ cosmogenic 10Be, in *Geophysical Research Abstracts Vol. 14, EGU2012-3573, 2012*, vol. 14, p. 3573.

Sibuet, J.-C., and S.-K. Hsu (2004), How was Taiwan created?, *Tectonophysics*, *379*(1-4), 159–181, doi:10.1016/j.tecto.2003.10.022.

Silver, E. A., and D. L. Reed (1988), Backthrusting in accretionary wedges, *J. Geophys. Res.*, *93*(B4), 3116–3126.

Simoes, M., and J.-P. Avouac (2006), Investigating the kinematics of mountain building in Taiwan from the spatiotemporal evolution of the foreland basin and western foothills, *J. Geophys. Res.*, *111*(B10), 1–25, doi:10.1029/2005JB004209.

Simoes, M., J.-P. Avouac, Y.-G. Chen, A. K. Singhvi, C.-Y. Wang, M. Jaiswal, Y.-C. Chan, and S. Bernard (2007a), Kinematic analysis of the Pakuashan fault tip fold, west central Taiwan: Shortening rate and age of folding inception, *J. Geophys. Res.*, *112*(B3), 1–30, doi:10.1029/2005JB004198.

Simoes, M., J.-P. Avouac, O. Beyssac, B. Goffé, K. a. Farley, and Y.-G. Chen (2007b), Mountain building in Taiwan: A thermokinematic model, *J. Geophys. Res.*, *112*(B11), 1–25, doi:10.1029/2006JB004824.

Simoes, M., O. Beyssac, and Y.-G. Chen (2012), Late Cenozoic metamorphism and mountain building in Taiwan: A review, *J. Asian Earth Sci.*, *46*(November), 92–119, doi:10.1016/j.jseaes.2011.11.009.

Stanley, R. S., L. B. Hill, H. C. Chang, and H. N. Hu (1981), A transect through the metamorphic core of the central mountains, southern Taiwan, *Mem. Geol. Soc. China*, *4*(4), 443–473.

Sternai, P., F. Herman, M. R. Fox, and S. Castelltort (2011), Hypsometric analysis to identify spatially variable glacial erosion, *J. Geophys. Res.*, *116*, 1–17, doi:10.1029/2010JF001823.

Stiiwe, K., and T. D. Barr (2000), On the relationship between surface uplift and gravitational extension, *Tectonics*, *19*(6), 1056–1064.

Stolar, D. B., S. D. Willett, and G. H. Roe (2006), Climatic and tectonic forcing of a critical orogen, in *Tectonics, Climate, and Landscape Evolution*, vol. 398, pp. 241–250.

Stolar, D. B., S. D. Willett, and D. R. Montgomery (2007), Characterization of topographic steady state in Taiwan, *Earth Planet. Sci. Lett.*, *261*(3-4), 421–431, doi:10.1016/j.epsl.2007.07.045.

Storti, F., and K. McClay (1995), Influence of syntectonic sedimentation on thrust wedges in analogue models, *Geology*, *23*(11), 999, doi:10.1130/0091-7613(1995)023<0999.

Strahler, A. (1952), Hypsometric (area-altitude) analysis of erosional topography, *Geol. Soc. Am. Bull.*, *63*, 1117–1142.

Stüwe, K. (2007), *Geodynamics of the Lithosphere: Quantitative decription of geological problems*, 2nd ed., Springer-Verlag.

Stüwe, K., and M. Hintermüller (2000), Topography and isotherms revisited: the influence of laterally migrating drainage divides, *Earth Planet. Sci. Lett.*, *184*(1), 287–303, doi:10.1016/S0012-821X(00)00315-0.

Stüwe, K., L. White, and R. Brown (1994), The influence of eroding topography on steady-state isotherms. Application to fission track analysis, *Earth Planet. Sci. Lett.*, *124*, 63–74.

Suppe, J. (1980a), A retrodeformable cross section of northern Taiwan, *Proceedings, Geol. Soc. China*, *23*, 46–55.

Suppe, J. (1980b), Imbricated structure of the western Foothills Belt, Central Taiwan, *Pet. Geol. Taiwan*, *17*, 1–16.

Suppe, J. (1981), Mechanics of mountain building and metamorphism in Taiwan, *Mem. Geol. Soc. China*, *4*, 67–89.

Suppe, J. (1984a), Kinematics of arc-continent collision, flipping of subduction, and back-arc spreading near Taiwan, *Mem. Geol. Soc. China*, *6*, 21–33.

Suppe, J. (1984b), *Principles of Structural Geology*, Prentice-Hall, Inc., Englewood Cliffs, New Jersey.

Suppe, J., and J. Namson (1979), Fault-bend origin of frontal folds of the Western Taiwan fold-and-thrust belt., *Pet. Geol. Taiwan*, *16*, 1–18.

Suppe, J., Y. Wang, J. Liou, and W. G. Ernst (1976), Observation of some contacts between the basement and Cenozoic cover in the Central Mountains, Taiwan, *Proc. Geol. Soc. China*, *19*, 59–70.

Tagami, T., and P. B. O'Sullivan (2005), Fundamentals of Fission-Track Thermochronology, *Rev. Mineral. Geochemistry*, *58*(1), 19–47, doi:10.2138/rmg.2005.58.2.

Tapponnier, P., G. Peltzer, and R. Armijo (1986), On the mechanism of collision between India and Asia., in *Collision Tectonics*, edited by M. P. Coward and A. C. Ries, pp. 115–157, Geological Society, London, Special Publications, 19,.

Teng, L. S. (1987), Stratigraphic records of the late Cenozoic Penglai orogeny of Taiwan, *Acta Geol. Taiwanica*, (25), 205–224.

Teng, L. S. (1990), Geotectonic evolution of late Cenozoic arc-continent in Taiwan, *Tectonophysics*, *183*, 57–76.

Teng, L. S. (1996), Extensional collapse of the northern Taiwan mountain belt, *Geology*, *24*(10), 949–952, doi:10.1130/0091-7613(1996)024<0949.

Teng, L. S., and A. T.-S. Lin (2004), Cenozoic tectonics of the China continental margin: insights from Taiwan, in *Aspects of Tectonic evolution of China*, vol. 226, edited by J. Malpas, C. J. N. Fletcher, J. Ali, and J. Aitchison, pp. 313–332, Geological Society, London, Special Publications 226.

Teng, L. S., Y. Wang, C. H. . Tang, C.-Y. Huang, T. . C. Huang, M. . S. Yu, and A. Ke (1991), Tectonic aspects of the Paleogene depositional basin of Northern Taiwan, *Proc. Geol. Soc. China*, *34*, 313–336.

Teng, L. S., C. T. Lee, Y. B. Tsai, and L.-Y. Hsiao (2000), Slab breakoff as a mechanism for flipping of subduction polarity in Taiwan, *Geology*, *28*(2), 155–158, doi:10.1130/0091-7613(2000)028<0155:SBAAMF>2.3.CO;2.

Tillman, K. S., and T. B. Byrne (1995), Kinematic analysis of the Taiwan Slate Belt, *Tectonics*, *14*(2), 322–341, doi:10.1029/94TC02451.

Tillman, K. S., and T. B. Byrne (1996), Out-of-sequence thrusting in the Taiwan slate belt, *J. Geol. Soc. China*, *39*(2), 189–208.

Tomita, Y. (1939), On the correlation of the topographical planes in Taiwan., *Rep. Japanese Assoc. Adv. Sci.*, *13*(3), 395–399.

Tomkin, J. H. (2007), Coupling glacial erosion and tectonics at active orogens: A numerical modeling study, *J. Geophys. Res.*, *112*(F2), F02015, doi:10.1029/2005JF000332.

Tomkin, J. H., and G. H. Roe (2007), Climate and tectonic controls on glaciated critical-taper orogens, *Earth Planet. Sci. Lett.*, *262*(3-4), 385–397, doi:10.1016/j.epsl.2007.07.040.

Tsao, S.-J. (1996), The geological significance of illite critallinity, zircon fission-track ages and K–Ar ages of metasedimentary rocks of the Central Range., 272 pp., National Taiwan University, Taipei, ROC.

Tsao, S.-J., T.-C. Li, J.-L. Tien, C.-H. Chen, T.-K. Liu, and C.-H. Chen (1992), Illite cristallinity and fission-track ages along the East Central cross-ilsland highway of Taiwan, *Acta Geol. Taiwanica*, (30), 45–64.

Usami, M., and T. Matsumoto (1940), Geologic map of Taiwan: Daibuzan sheet, *Beaureu Prod. Indus., Governement Gen. Taiwan*, (Scale 1: 100 000).

Ustaszewski, K., Y.-M. Wu, J. Suppe, H.-H. Huang, C.-H. Chang, and S. Carena (2012), Crust–mantle boundaries in the Taiwan–Luzon arc-continent collision system determined from local earthquake tomography and 1D models: Implications for the mode of subduction polarity reversal, *Tectonophysics*, *578*, 31–49, doi:10.1016/j.tecto.2011.12.029.

Valla, P. G., P. a. van der Beek, and J. Braun (2011), Rethinking low-temperature thermochronology data sampling strategies for quantification of denudation and relief histories: A case study in the French western Alps, *Earth Planet. Sci. Lett.*, *307*(3-4), 309–322, doi:10.1016/j.epsl.2011.05.003.

Wang Lee, C., and Y. Wang (1987), Tananao Terrane of Taiwan: its relation to the late mesozoic collision and accretion of the Southeast China margin, *Acta Geol. Taiwanica*, (25), 225–239.

Wang, P., and Q. Li (2009a), Oceanographic and geological backgrounds, in *The South China Sea*, edited by P. Wang and Q. Li, pp. 13–53, Springer, Dordrecht, The Netherlands.

Wang, P., and Q. Li (2009b), *The South China Sea*, Springer.

Wang, P.-L., L.-H. Lin, and C.-H. Lo (1998), 40Ar/39Ar dating of mylonitization in the Tananao schist, eastern Taiwan, *J. Geol. Soc. China*, *2*, 159–183.

Wang, T. K., M.-K. Chen, C.-S. Lee, and K. Xia (2006), Seismic imaging of the transitional crust across the northeastern margin of the South China Sea, *Tectonophysics*, *412*(3-4), 237–254, doi:10.1016/j.tecto.2005.10.039.

Wang, Y. (1979), Some strucural characyeristics of the Tertiary basement on Taiwan, *Mem. Geol. Soc. China*, *3*, 139–145.

Wegener, A. (1912), Die Entstehung der Kontinente, *Geol. Rund.*, *3*, 276–292.

Wei, K. (2006), Leg 195 synthesis: Site 1202 - Quaternary sedimentation and paleogeography in the southern Okinawa through, in *Proceedings of the Ocean Drilling Program, Scientific Results Volume 195*, vol. 195, edited by M. Shinohara, M. H. Salisbury, and C. Richter.

Whipple, K. X. (2009), The influence of climate on the tectonic evolution of mountain belts, *Nat. Geosci.*, *2*(2), 97–104, doi:10.1038/ngeo413.

Whipple, K. X., and B. Meade (2006), Orogen response to changes in climatic and tectonic forcing, *Earth Planet. Sci. Lett.*, *243*(1-2), 218–228, doi:10.1016/j.epsl.2005.12.022.

Widdowson, M. (1997), The geomorphological and geological importance of palaeosurfaces, *Geol. Soc. London, Spec. Publ.*, *120*, 1–12, doi:10.1144/GSL.SP.1997.120.01.01.

Willemin, J. H., and P. L. K. Knuepfer (1994), Kinematics of arc-continent collision in the eastern Central Range of Taiwan inferred from geomorphic analysis, *J. Geophys. Res.*, *99*(B10), 20267–20.

Willenbring, J. K., and F. von Blanckenburg (2010), Long-term stability of global erosion rates and weathering during late-Cenozoic cooling., *Nature*, *465*(7295), 211–4, doi:10.1038/nature09044.

Willett, S. D. (1999), Orogeny and orography: The effects of erosion on the structure of mountain belts, *J. Geophys. Res.*, *104*(B12), 28.957–28.981.

Willett, S. D. (2010), Late Neogene Erosion of the Alps: A Climate Driver?, *Annu. Rev. Earth Planet. Sci.*, *38*(1), 411–437, doi:10.1146/annurev-earth-040809-152543.

Willett, S. D., and M. T. Brandon (2002), On steady states in mountain belts, *Geology*, *30*(2), 175, doi:10.1130/0091-7613(2002)030<0175:OSSIMB>2.0.CO;2.

Willett, S. D., and M. T. Brandon (2013), Some analytical methods for converting thermochronometric age to erosion rate, *Geochemistry Geophys. Geosystems*, *in press*(14), 209–222, doi:10.1029/2012GC004279.

Willett, S. D., C. Beaumont, and P. Fullsack (1993), Mechanical model for the tectonics of doubly vergent compressional orogens, *Geology*, *21*(4), 371, doi:10.1130/0091-7613(1993)021<0371.

Willett, S. D., R. Slingerland, and N. Hovius (2001), Uplift, shortening, and steady state topography in active mountain belts, *Am. J. Sci.*, *301*, 455– 485.

Willett, S. D., D. M. Fisher, C. W. Fuller, Y. En-Chao, and L. Chia-Yu (2003), Erosion rates and orogenic-wedge kinematics in Taiwan inferred from fission-track thermochronometry, *Geology*, *31*(11), 945, doi:10.1130/G19702.1.

Willett, S. D., N. Hovius, M. T. Brandon, and D. M. Fisher (2006a), Introduction, in *Tectonic, Climate, and Landscape evolution*, vol. 398, edited by S. D. WIllett, N. Hovius, M. T. Brandon, and D. M. Fisher, pp. vii–xi, The Geological Society of America Special Paper.

Willett, S. D., F. Schlunegger, and V. Picotti (2006b), Messinian climate change and erosional destruction of the central European Alps, *Geology*, *34*(8), 613, doi:10.1130/G22280.1.

Willett, S. D., M. G. Fellin, and Y. G. Chen (2008), Detrital zircon fission track thermochronometry with implications for the topographic and exhumational history of Taiwan., in *Geochimica et Cosmochimica Acta 72, 12S (Goldschmidt Conference Abstracts)*, vol. 72, p. A1021.

Willett, S. D., S. W. McCoy, J. T. Perron, L. Goren, and C.-Y. Chen (2014), Dynamic Reorganization of River Basins, *Science (80-.).*, *343*(6175), doi:10.1126/science.1248765.

Wiltschko, D. V., L. Hassler, J.-H. Hung, and H.-S. Liao (2010), From accretion to collision: Motion and evolution of the Chaochou Fault, southern Taiwan, *Tectonics*, *29*(2), 1–23, doi:10.1029/2008TC002398.

Wu, F. T., R.-J. Rau, and D. Salzberg (1997), Taiwan orogeny: thin-skinned or lithospheric collision?, *Tectonophysics*, *274*(1-3), 191–220, doi:10.1016/S0040-1951(96)00304-6.

Wu, F. T., C. S. Chang, and Y.-M. Wu (2004), Precisely relocated hypocentres, focal mechanisms and active orogeny in Central Taiwan, *Geol. Soc. London, Spec. Publ.*, *226*(1), 333–353, doi:10.1144/GSL.SP.2004.226.01.18.

Wu, Y.-M., C.-H. Chang, L. Zhao, J. B. H. Shyu, Y.-G. Chen, K. Sieh, and J.-P. Avouac (2007), Seismic tomography of Taiwan: Improved constraints from a dense network of strong motion stations, *J. Geophys. Res.*, *112*(B8), 1–14, doi:10.1029/2007JB004983.

Yamato, P., P. Agard, E. Burov, L. Le Pourhiet, L. Jolivet, and C. Tiberi (2007), Burial and exhumation in a subduction wedge: Mutual constraints from thermomechanical modeling and natural P-T-t data (Schistes Lustrés, western Alps), *J. Geophys. Res.*, *112*(B7), 1–28, doi:10.1029/2006JB004441.

Yamato, P., F. Mouthereau, and E. Burov (2009), Taiwan mountain building: insights from 2D thermomechanical modelling of a rheologically stratified lithosphere, *Geophys. J. Int.*, *176*(1), 307–326, doi:10.1111/j.1365-246X.2008.03977.x.

Yan, P., H. Deng, H. Liu, Z. Zhang, and Y. Jiang (2006), The temporal and spatial distribution of volcanism in the South China Sea region, *J. Asian Earth Sci.*, *27*(5), 647–659, doi:10.1016/j.jseaes.2005.06.005.

Yang, K.-M., S.-T. Huang, J.-C. Wu, M. Lee, H.-H. Ting, and W.-W. Mei (2001), The characteristics of subsurface structure and evolution of the Tachien- shaneChukou thrust system., in *Annual Meeting of the Geological Society of China*, pp. 82–84.

Yang, T. F., J. Tien, C. Chen, T. Lee, and R. S. Punongbayang (1995), Fission-track dating of volcanics in the northern part of the Taiwan-Luzon Arc : eruption ages and evidence for crustal contamination, *J. Asian Earth Sci.*, *11*(2), 81–93.

Yang, T. F., C. Chen, R. L. Tien, S. R. Song, and T. K. Liu (2003), Remnant magmatic activity in the Coastal Range of East Taiwan after arc – continent collision : fission-track data and 3He/4He ratio evidence, *Radiat. Meas.*, *36*, 343–349, doi:10.1016/S1350-4487(03)00149-5.

Yeh, E.-C. (2004), Structural evolution of slates belts: examples from Tawain and eastern Pennsylvania., 207 pp., The Pennsylvania State University.

Yen, T. P. (1963), The metamorphic belts within the Tananao schist terrain of Taiwan, *Proc. Geol. Soc. China*, *6*, 72–74.

Yen, T. P., C. H. Wu, and T. Y. Chuang (1984), Geology along the Southern Taiwan east-west cross-mountain highway, *Spec. Pub. Cent. Geol. Surv.*, (3), 11–23.

Yen, T.-P., and Y.-T. Yang (1991), Miocene series and its basement strata in Taimali-Taiwu arera Southeastern Taiwan, *Proc. Geol. Soc. China*, *34*(1), 3–16.

Yu, S. (2001), Present-day crustal motion along the Longitudinal Valley Fault, eastern Taiwan, *Tectonophysics*, *333*(1-2), 199–217, doi:10.1016/S0040-1951(00)00275-4.

Yu, S., H.-Y. Chen, and L.-C. Kuo (1997), Velocity field of GPS stations in the Taiwan area, *Tectonophysics*, *274*(1-3), 41–59, doi:10.1016/S0040-1951(96)00297-1.

Yui, T.-F., and H.-T. Chu (2000), “Overturned” marble layers: evidence for upward extrusion of the Backbone Range of Taiwan, *Earth Planet. Sci. Lett.*, *179*(2), 351–361, doi:10.1016/S0012-821X(00)00119-9.

Yumul, G. P. (2007), Westward younging disposition of Philippine ophiolites and its implication for arc evolution, *Isl. Arc*, *16*(2), 306–317, doi:10.1111/j.1440-1738.2007.00573.x.

Zachos, J., M. Pagani, L. Sloan, E. Thomas, and K. Billups (2001), Trends , Rhythms , and Aberrations in Global Climate 65 Ma to Present, *Science (80-.).*, *292*(2001), 600–603, doi:10.1126/science.1059412.

Zhang, P. Z., P. Molnar, and W. R. Downs (2001), Increased sedimentation rates and grain sizes 2-4 Myr ago due to the influence of climate change on erosion rates., *Nature*, *410*(6831), 891–7, doi:10.1038/35073504.

Zhao, M., X. Qiu, S. Xia, H. Xu, P. Wang, T. K. Wang, C.-S. Lee, and K. Xia (2010), Seismic structure in the northeastern South China Sea: S-wave velocity and Vp/Vs ratios derived from three-component OBS data, *Tectonophysics*, *480*(1-4), 183–197, doi:10.1016/j.tecto.2009.10.004.

ANNEXES

Annex 1: Old geological map of southern Taiwan

Geologic map of Taiwan: Daibuzan sheet (Usami & Matsumoto, 1940)

Note that this and other Japanese geological maps can be found in the Central Geological Survey website: http://twgeoref.moeacgs.gov.tw/public/Data/f1293767115524.jpg



Geological map along the South Link Railroad *(Hu and Tsan, 1984)*

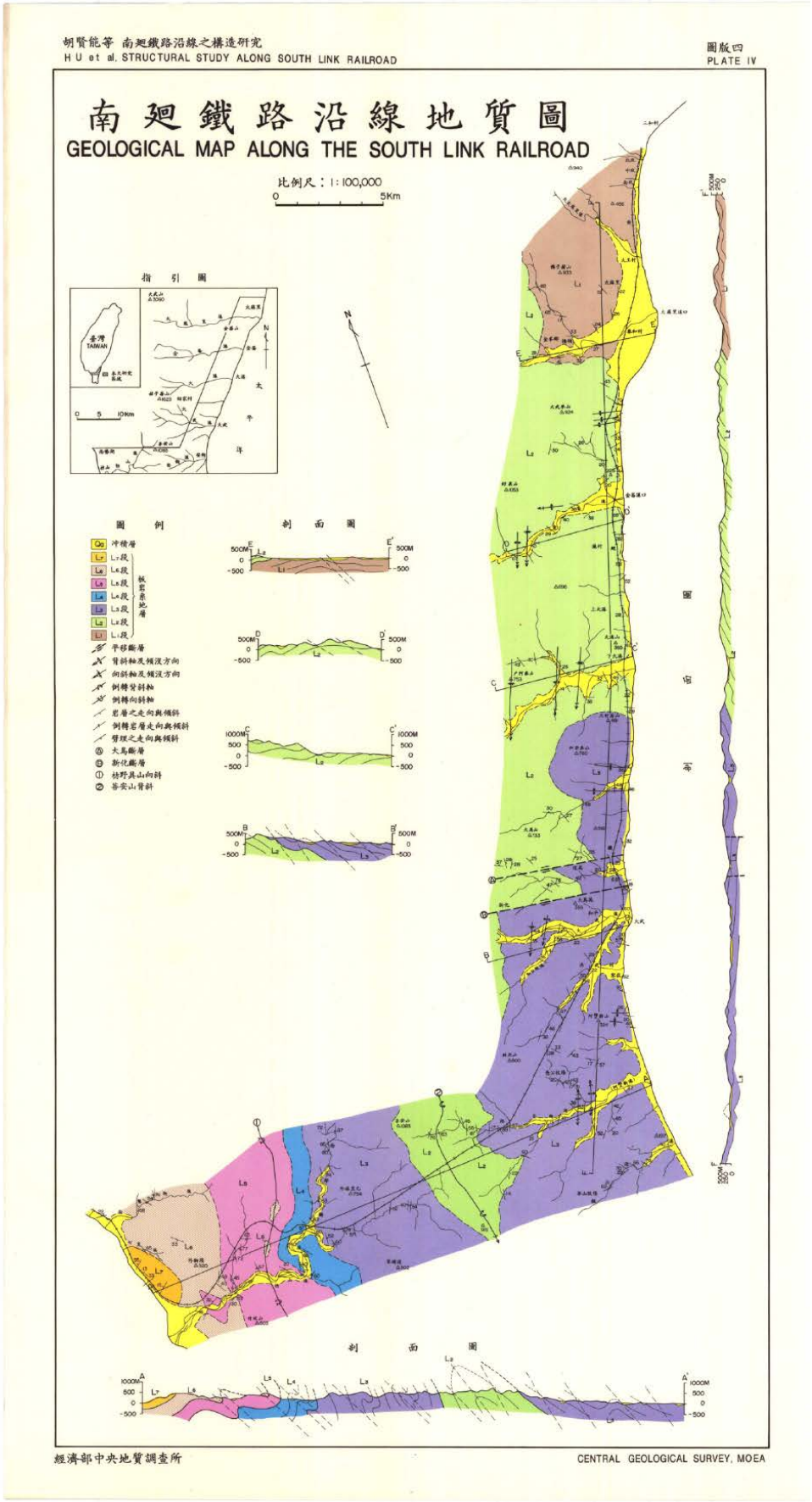

Annex 2: Summary of deformation phases from the main existing studies

Studies referred to

Reference	Area & Formation	Data used	Deformation phases & age (if any)
Stanley et al., 1981	TMC & Eo. Southern Cross island highway	Schistosity and folding cross-cutting relationships. Lithological correlations	**S1**= Criptic **F1** = parasitic folds **S2** = Penetrative axial surface **F2**= West vergent folds and faults (after counter-clockwise rotation of S2; i.e. after restoration); **F3** = East verging; hinge plunge NE **S3**= NE strike; W diping; Crenulation cleavage **F3**= NE plunging of axis **F4** =minor folds deforming **S4**= NE strike; NW dip **F5 &F6** = kink folds; variable orientation; flexing of dominant schistosity
Pelletier and Hu, 1984	Eo-Miocene Cover Southern Cross Island Highway & East and South Taiwan	Structural analysis	**P0** = southward directed slumps **D1**=EW to NW-SE compression **F1**= overturned towards the W; Axis are flat or plunge North or South **S1**=Axial planar **T1**= west vergent thrust Present in pro & retrowedge **F2**= kink-folds verging to the East; backfolding **S2**=Fracture cleavage not developed (in SE Tw) & Crenulation cleavage in the Western Southern Cross island highway **F3**= North verging, E-W axis No axial planar schisto.
Hu & Tsan, 1984	Miocene cover South and Southeastern Taiwan, Central Range (South Link Railroad)	Structural and sedimentological analysis (Folding and cleavage realtions) & Geological map	**F0** = NS (EW depositional folds) **S2**= NWW-SEE (NS-overturned tight folds & cleavage) **D3** = bending of S2 cleavage
Pelletier and Stephan, 1986]	Miocene cover Hengchun peninsula (S. Taiwan)	Sedimentological, geochemical (ophiolitic blocks) & structural analysis	**F0**=E-W axis of lithified sediments (no shisto), linked to listric faults **D1**= 5Ma (Mio-Plio boundary) or L. Miocene (NN15-NN1) **F1**= isoclinal, overturned to the W; N-S to N20 axis **S1**= axial planar **T1**=overthrusting of Kenting domain **D2**=3.5 Ma or between 3 and 5Ma **F2** = N160 axis Backthrusting and deposition of Lich mélange **D3**= coastal range westward thrusting; Middle Pleistocene to present
Faure et al 1991	Mainly TMC, also Eo-Miocene cover Central & Southern cross island highway	Micro-strucural analysis & synthesis of previous works	**S1**= fracture cleavage (in the W. slate belt) Axial planar cleavage (as we go E.); **F1**= overturned to the west (in slate belt); **L1**= non-coaxial, top to the NW shear sense (in slate belt & TMC, after restauration); **D2 =**3.5 Ma (from *Pelletier and Stephan*, 1986 **F2**= overturned to the E.; axis trend N100 (back folding); **S2**=Axial planar crenulation; **F3**= axis S.dipping **D4** = Normal faulting

Clark et al., 1992	Northern (Hsuhshan Range, HR) & Southern (Eo-TMC) cross-island highway. Deformation phases for the SCH unless indicated otherwise.	Microstructural analysis (syntectonic fibrous growth orientation)	D1; D2; D3=D2; D3;D4 of *Stanley et al., 1981* **S1** = dipping ~40SE; **L1**= updip; Clockwise rotation of elements + asymmetric folds and boudins –> non-coaxial (simple shear) **S2**= crenulation cleavage with fanning structure **F2**= west vergent folds & axis dipping ~35º to the NE **L2**= indicate fold-axis parallel extension & left-lateral shear Faults= sigma 3 plunge towards the NE, parallel to S2-extension **S3** = crenulation clavage diping NW, locally transposing S2 (in the east)
Clark and Fisher, 1995	Southern Cross-island –highway (Eo-TMC)	Microstructural (Chlorite-Mica aggregates)	Non-coaxial deformation with mineral growth
Fisher et al., 2002 & Fisher, 1999	HR (Eo-Oli-Mio) & Western backbone range –**WBB** (Eo-Mio) & Easternmost Backbone -**EBB** (TMC- Eo)	Structural & microstructural	**WBB**: NW vergent F1 SE dipping fold axial planes parallel to S1. Downdip L1 & non-coaxial stretching ~40%-460%; Deeper levels (Eo) more strain. **EBB**: SW-vergent meso-scale F1 with associated S1 and non-coaxial L1 sub-paralel to F1axis and gently plunging to NE, with stretching >180-500%. S1 changes from W-dipping to E-dipping from S to N. **WBB:** local crenulation cleavage S2 steeper then S1. **EBB**: local crenulation S2 steep to moderate W dipping. F2 axis gentle NE plunging. L2 moderatly NE dipping **WBB**: West-verging ou-of-seuqence thrusting Eo over Mio series concentrating strain. **EBB**: late W-dipping normal faults
Chu et al., 1995	Eocene cover Southern Central Range (Nandanwushan peak area)	Preliminary Litho-stratigraphic definition & nature of contacts	CR interpreted as a big scale anticlinorium (no cleavage-bedding relation interpreted)
Tillman and Byrne, 1995	HR & Mio-Eo cover (western SCH)	Structural & Micro-structural (incremental strain analysis)	**D1**= non-coaxial; top-to-the-NW simple shear. **T1**= bedding parallel thrust (flexural?) **S1**= strike NE, dip SE; axial planar **L1=** downdip, related to flexuaral slip; Finite strain increases from W to E **F2**= NW vergent asymetry **S2** = crenulation cleavage; axial planar to metter scale folds of S1; **L2** = sub-paralel to F2 avis **D4**= Late strike-slip conjugate faults
Tillman and Byrne, 1996	NCH (HR) & SCH (Eo-Mio cover)	Structural analysis	**D3**=out-of-sequence thrust; post-dates cleavages and metamorphism **F2**= tighter towards the faults **T3**= N20 dip ESE; slicken-size downdip(108º) and thrust sense
Lu et al., 2001 & Lu et al., 2002	Southeast Taiwan (Taimali-Dawu coast)	Structural analysis	**D1**= W vergent folding and thrusting **D2**=general shear due to back-folding; isoclinal folding **D3**=Transpression associated with E-W thrusting and folding & cleavage
Pulver et al., 2002	Norhern Cross-Island Highway (TMC&Eo)	Sructural and microstructural analysis	Plesitocen to recent **D1**= deformation in dislocation-creep regime (patchy , ondulose quartz) at ~300-400ºC **F1**=axis strike NE or SE, subhoryzontal; wide variety (tight , west-vergent, recumbent, open,symmetric) **S1**=strike NE, with varying dipping direction. **L1**= 30-45ºto the NE or SE S-C fabrics: left-lateral, top-to-the-NE or SW **S2**= widely spaced **D3**= Regional-scale block rotation: Semibrittle to ductile normal-sense shear zones and brittle normal faults

LX= stretching & mineral lienation; FX=folds; SX=schistosity plane; TMC = Tananao metamorphic complex; Eo-Mio = Central Range's Eocene-Miocene sedimentary cover.

Other structural studies not referenced in this table: [*Yen et al.*, 1984; *Wang Lee and Wang*, 1987; *Chang et al.*, 2003; *Yeh*, 2004]

Annex 3: Hypsometry of Taiwan's geological provinces.

Hypsometric curves of physiographic and geological areas of Taiwan.

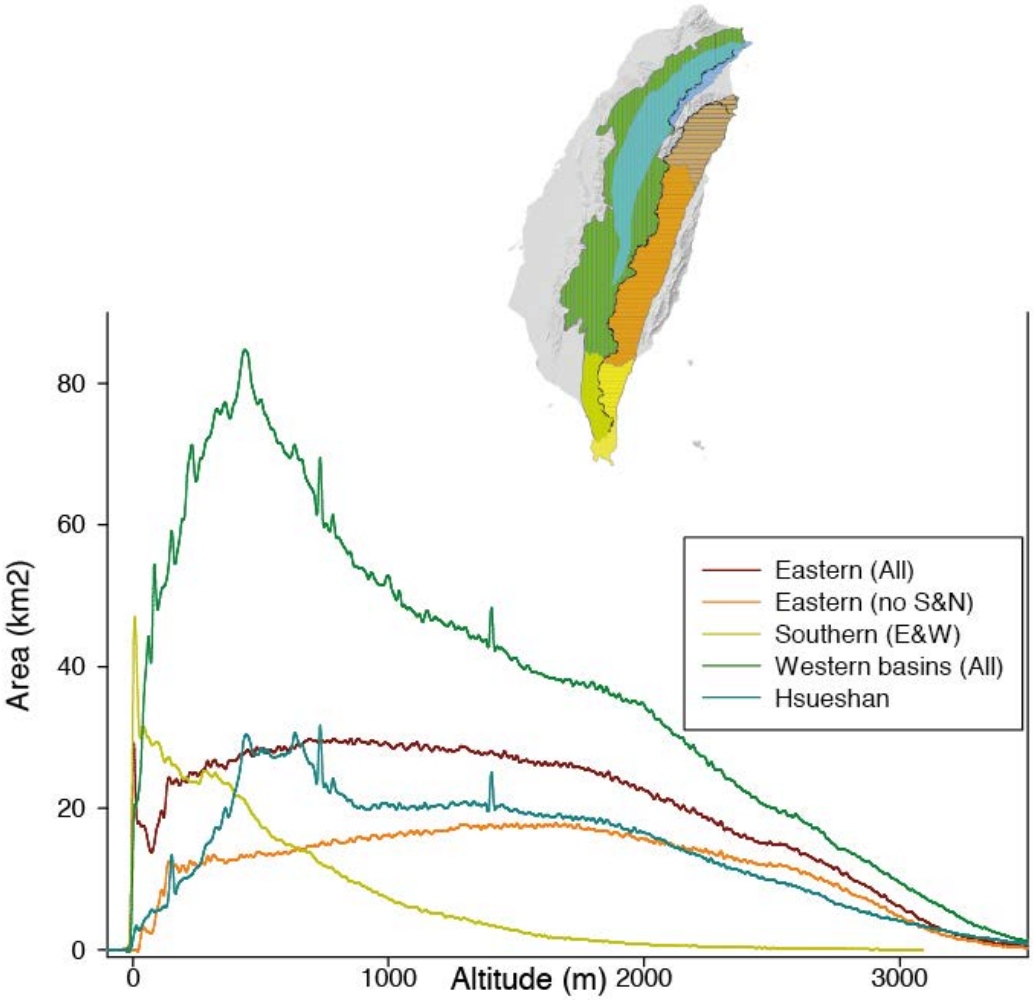

Fig. A4.1: Hyspometry of different geological and hydrological areas of Taiwan.

Annex 4: Thermochronological raw data

Below are the raw counting data with the parameters specific to the counter or irradiation. Ages and Uranium content extracted with Binomfit 1.1.60 [*Brandon*, 1992].

Zircon fission track:

Sample parameters, track counts and densities, uranium content and grain age.

PV4-3 (Taimali)

EFFECTIVE TRACK DENSITY FOR FLUENCE MONITOR (tracks/cm^2): 2.77E+05
RELATIVE ERROR (%): 1.11
EFFECTIVE URANIUM CONTENT OF MONITOR (ppm): 15.00
ZETA FACTOR AND STANDARD ERROR (yr cm^2): 135.42 15.20
SIZE OF COUNTER SQUARE (cm^2): 6.39E-07

Grain no.	ρ_s (tracks . cm^{-2}	Ns (tracks)	ρ_i (tracks . cm^{-2})	Ni (tracks)	Squares	Uranium (ppm) +/- 2 std. dev.		Age (Ma)	95% CI	
1	8.14E+05 (	13)	1.25E+06 (	20)	25	68	30	12.2	5.6	25.7
2	5.22E+05 (	5)	1.88E+06 (	18)	15	102	47	5.3	1.5	14.5
3	6.96E+05 (	4)	1.56E+06 (	9)	9	85	55	8.5	1.9	29.8
4	2.35E+06 (	18)	9.13E+05 (	7)	12	50	36	47.3	19.2	135.0
5	6.96E+05 (	4)	1.91E+06 (	11)	9	104	61	7.0	1.6	22.9
6	8.69E+05 (	5)	2.09E+06 (	12)	9	113	64	7.9	2.2	23.8
7	8.69E+05 (	5)	2.09E+06 (	12)	9	113	64	7.9	2.2	23.8
8	4.17E+06 (	24)	1.91E+06 (	11)	9	104	61	40.4	19.2	91.8
9	3.13E+06 (	18)	3.65E+06 (	21)	9	198	86	16.0	8.1	31.6
10	1.04E+06 (	6)	1.74E+06 (	10)	9	94	58	11.3	3.4	34.0
11	1.74E+05 (	1)	6.96E+05 (	4)	9	38	36	5.2	0.1	47.1
12	8.69E+05 (	5)	1.56E+06 (	9)	9	85	55	10.5	2.7	34.5
13	2.96E+06 (	17)	2.61E+06 (	15)	9	141	72	21.2	10.0	45.5
14	5.22E+05 (	3)	8.69E+05 (	5)	9	47	40	11.4	1.7	57.5
15	6.26E+06 (	36)	1.91E+06 (	11)	9	104	61	60.4	30.4	132.1
16	1.37E+06 (	14)	1.27E+06 (	13)	16	69	38	20.1	8.8	46.4
17	7.82E+05 (	8)	7.82E+05 (	8)	16	42	29	18.7	6.1	57.0
18	7.82E+05 (	8)	8.80E+05 (	9)	16	48	31	16.7	5.6	48.4
19	1.66E+06 (	17)	1.17E+06 (	12)	16	64	36	26.4	11.9	60.6
20	5.74E+06 (	33)	1.74E+06 (	10)	9	94	58	60.8	29.7	139.1
21	1.56E+06 (	9)	1.91E+06 (	11)	9	104	61	15.3	5.6	40.5
22	6.96E+05 (	4)	1.22E+06 (	7)	9	66	48	10.9	2.3	42.0
23	2.09E+06 (	12)	1.91E+06 (	11)	9	104	61	20.4	8.2	50.9
24	3.83E+06 (	22)	1.56E+06 (	9)	9	85	55	45.1	20.2	112.0
25	1.22E+06 (	7)	2.09E+06 (	12)	9	113	64	11.0	3.6	30.0

Pv4-1 (Taimali)

EFFECTIVE TRACK DENSITY FOR FLUENCE MONITOR (tracks/cm^2): 2.76E+05
RELATIVE ERROR (%): 1.41
EFFECTIVE URANIUM CONTENT OF MONITOR (ppm): 15.00
ZETA FACTOR AND STANDARD ERROR (yr cm^2): 135.42 15.20
SIZE OF COUNTER SQUARE (cm^2): 6.39E-07

Grain no.	ρ_s (tracks . cm^{-2}	Ns (tracks)	ρ_i (tracks . cm^{-2})	Ni (tracks)	Squares	Uranium (ppm) +/- 2 std. dev.		Age (Ma)	95% CI	
1	3.17E+06 (	81)	4.30E+06 (	110)	40	234	45	13.8	10.2	18.5
2	3.33E+06 (	34)	2.45E+06 (	25)	16	133	53	25.3	14.7	44.3
3	2.93E+05 (	3)	9.78E+05 (	10)	16	53	33	5.8	1.0	21.8
4	3.65E+06 (	21)	1.04E+06 (	6)	9	57	44	63.9	25.5	195.2
5	1.56E+06 (	9)	2.09E+06 (	12)	9	113	64	14.1	5.2	36.2

6	1.91E+06 (	11)	1.74E+06 (	10)	9	94	58	20.5	7.9	53.8
7	6.96E+05 (	4)	1.22E+06 (	7)	9	66	48	10.9	2.3	41.9
8	1.56E+06 (	12)	6.52E+05 (	5)	12	35	30	43.9	14.7	160.6
9	4.00E+06 (	23)	6.96E+05 (	4)	9	38	36	103.2	36.6	414.2
10	5.39E+06 (	31)	3.30E+06 (	19)	9	179	81	30.3	16.7	56.9
11	3.83E+06 (	22)	3.48E+06 (	20)	9	189	84	20.5	10.7	39.6
12	5.22E+05 (	3)	2.96E+06 (	17)	9	161	77	3.4	0.6	11.4
13	2.09E+06 (	12)	1.22E+06 (	7)	9	66	48	31.7	11.6	95.4
14	1.22E+06 (	7)	8.69E+05 (	5)	9	47	40	25.9	7.1	103.8
15	1.04E+06 (	6)	2.26E+06 (	13)	9	123	67	8.7	2.7	24.3
16	5.22E+05 (	3)	1.74E+05 (	1)	9	9	15	51.3	4.5	2425.5
17	3.48E+05 (	2)	1.74E+06 (	10)	9	94	58	4.0	0.4	17.5
18	1.56E+06 (	9)	6.96E+05 (	4)	9	38	36	41.0	11.7	184.3
19	5.22E+05 (	3)	8.69E+05 (	5)	9	47	40	11.4	1.7	57.4
20	1.74E+06 (	10)	1.56E+06 (	9)	9	85	55	20.7	7.6	57.5
21	6.96E+05 (	4)	1.56E+06 (	9)	9	85	55	8.5	1.9	29.7
22	8.69E+05 (	5)	6.96E+05 (	4)	9	38	36	23.2	5.0	116.8
23	5.22E+05 (	3)	2.26E+06 (	13)	9	123	67	4.5	0.8	15.7
24	3.30E+06 (	19)	1.56E+06 (	9)	9	85	55	39.0	17.0	98.4

PV4-0 (Taimali)

EFFECTIVE TRACK DENSITY FOR FLUENCE MONITOR (tracks/cm^2): 2.77E+05

RELATIVE ERROR (%): 1.11

EFFECTIVE URANIUM CONTENT OF MONITOR (ppm): 15.00

ZETA FACTOR AND STANDARD ERROR (yr cm^2): 135.42 15.20

SIZE OF COUNTER SQUARE (cm^2): 6.39E-07

Grain no.	ρ_s (tracks . cm^{-2}	Ns (tracks)	ρ_i (tracks . cm^{-2})	Ni (tracks)	Squares	Uranium (ppm) +/- 2 std. dev.		Age (Ma)	95% CI	
1	1.33E+06 (	23)	1.04E+06 (	18)	27	57	26	23.8	12.3	46.9
2	3.13E+06 (	16)	3.13E+06 (	16)	8	170	84	18.7	8.8	39.9
3	2.19E+06 (	35)	2.00E+06 (	32)	25	109	38	20.4	12.3	34.1
4	4.00E+06 (	23)	4.69E+06 (	27)	9	255	97	15.9	8.7	28.8
5	1.04E+06 (	6)	1.39E+06 (	8)	9	75	52	14.1	4.0	46.0
6	1.08E+06 (	11)	8.80E+05 (	9)	16	48	31	22.8	8.6	62.2
7	1.39E+06 (	8)	1.91E+06 (	11)	9	104	61	13.7	4.8	37.1
8	1.17E+06 (	9)	3.00E+06 (	23)	12	163	67	7.4	3.0	16.4
9	4.00E+06 (	23)	2.96E+06 (	17)	9	160	77	25.2	12.9	50.3
10	6.26E+05 (	8)	7.82E+05 (	10)	20	42	26	15.0	5.1	42.0
11	4.11E+06 (	42)	2.25E+06 (	23)	16	122	50	34.0	20.1	59.3
12	3.91E+05 (	6)	2.61E+05 (	4)	24	14	13	27.7	6.7	133.9
13	1.56E+06 (	25)	1.00E+06 (	16)	25	54	27	29.1	15.0	58.4
14	1.76E+06 (	9)	2.15E+06 (	11)	8	117	69	15.3	5.6	40.5
15	5.22E+05 (	3)	2.09E+06 (	12)	9	113	64	4.9	0.8	17.3
16	8.61E+06 (	66)	6.26E+06 (	48)	12	340	98	25.7	17.4	38.1
17	1.91E+06 (	11)	2.78E+06 (	16)	9	151	74	12.9	5.4	29.5
18	2.43E+06 (	14)	2.61E+06 (	15)	9	141	72	17.5	7.8	38.7
19	7.82E+06 (	80)	3.13E+06 (	32)	16	170	60	46.5	30.6	72.5
20	7.34E+06 (	75)	4.30E+06 (	44)	16	233	70	31.8	21.7	47.3
21	3.48E+05 (	2)	1.22E+06 (	7)	9	66	48	5.6	0.5	28.0
22	3.48E+05 (	2)	2.78E+06 (	16)	9	151	74	2.5	0.3	9.9
23	5.04E+06 (	29)	1.39E+06 (	8)	9	75	52	66.5	30.2	169.6
24	3.00E+06 (	23)	5.22E+05 (	4)	12	28	27	103.4	36.7	414.7

PV3-6B (Taimali)

EFFECTIVE TRACK DENSITY FOR FLUENCE MONITOR (tracks/cm^2): 2.77E+05

RELATIVE ERROR (%): 1.11
EFFECTIVE URANIUM CONTENT OF MONITOR (ppm): 15.00
ZETA FACTOR AND STANDARD ERROR (yr cm^2): 135.42 15.20
SIZE OF COUNTER SQUARE (cm^2): 6.39E-07

Grain no.	ρ_s (tracks . cm^{-2}	Ns (tracks)	ρ_i (tracks . cm^{-2})	Ni (tracks)	Squares	Uranium (ppm) +/- 2 std. dev.	Age (Ma)	95% CI
1	1.74E+05 (	1)	5.22E+05 (	3)	9	28 30	6.8	0.1 77.3
2	5.22E+05 (	3)	3.65E+06 (	21)	9	198 86	2.8	0.5 9.0
3	3.48E+05 (	2)	1.39E+06 (	8)	9	75 52	4.9	0.5 23.4
4	8.69E+05 (	5)	5.04E+06 (	29)	9	274 101	3.3	1.0 8.4
5	7.82E+05 (	8)	4.60E+06 (	47)	16	249 73	3.2	1.3 6.8
6	6.26E+05 (	4)	1.10E+06 (	7)	10	59 43	10.9	2.3 42.0
7	3.76E+05 (	6)	2.75E+06 (	44)	25	149 45	2.6	0.9 6.0
8	6.26E+05 (	8)	2.90E+06 (	37)	20	157 51	4.1	1.6 8.8
9	3.91E+05 (	4)	2.25E+06 (	23)	16	122 50	3.4	0.8 9.5
10	7.82E+05 (	8)	1.66E+06 (	17)	16	90 43	8.9	3.3 21.5
11	9.39E+05 (	18)	1.93E+06 (	37)	30	105 34	9.1	4.9 16.4
12	3.91E+05 (	3)	1.04E+06 (	8)	12	57 39	7.2	1.2 29.2
13	7.82E+05 (	8)	1.76E+06 (	18)	16	96 44	8.4	3.1 20.1
14	7.82E+05 (	8)	9.78E+05 (	10)	16	53 33	15.0	5.1 42.0
15	6.96E+05 (	4)	2.26E+06 (	13)	9	123 67	5.9	1.4 18.6
16	6.96E+05 (	4)	3.48E+06 (	20)	9	189 83	3.9	0.9 11.2
17	5.22E+05 (	3)	1.74E+06 (	10)	9	94 58	5.8	1.0 21.8
18	1.74E+05 (	1)	8.69E+05 (	5)	9	47 40	4.2	0.1 33.4
19	3.91E+05 (	6)	3.59E+06 (	55)	24	195 52	2.1	0.7 4.7
20	3.13E+05 (	4)	2.97E+06 (	38)	20	161 52	2.0	0.5 5.5
21	5.22E+05 (	8)	3.52E+06 (	54)	24	191 52	2.8	1.1 5.9
22	5.87E+05 (	6)	2.64E+06 (	27)	16	143 55	4.2	1.4 10.3
23	5.22E+05 (	3)	2.61E+06 (	15)	9	141 72	3.9	0.7 13.2
24	3.91E+05 (	6)	2.35E+06 (	36)	24	127 42	3.2	1.1 7.5

PV3-7 (Taimali)

EFFECTIVE TRACK DENSITY FOR FLUENCE MONITOR (tracks/cm^2): 2.77E+05
RELATIVE ERROR (%): 1.12
EFFECTIVE URANIUM CONTENT OF MONITOR (ppm): 15.00
ZETA FACTOR AND STANDARD ERROR (yr cm^2): 135.42 15.20
SIZE OF COUNTER SQUARE (cm^2): 6.39E-07

Grain no.	ρ_s (tracks . cm^{-2}	Ns (tracks)	ρ_i (tracks . cm^{-2})	Ni (tracks)	Squares	Uranium (ppm) +/- 2 std. dev.	Age (Ma)	95% CI
1	1.17E+06 (	6)	3.91E+06 (	20)	8	212 94	5.7	1.8 14.5
2	1.96E+05 (	2)	3.13E+06 (	32)	16	170 60	1.3	0.1 4.6
3	3.91E+05 (	3)	3.00E+06 (	23)	12	163 67	2.6	0.5 8.1
4	3.48E+05 (	2)	1.91E+06 (	11)	9	104 61	3.6	0.4 15.6
5	9.13E+05 (	7)	8.09E+06 (	62)	12	438 111	2.2	0.8 4.6
6	5.22E+05 (	3)	2.09E+06 (	12)	9	113 64	4.9	0.8 17.3
7	4.17E+05 (	4)	1.56E+06 (	15)	15	85 43	5.1	1.2 15.7
8	3.91E+05 (	5)	2.11E+06 (	27)	20	115 44	3.6	1.0 9.1
9	3.48E+05 (	2)	3.13E+06 (	18)	9	170 79	2.2	0.2 8.7
10	6.96E+05 (	4)	2.96E+06 (	17)	9	160 77	4.5	1.1 13.5
11	3.91E+05 (	3)	2.35E+06 (	18)	12	127 59	3.3	0.6 10.7
12	5.22E+05 (	4)	4.43E+06 (	34)	12	240 82	2.3	0.6 6.2
13	5.09E+05 (	13)	4.07E+06 (	104)	40	221 43	2.4	1.2 4.2
14	9.78E+05 (	15)	6.39E+06 (	98)	24	347 70	2.9	1.5 5.0
15	1.08E+06 (	9)	6.62E+06 (	55)	13	359 97	3.1	1.3 6.3
16	1.15E+06 (	11)	3.13E+06 (	30)	15	170 62	6.9	3.1 14.1
17	4.92E+05 (	11)	1.39E+06 (	31)	35	75 27	6.7	3.0 13.6
18	3.91E+05 (	5)	3.44E+06 (	44)	20	187 56	2.2	0.7 5.4
19	6.26E+05 (	6)	2.82E+06 (	27)	15	153 58	4.2	1.4 10.3
20	4.00E+05 (	11)	2.18E+06 (	60)	43	118 31	3.5	1.6 6.6

21	8.61E+05 (	22)	4.26E+06 (	109)	40	231	45	3.8	2.3	6.0
22	5.03E+05 (	9)	3.47E+06 (	62)	28	188	48	2.8	1.2	5.5
23	5.87E+05 (	6)	2.15E+06 (	22)	16	117	49	5.2	1.7	13.0
24	6.26E+05 (	6)	2.50E+06 (	24)	15	136	55	4.8	1.6	11.8

PV3-1 (Taimali)

EFFECTIVE TRACK DENSITY FOR FLUENCE MONITOR (tracks/cm^2): 2.76E+05
RELATIVE ERROR (%): 1.16
EFFECTIVE URANIUM CONTENT OF MONITOR (ppm): 15.00
ZETA FACTOR AND STANDARD ERROR (yr cm^2): 135.42 15.20
SIZE OF COUNTER SQUARE (cm^2): 6.39E-07

Grain no.	ρ_s (tracks . cm^{-2}	Ns (tracks)	ρ_i (tracks . cm^{-2})	Ni (tracks)	Squares	Uranium (ppm) +/- 2 std. dev.		Age (Ma)	95% CI	
1	5.22E+05 (	3)	1.91E+06 (	11)	9	104	61	5.3	0.9	19.3
2	6.26E+05 (	8)	2.58E+06 (	33)	20	140	49	4.6	1.8	10.0
3	4.89E+05 (	5)	2.64E+06 (	27)	16	143	55	3.6	1.0	9.1
4	8.69E+05 (	5)	1.91E+06 (	11)	9	104	61	8.6	2.3	26.5
5	8.69E+05 (	5)	4.87E+06 (	28)	9	264	99	3.4	1.0	8.8
6	5.22E+05 (	2)	3.13E+06 (	12)	6	170	96	3.3	0.3	14.0
7	3.48E+05 (	2)	2.61E+06 (	15)	9	142	72	2.7	0.3	10.7
8	9.13E+05 (	7)	3.13E+06 (	24)	12	170	69	5.5	2.0	13.1
9	6.96E+05 (	4)	2.96E+06 (	17)	9	160	77	4.5	1.1	13.5
10	2.93E+05 (	3)	1.08E+06 (	11)	16	58	34	5.3	0.9	19.3
11	5.22E+05 (	3)	3.13E+06 (	18)	9	170	79	3.3	0.6	10.7
12	5.22E+05 (	4)	1.96E+06 (	15)	12	106	54	5.1	1.2	15.7
13	7.82E+05 (	8)	2.35E+06 (	24)	16	127	52	6.3	2.4	14.3
14	4.89E+05 (	5)	2.64E+06 (	27)	16	143	55	3.6	1.0	9.1
15	6.85E+05 (	7)	7.82E+05 (	8)	16	42	29	16.4	5.1	51.5
16	5.22E+05 (	3)	1.04E+06 (	6)	9	57	44	9.6	1.5	43.7
17	3.48E+05 (	4)	6.96E+05 (	8)	18	38	26	9.5	2.1	34.8
18	3.48E+05 (	2)	3.13E+06 (	18)	9	170	79	2.2	0.2	8.7
19	3.91E+05 (	4)	4.89E+05 (	5)	16	27	23	15.1	3.0	69.2
20	3.91E+05 (	2)	1.76E+06 (	9)	8	96	62	4.4	0.4	20.1
21	5.22E+05 (	4)	1.17E+06 (	9)	12	64	41	8.5	1.9	29.7
22	1.39E+06 (	8)	3.65E+06 (	21)	9	198	86	7.2	2.7	16.7
23	8.69E+05 (	5)	1.56E+06 (	9)	9	85	55	10.5	2.7	34.5
24	6.96E+05 (4)	1.04E+06 (	6)	9	57	44	12.6	2.6	52.4	

PV3 (Taimali)

EFFECTIVE TRACK DENSITY FOR FLUENCE MONITOR (tracks/cm^2): 2.77E+05
RELATIVE ERROR (%): 1.11
EFFECTIVE URANIUM CONTENT OF MONITOR (ppm): 15.00
ZETA FACTOR AND STANDARD ERROR (yr cm^2): 135.42 15.20
SIZE OF COUNTER SQUARE (cm^2): 6.39E-07

Grain no.	ρ_s (tracks . cm^{-2}	Ns (tracks)	ρ_i (tracks . cm^{-2})	Ni (tracks)	Squares	Uranium (ppm) +/- 2 std. dev.		Age (Ma)	95% CI	
1	2.61E+05 (	2)	1.83E+06 (	14)	12	99	52	2.8	0.3	11.6
2	1.96E+06 (	15)	1.30E+06 (	10)	12	71	44	27.9	11.8	69.5
3	5.01E+05 (	8)	1.00E+06 (	16)	25	54	27	9.4	3.5	23.1
4	3.48E+05 (	2)	1.22E+06 (	7)	9	66	48	5.6	0.5	28.0
5	1.74E+06 (	10)	1.39E+06 (	8)	9	75	52	23.3	8.3	67.9
6	6.96E+05 (	4)	1.04E+06 (	6)	9	57	44	12.6	2.6	52.4
7	1.56E+06 (	12)	3.26E+06 (	25)	12	177	70	9.0	4.1	18.5
8	4.04E+06 (	31)	2.87E+06 (	22)	12	156	66	26.3	14.8	47.7
9	8.76E+05 (	14)	6.26E+05 (	10)	25	34	21	26.0	10.8	65.6

10	3.91E+05 (	4)	1.47E+06 (	15)	16	80	40	5.1	1.2	15.7
11	3.91E+05 (	5)	1.72E+06 (	22)	20	93	39	4.4	1.3	11.5
12	8.80E+05 (	9)	2.74E+06 (	28)	16	149	56	6.1	2.5	13.1
13	6.85E+05 (	7)	1.86E+06 (	19)	16	101	46	7.0	2.4	17.1
14	2.61E+06 (	15)	2.26E+06 (	13)	9	123	67	21.5	9.6	49.2
15	2.96E+06 (	17)	5.91E+06 (	34)	9	321	109	9.4	4.9	17.2
16	1.22E+06 (	7)	2.78E+06 (	16)	9	151	74	8.3	2.8	21.0
17	9.78E+05 (	10)	2.84E+06 (	29)	16	154	57	6.5	2.8	13.6
18	2.61E+06 (	15)	6.96E+05 (	4)	9	38	36	67.9	22.3	284.3
19	6.09E+06 (	35)	2.78E+06 (	16)	9	151	74	40.6	22.0	78.8
20	1.74E+06 (	10)	2.61E+06 (	15)	9	141	72	12.5	5.0	29.6
21	3.91E+05 (	4)	2.54E+06 (	26)	16	138	54	3.0	0.7	8.3
22	1.91E+06 (	11)	1.22E+06 (	7)	9	66	48	29.1	10.4	88.9
23	1.74E+06 (	10)	1.22E+06 (	7)	9	66	48	26.5	9.2	82.3
24	6.85E+05 (	7)	1.17E+06 (	12)	16	64	36	11.0	3.6	30.0

PV1-6 (Taimali)

EFFECTIVE TRACK DENSITY FOR FLUENCE MONITOR (tracks/cm^2): 2.76E+05
RELATIVE ERROR (%): 1.18
EFFECTIVE URANIUM CONTENT OF MONITOR (ppm):15.00
ZETA FACTOR AND STANDARD ERROR (yr cm^2): 135.42 15.20
SIZE OF COUNTER SQUARE (cm^2): 6.39E-07

Grain no.	ρ_s (tracks . cm^{-2}	Ns (tracks)	ρ_i (tracks . cm^{-2})	Ni (tracks)	Squares	Uranium (ppm) +/- 2 std. dev.		Age (Ma)	95% CI	
1	1.74E+05 (	1)	3.13E+06 (	18)	9	170	79	1.2	0.0	6.6
2	1.74E+05 (	1)	3.48E+06 (	20)	9	189	84	1.1	0.0	5.8
3	1.96E+05 (	1)	9.78E+05 (	5)	8	53	45	4.2	0.1	33.4
4	1.74E+05 (	1)	2.78E+06 (	16)	9	151	74	1.3	0.0	7.5
5	5.22E+05 (	3)	2.43E+06 (	14)	9	132	69	4.2	0.7	14.4
6	2.93E+05 (	3)	1.76E+06 (	18)	16	96	45	3.3	0.6	10.7
7	3.48E+05 (	2)	1.91E+06 (	11)	9	104	61	3.6	0.4	15.6
8	5.22E+05 (	3)	3.65E+06 (	21)	9	198	86	2.8	0.5	8.9
9	5.22E+05 (	4)	2.61E+06 (	20)	12	142	63	3.9	0.9	11.2
10	3.48E+05 (	2)	2.09E+06 (	12)	9	113	64	3.3	0.3	14.0
11	5.22E+05 (	3)	3.48E+06 (	20)	9	189	84	2.9	0.5	9.5
12	3.48E+05 (	2)	2.26E+06 (	13)	9	123	67	3.1	0.3	12.7
13	3.48E+05 (	2)	3.13E+06 (	18)	9	170	79	2.2	0.2	8.7
14	5.22E+05 (	3)	2.61E+06 (	15)	9	142	72	3.9	0.7	13.2
15	6.96E+05 (	4)	1.74E+06 (	10)	9	94	58	7.7	1.7	25.9
16	3.48E+05 (	2)	3.30E+06 (	19)	9	179	81	2.1	0.2	8.2
17	5.22E+05 (	4)	3.78E+06 (	29)	12	205	76	2.7	0.7	7.3
18	2.61E+05 (	2)	1.30E+06 (	10)	12	71	44	4.0	0.4	17.5
19	3.48E+05 (	2)	1.04E+06 (	6)	9	57	44	6.5	0.6	34.8
20	3.48E+05 (	2)	4.00E+06 (	23)	9	217	90	1.7	0.2	6.6
21	5.22E+05 (	3)	2.78E+06 (	16)	9	151	74	3.7	0.7	12.2
22	3.48E+05 (	2)	1.39E+06 (	8)	9	76	52	4.9	0.5	23.4
23	3.13E+05 (	2)	2.50E+06 (	16)	10	136	67	2.5	0.3	9.9

PV1-5 (Taimali)

EFFECTIVE TRACK DENSITY FOR FLUENCE MONITOR (tracks/cm^2): 2.76E+05
RELATIVE ERROR (%): 1.28
EFFECTIVE URANIUM CONTENT OF MONITOR (ppm):15.00
ZETA FACTOR AND STANDARD ERROR (yr cm^2): 135.42 15.20
SIZE OF COUNTER SQUARE (cm^2): 6.39E-07

Grain no.	ρ_s (tracks . cm^{-2}	Ns (tracks)	ρ_i	Ni (tracks)	Squares	Uranium (ppm)	Age (Ma)	95% CI

			(tracks . cm^{-2})			+/- 2 std. dev.				
1	5.22E+05	(5)	2.82E+06	(27)	15	153	58	3.6	1.0	9.1
2	1.96E+05	(1)	3.72E+06	(19)	8	202	92	1.1	0.0	6.2
3	3.13E+05	(2)	2.66E+06	(17)	10	144	69	2.3	0.2	9.3
4	6.96E+05	(4)	2.78E+06	(16)	9	151	74	4.8	1.1	14.5
5	6.96E+05	(4)	2.61E+06	(15)	9	142	72	5.1	1.2	15.6
6	1.74E+05	(1)	8.69E+05	(5)	9	47	40	4.2	0.1	33.4
7	3.48E+05	(2)	1.91E+06	(11)	9	104	61	3.6	0.4	15.6
8	6.52E+05	(5)	3.00E+06	(23)	12	163	67	4.2	1.2	10.9
9	1.74E+05	(1)	2.43E+06	(14)	9	132	70	1.5	0.0	8.8
10	3.48E+05	(2)	1.39E+06	(8)	9	76	52	4.9	0.5	23.4
11	5.22E+05	(4)	2.22E+06	(17)	12	120	58	4.5	1.1	13.5
12	7.82E+05	(10)	1.72E+06	(22)	20	93	39	8.6	3.6	18.7
13	3.48E+05	(2)	1.91E+06	(11)	9	104	61	3.6	0.4	15.6
14	3.91E+05	(3)	2.22E+06	(17)	12	120	58	3.4	0.6	11.4
15	5.22E+05	(3)	3.83E+06	(22)	9	208	88	2.7	0.5	8.5
16	3.48E+05	(2)	2.78E+06	(16)	9	151	74	2.5	0.3	9.9
17	1.74E+05	(1)	1.22E+06	(7)	9	66	48	3.0	0.1	20.8
18	3.91E+05	(3)	1.56E+06	(12)	12	85	48	4.9	0.8	17.3
19	6.52E+05	(5)	1.96E+06	(15)	12	106	54	6.4	1.8	18.0
20	6.96E+05	(4)	3.83E+06	(22)	9	208	88	3.5	0.9	10.0
21	7.82E+05	(8)	3.03E+06	(31)	16	165	59	4.9	1.9	10.7
22	3.13E+05	(3)	1.98E+06	(19)	15	108	49	3.1	0.6	10.0
23	3.48E+05	(2)	3.30E+06	(19)	9	179	81	2.1	0.2	8.2
24	6.96E+05	(4)	5.91E+06	(34)	9	321	110	2.3	0.6	6.2

PV1-3 (Taimali)

EFFECTIVE TRACK DENSITY FOR FLUENCE MONITOR (tracks/cm^2): 2.76E+05
RELATIVE ERROR (%): 1.25
EFFECTIVE URANIUM CONTENT OF MONITOR (ppm):15.00
ZETA FACTOR AND STANDARD ERROR (yr cm^2): 135.42 15.20
SIZE OF COUNTER SQUARE (cm^2): 6.39E-07

Grain no.	ρ_s (tracks . cm^{-2}	Ns (tracks)	ρ_i (tracks . cm^{-2})	Ni (tracks)	Squares	Uranium (ppm) +/- 2 std. dev.		Age (Ma)	95% CI	
1	1.74E+05	(1)	1.74E+05	(1)	9	9	15	18.7	0.2	1322.8
2	5.22E+05	(3)	1.39E+06	(8)	9	76	52	7.2	1.2	29.2
3	3.13E+05	(2)	1.72E+06	(11)	10	93	55	3.6	0.4	15.6
4	2.93E+05	(3)	7.82E+05	(8)	16	42	29	7.2	1.2	29.2
5	3.48E+05	(2)	2.96E+06	(17)	9	161	77	2.3	0.2	9.3
6	1.30E+05	(2)	4.56E+05	(7)	24	25	18	5.6	0.5	28.0
7	1.96E+05	(2)	1.96E+05	(2)	16	11	13	18.7	1.4	253.0
8	3.48E+05	(2)	1.56E+06	(9)	9	85	55	4.4	0.4	20.1
9	4.47E+05	(6)	1.94E+06	(26)	21	105	41	4.4	1.5	10.7
10	3.48E+05	(2)	1.91E+06	(11)	9	104	61	3.6	0.4	15.6
11	5.22E+05	(3)	2.96E+06	(17)	9	161	77	3.4	0.6	11.4
12	2.61E+05	(2)	1.30E+06	(10)	12	71	44	4.0	0.4	17.5
13	2.61E+05	(2)	6.52E+05	(5)	12	35	30	7.8	0.7	45.5
14	5.22E+05	(3)	3.30E+06	(19)	9	179	81	3.1	0.6	10.0
15	3.48E+05	(2)	2.96E+06	(17)	9	161	77	2.3	0.2	9.3
16	5.22E+05	(4)	4.69E+06	(36)	12	255	85	2.2	0.5	5.8
17	3.48E+05	(2)	5.91E+06	(34)	9	321	110	1.2	0.1	4.3
18	1.74E+05	(1)	2.09E+06	(12)	9	113	64	1.8	0.0	10.5
19	8.94E+05	(12)	4.69E+06	(63)	21	255	64	3.6	1.7	6.7
20	4.17E+05	(4)	2.50E+06	(24)	15	136	55	3.2	0.8	9.1
21	3.48E+05	(2)	4.35E+06	(25)	9	236	94	1.6	0.2	6.0
22	3.48E+05	(4)	3.30E+06	(38)	18	179	58	2.0	0.5	5.5
23	5.22E+05	(4)	5.09E+06	(39)	12	276	88	2.0	0.5	5.3
24	5.22E+05	(4)	3.39E+06	(26)	12	184	72	3.0	0.7	8.3
25	1.74E+05	(1)	1.56E+06	(9)	9	85	55	2.3	0.0	15.0
26	3.91E+05	(4)	3.13E+06	(32)	16	170	60	2.4	0.6	6.6

27	3.13E+05	(	3)	3.55E+06	(	34)	15	193	66	1.7	0.3	5.2
28	6.96E+05	(	4)	2.61E+06	(	15)	9	142	72	5.1	1.2	15.6
29	1.74E+05	(	1)	1.04E+06	(	6)	9	57	44	3.5	0.1	25.6
30	8.69E+05	(	5)	5.22E+06	(	30)	9	283	103	3.2	0.9	8.1
31	9.13E+05	(	7)	4.96E+06	(	38)	12	269	87	3.5	1.3	7.8
32	5.22E+05	(	4)	3.00E+06	(	23)	12	163	67	3.4	0.8	9.5
33	2.09E+05	(	2)	2.50E+06	(	24)	15	136	55	1.7	0.2	6.3
34	5.22E+05	(	3)	1.91E+06	(	11)	9	104	61	5.3	0.9	19.3
35	5.22E+05	(	3)	2.61E+06	(	15)	9	142	72	3.9	0.7	13.2
36	3.48E+05	(	2)	5.39E+06	(	31)	9	293	105	1.3	0.1	4.7
37	8.69E+05	(	5)	5.04E+06	(	29)	9	274	101	3.3	1.0	8.4
38	3.26E+05	(	5)	2.74E+06	(	42)	24	149	46	2.3	0.7	5.6

PV1-2B (Taimali)

EFFECTIVE TRACK DENSITY FOR FLUENCE MONITOR (tracks/cm^2): 2.76E+05
RELATIVE ERROR (%): 1.12
EFFECTIVE URANIUM CONTENT OF MONITOR (ppm):15.00
ZETA FACTOR AND STANDARD ERROR (yr cm^2): 135.42 15.20
SIZE OF COUNTER SQUARE (cm^2): 6.39E-07

Grain no.	ρ_s (tracks . cm^{-2}	Ns (tracks)	ρ_i (tracks . cm^{-2})	Ni (tracks)	Squares	Uranium (ppm) +/- 2 std. dev.		Age (Ma)	95% CI	
1	3.48E+05 (	2)	1.56E+06 (	9)	9	85	55	4.4	0.4	20.1
2	3.91E+05 (	4)	1.66E+06 (	17)	16	90	43	4.5	1.1	13.5
3	6.96E+05 (	4)	5.04E+06 (	29)	9	274	101	2.7	0.7	7.4
4	7.82E+05 (	8)	3.13E+06 (	32)	16	170	60	4.7	1.9	10.4
5	3.48E+05 (	2)	2.78E+06 (	16)	9	151	74	2.5	0.3	9.9
6	1.74E+05 (	1)	1.91E+06 (	11)	9	104	61	1.9	0.0	11.7
7	1.04E+06 (	6)	2.96E+06 (	17)	9	160	77	6.7	2.1	17.5
8	5.22E+05 (	3)	2.61E+06 (	15)	9	142	72	3.9	0.7	13.2
9	3.48E+05 (	2)	2.09E+06 (	12)	9	113	64	3.3	0.3	14.0
10	3.48E+05 (	2)	1.39E+06 (	8)	9	75	52	4.9	0.5	23.4
11	3.91E+05 (	3)	3.39E+06 (	26)	12	184	72	2.3	0.4	7.0
12	3.48E+05 (	2)	2.26E+06 (	13)	9	123	67	3.1	0.3	12.7
13	8.94E+04 (	4)	1.30E+06 (	58)	70	70	18	1.3	0.3	3.5
14	2.61E+05 (	2)	7.82E+05 (	6)	12	42	33	6.5	0.6	34.8
15	5.22E+05 (	3)	3.65E+06 (	21)	9	198	86	2.8	0.5	9.0
16	2.93E+05 (	3)	2.84E+06 (	29)	16	154	57	2.0	0.4	6.2
17	6.96E+05 (	4)	2.61E+06 (	15)	9	142	72	5.1	1.2	15.7
18	5.22E+05 (	3)	3.13E+06 (	18)	9	170	79	3.3	0.6	10.7
19	2.61E+05 (	3)	2.09E+06 (	24)	18	113	46	2.4	0.5	7.7
20	1.74E+05 (	1)	2.96E+06 (	17)	9	160	77	1.3	0.0	7.0
21	1.74E+05 (	1)	8.69E+05 (	5)	9	47	40	4.2	0.1	33.4
22	7.82E+05 (	6)	4.69E+06 (	36)	12	255	85	3.2	1.1	7.5
23	6.96E+05 (	4)	2.61E+06 (	15)	9	142	72	5.1	1.2	15.7
24	8.24E+05 (	10)	3.95E+06 (	48)	19	215	62	3.9	1.8	7.8

PV1-1 (Taimali)

EFFECTIVE TRACK DENSITY FOR FLUENCE MONITOR (tracks/cm^2): 2.76E+05
RELATIVE ERROR (%): 1.45
EFFECTIVE URANIUM CONTENT OF MONITOR (ppm): 15.00
ZETA FACTOR AND STANDARD ERROR (yr cm^2): 135.42 15.20
SIZE OF COUNTER SQUARE (cm^2): 6.39E-07

Grain no.	ρ_s (tracks . cm^{-2}	Ns (tracks)	ρ_i (tracks . cm^{-2})	Ni (tracks)	Squares	Uranium (ppm) +/- 2 std. dev.		Age (Ma)	95% CI	
1	5.22E+05 (	4)	9.13E+05 (	7)	12	50	36	10.9	2.3	41.9

2	3.91E+05 (	6)	1.76E+06 (	27)	24	96	37	4.2	1.4	10.3
3	4.38E+05 (	7)	1.82E+06 (	29)	25	99	36	4.6	1.7	10.5
4	5.22E+05 (	3)	1.04E+06 (	6)	9	57	44	9.6	1.5	43.6
5	2.35E+05 (	3)	9.39E+05 (	12)	20	51	29	4.9	0.8	17.3
6	1.22E+06 (	7)	5.74E+06 (	33)	9	312	108	4.0	1.5	9.1
7	3.91E+05 (	3)	1.30E+06 (	10)	12	71	44	5.8	1.0	21.8
8	2.87E+05 (	9)	8.94E+05 (	28)	49	49	18	6.1	2.5	13.1
9	3.91E+05 (	4)	1.08E+06 (	11)	16	58	35	7.0	1.6	22.9
10	7.82E+05 (	6)	3.13E+06 (	24)	12	170	69	4.8	1.6	11.7
11	1.17E+06 (	9)	3.52E+06 (	27)	12	191	73	6.3	2.6	13.6
12	8.35E+05 (	8)	1.36E+06 (	13)	15	74	40	11.6	4.1	29.9
13	3.48E+05 (	2)	1.22E+06 (	7)	9	66	48	5.6	0.5	28.0
14	4.89E+05 (	5)	3.52E+06 (	36)	16	191	64	2.7	0.8	6.6
15	3.26E+05 (	5)	1.70E+06 (	26)	24	92	36	3.7	1.1	9.5
16	5.22E+05 (	8)	1.89E+06 (	29)	24	103	38	5.2	2.0	11.6
17	2.93E+05 (	3)	2.45E+06 (	25)	16	133	53	2.3	0.4	7.4
18	6.52E+05 (	15)	3.13E+06 (	72)	36	170	40	3.9	2.1	6.9
19	1.96E+05 (	2)	5.87E+05 (	6)	16	32	25	6.5	0.6	34.8
20	2.68E+05 (	6)	2.06E+06 (	46)	35	112	33	2.5	0.9	5.7
21	3.58E+05 (	16)	2.03E+06 (	91)	70	111	23	3.3	1.8	5.6
22	3.13E+05 (	4)	2.11E+06 (	27)	20	115	44	2.9	0.7	7.9
23	5.22E+05 (	5)	2.40E+06 (	23)	15	130	54	4.2	1.2	10.9
24	2.09E+05 (	4)	1.51E+06 (	29)	30	82	30	2.7	0.7	7.3

Ph0 (Taimali)

EFFECTIVE TRACK DENSITY FOR FLUENCE MONITOR (tracks/cm^2): 2.76E+05
RELATIVE ERROR (%): 1.31
EFFECTIVE URANIUM CONTENT OF MONITOR (ppm):15.00
ZETA FACTOR AND STANDARD ERROR (yr cm^2): 135.42 15.20
SIZE OF COUNTER SQUARE (cm^2): 6.39E-07

Grain no.	ρ_s (tracks . cm^{-2}	Ns (tracks)	ρ_i (tracks . cm^{-2})	Ni (tracks)	Squares	Uranium (ppm) +/- 2 std. dev.		Age (Ma)	95% CI	
1	3.91E+05 (	10)	3.33E+06 (	85)	40	181	39	2.2	1.0	4.2
2	6.96E+05 (	4)	3.30E+06 (	19)	9	179	81	4.1	1.0	11.8
3	6.96E+05 (	4)	4.69E+06 (	27)	9	255	97	2.9	0.7	8.0
4	3.48E+05 (	2)	1.91E+06 (	11)	9	104	61	3.6	0.4	15.6
5	4.38E+05 (	7)	2.00E+06 (	32)	25	109	38	4.2	1.5	9.4
6	4.89E+05 (	5)	2.54E+06 (	26)	16	138	54	3.7	1.1	9.5
7	8.69E+05 (	5)	4.52E+06 (	26)	9	246	96	3.7	1.1	9.5
8	2.93E+05 (	3)	3.81E+06 (	39)	16	207	66	1.5	0.3	4.5
9	8.69E+05 (	5)	2.09E+06 (	12)	9	113	64	7.9	2.1	23.7
10	2.61E+05 (	2)	2.09E+06 (	16)	12	113	56	2.5	0.3	9.9
11	5.22E+05 (	3)	1.74E+06 (	10)	9	94	58	5.8	1.0	21.8
12	1.44E+06 (	23)	6.07E+06 (	97)	25	330	67	4.5	2.7	7.0
13	6.96E+05 (	4)	4.87E+06 (	28)	9	264	99	2.8	0.7	7.6
14	8.35E+05 (	8)	4.59E+06 (	44)	15	249	75	3.5	1.4	7.3
15	3.48E+05 (	2)	1.04E+06 (	6)	9	57	44	6.5	0.6	34.8
16	1.41E+06 (	18)	9.39E+06 (	120)	20	510	94	2.8	1.6	4.6
17	1.08E+06 (	11)	5.58E+06 (	57)	16	303	80	3.7	1.7	7.0
18	8.69E+05 (	5)	3.65E+06 (	21)	9	198	86	4.6	1.3	12.1
19	6.96E+05 (	4)	1.91E+06 (	11)	9	104	61	7.0	1.6	22.9
20	6.52E+05 (	5)	2.74E+06 (	21)	12	149	64	4.6	1.3	12.1
21	8.69E+05 (	5)	4.52E+06 (	26)	9	246	96	3.7	1.1	9.5
22	5.63E+05 (	9)	4.26E+06 (	68)	25	231	56	2.5	1.1	5.0
23	3.91E+05 (	4)	1.37E+06 (	14)	16	74	39	5.5	1.3	17.0
24	5.22E+05 (	3)	1.22E+06 (	7)	9	66	48	8.2	1.3	35.0

Ph60 (Taimali)

EFFECTIVE TRACK DENSITY FOR FLUENCE MONITOR (tracks/cm^2): 2.76E+05
RELATIVE ERROR (%): 1.22

EFFECTIVE URANIUM CONTENT OF MONITOR (ppm):15.00
ZETA FACTOR AND STANDARD ERROR (yr cm^2): 135.42 15.20
SIZE OF COUNTER SQUARE (cm^2): 6.39E-07

Grain no.	ρ_s (tracks . cm^{-2}	Ns (tracks)	ρ_i (tracks . cm^{-2})	Ni (tracks)	Squares	Uranium (ppm) +/- 2 std. dev.		Age (Ma)	95% CI	
1	1.74E+05	(1)	6.96E+05	(4)	9	38	36	5.2	0.1	47.1
2	2.61E+05	(3)	2.35E+06	(27)	18	127	49	2.2	0.4	6.8
3	3.48E+05	(2)	5.22E+05	(3)	9	28	30	12.8	1.0	108.0
4	3.13E+05	(3)	1.56E+06	(15)	15	85	43	3.9	0.7	13.2
5	1.74E+05	(1)	1.22E+06	(7)	9	66	48	3.0	0.1	20.8
6	1.74E+05	(1)	1.56E+06	(9)	9	85	55	2.3	0.0	15.0
7	5.22E+05	(3)	1.91E+06	(11)	9	104	61	5.3	0.9	19.3
8	5.22E+05	(3)	6.96E+06	(40)	9	378	119	1.5	0.3	4.4
9	5.22E+05	(5)	1.15E+06	(11)	15	62	37	8.6	2.3	26.5
10	3.91E+05	(2)	2.15E+06	(11)	8	117	69	3.6	0.4	15.6
11	3.91E+05	(2)	1.17E+06	(6)	8	64	50	6.5	0.6	34.8
12	3.91E+05	(3)	2.87E+06	(22)	12	156	66	2.7	0.5	8.5
13	6.96E+05	(4)	4.00E+06	(23)	9	217	90	3.4	0.8	9.5
14	3.48E+05	(2)	1.22E+06	(7)	9	66	48	5.6	0.5	28.0
15	5.22E+05	(3)	1.74E+06	(10)	9	94	58	5.8	1.0	21.8
16	3.48E+05	(2)	1.04E+06	(6)	9	57	44	6.5	0.6	34.8
17	1.74E+05	(1)	5.22E+05	(3)	9	28	30	6.8	0.1	77.2
18	2.61E+05	(1)	1.04E+06	(4)	6	57	53	5.2	0.1	47.1
19	5.22E+05	(3)	3.13E+06	(18)	9	170	79	3.3	0.6	10.7
20	2.87E+06	(22)	2.74E+06	(21)	12	149	64	19.6	10.3	37.4
21	1.83E+06	(7)	2.61E+06	(10)	6	142	87	13.2	4.2	38.0
22	5.22E+05	(3)	1.39E+06	(8)	9	76	52	7.2	1.2	29.2
23	6.96E+05	(4)	8.69E+05	(5)	9	47	40	15.1	3.0	69.2
24	5.87E+05	(3)	9.78E+05	(5)	8	53	45	11.4	1.7	57.5
25	3.48E+05	(2)	2.78E+06	(16)	9	151	74	2.5	0.3	9.9
26	9.39E+05	(12)	4.54E+06	(58)	20	246	65	3.9	1.9	7.3
27	3.48E+05	(2)	1.74E+06	(10)	9	94	58	4.0	0.4	17.5
28	2.50E+06	(16)	7.82E+05	(5)	10	42	36	58.3	20.9	205.7
29	3.48E+05	(2)	8.69E+05	(5)	9	47	40	7.8	0.7	45.6
30	3.83E+06	(22)	3.30E+06	(19)	9	179	81	21.6	11.2	42.2
31	5.22E+05	(3)	1.39E+06	(8)	9	76	52	7.2	1.2	29.2
32	2.48E+06	(19)	2.61E+06	(20)	12	142	63	17.8	9.0	35.0
33	6.96E+06	(40)	2.61E+06	(15)	9	142	72	49.4	26.9	96.6
34	3.76E+06	(24)	2.50E+06	(16)	10	136	67	27.9	14.3	56.3
35	7.30E+06	(42)	2.61E+06	(15)	9	142	72	51.8	28.4	101.0
36	1.22E+06	(7)	3.13E+06	(18)	9	170	79	7.4	2.6	18.2
37	2.24E+05	(3)	1.12E+06	(15)	21	61	31	3.9	0.7	13.2
38	5.04E+06	(29)	2.96E+06	(17)	9	160	77	31.7	16.9	61.7
39	4.35E+06	(25)	1.56E+06	(9)	9	85	55	51.2	23.4	125.4
40	4.87E+06	(28)	3.83E+06	(22)	9	208	88	23.7	13.1	43.6
41	3.13E+06	(18)	1.91E+06	(11)	9	104	61	30.4	13.7	71.4
42	6.43E+06	(37)	1.56E+06	(9)	9	85	55	75.4	36.3	178.8
43	2.61E+06	(15)	1.74E+06	(10)	9	94	58	27.9	11.8	69.5

Ph6' (Taimali)

EFFECTIVE TRACK DENSITY FOR FLUENCE MONITOR (tracks/cm^2): 2.76E+05
RELATIVE ERROR (%): 1.49
EFFECTIVE URANIUM CONTENT OF MONITOR (ppm):15.00
ZETA FACTOR AND STANDARD ERROR (yr cm^2): 135.42 15.20
SIZE OF COUNTER SQUARE (cm^2): 6.39E-07

Grain no.	ρ_s (tracks . cm^{-2}	Ns (tracks)	ρ_i (tracks . cm^{-2})	Ni (tracks)	Squares	Uranium (ppm) +/- 2 std. dev.		Age (Ma)	95% CI	
1	4.52E+06	(26)	6.96E+05	(4)	9	38	36	116.5	42.0	462.3
2	5.04E+06	(29)	1.91E+06	(11)	9	104	61	48.7	23.8	108.5

3	3.48E+06	(	20)	1.39E+06	(	8)	9	76	52	46.0	19.7	121.6
4	3.91E+05	(	2)	1.96E+06	(	10)	8	106	66	4.0	0.4	17.5
5	5.22E+05	(	3)	1.22E+06	(	7)	9	66	48	8.2	1.3	35.0
6	5.22E+05	(	3)	1.22E+06	(	7)	9	66	48	8.2	1.3	35.0
7	1.83E+06	(	7)	1.83E+06	(	7)	6	99	72	18.7	5.6	62.2
8	1.04E+06	(	6)	2.26E+06	(	13)	9	123	67	8.7	2.7	24.3
9	4.89E+05	(	5)	2.15E+06	(	22)	16	117	49	4.4	1.3	11.5
10	3.48E+05	(	2)	1.91E+06	(	11)	9	104	61	3.6	0.4	15.6
11	3.48E+05	(	2)	1.56E+06	(	9)	9	85	55	4.4	0.4	20.1
12	5.22E+05	(	3)	1.22E+06	(	7)	9	66	48	8.2	1.3	35.0
13	3.48E+05	(	2)	1.22E+06	(	7)	9	66	48	5.6	0.5	28.0
14	3.48E+05	(	2)	1.74E+06	(	10)	9	94	58	4.0	0.4	17.5
15	3.13E+05	(	5)	1.88E+05	(	3)	25	10	11	30.5	6.1	197.6
16	2.93E+05	(	3)	2.05E+06	(	21)	16	112	48	2.8	0.5	8.9
17	7.30E+05	(	7)	1.98E+06	(	19)	15	108	49	7.0	2.4	17.1
18	7.82E+05	(	6)	1.43E+06	(	11)	12	78	46	10.3	3.1	30.0
19	2.61E+06	(	15)	6.96E+05	(	4)	9	38	36	67.8	22.3	283.9
20	3.48E+05	(	2)	4.35E+06	(	25)	9	236	94	1.6	0.2	6.0
21	1.74E+05	(	1)	1.22E+06	(	7)	9	66	48	3.0	0.1	20.8
22	3.48E+06	(	20)	1.04E+06	(	6)	9	57	44	60.9	24.1	187.0
23	5.91E+06	(	34)	1.04E+06	(	6)	9	57	44	102.8	43.8	301.7
24	5.22E+05	(	8)	3.65E+06	(	56)	24	198	53	2.7	1.1	5.6
25	1.04E+06	(	6)	1.15E+07	(	66)	9	623	154	1.7	0.6	3.9
26	2.61E+05	(	1)	2.61E+06	(	10)	6	142	88	2.1	0.0	13.1
27	5.22E+05	(	4)	1.56E+06	(	12)	12	85	48	6.4	1.5	20.5
28	8.69E+05	(	5)	1.39E+06	(	8)	9	76	52	11.8	3.0	40.4
29	1.56E+06	(	12)	1.56E+06	(	12)	12	85	48	18.7	7.7	45.4
30	2.61E+05	(	2)	1.04E+06	(	8)	12	57	39	4.9	0.5	23.4
31	5.22E+05	(	3)	2.26E+06	(	13)	9	123	67	4.5	0.8	15.7
32	3.48E+05	(	2)	1.74E+06	(	10)	9	94	58	4.0	0.4	17.5

Ph5 (Taimali)

EFFECTIVE TRACK DENSITY FOR FLUENCE MONITOR (tracks/cm^2): 2.76E+05
RELATIVE ERROR (%): 1.34
EFFECTIVE URANIUM CONTENT OF MONITOR (ppm):15.00
ZETA FACTOR AND STANDARD ERROR (yr cm^2): 135.42 15.20
SIZE OF COUNTER SQUARE (cm^2): 6.39E-07

Grain no.	ρ_s (tracks . cm^{-2}	Ns (tracks)	ρ_i (tracks . cm^{-2})	Ni (tracks)	Squares	Uranium (ppm) +/- 2 std. dev.		Age (Ma)	95% CI	
1	1.74E+05	(1)	5.22E+05	(3)	9	28	30	6.8	0.1	77.2
2	6.96E+05	(4)	1.22E+06	(7)	9	66	48	10.9	2.3	41.9
3	3.48E+05	(2)	1.22E+06	(7)	9	66	48	5.6	0.5	28.0
4	1.22E+06	(7)	2.43E+06	(14)	9	132	70	9.5	3.2	24.7
5	8.69E+05	(5)	3.48E+06	(20)	9	189	84	4.8	1.4	12.8
6	2.61E+05	(1)	5.22E+05	(2)	6	28	36	9.9	0.2	177.2
7	1.96E+05	(1)	1.56E+06	(8)	8	85	58	2.6	0.1	17.4
8	1.96E+05	(3)	2.15E+06	(33)	24	117	41	1.8	0.3	5.4
9	1.74E+05	(1)	3.48E+05	(2)	9	19	24	9.9	0.2	177.2
10	3.13E+05	(2)	9.39E+05	(6)	10	51	40	6.5	0.6	34.8
11	9.78E+05	(5)	2.54E+06	(13)	8	138	75	7.3	2.0	21.5
12	4.17E+05	(4)	1.56E+06	(15)	15	85	43	5.1	1.2	15.6
13	1.74E+05	(1)	1.04E+06	(6)	9	57	44	3.5	0.1	25.6
14	3.13E+05	(2)	1.56E+06	(10)	10	85	53	4.0	0.4	17.5
15	3.48E+05	(2)	5.22E+05	(3)	9	28	30	12.8	1.0	108.0
16	5.22E+05	(2)	2.61E+06	(10)	6	142	88	4.0	0.4	17.5
17	2.61E+05	(1)	1.83E+06	(7)	6	99	72	3.0	0.1	20.8
18	3.13E+05	(2)	7.82E+05	(5)	10	42	36	7.8	0.7	45.5
19	5.22E+05	(4)	1.70E+06	(13)	12	92	50	5.9	1.4	18.6
20	4.69E+05	(3)	1.56E+06	(10)	10	85	53	5.8	1.0	21.8
21	2.61E+05	(2)	2.61E+06	(20)	12	142	63	2.0	0.2	7.7
22	1.74E+05	(1)	1.56E+06	(9)	9	85	55	2.3	0.0	15.0
23	3.48E+05	(2)	2.26E+06	(13)	9	123	67	3.1	0.3	12.7
24	1.04E+06	(4)	4.96E+06	(19)	6	269	122	4.1	1.0	11.8

Ph3 (Taimali)

EFFECTIVE TRACK DENSITY FOR FLUENCE MONITOR (tracks/cm^2): 2.76E+05
RELATIVE ERROR (%): 1.37
EFFECTIVE URANIUM CONTENT OF MONITOR (ppm):15.00
ZETA FACTOR AND STANDARD ERROR (yr cm^2): 135.42 15.20
SIZE OF COUNTER SQUARE (cm^2): 6.39E-07

Grain no.	ρ_s (tracks . cm^{-2}	Ns (tracks)	ρ_i (tracks . cm^{-2})	Ni (tracks)	Squares	Uranium (ppm) +/- 2 std. dev.		Age (Ma)	95% CI	
1	3.13E+05 (	2)	4.69E+05 (	3)	10	26	27	12.7	1.0	107.9
2	4.69E+05 (	3)	1.56E+06 (	10)	10	85	53	5.8	1.0	21.8
3	6.96E+05 (	4)	1.56E+06 (	9)	9	85	55	8.5	1.9	29.7
4	3.48E+05 (	2)	1.74E+06 (	10)	9	94	58	4.0	0.4	17.5
5	2.61E+05 (	4)	9.78E+05 (	15)	24	53	27	5.1	1.2	15.6
6	2.61E+05 (	3)	2.09E+06 (	24)	18	113	46	2.4	0.5	7.7
7	2.61E+05 (	2)	1.43E+06 (	11)	12	78	46	3.6	0.4	15.6
8	4.89E+05 (	5)	1.96E+06 (	20)	16	106	47	4.8	1.4	12.8
9	2.61E+05 (	1)	3.39E+06 (	13)	6	184	100	1.6	0.0	9.6
10	1.96E+05 (	2)	4.89E+05 (	5)	16	27	23	7.8	0.7	45.5
11	3.91E+05 (	3)	2.35E+06 (	18)	12	128	59	3.3	0.6	10.7
12	1.74E+05 (	1)	1.74E+05 (	1)	9	9	15	18.7	0.2	1322.4
13	3.35E+05 (	3)	1.34E+06 (	12)	14	73	41	4.9	0.8	17.3
14	1.74E+05 (	1)	5.22E+05 (	3)	9	28	30	6.8	0.1	77.2
15	1.74E+05 (	1)	2.96E+06 (	17)	9	161	77	1.2	0.0	7.0
16	2.61E+05 (	2)	2.35E+06 (	18)	12	128	59	2.2	0.2	8.7
17	6.96E+05 (	4)	2.96E+06 (	17)	9	161	77	4.5	1.1	13.5
18	3.91E+05 (	2)	2.15E+06 (	11)	8	117	69	3.6	0.4	15.6
19	3.13E+05 (	2)	1.88E+06 (	12)	10	102	58	3.3	0.3	14.0
20	1.04E+06 (	6)	4.35E+06 (	25)	9	236	94	4.6	1.5	11.2
21	2.61E+05 (	1)	1.04E+06 (	4)	6	57	53	5.2	0.1	47.1
22	1.74E+05 (	1)	2.26E+06 (	13)	9	123	67	1.6	0.0	9.6
23	6.96E+05 (	4)	2.78E+06 (	16)	9	151	75	4.8	1.1	14.5
24	3.48E+05 (	2)	1.56E+06 (	9)	9	85	55	4.4	0.4	20.1

Ph2 (Taimali)

EFFECTIVE TRACK DENSITY FOR FLUENCE MONITOR (tracks/cm^2): 2.77E+05
RELATIVE ERROR (%): 1.14
EFFECTIVE URANIUM CONTENT OF MONITOR (ppm):15.00
ZETA FACTOR AND STANDARD ERROR (yr cm^2): 135.42 15.20
SIZE OF COUNTER SQUARE (cm^2): 6.39E-07

Grain no.	ρ_s (tracks . cm^{-2}	Ns (tracks)	ρ_i (tracks . cm^{-2})	Ni (tracks)	Squares	Uranium (ppm) +/- 2 std. dev.		Age (Ma)	95% CI	
1	2.09E+05 (	4)	3.08E+06 (	59)	30	167	43	1.3	0.3	3.4
2	5.87E+05 (	3)	2.74E+06 (	14)	8	149	78	4.2	0.7	14.4
3	6.96E+05 (	4)	2.96E+06 (	17)	9	160	77	4.5	1.1	13.5
4	7.82E+05 (	6)	3.52E+06 (	27)	12	191	73	4.2	1.4	10.3
5	5.22E+05 (	4)	3.52E+06 (	27)	12	191	73	2.9	0.7	8.0
6	3.48E+05 (	2)	1.91E+06 (	11)	9	104	61	3.6	0.4	15.6
7	5.22E+05 (	3)	1.22E+06 (	7)	9	66	48	8.3	1.3	35.1
8	3.48E+05 (	2)	1.56E+06 (	9)	9	85	55	4.4	0.4	20.1
9	3.48E+05 (	2)	8.69E+05 (	5)	9	47	40	7.8	0.7	45.6
10	6.52E+05 (	5)	2.22E+06 (	17)	12	120	58	5.6	1.6	15.5
11	3.48E+05 (	2)	2.78E+06 (	16)	9	151	74	2.5	0.3	10.0
12	1.74E+05 (	1)	8.69E+05 (	5)	9	47	40	4.2	0.1	33.4
13	1.74E+05 (	1)	2.96E+06 (	17)	9	160	77	1.3	0.0	7.0
14	3.91E+05 (	2)	1.76E+06 (	9)	8	95	62	4.4	0.4	20.1

15	3.48E+05 (	2)	1.22E+06 (	7)	9	66	48	5.6	0.5	28.1
16	4.89E+05 (	5)	1.66E+06 (	17)	16	90	43	5.6	1.6	15.5
17	1.74E+05 (	1)	6.96E+05 (	4)	9	38	36	5.2	0.1	47.2
18	1.74E+05 (	1)	3.48E+05 (	2)	9	19	24	10.0	0.2	177.5
19	7.82E+05 (	3)	3.13E+06 (	12)	6	170	96	4.9	0.8	17.3
20	5.22E+05 (	3)	1.04E+06 (	6)	9	57	44	9.6	1.5	43.7
21	5.22E+05 (	3)	2.26E+06 (	13)	9	123	67	4.5	0.8	15.7
22	1.74E+05 (	1)	2.43E+06 (	14)	9	132	69	1.5	0.0	8.8
23	3.48E+05 (	2)	1.39E+06 (	8)	9	75	52	4.9	0.5	23.4
24	3.48E+05 (	2)	1.39E+06 (	8)	9	75	52	4.9	0.5	23.4

Ph1 (Taimali)

EFFECTIVE TRACK DENSITY FOR FLUENCE MONITOR (tracks/cm^2): 2.77E+05
RELATIVE ERROR (%): 1.13
EFFECTIVE URANIUM CONTENT OF MONITOR (ppm):15.00
ZETA FACTOR AND STANDARD ERROR (yr cm^2): 135.42 15.20
SIZE OF COUNTER SQUARE (cm^2): 6.39E-07

Grain no.	ρ_s (tracks . cm^{-2}	Ns (tracks)	ρ_i (tracks . cm^{-2})	Ni (tracks)	Squares	Uranium (ppm) +/- 2 std. dev.	Age (Ma)	95% CI
1	3.13E+05 (	1)	7.20E+06 (	23)	5	390 161	0.9	0.0 5.0
2	3.91E+05 (	2)	1.17E+06 (	6)	8	64 50	6.6	0.6 34.8
3	1.74E+05 (	1)	1.74E+06 (	10)	9	94 58	2.1	0.0 13.2
4	5.22E+05 (	3)	2.26E+06 (	13)	9	123 67	4.5	0.8 15.7
5	2.61E+05 (	1)	1.04E+06 (	4)	6	57 53	5.2	0.1 47.2
6	1.74E+05 (	1)	1.39E+06 (	8)	9	75 52	2.6	0.1 17.4
7	3.91E+05 (	2)	4.50E+06 (	23)	8	244 101	1.7	0.2 6.6
8	1.15E+07 (	66)	1.74E+05 (	1)	9	9 15	999.4	210.7 13936.4
9	9.29E+05 (	19)	6.11E+06 (	125)	32	332 60	2.9	1.7 4.6
10	3.48E+05 (	2)	1.04E+06 (	6)	9	57 44	6.6	0.6 34.8
11	3.48E+05 (	2)	5.04E+06 (	29)	9	273 101	1.4	0.1 5.1
12	2.61E+05 (	1)	1.30E+06 (	5)	6	71 60	4.2	0.1 33.4
13	2.61E+05 (	1)	2.35E+06 (	9)	6	127 83	2.3	0.0 15.0
14	2.61E+05 (	1)	4.17E+06 (	16)	6	226 112	1.3	0.0 7.5
15	6.96E+05 (	4)	2.78E+06 (	16)	9	151 74	4.8	1.1 14.5
16	3.48E+05 (	2)	6.09E+06 (	35)	9	330 111	1.1	0.1 4.2
17	0.00E+00 (	0)	3.13E+06 (	12)	6	170 96	1.1	0.0 6.7
18	0.00E+00 (	0)	2.96E+06 (	17)	9	160 77	0.8	0.0 4.5
19	0.00E+00 (	0)	1.91E+06 (	11)	9	104 61	1.2	0.0 7.5
20	0.00E+00 (	0)	1.22E+06 (	7)	9	66 48	1.9	0.1 13.0
21	0.00E+00 (	0)	1.83E+06 (	7)	6	99 72	1.9	0.1 13.0
22	0.00E+00 (	0)	2.78E+06 (	16)	9	151 74	0.8	0.0 4.9
23	0.00E+00 (	0)	1.04E+06 (	6)	9	57 44	2.3	0.1 15.9

0810-03 (Laonung)

2 mounts

EFFECTIVE TRACK DENSITY FOR FLUENCE MONITOR (tracks/cm^2): 2.11E+05
RELATIVE ERROR (%): 1.44
EFFECTIVE URANIUM CONTENT OF MONITOR (ppm):15.00
ZETA FACTOR AND STANDARD ERROR (yr cm^2): 135.42 15.20
SIZE OF COUNTER SQUARE (cm^2): 6.39E-07

Grain no.	ρ_s (tracks . cm^{-2}	Ns (tracks)	ρ_i (tracks . cm^{-2})	Ni (tracks)	Squares	Uranium (ppm) +/- 2 std. dev.	Age (Ma)	95% CI
1	3.48E+05	(2)	1.74E+05	(1)	9	12 20	26.9	1.5 1500.5
2	2.09E+05	(2)	2.30E+06	(22)	15	163 69	1.4	0.1 5.3

3	5.74E+06	(33)	8.69E+05	(5)	9	62	53	91.3	36.5	302.9
4	1.01E+07	(58)	2.09E+06	(12)	9	148	84	68.1	36.6	140.1
5	3.65E+06	(28)	1.30E+05	(1)	12	9	15	342.5	65.9	8154.6
6	2.43E+06	(14)	1.04E+06	(6)	9	74	58	32.8	12.0	105.2
7	1.88E+07	(108)	1.91E+06	(11)	9	136	80	137.2	75.0	283.8
8	6.43E+06	(37)	1.22E+06	(7)	9	86	63	73.8	33.2	198.2
9	5.22E+06	(80)	1.11E+06	(17)	24	79	38	66.5	39.4	120.3
10	3.13E+06	(24)	1.30E+06	(10)	12	93	57	33.9	15.8	80.0
11	1.32E+07	(76)	4.52E+06	(26)	9	321	125	41.5	26.4	67.8
12	3.65E+06	(21)	1.04E+06	(6)	9	74	58	49.0	19.5	150.0
13	1.12E+07	(86)	2.35E+06	(18)	12	167	78	67.6	40.6	119.8
14	3.78E+06	(29)	1.17E+06	(9)	12	83	54	45.4	21.2	109.9
15	1.38E+07	(106)	9.13E+05	(7)	12	65	47	208.7	100.8	530.1
16	2.09E+06	(12)	2.09E+06	(12)	9	148	84	14.3	5.9	34.8
17	2.43E+06	(14)	5.22E+05	(3)	9	37	40	63.9	18.6	352.8
18	7.48E+06	(43)	2.43E+06	(14)	9	173	91	43.5	23.5	86.5
19	7.82E+06	(45)	1.22E+06	(7)	9	86	63	89.6	41.0	237.6
20	1.50E+07	(86)	2.26E+06	(13)	9	160	87	93.0	52.3	182.6
21	1.25E+07	(72)	3.48E+05	(2)	9	25	31	462.2	136.1	3317.2
22	1.03E+07	(59)	1.74E+06	(10)	9	123	76	82.8	42.7	182.7
23	6.91E+06	(53)	7.82E+05	(6)	12	56	44	122.3	54.1	350.5
24	3.52E+06	(27)	1.70E+06	(13)	12	120	66	29.5	14.8	62.5
25	2.36E+06	(68)	4.87E+05	(14)	45	35	18	68.5	38.6	132.6
26	7.43E+06	(57)	5.22E+05	(4)	12	37	35	193.7	75.0	731.4
27	1.74E+05	(1)	1.56E+06	(9)	9	111	72	1.8	0.0	11.5
28	2.35E+05	(3)	7.82E+04	(1)	20	6	9	39.3	3.4	1933.7
29	9.19E+06	(94)	8.80E+05	(9)	16	62	41	145.4	75.0	328.8
30	1.96E+06	(20)	2.93E+06	(30)	16	208	76	9.6	5.1	17.4
31	9.91E+06	(57)	3.13E+06	(18)	9	222	103	44.9	26.2	81.4
32	7.82E+06	(45)	1.74E+06	(10)	9	123	76	63.3	31.9	141.9
33	5.09E+06	(52)	1.37E+06	(14)	16	97	51	52.5	28.9	103.1
34	1.91E+06	(11)	8.69E+05	(5)	9	62	53	30.9	10.1	114.6
35	3.83E+06	(22)	1.04E+06	(6)	9	74	58	51.3	20.6	156.4
36	1.56E+06	(12)	9.13E+05	(7)	12	65	47	24.3	8.9	73.2
37	2.61E+06	(15)	1.74E+06	(10)	9	123	76	21.3	9.0	53.3
38	8.52E+06	(49)	1.04E+06	(6)	9	74	58	113.2	49.8	325.8
39	9.22E+06	(53)	1.22E+06	(7)	9	86	63	105.4	48.9	276.7
40	4.69E+06	(27)	3.48E+05	(2)	9	25	31	177.9	48.4	1491.0

EFFECTIVE TRACK DENSITY FOR FLUENCE MONITOR (tracks/cm^2): 2.11E+05
RELATIVE ERROR (%): 1.49
EFFECTIVE URANIUM CONTENT OF MONITOR (ppm):15.00
ZETA FACTOR AND STANDARD ERROR (yr cm^2): 135.42 15.20
SIZE OF COUNTER SQUARE (cm^2): 6.39E-07

Grain no.	ρ_s (tracks . cm^{-2}	Ns (tracks)	ρ_i (tracks . cm^{-2})	Ni (tracks)	Squares	Uranium (ppm) +/- 2 std. dev.	Age (Ma)	95% CI
41	1.74E+05	(1)	3.13E+06	(18)	9	222 104	0.9	0.0 5.0
42	3.48E+05	(2)	1.22E+06	(7)	9	86 63	4.3	0.4 21.4
43	7.30E+06	(42)	6.96E+05	(4)	9	49 47	143.3	54.2 552.4
44	4.30E+06	(33)	3.91E+05	(3)	12	28 30	148.4	49.1 755.8
45	6.94E+06	(71)	1.76E+06	(18)	16	125 58	55.8	33.1 99.9
46	1.43E+07	(146)	2.84E+06	(29)	16	201 74	71.3	47.8 110.4
47	1.37E+06	(14)	5.87E+05	(6)	16	42 33	32.8	12.0 105.1
48	5.22E+05	(3)	1.39E+06	(8)	9	99 68	5.5	0.9 22.3
49	5.22E+05	(3)	3.30E+06	(19)	9	235 107	2.4	0.4 7.7
50	4.35E+06	(25)	8.69E+05	(5)	9	62 53	69.3	26.8 234.9
51	9.39E+06	(54)	2.43E+06	(14)	9	173 91	54.5	30.1 106.7
52	4.79E+06	(49)	1.66E+06	(17)	16	118 57	40.8	23.3 76.0
53	7.82E+06	(45)	2.26E+06	(13)	9	161 88	48.9	26.2 99.3
54	5.87E+05	(6)	9.78E+04	(1)	16	7 11	76.4	10.4 3079.3
55	4.79E+06	(49)	1.27E+06	(13)	16	90 49	53.2	28.7 107.5

56	9.04E+06	(52)	6.96E+05	(4)	9	49	47	176.8	68.0	671.8
57	8.00E+06	(46)	1.22E+06	(7)	9	86	63	91.5	42.0	242.2
58	2.45E+06	(25)	6.85E+05	(7)	16	49	36	50.0	21.4	138.4
59	6.26E+06	(64)	1.17E+06	(12)	16	83	47	75.0	40.6	153.5
60	6.39E+06	(49)	5.22E+05	(4)	12	37	35	166.8	63.9	636.2
61	4.29E+06	(137)	5.32E+05	(17)	50	38	18	113.3	69.0	200.6
62	8.87E+06	(68)	2.09E+06	(16)	12	148	73	60.0	34.7	111.4
63	8.45E+06	(81)	5.22E+05	(5)	15	37	32	221.0	94.5	694.2
64	1.21E+07	(93)	1.30E+06	(10)	12	93	57	129.8	68.7	280.5
65	3.48E+06	(20)	2.96E+06	(17)	9	210	101	16.8	8.4	34.1
66	5.48E+06	(42)	3.13E+06	(24)	12	222	90	24.9	14.8	43.1
67	4.69E+06	(36)	1.70E+06	(13)	12	120	66	39.2	20.5	80.9
68	8.00E+06	(46)	1.39E+06	(8)	9	99	68	80.4	38.3	198.7
69	7.17E+06	(55)	5.22E+05	(4)	12	37	35	186.8	72.1	707.2
70	7.64E+06	(122)	5.63E+05	(9)	25	40	26	187.9	98.0	420.3
71	4.11E+06	(42)	4.89E+05	(5)	16	35	30	115.8	47.4	377.9
72	3.72E+06	(38)	3.91E+05	(4)	16	28	26	129.8	48.7	504.0
73	6.96E+06	(40)	6.96E+05	(4)	9	49	47	136.6	51.5	528.3

0810-02 (Laonung)

2mounts

EFFECTIVE TRACK DENSITY FOR FLUENCE MONITOR (tracks/cm^2): 2.12E+05
RELATIVE ERROR (%): 1.39
EFFECTIVE URANIUM CONTENT OF MONITOR (ppm):15.00
ZETA FACTOR AND STANDARD ERROR (yr cm^2): 135.42 15.20
SIZE OF COUNTER SQUARE (cm^2): 6.39E-07

Grain no.	ρ_s (tracks . cm^{-2}	Ns (tracks)	ρ_i (tracks . cm^{-2})	Ni (tracks)	Squares	Uranium (ppm) +/- 2 std. dev.		Age (Ma)	95% CI	
1	6.78E+06	(39)	2.43E+06	(14)	9	173	91	39.5	21.1	79.1
2	5.22E+05	(3)	1.04E+06	(6)	9	74	58	7.3	1.2	33.5
3	9.39E+06	(72)	1.04E+06	(8)	12	74	51	125.4	61.7	302.8
4	9.78E+05	(5)	3.33E+06	(17)	8	236	113	4.3	1.2	11.9
5	6.09E+06	(35)	1.56E+06	(9)	9	111	72	54.7	26.2	130.5
6	5.56E+06	(32)	4.52E+06	(26)	9	321	125	17.6	10.2	30.7
7	9.74E+06	(56)	2.09E+06	(12)	9	148	84	65.8	35.3	135.6
8	1.12E+07	(43)	7.82E+05	(3)	6	55	59	192.8	65.3	959.6
9	7.48E+06	(43)	1.91E+06	(11)	9	136	80	55.1	28.3	119.3
10	3.30E+06	(19)	3.13E+06	(18)	9	222	103	15.1	7.5	30.5
11	3.83E+06	(22)	1.74E+05	(1)	9	12	20	271.1	50.7	7119.6
12	9.56E+06	(55)	2.26E+06	(13)	9	160	87	59.7	32.6	119.9
13	1.74E+06	(10)	2.26E+06	(13)	9	160	87	11.0	4.3	27.2
14	3.91E+06	(20)	2.15E+06	(11)	8	153	90	25.8	11.9	59.9
15	1.60E+07	(123)	2.61E+06	(20)	12	185	82	86.9	54.3	147.6
16	8.35E+06	(48)	1.22E+06	(7)	9	86	63	95.6	44.0	252.4
17	6.61E+06	(38)	5.22E+05	(3)	9	37	40	170.7	57.3	859.0
18	4.69E+06	(36)	2.35E+06	(18)	12	166	78	28.5	15.8	53.4
19	1.29E+07	(74)	4.69E+06	(27)	9	333	127	39.0	24.9	63.2
20	1.25E+07	(72)	8.69E+05	(5)	9	62	53	197.2	83.8	623.5
21	2.93E+06	(15)	1.17E+06	(6)	8	83	65	35.1	13.1	111.7
22	9.19E+06	(47)	1.76E+06	(9)	8	125	81	73.3	36.1	171.4
23	2.26E+06	(13)	8.69E+05	(5)	9	62	53	36.4	12.4	132.1
24	8.52E+06	(49)	2.61E+06	(15)	9	185	94	46.3	25.7	89.3
25	1.52E+07	(146)	3.03E+06	(29)	15	215	79	71.4	47.9	110.6
26	1.98E+07	(152)	3.13E+06	(24)	12	222	90	89.6	58.4	144.4
27	9.22E+06	(53)	1.04E+06	(6)	9	74	58	122.4	54.2	350.6
28	9.04E+06	(52)	1.04E+06	(6)	9	74	58	120.1	53.1	344.4
29	2.09E+06	(12)	6.96E+05	(4)	9	49	47	41.7	13.0	180.3
30	2.93E+06	(15)	1.56E+06	(8)	8	111	76	26.6	10.7	72.8
31	6.94E+06	(71)	1.56E+06	(16)	16	111	55	62.7	36.4	116.2
32	1.37E+07	(79)	1.39E+06	(8)	9	99	68	137.4	68.0	330.5
33	4.69E+06	(27)	3.48E+05	(2)	9	25	31	178.0	48.4	1491.5

34	2.35E+06	(12)	1.56E+06	(8)	8	111	76	21.3	8.1	60.3
35	1.67E+07	(149)	2.24E+06	(20)	14	159	70	105.1	66.3	177.4
36	1.48E+07	(85)	2.09E+06	(12)	9	148	84	99.5	54.9	201.0
37	2.26E+06	(13)	2.78E+06	(16)	9	197	97	11.7	5.1	25.8
38	3.83E+06	(22)	1.22E+06	(7)	9	86	63	44.2	18.5	123.6
39	1.08E+07	(69)	3.13E+06	(20)	10	222	98	48.9	29.6	85.3
40	5.29E+06	(71)	6.41E+06	(86)	21	455	99	11.8	8.5	16.4
41	2.26E+06	(13)	8.69E+05	(5)	9	62	53	36.4	12.4	132.1
42	1.53E+07	(88)	3.48E+06	(20)	9	247	109	62.3	38.3	107.3
43	1.47E+07	(94)	2.35E+06	(15)	10	166	85	88.3	51.5	164.7

EFFECTIVE TRACK DENSITY FOR FLUENCE MONITOR (tracks/cm^2): 2.11E+05
RELATIVE ERROR (%): 1.41
EFFECTIVE URANIUM CONTENT OF MONITOR (ppm):15.00
ZETA FACTOR AND STANDARD ERROR (yr cm^2): 135.42 15.20
SIZE OF COUNTER SQUARE (cm^2): 6.39E-07

Grain no.	ρ_s (tracks . cm^{-2}	Ns (tracks)	ρ_i (tracks . cm^{-2})	Ni (tracks)	Squares	Uranium (ppm) +/- 2 std. dev.	Age (Ma)	95% CI
44	2.61E+06	(15)	2.43E+06	(14)	9	173 91	15.3	6.9 34.2
45	2.26E+06	(13)	1.74E+06	(10)	9	123 76	18.5	7.5 47.3
46	2.61E+06	(20)	6.52E+05	(5)	12	46 39	55.7	20.8 192.4
47	1.45E+07	(65)	8.94E+05	(4)	7	63 60	220.4	86.0 824.5
48	1.02E+06	(13)	2.35E+06	(30)	20	167 61	6.2	3.0 12.3
49	6.43E+06	(37)	6.96E+05	(4)	9	49 47	126.6	47.4 492.3
50	2.09E+06	(12)	3.83E+06	(22)	9	271 115	7.9	3.5 16.5
51	6.46E+06	(33)	1.76E+06	(9)	8	125 81	51.6	24.5 123.6
52	8.74E+06	(67)	1.96E+06	(15)	12	139 71	63.1	36.0 119.5
53	1.07E+07	(41)	3.65E+06	(14)	6	259 136	41.5	22.3 82.8
54	3.83E+06	(22)	1.04E+06	(6)	9	74 58	51.3	20.6 156.4
55	1.06E+07	(61)	1.22E+06	(7)	9	86 63	121.1	56.7 315.6
56	4.50E+06	(46)	4.69E+06	(48)	16	333 96	13.7	8.9 21.0
57	6.52E+06	(50)	2.09E+06	(16)	12	148 73	44.3	25.0 83.7
58	4.47E+06	(40)	3.80E+06	(34)	14	270 92	16.8	10.4 27.4
59	3.83E+06	(22)	3.83E+06	(22)	9	271 115	14.3	7.6 27.1
60	7.82E+06	(45)	3.30E+06	(19)	9	234 106	33.6	19.4 61.1
61	6.26E+06	(36)	7.82E+06	(45)	9	555 165	11.5	7.2 18.1
62	8.74E+06	(67)	6.52E+05	(5)	12	46 39	183.6	77.7 583.0
63	1.48E+07	(85)	4.35E+06	(25)	9	308 122	48.3	30.7 79.0
64	2.48E+07	(127)	6.26E+06	(32)	8	444 156	56.3	38.1 86.1
65	9.91E+06	(57)	2.09E+06	(12)	9	148 84	66.9	35.9 137.8
66	1.15E+07	(59)	1.17E+06	(6)	8	83 65	136.0	60.6 387.3
67	6.26E+06	(32)	9.78E+05	(5)	8	69 59	88.6	35.3 294.5
68	6.26E+06	(56)	1.23E+06	(11)	14	87 52	71.6	37.6 152.5
69	9.39E+06	(66)	4.41E+06	(31)	11	313 112	30.3	19.6 48.2
70	7.82E+06	(60)	2.09E+06	(16)	12	148 73	53.1	30.4 99.2
71	8.76E+06	(56)	1.88E+06	(12)	10	133 75	65.8	35.3 135.6
72	5.39E+06	(31)	6.96E+05	(4)	9	49 47	106.3	39.1 418.8
73	5.61E+06	(43)	1.17E+06	(9)	12	83 54	67.1	32.8 157.7

0810-01 (Laonung)

2 mounts

EFFECTIVE TRACK DENSITY FOR FLUENCE MONITOR (tracks/cm^2): 2.12E+05
RELATIVE ERROR (%): 1.34
EFFECTIVE URANIUM CONTENT OF MONITOR (ppm):15.00
ZETA FACTOR AND STANDARD ERROR (yr cm^2): 135.42 15.20
SIZE OF COUNTER SQUARE (cm^2): 6.39E-07

Grain no.	ρ_s (tracks . cm^{-2}	Ns (tracks)	ρ_i (tracks . cm^{-2})	Ni (tracks)	Squares	Uranium (ppm) +/- 2 std. dev.		Age (Ma)	95% CI	
1	7.30E+06 (	42)	1.91E+06 (	11)	9	136	80	53.9	27.6	116.8
2	1.62E+07 (	124)	1.04E+06 (	8)	12	74	51	214.3	108.3	505.7
3	2.61E+05 (	2)	6.52E+05 (	5)	12	46	39	6.0	0.5	34.9
4	1.00E+07 (	77)	9.13E+05 (	7)	12	65	47	152.5	72.5	393.0
5	1.32E+07 (	76)	3.48E+05 (	2)	9	25	31	487.3	143.9	3459.1
6	6.26E+06 (	48)	6.52E+05 (	5)	12	46	39	132.3	54.8	428.3
7	2.93E+05 (	3)	4.89E+05 (	5)	16	35	30	8.8	1.3	44.0
8	5.22E+06 (	50)	5.22E+05 (	5)	15	37	32	137.7	57.2	444.9
9	6.52E+06 (	50)	9.13E+05 (	7)	12	65	47	99.6	46.0	262.3
10	1.36E+07 (	78)	4.00E+06 (	23)	9	284	117	48.2	30.1	80.6
11	1.15E+07 (	66)	2.09E+06 (	12)	9	148	84	77.5	42.1	158.3
12	9.39E+05 (	9)	3.13E+05 (	3)	15	22	24	41.4	10.7	242.3
13	1.86E+07 (	107)	2.61E+06 (	15)	9	185	94	100.5	59.0	186.4
14	1.49E+07 (	229)	2.15E+06 (	33)	24	153	53	98.2	68.4	146.4
15	8.66E+06 (	83)	1.77E+06 (	17)	15	126	60	69.0	41.0	124.6
16	4.23E+06 (	27)	2.35E+06 (	15)	10	166	85	25.6	13.2	52.0
17	1.22E+06 (	7)	1.74E+05 (	1)	9	12	20	88.9	12.9	3425.5
18	2.96E+06 (	17)	1.56E+06 (	9)	9	111	72	26.8	11.4	68.6
19	6.00E+06 (	46)	1.30E+06 (	10)	12	92	57	64.7	32.7	144.9
20	4.00E+06 (	23)	1.91E+06 (	11)	9	136	80	29.7	14.0	67.7
21	1.15E+07 (	66)	1.39E+06 (	8)	9	99	68	115.1	56.3	279.1
22	8.05E+06 (	72)	2.12E+06 (	19)	14	151	68	53.7	32.3	94.7

EFFECTIVE TRACK DENSITY FOR FLUENCE MONITOR (tracks/cm^2): 2.12E+05
RELATIVE ERROR (%): 1.37
EFFECTIVE URANIUM CONTENT OF MONITOR (ppm):15.00
ZETA FACTOR AND STANDARD ERROR (yr cm^2): 135.42 15.20
SIZE OF COUNTER SQUARE (cm^2): 6.39E-07

Grain no.	ρ_s (tracks . cm^{-2}	Ns (tracks)	ρ_i (tracks . cm^{-2})	Ni (tracks)	Squares	Uranium (ppm) +/- 2 std. dev.		Age (Ma)	95% CI	
23	3.83E+06 (	22)	1.04E+06 (	6)	9	74	58	51.3	20.6	156.5
24	6.61E+06 (	38)	3.48E+05 (	2)	9	25	31	248.8	69.9	1988.9
25	1.22E+06 (	7)	1.39E+06 (	8)	9	99	68	12.6	3.9	39.5
26	1.32E+07 (	76)	2.09E+06 (	12)	9	148	84	89.1	48.8	180.9
27	1.62E+07 (	93)	3.13E+06 (	18)	9	222	103	73.1	44.2	129.1
28	1.91E+06 (	11)	6.61E+06 (	38)	9	468	152	4.2	1.9	8.3
29	9.39E+06 (	54)	1.04E+06 (	6)	9	74	58	124.7	55.3	356.9
30	2.70E+06 (	31)	2.61E+05 (	3)	18	18	20	139.8	46.0	715.8
31	1.22E+07 (	164)	9.69E+05 (	13)	21	69	37	176.2	101.9	337.9
32	6.43E+06 (	37)	3.48E+05 (	2)	9	25	31	242.4	68.0	1945.3
33	1.21E+07 (	93)	3.91E+06 (	30)	12	277	101	44.1	29.1	69.2
34	5.74E+06 (	33)	1.04E+06 (	6)	9	74	58	76.6	32.5	226.2
35	8.35E+06 (	48)	4.87E+06 (	28)	9	345	130	24.5	15.1	40.6
36	8.17E+06 (	47)	1.22E+06 (	7)	9	86	63	93.7	43.0	247.6
37	8.87E+06 (	51)	1.39E+06 (	8)	9	99	68	89.2	42.9	219.2
38	1.04E+07 (	80)	1.30E+06 (	10)	12	92	57	112.0	58.9	243.6
39	1.34E+07 (	128)	4.17E+06 (	40)	15	296	93	45.6	31.8	66.9
40	1.43E+07 (	82)	4.69E+06 (	27)	9	333	127	43.2	27.8	69.6
41	1.06E+07 (	61)	1.04E+06 (	6)	9	74	58	140.7	62.9	399.9
42	1.95E+07 (	112)	3.13E+06 (	18)	9	222	103	87.9	53.6	154.2
43	6.26E+06 (	36)	1.39E+06 (	8)	9	99	68	63.2	29.4	158.7
44	7.82E+06 (	60)	1.30E+06 (	10)	12	92	57	84.3	43.5	185.8
45	3.13E+05 (	2)	4.69E+05 (	3)	10	33	36	9.8	0.8	82.9

0510-01 (Laonung)

EFFECTIVE TRACK DENSITY FOR FLUENCE MONITOR (tracks/cm^2): 2.12E+05
RELATIVE ERROR (%): 1.18
EFFECTIVE URANIUM CONTENT OF MONITOR (ppm):15.00
ZETA FACTOR AND STANDARD ERROR (yr cm^2): 135.42 15.20
SIZE OF COUNTER SQUARE (cm^2): 8.30E-07

Grain no.	ρ_s (tracks . cm^{-2}	Ns (tracks)	ρ_i (tracks . cm^{-2})	Ni (tracks)	Squares	Uranium (ppm) +/- 2 std. dev.		Age (Ma)	95% CI	
1	2.17E+07 (	216)	2.01E+06 (	20)	12	142	63	152.3	97.3	254.3
2	4.02E+06 (	30)	2.41E+06 (	18)	9	170	79	23.8	12.9	45.5
3	1.18E+07 (	98)	1.20E+06 (	10)	10	85	53	137.4	73.0	296.2
4	1.18E+07 (	88)	1.47E+06 (	11)	9	104	61	112.5	60.9	234.5
5	1.41E+07 (	140)	1.71E+06 (	17)	12	121	58	116.3	70.9	205.8
6	3.88E+06 (	29)	5.76E+06 (	43)	9	407	124	9.7	5.8	15.9
7	1.15E+07 (	86)	1.34E+06 (	10)	9	95	58	120.7	63.7	261.7
8	5.27E+06 (	35)	1.96E+06 (	13)	8	138	75	38.3	19.9	79.3
9	6.22E+06 (	62)	2.71E+06 (	27)	12	192	73	32.8	20.6	53.8
10	8.43E+06 (	63)	2.28E+06 (	17)	9	161	77	52.7	30.7	96.4
11	1.62E+07 (	121)	4.28E+06 (	32)	9	303	106	53.9	36.4	82.5
12	4.82E+06 (	32)	2.26E+06 (	15)	8	160	81	30.4	16.1	60.7
13	1.06E+07 (	79)	2.14E+06 (	16)	9	151	75	70.0	41.0	129.0
14	2.03E+07 (	135)	3.01E+06 (	20)	8	213	94	95.6	60.1	162.0
15	8.84E+06 (	44)	1.81E+06 (	9)	6	128	83	68.9	33.8	161.8

0210-01 (Laonung)
2mounts

EFFECTIVE TRACK DENSITY FOR FLUENCE MONITOR (tracks/cm^2): 2.14E+05
RELATIVE ERROR (%): 1.20
EFFECTIVE URANIUM CONTENT OF MONITOR (ppm):15.00
ZETA FACTOR AND STANDARD ERROR (yr cm^2): 135.42 15.20
SIZE OF COUNTER SQUARE (cm^2): 8.30E-07

Grain no.	ρ_s (tracks . cm^{-2}	Ns (tracks)	ρ_i (tracks . cm^{-2})	Ni (tracks)	Squares	Uranium (ppm) +/- 2 std. dev.		Age (Ma)	95% CI	
1	6.29E+06 (	47)	6.69E+05 (	5)	9	47	40	131.0	54.1	424.4
2	1.11E+07 (	83)	1.87E+06 (	14)	9	131	69	84.5	48.2	161.9
3	1.19E+07 (	89)	1.47E+06 (	11)	9	103	61	114.6	62.1	238.8
4	1.08E+07 (	81)	1.74E+06 (	13)	9	122	66	88.7	49.7	174.4
5	1.18E+07 (	118)	1.51E+06 (	15)	12	106	54	111.9	66.0	206.8
6	1.57E+07 (	117)	3.48E+06 (	26)	9	244	95	64.5	42.2	103.1
7	7.76E+06 (	58)	1.20E+06 (	9)	9	84	55	91.3	45.7	210.9
8	1.19E+07 (	89)	2.68E+06 (	20)	9	188	83	63.7	39.2	109.7
9	9.91E+06 (	74)	1.07E+06 (	8)	9	75	52	130.2	64.2	314.1
10	7.10E+06 (	53)	1.87E+06 (	14)	9	131	69	54.1	29.9	106.2
11	1.22E+07 (	91)	1.87E+06 (	14)	9	131	69	92.5	53.1	176.6
12	1.34E+07 (	100)	3.61E+06 (	27)	9	253	97	53.2	34.7	84.9
13	1.15E+07 (	86)	8.03E+05 (	6)	9	56	44	199.4	90.9	556.8
14	1.51E+07 (	113)	2.28E+06 (	17)	9	160	76	94.8	57.2	168.9
15	8.03E+06 (	60)	9.37E+05 (	7)	9	66	48	120.5	56.4	314.3
16	1.35E+07 (	168)	1.20E+06 (	15)	15	84	43	158.6	94.8	289.8
17	1.60E+07 (	159)	2.01E+06 (	20)	12	141	62	113.3	71.6	190.9

EFFECTIVE TRACK DENSITY FOR FLUENCE MONITOR (tracks/cm^2): 2.13E+05
RELATIVE ERROR (%): 1.10
EFFECTIVE URANIUM CONTENT OF MONITOR (ppm):15.00

ZETA FACTOR AND STANDARD ERROR (yr cm^2): 135.42 15.20
SIZE OF COUNTER SQUARE (cm^2): 8.30E-07

Grain no.	ρ_s (tracks . cm^{-2}	Ns (tracks)	ρ_i (tracks . cm^{-2})	Ni (tracks)	Squares	Uranium (ppm) +/- 2 std. dev.		Age (Ma)	95% CI	
18	1.16E+07 (241)		2.07E+06 (	43)	25	146	44	80.1	57.9	113.7
19	1.54E+07 (205)		2.86E+06 (	38)	16	202	65	77.1	54.6	112.2
20	1.38E+07 (137)		1.91E+06 (	19)	12	134	61	102.4	63.8	175.7
21	1.00E+07 (	75)	1.87E+06 (	14)	9	132	69	76.1	43.1	146.5
22	1.19E+07 (	89)	1.20E+06 (	9)	9	85	55	138.8	71.4	314.4
23	8.89E+06 (177)	1.36E+06 (27)			24	95	36	93.4	62.5	145.9

Lk03 (Linkou fm.)

EFFECTIVE TRACK DENSITY FOR FLUENCE MONITOR (tracks/cm^2): 2.77E+05
RELATIVE ERROR (%): 1.25
EFFECTIVE URANIUM CONTENT OF MONITOR (ppm):15.00
ZETA FACTOR AND STANDARD ERROR (yr cm^2): 135.42 15.20
SIZE OF COUNTER SQUARE (cm^2): 6.39E-07

Grain no.	ρ_s (tracks . cm^{-2}	Ns (tracks)	ρ_i (tracks . cm^{-2})	Ni (tracks)	Squares	Uranium (ppm) +/- 2 std. dev.		Age (Ma)	95% CI	
1	6.52E+05	(5)	2.22E+06	(17)	12	120	58	5.6	1.6	15.6
2	1.39E+06	(8)	1.74E+06	(10)	9	94	58	15.0	5.1	42.1
3	9.39E+06	(54)	3.83E+06	(22)	9	207	88	45.6	27.5	78.9
4	2.93E+05	(3)	7.82E+05	(8)	16	42	29	7.3	1.2	29.2
5	9.78E+05	(10)	2.45E+06	(25)	16	133	53	7.6	3.2	16.2
6	1.41E+07	(81)	3.83E+06	(22)	9	207	88	68.3	42.5	115.2
7	8.09E+06	(62)	9.13E+05	(7)	12	49	36	160.6	75.5	416.4
8	5.67E+06	(58)	1.08E+06	(11)	16	58	34	96.9	51.1	205.6
9	3.48E+05	(2)	5.22E+05	(3)	9	28	30	12.8	1.0	108.2
10	1.04E+06	(6)	1.56E+06	(9)	9	85	55	12.6	3.7	39.2
11	2.93E+05	(3)	2.15E+06	(22)	16	117	49	2.7	0.5	8.5
12	1.30E+05	(1)	1.43E+06	(11)	12	78	46	1.9	0.0	11.7
13	2.45E+06	(25)	1.17E+06	(12)	16	64	36	38.7	18.9	84.8
14	6.96E+05	(4)	2.09E+06	(12)	9	113	64	6.4	1.5	20.6
15	1.74E+05	(1)	3.13E+06	(18)	9	170	79	1.2	0.0	6.6
16	2.61E+05	(2)	1.30E+06	(10)	12	71	44	4.0	0.4	17.6
17	1.22E+07	(70)	2.96E+06	(17)	9	160	77	76.2	44.8	138.5
18	6.52E+05	(5)	1.30E+06	(10)	12	71	44	9.5	2.5	30.0
19	3.48E+05	(2)	1.56E+06	(9)	9	85	55	4.4	0.4	20.1
20	1.39E+06	(8)	5.39E+06	(31)	9	292	104	4.9	1.9	10.8
21	9.78E+04	(1)	1.08E+06	(11)	16	58	34	1.9	0.0	11.7
22	7.14E+06	(73)	2.84E+06	(29)	16	154	57	46.8	30.2	74.9
23	5.87E+05	(6)	7.82E+05	(8)	16	42	29	14.1	4.0	46.1
24	1.10E+06	(7)	6.57E+06	(42)	10	356	110	3.2	1.2	7.0
25	1.96E+05	(2)	1.08E+06	(11)	16	58	34	3.6	0.4	15.6
26	8.35E+06	(64)	1.30E+06	(10)	12	71	44	117.2	60.9	257.0
27	6.96E+05	(4)	1.56E+06	(9)	9	85	55	8.5	1.9	29.8
28	1.39E+06	(8)	1.22E+06	(7)	9	66	48	21.3	6.8	69.0
29	1.74E+06	(40)	1.78E+06	(41)	36	97	30	18.3	11.5	28.9
30	5.87E+05	(6)	3.42E+06	(35)	16	186	62	3.3	1.1	7.7
31	1.04E+06	(8)	4.69E+06	(36)	12	254	84	4.2	1.7	9.1
32	1.66E+06	(17)	3.72E+06	(38)	16	201	65	8.4	4.4	15.2
33	1.74E+05	(1)	1.56E+06	(9)	9	85	55	2.3	0.0	15.0
34	7.82E+05	(8)	3.23E+06	(33)	16	175	61	4.6	1.8	10.0
35	1.96E+05	(2)	2.54E+06	(26)	16	138	54	1.5	0.2	5.8
36	9.78E+04	(1)	1.47E+06	(15)	16	80	40	1.4	0.0	8.1
37	5.74E+05	(11)	2.45E+06	(47)	30	133	39	4.4	2.1	8.6

38	5.48E+05	(7)	5.71E+06	(73)	20	310	73	1.8	0.7	3.9
39	7.24E+06	(74)	1.47E+06	(15)	16	80	40	91.0	52.4	171.3
40	7.30E+06	(56)	1.83E+06	(14)	12	99	52	73.9	41.0	144.3
41	7.48E+06	(43)	2.61E+06	(15)	9	141	72	53.1	29.2	103.3
42	4.89E+05	(5)	1.47E+06	(15)	16	80	40	6.4	1.8	18.1
43	6.96E+05	(4)	1.91E+06	(11)	9	104	61	7.0	1.6	23.0
44	3.91E+05	(3)	1.96E+06	(15)	12	106	54	3.9	0.7	13.2
45	3.76E+05	(6)	2.57E+06	(41)	25	139	43	2.8	1.0	6.5
46	8.14E+05	(26)	3.10E+06	(99)	50	168	34	4.9	3.1	7.6
47	1.74E+06	(10)	5.91E+06	(34)	9	320	109	5.6	2.4	11.4
48	2.35E+05	(3)	9.39E+05	(12)	20	51	29	4.9	0.8	17.3
49	2.96E+06	(17)	3.65E+06	(21)	9	198	85	15.2	7.5	30.1
50	6.96E+05	(4)	3.48E+05	(2)	9	19	24	36.1	5.4	401.7
51	1.30E+05	(1)	1.04E+06	(8)	12	57	39	2.6	0.1	17.5
52	1.06E+07	(61)	1.56E+06	(9)	9	85	55	123.9	62.4	284.7
53	3.91E+05	(4)	8.80E+05	(9)	16	48	31	8.5	1.9	29.8
54	8.17E+06	(47)	2.26E+06	(13)	9	122	67	66.8	35.9	135.2
55	6.96E+05	(4)	1.56E+06	(9)	9	85	55	8.5	1.9	29.8
56	3.91E+05	(4)	5.87E+05	(6)	16	32	25	12.6	2.6	52.5
57	3.48E+05	(2)	4.35E+06	(25)	9	236	93	1.6	0.2	6.0
58	6.26E+06	(36)	2.43E+06	(14)	9	132	69	47.7	25.3	96.1
59	7.51E+05	(12)	3.88E+06	(62)	25	210	53	3.7	1.8	6.8
60	1.27E+07	(73)	4.17E+06	(24)	9	226	92	56.5	35.4	93.9
61	3.91E+05	(3)	4.43E+06	(34)	12	240	82	1.7	0.3	5.3
62	1.74E+06	(10)	1.74E+06	(10)	9	94	58	18.7	7.0	50.0
63	1.22E+06	(7)	7.30E+06	(42)	9	396	122	3.2	1.2	7.0
64	1.55E+07	(89)	2.43E+06	(14)	9	132	69	116.9	67.0	223.0
65	1.39E+06	(8)	1.22E+06	(7)	9	66	48	21.3	6.8	69.0
66	9.78E+04	(1)	2.15E+06	(22)	16	117	49	1.0	0.0	5.3
67	8.69E+05	(5)	1.56E+06	(9)	9	85	55	10.6	2.7	34.5
68	2.09E+05	(2)	1.25E+06	(12)	15	68	38	3.3	0.3	14.0
69	9.13E+05	(7)	3.39E+06	(26)	12	184	72	5.1	1.8	11.9
70	4.89E+05	(5)	2.74E+06	(28)	16	148	56	3.4	1.0	8.8
71	8.69E+05	(5)	3.30E+06	(19)	9	179	81	5.0	1.4	13.6
72	6.52E+05	(5)	1.96E+06	(15)	12	106	54	6.4	1.8	18.1
73	7.82E+06	(45)	6.96E+05	(4)	9	38	36	200.3	76.4	760.8
74	3.48E+05	(2)	1.56E+06	(9)	9	85	55	4.4	0.4	20.1
75	7.30E+06	(42)	1.22E+06	(7)	9	66	48	109.4	49.8	290.2
76	1.96E+05	(2)	2.93E+05	(3)	16	16	17	12.8	1.0	108.2
77	1.56E+06	(9)	8.69E+05	(5)	9	47	40	33.2	10.1	126.9
78	6.13E+06	(47)	1.43E+06	(11)	12	78	46	78.7	40.8	169.1
79	4.89E+05	(5)	4.89E+05	(5)	16	27	23	18.7	4.3	81.0
80	5.22E+05	(3)	1.91E+06	(11)	9	104	61	5.3	0.9	19.3
81	1.74E+05	(1)	1.22E+06	(7)	9	66	48	3.0	0.1	20.8
82	6.26E+05	(10)	2.63E+06	(42)	25	142	44	4.5	2.0	9.0
83	7.82E+05	(6)	5.22E+06	(40)	12	283	89	2.9	1.0	6.7

Lk04 (Linkou Fm.)

2 mounts

EFFECTIVE TRACK DENSITY FOR FLUENCE MONITOR (tracks/cm^2): 2.77E+05
RELATIVE ERROR (%): 1.30
EFFECTIVE URANIUM CONTENT OF MONITOR (ppm):15.00
ZETA FACTOR AND STANDARD ERROR (yr cm^2): 135.42 15.20
SIZE OF COUNTER SQUARE (cm^2): 6.39E-07

Grain no.	ρ_s (tracks . cm^{-2}	Ns (tracks)	ρ_i (tracks . cm^{-2})	Ni (tracks)	Squares	Uranium (ppm) +/- 2 std. dev.	Age (Ma)	95% CI
84	5.07E+06	(81)	1.13E+06	(18)	25	61 28	83.2	49.9 147.8

85	8.02E+06	(82)	7.82E+05	(8)	16	42	29	185.9	92.3	444.4
86	1.56E+06	(12)	1.04E+06	(8)	12	57	39	27.9	10.6	78.8
87	1.39E+06	(8)	1.22E+06	(7)	9	66	48	21.3	6.8	69.0
88	4.52E+06	(26)	8.69E+05	(5)	9	47	40	94.3	36.7	317.2
89	4.00E+06	(23)	1.22E+06	(7)	9	66	48	60.3	25.5	167.8
90	3.13E+06	(18)	1.04E+06	(6)	9	57	44	55.0	21.3	170.8
91	4.17E+06	(24)	1.22E+06	(7)	9	66	48	62.9	26.8	174.3
92	2.78E+06	(16)	8.69E+05	(5)	9	47	40	58.4	21.0	206.1
93	2.61E+06	(15)	1.22E+06	(7)	9	66	48	39.6	15.4	115.4
94	1.50E+07	(86)	2.09E+06	(12)	9	113	64	131.4	72.6	264.7
95	6.61E+06	(38)	8.69E+05	(5)	9	47	40	137.1	55.7	447.9
96	1.74E+06	(10)	1.22E+06	(7)	9	66	48	26.5	9.2	82.4
97	6.43E+06	(37)	2.09E+06	(12)	9	113	64	57.0	29.4	120.7
98	2.26E+06	(13)	6.96E+05	(4)	9	38	36	59.0	18.8	251.5
99	9.22E+06	(53)	1.56E+06	(9)	9	85	55	107.8	53.7	249.7
100	8.35E+06	(48)	2.26E+06	(13)	9	122	67	68.2	36.8	137.8
101	4.69E+06	(27)	1.56E+06	(9)	9	85	55	55.3	25.6	134.5
102	4.69E+06	(27)	1.22E+06	(7)	9	66	48	70.7	30.6	193.8
103	1.37E+06	(14)	8.80E+05	(9)	16	48	31	28.9	11.7	75.9
104	4.99E+06	(51)	1.37E+06	(14)	16	74	39	67.3	37.1	132.3
105	6.55E+06	(67)	1.66E+06	(17)	16	90	43	72.9	42.7	132.9
106	7.13E+06	(41)	1.39E+06	(8)	9	75	52	93.8	44.3	233.1
107	6.43E+06	(37)	2.96E+06	(17)	9	160	77	40.5	22.3	76.8
108	3.65E+06	(21)	1.56E+06	(9)	9	85	55	43.1	19.2	107.6
109	6.78E+06	(52)	2.74E+06	(21)	12	148	64	46.0	27.4	80.7
110	5.56E+06	(32)	2.43E+06	(14)	9	132	69	42.4	22.2	86.4
111	1.74E+06	(10)	1.22E+06	(7)	9	66	48	26.5	9.2	82.4
112	6.43E+06	(37)	3.30E+06	(19)	9	179	81	36.2	20.4	66.9
113	4.23E+06	(27)	1.72E+06	(11)	10	93	55	45.4	22.0	102.0
114	1.03E+07	(105)	4.30E+06	(44)	16	233	70	44.5	31.1	64.9
115	8.17E+06	(47)	3.65E+06	(21)	9	198	86	41.6	24.5	73.5
116	8.17E+06	(47)	2.43E+06	(14)	9	132	69	62.1	33.9	122.6
117	1.01E+07	(58)	2.26E+06	(13)	9	122	67	82.3	45.1	164.3
118	6.78E+06	(39)	2.96E+06	(17)	9	160	77	42.6	23.7	80.6
119	1.06E+07	(61)	2.26E+06	(13)	9	122	67	86.5	47.6	172.3
120	7.13E+06	(41)	1.91E+06	(11)	9	104	61	68.7	35.1	149.0
121	1.32E+07	(76)	2.43E+06	(14)	9	132	69	100.0	56.8	192.1
122	7.30E+06	(42)	2.26E+06	(13)	9	122	67	59.8	31.8	121.9
123	6.96E+05	(4)	8.69E+05	(5)	9	47	40	15.1	3.0	69.3
124	9.04E+06	(52)	2.09E+06	(12)	9	113	64	79.9	42.6	165.1
125	3.23E+06	(33)	5.87E+05	(6)	16	32	25	100.1	42.5	294.3
126	8.00E+06	(46)	1.39E+06	(8)	9	75	52	105.1	50.1	259.2
127	2.84E+06	(29)	5.87E+05	(6)	16	32	25	88.1	36.8	261.6
128	2.09E+06	(12)	1.22E+06	(7)	9	66	48	31.7	11.6	95.6
129	5.39E+06	(31)	2.43E+06	(14)	9	132	69	41.1	21.4	83.9
130	5.22E+05	(3)	1.39E+06	(8)	9	75	52	7.3	1.2	29.2
131	3.13E+06	(18)	1.74E+06	(10)	9	94	58	33.4	14.7	81.3
132	8.87E+06	(51)	1.91E+06	(11)	9	104	61	85.3	44.5	182.4
133	1.39E+06	(8)	1.22E+06	(7)	9	66	48	21.3	6.8	69.0
134	2.61E+06	(15)	1.22E+06	(7)	9	66	48	39.6	15.4	115.4
135	2.09E+06	(12)	1.39E+06	(8)	9	75	52	27.9	10.6	78.8
136	4.43E+06	(34)	1.56E+06	(12)	12	85	48	52.4	26.8	111.7
137	6.96E+06	(40)	1.74E+06	(10)	9	94	58	73.6	36.7	166.0
138	6.78E+06	(39)	8.69E+05	(5)	9	47	40	140.6	57.3	458.7
139	3.30E+06	(19)	1.04E+06	(6)	9	57	44	58.0	22.7	179.1
140	6.96E+05	(4)	2.09E+06	(12)	9	113	64	6.4	1.5	20.6
141	1.74E+06	(10)	5.22E+05	(3)	9	28	30	60.0	16.1	344.0
142	6.61E+06	(38)	1.22E+06	(7)	9	66	48	99.1	44.7	264.6
143	8.35E+06	(48)	1.91E+06	(11)	9	104	61	80.4	41.7	172.4

EFFECTIVE TRACK DENSITY FOR FLUENCE MONITOR (tracks/cm^2): 2.77E+05
RELATIVE ERROR (%): 1.34
EFFECTIVE URANIUM CONTENT OF MONITOR (ppm):15.00
ZETA FACTOR AND STANDARD ERROR (yr cm^2): 135.42 15.20
SIZE OF COUNTER SQUARE (cm^2): 6.39E-07

Grain no.	ρ_s (tracks . cm^{-2}	Ns (tracks)	ρ_i (tracks . cm^{-2})	Ni (tracks)	Squares	Uranium (ppm) +/- 2 std. dev.	Age (Ma)	95% CI
144	1.25E+06	(12)	2.09E+05	(2)	15	11 14	104.9	25.0 959.6
145	5.22E+05	(4)	3.91E+05	(3)	12	21 23	24.6	4.2 168.4
146	9.04E+06	(52)	1.74E+06	(10)	9	94 58	95.5	48.8 211.7
147	2.87E+06	(22)	7.82E+05	(6)	12	42 33	67.1	27.0 204.0
148	5.04E+06	(29)	1.04E+06	(6)	9	57 44	88.1	36.8 261.6
149	2.09E+06	(20)	3.13E+05	(3)	15	17 18	118.5	36.9 625.4
150	6.89E+05	(11)	4.38E+05	(7)	25	24 17	29.1	10.4 89.0
151	1.04E+06	(6)	3.48E+05	(2)	9	19 24	53.3	10.0 546.0
152	2.96E+06	(17)	3.48E+05	(2)	9	19 24	147.5	37.7 1284.9
153	1.38E+06	(22)	4.38E+05	(7)	25	24 17	57.7	24.2 161.3
154	3.48E+06	(20)	1.39E+06	(8)	9	75 52	46.1	19.7 121.9
155	4.35E+06	(25)	1.74E+06	(10)	9	94 58	46.2	21.7 108.5
156	7.43E+06	(57)	1.30E+06	(10)	12	71 44	104.6	53.8 230.6
157	5.56E+06	(32)	5.22E+05	(3)	9	28 30	188.0	62.2 947.4
158	4.17E+06	(24)	5.22E+05	(3)	9	28 30	141.8	45.4 734.6
159	5.48E+06	(42)	1.83E+06	(14)	12	99 52	55.6	30.0 110.6
160	1.01E+07	(58)	2.61E+06	(15)	9	141 72	71.5	40.4 136.3
161	3.13E+06	(18)	1.04E+06	(6)	9	57 44	55.0	21.3 170.8
162	6.43E+06	(37)	1.22E+06	(7)	9	66 48	96.5	43.4 258.2
163	3.48E+06	(20)	1.56E+06	(9)	9	85 55	41.1	18.1 103.1
164	1.74E+05	(1)	6.96E+05	(4)	9	38 36	5.2	0.1 47.2
165	3.83E+06	(22)	5.22E+05	(3)	9	28 30	130.2	41.1 680.3
166	4.52E+06	(26)	1.04E+06	(6)	9	57 44	79.1	32.6 237.0
167	7.14E+06	(73)	9.78E+05	(10)	16	53 33	133.5	69.9 290.7
168	8.69E+06	(50)	1.56E+06	(9)	9	85 55	101.8	50.5 236.6
169	3.65E+06	(21)	6.96E+05	(4)	9	38 36	94.6	33.1 382.8
170	1.43E+06	(11)	7.82E+05	(6)	12	42 33	33.9	11.6 112.2
171	5.22E+06	(30)	1.56E+06	(9)	9	85 55	61.4	28.8 148.0
172	3.83E+06	(22)	1.22E+06	(7)	9	66 48	57.7	24.2 161.3
173	3.65E+06	(21)	8.69E+05	(5)	9	47 40	76.4	28.8 261.9
174	1.91E+06	(11)	5.22E+05	(3)	9	28 30	65.9	18.1 372.7
175	2.74E+06	(28)	1.47E+06	(15)	16	80 40	34.7	18.0 70.1
176	3.52E+06	(36)	4.89E+05	(5)	16	27 23	130.0	52.5 426.3
177	6.43E+06	(37)	1.04E+06	(6)	9	57 44	112.0	48.1 326.8
178	5.22E+06	(40)	2.61E+06	(20)	12	141 63	37.2	21.4 67.4
179	4.69E+06	(27)	2.09E+06	(12)	9	113 64	41.7	20.6 90.8
180	2.96E+06	(17)	1.04E+06	(6)	9	57 44	52.0	19.9 162.5
181	1.11E+07	(64)	1.39E+06	(8)	9	75 52	145.7	71.3 352.5
182	5.04E+06	(29)	1.74E+06	(10)	9	94 58	53.6	25.7 123.9
183	1.11E+07	(64)	1.91E+06	(11)	9	104 61	106.8	56.8 225.5
184	6.96E+05	(4)	1.04E+06	(6)	9	57 44	12.6	2.6 52.5
185	1.56E+06	(9)	5.22E+05	(3)	9	28 30	54.1	14.0 315.1
186	1.04E+07	(60)	2.61E+06	(15)	9	141 72	73.9	41.9 140.7
187	5.67E+06	(58)	1.27E+06	(13)	16	69 38	82.3	45.1 164.3
188	1.04E+06	(6)	1.22E+06	(7)	9	66 48	16.1	4.5 55.6
189	3.83E+06	(22)	3.48E+05	(2)	9	19 24	189.8	50.5 1594.5
190	5.35E+06	(41)	2.61E+06	(20)	12	141 63	38.1	21.9 68.9
191	6.96E+06 (40)	1.74E+06 (10)			9	94 58	73.6	36.7 166.0

0510-15 (Liukuei fm.)
2mounts

EFFECTIVE TRACK DENSITY FOR FLUENCE MONITOR (tracks/cm^2): 2.12E+05
RELATIVE ERROR (%): 1.19
EFFECTIVE URANIUM CONTENT OF MONITOR (ppm):15.00
ZETA FACTOR AND STANDARD ERROR (yr cm^2): 135.42 15.20
SIZE OF COUNTER SQUARE (cm^2): 8.30E-07

Grain no.	ρ_s (tracks . cm^{-2}	Ns (tracks)	ρ_i (tracks . cm^{-2})	Ni (tracks)	Squares	Uranium (ppm) +/- 2 std. dev.	Age (Ma)	95% CI

1	4.14E+05	(11)	1.24E+06	(33)	32	88	30	4.8	2.2	9.7
2	9.30E+06	(193)	1.45E+06	(30)	25	102	37	91.4	62.3	139.3
3	2.75E+05	(8)	1.27E+06	(37)	35	90	29	3.2	1.2	6.8
4	4.02E+06	(80)	4.02E+05	(8)	24	28	19	139.6	69.1	335.5
5	5.78E+05	(12)	1.20E+06	(25)	25	85	34	6.9	3.2	14.2
6	6.10E+06	(81)	2.03E+06	(27)	16	144	55	42.8	27.5	69.0
7	8.67E+05	(18)	7.71E+05	(16)	25	55	27	16.1	7.8	33.8
8	1.25E+06	(26)	2.36E+06	(49)	25	167	48	7.6	4.5	12.5
9	9.04E+05	(12)	1.51E+06	(20)	16	106	47	8.7	3.8	18.5
10	5.22E+05	(13)	2.81E+05	(7)	30	20	15	26.4	9.9	78.5
11	8.96E+06	(223)	1.93E+06	(48)	30	136	39	66.2	48.5	92.6
12	8.73E+05	(29)	2.77E+06	(92)	40	196	41	4.5	2.9	6.9
13	4.22E+05	(7)	6.63E+05	(11)	20	47	28	9.2	3.0	25.8
14	5.12E+06	(136)	1.88E+06	(50)	32	133	38	38.9	28.0	55.0
15	8.43E+05	(14)	1.87E+06	(31)	20	132	47	6.5	3.2	12.6
16	1.11E+06	(23)	5.20E+06	(108)	25	368	71	3.1	1.9	4.8
17	4.02E+05	(4)	1.20E+06	(12)	12	85	48	4.9	1.1	15.8
18	7.71E+05	(32)	2.41E+05	(10)	50	17	11	45.3	22.0	104.1
19	5.62E+05	(7)	1.69E+06	(21)	15	119	52	4.9	1.7	11.7
20	5.35E+05	(8)	1.47E+06	(22)	18	104	44	5.3	2.0	12.2
21	6.02E+05	(9)	1.20E+06	(18)	18	85	40	7.2	2.8	16.8
22	1.72E+05	(2)	2.67E+06	(31)	14	189	67	1.0	0.1	3.6
23	2.41E+06	(50)	1.54E+06	(32)	25	109	38	22.4	14.1	36.1
24	6.48E+06	(86)	1.66E+06	(22)	16	117	49	55.6	34.7	93.6
25	6.43E+06	(128)	2.16E+06	(43)	24	153	46	42.5	30.0	61.7
26	2.41E+05	(4)	6.63E+05	(11)	20	47	28	5.4	1.2	17.6
27	1.20E+05	(2)	2.53E+06	(42)	20	179	55	0.7	0.1	2.6
28	8.61E+05	(15)	1.55E+06	(27)	21	109	42	8.0	3.9	15.5
29	1.10E+07	(320)	1.51E+06	(44)	35	107	32	103.3	75.6	145.2
30	2.81E+05	(7)	9.64E+05	(24)	30	68	28	4.3	1.5	10.0
31	1.23E+07	(286)	2.02E+06	(47)	28	143	42	86.6	63.7	120.7
32	5.62E+05	(28)	1.57E+06	(78)	60	111	25	5.2	3.2	8.0
33	1.33E+06	(31)	3.18E+06	(74)	28	225	52	6.0	3.8	9.3
34	1.07E+07	(222)	1.98E+06	(41)	25	140	43	77.1	55.3	110.5
35	6.63E+06	(154)	1.59E+06	(37)	28	113	37	59.3	41.4	87.6
36	5.30E+05	(11)	1.16E+06	(24)	25	82	33	6.6	2.9	14.0
37	1.63E+06	(135)	1.57E+05	(13)	100	11	6	145.9	83.8	281.4
38	6.33E+05	(21)	4.82E+05	(16)	40	34	17	18.8	9.4	38.6
39	5.65E+05	(15)	5.65E+05	(15)	32	40	20	14.4	6.5	31.5
40	1.11E+07	(83)	2.68E+05	(2)	9	19	24	531.7	158.0	3704.9
41	1.20E+06	(9)	1.47E+06	(11)	9	104	61	11.8	4.3	31.1
42	1.04E+07	(156)	2.21E+06	(33)	18	156	54	67.3	46.2	101.4
43	9.64E+04	(2)	4.82E+05	(10)	25	34	21	3.0	0.3	13.5
44	8.43E+05	(14)	2.47E+06	(41)	20	175	54	4.9	2.5	9.2
45	1.17E+07	(195)	1.87E+06	(31)	20	132	47	89.4	61.3	135.3
46	4.40E+06	(146)	9.34E+05	(31)	40	66	24	67.0	45.5	102.5
47	2.25E+06	(28)	3.21E+06	(40)	15	227	72	10.1	6.0	16.7
48	1.31E+06	(26)	2.11E+06	(42)	24	149	46	8.9	5.2	14.8
49	4.15E+06	(31)	1.34E+06	(10)	9	95	58	43.9	21.2	101.1
50	6.02E+05	(8)	1.81E+06	(24)	16	128	52	4.9	1.9	11.0
51	7.63E+05	(19)	1.69E+06	(42)	30	119	37	6.5	3.6	11.4
52	4.62E+06	(46)	1.31E+06	(13)	12	92	50	50.2	26.9	101.8
53	4.82E+05	(6)	1.20E+06	(15)	15	85	43	5.8	1.8	15.7
54	8.53E+05	(17)	2.11E+06	(42)	24	149	46	5.8	3.1	10.4
55	1.69E+06	(21)	2.65E+06	(33)	15	187	65	9.2	5.0	16.3
56	1.41E+06	(14)	3.21E+06	(32)	12	227	80	6.3	3.1	12.1
57	1.58E+06	(21)	2.71E+06	(36)	16	192	64	8.4	4.6	14.7
58	5.09E+06	(228)	1.76E+06	(79)	54	125	28	41.3	31.9	54.1
59	2.11E+06	(21)	1.91E+06	(19)	12	135	61	15.8	8.1	31.2
60	3.77E+05	(5)	8.28E+05	(11)	16	59	35	6.6	1.8	20.4
61	7.53E+05	(10)	1.13E+06	(15)	16	80	41	9.6	3.8	22.8
62	8.77E+06	(291)	2.29E+06	(76)	40	162	37	54.7	42.4	71.5
63	4.89E+06	(73)	1.47E+06	(22)	18	104	44	47.3	29.2	80.2
64	2.81E+06	(28)	3.21E+06	(32)	12	227	80	12.6	7.3	21.5
65	2.68E+05	(2)	1.74E+06	(13)	9	123	67	2.4	0.2	9.8

EFFECTIVE TRACK DENSITY FOR FLUENCE MONITOR (tracks/cm^2): 2.12E+05
RELATIVE ERROR (%): 1.21
EFFECTIVE URANIUM CONTENT OF MONITOR (ppm):15.00
ZETA FACTOR AND STANDARD ERROR (yr cm^2): 135.42 15.20
SIZE OF COUNTER SQUARE (cm^2): 8.30E-07

Grain no.	ρ_s (tracks . cm^{-2}	Ns (tracks)	ρ_i (tracks . cm^{-2})	Ni (tracks)	Squares	Uranium (ppm) +/- 2 std. dev.		Age (Ma)	95% CI	
66	5.42E+06 (	54)	9.04E+05 (	9)	12	64	41	84.3	42.0	195.6
67	9.37E+05 (	7)	2.54E+06 (	19)	9	180	82	5.4	1.9	13.1
68	2.56E+06 (	34)	3.77E+05 (	5)	16	27	23	94.4	37.9	312.3
69	7.63E+06 (	57)	5.35E+05 (	4)	9	38	36	194.3	75.2	733.6
70	1.20E+06 (	20)	1.93E+06 (	32)	20	136	48	9.0	4.9	16.2
71	1.10E+07 (	82)	2.01E+06 (	15)	9	142	72	77.3	44.8	145.0
72	1.20E+06 (	24)	1.51E+06 (	30)	24	107	39	11.5	6.4	20.3
73	3.77E+05 (	5)	1.58E+06 (	21)	16	112	48	3.5	1.0	9.3
74	1.73E+07 (	172)	2.41E+06 (	24)	12	170	69	101.5	66.5	163.1
75	1.05E+07 (	280)	1.66E+06 (	44)	32	117	35	90.5	65.9	127.5
76	9.34E+06 (	248)	1.13E+06 (	30)	32	80	29	117.1	80.5	177.4
77	8.28E+05 (	11)	1.88E+06 (	25)	16	133	53	6.4	2.8	13.3
78	3.45E+06 (	43)	2.17E+06 (	27)	15	153	59	22.8	13.8	38.4
79	2.81E+05 (	14)	2.75E+06 (	137)	60	195	34	1.5	0.8	2.5
80	9.79E+05 (	13)	1.88E+06 (	25)	16	133	53	7.5	3.5	15.2
81	5.67E+06 (	113)	1.66E+06 (	33)	24	117	41	48.8	33.0	74.5
82	5.62E+06 (	56)	1.81E+06 (	18)	12	128	60	44.3	25.8	80.3
83	1.43E+06 (	19)	3.46E+06 (	46)	16	245	72	6.0	3.3	10.3
84	1.83E+07 (	137)	3.35E+06 (	25)	9	237	94	77.8	50.9	124.7
85	5.05E+06 (	67)	1.20E+06 (	16)	16	85	42	59.4	34.4	110.3
86	1.74E+06 (	13)	3.48E+06 (	26)	9	246	96	7.2	3.4	14.5
87	1.66E+06 (	22)	3.54E+06 (	47)	16	250	73	6.7	3.9	11.4
88	1.28E+06 (	17)	2.03E+06 (	27)	16	144	55	9.1	4.6	17.2

0510-17 (Liukuei fm.)

2mounts

EFFECTIVE TRACK DENSITY FOR FLUENCE MONITOR (tracks/cm^2): 2.12E+05
RELATIVE ERROR (%): 1.22
EFFECTIVE URANIUM CONTENT OF MONITOR (ppm):15.00
ZETA FACTOR AND STANDARD ERROR (yr cm^2): 135.42 15.20
SIZE OF COUNTER SQUARE (cm^2): 6.39E-07

Grain no.	ρ_s (tracks . cm^{-2}	Ns (tracks)	ρ_i (tracks . cm^{-2})	Ni (tracks)	Squares	Uranium (ppm) +/- 2 std. dev.		Age (Ma)	95% CI	
89	6.52E+05	(5)	6.52E+05	(5)	12	46	39	14.3	3.3	62.1
90	1.01E+07	(58)	1.22E+06	(7)	9	86	63	115.6	54.0	302.0
91	4.69E+06	(36)	2.48E+06	(19)	12	175	79	27.0	15.2	50.1
92	2.09E+06	(12)	1.74E+05	(1)	9	12	20	150.6	25.4	4913.6
93	2.61E+06	(15)	2.26E+06	(13)	9	160	87	16.5	7.3	37.8
94	5.74E+06	(55)	2.09E+05	(2)	15	15	19	357.4	103.4	2693.6
95	7.48E+06	(43)	1.74E+06	(10)	9	123	76	60.7	30.5	136.4
96	1.17E+06	(15)	8.61E+05	(11)	20	61	36	19.5	8.4	47.0
97	3.65E+06	(21)	8.69E+05	(5)	9	61	52	58.6	22.1	201.6
98	2.09E+06	(12)	1.56E+06	(9)	9	111	72	19.0	7.4	51.3
99	3.30E+06	(19)	1.39E+06	(8)	9	98	68	33.6	14.2	89.5
100	6.96E+06	(40)	1.22E+06	(7)	9	86	63	80.0	36.3	213.6
101	2.61E+06	(15)	4.17E+06	(24)	9	295	119	9.0	4.4	17.8

102	5.56E+06	(32)	5.22E+05	(3)	9	37	39	144.6	47.7	738.1
103	9.74E+06	(56)	4.69E+06	(27)	9	332	127	29.6	18.5	48.9
104	1.17E+06	(9)	2.48E+06	(19)	12	175	79	6.9	2.7	15.8
105	1.67E+06	(16)	5.22E+05	(5)	15	37	31	44.8	16.1	158.5
106	2.09E+06	(12)	2.26E+06	(13)	9	160	87	13.3	5.5	31.5
107	9.74E+06	(56)	2.26E+06	(13)	9	160	87	61.0	33.3	122.2
108	4.35E+06	(25)	4.17E+06	(24)	9	295	119	14.9	8.2	27.3
109	8.90E+06	(91)	1.17E+06	(12)	16	83	47	106.7	59.1	215.0
110	1.66E+06	(17)	4.89E+05	(5)	16	35	30	47.6	17.3	167.2
111	3.65E+06	(21)	1.39E+06	(8)	9	98	68	37.1	16.0	97.7
112	4.35E+06	(25)	2.09E+06	(12)	9	148	84	29.6	14.5	65.1
113	1.60E+07	(92)	5.56E+06	(32)	9	394	138	41.0	27.3	63.6
114	3.83E+06	(22)	5.22E+05	(3)	9	37	39	100.0	31.6	527.6
115	2.78E+06	(16)	3.30E+06	(19)	9	234	106	12.1	5.8	24.8
116	1.39E+06	(8)	5.22E+05	(3)	9	37	39	37.0	9.2	220.4
117	1.22E+06	(7)	2.61E+06	(15)	9	184	94	6.8	2.3	17.4
118	8.69E+06	(50)	2.61E+06	(15)	9	184	94	47.3	26.4	91.2

EFFECTIVE TRACK DENSITY FOR FLUENCE MONITOR (tracks/cm^2): 2.12E+05
RELATIVE ERROR (%): 1.24
EFFECTIVE URANIUM CONTENT OF MONITOR (ppm):15.00
ZETA FACTOR AND STANDARD ERROR (yr cm^2): 135.42 15.20
SIZE OF COUNTER SQUARE (cm^2): 6.39E-07

Grain no.	ρ_s (tracks . cm^{-2}	Ns (tracks)	ρ_i (tracks . cm^{-2})	Ni (tracks)	Squares	Uranium (ppm) +/- 2 std. dev.		Age (Ma)	95% CI	
119	2.06E+06	(46)	5.37E+05	(12)	35	38	21	54.3	28.6	113.2
120	1.04E+07	(60)	2.43E+06	(14)	9	172	91	60.7	33.9	118.2
121	1.77E+07	(170)	1.25E+06	(12)	15	89	50	197.7	112.4	389.6
122	2.12E+06	(19)	2.24E+06	(20)	14	158	70	13.6	6.9	26.9
123	3.36E+06	(43)	1.33E+06	(17)	20	94	45	36.0	20.2	67.6
124	2.43E+06	(14)	1.04E+06	(6)	9	74	58	32.9	12.1	105.5
125	2.57E+06	(41)	4.38E+05	(7)	25	31	23	82.0	37.2	218.5
126	2.74E+06	(21)	1.56E+06	(12)	12	111	63	24.9	11.8	55.8
127	2.02E+07	(116)	1.91E+06	(11)	9	135	80	147.7	81.0	304.5
128	4.16E+06	(149)	1.03E+06	(37)	56	73	24	57.4	39.9	84.8
129	5.48E+06	(42)	6.52E+05	(5)	12	46	39	116.2	47.6	379.3
130	5.74E+06	(66)	9.56E+05	(11)	18	68	40	84.5	45.0	178.5
131	5.61E+06	(43)	1.17E+06	(9)	12	83	54	67.3	32.9	158.1
132	1.56E+06	(16)	1.86E+06	(19)	16	131	60	12.1	5.8	24.8
133	7.43E+06	(76)	1.96E+06	(20)	16	138	61	54.0	32.9	93.7
134	3.03E+06	(31)	3.91E+05	(4)	16	28	26	106.6	39.2	420.0
135	1.49E+07	(152)	3.13E+06	(32)	16	221	78	67.6	46.1	102.5
136	4.53E+06	(81)	1.34E+06	(24)	28	95	38	48.0	30.3	79.5
137	3.39E+06	(117)	1.25E+06	(43)	54	88	27	38.8	27.2	56.6
138	6.94E+06	(71)	1.96E+06	(20)	16	138	61	50.5	30.6	87.8
139	1.61E+07	(216)	1.64E+06	(22)	21	116	49	138.5	90.0	225.8
140	7.69E+06	(118)	2.48E+06	(38)	24	175	57	44.3	30.6	65.8
141	1.18E+07	(113)	3.13E+06	(30)	15	221	80	53.6	35.8	83.3
142	1.16E+07	(223)	2.14E+06	(41)	30	151	47	77.4	55.5	110.9
143	8.22E+06	(84)	1.76E+06	(18)	16	125	58	66.2	39.8	117.5
144	3.23E+06	(33)	5.87E+05	(6)	16	42	33	76.8	32.6	226.6
145	1.56E+06	(16)	3.91E+05	(4)	16	28	26	55.5	18.5	231.9
146	2.93E+06	(30)	6.46E+06	(66)	16	457	113	6.5	4.1	10.2
147	1.56E+06	(25)	5.01E+05	(8)	25	35	24	44.1	19.6	114.1
148	2.00E+06	(23)	2.61E+05	(3)	18	18	20	104.4	33.2	548.7
149	3.91E+05	(4)	6.85E+05	(7)	16	48	35	8.3	1.8	32.2
150	7.82E+05	(8)	2.93E+05	(3)	16	21	22	37.0	9.2	220.3
151	1.25E+07	(128)	1.27E+06	(13)	16	90	49	138.3	79.2	267.2
152	2.24E+06	(30)	5.22E+05	(7)	21	37	27	60.2	26.4	163.9
153	3.62E+06	(37)	5.87E+05	(6)	16	42	33	86.0	36.9	251.7
154	1.00E+07	(77)	9.13E+05	(7)	12	65	47	152.8	72.6	393.7
155	2.93E+06	(30)	9.78E+04	(1)	16	7	11	367.1	71.2	8479.1
156	1.12E+06	(20)	6.15E+05	(11)	28	44	26	25.9	11.9	60.1
157	6.26E+05	(4)	1.41E+06	(9)	10	100	65	6.5	1.4	22.8
158	2.26E+06	(13)	1.56E+06	(9)	9	111	72	20.6	8.2	54.8

159	1.56E+06	(9)	2.09E+06	(12)	9	148	84	10.8	4.0	27.8
160	5.22E+05	(3)	1.56E+06	(9)	9	111	72	4.9	0.8	19.2
161	1.22E+06	(7)	8.69E+05	(5)	9	62	52	19.9	5.5	79.8
162	1.04E+06	(6)	1.39E+06	(8)	9	98	68	10.8	3.1	35.3
163	1.39E+06	(8)	1.74E+05	(1)	9	12	20	101.4	15.4	3755.4
164	7.82E+05	(8)	1.96E+06	(20)	16	138	61	5.8	2.2	13.6
165	6.26E+05	(4)	1.10E+06	(7)	10	78	57	8.3	1.8	32.2
166	4.35E+06	(25)	1.91E+06	(11)	9	135	80	32.3	15.5	73.1

0510-18 (Liukuei fm.)

2 mounts

EFFECTIVE TRACK DENSITY FOR FLUENCE MONITOR (tracks/cm^2): 2.12E+05
RELATIVE ERROR (%): 1.26
EFFECTIVE URANIUM CONTENT OF MONITOR (ppm):15.00
ZETA FACTOR AND STANDARD ERROR (yr cm^2): 135.42 15.20
SIZE OF COUNTER SQUARE (cm^2): 8.30E-07

Grain no.	ρ_s (tracks . cm^{-2}	Ns (tracks)	ρ_i (tracks . cm^{-2})	Ni (tracks)	Squares	Uranium (ppm) +/- 2 std. dev.		Age (Ma)	95% CI	
167	1.29E+07	(128)	3.31E+06	(33)	12	235	81	55.2	37.6	83.8
168	1.09E+07	(109)	2.01E+05	(2)	12	14	18	688.4	207.9	4515.0
169	4.74E+06	(59)	9.64E+05	(12)	15	68	39	69.4	37.4	142.7
170	8.43E+06	(126)	2.74E+06	(41)	18	194	61	43.8	30.7	64.1
171	1.00E+07	(75)	1.20E+06	(9)	9	85	55	116.6	59.4	266.2
172	7.11E+06	(118)	2.05E+06	(34)	20	145	50	49.4	33.6	74.9
173	6.91E+06	(86)	1.45E+06	(18)	15	102	48	67.7	40.7	120.1
174	5.22E+06	(52)	1.00E+06	(10)	12	71	44	73.2	37.4	162.7
175	9.09E+06	(181)	1.76E+06	(35)	24	124	42	73.5	51.2	109.0
176	5.49E+06	(41)	2.41E+06	(18)	9	171	79	32.4	18.3	60.2
177	6.27E+06	(78)	1.20E+06	(15)	15	85	43	73.5	42.4	138.2
178	1.14E+07	(114)	3.21E+06	(32)	12	227	80	50.7	34.2	77.8
179	5.12E+06	(68)	5.27E+05	(7)	16	37	27	135.1	63.8	350.2
180	6.75E+06	(112)	2.95E+06	(49)	20	209	60	32.7	23.2	46.7
181	7.03E+06	(70)	2.21E+06	(22)	12	156	66	45.3	27.9	77.0
182	5.42E+06	(54)	2.11E+06	(21)	12	149	64	36.6	21.9	64.0
183	6.02E+06	(60)	1.71E+06	(17)	12	121	58	50.1	29.1	92.0
184	6.61E+06	(351)	1.05E+06	(56)	64	75	20	89.1	67.2	120.5
185	1.08E+07	(359)	2.32E+06	(77)	40	164	38	66.4	51.9	86.3
186	6.43E+06	(48)	2.54E+06	(19)	9	180	82	36.0	20.9	65.0
187	8.84E+06	(88)	2.11E+06	(21)	12	149	64	59.5	36.9	101.2
188	4.90E+06	(61)	5.62E+05	(7)	15	40	29	121.4	56.9	316.3
189	5.54E+06	(115)	2.02E+06	(42)	25	143	44	39.1	27.3	57.2
190	5.90E+06	(98)	2.89E+06	(48)	20	205	59	29.2	20.5	42.2
191	6.33E+06	(63)	9.04E+05	(9)	12	64	42	98.1	49.5	225.8
192	1.59E+07	(119)	3.35E+06	(25)	9	237	94	67.6	43.9	108.9
193	7.71E+06	(96)	9.64E+05	(12)	15	68	39	112.4	62.4	226.0
194	5.62E+06	(42)	2.68E+06	(20)	9	190	84	29.9	17.3	54.0
195	7.50E+06	(56)	2.54E+06	(19)	9	180	82	41.9	24.7	75.0
196	1.10E+07	(91)	4.46E+06	(37)	10	316	103	35.1	23.8	53.0
197	8.03E+06	(60)	2.28E+06	(17)	9	161	77	50.1	29.1	92.0
198	6.10E+06	(76)	8.03E+05	(10)	15	57	35	106.6	55.9	232.4
199	8.43E+06	(210)	1.16E+06	(29)	30	82	30	102.6	69.8	157.2
200	1.07E+07	(160)	1.81E+06	(27)	18	128	49	84.0	56.0	131.8
201	5.42E+06	(126)	1.55E+06	(36)	28	110	36	49.9	34.3	74.5
202	1.02E+07	(153)	6.69E+05	(10)	18	47	29	212.7	115.1	451.1
203	2.61E+06	(65)	1.24E+06	(31)	30	88	31	29.9	19.3	47.6
204	1.22E+07	(244)	3.51E+06	(70)	24	249	60	49.7	38.0	66.0
205	4.28E+06	(32)	1.34E+06	(10)	9	95	59	45.2	22.0	103.9

206	6.27E+06	(130)	1.83E+06	(38)	25	130	42	48.8	33.8	72.1
207	1.67E+07	(332)	1.61E+06	(32)	24	114	40	146.5	102.5	217.7
208	1.82E+07	(136)	4.95E+06	(37)	9	351	115	52.4	36.3	77.7
209	1.50E+07	(435)	3.06E+06	(89)	35	217	46	69.7	55.4	88.6
210	1.37E+07	(102)	3.35E+06	(25)	9	237	94	58.0	37.4	94.0
211	1.05E+07	(139)	2.64E+06	(35)	16	187	63	56.5	38.9	84.6
212	1.00E+07	(75)	3.48E+06	(26)	9	246	96	41.1	26.1	67.1
213	1.34E+07	(100)	3.08E+06	(23)	9	218	90	61.7	39.2	102.1
214	1.55E+07	(129)	3.86E+06	(32)	10	273	96	57.4	38.9	87.5
215	1.60E+07	(199)	4.98E+06	(62)	15	353	90	45.8	34.3	62.1
216	5.29E+06	(79)	1.47E+06	(22)	18	104	44	51.0	31.7	86.3

EFFECTIVE TRACK DENSITY FOR FLUENCE MONITOR (tracks/cm^2): 2.12E+05
RELATIVE ERROR (%): 1.28
EFFECTIVE URANIUM CONTENT OF MONITOR (ppm):15.00
ZETA FACTOR AND STANDARD ERROR (yr cm^2): 135.42 15.20
SIZE OF COUNTER SQUARE (cm^2): 6.39E-07

Grain no.	ρ_s (tracks . cm^{-2}	Ns (tracks)	ρ_i (tracks . cm^{-2})	Ni (tracks)	Squares	Uranium (ppm) +/- 2 std. dev.		Age (Ma)	95% CI	
217	5.04E+06	(29)	5.22E+05	(3)	9	37	40	131.1	42.8	674.8
218	2.43E+06	(14)	6.96E+05	(4)	9	49	46	48.6	15.7	206.2
219	6.26E+06	(36)	1.39E+06	(8)	9	99	68	63.2	29.4	158.8
220	1.24E+07	(127)	2.35E+06	(24)	16	166	67	75.0	48.6	121.7
221	5.38E+06	(55)	6.85E+05	(7)	16	48	35	109.5	51.0	287.0
222	1.50E+07	(86)	1.39E+06	(8)	9	99	68	149.6	74.4	358.5
223	7.30E+06	(42)	3.48E+05	(2)	9	25	31	274.6	77.8	2162.2
224	1.05E+07	(167)	1.31E+06	(21)	25	93	40	112.3	71.8	186.5
225	5.56E+06	(32)	2.26E+06	(13)	9	160	87	34.9	18.0	72.9
226	1.67E+06	(16)	2.09E+06	(20)	15	148	65	11.5	5.6	23.3
227	4.87E+06	(28)	2.26E+06	(13)	9	160	87	30.6	15.5	64.7
228	1.45E+07	(148)	2.64E+06	(27)	16	187	71	77.8	51.7	122.2
229	1.03E+07	(59)	1.56E+06	(9)	9	111	72	91.9	46.1	212.3
230	1.10E+06	(7)	1.10E+06	(7)	10	78	57	14.3	4.3	47.8
231	6.52E+06	(125)	8.35E+05	(16)	30	59	29	110.1	66.0	199.1
232	1.15E+07	(66)	1.56E+06	(9)	9	111	72	102.7	51.9	235.8
233	4.87E+06	(28)	2.09E+06	(12)	9	148	84	33.1	16.5	71.9
234	2.61E+06	(15)	1.22E+06	(7)	9	86	63	30.3	11.8	88.5
235	9.91E+06	(57)	2.09E+06	(12)	9	148	84	67.1	36.0	138.1
236	5.09E+06	(52)	5.87E+05	(6)	16	42	33	120.3	53.2	344.9
237	1.69E+06	(27)	4.38E+05	(7)	25	31	23	54.2	23.4	148.8
238	3.33E+06	(34)	2.93E+05	(3)	16	21	22	153.3	50.9	778.4
239	2.78E+06	(16)	6.96E+05	(4)	9	49	46	55.5	18.5	231.7
240	4.40E+06	(45)	9.78E+05	(10)	16	69	43	63.4	32.0	142.1
241	6.94E+06	(71)	1.08E+06	(11)	16	76	45	90.8	48.5	191.0
242	5.74E+06	(33)	2.26E+06	(13)	9	160	87	36.0	18.6	75.0
243	6.96E+06	(40)	6.96E+05	(4)	9	49	46	137.0	51.6	529.7
244	1.29E+07	(74)	3.13E+06	(18)	9	222	103	58.3	34.7	104.1
245	4.69E+06	(27)	5.22E+05	(3)	9	37	40	122.1	39.6	632.9
246	4.28E+06	(41)	5.22E+05	(5)	15	37	32	113.4	46.3	370.6
247	8.69E+06	(50)	1.39E+06	(8)	9	99	68	87.5	42.0	215.4
248	2.15E+06	(22)	2.93E+05	(3)	16	21	22	99.8	31.5	526.9

0510-20 (Liukuei fm.)

EFFECTIVE TRACK DENSITY FOR FLUENCE MONITOR (tracks/cm^2): 2.12E+05
RELATIVE ERROR (%): 1.30
EFFECTIVE URANIUM CONTENT OF MONITOR (ppm):15.00
ZETA FACTOR AND STANDARD ERROR (yr cm^2): 135.42 15.20
SIZE OF COUNTER SQUARE (cm^2): 6.39E-07

Grain no.	ρ_s (tracks . cm^{-2}	Ns (tracks)	ρ_i (tracks . cm^{-2})	Ni (tracks)	Squares	Uranium (ppm) +/- 2 std. dev.		Age (Ma)	95% CI	
249	9.22E+06	(53)	1.74E+06	(10)	9	123	76	74.6	38.1	165.5
250	8.20E+06	(110)	1.04E+06	(14)	21	74	39	110.6	64.0	209.5
251	4.96E+06	(38)	2.87E+06	(22)	12	203	86	24.6	14.3	43.9
252	1.22E+06	(7)	1.74E+05	(1)	9	12	20	89.0	12.9	3428.0
253	1.22E+07	(70)	5.22E+05	(3)	9	37	40	310.9	108.9	1478.8
254	3.65E+06	(28)	1.43E+06	(11)	12	102	60	36.1	17.6	80.8
255	1.15E+07	(147)	3.21E+06	(41)	20	227	71	51.1	36.0	74.2
256	1.17E+07	(67)	1.91E+06	(11)	9	135	80	85.7	45.6	180.8
257	7.82E+05	(6)	2.09E+06	(16)	12	148	73	5.5	1.7	14.5
258	5.22E+05	(4)	1.04E+06	(8)	12	74	51	7.3	1.6	26.7
259	9.56E+06	(110)	1.56E+06	(18)	18	111	52	86.4	52.7	151.6
260	1.30E+06	(30)	2.43E+06	(56)	36	172	46	7.7	4.8	12.2
261	5.22E+05	(5)	1.98E+06	(19)	15	140	64	3.9	1.1	10.4
262	4.30E+06	(33)	3.91E+05	(3)	12	28	30	148.8	49.3	757.8
263	2.26E+06	(13)	1.22E+06	(7)	9	86	63	26.3	9.9	78.4
264	9.74E+06	(56)	6.96E+05	(4)	9	49	46	190.7	73.7	720.8
265	8.69E+05	(5)	4.52E+06	(26)	9	320	125	2.8	0.8	7.3
266	7.65E+06	(44)	2.61E+06	(15)	9	185	94	41.6	22.9	80.9
267	1.06E+06	(17)	3.69E+06	(59)	25	262	68	4.2	2.3	7.2
268	1.08E+07	(62)	3.13E+06	(18)	9	222	103	48.9	28.8	88.2
269	1.04E+06	(6)	2.96E+06	(17)	9	209	100	5.1	1.6	13.4
270	7.13E+06	(41)	6.96E+05	(4)	9	49	46	140.3	53.0	541.8
271	8.56E+06	(82)	1.88E+06	(18)	15	133	62	64.5	38.7	114.7
272	6.52E+06	(50)	7.82E+05	(6)	12	55	43	115.7	51.0	332.5
273	9.78E+05	(15)	9.13E+05	(14)	24	65	34	15.3	6.9	34.3
274	5.22E+05	(5)	8.35E+05	(8)	15	59	41	9.1	2.3	31.0
275	1.10E+06	(14)	1.17E+06	(15)	20	83	42	13.4	6.0	29.7
276	5.91E+06	(34)	1.91E+06	(11)	9	135	80	43.7	21.9	96.3
277	4.69E+06	(27)	2.43E+06	(14)	9	172	91	27.4	14.0	56.8
278	5.04E+06	(29)	1.74E+06	(10)	9	123	76	41.0	19.7	95.0
279	6.91E+06	(53)	1.04E+06	(8)	12	74	51	92.7	44.7	227.4
280	5.61E+06	(43)	1.17E+06	(9)	12	83	54	67.2	32.8	158.0
281	2.61E+06	(20)	1.83E+06	(14)	12	129	68	20.4	9.8	43.7
282	6.89E+05	(11)	3.38E+06	(54)	25	239	65	3.0	1.4	5.7
283	8.14E+06	(78)	6.26E+05	(6)	15	44	35	179.4	81.3	503.5
284	4.80E+06	(46)	2.50E+06	(24)	15	177	72	27.3	16.4	46.9
285	5.55E+06	(149)	1.49E+06	(40)	42	106	33	53.0	37.3	77.4
286	7.65E+06	(44)	1.04E+06	(6)	9	74	58	102.0	44.5	295.2
287	8.69E+05	(5)	3.48E+06	(20)	9	246	109	3.7	1.1	9.8
288	6.96E+05	(4)	2.96E+06	(17)	9	209	100	3.5	0.8	10.3
289	3.26E+06	(25)	1.17E+06	(9)	12	83	54	39.3	18.0	96.3
290	2.43E+06	(14)	2.43E+06	(14)	9	172	91	14.3	6.3	32.4
291	7.34E+06	(75)	1.27E+06	(13)	16	90	49	81.4	45.4	160.6
292	9.56E+06	(55)	1.22E+06	(7)	9	86	63	109.5	50.9	286.9
293	1.12E+07	(86)	2.87E+06	(22)	12	203	86	55.5	34.6	93.5
294	7.82E+06	(45)	3.48E+05	(2)	9	25	31	293.6	83.7	2287.9
295	3.48E+05	(2)	1.91E+06	(11)	9	135	80	2.8	0.3	11.9
296	5.04E+06	(29)	8.69E+05	(5)	9	62	53	80.5	31.7	269.6
297	8.69E+05	(5)	2.43E+06	(14)	9	172	91	5.2	1.4	15.0
298	5.22E+06	(30)	1.22E+06	(7)	9	86	63	60.1	26.4	163.7
299	9.91E+06	(57)	6.96E+06	(40)	9	493	155	20.4	13.4	31.4
300	1.98E+07	(114)	3.30E+06	(19)	9	234	106	84.9	52.4	146.6
301	4.89E+05	(5)	2.35E+06	(24)	16	166	67	3.1	0.9	8.0
302	6.65E+06	(68)	1.17E+06	(12)	16	83	47	79.9	43.5	163.0
303	3.91E+05	(5)	1.02E+06	(13)	20	72	39	5.6	1.5	16.5
304	1.23E+07	(94)	3.91E+06	(30)	12	277	101	44.6	29.4	69.9
305	6.18E+06	(79)	5.48E+05	(7)	20	39	28	156.6	74.5	403.0
306	2.64E+06	(27)	2.93E+06	(30)	16	208	75	12.9	7.4	22.4
307	6.36E+06	(65)	1.37E+06	(14)	16	97	51	65.6	36.9	127.3
308	1.46E+07	(84)	1.39E+06	(8)	9	99	68	146.2	72.6	350.6
309	3.72E+06	(38)	5.87E+05	(6)	16	42	33	88.2	38.0	257.8

310	6.85E+05	(7)	1.47E+06	(15)	16	104	53	6.8	2.3	17.4
311	9.29E+06	(95)	4.89E+05	(5)	16	35	30	259.1	111.7	806.1
312	1.06E+07	(61)	2.26E+06	(13)	9	160	87	66.3	36.4	132.2
313	6.96E+06	(40)	1.91E+06	(11)	9	135	80	51.4	26.2	111.8
314	6.26E+05	(8)	2.50E+06	(32)	20	177	62	3.6	1.4	7.9
315	1.43E+06	(11)	4.69E+06	(36)	12	332	110	4.4	2.0	8.8
316	5.35E+06	(41)	7.82E+05	(6)	12	55	43	95.1	41.2	276.5
317	8.87E+06	(51)	1.56E+06	(9)	9	111	72	79.6	39.5	185.2
318	7.48E+06	(43)	1.74E+06	(10)	9	123	76	60.6	30.4	136.2
319	4.69E+05	(9)	3.08E+06	(59)	30	218	57	2.2	1.0	4.4
320	6.43E+06	(37)	1.91E+06	(11)	9	135	80	47.6	24.0	104.0
321	6.43E+06	(37)	3.48E+05	(2)	9	25	31	242.6	68.0	1946.7
322	1.27E+07	(73)	3.83E+06	(22)	9	271	114	47.2	29.1	80.1
323	9.91E+06	(57)	4.52E+06	(26)	9	320	125	31.3	19.4	51.9
324	2.03E+07	(117)	1.74E+06	(10)	9	123	76	163.2	87.4	349.6
325	5.09E+06	(52)	7.82E+05	(8)	16	55	38	91.0	43.8	223.4
326	7.65E+06	(44)	1.74E+06	(10)	9	123	76	62.0	31.2	139.2
327	1.10E+07	(63)	2.26E+06	(13)	9	160	87	68.4	37.7	136.3
328	3.48E+06	(20)	1.04E+06	(6)	9	74	58	46.8	18.5	143.9
329	7.82E+05	(6)	1.43E+06	(11)	12	102	60	7.9	2.4	23.0
330	1.18E+07	(68)	1.22E+06	(7)	9	86	63	135.0	63.7	350.0
331	5.48E+06	(84)	5.22E+05	(8)	24	37	25	146.2	72.6	350.6
332	1.39E+06 (	8)	3.65E+06 (21)		9	259	112	5.5	2.1	12.8

NA02 (Nanshilun fm.)

2mounts

EFFECTIVE TRACK DENSITY FOR FLUENCE MONITOR (tracks/cm^2): 2.77E+05
RELATIVE ERROR (%): 1.20
EFFECTIVE URANIUM CONTENT OF MONITOR (ppm):15.00
ZETA FACTOR AND STANDARD ERROR (yr cm^2): 135.42 15.20
SIZE OF COUNTER SQUARE (cm^2): 6.39E-07

Grain no.	ρ_s (tracks . cm^{-2}	Ns (tracks)	ρ_i (tracks . cm^{-2})	Ni (tracks)	Squares	Uranium (ppm) +/- 2 std. dev.		Age (Ma)	95% CI	
1	1.63E+07	(94)	1.39E+06	(8)	9	75	52	212.6	106.3	504.7
2	2.35E+06	(18)	1.17E+06	(9)	12	64	41	37.0	16.0	94.0
3	1.03E+07	(59)	3.48E+05	(2)	9	19	24	494.6	144.7	3513.2
4	3.83E+06	(22)	6.96E+05	(4)	9	38	36	99.0	34.9	398.8
5	1.39E+06	(8)	1.74E+05	(1)	9	9	15	132.0	20.1	4569.9
6	1.70E+07	(98)	2.26E+06	(13)	9	123	67	138.2	78.3	269.1
7	1.46E+07	(84)	1.56E+06	(9)	9	85	55	169.8	87.2	384.1
8	4.50E+06	(23)	1.17E+06	(6)	8	64	50	70.0	28.4	212.2
9	1.22E+06	(7)	1.74E+05	(1)	9	9	15	116.0	16.8	4195.0
10	1.37E+06	(7)	9.78E+05	(5)	8	53	45	25.9	7.2	104.0
11	2.36E+07	(136)	1.56E+06	(9)	9	85	55	272.5	143.1	603.5
12	1.03E+07	(59)	1.91E+06	(11)	9	104	61	98.5	52.0	208.8
13	1.72E+07	(99)	1.91E+06	(11)	9	104	61	164.3	89.6	339.8
14	7.39E+06	(118)	8.76E+05	(14)	25	48	25	154.4	89.8	291.1
15	1.15E+07	(66)	1.74E+05	(1)	9	9	15	999.7	210.8	13938.4
16	1.98E+06	(19)	1.15E+06	(11)	15	62	37	32.1	14.6	74.9
17	6.43E+06	(37)	8.69E+05	(5)	9	47	40	133.5	54.1	436.9
18	1.70E+07	(98)	2.43E+06	(14)	9	132	69	128.5	74.1	244.1
19	5.22E+06	(30)	3.48E+05	(2)	9	19	24	256.9	70.9	2060.0
20	9.22E+06	(53)	3.83E+06	(22)	9	207	88	44.8	26.9	77.5
21	9.04E+06	(52)	3.48E+06	(20)	9	189	83	48.3	28.5	85.6
22	1.29E+07	(74)	2.61E+06	(15)	9	141	72	91.0	52.3	171.2
23	1.63E+07	(94)	8.69E+05	(5)	9	47	40	333.0	144.0	1024.3
24	1.18E+07	(68)	1.22E+06	(7)	9	66	48	175.9	83.1	453.6
25	1.04E+07	(80)	2.35E+06	(18)	12	127	59	82.2	49.3	146.0
26	4.35E+06	(25)	1.39E+06	(8)	9	75	52	57.5	25.5	148.5
27	1.30E+07	(75)	1.91E+06	(11)	9	104	61	124.9	67.1	261.5
28	5.39E+06	(31)	1.22E+06	(7)	9	66	48	81.0	35.7	219.5
29	6.78E+06	(39)	1.04E+06	(6)	9	57	44	118.0	51.0	342.8
30	1.18E+07	(68)	2.26E+06	(13)	9	123	67	96.3	53.4	190.6
31	1.04E+06	(6)	5.22E+05	(3)	9	28	30	36.4	8.0	227.5

32	6.26E+06	(36)	1.56E+06	(9)	9	85	55	73.5	35.3	174.6
33	2.33E+07	(134)	2.78E+06	(16)	9	151	74	153.6	92.4	276.5
34	1.22E+06	(7)	6.96E+05	(4)	9	38	36	32.2	8.3	151.0
35	1.22E+06	(7)	5.22E+05	(3)	9	28	30	42.3	10.0	256.9
36	6.78E+06	(52)	1.04E+06	(8)	12	57	39	118.6	57.2	290.3
37	8.45E+06	(135)	8.14E+05	(13)	25	44	24	189.5	109.0	364.5
38	7.43E+06	(38)	2.93E+06	(15)	8	159	81	47.0	25.4	92.3
39	8.52E+06	(49)	2.78E+06	(16)	9	151	74	56.7	32.0	107.2
40	6.43E+06	(37)	3.48E+05	(2)	9	19	24	315.1	88.8	2441.9
41	1.11E+07	(64)	4.87E+06	(28)	9	264	99	42.5	27.0	69.0
42	1.03E+07	(59)	1.22E+06	(7)	9	66	48	152.9	71.6	397.4
43	1.05E+07	(202)	3.18E+06	(61)	30	173	44	61.6	46.2	83.6
44	6.61E+06	(38)	2.43E+06	(14)	9	132	69	50.3	26.9	100.9
45	4.52E+06	(26)	4.00E+06	(23)	9	217	90	21.1	11.6	38.8
46	1.39E+06	(8)	8.69E+05	(5)	9	47	40	29.6	8.6	115.4
47	9.65E+06	(74)	4.04E+06	(31)	12	219	78	44.4	28.9	70.1
48	4.35E+06	(25)	3.65E+06	(21)	9	198	86	22.2	12.0	41.8
49	1.46E+07	(112)	4.56E+06	(35)	12	247	83	59.5	40.5	89.8
50	6.94E+06	(71)	7.82E+05	(8)	16	42	29	161.3	79.4	388.2
51	1.13E+07	(116)	4.40E+06	(45)	16	239	71	48.0	33.8	69.4
52	6.78E+06	(39)	8.69E+05	(5)	9	47	40	140.6	57.3	458.5
53	9.91E+06	(57)	3.30E+06	(19)	9	179	81	55.6	32.8	99.3
54	1.13E+07	(65)	3.13E+06	(18)	9	170	79	66.9	39.5	120.1
55	1.22E+07	(70)	3.13E+06	(18)	9	170	79	72.0	42.8	128.8
56	5.91E+06	(34)	2.26E+06	(13)	9	123	67	48.4	25.1	100.4
57	9.26E+06	(71)	2.61E+06	(20)	12	141	63	65.8	39.9	114.4
58	1.06E+07	(61)	1.39E+06	(8)	9	75	52	138.9	67.7	336.9
59	5.56E+06	(32)	1.22E+06	(7)	9	66	48	83.6	37.0	226.0
60	8.52E+06	(49)	1.56E+06	(9)	9	85	55	99.7	49.4	232.0
61	1.70E+07	(98)	2.96E+06	(17)	9	160	77	106.3	63.8	190.1
62	1.22E+07	(70)	1.39E+06	(8)	9	75	52	159.0	78.3	383.1
63	8.87E+06	(68)	1.17E+06	(9)	12	64	41	137.9	69.9	315.1
64	1.06E+07	(61)	2.78E+06	(16)	9	151	74	70.5	40.5	131.4

EFFECTIVE TRACK DENSITY FOR FLUENCE MONITOR (tracks/cm^2): 2.77E+05
RELATIVE ERROR (%): 1.22
EFFECTIVE URANIUM CONTENT OF MONITOR (ppm):15.00
ZETA FACTOR AND STANDARD ERROR (yr cm^2): 135.42 15.20
SIZE OF COUNTER SQUARE (cm^2): 6.39E-07

Grain no.	ρ_s (tracks . cm^{-2}	Ns (tracks)	ρ_i (tracks . cm^{-2})	Ni (tracks)	Squares	Uranium (ppm) +/- 2 std. dev.	Age (Ma)	95% CI
65	1.46E+07	(234)	1.94E+06	(31)	25	105 38	139.3	96.2 209.6
66	1.69E+07	(97)	1.74E+06	(10)	9	94 58	176.7	94.0 379.7
67	1.20E+07	(115)	2.19E+06	(21)	15	119 51	101.2	63.7 169.9
68	9.52E+06	(73)	7.82E+05	(6)	12	42 33	218.7	99.0 611.7
69	7.17E+06	(55)	1.56E+06	(12)	12	85 48	84.4	45.3 173.9
70	2.61E+05	(2)	1.30E+05	(1)	12	7 12	35.1	2.0 1901.1
71	1.06E+07	(61)	1.74E+05	(1)	9	9 15	929.4	194.5 13498.8
72	1.20E+07	(69)	3.48E+05	(2)	9	19 24	574.7	170.0 3947.2
73	3.76E+06	(60)	9.39E+05	(15)	25	51 26	73.9	41.9 140.6
74	5.91E+06	(34)	1.39E+06	(8)	9	75 52	77.9	36.1 196.2
75	6.26E+06	(36)	1.74E+06	(10)	9	94 58	66.3	32.7 150.7
76	1.23E+07	(71)	2.61E+06	(15)	9	141 72	87.3	50.1 164.7
77	7.82E+06	(45)	3.48E+05	(2)	9	19 24	381.0	109.2 2852.7
78	3.65E+06	(21)	1.04E+06	(6)	9	57 44	64.0	25.5 195.7
79	4.96E+06	(38)	3.91E+05	(3)	12	21 23	222.4	74.8 1102.2
80	4.17E+06	(24)	3.48E+05	(2)	9	19 24	206.6	55.6 1713.8
81	7.65E+06	(44)	1.39E+06	(8)	9	75 52	100.6	47.8 248.7
82	7.65E+06	(44)	3.13E+06	(18)	9	170 79	45.4	25.9 83.7
83	1.74E+06	(10)	3.48E+05	(2)	9	19 24	87.7	19.9 824.5
84	8.48E+06	(65)	1.70E+06	(13)	12	92 50	92.1	50.9 182.8

Apatite fission track

LK 02 (Nanshilun fm.)

EFFECTIVE TRACK DENSITY FOR FLUENCE MONITOR (tracks/cm^2): 6.99E+05
RELATIVE ERROR (%): 1.06
EFFECTIVE URANIUM CONTENT OF MONITOR (ppm):15.00
ZETA FACTOR AND STANDARD ERROR (yr cm^2): 268.37 7.61
SIZE OF COUNTER SQUARE (cm^2): 8.30E-07

Grain no.	ρ_s (tracks . cm^{-2}	Ns (tracks)	ρ_i (tracks . cm^{-2})	Ni (tracks)	Squares	Uranium (ppm) +/- 2 std. dev.		Age (Ma)	95% CI	
1	3.01E+05 (	3)	1.00E+05 (	1)	12	2	4	253.2	22.5 7	679.8
2	8.61E+04 (	2)	3.87E+05 (	9)	28	8	5	22.0	2.2	99.9
3	2.87E+05 (	5)	1.61E+06 (	28)	21	34	13	17.2	5.0	43.8
4	1.00E+05 (	1)	6.02E+05 (	6)	12	13	10	17.4	0.3	127.6
5	1.26E+05 (	5)	8.79E+05 (	35)	48	19	6	13.8	4.1	34.3
6	2.41E+05 (	2)	5.54E+06 (	46)	10	119	35	4.4	0.5	15.6
7	6.02E+04 (	1)	1.69E+06 (	28)	20	36	14	3.8	0.1	20.2
8	4.02E+05 (	5)	8.03E+04 (	1)	15	2	3	408.8	52.3	
9610.5										

LK03 (Linkou fm)

EFFECTIVE TRACK DENSITY FOR FLUENCE MONITOR (tracks/cm^2): 7.06E+05
RELATIVE ERROR (%): 1.17
EFFECTIVE URANIUM CONTENT OF MONITOR (ppm):15.00
ZETA FACTOR AND STANDARD ERROR (yr cm^2): 268.37 7.61
SIZE OF COUNTER SQUARE (cm^2): 8.30E-07

Grain no.	ρ_s (tracks . cm^{-2}	Ns (tracks)	ρ_i (tracks . cm^{-2})	Ni (tracks)	Squares	Uranium (ppm) +/- 2 std. dev.		Age (Ma)	95% CI	
1	3.77E+04 (	1)	1.47E+06 (	39)	32	31	10	2.8	0.1	14.3
2	4.30E+04 (	1)	9.47E+05 (	22)	28	20	8	4.9	0.1	26.6
3	1.34E+05 (	2)	2.41E+06 (	36)	18	51	17	5.6	0.6	20.4
4	6.02E+04 (	1)	1.81E+05 (	3)	20	4	4	34.3	0.6	381.7
5	4.82E+04 (	1)	9.64E+05 (	20)	25	20	9	5.4	0.1	29.6
6	3.44E+04 (	1)	6.88E+04 (	2)	35	1	2	50.2	0.8	851.0
7	6.02E+04 (	1)	2.05E+06 (	34)	20	44	15	3.2	0.1	16.6
8	9.64E+04 (	2)	3.76E+06 (	78)	25	80	18	2.6	0.3	9.1
9	1.51E+05 (	2)	3.92E+06 (	52)	16	83	23	3.9	0.4	13.8
10	1.00E+05 (	2)	6.02E+05 (	12)	24	13	7	16.8	1.7	70.5
11	1.20E+05 (	2)	5.42E+05 (	9)	20	12	7	22.2	2.2	100.9
12	7.53E+04 (	1)	2.26E+05 (	3)	16	5	5	34.3	0.6	381.7
13	8.92E+04 (	2)	6.69E+05 (	15)	27	14	7	13.5	1.4	54.1
14	7.53E+04 (	1)	1.51E+06 (	20)	16	32	14	5.4	0.1	29.6
15	4.02E+04 (	1)	1.24E+06 (	31)	30	26	9	3.5	0.1	18.3
16	6.02E+04 (	1)	8.43E+05 (	14)	20	18	9	7.7	0.2	44.3
17	0.00E+00 (	0)	1.08E+06 (	25)	28	23	9	2.7	0.1	15.0

Lk 04 (Linkou fm.)

EFFECTIVE TRACK DENSITY FOR FLUENCE MONITOR (tracks/cm^2): 7.08E+05
RELATIVE ERROR (%): 1.23
EFFECTIVE URANIUM CONTENT OF MONITOR (ppm):15.00
ZETA FACTOR AND STANDARD ERROR (yr cm^2): 268.37 7.61
SIZE OF COUNTER SQUARE (cm^2): 8.30E-07

Grain no.	ρ_s (tracks . cm^{-2}	Ns (tracks)	ρ_i (tracks . cm^{-2})	Ni (tracks)	Squares	Uranium (ppm) +/- 2 std. dev.		Age (Ma)	95% CI	
1	9.64E+04 (	2)	5.30E+05 (	11)	25	11	7	18.3	1.9	78.7
2	4.82E+04 (	1)	9.64E+04 (	2)	25	2	3	50.4	0.8	853.7

0510-15 (Liukuei fm.)

EFFECTIVE TRACK DENSITY FOR FLUENCE MONITOR (tracks/cm^2): 6.85E+05
RELATIVE ERROR (%): 1.18
EFFECTIVE URANIUM CONTENT OF MONITOR (ppm):15.00
ZETA FACTOR AND STANDARD ERROR (yr cm^2): 268.37 7.61
SIZE OF COUNTER SQUARE (cm^2): 8.30E-07

Grain no.	ρ_s (tracks . cm^{-2}	Ns (tracks)	ρ_i (tracks . cm^{-2})	Ni (tracks)	Squares	Uranium (ppm) +/- 2 std. dev.		Age (Ma)	95% CI	
1	1.20E+05 (	4)	2.74E+06 (	91)	40	60	13	4.2	1.1	10.7
2	9.64E+04 (	2)	5.30E+05 (	11)	25	12	7	17.7	1.8	76.2
3	4.92E+04 (	2)	6.88E+05 (	28)	49	15	6	7.0	0.8	26.0
4	8.03E+04 (	2)	4.82E+05 (	12)	30	11	6	16.3	1.7	68.5
5	4.52E+04 (	3)	9.64E+05 (	64)	80	21	5	4.5	0.9	13.2
6	6.88E+04 (	2)	5.51E+05 (	16)	35	12	6	12.3	1.3	48.7
7	6.02E+04 (	2)	1.63E+06 (	54)	40	36	10	3.7	0.4	12.9
8	4.02E+04 (	1)	3.21E+05 (	8)	30	7	5	12.9	0.3	85.2
9	1.03E+05 (	3)	2.31E+06 (	67)	35	50	12	4.3	0.8	12.6
10	9.04E+04 (	3)	1.02E+06 (	34)	40	22	8	8.5	1.6	25.8
11	2.51E+04 (	1)	2.26E+05 (	9)	48	5	3	11.5	0.2	73.3
12	1.45E+05 (	3)	8.67E+05 (	18)	25	19	9	16.0	2.9	52.3
13	1.45E+05 (	3)	2.41E+06 (	50)	25	53	15	5.8	1.1	17.1
14	4.82E+04 (	1)	1.93E+05 (	4)	25	4	4	25.3	0.5	228.3
15	0.00E+00 (	0)	8.19E+05 (	17)	25	18	9	3.8	0.1	22.3
16	0.00E+00 (	0)	3.44E+05 (	10)	35	8	5	6.6	0.2	40.9
17	0.00E+00 (	0)	1.39E+06 (	81)	70	31	7	0.8	0.0	4.3
18	0.00E+00 (	0)	1.69E+06 (	42)	30	37	11	1.5	0.1	8.4

0510-20 (Liukuei fm.)

2mounts

EFFECTIVE TRACK DENSITY FOR FLUENCE MONITOR (tracks/cm^2): 6.90E+05
RELATIVE ERROR (%): 1.09
EFFECTIVE URANIUM CONTENT OF MONITOR (ppm):15.00
ZETA FACTOR AND STANDARD ERROR (yr cm^2): 268.37 7.61
SIZE OF COUNTER SQUARE (cm^2): 8.30E-07

Grain no.	ρ_s (tracks . cm^{-2}	Ns (tracks)	ρ_i (tracks . cm^{-2})	Ni (tracks)	Squares	Uranium (ppm) +/- 2 std. dev.		Age (Ma)	95% CI	
1	7.23E+04 (	3)	9.64E+05 (	40)	50	21	7	7.3	1.4	21.8
2	1.67E+05 (	5)	1.81E+06 (	54)	36	39	11	8.8	2.7	21.2
3	1.20E+05 (	3)	2.09E+06 (	52)	30	45	13	5.6	1.1	16.5
4	6.88E+04 (	4)	5.16E+05 (	30)	70	11	4	12.8	3.2	34.9
5	2.01E+04 (	1)	1.69E+06 (	84)	60	37	8	1.3	0.0	6.3
6	2.41E+04 (	1)	8.19E+05 (	34)	50	18	6	3.1	0.1	16.2

7	1.76E+05 (	7)	3.41E+06 (	136)	48	74	13	4.9	1.9	10.1
8	2.41E+04 (	1)	2.41E+05 (	10)	50	5	3	10.4	0.2	64.8
9	9.04E+04 (	3)	3.64E+06 (	121)	40	79	14	2.4	0.5	6.9
10	2.01E+04 (	1)	1.08E+06 (	54)	60	24	6	2.0	0.0	10.0
11	4.02E+04 (	1)	4.02E+05 (	10)	30	9	5	10.4	0.2	64.8
12	5.74E+04 (	3)	1.72E+05 (	9)	63	4	2	31.8	5.4	122.5
13	3.44E+04 (	1)	9.64E+05 (	28)	35	21	8	3.8	0.1	20.0
14	6.02E+04 (	2)	1.99E+06 (	66)	40	43	11	3.0	0.3	10.5

EFFECTIVE TRACK DENSITY FOR FLUENCE MONITOR (tracks/cm^2): 6.92E+05
RELATIVE ERROR (%): 1.06
EFFECTIVE URANIUM CONTENT OF MONITOR (ppm):15.00
ZETA FACTOR AND STANDARD ERROR (yr cm^2): 268.37 7.61
SIZE OF COUNTER SQUARE (cm^2): 8.30E-07

Grain no.	ρ_s (tracks . cm^{-2}	Ns (tracks)	ρ_i (tracks . cm^{-2})	Ni (tracks)	Squares	Uranium (ppm) +/- 2 std. dev.		Age (Ma)	95% CI	
15	1.20E+05 (	2)	1.02E+06 (	17)	20	22	11	11.7	1.2	45.9
16	1.00E+05 (	3)	2.11E+06 (	63)	36	46	12	4.6	0.9	13.5
17	6.69E+04 (	1)	2.14E+06 (	32)	18	46	16	3.3	0.1	17.4
18	8.03E+04 (	1)	2.41E+05 (	3)	15	5	6	33.6	0.6	374.5
19	4.02E+04 (	1)	6.83E+05 (	17)	30	15	7	6.2	0.1	34.8
20	2.87E+04 (	1)	5.74E+04 (	2)	42	1	2	49.2	0.8	835.5
21	6.02E+04 (	2)	7.53E+05 (	25)	40	16	6	8.0	0.9	29.7
22	2.41E+04 (	1)	2.17E+05 (	9)	50	5	3	11.6	0.2	74.1
23	4.02E+04 (	2)	1.16E+06 (	58)	60	25	7	3.4	0.4	12.1
24	2.41E+04 (	1)	1.40E+06 (	58)	50	30	8	1.8	0.0	9.3
25	2.41E+04 (	1)	1.95E+06 (	81)	50	42	9	1.3	0.0	6.6
26	4.02E+04 (	1)	2.65E+06 (	66)	30	57	14	1.6	0.0	8.1
27	1.00E+05 (	5)	1.35E+06 (	67)	60	29	7	7.1	2.2	17.0
28	1.43E+05 (	5)	8.61E+04 (	3)	42	2	2	150.0	30.0	927.0
29	8.61E+04 (	3)	2.29E+06 (	80)	42	50	11	3.7	0.7	10.5
30	0.00E+00 (	0)	2.68E+05 (	10)	45	6	4	6.7	0.2	41.3
31	0.00E+00 (	0)	2.01E+04 (	1)	60	0	1	92.2	2.4	2874.5
32	0.00E+00 (	0)	1.72E+05 (	5)	35	4	3	13.8	0.5	100.6

0210-01 (Laonung)

EFFECTIVE TRACK DENSITY FOR FLUENCE MONITOR (tracks/cm^2): 6.81E+05
RELATIVE ERROR (%): 1.32
EFFECTIVE URANIUM CONTENT OF MONITOR (ppm):15.00
ZETA FACTOR AND STANDARD ERROR (yr cm^2): 268.37 7.61
SIZE OF COUNTER SQUARE (cm^2): 8.30E-07

Grain no.	ρ_s (tracks . cm^{-2}	Ns (tracks)	ρ_i (tracks . cm^{-2})	Ni (tracks)	Squares	Uranium (ppm) +/- 2 std. dev.		Age (Ma)	95% CI	
1	2.01E+05 (	6)	2.41E+06 (	72)	36	53	13	7.8	2.7	17.4
2	1.20E+05 (	3)	9.24E+05 (	23)	30	20	8	12.4	2.3	39.3
3	1.93E+05 (	4)	2.65E+06 (	55)	25	58	16	6.9	1.7	18.0
4	6.02E+04 (	1)	6.63E+05 (	11)	20	15	9	9.4	0.2	56.9
5	1.81E+05 (	3)	6.39E+06 (	106)	20	141	28	2.7	0.5	7.8
6	7.53E+04 (	3)	9.79E+05 (	39)	48	22	7	7.4	1.4	22.1
7	1.61E+05 (	2)	2.41E+06 (	30)	15	53	19	6.5	0.7	24.0
8	1.45E+05 (	6)	2.12E+06 (	88)	50	47	10	6.4	2.2	14.1
9	6.02E+04 (	1)	4.82E+05 (	8)	20	11	7	12.8	0.3	84.6
10	2.01E+05 (	4)	1.20E+06 (	24)	24	27	11	15.7	3.8	44.2
11	1.45E+05 (	3)	1.98E+06 (	41)	25	44	14	7.0	1.3	20.9
12	2.89E+05 (	12)	3.61E+06 (	150)	50	80	13	7.4	3.7	13.1
13	5.74E+04 (	1)	2.35E+06 (	41)	21	52	16	2.5	0.1	13.1
14	2.01E+05 (	5)	1.85E+06 (	46)	30	41	12	10.2	3.1	24.9
15	6.88E+04 (	2)	1.34E+06 (	39)	35	30	9	5.0	0.5	18.1
16	1.07E+06 (	8)	2.68E+05 (	2)	9	6	7	336.8	72.5	2816.4
17	2.01E+05 (	2)	6.02E+05 (	6)	12	13	10	31.9	3.0	168.1
18	3.51E+05 (	7)	5.07E+06 (	101)	24	112	22	6.5	2.5	13.5
19	0.00E+00 (	0)	2.01E+05 (	4)	24	4	4	17.3	0.6	136.9
20	0.00E+00 (	0)	6.02E+05 (	8)	16	13	9	8.3	0.3	53.3
21	0.00E+00 (	0)	6.63E+05 (	11)	20	15	9	5.9	0.2	36.3
22	0.00E+00 (	0)	5.02E+05 (	5)	12	11	9	13.6	0.5	98.9
23	0.00E+00	(0)	1.81E+05	(6)	40	4	3	11.2	0.4	

77.1

0510-01 (Laonung)

EFFECTIVE TRACK DENSITY FOR FLUENCE MONITOR (tracks/cm^2): 6.83E+05
RELATIVE ERROR (%): 1.25
EFFECTIVE URANIUM CONTENT OF MONITOR (ppm):15.00
ZETA FACTOR AND STANDARD ERROR (yr cm^2): 268.37 7.61
SIZE OF COUNTER SQUARE (cm^2): 8.30E-07

Grain no.	ρ_s (tracks . cm^{-2}	Ns (tracks)	ρ_i (tracks . cm^{-2})	Ni (tracks)	Squares	Uranium (ppm) +/- 2 std. dev.		Age (Ma)	95% CI	
1	7.09E+04 (	1)	2.13E+05 (	3)	17	5	5	33.2	0.6	369.7
2	0.00E+00 (	0)	3.21E+05 (	4)	15	7	7	17.3	0.6	137.4
3	0.00E+00 (	0)	3.44E+05 (	4)	14	8	7	17.3	0.6	137.4
4	7.53E+04 (	1)	1.05E+06 (	14)	16	23	12	7.4	0.2	42.9
5	1.20E+05 (	1)	4.82E+05 (	4)	10	11	10	25.2	0.5	227.5
6	6.02E+04 (	1)	1.57E+06 (	26)	20	34	13	4.0	0.1	21.4
7	0.00E+00 (	0)	6.02E+05 (	8)	16	13	9	8.3	0.3	53.5

PI56 (Laonung)

EFFECTIVE TRACK DENSITY FOR FLUENCE MONITOR (tracks/cm^2): 7.10E+05
RELATIVE ERROR (%): 1.30
EFFECTIVE URANIUM CONTENT OF MONITOR (ppm):15.00
ZETA FACTOR AND STANDARD ERROR (yr cm^2): 268.37 7.61
SIZE OF COUNTER SQUARE (cm^2): 8.30E-07

Grain no.	ρ_s (tracks . cm^{-2}	Ns (tracks)	ρ_i (tracks . cm^{-2})	Ni (tracks)	Squares	Uranium (ppm) +/- 2 std. dev.		Age (Ma)	95% CI	
1	1.00E+05 (	1)	5.02E+05 (	5)	12	11	9	21.1	0.4	168.2
2	6.02E+04 (	1)	3.61E+05 (	6)	20	8	6	17.7	0.3	129.7
3	5.74E+04 (	1)	1.95E+06 (	34)	21	41	14	3.2	0.1	16.7
4	1.34E+05 (	1)	6.69E+05 (	5)	9	14	12	21.1	0.4	168.2
5	5.02E+05 (	5)	2.51E+06 (	25)	12	53	21	19.5	5.7	50.5
6	5.02E+05 (	5)	5.42E+06 (	54)	12	114	31	9.1	2.8	21.9
7	4.82E+04 (	1)	1.20E+06 (	25)	25	25	10	4.3	0.1	23.3
8	5.02E+04 (	1)	1.26E+06 (	25)	24	26	11	4.3	0.1	23.3
9	7.53E+04 (	1)	5.27E+05 (	7)	16	11	8	15.2	0.3	105.2
10	4.02E+04 (	1)	1.61E+05 (	4)	30	3	3	26.2	0.5	236.5
11	6.69E+04 (	1)	6.02E+05 (	9)	18	13	8	11.9	0.2	76.0
12	4.02E+04 (	1)	8.03E+04 (	2)	30	2	2	50.5	0.8	856.3
13	0.00E+00 (	0)	1.71E+06 (	17)	12	36	17	4.0	0.1	23.1
14	0.00E+00 (	0)	8.03E+04 (	1)	15	2	3	94.6	2.4	2935.6
15	0.00E+00 (	0)	2.68E+05 (	4)	18	6	5	18.0	0.6	142.9
16	0.00E+00 (	0)	2.28E+06 (	17)	9	48	23	4.0	0.1	23.1
17	0.00E+00 (	0)	4.02E+05 (	4)	12	8	8	18.0	0.6	142.9
18	0.00E+00 (	0)	1.00E+06 (	10)	12	21	13	6.8	0.2	42.4
19	0.00E+00 (	0)	2.41E+05 (	4)	20	5	5	18.0	0.6	142.9
20	0.00E+00 (	0)	1.93E+06 (	24)	15	41	16	2.8	0.1	15.8

0810-01 (Laonung)

EFFECTIVE TRACK DENSITY FOR FLUENCE MONITOR (tracks/cm^2): 6.94E+05

RELATIVE ERROR (%): 1.04

EFFECTIVE URANIUM CONTENT OF MONITOR (ppm):15.00

ZETA FACTOR AND STANDARD ERROR (yr cm^2): 268.37 7.61

SIZE OF COUNTER SQUARE (cm^2): 8.30E-07

Grain no.	ρ_s (tracks . cm^{-2}	Ns (tracks)	ρ_i (tracks . cm^{-2})	Ni (tracks)	Squares	Uranium (ppm) +/- 2 std. dev.		Age (Ma)	95% CI	
1	1.15E+05 (	2)	2.29E+05 (	4)	21	5	5	48.1	4.2	317.2
2	5.02E+04 (	1)	1.91E+06 (	38)	24	41	13	2.8	0.1	14.5
3	1.03E+05 (	3)	4.23E+06 (	123)	35	91	17	2.4	0.5	6.8
4	0.00E+00 (	0)	9.47E+05 (	33)	42	20	7	2.0	0.1	11.0
5	0.00E+00 (	0)	9.64E+04 (	2)	25	2	3	38.5	1.2	478.1
6	0.00E+00 (	0)	6.88E+04 (	2)	35	1	2	38.5	1.2	478.1
7	0.00E+00 (	0)	1.36E+06 (	27)	24	29	11	2.4	0.1	13.6
8	0.00E+00 (	0)	1.45E+06 (	42)	35	31	10	1.6	0.1	8.6
9	0.00E+00 (	0)	8.03E+05 (	8)	12	17	12	8.4	0.3	54.4
10	0.00E+00 (	0)	5.24E+04 (	1)	23	1	2	92.5	2.4	2882.3
11	0.00E+00 (	0)	1.81E+06 (	36)	24	39	13	1.8	0.1	10.0
12	0.00E+00 (	0)	1.20E+05 (	2)	20	3	3	38.5	1.2	478.1
13	0.00E+00 (	0)	5.30E+05 (	11)	25	11	7	6.1	0.2	37.0
14	0.00E+00 (	0)	1.10E+06 (	22)	24	24	10	3.0	0.1	17.0
15	0.00E+00 (	0)	5.52E+05 (	11)	24	12	7	6.1	0.2	37.0

0810-03 (Laonung)

NOTE: no age could be extracted from this sample due to the fact that no spontaneous tracks could be counted, which is equivalent to an effective age equal to zero. Below are the original track count and the counting parameters.

EFFECTIVE TRACK DENSITY FOR FLUENCE MONITOR (tracks/cm^2): 6.966E+05

RELATIVE ERROR (%): 1.04

EFFECTIVE URANIUM CONTENT OF MONITOR (ppm): 15.00

ZETA FACTOR AND STANDARD ERROR (yr cm^2): 268.37 7.61

SIZE OF COUNTER SQUARE (cm^2): 8.30E

Spontaneous tracks	Induced track	Squares
0	1	42
0	1	35

0	2	56
0	9	38
0	1	42
0	1	57
0	1	60
0	2	36
0	4	50
0	1	50
0	5	29
0	9	25
0	2	28
0	2	40
0	51	60
0	1	35
0	1	32